Distribution Category:
Materials (UC-25)

ANL-82-80

ANL--82-80

DE83 008718

ARGONNE NATIONAL LABORATORY
9700 South Cass Avenue
Argonne, Illinois 60439

ICANS-VI

Proceedings of the Sixth Meeting of the INTERNATIONAL COLLABORATION ON ADVANCED NEUTRON SOURCES

Argonne National Laboratory
June 28 - July 2, 1982

January 1983

Contract W-31-109-Eng-38

LEGIBILITY NOTICE

A major purpose of the Technical Information Center is to provide the broadest dissemination possible of information contained in DOE's Research and Development Reports to business, industry, the academic community, and federal, state and local governments.

Although a small portion of this report is not reproducible, it is being made available to expedite the availability of information on the research discussed herein.

Preface

Representatives of the Laboratories of the International Collaboration on Advanced Neutron Sources gathered between 28 June and 2 July, 1982 at Argonne National Laboratory for their sixth meeting, ICANS-VI. The meeting was the first opportunity for participants to see Argonne's Intense Pulsed Neutron Source, which went into full operation in August, 1981, and in an important sense celebrated the coming-on-line of this most recent entry into the world's complement of the new generation of neutron sources.

The main topics of the meeting were "Targets and Moderators" and "Neutron Scattering Instrumentation", following what has become the customary rotation of subjects. An additional topic, "Nuclear Data and Codes" emerged this time as a separate entity, closely related to the Targets and Moderators subjects.

As usual, we devoted the first sessions to Status Reports from the different projects. In addition, Günter Bauer provided an informal report on progress on new neutron sources in the Soviet Union, based on his attendance of the Dubna meeting in June.

On the second and third days, participants presented prepared papers in two separate sessions devoted to the two main topics of the meeting. We made a deliberate effort to provide as much time as possible for open discussions in a "workshop" style. This attempt was a response to a call raised at the end of each of the recent meetings, to provide more such opportunity. It seemed that we happily succeeded in this, but at a cost which we recognized, of making very tight schedules for formal presentations.

These Proceedings are organized roughly in the order and organization of presentations. In addition, we include a record of some of the discussions following each Status Report, and separate summaries of discussions on various subjects of the topical sessions. We have reproduced the manuscripts essentially as received. The Editor expresses his deep gratitude to all participants for their contributions, for the help of those who agreed to chair the sessions, and for the efforts of those who prepared discussion summaries. All contributed to the success of the meeting.

We all express our thanks to Ms. Miriam Holden and her staff of Argonne's Conference Planning and Management group, for so smoothly attending to organizational details and participants travel and communication needs. It is all too easy to take this for granted, but we do not. Their excellent efforts and broad experience were fundamental to the success of the meeting. As conference organizer, I cannot express sufficient thanks to Dr. Gerard Lander, Director, IPNS Program, for his essential help and encouragement throughout.

In broad summary, we can say that the activities and results reported, and the productive discussions that took place, show that the spallation neutron sources are developing in a healthy way, and that the objectives of the ICANS are served well by our meetings.

Argonne, Illinois
November, 1982

J. M. Carpenter

Contents

ICANS-VI

INTERNATIONAL COLLABORATION ON ADVANCED NEUTRON SOURCES

June 27 - July 2, 1982

PROGRESS ON THE CONSTRUCTION OF THE SPALLATION NEUTRON SOURCE AT THE RUTHERFORD APPLETON LABORATORY

David A Gray

Rutherford Appleton Laboratory

ABSTRACT

This paper gives details of progress on the Spallation Neutron Source which is due to produce first neutrons in 1984. It updates similar reports given at ICANS-IV and ICANS-V.

PROGRESS ON THE CONSTRUCTION OF THE SPALLATION NEUTRON SOURCE AT THE RUTHERFORD APPLETON LABORATORY

David A Gray
Rutherford Appleton Laboratory

1. INTRODUCTION

This report is an update of reports given by G Manning at ICANS-IV and by myself at ICANS-V. A recapitulation of the main parameters of the SNS is given in Table 1 and the layout of the facility in Figure 1. A full description of the project is given in Reference 1.

2. FINANCE

The financial approvals for capital are in the process of being updated to £15.04M for the machine and target station and £2.31M for the 7 (out of 15) approved instruments. The update is purely for inflation. This does not include costs for staff nor for design, research and development costs. The allocation to cover all costs for the SNS in the current financial year is £8.53M with similar figures foreseen in Forward Look projections. The money is consistent with providing first neutrons in mid-1984 with 5 instruments available at that time.

Approximately £9M worth of equipment has been ordered for the machine and target station and £0.3M for the instruments.

3. PROGRESS

3.1 Injection

The ion source (Figure 2) and pre-injector were successfully run to produce H^- beam at 665 keV during February. During several runs since then improvements have been made to power supplies for the ion source and to reduce damage to electronic components caused when there is a spark-over in the accelerating column. Computer control of the ion source is now being implemented.

TABLE 1: MAIN PARAMETERS OF THE SNS

Proton design energy		800 MeV
Proton design intensity		200 μA
Nominal repetition frequency		50 Hz
Injection scheme		H^- charge exchange
Injection interval		376 μs
Injection energy (protons)		70.44 MeV
Injected protons/pulse		5×10^{13}
Emittance H^- ions		$25\pi \times 10^{-6}$ rad m
Mean radius of synchrotron		26.0 m
Number of superperiods		10
Dipole field at 70.44 MeV		0.1764 T
Dipole field at 800 MeV		0.6970 T
Betatron tune (Q_h, Q_v)		4.31, 3.83
Beam emittance at 70.44 MeV	H	$540\pi \times 10^{-6}$ rad m
	V	$430\pi \times 10^{-6}$ rad m
Number of RF cavities		6
Frequency swing (harmonic No. = 2)		1.34 to 3.09 MHz
Vacuum chamber in magnet		Ceramic
Target material		Depleted Uranium
Fast neutron production rate		3×10^{16} n per sec
Neutron current from surface of moderator		$10^{15} - 10^{13}$ s^{-1} $ster^{-1}$ eV^{-1} (.01 eV - 1 eV)

During March 10 MeV beam was accelerated through the first of the 4 linac tanks. Further linac beam will not be run until the whole linac is ready for 70 MeV tests which is programmed for October.

The linac has been aligned and the tanks flattened to produce the required RF field law.

The October 70 MeV beam date is determined by the build and test and the modulators for the RF valves driving the tanks. This work is going to programme.

The 70 MeV beam transport line between the linac and the synchrotron is being installed.

The injection septum magnet which steers the H^- ions on to the stripping foil has been delivered. Its power supply has been installed and it is about to be powered. Components have been delivered for the 4 beam bump magnets which change during injection the circulating proton closed orbit to make it pass through the stripping foil. The first has been assembled. The beam bump magnet power supply will be delivered shortly.

Development work on stripping foils is continuing with good results. Circular foils, 50mm in diameter, of the required thickness, 0.25μ, with a conducting coating of alumina and supported all round are routinely made. These foils have been tested with 70 MeV proton beam at SIN, Zurich, and initial indications are that they last for the equivalent of 10 hours of full SNS intensity as expected. Work is now proceeding on improving techniques for making the required 120 x 30 mm foils with one unsupported edge of which some have already been made.

A rectangular foil supported all round is shown in Figure 3.

3.2 Synchrotron ring magnets

There has been a delay in the delivery of the 10 dipole magnets. The prototype was delivered 14 months late in January. The configuration was determined using computer calculations. The central field and field gradient was as computed within the measurement accuracy ($\Delta B/B \sim 10^{-4}$).

The end fields similarly tied up with calculations. Since the prototype was ordered further refinement of the beam dynamics has changed the required average gradient in the magnet. This will be accommodated by changing the end shapes of the dipoles which have now been determined. Losses in the core and coils have been as the predictions. The inductance is about 10% higher than calculated.

The 10 main quadrupole doublets have been assembled in modules with a trim quadrupole doublet and have been installed in the synchrotron room (Figure 4).

The 10 singlet quadrupole magnets have been delivered, as have the steering magnets for closed orbit correction.

The support frames for all the main magnets have been surveyed into position. In the case of the dipoles, see foreground of Figure 4, this was done using the dipole base with dummy targets.

3.3 Magnet power supplies

All components for the main magnet power supply have been delivered. Part of the capacitor bank has been used to power the dipole prototype.

All 30 of the programmable power supplies needed for the trim quadrupole and correction magnets have been delivered and are being positioned in the centre of the synchrotron room which has sufficient shielding to protect electronic components.

3.4 Main ring vacuum

The ceramic chambers for the quadrupole modules have been installed and the singlet chambers manufactured. The 10 5m long 36° chambers for the dipoles (Figure 5) have been manufactured. Shorter ceramic chambers for straight section modules containing steering magnets are being manufactured.

Components for the roughing line are available and the ion pump controls have been installed.

3.5 RF shields

The design of the RF shields which fit inside the ceramic chambers is complete. The inside dimensions of the doublet ceramic chambers have been measured. The supports for the wires in the shield are individually machined to put the shield accurately around the beam. The first doublet shield is being assembled. Components for the dipole shields are being manufactured.

3.6 Main ring RF system

The prototype RF cavity has been tested successfully to full voltage with the correct frequency swing and swing rate (Figure 6). Two production cavities have been installed in the synchrotron room.

The prototype amplifier chain which powers the cavity has been shown to provide sufficient power. There have been problems with parasitic oscillations at high frequency emanating from either inside the valve or associated with the mounting of the valve which are in the process of resolution. Preliminary work has been done on the parallel chain which compensates for the beam loading of the intense proton pulses. The production amplifiers are being built up.

The DC bias supplies have been installed and the 6 anode power supplies are nearly complete. A new bias regulator using larger transistors has been designed and the prototype is under construction. The low power RF system has been used in the cavity tests.

3.7 Diagnostics

Position monitors, profile monitors, intensity monitors and the Q-measuring system for the synchrotron are being manufactured. The high quality co-axial cables have been installed. Electronics are being manufactured and installed.

3.8 Extraction

The extraction team have been diverted during the year to help with the injector. The extraction work is now continuing and components are

being ordered.

3.9 Extracted proton beam

The new components required have been ordered. Stands for the EPB which has to go over and back across the synchrotron will be of concrete and have been designed.

3.10 Target station

A Carne will be dealing with this item in detail at this meeting. Highlights of progress have been the successful production of two uranium target plates encased in Zircaloy and the build-up of target station shielding to include the installation on one side of the 'inserts' which will allow individual collimators for each of the neutron lines. The shutter system has been designed and the lower shielding wedges which go radially between the shutters have been ordered.

The 3.2m diameter target void vessel which contains the target, moderator, reflector assembly and which has been designed to ASME 3 Class A standard, has been ordered. The target, moderator, reflector assembly has been specified following neutronic measurements at Los Alamos.

Development work continues on the remote handling system.

3.11 Controls

One of the 3 satellite computers is being used progressively to control components of the injector (Figure 7). The second satellite, for the synchrotron, has been installed and is being used for development of the diagnostics and other systems. Development of system hardware continues and interface hardware modules are in various stages of manufacture.

3.12 Experimental facilities

Of the 7 approved instruments[2], the Liquids and Amorphous Materials Diffractometer (LAD) has been installed on the Harwell linac and commissioned successfully. The components for the High Throughput Inelastic Spectrometer (HTIS) have been delivered. Installation on the Harwell

linac is expected this month. The type of system for the HUB computer has been chosen and the approval procedure is underway to buy the initial components for this system so that software development can be done.

4. OTHER USES OF THE SNS

Other uses of the SNS are being considered. These include facilities for research using the μSR technique, neutrinos, fast neutrons for irradiation studies, pions for radiobiology and charged particles for setting up detectors for particle physics research. These facilities are described in more detail in Alan Carne's paper at this meeting.

References

1. Spallation Neutron Source: Description of Accelerator and Target. B Boardman (Ed). RL-82-006, March 1982.

2. ICANS-V. Proc. of 5th meeting, Jülich 22-26 June 81, p.63. Jül-Conf-45, Oct 81.

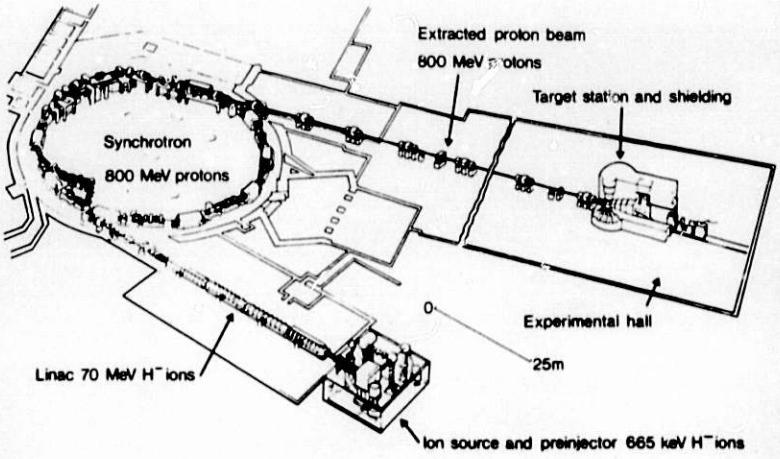

Fig. 1. Layout of the SNS

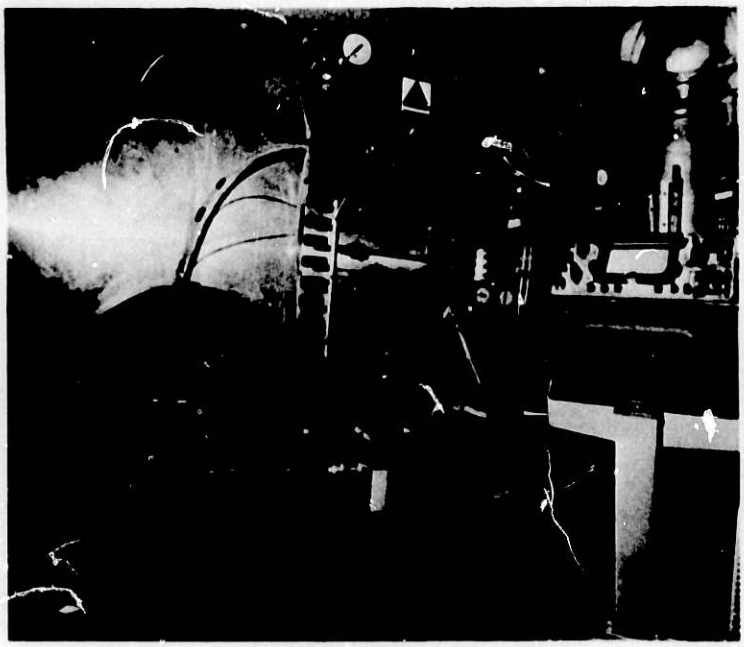

Fig. 2. H^- ion source on EHT platform

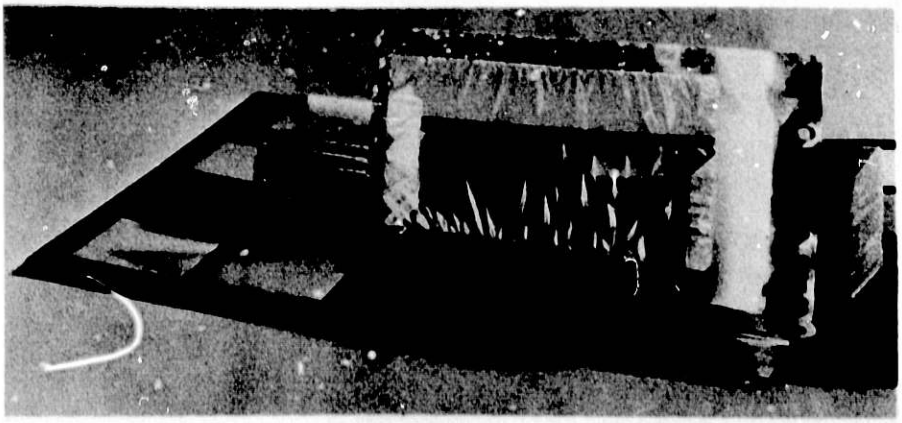

Fig. 3. Experimental stripping foil

Fig. 4. The SNS synchrotron room

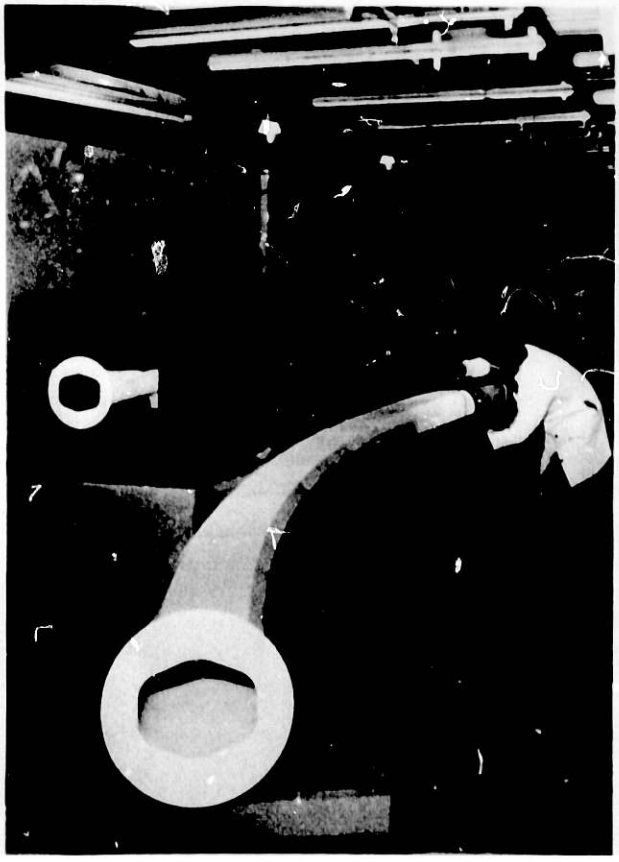

Fig. 5

5m long dipole ceramic vacuum chamber

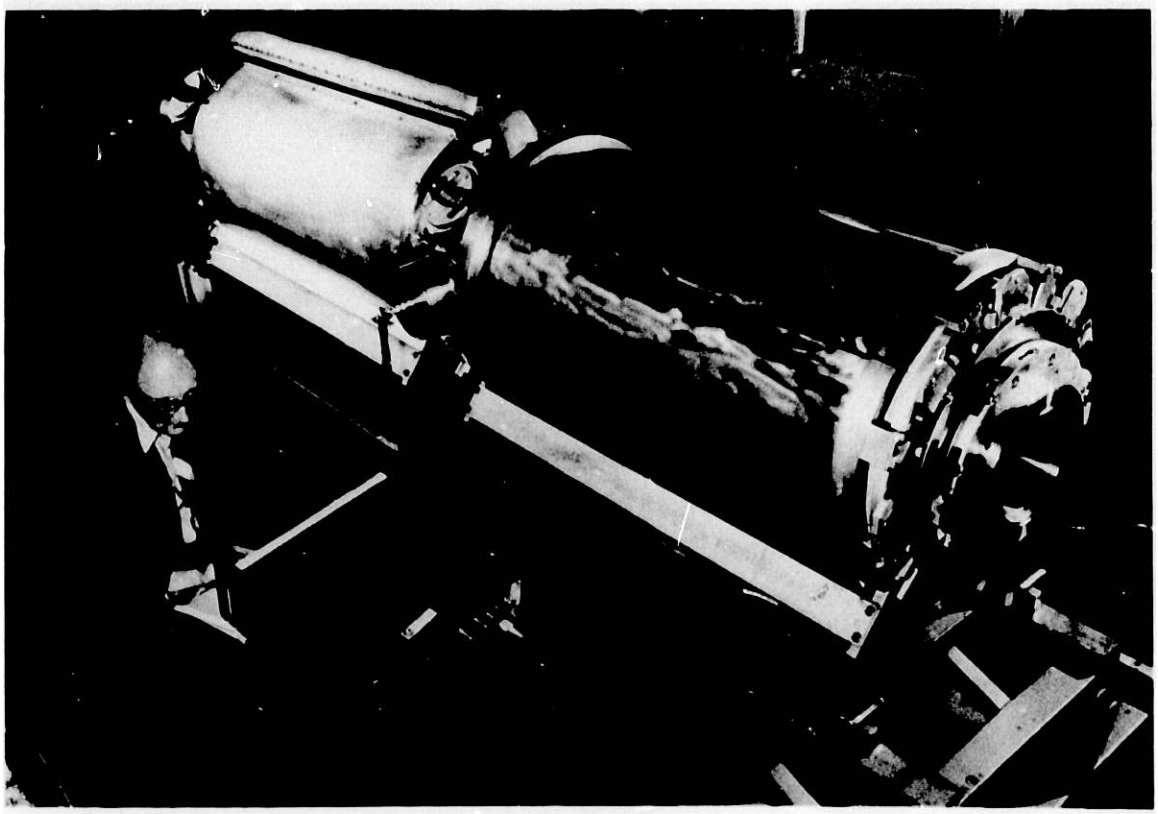

Fig. 6. One of the 6 RF cavities

Fig. 7. Injector Control Centre

SNS - D. A. Gray

J. Meese	Q	What is the maximum Q shift achievable with the trim quads?
D. A. Gray	A	0.25
R. Kustom		Comment - I'm concerned about the durability of the ceramic vacuum vessel under proton bombardment. What tests had been done on the material?
D. A. Gray	A	Tests had been done using the Harwell cyclotron at beam intensities corresponding to the maximum loss expected in SNS.
R. Kustom	Q	Can you change the vacuum vessels and how long would it take?
D. A. Gray	A	Yes we can change them but the time to do so cannot yet be assessed.
A. D. Taylor	Q	Can you extract a single beam bunch rather than 2, to get shorter neutron pulses?
D. A. Gray	A	We could kick out one pulse in principle and send it to a second target station or a beam dump, but we cannot trap and accelerate a single bunch to 800 MeV with the present RF system.
J. M. Carpenter	Q	What is the present position on glueing the dipole magnet laminations together?
D. A. Gray	A	The problem has now been solved by the manufacturers.
R. Moon	Q	What are the first 5 instruments?
H. Wroe	A	A liquids and amorphous materials diffractometer (LAD now operating initially on the Harwell linac); a high throughput, inelastic spectrometer using the Be filter techniques (HTIS) is being assembled ready for initial operation on the linac; parts are being ordered a high resolution powder diffractometer (HRPD) on a 100 m guide tube; designs

are being finalized on a high energy transfer spectrometer (HET) using a fast chopper to monochromate the incident beam and finally the incident flight path for a quasielastic instrument will be built to serve a beryllium-beryllium window spectrometer to be supplied by the Bhaba Institute in Bombay. A polarized neutron spectrometer using filters is also being built as a development project, initially for use on the Harwell linac.

J. Meese Q What run time do you expect?

H. Wroe A Probably the best feel for that is given by some figures Colin Windsor has produced comparing estimated run times on the SNS with actual times on the linac for the same measurement. The SNS times are a few minutes in some cases. In practice you would do harder experiments say with small samples or at high resolution.

ICANS-VI

INTERNATIONAL COLLABORATION ON ADVANCED NEUTRON SOURCES

June 27 - July 2, 1982

STATUS AND NEUTRON SCATTERING EXPERIMENTS AT KENS

Noboru Watanabe and Hiroshi Sasaki

National Laboratory for High Energy Physics
Oho-machi, Tsukuba-gun, Ibaraki, 305, Japan

Yoshikazu Ishikawa and Yasuo Endoh

Physics Department, Tohoku University
Sendai, 982, Japan

Kazuhiko Inoue

Department of Nuclear Engineering, Hokkaido University
Sapporo, 060, Japan

ABSTRACT

This paper reports present status of the KENS facility, progress in neutron scattering experiments and instrumental developments, and status of the KENS-I' program. A design study of a high intensity rapid-cycle 800 MeV proton synchrotron for proposed new pulsed neutron (KENS-II) and meson source is also described.

STATUS AND NEUTRON SCATTERING EXPERIMENTS AT KENS

Noboru Watanabe and Hiroshi Sasaki
National Laboratory for High Energy Physics
Oho-machi, Tsukuba-gun, Ibaraki, 305, Japan

Yoshikazu Ishikawa and Yasuo Endoh
Physics Department, Tohoku University
Sendai, 982, Japan

Kazuhiko Inoue
Department of Nuclear Engineering, Hokkaido University
Sapporo, 060, Japan

1. PRESENT STATUS OF KENS

In FY 1981 (April 1, 1981 - March 31, 1982), the booster synchrotron at KEK has been operated for 3280 hours, 88 per cent of which has been delivered to the Booster Synchrotron Utilization Facility (BSF). The spallation neutron source KENS has been operated successfully throughout this period. Total operation time for KENS was about 1450 hours, because we shared the machine time with Booster Meson Facility (Boom) of Meson Science Laboratory, University of Tokyo.

Many research programs were proposed for FY 1982. Number of proposals are listed in Table 1. Among the existing spectrometers, the small angle scattering spectrometer SAN is the busiest. In order to relieve machine time congestion, the construction of a new small angle scattering machine has been proposed, which will be authorized in the next fiscal year. The machine will be equipped with a 2-dimensional PSD made of Li-6 glass scintillators, and installed at a beam hole viewing the room temperature moderator. Shortage in neutron machine time becomes more serious this year, because the BSF has started to deliver proton beams to the new facility, Particle Radiation Medical Science Center, University of Tsukuba, which is located in the next door of KENS. Furthermore, the proton accelerators at KEK will be shut down for about one year probably in 1984, due to the TRISTAN tunnel construction under the existing accelerators.

Table 1 Number of Proposals

Type	Definition	Total machine time (%)	No. of proposals accepted/No. of proposals	
			FY 1981	FY 1982
A1	Big project for the construction of a new spectrometer with instrumental development	100	2/2	3/3*
A2	Program for instrumental development	100	4/4	4/4**
B1	Big research program using a existing spectrometer by the instrument group responsible for the spectrometer	70	5/5	5/5**
B2	Small research program using existing spectrometers	30	9/20	13/19

* Two proposals are the continuation from the FY 1981.
** All proposals are the continuation from the FY 1981.

The tungsten target was renewed at the end of this period, because the outer-surface of the target container and the coolant pipe suffered from serious erosion, even though the material was SUS-316. This is probably due to the high concentration NO_x gas formation in the final section ($\sim$ 2 m long) of the proton beam line where air is confined instead of helium gas. Change to helium atmosphere is necessary.

There has been a considerable improvement in the remote handling devices for the active target-moderator-reflector assembly. A robot arm crane was constructed which enables the precise mounting or the demounting of the assembly or the cold neutron moderator system on (from) the target station with full remote mode. An iron cell has been built which is necessary for the maintenance of the assembly, and also for the reconstruction of the KENS-I' advanced system. A photograph of the robot arm crane is shown in Fig. 1.

2. NEUTRON SCATTERING EXPERIMENT WITH EXISTING SPECTROMETERS

Neutron scattering experiments with the existing five spectrometers HIT, LAM, MAX, SAN and TOP were very active during the last fiscal year. Many results have already been obtained. We will briefly summarize some

of these research activities. (All of the experimental results which have been achieved last year are being published as KENS Report-III, KEK Internal (1982).)

1. High Intensity Total Scattering Spectrometer (HIT)

More than hundred samples have been measured with HIT last year. Short-range structures of metal-metal alloy glasses such as Ni-Ti and Cu-Ti, and those of archetypical metal-metalloid alloy glass of Ni-B have been determined, and it was concluded that (i) the atomic arrangement of alloy glasses preserves the chemical short-range order analogous to that found in the corresponding crystalline compounds, (ii) glass formation composition ranges are likely to be dominated by the nature of the chemical short-range order inherent in these alloy glasses. As an example of measured data, S(Q)'s and g(r)'s of Ni-B alloy glasses are shown in Fig. 2. Atomic sites of deuteriums in deuterided metallic glasses such as $Pd_{0.35}Zr_{0.65}D_x$; structure changes of Pd-17at%Si alloy glass by cold rolling; and structures of silicate glasses, binary amorphous alloys and amorphous As-chalcogenids were also studied. Nuclear and magnetic structure of Fe-B alloy glasses has been measured. Instrumental improvement is also in progress; annulus detectors of Li-6 glass scintillator at small angles are under construction.

2.2 Large Analyzer Mirror Spectrometer (LAM)

Several improvements were made on the LAM since last ICANS. One of them, the increase of the number of analyzers from four to eight (see Fig. 3), provided more information about the Q dependence of the quasielastic spectral profile, and the evacuated housing of the whole spectrometer improved drastically the S/N ratio. Fig. 4-a gives some raw data of the quasielastic spectrum of chloroprene. We can definitely distinguish the quasielastic and the elastic parts in the spectrum. Fig. 4-b shows the measured elastic incoherent structure factor (EISF) where the solid line is a theoretical curve of EISF in a model describing

migration of kinks in the rubber polymer. Many other low energy fluctuational motions involved in molecular and spin systems were studied. In the case of the former, diffusion in liquids such as water, methanol aqueous solutions, cycrohexane, benzene, etc; rotational diffusion in plastic crystals; micro-Brawnian motion of polymer chains; and diffusion of hydrogen in TiH_x were studied. Similar studies concerning poly- and oligo-ethers, α-lactalbumin solution and polyelectrolyte solutions were also done. Concerning spin systems, experiments were performed to measure the temperature and magnetic field dependence of crystal field splitting in CeBi.

2.3 Multi-Analyzer Crystal Spectrometer (MAX)

One of the progress MAX made last year was the success of the intensity mapping of the magnetic excitations over the whole Brillouin zone. An example is shown in Fig. 5 where the magnetic excitations in a $\gamma Fe_{0.7}Mn_{0.3}$ alloy at various temperatures up to $1.5T_N$ are displayed as the contour maps of the scattering intensity. The data show clearly that the low energy excitations are renormalized near T_C, while the higher energy excitations remain almost unchanged even above T_N.

2.4 Small Angle Scattering Spectrometer (SAN)

The SAN, small angle scattering machine has also been improved further this year. The large external memory bank of 2 M bite was attatched to it in order to make the measurement of the time dependent phenomena possible. The measurements under various circumstances as at different temperatures ($10 \leq T \leq 1{,}000$ K) or in a magnetic field ($H \leq 5$ kG) become also possible. The subjects studied by this spectrometer included the magnetic systems, phase separation in alloys as well as polymer and biological problems. A complete study of the magnetic correlation was carried out on a single crystal of $0.88FeTiO_3$-$0.12Fe_2O_3$ at different temperatures ($10 \leq T \leq 300$ K) in various magnetic fields. Two dimensional displays of the scattering profiles at low temperatures

are shown in Fig. 6. A significant change of the profiles occurs between 40 K and 45 K corresponding to the existence of the spin glass temperature at 38 K. The magnetic phase diagram of MnSi near T_N has also been established. The spinodal decomposition process of $Fe_{1-x}Cr_x$ alloys was studied for various compositions (x = 0.2, 0.3, 0.4 and 0.6) and the important contributions of thermal fluctuations and nonlinear effects are recognized. By the study of the semi-dilute polymer solutions around the compensation temperature, the binary cluster integral of polymer segments and the ternary cluster integral were separately obtained. The structure of nucleosome core from chicken erythrocytes were studied in a dilute solution with different Na^+ and an interesting ionic strength dependence of core sizes was found.

2.5 Time-of-Flight Spectrometer with Optical Polarizer (TOP)

After completion of the performance test of TOP it has been operated as the polarized neutron diffractometer with a polarization analyzer. Though polarization is not completely satisfied, the flipping efficiency and the reflectivity of the polarizer is 100 % and 90 % respectively, which is excellent.

Numbers of experiments have been carried out during a year, namely polarized neutron diffraction studies on the Fe-Pd, Fe-Sb and Fe-V artificial superlattice films. We could find unusual magnetic form factor due to the interfacial effects on the ferromagnetism of Fe layers. We also measured similar effects of the magnetic form factor of Ni ultra fine particles. Besides these studies, we have found novel feature of the dynamical depolarization of the transmitted neutrons through ferromagnetic alloys. We illustrate the typical examples in Fig. 7, where the depolarization is dependent of the velocity of neutrons when they pass through a quenched $Fe_{0.85}Cr_{0.15}$ alloy, whereas polarization is maintained completely in the case of the transmission through an anealed $Fe_{0.85}Cr_{0.15}$ alloy. It must be concluded that the comparable size of micro magnetic domains as the Larmor period are distributed in the quenched alloy which disappear by anealing.

3. NEW SPECTROMETERS AND INSTRUMENTAL DEVELOPMENTS

There have been a considerable progress in the instrumental development since last ICANS. Three spectrometers, FOX, CAT and DIX have been constructed and operated, and other two named PEN and RAT are now under construction. RAT and CAT are installed at the same beam hole H-7, and the combination is called RAC. CAT and DIX are the tentative machine for the instrumental development. A test machine for the PEN which is called Pre-PEN was constructed and operated. A prototype machine of RAT has also been constructed and the test experiments are in progress.

3.1 Four-circle Single Crystal Diffractometer (FOX)

FOX is a TOF type single crystal diffractometer, equipped with a large χ-circle (50 cm in diam.) and a conventional He-3 counter. The instrument has been installed at the H-1 beam hole. Single crystals of Si, $BaTiO_3$, V and pyrographite have been measured for the performance test with satisfactory results; the distinct Bragg reflections were observed for V, and higher order reflections were detected up to 0 0 26 for pyrographite. One dimensional Li-6 glass scintillation detector system will be ready at the end of this fiscal year.

3.2 Polarized Epithermal Neutron Spectrometer (PEN)

The Pre-PEN is a test machine of the PEN which was installed at the H-8 beam hole to produce a white polarized beam of epithermal neutrons by means of a dynamically polarized proton filter. Extensive tests have been carried out to improve the neutron polarization and to identify it. Neutron polarization of about 0.65 at 0.1 eV, 0.45 beyond 1 eV have already been attained with the proton polarization of 43 %. Details are given in a separate paper for this meeting[1]. PEN is under construction which will be completed at the end of FY 1982.

3.3 Cystal Analyzer TOF Spectrometer (CAT)

CAT is a inverted geometry type machine designed to measure the incoherent high energy excitation in the range 50 - 1,000 meV, with good resolution ($\Delta\hbar\omega/\hbar\omega$ = 0.02 $\sim$ 0.03), and with good efficiency. Since the two-dimensional focussing geometry is adopted in the scattered neutron path, larger planar sample can be used without sacrificing the resolution. In order to test the instrumental performance, local modes of hydrogens in the various metallic hydrides have been measured. It was found that the spectrometer can provide spectrum with extremely low background and with excellent resolution. For instance, in case of TiH_2, higher harmonics have been detected up to 5th order with respective fine structures. Details are given in a separate paper for this meeting[2].

3.4 Resonance Detector Analyzer TOF Spectrometer (RAT)

RAT is a resonance detector spectrometer. The instrument of this type will make possible spectroscopy with scattered neutron energies in the range 1 - 10 eV, with resolution in the neighborhood of 50 meV. The system uses a resonantly-absorbing material, which captures scattered neutrons of fixed energy; a scintillation counter registeres the resulting gamma ray cascade. Time of flight disperses the energy spectrum as a function of incident neutron energy. We have constructed and operated a prototype machine to understand the principle of the instrument and to develop it, in collaboration with J. M. Carpenter from Argonne National Lab.

By extensive tests to identify sources of background and find corrective measures, we arrived at some general understandings which guided our development, and some spesific principles.

We have tested various scintillators for the gamma ray detection, and found bismuth germanate (BGO) scintillator is the best for this application. We have examined a fast and a slow electronics to handle the detector signal and found that the fast system workes well. We have

tested and used three resonance absorbers, Ta-181, Sb-121 and Sm-149 both at room temperature and at reduced temperature. Figure 8(a) shows the time distribution of the measured detecting probability for a 12 μm thick Ta foil with a calculated curve.

We have measured and understood the inelastic scattering at large wave-vector change ($Q > 60\ A^{-1}$) from graphite, vanadium, lead and bismuth; we have measured and understood the scattering at smaller wave-vector change ($Q = 10\ A^{-1}$) from graphite and hydrogen gas. Figure 8(b) shows typical TOF spectra measured for bismuth at room temperature with Ta detector.

The resolution accomplished so far is only modest, around 100 meV, limited by the fact that absorbers have been subject to room-temperature Doppler broadening, as well as by the lack of a uranium-238 absorber (which has the narrowest resonance we are aware of). Counting rates have enabled measurements to be completed in about 1/2 day. Details of the measurements and the analysis will be given in separate article[3].

The construction of the RAT will be completed within FY 1983.

3.5 DIX

Another crystal spectrometer called DIX has been constructed and installed at the H-6 beam hole which views the polyethylene moderator at room temperature. The instrument has a large analyzer mirror which is similar to that of the LAM, but designed to measure the incoherent scattering in the range $\hbar\omega = 5 \sim 50$ meV with the resolution of about 0.5 meV. Test experiments are in progress.

3.6 UCN

The project for the ultra cold neutron production by means of excitations of HeII (UCN) is also in progress. A thin window (90 μm Al)

He-3 counter was developed for detecting ultra cold neutrons. The He-3 cryostat producing UCN is being tested. First cooling will be started in the fall of 1982.

3.7 PSD

The position sensitive detectors (PSD) employing the Li-6 glass scintillator is also under development. The PSD (3 x 28 arrays) based on a fibre optic encoding method was constructed, and the performance was tested by using the Bragg reflections from a single crystal of KBr.

4. STATUS OF KENS-I' PROGRAM

KENS-I' program has been proposed[4] which aimed to increase the neutron beam intensity about one order of magnitude by the improvements of the present accelerators and the target-moderator system.

A charge exchange injection system with H^- ion to increase the proton beam current is now under construction and the operation test is scheduled in next autumn. Energy up of the present 20 MeV proton linac is also being discussed in the accelerator group at KEK, but no decision has been made yet.

A grooved surface solid methane moderator has been proposed at KENS in order to increase the cold neutron beam intensity. A prototype cryogenic moderator chamber with a grooved surface has been constructed and extensive test experiments are now in progress, using the pulsed cold neutron facility at Hokkaido linac.

In Fig. 9 is demonstrated a measured spectrum obtained from the grooved solid methane at 20 K, compared with that from a flat one. A gain factor of about two has already been recognized at the cold neutron region. The results proves that the grooved surface is also very useful for the cold moderator as for the thermal neutron moderator. A first

installation of a grooved solid methane moderator to the KENS target station will be completed at the end of this fiscal year. Details of the prototype experiment is given in a separate paper for this meeting[5].

The convension of the present tungsten target to a depleted uranium is one of the most important project in KENS-I' program. The rectangular target is necessary to keep the good coupling efficiency. We are hopping to realize this by the collaboration with Argonne National Lab. Some calculations and mock up tests are now in progress.

5. KENS-II PROGRAM

KENS-II program is a future project to construct a intense pulsed spallation neutron source at KEK. A tentative program has been presented at the meeting on future program of BSF last March. This was first formal presentation in KEK. Since the construction of a high intensity proton synchrotron is the most important part of the program, a design study has just started.

Design study of a proton synchrotron, which is the generator of the meson-intense and neutron-intense beam, Gemini, is in progress. This 800 MeV synchrotron is aimed to deliver an intense proton beam, e.g., 500 μA in time average. Such a beam intensity, for instance, will be achieved by accelerating 6×10^{13} protons per pulse with the repetition rate of 50 Hz. This machine also should play the role of the injector to the present KEK 12 GeV proton synchrotron on behalf of the 500 MeV booster synchrotron. The circumference of the machine, therefore, was determined to be a half of that in the 12 GeV synchrotron. The machine parameters are listed in Table 2. The accelerator will consist of an H^- ion source, preaccelerator including RFQ, 80 MeV Alvarez-type linac, and 800 MeV rapid-cycling synchrotron.

The requirements on the ion source are that 30 mA of H^- ion beam is injected into the synchrotron with the pulse width of at least 350 μsec to realize the beam intensity of 6×10^{13} protons per pulse. Since

the beam loading on the linac is relatively small, a conventional Alvarez-type linac would be constructed. To simplify the RF power system, 400 MHz klystrons of 2 MW will be used, which drive five tank structures.

The rapid-cycling 800 MeV synchrotron of 54 m in diameter consists of 24 FBDO cell-structures. In order to attain high space-charge limit, the horizontal and vertical tunes are chosen to be relatively high, i.e., 6.8 and 7.3 respectively. Figure 10 shows the layout of the accelerator ring and the cell structure.

The emittance of H^- beam used for the injection at 80 MeV is small compared to the desired 97 x 84 $(cm \cdot mrad)^2$ initial emittance for 6 x 10^{13} protons circulating in the synchrotron. To produce these emittances, the H^- beam must move both horizontally and vertically with respect to their orbits during injection. In the horizontal plane, especially, the beam emittance will be regulated by decaying the injection bump orbit, which is formed with a pair of bump magnets.

Beam extraction is basically the single-turn extraction, which makes possible the maximum use of the pulse structure of the beam in the neutron and muon physics. The emittance of the extracted beam is assumed to be twice of the expected one from the adiavatic damping of the initial emittance. For the extraction of such a beam with a total 2 % momentum spread, it is sufficient that each of two kicker magnets of 2.5 m in length deflects the beam by 15 mrad in cooperation with some bump magnets. The beam is extracted outwardly by angles of 110 and 380 mrad in two septum magnets, respectively. Since the bunch spacing at 800 MeV is about 160 nsec for the RF system with the harmonic number of 2, the rise time of the ferrite loaded kicker magnet has to be less than 150 nsec.

The accelerator ring is made of 24 bending magnets and 48 quadrupole magnets. The required semi-aperture of the good field region is 11.5 cm x 9.2 cm for the bending magnet and 13.5 cm x 11.0 cm for the quadrupole magnet. This defines the usable semi-size of the vacuum chamber. It is necessary to add 3 and 4 cm in horizontal aperture of the bending and

quadrupole magnet respectively, to allow the room for the injection and extraction of the beam. The synchrotron ring magnet is excited by 50 Hz, dc-biased sine-wave current. All of the bending and quadrupole magnets are devided into eight or twelve groups. These are connected in series through resonant capacitors and forms a ring circuit. The dc bypass for the capacitors is provided by installing chokes in parallel to the capacitors and resonating the resultant tank circuits to 50 Hz. In order to reduce the RF accelerating voltage, the magnet system would be excited by a bi-resonant frequency system with the resonant frequencies of 33 and 100 Hz as proposed by M. Foss and W. Praeg at ANL. Even in this case, the max. voltage imposed on the exciting coil of the magnet will be kept within 10 kV to the earth. This is achieved by using hollow conductors of parallel current paths and by transposing those paths each other at the connection points between coil pancakes. This procedure will reduce eddy current loss as successfully applied at the KEK booster synchrotron magnet.

It should be guaranteed that a single bunched beam is always supplied to each of the neutron and meson experimental facility. This determines uniquely the harmonic number of RF acceleration system is 2. With the 80 MeV linac beam of 0.75 % full momentum spread, the emittance of such an injected beam is 0.84 eV•sec. If the RF bucket area has to be twice of this emittance, the required maximum RF voltage is 200 kV for the 50 Hz operation and 150 kV for the 33 Hz operation of the guide field magnet, respectively. Eight RF stations will provide with this accelerating voltage, each of which is installed in a 3 m long straight section. The reduction of RF bucket area due to space charge will require higher RF voltage. Therefore, the application of the bi-resonant frequency system to the excitation of the guide magnet is significant.

The design study of this machine is only on the start point. In addition to refining concept and hardware for each accelerator component, the problem remains to be solved on the radiation protection and handling. And also, some aspects of the designs may be changed in the process of the design work.

Table 2 Parameters of the proposed accelerator

Maximum kinetic energy	800 MeV
Maximum intensity	6×10^{13} p/p
Repetition rate	50 Hz (100/3 Hz & 100 Hz)
Average beam current	500 μA
Injection energy	80 MeV
Injection beam	30 mA H^-
Number of turns of injected beam	>240
Beam pulse width of injected beam	>350 μs
Magnet radius	7.00 m
Average radius	27.00 m
Number of period	24
Length of straight section	3.008 m
Structure	FBDO
Betatron frequency	
Horizontal	6.8
Vertical	7.3
Revolution frequency	0.687 - 1.489 MHz
Maximum beta-function	
Horizontal	12.4 m
Vertical	12.9 m
Momentum compaction factor	2.71×10^{-2}
Transistion energy/rest energy	6.07
Beam emittance	
800 MeV	0.26 x 0.23 $(\pi \text{ mm rad})^2$
80 MeV	0.97 x 0.84 $(\pi \text{ mm rad})^2$
Number of bending magnets	24
Length of bending magnets	1.833 m
Length of quadrupole magnets	
Focussing magnet	0.505 m
Defocussing magnet	0.547 m
Bending magnet field	
800 MeV	0.697 T
80 MeV	0.189 T
Quadrupole magnet peak field gradient	4.34 T/m
Peak energy gain per turn	94.9 keV (63.3 keV)
Harmonic number	2
RF frequency	1.374 - 2.978 MHz
Max. RF voltage	200 kV (150 kV)
RF bucket area	1.67 eV.sec
Number of RF stations	8
Incoherent space charge limit	7.7×10^{13} p

REFERENCES

1) M. Kohgi, et al., presented paper to this meeting (1982).

2) N. Watanabe, S. Ikeda and K. Kai, presented paper to this meeting (1982).

3) J. M. Carpenter, N. Watanabe, S. Ikeda, Y. Masuda and S. Sato, to be published.

4) N. Watanabe, H. Sasaki, Y. Ishikawa, Y. Endoh and K. Inoue, Proc. ICANS-V (Jülich, June 22 - 26, 1981) p. 21.

5) K. Inoue, et al., presented paper to this meeting (1982).

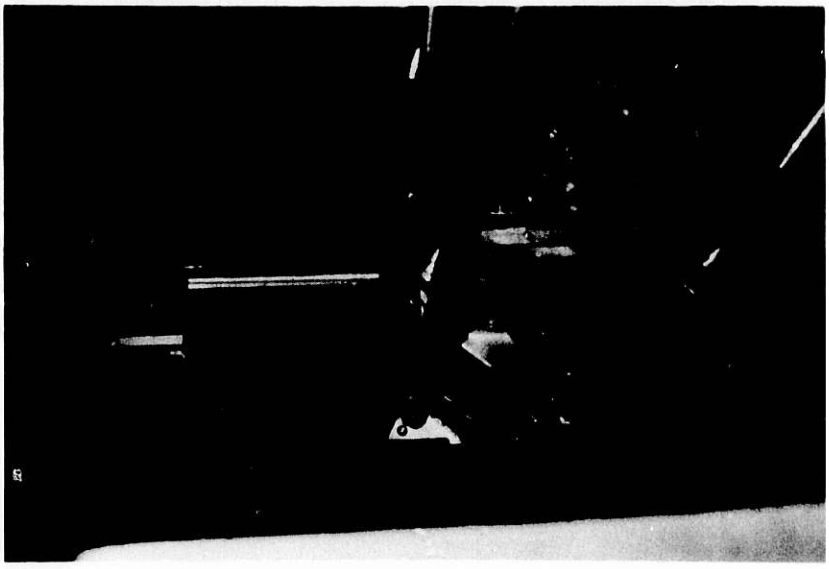

Fig. 1 Photograph of robot arm crane

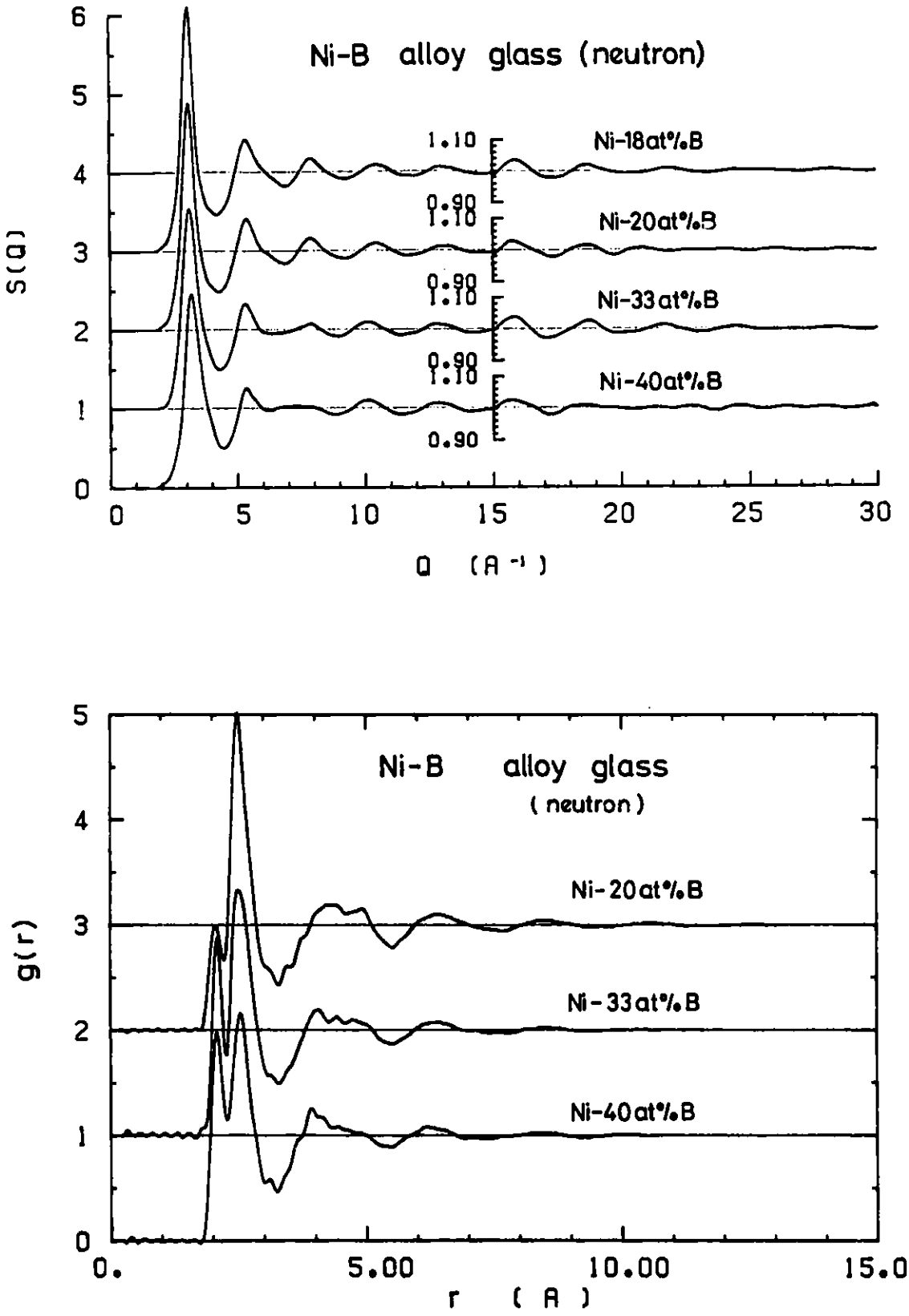

Fig. 2 S(Q)'s (a) and g(r)'s (b) of Ni-B alloy glass

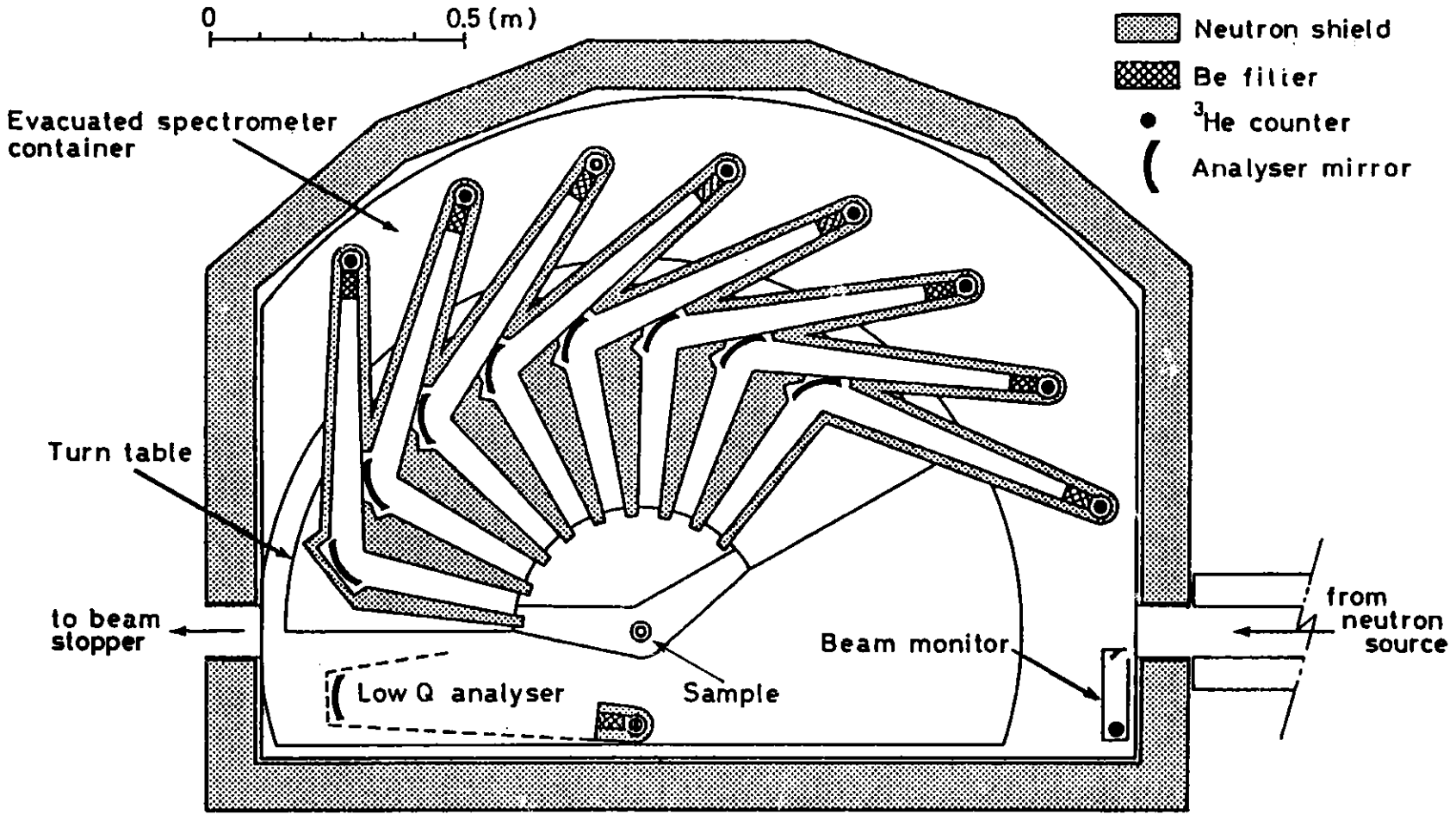

Fig. 3 Configuration of the improved LAM

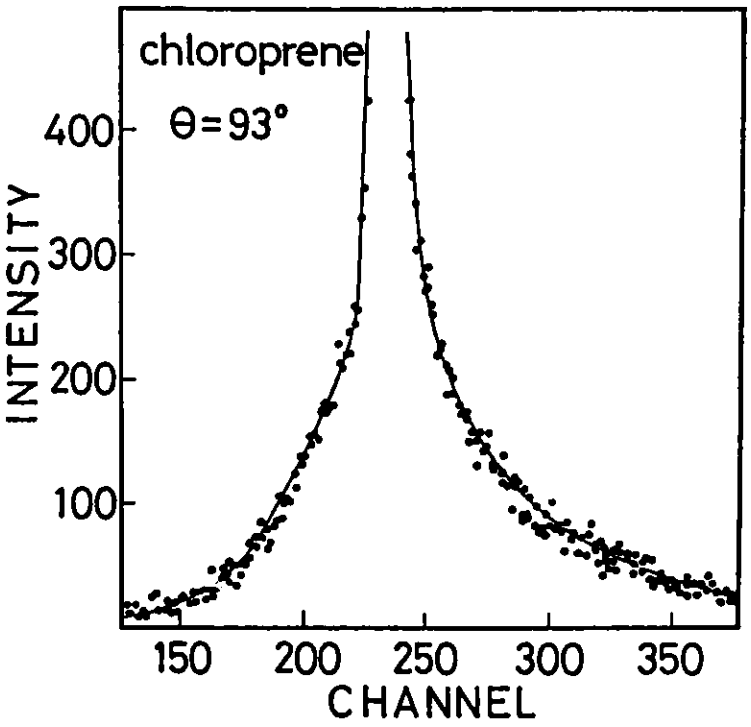

(a)

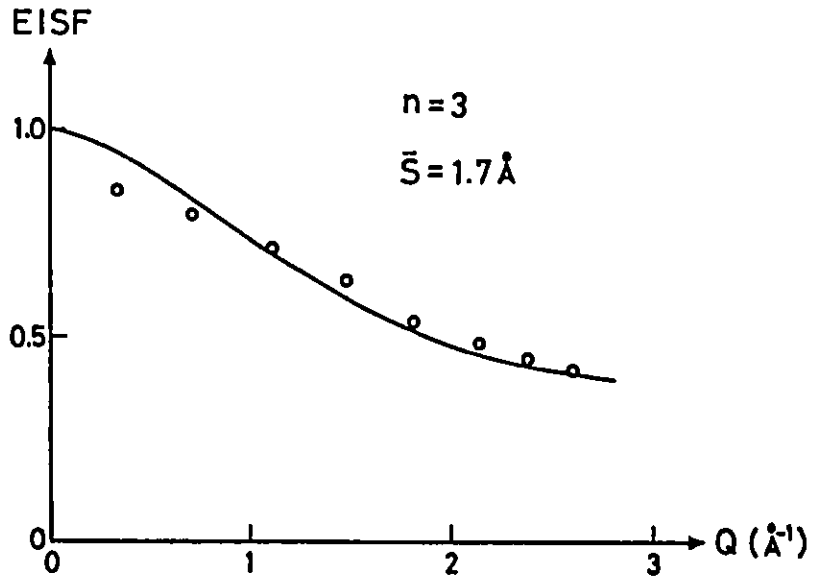

(b)

Fig. 4 TOF spectrum (a) and calculated (solid curve) and measured (open circle) EISF (b) for chloroprene at room temperature

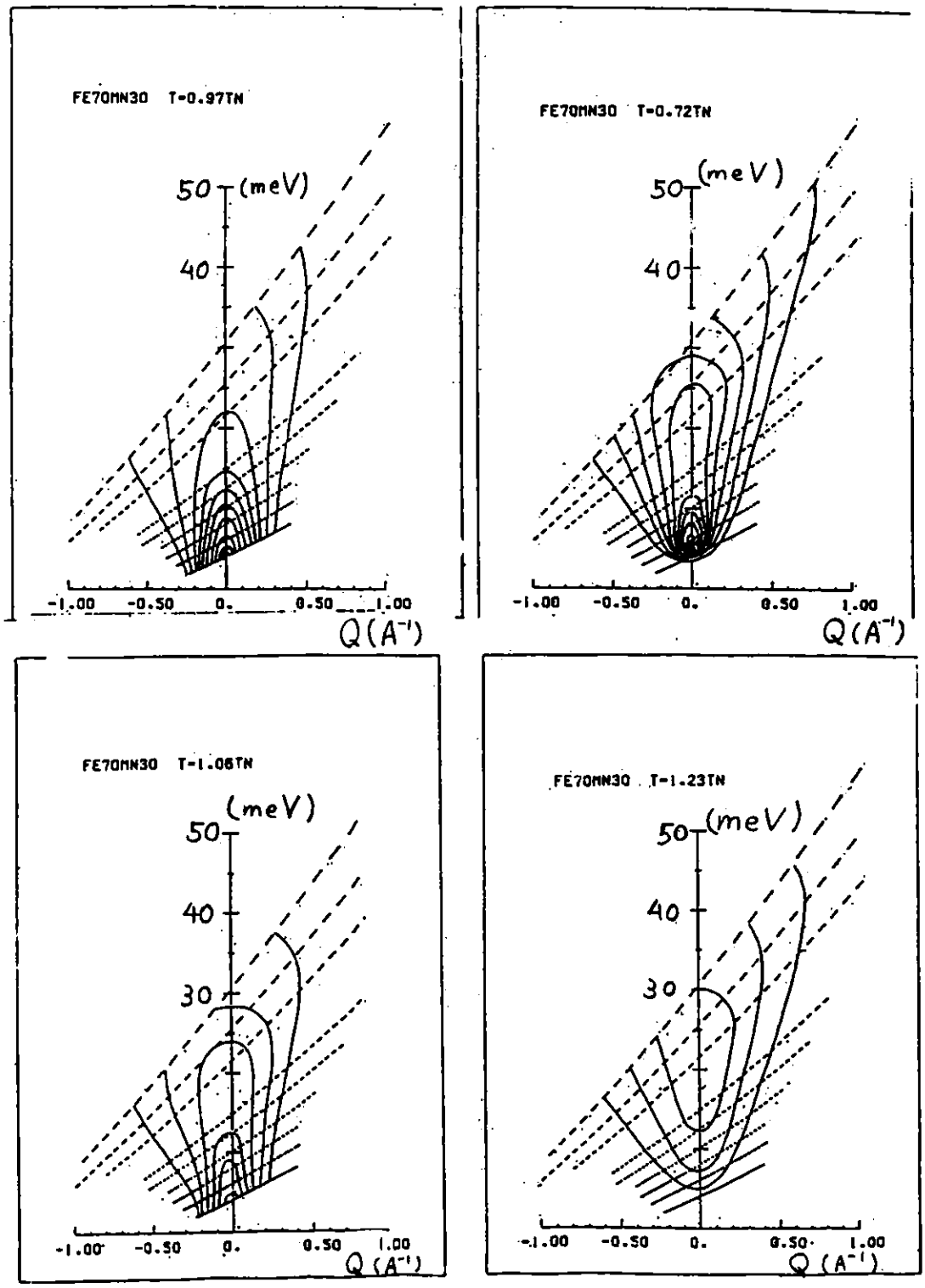

Fig. 5 Intensity mapping of the magnetic excitations in a $\gamma Fe_{0.7}Mn_{0.3}$ alloy at various temperature

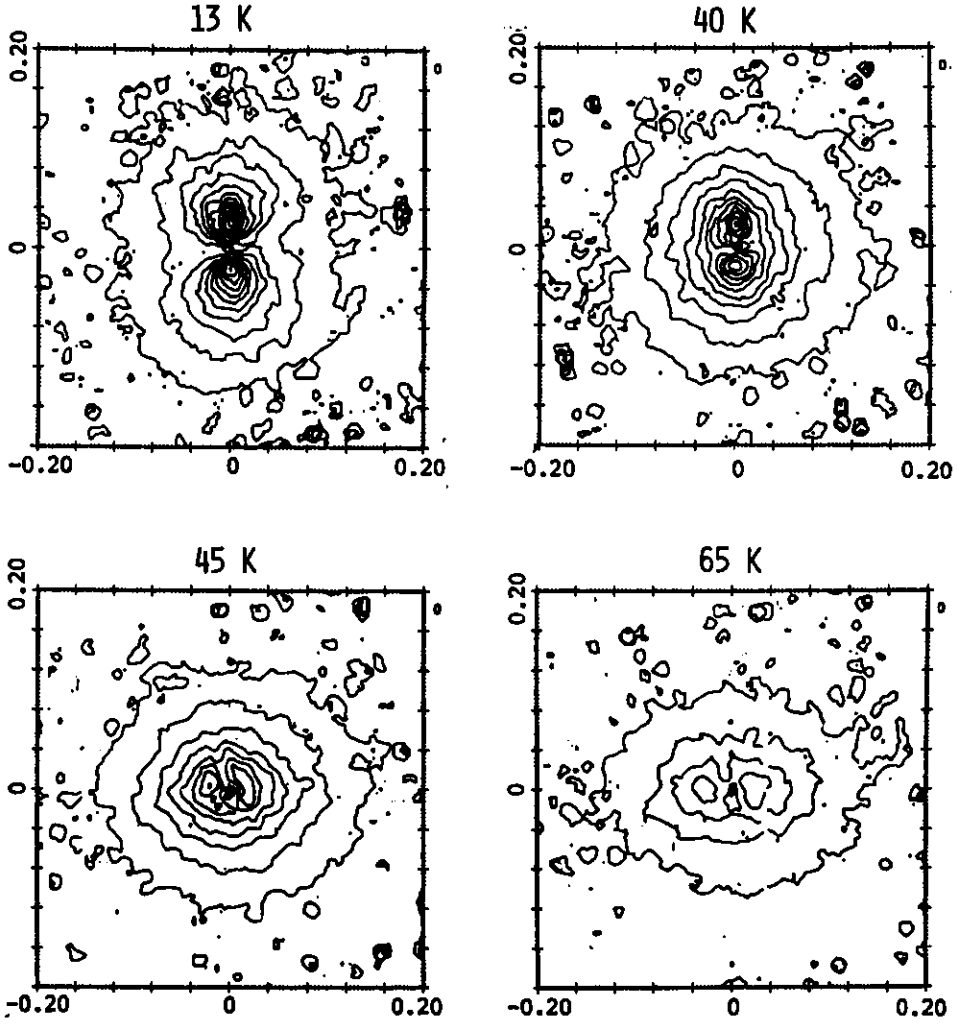

Fig. 6 Two dimensional display of magnetic correlation in $0.88FeTiO_3$ - $0.12Fe_2O_3$

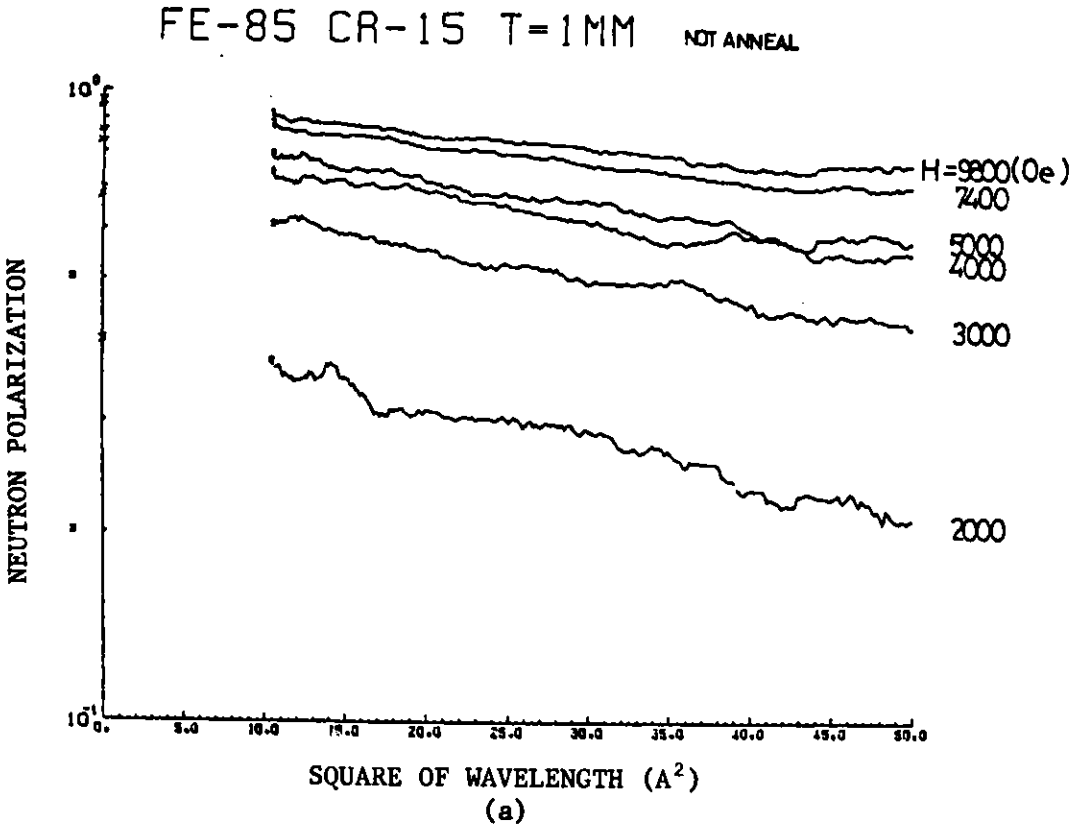

Fig. 7 Polarization of neutron beams after transmission through 1 mm thick $Fe_{0.85}Cr_{0.15}$ crystal, quenched from molten state (a), and after annealing (b)

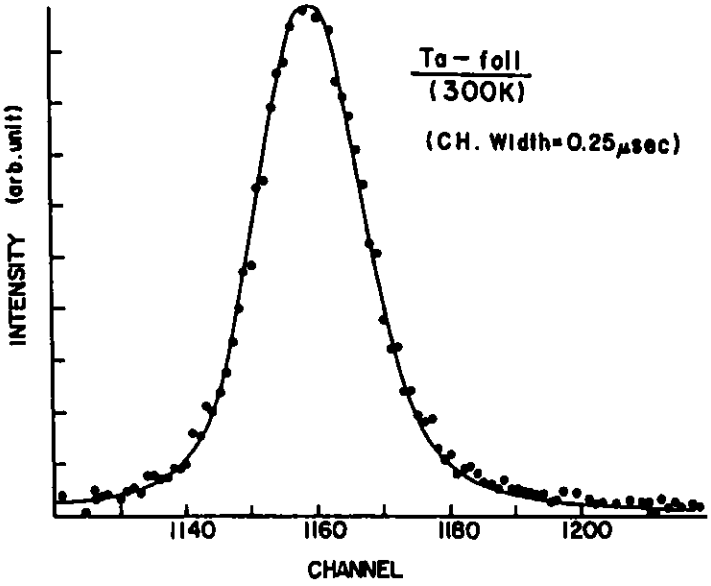

(a)

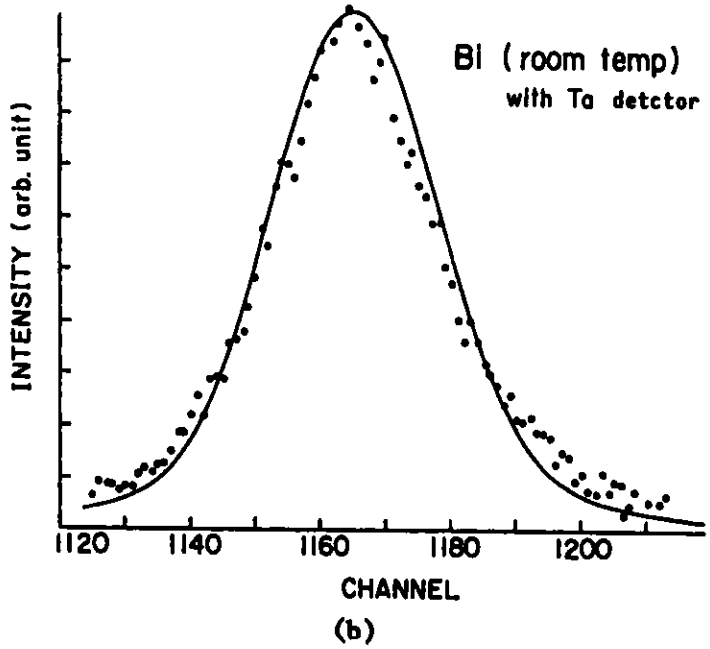

(b)

Fig. 8 Measured (solid circles) and calculated (solid curves) time distributions of detecting probability for 12 μm thick Ta foil at room Temp. (a), and time spectra of scattered neutrons from Bi at room temp. measured by Ta detector (b)

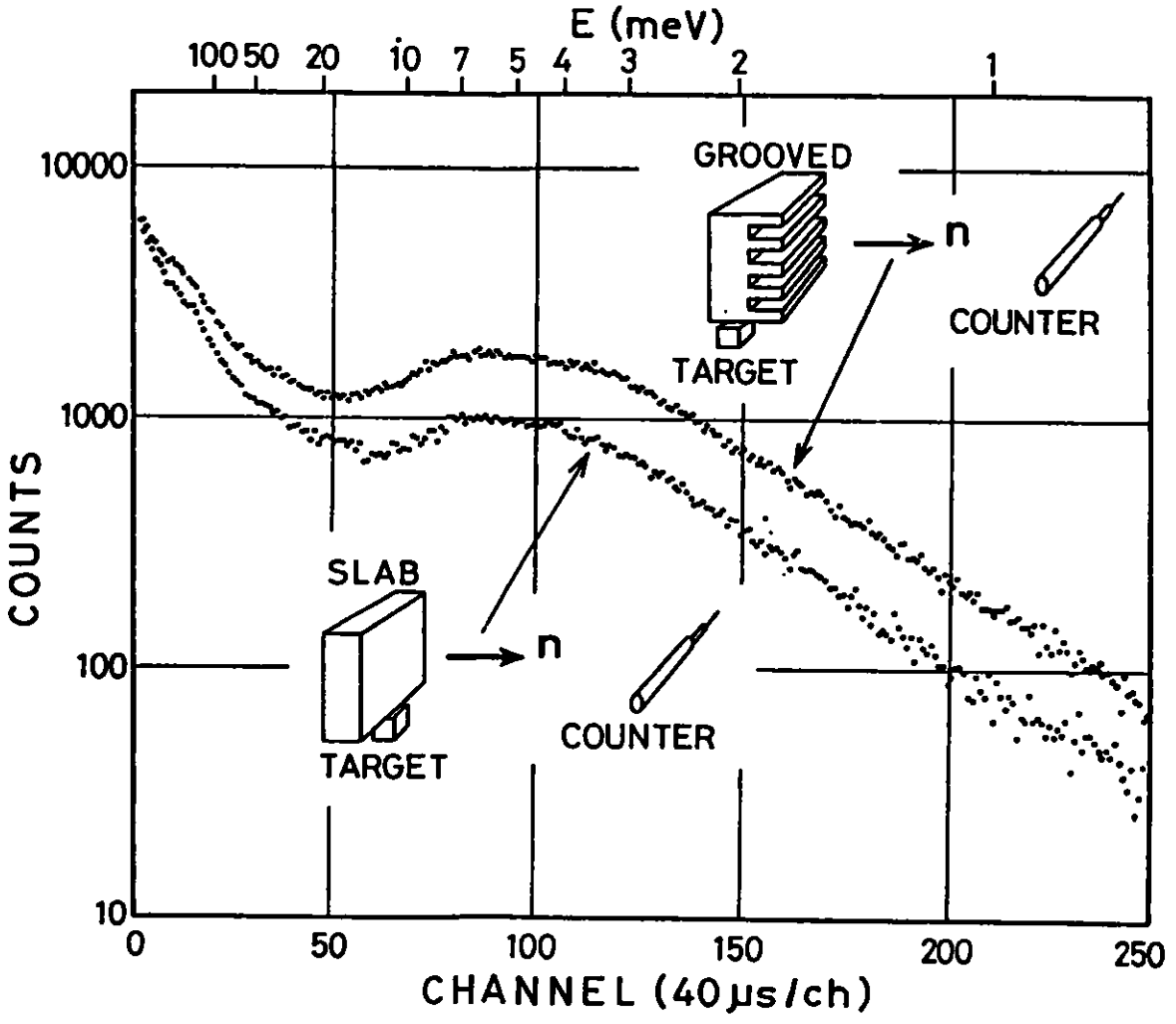

Fig. 9 TOF spectrum from a grooved solid methane moderator at 20 K compared with that from a slab one

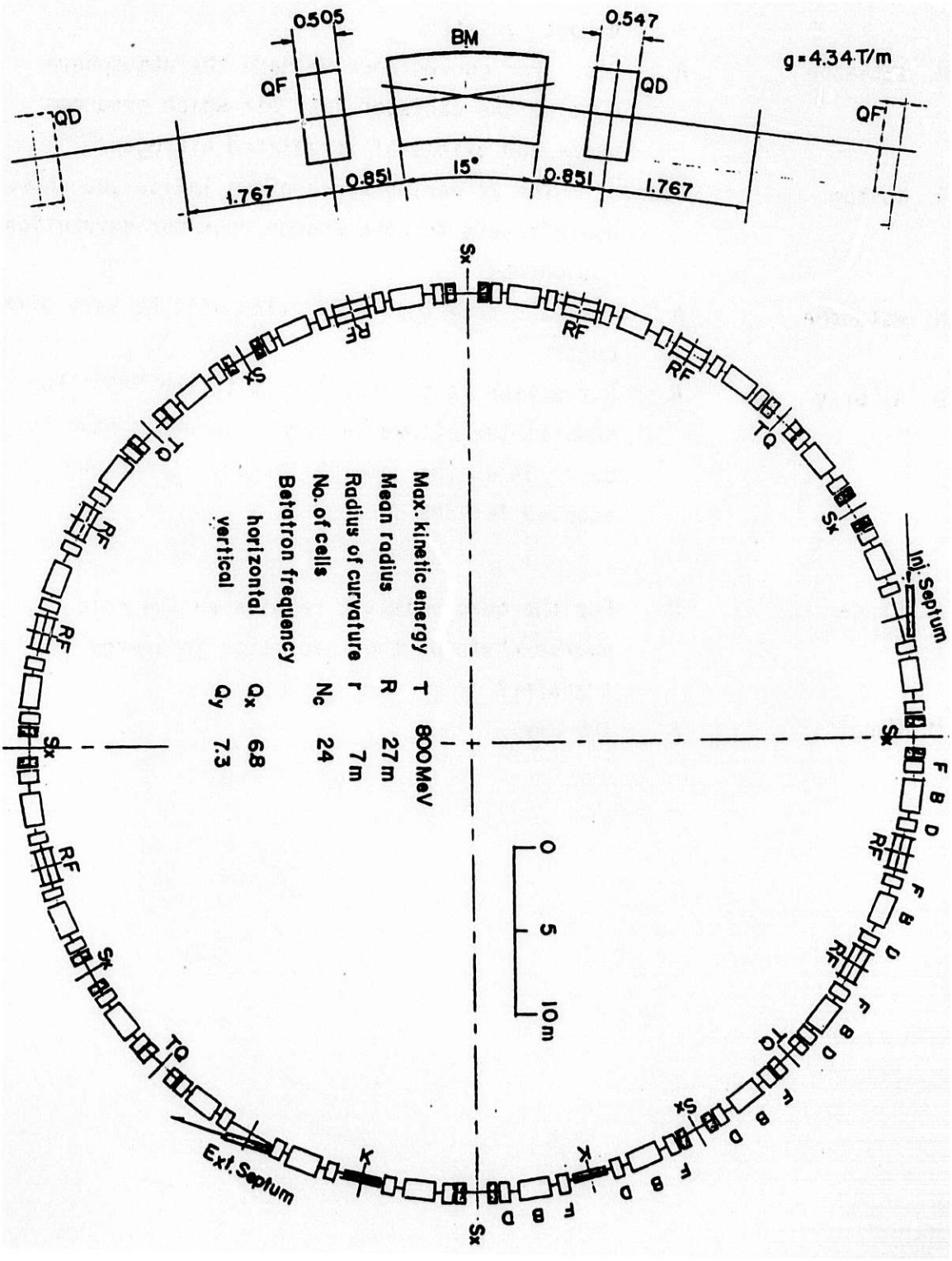

Fig. 10 Layout and lattice structure of the proposed accelerator

Russell	Q	Was the corrosion you mentioned outside the target canister?
N. Watanabe	A	Yes. For convenience we made the atmosphere outside the canister just air which produces ozone and oxides of irradiated nitrogen.
R. Kustom	Comment -	The 24 period synchrotron latice you showed doesn't seem to have enough room for extraction components.
N. Watanabe	A	Yes it's true that extraction will be very difficult!
D. A. Gray	A	Extraction is already hard with the SNS. For KENS-II the allowable beam loss would have to be < .3% on the same philosophy as the one adopted for SNS.
G. Lander	Q	For the quasi-elastic results on the cold source what was the resolution in energy transfer?
M. Kohgi	A	100 μeV.

ICANS-VI
INTERNATIONAL COLLABORATION ON ADVANCED NEUTRON SOURCES
June 27 - July 2, 1982

STATUS OF THE SNQ PROJECT AT KFA JÜLICH

G. S. Bauer
Institut für Festkörperforschung/Projekt Spallationsneutronenquelle
Kernforschungsanlage Jülich
D-5170 Jülich

ABSTRACT

The study for a high power spallation neutron source carried out jointly by the Kernforschungszentrum Karlsruhe and the Kernforschungsanlage Jülich has been completed in May 1981. In Feb. 1982 the KFA Jülich was selected as the site for a future spallation neutron source in Germany. A final decision about it construction does, however, require more planning work which will be carried out by KFA until the end of 1983. A formal project SNQ has been established at KFA, starting July 1, 1982. A staged concept for the realization of the facility will be studied.

STATUS OF THE SNQ PROJECT AT KFA JÜLICH

G. S. Bauer
Institut für Festkörperforschung/Projekt Spallationsneutronenquelle
Kernforschungsanlage Jülich
D-5170 Jülich

In March 1979, a special advisory panel to the German Ministry for Research and Technology recommended to study the possibility of building a high power spallation neutron source as a new central neutron research facility in the Federal Republic of Germany. The chairman of this panel was G. zu Putlitz. About two months later, in May 1979 the two major German laboratories for nuclear research, the Kernforschungszentrum Karlsruhe and the Kernforschungsanlage Jülich established a collaboration to carry out such a study. The goal was to finish the study work within two years. About half way through, in May 1980, an intermediate report was prepared for a panel (Pinkau-panel) appointed to evaluate major proposed projects for foundamental research in Germany. Based on this intermediate report, this panel concluded in February 1981 that a new neutron source should be built in Germany and that, if feasible, this should be a spallation neutron source. A further 3 to 4 year study period was recommended to prove the technical feasibility of components which were considered as being critical to the success of the facility. The SNQ-study was completed in June 1982, with the result that a spallation neutron source which could be competitive with a high flux reactor in terms of time average neutron flux and which would allow the users to benefit greatly from its time structure was feasible with present-day technology. This conclusion was based on numerous experimental and theoretical investigations and had been essentially confirmed by an international group of experts to whom the results had been presented at Heidelberg. It was, however, clear that prototypes should be built for certain components. The complete study report, which consists of three parts in 16 volumes was handed over to the Ministry of Research and Technology in September 1981.

The general plan of the facility is shown in Fig. 1 and the main data of the reference concept as worked out in the SNQ-study are summarized in Table 1.

The estimated cost of the facility was about 540 million DM for the accelerator and proton experimental areas, 140 million DM for the target station and 130 million DM for the proton pulse compressor ring.

Accelerator type:	Linac
Type of particles:	Protons (H^-)
Mean proton current:	5 mA
Peak proton current:	100 mA
Pulse repetition rate:	100 Hz
Injection an preacceleration:	450 keV dc
Low energy accelerating structure:	Alvarez, 108 MHz, 450 keV-105 MeV
High energy accelerating stucture:	Disk and washer, 324 MHz, 105-1100 MeV
Total length of accelerator:	650 m
Total power consumption:	50 MW (whole facility)
Target type:	Rotating target, H_2O cooled
Target material:	Pb, Al-clad
Power dissipated in target:	2,9 MW
Moderators:	H_2O, D_2O, Cold Source
Time average thermal neutron flux:	$7 \cdot 10^{14}$ $cm^{-2}s^{-1}$
Peak thermal neutron flux:	$1.3 \cdot 10^{16}$ $cm^{-2}s^{-1}$
Thermal neutron pulse width:	510 µs
Number of thermal neutron beam tubes:	12
Number of cold neutron beam tubes:	2
Number of neutron guides:	12
Experimental areas:	350 MeV proton hall
	1100 MeV proton hall
	Target hall (thermal neutrons)
	Neutron guide hall
	Neutrino cavern
	Target top hall (irradiation stations)
Options:	U-238 target (flux doubling)
	10 mA proton beam (1 ms pulses)
	Proton pulse compressor (0.5 µs pulses)
	Target station with pulsed source

Table 1: Main parameters of the SNQ reference concept

Two possibilities were considered, to build the facility in a staged way such as to be able to produce neutrons already well before the full sum has been spent.

One possibility would be to build the target station as conceived and the linac tunnel, but to equip the linac with accelerating structure only up to a fraction of the final energy. It has been estimated that this energy could be of the order of 350 MeV if about half of the total cost was to be spent on stage 1. This would make it possible to serve the 350 MeV experimental area and to produce neutrons in the target. The neutron flux levels achievable in this way would be about 25% of those of the reference concept, but with the early use of depleted uranium it could be brought up to $\bar{\Phi}_{th} = 3 \cdot 10^{14}$ $cm^{-2}s^{-1}$ and $\hat{\Phi} = 6 \cdot 10^{15}$ $cm^{-2}s^{-1}$. The pulse length would be 510 μs. Further accelerating structures could be added as funding becomes available, each time increasing the neutron flux in the target. With growing operating experience with the U-238 target, this might allow to achieve a time average thermal neutron flux of $1.4 \cdot 10^{15}$ $cm^{-2}s^{-1}$ and a peak flux of $2.6 \cdot 10^{16}$ $cm^{-2}s^{-1}$ when the 1.1 GeV beam is available and the target of depleted uranium is retained. As a last step the proton pulse compressor would be built to provide a time structure suitable for work with epithermal neutrons.

Another possibility for a staged realization would be to partly invert the sequence of construction and to build the target station and the ring first. The ring would than be laid out as a synchrotron initially, but its design would take into account its later conversion into a proton pulse compressor. Desirable specifications for such a synchrotron would be a proton energy of 1.1 GeV, a repetition rate of 50 Hz and a time average proton current of 0.5 mA with proton pulses of no more than 200 ns duration. This last requirement comes from the desire to provide a good time structure for neutrino research and certain applications of mesons right from the beginning. It would be tolerable if two or three such pulses would be extracted from the ring at 10 μs separation. For the thermal neutron pulse in the non-decoupled and unpoisonned moderator this would hardly affect the pulse width, which is of the order of 150 μs. On the other hand, for work with neutrons in the epithermal regime those subpulses should be joined together to give one pulse of less than 1 μs duration. A synchrotron of these ratings may be close to the limits of feasibility, but is still within reasonable extrapolation from existing concepts.

With a target of depleted uranium, a time average thermal neutron flux of $1.5 \cdot 10^{14}$ $cm^{-2}s^{-1}$ and a peak flux of $1.6 \cdot 10^{16}$ $cm^{-2}s^{-1}$ would be anticipated. The high peak-to-average flux ratio results from (a) the reduction in pulse frequency by a factor of two and (b) the shortening of the proton pulses which gives a factor of about 3 in thermal neutron peak flux. While this peak flux is higher than achieved in any neutron source so far, the time average flux of this first stage would still be on the same level as that of the most powerful research reactor presently operating in Germany (the FRJ-2, DIDO, in Jülich). It is a particularly attractive feature of this first stage that all the essential design characteristics of the final concept are already realized, although at only 10% of the intensity. Besides providing very good working conditions for those disciplines which need short proton pulses, it would allow to gain all the necessary experience e.g. in shielding requirements, target operation and instrument design at the correct energy and time structure. The linear accelerator needed for the injection into this synchrotron could be similar in design to the high current linac to be built in stage II. It would, however, operate at reduced load levels and thus allow to collect valuable experience. Also, its final energy would be likely to be of the order of 100-120 MeV and it would thus make an ideal test bed for the high energy accelerating structure of the linac which is yet to be examined under practical beam-load conditions. Based on the experience from the injector, the high power linac would be built in stage II. The goal should be to achieve a peak current of 200 mA, while retaining the 5 mA time average value. Due to the shorter proton pulses and with a target of depleted uranium, the flux levels in the moderators would then be $\bar{\Phi} = 1.4 \cdot 10^{15}$ $cm^{-2}s^{-1}$ and $\hat{\Phi} = 5.2 \cdot 10^{16}$ $cm^{-2}s^{-1}$. In stage III the synchrotron would finally be converted into a proton pulse compressor with similar pulse characteristics as before but with 10-fold higher intensity (i.e. accommodating the full linac beam). Since the implementation of stage II and III in this concept would not interfere with the operation of stage I respectively II, transition from one stage to the other could be done with only minor shut down periods. Also, since the operation of the linac with H^--ions, which is required for the injection into the synchrotron may be quite difficult to achieve, it would be conceivable that the synchrotron and the linac could be working in alternating periods and thus ensure good time structure or high flux values as dictated by the experimental program.

Table 2 gives a comparison of the two stages of the target station DIANE according to this scheme (with synchrotron and with 200 mA linac) to other leading neutron sources in the world.

In February 1982 a decision was taken by the Federal Ministry of Research and Technology in Germany that, if a spallation neutron source was to be built, it would be located at KFA Jülich. KFA was asked to work out a detailed concept for a staged realization of the facility and to establish a project plan.

Following this decision, the spallation neutron source was made one of the prime research goals at KFA and the process of formal establishing the SNQ project was initiated. On June 9 the supervisory board of the laboratory gave its agreement to the foundation of the project. Fig. 2 gives a scheme of the planned organization.

Following the Ministry's request, KFA will carry out studies for both of the above staging concepts to a sufficient degree of detail that a decision, which one to pursue further, can be made. Such a decision is envisaged for early 1983. For the concept selected, a more detailed plan and cost estimate together with a general project plan will be worked out and submitted to the ministry to serve as a basis for the decision, whether or not the source should be built.

	HFR (ILL)	IBR II	DIANE*	DIANE I	DIANE II	SNS
Peak thermal flux Φ ($cm^{-2}s^{-1}$)	10^{15}	$2 \cdot 10^{16}$	$1.3 \cdot 10^{16}$	$1.7 \cdot 10^{16}$	$5.2 \cdot 10^{16}$	$4.5 \cdot 10^{15}$
Average thermal flux $\bar{\Phi}$ ($cm^{-2}s^{-1}$)	10^{15}	$2 \cdot 10^{13}$	$7 \cdot 10^{14}$	$1.5 \cdot 10^{14}$	$1.4 \cdot 10^{15}$	$7 \cdot 10^{12}$
Pulse repetition rate ν (s^{-1})	-	5	100	50	100	50
Pulse width τ (μs)	-	150	510	150	270	30
Fuel or target	U-235 (HEU)	Pu	Pb	U-238	U-238	U-238
Mode of operation	critical	periodically super critical	non-critical	non-critical	non-critical	non-critical
Coolant	D_2O	Na	H_2O	H_2O	H_2O	D_2O
Average thermal power (MW)	57	4	2.9	1	10	0.25
Moving parts	-	Reflector (5u.25Hz)	Target (0.5Hz)	Target (0.25Hz)	Target (0.5Hz)	-
Options and extensions	-	Electron Induction Linac Source-pulse 7 μs	U-Target, Compressor-ring Source-pulse 0.7 μs	multiplying target	Compressor-ring (?)	

* as studied in SNQ-report, $I_{max} = 100$ mA, $I_{av} = 5$ mA, Pb Target

DIANE I: $I_{av} = 0.5$ mA, U-238 Target

DIANE II: $I_{av} = 5$ mA, $I_{max} = 200$ mA, U-238 Target

Table 2: Comparison of modern neutron sources

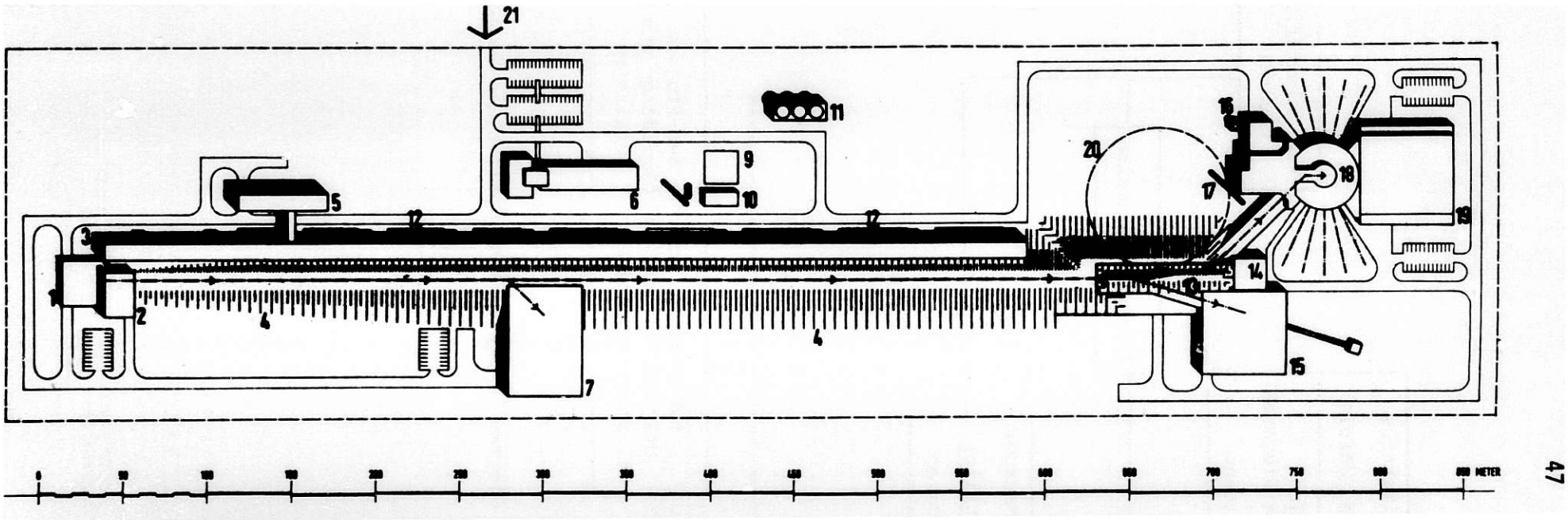

1	Injector building	8	Air stack	15	1100 MeV experimental area
2	Assembly hall	9	Switchyard	16	Cooling towers
3	RF-galery	10	20 kV power distribution	17	Airstack
4	Dirt shielding	11	Cooling towers	18	Target building
5	Test and assembly building	12	RF power supplies	19	Neutron guide hall
6	Operations building	13	High energy beam switchyard	20	Proton pulse compressor
7	350 MeV experimental hall	14	Assembly hall	21	Site entrance

Fig. 1: Site Planning of the SNQ reference concept

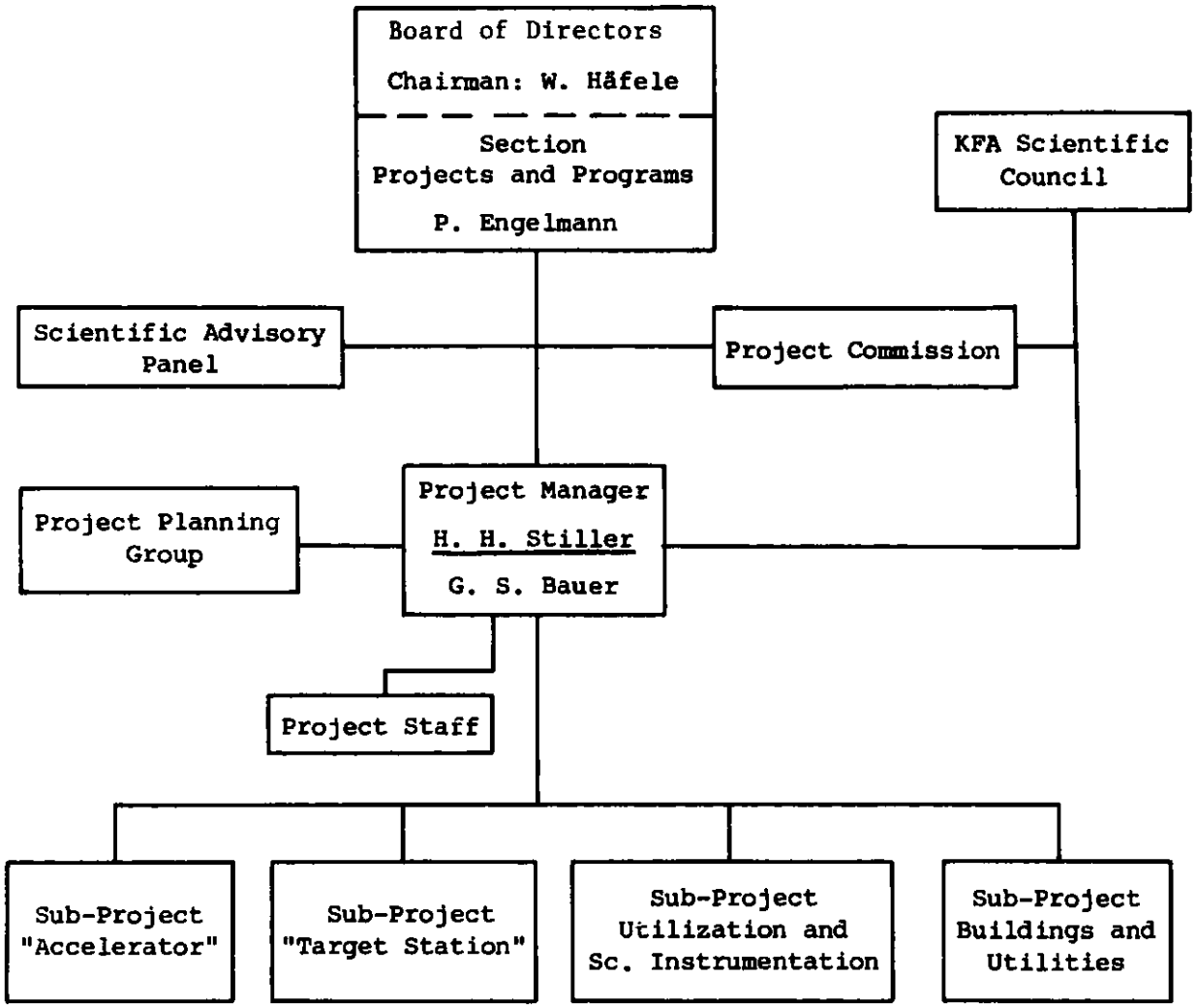

Fig. 2: Preliminary Organizational Diagram of the Project Spallations-Neutronenquelle at KFA Jülich

SNQ - G. Bauer

R. Silver	Q	What is the cost of stage 1 of SNQ?
G. Bauer	A	400 M DM.
W. E. Fischer	Q	What is the neutron flux produced by stage 1?
G. Bauer	A	At 350 MeV with a U target $\bar{\phi} = 3 \times 10^{14}$ and $\hat{\phi}$ is 20 times higher.
F. Mezei	Comment -	It is not correct that all instruments will use the mean flux. Spin echo would have velocity selectors using ~ 20% of the wavelength range so the relevant flux is the peak.
B. Brown	Q	What is the status of the radiation effects facility?
G. Bauer	A	There is nothing very special in mind. We are thinking of a low temperature facility which could be put into the reflector tank or target area when needed.

ICANS-VI

INTERNATIONAL COLLABORATION ON ADVANCED NEUTRON SOURCES

June 27 - July 2, 1982

STATUS OF THE WNR/PSR AT LOS ALAMOS

R. N. Silver
Physics Division
Los Alamos National Laboratory
Los Alamos, NM 87545

ABSTRACT

A proton storage ring is presently under construction at Los Alamos for initial operation in 1985 to provide the world's highest peak neutron flux for neutron scattering experiments. The operational WNR pulsed neutron source is in use for TOF instrument development and condensed matter research. Experimental results have been obtained in incoherent inelastic scattering, liquids and powder diffraction, single crystal diffraction and eV spectroscopy using nuclear resonances. Technical problems being addressed include chopper phasing, scintillator detector development, shielding and collimation. A crystal analyzer spectrometer in the "constant Q" configuration is being assembled. The long range plan for the WNR/PSR facility is described.

The Los Alamos pulsed spallation neutron source, the WNR/PSR is progressing toward its goal of a world class facility in 1985. This will provide a peak thermal flux of 10^{16} n/cm^2-s at 12Hz, with a time average current of 100 μA of 800 MeV protons. Construction has commenced on the Proton Storage Ring (PSR), which will compress the 750 μ sec long macropulses from the LAMPF accelerator to a .27 μsec proton pulse width more suitable for time of flight neutron scattering experiments. Construction is presently on schedule and within cost, with the first proton beam expected in March 1985.

In this paper, the emphasis will be on the progress and plans of the neutron scattering research program and instrumentation at Los Alamos. The WNR is presently an operational spallation neutron source, with a time average current of 4-5 μA of 800 MeV protons at a proton pulse width of 5 μsec and a repetition rate of 120Hz. This makes it possible to test novel TOF instrument developments, to explore the unique science made possible by these sources, and to develop the expertise of the scientific staff by research experience. The goal is to have mature instrumentation, research programs, and staff by 1986 to maximize the scientific impact of the much superior source characteristics of the PSR.

Neutron scattering instrumentation at Los Alamos has advanced considerably since the last report at ICANS IV. Figure 1 shows the current layout of instrumentation at the WNR. Three instruments, which were in an assembly or testing stage two years ago, are presently in a production mode for condensed matter research. These are: 1) a general purpose diffractometer (GPD) for powder,

liquids, and amorphous materials diffraction; 2) a single crystal diffractometer (SCD) based on the Laue-TOF technique; and 3) a Be-BeO filter difference spectrometer (FDS) for incoherent inelastic scattering. A prototype eV spectrometer using nuclear resonance filters (EVS) is operational. Testing and assembly has commenced on a constant Q spectrometer for the measurement of elementary excitations in single crystals, particularly at high energies. In addition, the vexing problem of phasing neutron choppers to the power line used to trigger LAMPF has been solved. Systematic studies have commenced of shielding and data acquisition requirements for the much higher intensities of the PSR era.

The filter difference spectrometer, shown in Figure 2, uses the differing Bragg cutoffs of Be and BeO to improve the resolution of the filter detector techniques (see the article by J. A. Goldstone, et.al., in these proceedings). Figure 3a shows the raw Be filter spectrum from KH Maleate, while Figure 3b shows the improvement in resolution obtained by taking the difference of Be and BeO filter spectra. A comparison of the performance of the FDS with the crystal analyzer spectrometer (CAS) (Figure 4) is shown in Figure 5. These were obtained on approximately 30g samples with 100 μA-hrs of beam. The FDS has comparable resolution to the CAS with greatly improved count rate. In the final version, a further factor of 4 improvement will be obtained for the FDS by cooling the filters to 77°K and increasing the detector solid angle. An example of research with the FDS is shown in Figure 6 and 7. Ni-Dimethylgloxine is a molecule with an intramolecular hydrogen

bond. The vibrational frequency of the out of plane bending mode γ(OHO) of this hydrogen is obtained by observing the change in spectrum upon deuteration (Figure 6). Measurements of this kind were used in a systematic study of the variation of the vibrational frequency with bond length. The question was whether the trend observed with the longer bonds of the intermolecular cases would continue for the shorter bonds of the intramolecular cases. The results (Figure 7) show a clearly different trend. The FDS and CAS have also been used for studies of hydrogen optic modes in metal hydrides and for complementary measurements to IR and Raman in chemical spectroscopy.

The general purpose diffractometer is shown in Figure 7. The 150° bank provides for medium resolution ($\Delta d/d \sim .45\%$) powder diffraction. The low angle banks at 40° and 10° are especially important to minimizing inelasticity connections in liquids diffraction. In this paper, the emphasis will be on recent work on the structure of water with the GPD. The quantity sought in a diffraction experiment is the static structure factor S(Q). However, the quantity measured is a differential cross section $\Sigma(Q)$. These are simply related to each other only in the case of completely elastic scattering. In the case of light elements, the recoil of the particle from which the neutron scatters leads to large inelasticity corrections required to extract S(Q) from $\Sigma(Q)$. Examination of the kinematics shows that the corrections can be minimized by scattering at low angles with high energy neutrons to achieve a given Q. This is demonstrated in a comparison of the

performance of the GPD with the D4 instrument at the ILL shown in Figure 8. The structure factor S(Q) is expected to oscillate about the static self scattering limit at high Q. However, the measured cross section at the ILL droops far below the self scattering limit. At a reactor, high Q is reached at a fixed wavelength by scattering at large angles with a consequent large inelasticity correction. In contrast, the result for the GPD at 40° is much closer to the static limit because high energy neutrons (up to 1.7 eV at 20Å^{-1}) are used to reach high Q. Thus, it is possible at the WNR to analyze liquids diffraction data without introducing questionable models for the inelastic scattering. Note also the competitive count rate of the GPD and the larger Q range obtainable. The water experiment involved taking a linear combination of cross sections obtained on isotope substituted samples (H_2O, D_2O, and an H_2O:D_2O mixture), to extract the HH distinct cross section. Because of the minimal inelasticity effects, this can be compared directly with molecular dynamics simulations of the structure of water as shown in Figure 9. Remarkable overall agreement is obtained between theory and our model independent experiment. The differences correspond to a somewhat smaller coordination number and bond lengths in the experiment compared to the simulations.

The single crystal diffractometer shown in Figure 10 uses a 25 x 25 cm He^3 multiwire area detector to collect data in a time resolved Laue technique. Figure 11a shows the intensity as a function of x and y on the detector for the sum of all time channels

in a sapphire sample. Figure 11b shows a single time channel with a single Bragg peak. We have worked closely with ANL in the development of software to derive integrated intensities from the data. Structural refinements on test crystals have produced R factors, thermal parameters, and lattice positions comparable to X-ray and single wavelength reactor experiments. One very encouraging result is that data rates with this instrument at the present WNR are comparable to a four circle diffractometer at BNL. This shows the advantages of the combination of white beams with multidetectors to obtain high data rates. However, backgrounds were much higher than at BNL primarily due to the poor shielding currently available. Upgrade of the instrument will include improved shielding and collimation, a two-axis goniometer, and the use of position sensitive scintillator detectors.

Two instruments are being tested in prototype form. We have developed an eV spectrometer based on the use of nuclear resonances for energy selection (see the article by Brugger, et.al., in these proceedings). The technique is to take the difference between spectra with resonance filters in the beam and removed. Figure 12 shows the scattering from liquid He using the U^{238} resonance at 6.6 eV in a direct geometry. The peak at 3.5 eV energy transfer is from the He while the peak at .69 eV is from the Al container. Tests of resolution in direct, inverted, and sample geometries have been carried out. We are currently examining possible detector configurations. The initial experimental effort is on momentum distributions in hydrogenic systems. We are also developing a

constant Q spectrometer similar to C. Windsor's design primarily for the measurement of high energy elementary excitations in single crystals such as magnons. Considerable attention is being paid to the calibration and alignment of the spectrometer. Resolution calculations suggest that the constant Q machine will have complementary characteristics to triple axis spectrometers at reactors. Preliminary experiments have suggested that competitive data rates will be obtained with the PSR.

We are also addressing several of the technical problems of pulsed sources. This includes chopper phasing (see the article by Bolie, et. al., in these proceedings), beam line collimation and shielding, and scintillator detector development. The approach to collimation and shielding has included empirical tests, the development of detectors to measure neutron energy spectra, and Monte Carlo simulations. The detector effort has concentrated on improving the speed and lowering the γ sensitivity of Anger scintillator cameras.

The long range plan for the WNR/PSR is to have a total of eight neutron scattering instruments operational by 1986 when the PSR is expected to come into reliable operation. These include upgraded versions of the filter difference spectrometer (FDS) and single crystal diffractometer (SCD) currently in operation. The present general purpose diffractometer will be replaced by two instruments: one a low resolution (1-2%) machine with small angle capability optimized for liquids, amorphous and special environment diffraction (LIQ); and the other a high resolution (.15%) powder

diffractometer (HRPD) on a 35 m flight path. We also expect to have a high resolution chopper spectrometer (CS), an eV spectrometer (eVS) and a constant Q machine (CQS) all optimized by research experience on the present WNR. Figure 13 shows a possible layout of condensed matter instruments at the WNR in 1986, where we have added a quasielastic backscattering spectrometer (BSS). The figure also shows the powder diffractometer in low resolution (10m) configuration (LRPD) prior to PSR operation. We show on f.p. 11 that it is possible to place more than one instrument on a beam line if the flight paths are long.

This is a report of work by personnel and collaborators of the neutron scattering group, P-8, at Los Alamos. This includes A. Soper, J. Eckert, J. Goldstone, P. Seeger, P. Vergamini, A. Larson, R. Alkire, R. Brugger (MURR), A. Taylor (Rutherford-Appleton Laboratory) and R. Pynn (ILL).

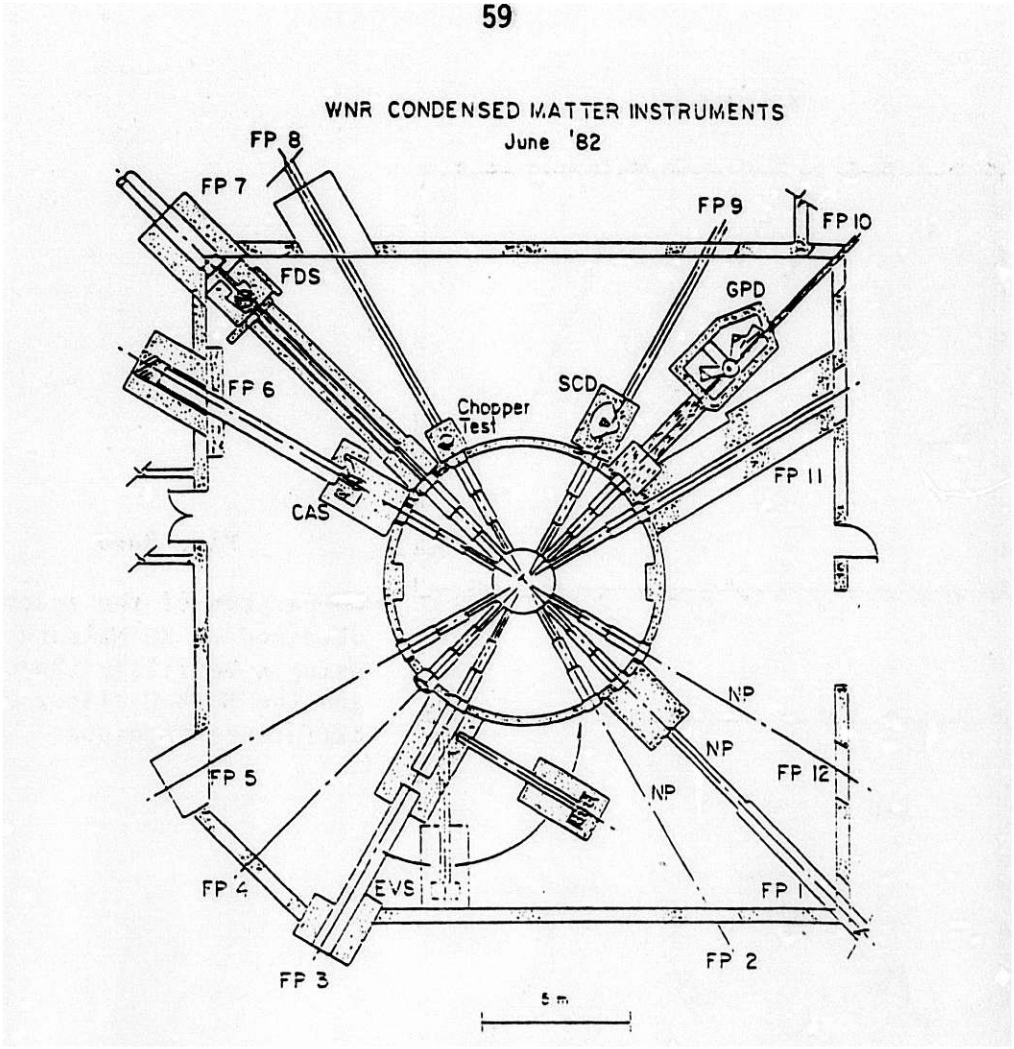

Fig. 1. Current layout of neutron scattering instrumentation at the WNR. NP stands for flight paths assigned to nuclear physics. GPD is the general purpose diffractometer, SCD the single crystal diffractometer, FDS the filter difference spectrometer, CAS the crystal analyzer spectrometer, and EVS the electron volt spectrometer.

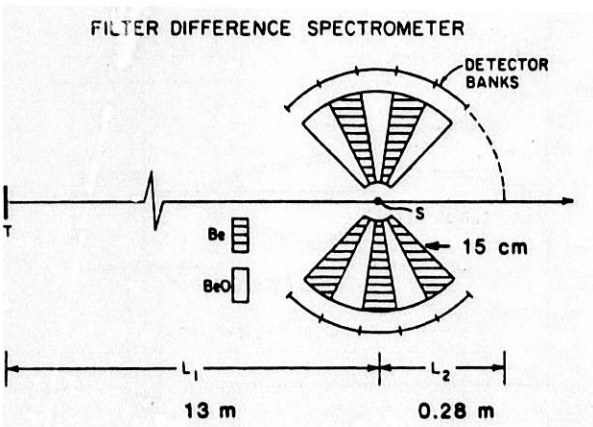

Fig. 2

Schematic layout of the Filter Difference Spectrometer for incoherent inelastic scattering. The filter provides a Bragg cutoff to the final energy bandpass. The difference between Be and BeO filter spectra is taken to improve the resolution of the filter technique. (3b)

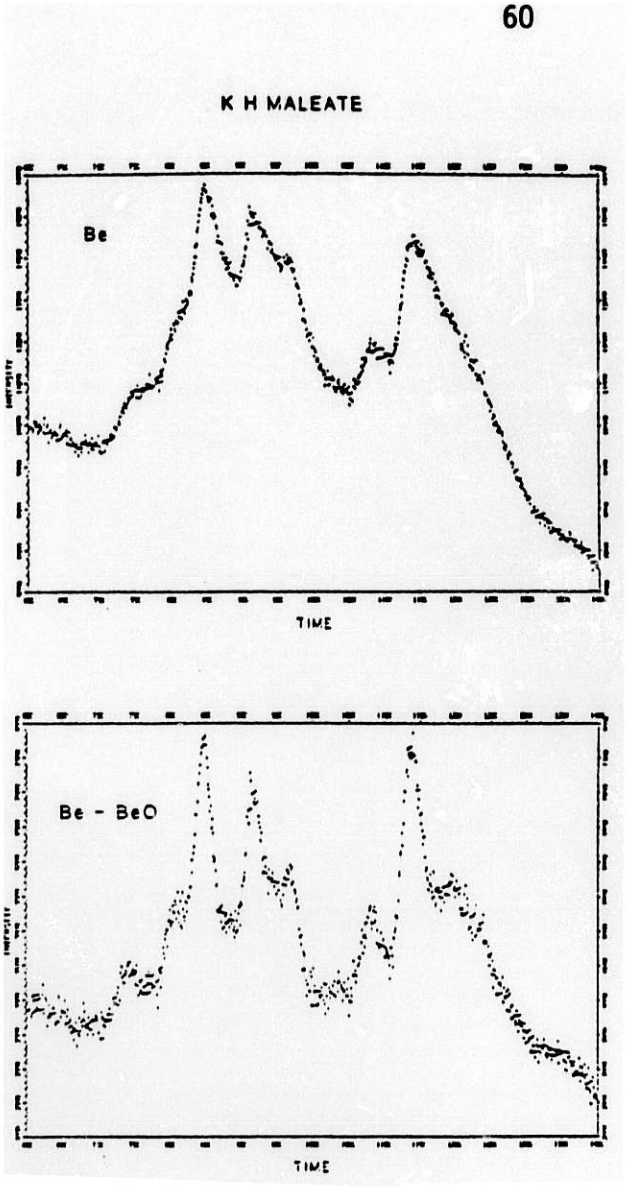

Fig. 3a&b

Comparison of the spectra obtained on KH Maleate using a Be filter (3a) and the Be-BeO filter difference tecnique.

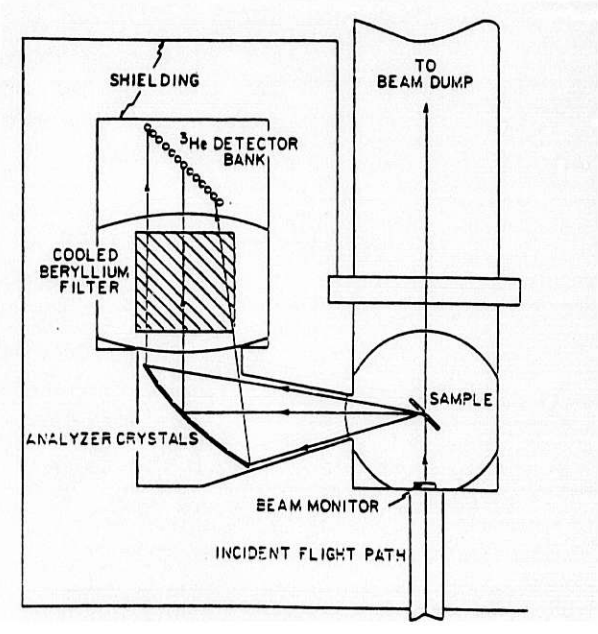

Fig. 4

Schematic layout of the crystal analyzer spectrometer. The analyzer crystals are pyrolytic graphite.

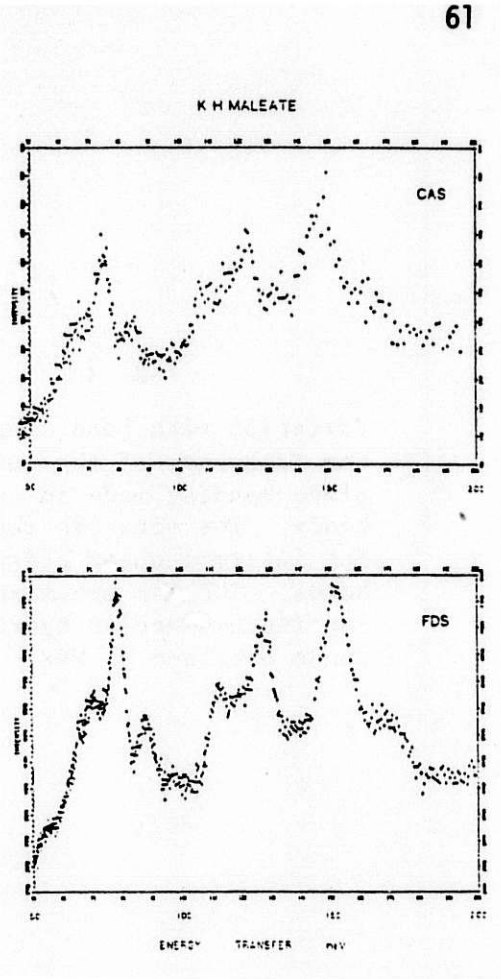

Fig. 5a&b

Comparison of spectra obtained on KH Maleate using the crystal analyzer spectrometer (5a) and the filter difference spectrometer (5b). The FDS has comparable resolution with better count rates. The FDS will be improved another factor of four by cooling the filters and increasing the detector solid angle.

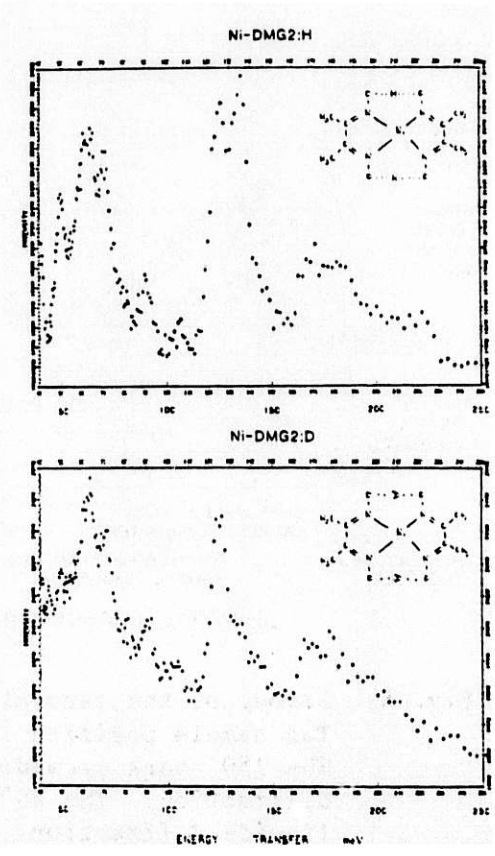

Fig. 5a&b

Incoherent inelastic neutron spectra of nickel dimethylgloxine. H/D substitution is used to identify modes due to the intramolecular hydrogen bond.

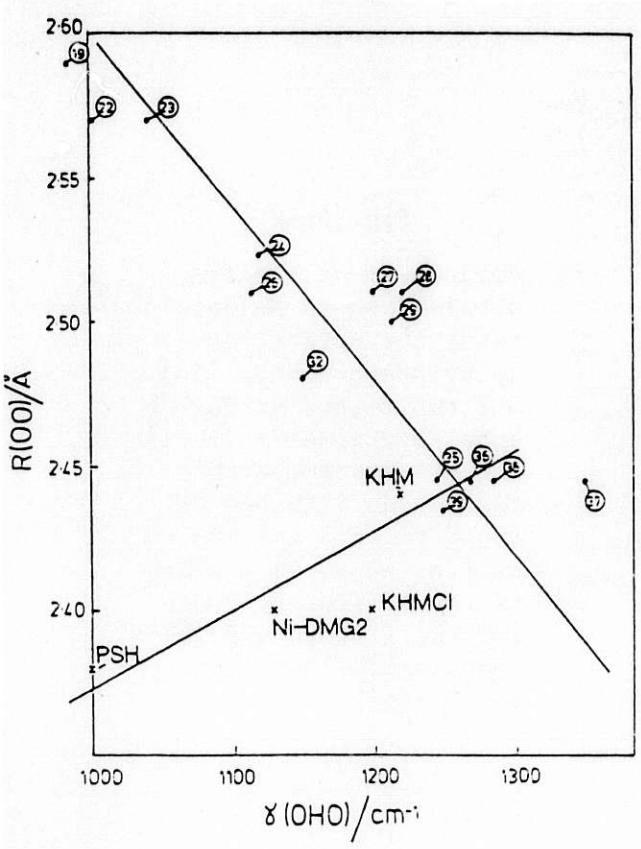

Fig. 7

Variation with bond length of the frequency of the out of plane bending mode in hydrogen bonds. The dots are results for intermolecular hydrogen bonds. The X's are results for intramolecular hydrogen bonds obtained at WNR.

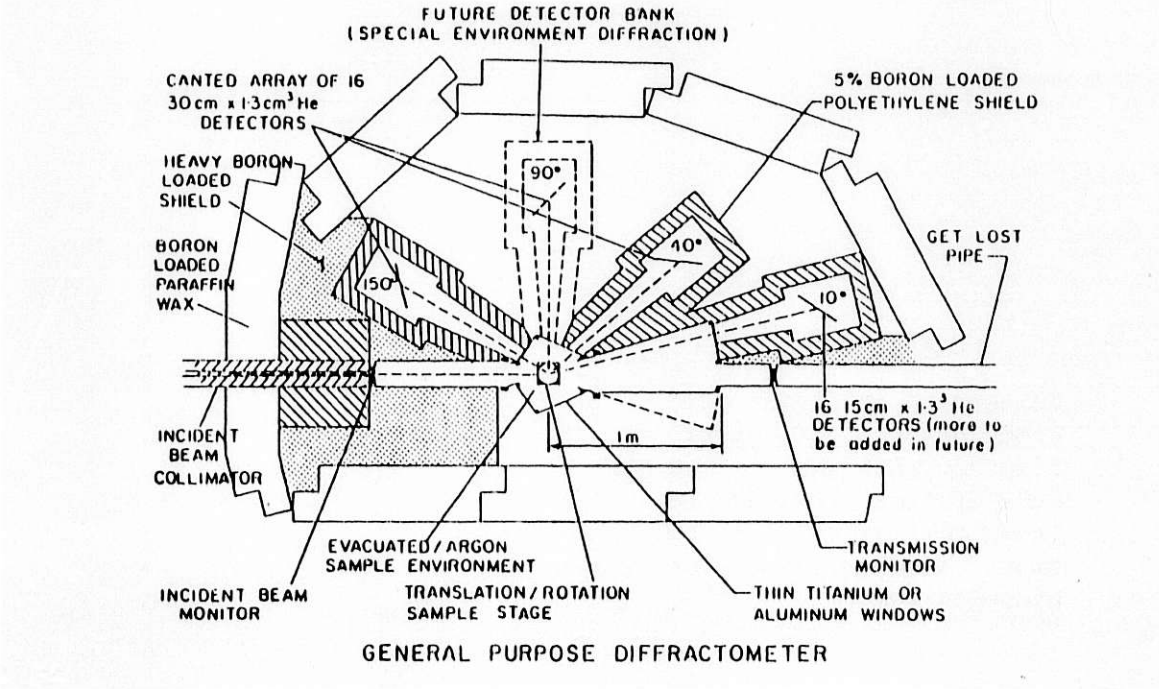

Fig. 8. Layout of the general purpose diffractometer. The sample position is at 10m from the source. The 150° bank provides .45% resolution powder diffraction. The 40° and 10° banks are for liquids diffraction. The evacuated/argon sample environment is under construction.

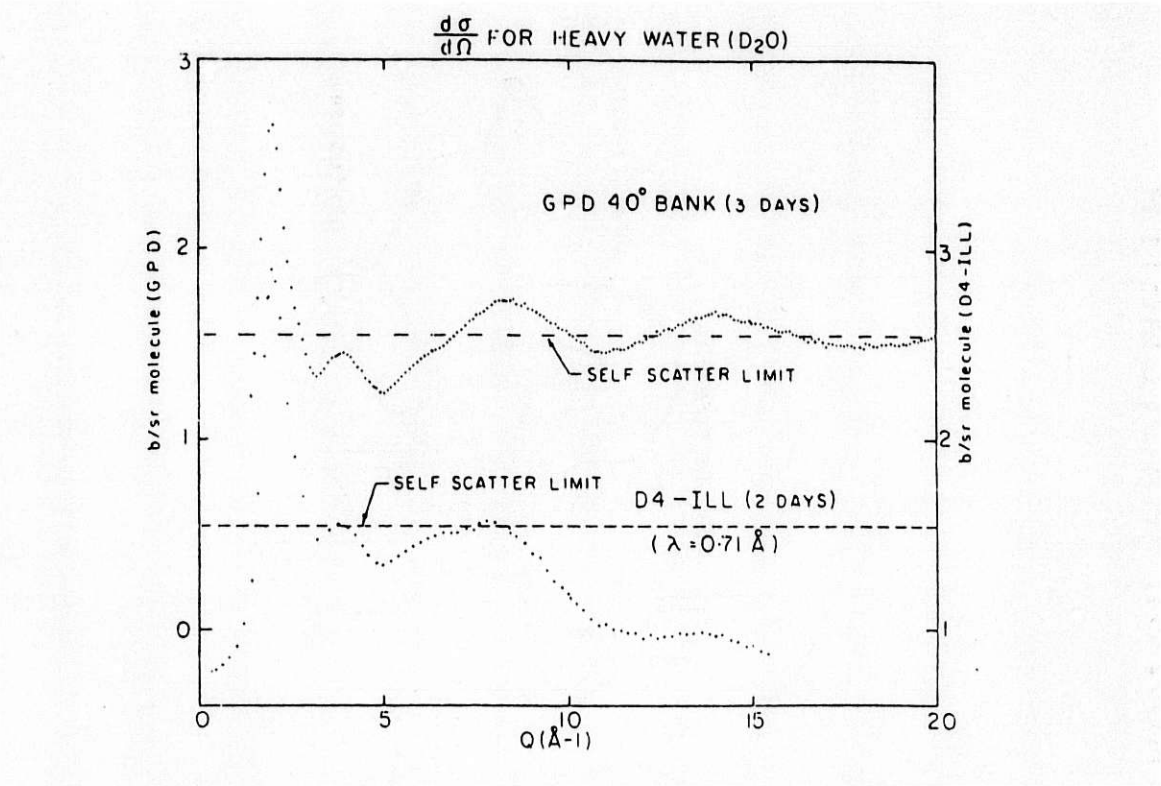

Fig. 9. Comparison of the performance of the GPD at the WNR with the D4 instrument at the ILL. Because inelasticity effects are minimized by reaching high Q with epithermal neutrons at low angles, the GPD results are much closer to the self scattering static limit than the D4 results. Note also the competitive statistics and larger Q range obtainable.

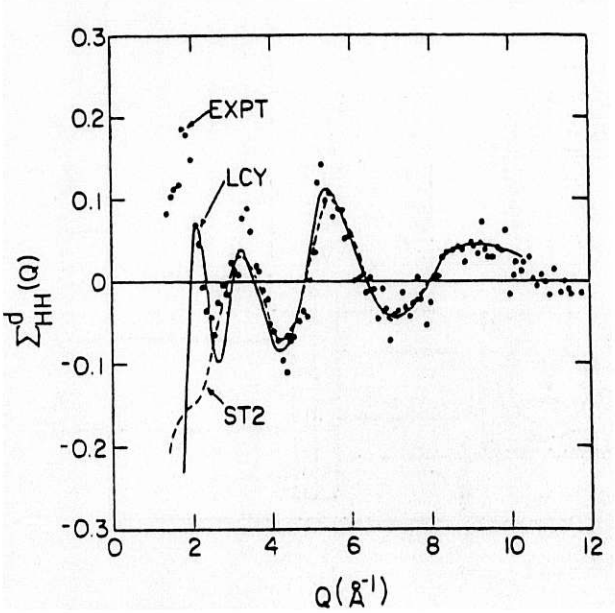

Fig. 10

Distinct hydrogen-hydrogen cross section for liquid water obtained at the WNR. Data are compared to molecular dynamics simulations of water structure using model potentials. LCY stands for Lie, Clementi and Yoshimine. ST2 is the result of Stillinger and Rahman. Data stop at 1.4A^{-1} due to frame overlap on the 40° bank at 120Hz. Data above 12A^{-1} are not shown because of poor statistics. Both problems will be reduced with PSR operation.

SINGLE CRYSTAL PULSED NEUTRON DIFFRACTOMETER

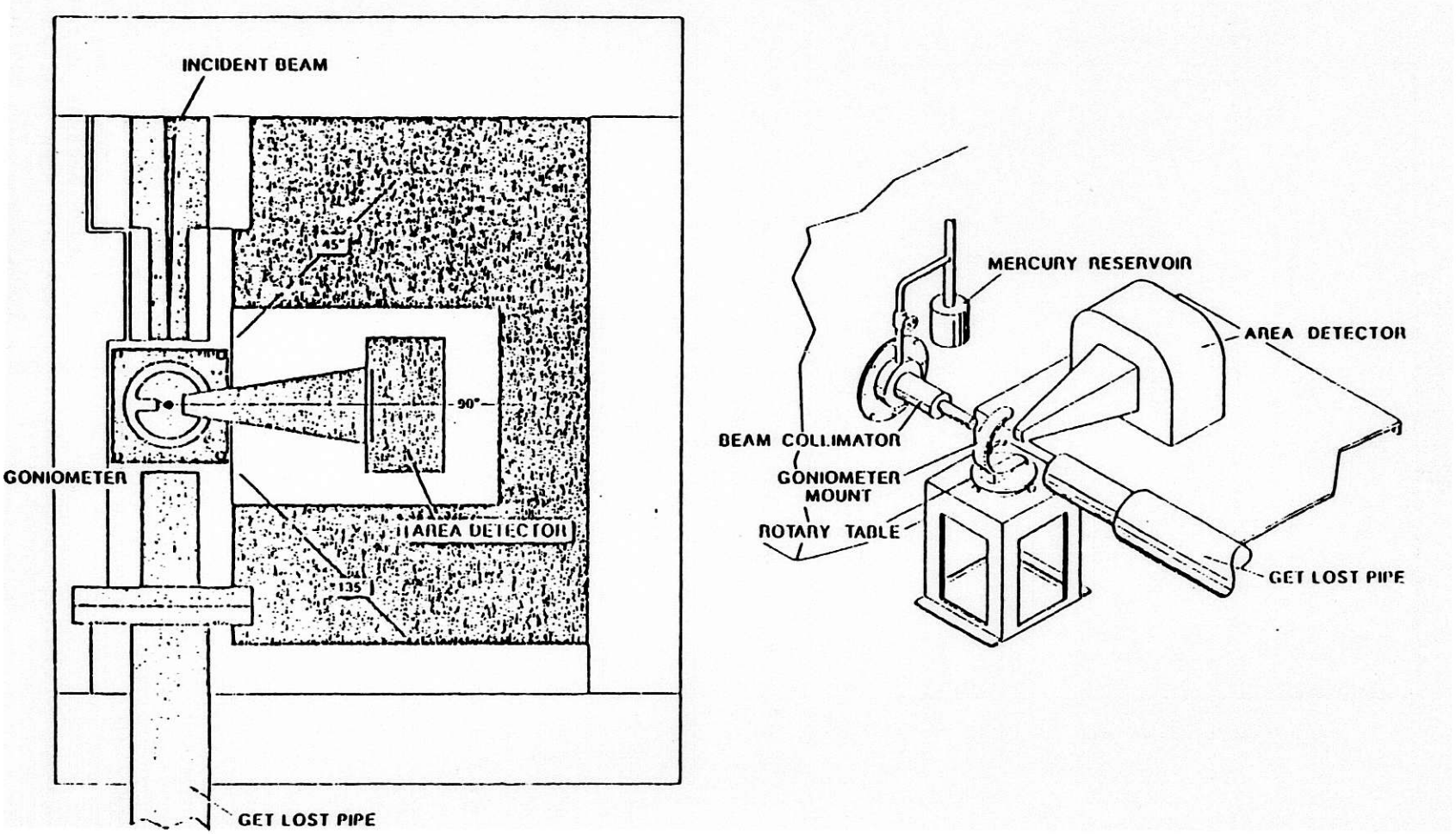

Fig. 11. Layout of the Laue-TOF single crystal diffractometer. The detector is a He^3 multiwire counter.

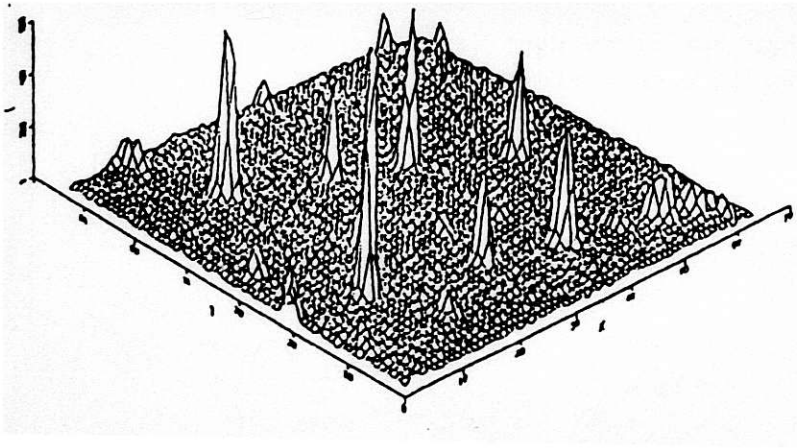

Fig. 12a. Intensity vs position on the area detector for a sapphire crystal with all time channels compressed.

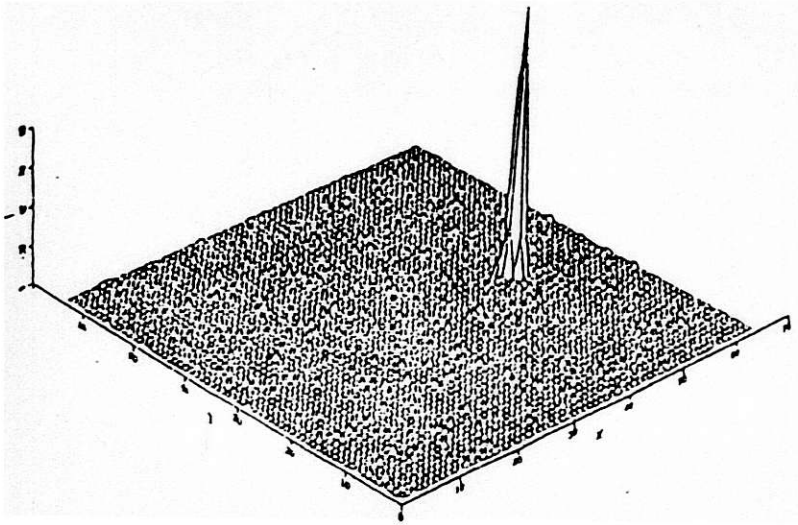

Fig. 12b. Intensity vs position on the area detector for a sapphire crystal and a single time channel.

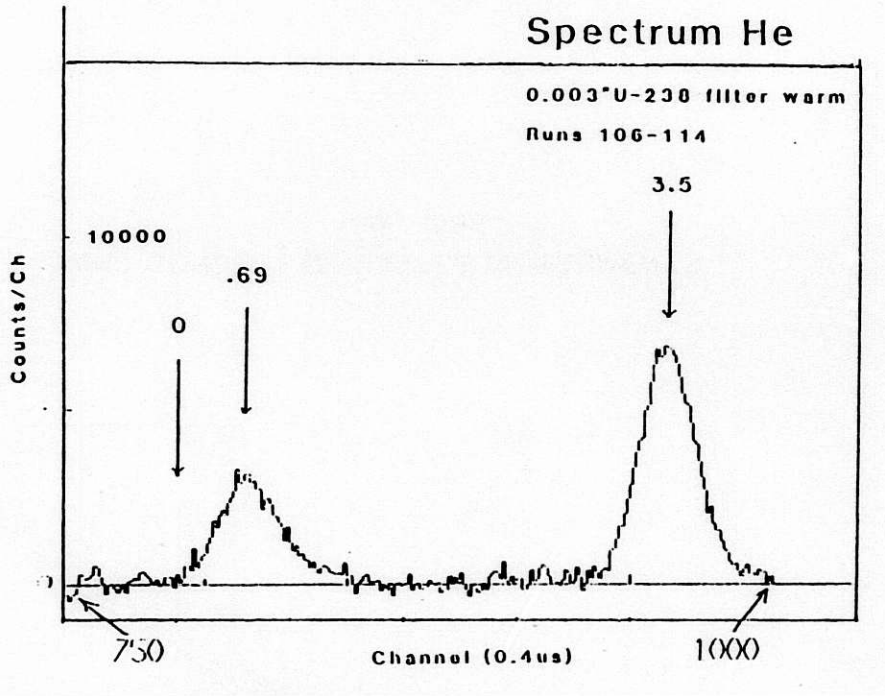

Fig. 13. Inelastic neutron scattering data on liquid He obtained with the electron volt spectrometer using a warm U^{238} filter with a resonance at 6.6 eV. The peak at 3.5 eV transfer is due to the He. The peak at .69 eV transfer is due to the Al container.

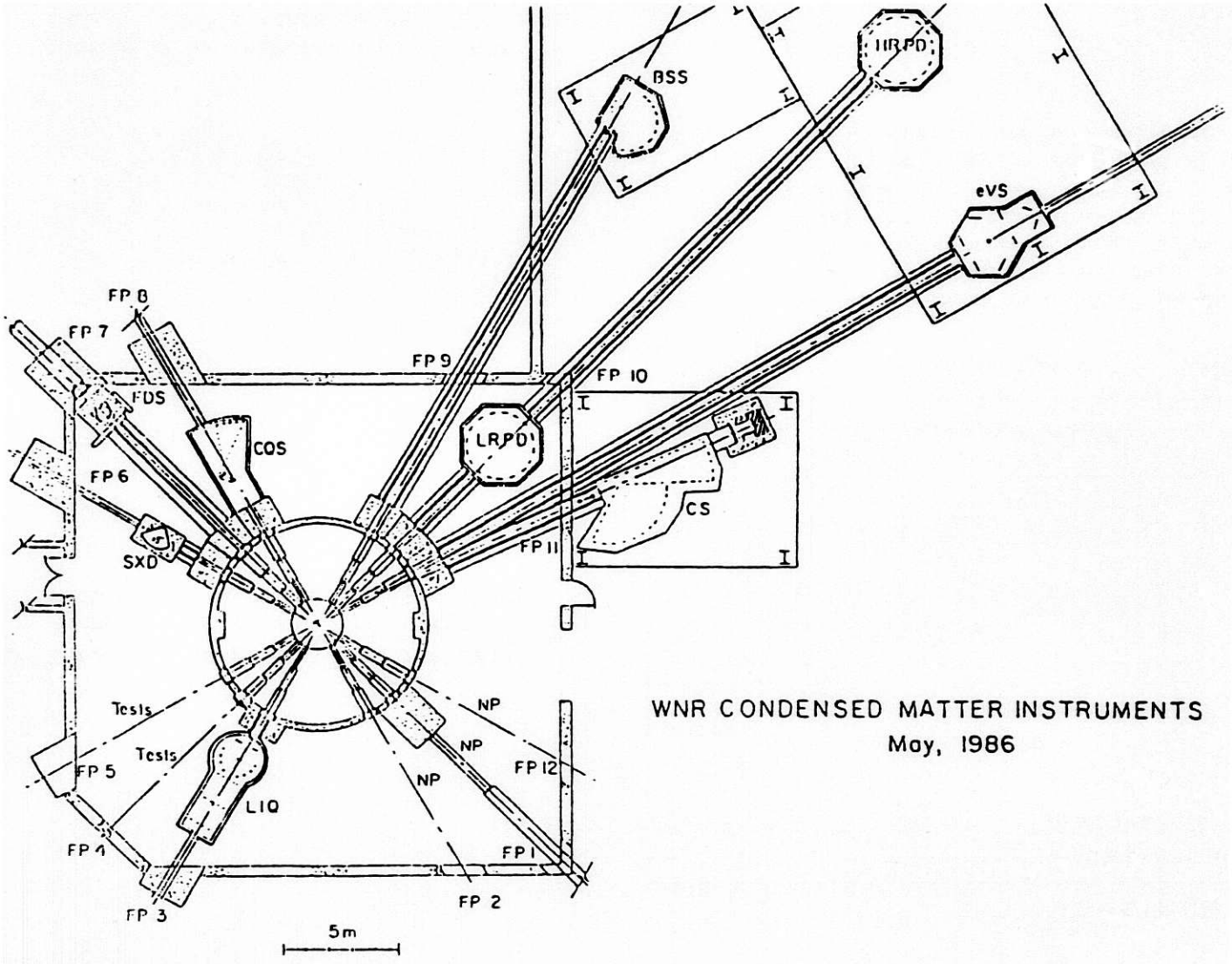

Fig. 14. Possible layout of neutron scattering instruments at the WNR in 1986 after the PSR begins operation. Labels are as in test.

J. Meese	Q	What are the milestones for construction of PSR?
R. Woods	A	All components should have been delivered in 1984 and construction complete in 1985.
J. M. Carpenter	Comment -	You may have been unfair to your results in comparing WNR diffraction data with that from BNL because the BNL background is in 2 dimensions whereas yours is in 3 as a TOF measurement.
A. D. Taylor	Comment -	Improving the shielding in a neighboring instrument (the Be filter) reduced the background in the single crystal diffractometer by an order of magnitude.
S. K. Satija	Q	What is the background like on the GPD?
A. D. Taylor	A	In this case the background arises from air scattering inside the GPD itself.
H. Wroe	Q	How long do you think you will take to work PSR up to full intensity?
R. Silver	A	About 1 to 2 years.

STATUS REPORT ON THE SIN NEUTRON SOURCE

Walter E. Fischer for
the Project Group
Schweizerisches Institut für Nuklearforschung
CH-5234 Villigen, Switzerland

1. OVERALL EXPERIMENTAL FACILITY LAYOUT

Figure 1 shows the proposed layout of the SIN accelerator system and experimental facilities following the installation of the Injector II. At present Injector I feeds the Ring Cyclotron with a 100 to 150 µA proton beam for routine operation. Injector II is designed to deliver a beam current of at least 1 mA. Ultimately the current should be further increased by a factor which at the present time is only vaguely known: Operational experience will in fact set the final limit.

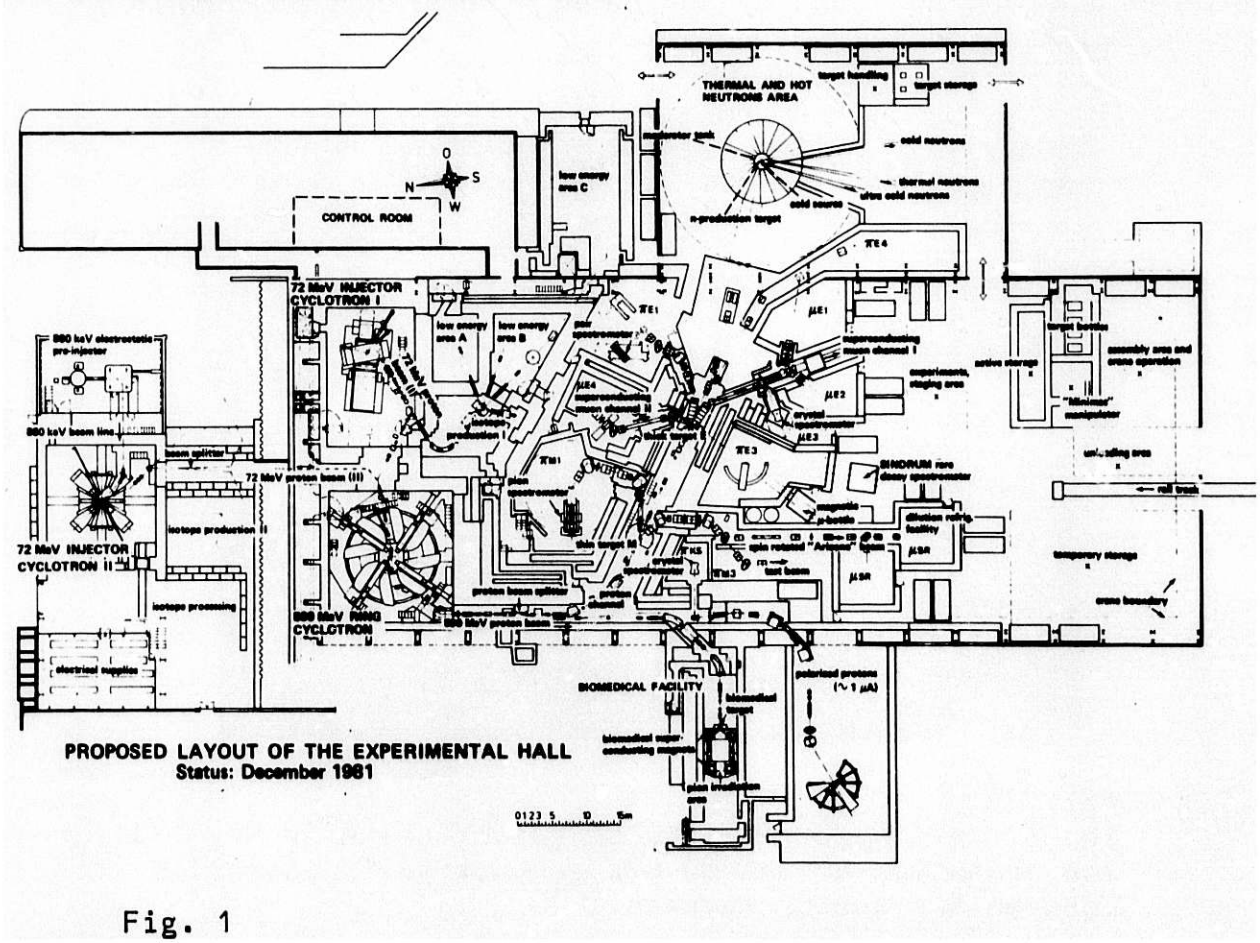

Fig. 1

The present status is as follows:

Injector II is under construction.

Improvement of the proton channel for high current operation is in the design stage.

The spallation neutron source design is progressing.

2. TIME SCHEDULE

First beam from Injector II is expected towards the end of 1983. During 1984 and 1985 the intensity limits will be explored. In order to accelerate a 1 mA beam in the Ring Cyclotron to 590 MeV; the RF-power has to be increased. The proton channel, including the meson target stations, need considerable improvement to allow full exploitation of this higher current. This task will now be accomplished during two long shutdown-periods, presumably those in 1984/85 and 1986/87.

The spallation neutron source, recommended by the Federal Science Council, and now approved by the Federal Schools Council, is scheduled for funding as from 1985.

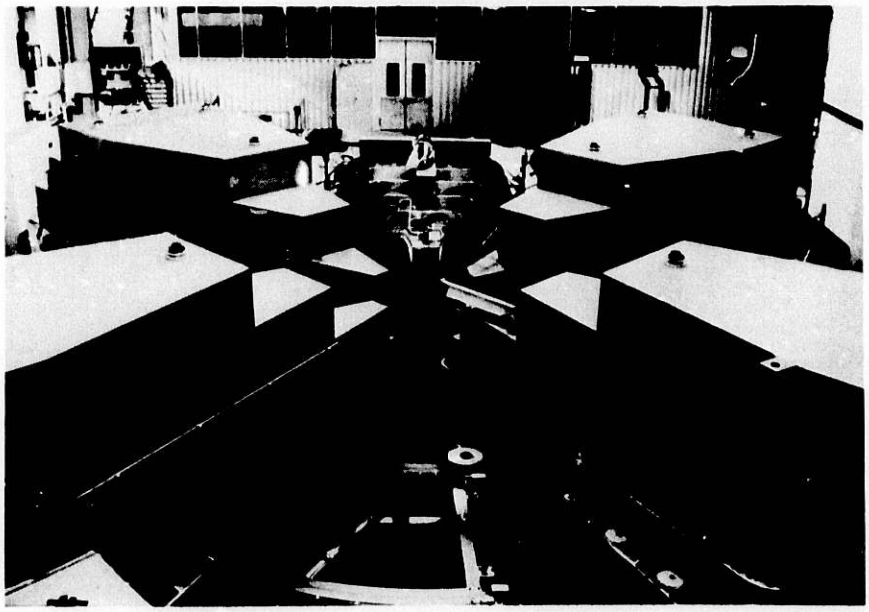

Fig. 2
The 72 MeV Injector II under construction in May 1981. The prototype of the 50 MHz-resonators is installed between two sector magnets.

3. INJECTOR II

This is a 72 MeV Isochronous Cyclotron, and is, in its principles, very similar to the 590 MeV Ring Machine. Figure 2 gives an impression during the state of construction. It will be fed by a 860 kV Cockcroft-Walton generator as a pre-accelerator.

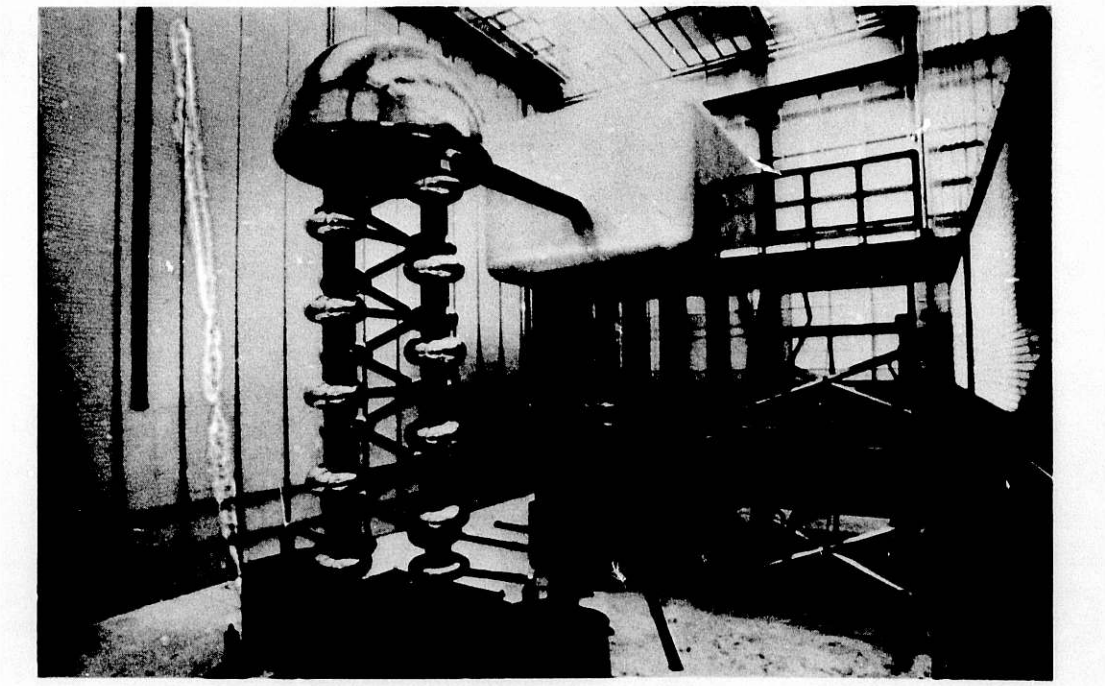

Fig. 3
View showing the main components of the 860 keV pre-accelerator: The Cockcroft-Walton generator designed for 900 kV (left) and the high voltage dome (right) which will house the ion source and the 60 keV beam line.

An artist's impression of the beam transport from the Cockcroft-Walton generator and the vertical injection system are shown in Fig. 4.

4. NEUTRON SOURCE

Among the different versions discussed at the last ICANS-meetings, we now prefer the arrangement with a vertical liquid metal target (beam injected from below) using natural convection as cooling mechanism. A cross section, showing the principle of this source type, is given in Fig. 5.

The design of a vertical Pb/Bi-target needs a rather careful investigation of the thermo-fluid dynamics which is driven by the

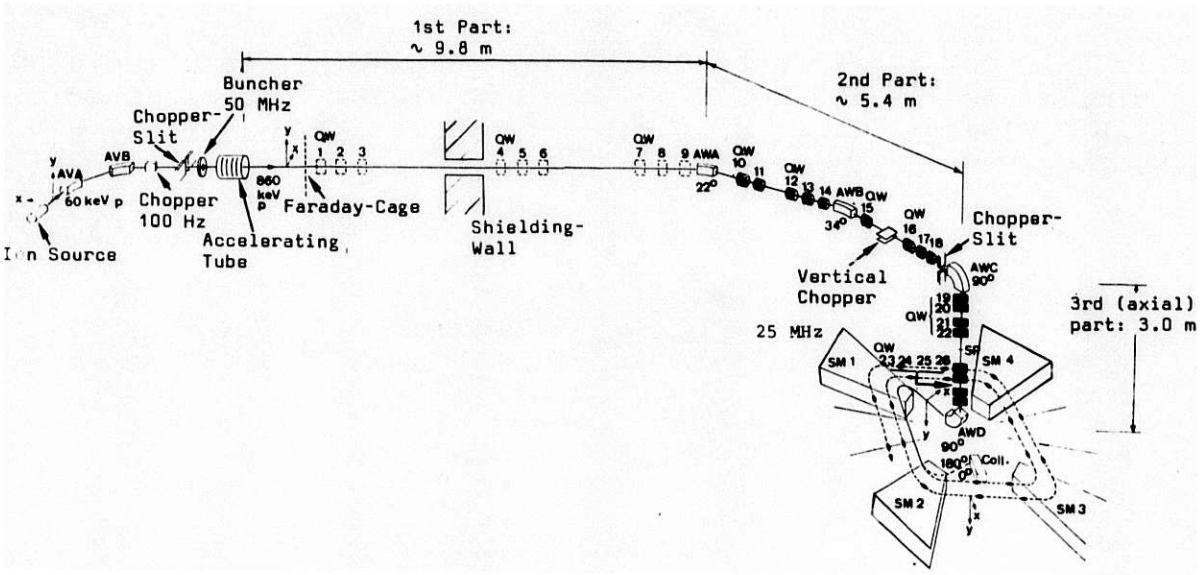

Fig. 4
Schematic presentation of the 860 keV beam transport system between pre-accelerator (left) and 72 MeV Injector II. The length of the horizontal section is 14.2 m (measured from the Faraday cage wall) whereas the length of the vertical section is 3.0 m.

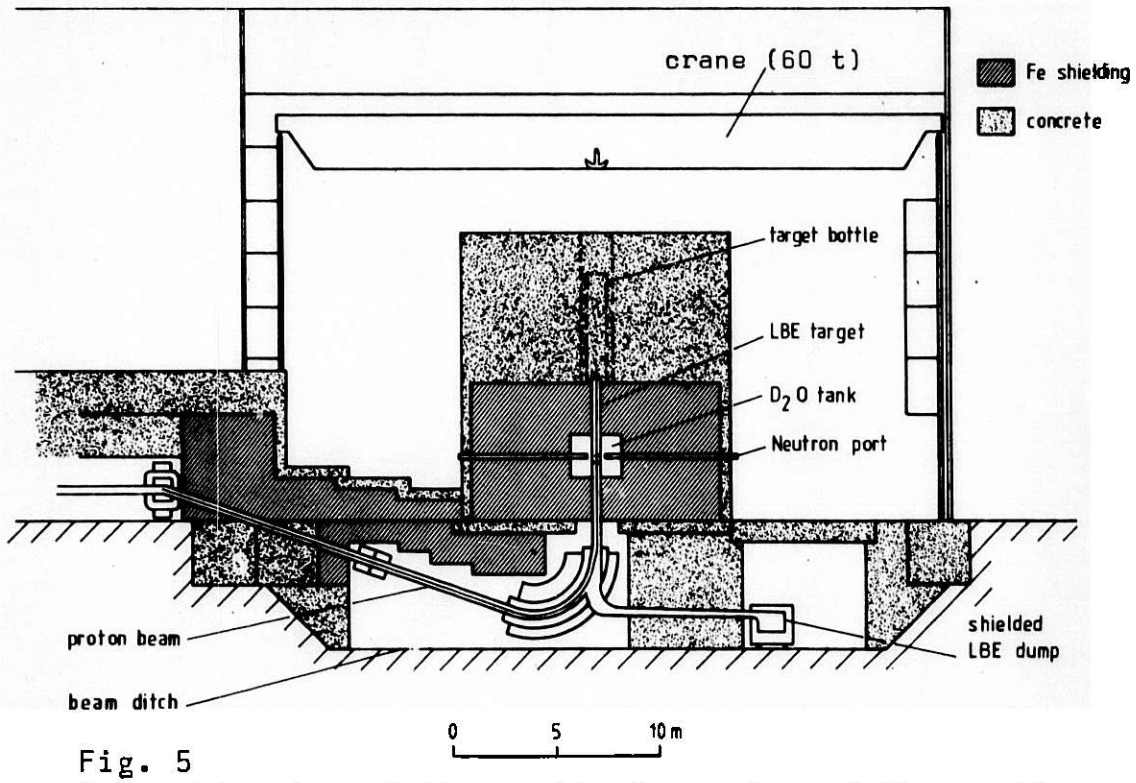

Fig. 5
Schematic view of the vertical version of the spallation neutron source. LBE = lead-bismuth eutectics.

buoyancy force caused by the heating of the lower part of the target by the proton beam. A program of work to study the behaviour of such systems theoretically and experimentally is under way. In Fig. 6 we show a typical set of flow-patterns and temperature distributions for some time sequence after switching on a beam. This subject will be treated in a special paper to this Conference [1]. Some effort is still needed to find the optimal configuration of the target for most effective cooling.

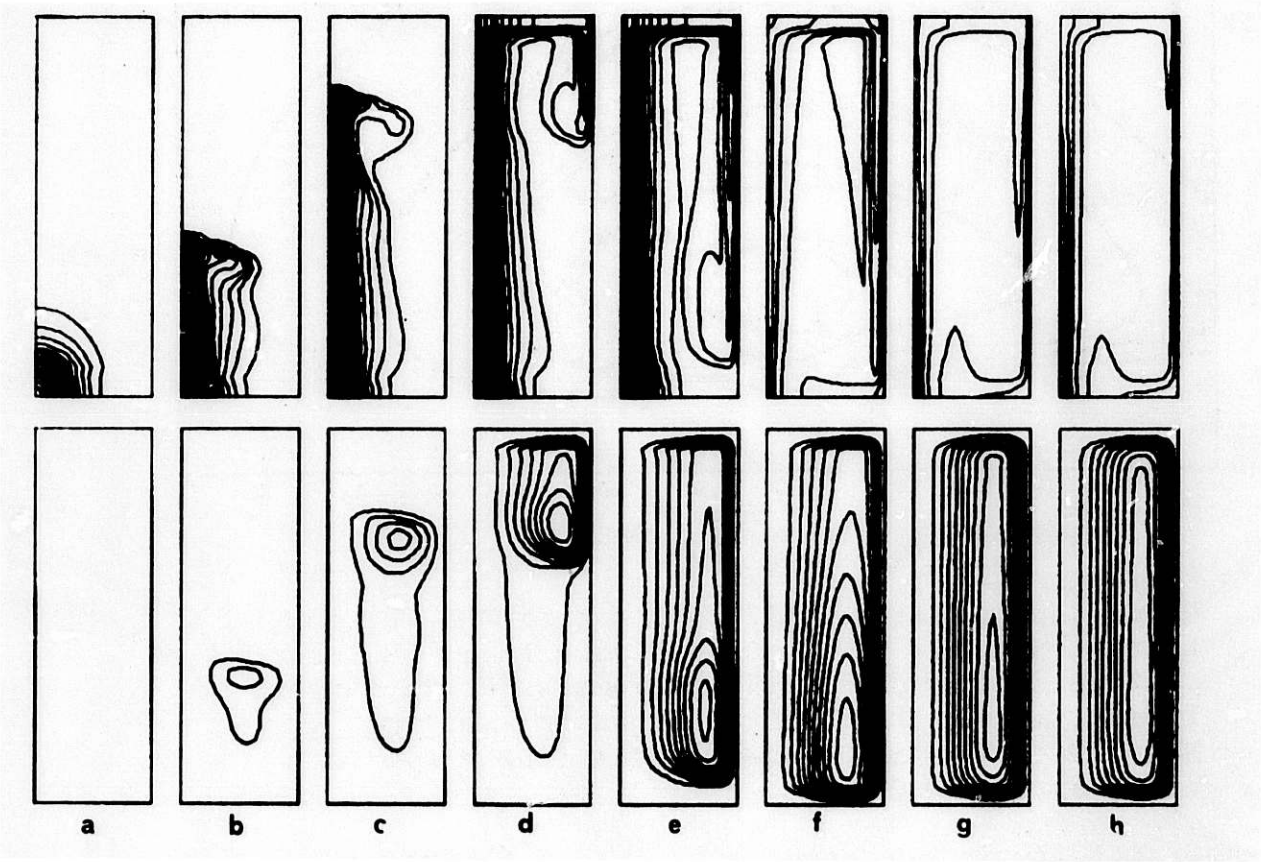

Fig. 6
Transient behaviour for 3 m target of 15 cm radius. Beam current is 100 μA. Contour-maps are for temperature (above) and stream function (below). For temperature contours, the lowest line is 3.1 °C above melting point, and line interval is also 3.1 °C. "a" is at 2.55 sec, and interval between two figures is 5.10 sec.

On the neutronics side, further measurements of flux distributions in moderators have been made by the Jülich-Karlsruhe-SIN collaboration. One of the flux maps, relevant to the planned SIN-source, is shown together with its comparison with a Monte-Carlo simulation (Fig. 7). This setup had an annular void gap between target and moderator. Other configurations and their comparisons are presented in another paper to this Conference [2]. By means of these flux distributions for thermal neutrons in the D_2O moder-

ator, we may find the optimal position of the cold source as well as the position and size of the beam tubes.

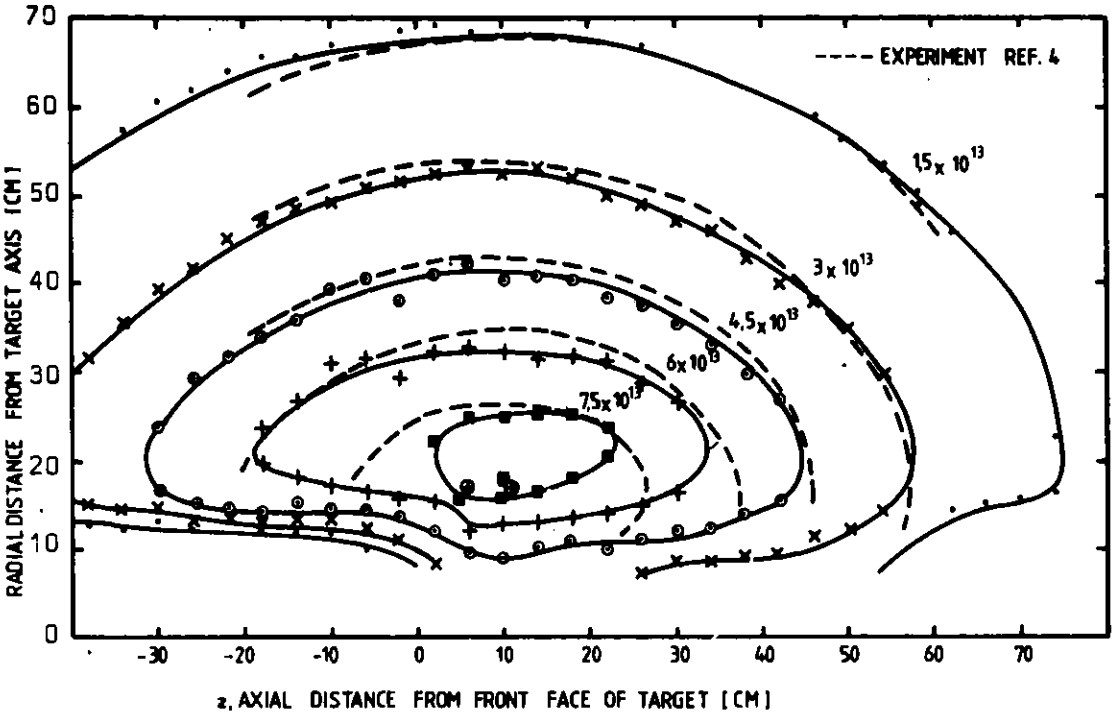

Fig. 7
Comparison of calculation and experiment for the thermal neutron flux in a D_2O moderator. 590 MeV protons incident on a 15 cm diameter Pb/Bi-target. Intensities in units of neutrons $cm^{-2}sec^{-1}mA^{-1}$. Measured ⊕ and calculated ■ peak flux = $8.6 \cdot 10^{13}$ neutrons $cm^{-2}sec^{-1}mA^{-1}$.

Further activity is concerned with the heat dissipation in the vicinity of the spallation target - a topic particularly important for the design of the cold source. Model calculations for an experimental setup at the TRIUMF-source have been done for several sample materials. The results are presented in a third paper to this Conference [3]. The experimental run is scheduled at TRIUMF for November 1982.

5. ACTIVITIES FOR THE NEAR FUTURE

Below we give a list of experimental activities planned to be realized during the second part of 1982 and in 1983:

(i) Irradiation tests of window materials at LAMPF.

(ii) Heat dissipation measurements in the vicinity of a spallation target. This experiment will be done at TRIUMF in collaboration with KFA-Jülich.

(iii) Model experiments for thermo-fluid dynamics of the liquid metal target
a) water model
b) Pb/Bi model

(iv) Mock-up experiment at the SIN proton beam for tests of several configurations of cold sources; in collaboration with KFA-Jülich and TU-Munich.

6. INSTRUMENTATION

A list of spectrometers to be installed at the source has been given at ICANS-V. A recent reinvestigation among the present users in Switzerland of neutron scattering facilities has not changed this situation.

Presently there are five neutron spectrometers at the reactor "Saphir" fully booked up. Furthermore, spectrometer time abroad - mainly in Grenoble and Risø - is used by Swiss groups. According to the investigations there will be requirement for about twice the present number of spectrometers in future. In this sense, the SIN spallation source may be exploited by experiments of our own research groups.

International participation in the experimental program, especially at the guides for cold neutrons, where some spare time is likely to be available, is however strongly urged.

REFERENCES

[1] Y. Takeda, Thermofluid Dynamics of the Liquid Lead-Bismuth Target for the Spallation Neutron Source at SIN, These proceedings

[2] F. Atchison, W.E. Fischer and B. Sigg, Some Aspects of the Neutronics of the SIN Neutron Source, These proceedings

[3] Monte Carlo Study of the Energy Deposition of a Flux of Spallation Neutrons in Various Samples, These proceedings

SIN - W. Fischer

D. A. Gray	Q	Will you have space charge problems in the 860 kV beam in injector??
W. Fischer	A	Yes we probably will. That's why we've allowed 1-2 years to work up. The 40 eV beam from the source has been operated at full intensity space charge neutralisation occurs when argon at 10^{-5} Torr is the background gas.
A. Carne	Q	Have you integrated the flux to get the neutron yields?
W. Fischer	A	Yes and we also have other estimates at yields. We think there will be 10n/proton at 590 MeV.
H. Wroe	Q	How many hours a year will you run?
W. Fischer	A	We haven't got an exact figure yet, but the neutron source parasites on the main machine which has only one long shutdown of 1 month in a year.

ICANS-VI

INTERNATIONAL COLLABORATION ON ADVANCED NEUTRON SOURCES

June 27 - July 2, 1982

INTENSE PULSED NEUTRON SOURCE (IPNS) AT ARGONNE NATIONAL LABORATORY (ANL): A STATUS REPORT AS OF JUNE, 1982

J. M. Carpenter, C. W. Potts and G. H. Lander

Argonne National Laboratory, Argonne, Illinois 60439 U.S.A.

ABSTRACT

In this status report a general overview is given of the IPNS program. The facility has been operating since August 1981 and in a routine way for outside users since November 1981. The accelerator performance has been exceptional. Most instruments are now operational, or nearly so. For details of the individual instruments and experimental program the reader is referred to papers later in these Proceedings.

Paper to be published in an Argonne National Laboratory Internal Report as part of the Proceedings of the International Collaboration on Advanced Neutron Sources (ICANS-VI) held at ANL, June 27-July 2, 1982.

INTENSE PULSED NEUTRON SOURCE (IPNS) AT ARGONNE NATIONAL LABORATORY (ANL): A STATUS REPORT AS OF JUNE 1982

J. M. Carpenter, C. W. Potts, and G. H. Lander
Argonne National Laboratory, Argonne, Illinois 60439

1. INTRODUCTION

The Intense Pulsed Neutron Source (IPNS) has been operating since October 1981. The performance of the accelerator has been exceptional. From November 1 to May 5 it delivered protons for a total of 2175 hours at an average current of 8 μA and an operating efficiency of 88%. In this period of time some 80 experiments have been run at IPNS. Details of some of these will be found in the individual instrument papers. Figure 1 shows the layout of the experimental facilities. At this time three beams are unassigned, although two of them are being temporarily used for radiation damage experiments. As will be discussed in more detail, we now have 6 operational scattering instruments, 2 instruments in the testing stage, and 3 special experiments that are being set up on the neutron beams. Two cryogenic fast neutron irradiation facilities are operating.

2. IPNS-I ACCELERATOR SYSTEM

At the time of the ICANS-V meeting, the Rapid Cycling Synchrotron (RCS) was just in the process of turning back on after a lengthy shutdown for apparatus improvement and for relocation of the extraction components to deliver the proton beam to the IPNS-I targets. A report[1] at that conference detailed many improvements and gave preliminary assessments of their value. Reference to the 1982 operating records in Table I below indicates the overall success of the improvement program.

TABLE I

ACCELERATOR OPERATING SUMMARY

	1980	(Nov-June) 1981-82
Operating Energy	300 MeV	400 MeV
Average Beam Current	4.72 μA	7.98 μA
Operating Efficiency	85.2%	88.0%
Scheduled Operating Time	2569.2 hours	2471.0 hours
Available Operating Time	2187.8 hours	2175.3 hours
Total Pulses on Target	1.98×10^{8}	2.17×10^{8}
Total Protons on Target	2.25×10^{20}	3.60×10^{20}

The accelerator turned on in April of 1981 and made some brief tests with the proton beam to assure that no gross problems existed. RCS first delivered protons to the Radiation Effects Facility on May 5, 1981. First runs for neutron scattering instrument calibration began August 4. These runs were at a proton energy of 500 MeV. While average currents of 5 μA were achieved, reliability was poor and the continuity required for studies to increase the beam current was impaired by all too frequent operating interruptions.

The reliability problems were primarily in the charge storage cabling of the kicker magnet power supplies and in the rf system. The problems encountered were a type that took several million pulses to develop and the limited prior running had not revealed them.

400 MeV Operation

A decision was made at that time to operate temporarily at a proton energy of 400 MeV to allow the accelerator some time to sort out its problems. This was consistent with the experimenters needs also since lower electrical power costs allowed more running time for instrument development and the powder diffractometers, the workhorses of the early IPNS-I program, were quite effective with the neutrons available at 400 MeV.

The summer test running of the RCS had convinced the operators that the intensity dependent high energy beam instabilities that had previously plagued the RCS were not related to betatron tune and were not correctable

with the new programmable optupoles.[2] Evidence indicated that the instability depended on rf voltage amplitude and at that time it was felt that enough additional protons could be accelerated at 400 MeV with better reliability to more than make up for the decrease in neutrons per proton at 400 MeV. The improvement in beam current and reliability shown in Figures 2 (a) & (b) during 400 MeV operation dramatically indicate the correctness of this assumption.

Reliable operation has allowed the accelerator crews the time to attack specific problems of the operation with gratifying results. The kicker cable problems were found to be the result of faulty cables and consultation with the manufacturer helped straighten these out. Modifications were also made in the terminating resistors to allow lower voltage operation. The rf problems were quite varied in nature but are now under control. Very early in the 400 MeV running period improvements were made in the beam phase feedback system which moved the beam intensity instability threshold from about 1.4×10^{12} protons per pulse to over 2×10^{12} protons per pulse (at 400 MeV). Machine studies have been done at 450 MeV with the accelerator easily achieving an extracted beam current of 8 μA.

Plans are to increase the energy to 450 MeV in September, evaluate the effectiveness of operation at this energy for 2-3 months, then begin operation at 500 MeV if no new problems develop at 450 MeV.

Chopper Controlled Operation

Almost all the RCS operation has been carried out with the entire accelerator timing system under control of a crystal oscillator. This oscillator also provides timing reference to one or more neutron choppers. Some of the accelerator modifications to permit this type of operation have previously been described.[3] Since all the accelerator power supplies have a voltage ripple which is synchronized to the power line, chopper controlled operation tends to be more unstable and lossy than power line synchronized operation. Accelerator personnel have continuously worked to decrease this instability so that chopper controlled operation is just as free of proton loss as line synchronized operation.

One of the approaches phase locked the chopper motor to the power line with a very slowly responding circuit. This provided significant improvement in accelerator performance and is acceptable to the chopper user as

long as only one chopper is in use. This method is not acceptable for the more general case of several choppers in operation each with different moments of inertia, since only one can be in control of accelerator proton extraction timing. As of this writing, the accelerator runs quite cleanly under chopper control, but still requires a lot more operator attention than line synchronized operation.

Present Status

The accelerator has now operated in a production mode for 22 weeks and performance has exceeded expectations. A most vital ingredient required to make this a production facility has been control of the proton losses in the accelerator tunnel. This has been partially accomplished by added diagnostics, some of which automatically shutdown faulty operation. While Table I tells the success story of the IPNS-I accelerator, some other points are worth noting. The accelerator has reached peak currents of 11.2 μA for short periods under acceptable operating conditions and 24 hour averages of 10 μA. Accelerator study periods have produced 2.4×10^{12} protons per pulse at 5 Hz. The limiting component of the system is now clearly the H^- ion source. The synchrotron and linac can efficiently handle all the H^- current presently available, at least at 400 MeV. It may be possible to edge the average current up to 10 μA with the present source, but that will be about the limit.

Stripping foils have been something of a problem since they have to be replaced about every 5 million pulses. A new foil must be conditioned for about 4 hours at reduced current. This significantly reduces average current so that we are considering better foil materials.

Future Plans

Machine studies have revealed no serious injection space charge problems with 3×10^{12} protons injected. The operating ion source provides such beams at 5 Hz but at 30 Hz only about 2.2×10^{12} can be delivered regularly to the synchrotron. This source produces a current of 15 mA at an energy of 750 keV. Linac personnel have adapted a 15 Hz Fermilab magnetron H^- source to run at 30 Hz. This new source reliably produces 40-50 mA H^- beams at 32 Hz on the test stand. Plans are to install this source about March of 1983.

While we cannot fully evaluate the RCS capability with the present ion source, we believe it should be possible with the new ion source in operation

to get the average current up to about 12 μA without any further significant changes in equipment. Added rf voltage will probably be required to increase the beam current above 12 μA. With some compromise in rf reliability, about 10% more voltage can be achieved with the present cavities. A third rf system is actively being considered as a major future improvement.

3. TARGETS AND MODERATORS

The IPNS Zircaloy-2-clad uranium targets have been in use in both the Neutron Scattering Facility (NSF) and the Radiation Effects Facility (REF) since startup time. Completely-assembled tantalum targets are available for both facilities, as are spare uranium target assemblies. We have not yet used either. The targets and (independent, interchangeable) cooling systems have operated completely trouble-free, and according to design expectations.

The uranium targets consist of eight, 25-mm-thick, 100-mm-diameter uranium-alloy disks, clad with 0.5-mm Zircaloy-2, (1.5 mm on circumference) cooled by light water flowing in 1-mm channels between disks. Disks 1,3,5, and 7 contain small, steel-sheathed thermocouples in Zircaloy wells at their centers.

The entirely-conventional cooling systems have two loops; the primary loop contains a helium-gas-covered surge tank with hydrogen recombiner, filters, ion-exchange column, the pump and heat exchanger. Radiation monitors near the exchange column detect gross changes in radiation levels, which are primarily due to positron-annihilation and nitrogen-16 gammas. Periodic sampling and gamma-ray spectral analysis of primary water and cover gas gives us the most sensitive, longer-term indication of trouble such as a breach of cladding. Normal gas and water samples contain isotopes identified as spallation and activation products of 300 series stainless steel, Zircaloy and water. No excess hydrogen is evolved, gratifyingly contrary to ZING-P′ experience.

The target temperatures behave according to design, with disk 1 centerline temperature rising approximately 14 degrees C above coolant temperature, per microamp of 400 MeV protons on the NSF. The temperature in the REF is somewhat higher, presumably due to sharper focussing of the proton beam.

We have measured the transient temperature response of the uranium

disks: they respond to proton beam intensity variations in a fashion described by two time constants, 6.7 and 2.1 sec, in accordance with calculations. (Measured thermocouple response times are less than about .5 seconds.) Thus even beam power fluctuations on the times scale of 10 seconds give fully-reversed thermal stress cycles. (We identified cladding thermal stress cycling fatigue as the mechanism of failure of our targets at the original design current of 22 microamps, 500 MeV.) At 8 microamps proton current, we are operating at stresses just below the level of infinite fatigue cycle lifetime.

The shielding provides general background levels of .5 to 1. mrem/hr, at 8 microamps of proton current. We find exceptions up 3. to 10. mrem/hr in locations close to the neutron beam tubes at the shield face. At the shield top, where a corner of the central iron shield has no concrete shielding (an unoccupied area), we find several hundred mrem/hr, which we have attributed to 25 keV "iron-window" neutrons. Near the LRMECS chopper, shielded with only 30. cm of hydrogenous material, the dose rate is about 25 mrem/hr with 8 microamps of protons on the target. The beam stops are quite simple; we use second-hand shipping casks and reactor beam stops about which we admit we know little. Unmodified, these bring the dose rates down to levels of about 1 mrem/hr, except in the case of LRMECS, where we added 30. cm of iron in the beam direction to accomplish this level.

We have not yet installed the cryogenic moderator system, which originally was to consist of two liquid methane moderators at approximately about 100 Kelvin, and two liquid hydrogen moderators at approximately 25 Kelvin. This was due to problems of time dependent and static differential thermal contraction, material flaws, thermal shorts in the cryogenic heat exchangers, and some central instabilities. We have now repaired the moderator and reflector assembly, and will circulate liquid methane in all four moderators. We expect to be operating with the cryogenic moderator system beginning with the start-up this October.

Meanwhile, since startup of the NSF, we have used a system consisting of three ambient-temperature polyethylene moderators, with inner graphite and outer beryllium reflectors, and cadmium decoupling and void liners throughout. (In this temporary assembly, we provide no vertical beam moderator.) The assembly is uncooled. Figure 3 illustrates the temporary assembly.)

We have measured epithermal beam currents from each of the temporary moderators. The table compares the results of these measurements with Monte Carlo calculations for the beryllium-reflected, cryogenic moderator system.

		Epithermal Neutron Beam Current $EI_p(E)_{1\ ev}$, n/s-μA-sec		
Beam	(Instrument)	Calculated for	(Material)	Measured
H-1	(SCD)	$3.25 \pm .56 \times 10^{10}$	(CH_4)	$3.42 \pm .1 \times 10^{10}$
C-1	(SAD)	$2.09 \pm .38 \times 10^{10}$	(H_2)	$0.129 \pm 0.4 \times 10^{10}$ (a) $1.71 \pm .5 \times 10^{10}$ (b)
F-5	(SEPD)	$2.95 \pm .50 \times 10^{10}$	(CH_4)	$2.91 \pm .1 \times 10^{10}$
F-2	(GPPD)	$3.26 \pm .54 \times 10^{10}$	(CH_4)	----------

(a) As measured, with effect of collimation.

(b) Corrected for collimation by ratio (Moderator area viewed through collimation/(Total moderator area).

The proton energy for the measurements was 401 MeV. That assumed in the calculation was 500 MeV. The results contain several surprises. First, that the measured and calculated intensities for most cases are in agreement, even though the proton energies are different. Measurements should be lower than calculation by a factor of about 1.36, the ratio of neutron yields, on this account. Second, we expect the present, temporary assembly, to be significantly inferior to the Be reflected CH_4 assembly, especially on account of degeneration of the polyethylene due to irradiation. The proton current normalization was from the toroid nearest the target.

4. NEUTRON SCIENCE

(a) Instruments

The instrumental parameters are specified in Table I. More complete descriptions of most of these instruments appear in later sections in this proceedings. What we shall do here is briefly outline the classes of instruments and their fields of study.

Powder Diffractometers

From the first prototype spallation source up to the present day it has been clear that these machines would open up new areas of research. There are two powder diffractometers at IPNS, as the table indicates, and both are fully operational. There are two primary reasons for this; first the abundance of epithermal neutrons has allowed measurements out to much higher Q values, possibly up to ~ 100 Å^{-1}, and secondly, the short pulse width, together with long flight times has allowed new standards of resolution to be attained. For example, both instruments have a resolution of $\Delta Q/Q \simeq 0.003$, which is independent of Q. At the present time three main areas of study have been pursued: (i) Structural work. At present the heaviest demand is for this area, and since a data set can be collected from a reasonable (~5g) size sample in ~24 hrs the machines service a good number of users. In fact about half our present users fit into this category, although this may be misleading as not all our instruments are fully operational. What is of great importance is that the software package for handling this data is "on-line" at ANL. FORTRAN software for the display and analysis of time-of-flight (TOF) neutron powder data from the powder diffractometers is operational on our IPNS-dedicated VAX 11/780 computer. At the heart of this software package are the routines TOFPRP and TOFLS (written by R. B. von Dreele of Arizona State University and used extensively at Argonne over the past 2-½ years) which perform full-matrix least-squares refinement of crystal structure and peak shape parameters (Rietveld analysis) based on powder data. Programs to determine Bragg reflections for a given structure, to calculate Fourier syntheses, to calculate distances, angles and associated standard deviations from refined structures and to illustrate the atomic arrangement of a given structure have been adapted for use in this package. A user's guide to the Rietveld analysis of powder data at IPNS is in preparation. Users who have stayed an extra day or two after data collection have been able to leave with nearly complete Rietveld refinements. In addition, we are running a short course on Powder Diffraction and Rietveld Analysis at ANL from July 13-16, 1982.

(ii) Glasses, liquids and amorphous systems. For these studies the high Q capability is particularly important and this has already been exploited in a study of P_xSe_{1-x} glasses by Misawa, Price, and Susman. Another interesting

application of the powder diffractometers was in determination of the magnetic scattering from an amorphous ferromagnet $Fe_{0.82}$ Y $B_{0.18}$ by Guttman, et al. Here the experimenters used banks of detectors placed symmetrically left and right of the incident beam, and applied a magnetic field $\vec{H}$ so that for one set of detectors $\vec{Q} \parallel \vec{H}$, and for another $\vec{Q} \perp \vec{H}$. Under these conditions the magnetic scattering appears in the $\vec{Q} \perp \vec{H}$ detectors only and can be separated out. Note that with the time-of-flight method this condition is true for all $\vec{Q}$.

(iii) Measurements of residual grain interaction stresses in deformed alloys. MacEwan et al have exploited the high resolution at all Q values to observe the shifts of individual peaks after materials have been permanently strained. They estimate that residual bulk strains of order 10^{-5} can be detected using the high resolution configuration.

Single-Crystal Diffractometer

This instrument, based on the wavelength-resolved Laue method, uses a 30 x 30 cm position sensitive ^{6}Li-glass scintillation detector developed by M. G. Strauss and others in the Electronics Division at ANL. The smaller-scale prototype built up at ZING-P′ was the first of its kind. As this technique is capable of viewing large portions of reciprocal space it has a wide variety of potential applications. The first experiments have concentrated on crystallography and the crystal structure of $Mn(CO)_3$ $(C_6H_8CH_3)$ at 25K was solved by a joint group from ANL and the University of North Carolina at Chapel Hill. The low-temperature structure was solved independently by direct methods - to our knowledge, the first such case with time-of-flight data.

Other types of experiments which are being performed with this instrument include searches for diffuse scattering, satellite peaks, and superlattice reflections. The versatility of the instrument is certain to make it particularly attractive for these latter studies. There are a few small difficulties still to be worked on, for example, involving dead time and minor aberrational effects and fast neutron background when the minimum wavelength is below ~0.6Å. However, the instrument is clearly operational and we expect these problems to be overcome and new uses to emerge.

Small-Angle Diffractometer

The SAD is another recently-developed instrument. As such, one expects to encounter new challenges, and the most difficult one is to diminish the background scattering from fast neutrons. The instrument has a 2-dimensional gas-filled proportional counter that sits directly in the incident beam, but the background is now a factor 10^6 lower than the direct beam flux. At present the minimum usable Q is limited to ~ 0.02 $\mathring{A}^{-1}$; however, once the cold moderator is installed, the Q range will be 7×10^{-3} to 0.35 $\mathring{A}^{-1}$. Experiments are being conducted on both metallurgical as well as biological samples, and we expect to receive proposals for this instrument for the first time in September.

Chopper Spectrometers

The inelastic scattering experiments at IPNS are of special interest because they attempt to exploit in a direct way the high epithermal flux, which is a unique capability of spallation sources. Both these machines run in the so-called 'direct' geometry, i.e. the incident energy E_o is defined. So far runs have been made with E_o = 160 and 500 meV.

The Medium-Energy Chopper Spectrometers at IPNS are designed for inelastic scattering experiments over a wide range of energy transfer (0-500 meV) and momentum transfer (0.1-20 $\mathring{A}^{-1}$). The high-intensity, low-resolution instrument (LRMECS) has been operating for several months and experiments approved by the Program Committee are underway. Measurements of the vibrational densities of states of amorphous SiO_2 and amorphous P have been completed. The electronics for the phasing of chopper and accelerator have been improved and the time in which the accelerator-chopper phase relationship is acceptable ($t_o - t_c < \Delta T_c$, typically 2 μsec) is now essentially 100%.

The second chopper machine (High resolution medium energy chopper spectrometer, HRMECS) is now installed and initial tests have been run. Of particular importance is that we are able to run two choppers simultaneously, which presents a complex phasing problem since only one chopper can be used to trigger accelerator extraction. Tests have now shown that two (or more) choppers controlled by a fixed-frequency oscillator can be maintained in acceptable phase relationship with the accelerator.

As expected, the chopper spectrometers have been under great demand for experiments. At the last program committee meeting only 43% of the proposals

on LRMECS could be accommodated. Although this situation may get better when HRMECS comes on line, the low percentage reflects both the long time required for these experiments and the high interest.

The readcr is referred to the specific article on chopper spectrometers for further details of the experiments that have been performed and are planned.

Crystal Analyzer Spectrometer

This machine uses the 'inverse' geometry technique in which the final energy is defined by a cooled Be filter and focussed graphite crystals to be 3.6 meV. The time-of-flight technique is then used to determine the initial energy and thus the energy transfer is known. The CAS is being constructed primarily for studying vibrational modes at hydrogen in metals. The CAS can be used effectively for other studies such as vibrational densities of states and molecular spectroscopy.

(b) Radiation Effects Facility

The Radiation Effects Facility (REF) at IPNS has been in operation since January 1982. Two fast-neutron irradiation positions operate independently at controlled temperatures between 4.2K and about 500 C. Neutron fluxes, energy spectra, and flux gradiants have been accurately determined in these 2 temperature irradiation positions. Secondary proton and gamma fluxes have also been measured and found to be within acceptable limits. The fast-neutron flux is typically 1 x 10^{12} n/cm^2-sec (E_n > 0.2 MeV) and has an energy spectrum quite similar to a slightly degraded fission-neutron spectrum. Computer controlled data acquisition systems for in-situ experiments are in use for the 2 temperature controlled irradiation positions. The REF is available for user's experiments approximately 1/4 of the total IPNS running, or about 6 weeks through the year. More details can be found in the specific article on the REF.

(c) Special experiments at IPNS

In addition to the experimental facilities described above that are open to the entire user community on an experiment by experiment basis, three proposals were accepted by the Program Committee in June 1981 for long-term assignment of beams. These are described briefly below. In each

case they represent a considerable effort, often collaborative with other institutions.

Nuclear magnetic ordering in ^{3}He at very low temperature

This experiment is designed to observe antiferromagnetic Bragg reflections from single crystals of solid ^{3}He below 0.001K. The facility is now in the final stages of assembly.

A vibration-free support structure to hold the cryostat has been completed and the dilution refrigerator has been installed at IPNS. In previous testing before this installation it cooled below 0.006K. The nuclear cooling stage is now being installed. The sample cell with a single-crystal silicon window is being leak tested.

Other necessary components such as filters, the chopper assembly, position-sensitive detectors, and shielding are now almost completed. Studies of solid ^{3}He crystal growth will begin soon, and the actual experiments later this summer.

Polarized Neutron Mirror at IPNS

An optical instrument is being installed for neutron reflection studies. The object is to determine the magnetic induction $\vec{B}$ (z) close to the surface of materials. In many instances $\vec{B}$ varies as a function of the distance z from the surface until it reaches a value $\vec{B}_0$ for the bulk. The goal is attained by measuring the spin dependent reflectivity of the neutron beam by the surface, since this quantity is related by optical laws to $\vec{B}$ (z). The perturbation of the magnetic induction at the surface is detected if significantly different from the bulk over a region not smaller than 5 Å, nor larger than 1000 Å.

A filtered neutron beam is reflected by a magnetized cobalt mirror. This reflects only the neutrons whose spin is parallel to the magnetization of the cobalt. The polarized beam is brought on the sample, which has a well-polished surface and is kept in a magnetic field paralled to that of the cobalt mirror. The neutrons are partially reflected by the surface of the sample; the reflectivity as a function of the wavelength is measured by a time-of-flight detector. The insertion of a flipping coil in the space between the mirror and the sample allows the reversal of the neutron spins

with respect to the laboratory magnetic fields; in this way the spin-dependent reflectivity of the sample is exactly identified.

The instrument is scheduled to start operating in June 1982. With an initial round of experiments devoted to the detection of the penetration length of an applied magnetic field in superconducting $ErRh_4B_4$, and the determination of the magnetic critical exponents at the surface of ferromagnetic nickel. The special environments for the samples are presently under construction.

Ultracold Neutron Experiments

The ultimate aim of this experiment is to measure the electric dipole moment (EDM) of the neutron as a test of time reversal invariance. A finite EDM would show failure of time reversal. We have demonstrated a practical system for producing ultracold neutrons (UCN) at high density from a pulsed neutron source using ZING-P′. We now need to show that we can hold these neutrons in a bottle for 100 seconds or so.

To do this we have (1) built a window that separates the bad vacuum of our source (a rapidly moving mica crystal which reflects 400 m/sec neutrons) (2) polished the surface of our bottle and (3) built pneumatically operated valves with minimum leakage to control the neutrons. We need a high flux of 400 m/sec neutrons to test the source and bottle and we hope to have this from the refrigerated moderator in IPNS.

To be competitive with other measurements of the EDM we need a density of about 10 UCN/cc stored in our bottle.

(d) Data Acquisition System

Ease of use, flexibility, and reliability were the primary goals in the design of the IPNS Data Acquisition System (DAS) and these goals have been met very well. Very little time has been lost through problems with the DAS and users have been able to begin using the system with a minimum of instruction. This is the first neutron scattering data acquisition system with the sophistication to do electronic time focussing on the fly, enabling the use of large detector banks in simple arrangements. The IPNS DAS includes a powerful and compatible host computer (a VAX 11/780) to permit rapid analysis of acquired data. This allows us to run an efficient user program despite the complex nature of the data. Outside users are usually able to complete most of their analysis before leaving the Laboratory if they are

with respect to the laboratory magnetic fields; in this way the spin-dependent reflectivity of the sample is exactly identified.

The instrument is scheduled to start operating in June 1982. With an initial round of experiments devoted to the detection of the penetration length of an applied magnetic field in superconducting $ErRh_4B_4$, and the determination of the magnetic critical exponents at the surface of ferromagnetic nickel. The special environments for the samples are presently under construction.

Ultracold Neutron Experiments

The ultimate aim of this experiment is to measure the electric dipole moment (EDM) of the neutron as a test of time reversal invariance. A finite EDM would show failure of time reversal. We have demonstrated a practical system for producing ultracold neutrons (UCN) at high density from a pulsed neutron source using ZING-P′. We now need to show that we can hold these neutrons in a bottle for 100 seconds or so.

To do this we have (1) built a window that separates the bad vacuum of our source (a rapidly moving mica crystal which reflects 400 m/sec neutrons) (2) polished the surface of our bottle and (3) built pneumatically operated valves with minimum leakage to control the neutrons. We need a high flux of 400 m/sec neutrons to test the source and bottle and we hope to have this from the refrigerated moderator in IPNS.

To be competitive with other measurements of the EDM we need a density of about 10 UCN/cc stored in our bottle.

(d) Data Acquisition System

Ease of use, flexibility, and reliability were the primary goals in the design of the IPNS Data Acquisition System (DAS) and these goals have been met very well. Very little time has been lost through problems with the DAS and users have been able to begin using the system with a minimum of instruction. This is the first neutron scattering data acquisition system with the sophistication to do electronic time focussing on the fly, enabling the use of large detector banks in simple arrangements. The IPNS DAS includes a powerful and compatible host computer (a VAX 11/780) to permit rapid analysis of acquired data. This allows us to run an efficient user program despite the complex nature of the data. Outside users are usually able to

complete most of their analysis before leaving the Laboratory if they are willing to stay a day or two after their experiments are completed.

The DAS currently serves seven instruments: The SEPD, GPPD, LRMECS, SCD, CAS, HRMECS and the Solid He^3 Experiment (and on a temporary basis, the Polarized Neutron Experiment). The SAD instrument does not yet use the main IPNS DAS but instead uses an upgraded form of the data acquisition system which was used for this instrument at ZING-P'. All IPNS users analyze data on the IPNS VAX 11/780.

Many unique capabilities and a great deal of flexibility are provided by the IPNS DAS. The user can choose the range of times-of-flight over which data is collected, channel widths, grouping and/or time-focussing of detectors, and method of monitoring collection. Time-focussing corrections which can be made before recording each event include scaling of the time to correct for different flight paths, and/or scattering angles and corrections for time delays. This has permitted a simple symmetric design for the powder diffractometers with the detectors mounted on a circle surrounding the sample. Three types of time delay corrections are possible so corrections can be made for different types of instruments. Data from different detectors may be collected over the same or different ranges and a given event may be histogrammed more than once to allow collection with and without corrections such as time-focussing. Each powder instrument has, on occasion, collected data simultaneously into more than 220,000 channels. The Single Crystal Diffractometer can collect data into over one million channels at a time.

5. USER PROGRAM

IPNS is a national user facility. What this means is that we encourage and actively seek use of the various instruments by outside users. To achieve this effectively we have developed the following policy:

- o Program Committee (chaired by a non-Argonne scientist -- majority of members from outside Argonne) will review experiment proposals and allocate time to optimize the production of good science.

- Instrument Scientists will be allotted 25% of time on each instrument for checking, upgrading, calibration and their own experiments, remaining 75% will be allocated by Program Committee.

- Some beams will be left free for special experiments in which all experimental equipment will be provided by the users.

- Users will generally provide any non-standard equipment required (beyond conventional sample environment equipment).

- Users will provide their own travel support (Argonne Universities Association may be able to help university users in special cases).

- Neutrons will be provided free of charge for scientific experiments meeting criteria established by the Department of Energy.

- Proprietary experiments may be scheduled with appropriate cost recovery according to the Department of Energy guidelines.

The question is how well has this worked. On the whole extremely well. So far (Nov. 1981 - June 1982) we have run 80 experiments. About 60 outside users have been involved with these experiments, and of these about 30 have actually been at ANL to do their experiments. This is a promising start.

A summary of the research proposals submitted in February 1982 for the experimental period April 1982 - October 1982 is given below. The decisions on which proposals were accepted are those of the Program Committee which met at Argonne on March 1, 1982. The next proposal deadline is September 15. Proposal forms, experimental report forms, and a user handbook describing the instruments in detail are available by writing to the Scientific Secretary, IPNS-372, Argonne Natonal Laboratory, Argonne, Illinois 60439, telephone (312) 972-5518.

Instrument	Number Submitted			No. Accepted[3]	
	Outside Users	ANL	Total	Outside Users	Total
Special Environment Powder Diff.	10	10	20	6	13
General Purpose Powder Diff.	10	7	17	10	15
Low-Res. Medium-Energy Chopper Spectr.	6	5	11	2	4
Single Crystal Diff.	7[2]	1	8	6[1]	7[1]
Radiation Effects Fac.	7	8	15	7	13
Special Experiments	1	2	3	1	3
TOTAL NUMBER[2]	41	33	74	32	55

(1) Final experiments to be selected depending on results of screening measurements. One of these proposals includes 44 individual proposals from scientists representing 32 U.S. institutions.

(2) Counts proposals with multiple samples as one proposal.

(3) In most cases time allocated was less than requested.

Proposals were also received for the Small Angle Diffractometer. and High-Resolution Medium-Energy Chopper Spectrometer. These are not included here because these instruments are still in a testing stage.

6. FUTURE PLANS

For many years Argonne has been in the lead with thinking and developing spallation sources for neutron science. ZING-P in 1974 was the first source based on a proton accelerator in the world. The IPNS concept was developed and documented at ANL in 1978 (see ANL publication 78-88 compiled by J. M. Carpenter, D. L. Price, and N. J. Swanson, 291 pages) and included detailed specifications for both IPNS-I, which we now have operating, and IPNS-II, a more intense machine designed for 800 MeV energy and 500 μA current. Work on this latter machine is not at present continuing, since not only is funding unavailable but better ideas have also emerged in the intervening 4 years. The United States is looking to the WNR/PSR option at Los

Alamos as a high intensity source in the late 1980's. As a major center for pulsed neutron research, the staff at ANL are actively involved in collaborations with Los Alamos personnel on designing instruments and planning or continuing research programs at the WNR/PSR.

In addition some effort is being made at Argonne to think of new accelerator based systems. Since the research reactors in the U.S. were commissioned in 1966, and the LAMPF accelerator in 1972, this is a necessary step if we are to have a competitive source ten years from now. Dr. R. L. Kustom is in charge of these efforts and further details may be obtained by writing directly to him. Some of the ideas, particularly those involving the fixed field alternating gradient (FFAG) synchrotron, appear very promising from the viewpoint of neutron science.

7. CONCLUSION

IPNS-I is now working well. We are learning how to optimize the instruments to do the best science with pulsed neutrons. The accelerator is working well and we plan to increase the energy to 450 MeV in September. A new ion source will be installed next March, which will result in a large increase in current. Optimistically we hope a year from now that IPNS will have $\sim 2\frac{1}{2}$ times the flux it now has. On the neutron science front we expect to have 13 instruments in operation and perhaps one or two new spectrometers in the early stages of design. Our efforts with pulsed neutrons has drawn worldwide attention and we expect a large number of visitors, both from the U.S. and outside, who are interested and wish to contribute to getting the best science from these sources. We urge you to submit proposals!

REFERENCES

1. Potts, C. W., "Improvements in the Rapid Cycling Synchrotron", Proc. ICANS-V, p. 53 (October 1981).

2. Potts, C., Faber, M., Gunderson, G., Knott, M., and Voss, D., "Tune Control Improvements on the Rapid Cycling Synchrotron", IEEE Trans. Nucl. Sci., Vol. NS-28, No. 3, p. 3020 (June 1981).

3. Praeg, W., McGhee, D., and Volk, G., "Phase Lock of Rapid Cycling Synchrotron and Neutron Choppers", IEEE Trans. Nucl. Sci., Vol. NS-28, No. 3, p. 2171 (June 1981).

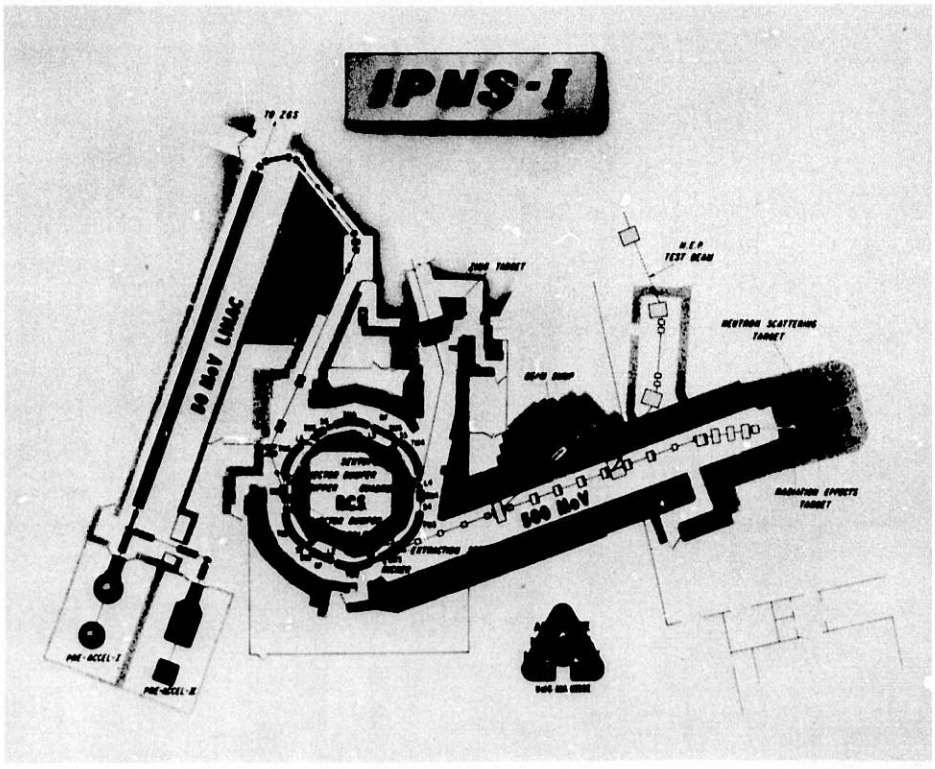

Fig. 1 Experimental Facilities at IPNS.

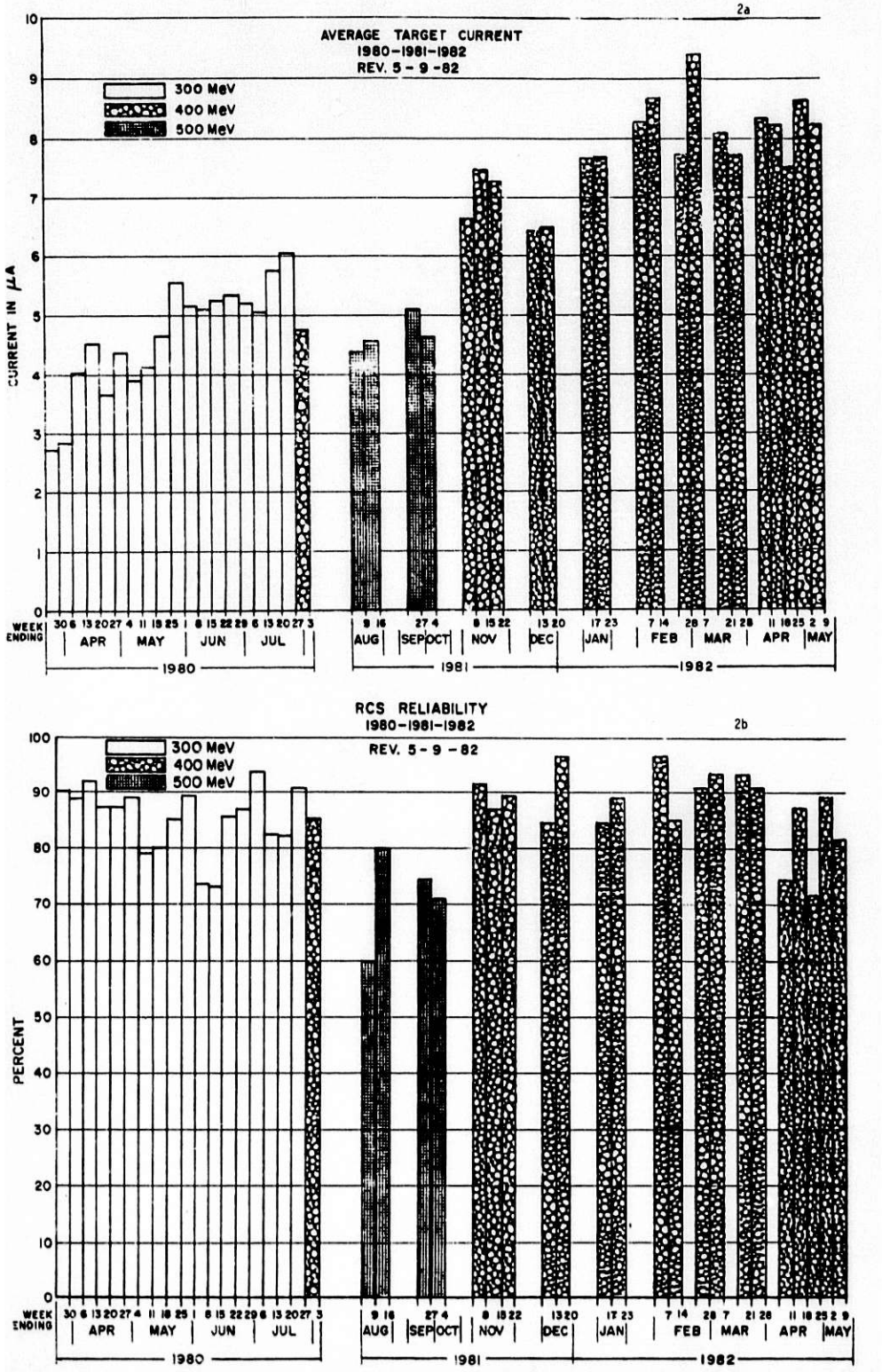

Fig. 2 (a) Average target current and (b) reliability since 1980 of the IPNS Accelerator system.

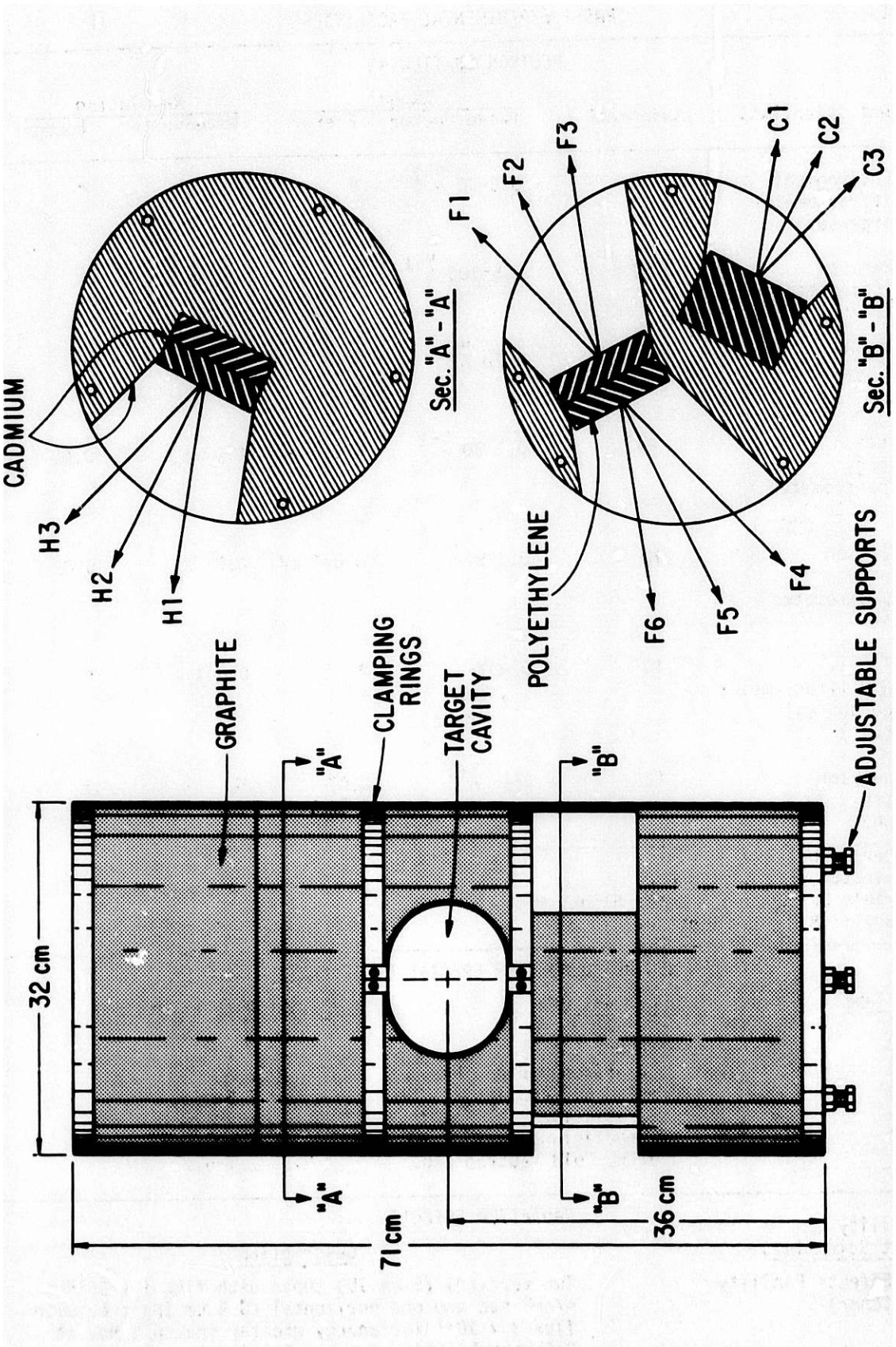

Fig. 3 The temporary moderator-reflector assembly. The three moderators are of polyethylene, reflected by graphite decoupled and heterogeneously poisoned by .5mm thick cadmium.

TABLE I IPNS-I EXPERIMENTAL FACILITIES

NEUTRON SCATTERING

Facility (Instrument Scientist)	Assignment	Range		Resolution	
		†Wave-vector	Energy	Wave-vector	Energy
Special Environment Powder Diffractometer (J. D. Jorgensen)	F5	0.5-40 $Å^{-1}$	*	0.35%	*
General Purpose Powder Diffractometer (J. Faber, Jr.)	F2	0.5-100 $Å^{-1}$	*	0.25%	*
Single Crystal Diffractometer (A. J. Schultz)	H1	2-20 $Å^{-1}$	*	2%	*
Low-Resolution Medium-Energy Chopper Spectrometer (J. M. Carpenter)	F4	0.1-30 $Å^{-1}$	0-0.6 eV	0.02 K_o	0.05 E_o
High-Resolution Medium-Energy Chopper Spectrometer (D. L. Price)	H3	0.3-9 $Å^{-1}$	0-0.4 eV	0.01 K_o	0.02 E_o
Small-Angle Scattering Diffractometer (J. E. Epperson (a), C. Borso (b))	C1	0.001-0.3 $Å^{-1}$	*	0.004 $Å^{-1}$	*
Crystal Analyzer Spectrometer (T. O. Brun)	F1	3-16 $Å^{-1}$	0.02-0.5 eV	3%	2%

* No energy analysis
† Wave-vector, $K = 4\pi \sin\theta/\lambda$
(a) Materials Science -- 3 Meter Flight Path
(b) Biology -- 8 Meter Flight Path

NEUTRON BEAMS FOR [illegible]AL EXPERIMENTS

Beam Tube	Current Use	Flight Path Length (m)
F3	Vacant	6-70
C2	Polarized Neutron Exp.	6-40
C3	Solid He^3 Project	7.5-25
F6	Irradiations	6-20
H2	Irradiations	6-20
V1	Ultra-Cold Neutron Exp.	2.7-6.7

RADIATION EFFECTS

Facility (Instrument Scientist)	Description
Radiation Effects Facility (R. C. Birtcher)	Two vertical (5 cm ID) tubes with flux 1×10^{12} n/cm^2 sec and one horizontal (3.8 cm ID) tube with flux 3×10^{11} for energy greater than 0.1 MeV at 8μA; capabilities for maintaining two samples at liquid helium temperature (4°K) and above

IPNS - G. H. Lander

H. Wroe	Comment - I noticed that in scheduling you allowed 25% of the beam time for in-house use. On SNS we have allowed a commissioning period for a new instrument but once it's scheduled in-house scientists have to compete for time through the same procedure as the university user.
G. Lander	Response - In practice the 25% rule is not applied across the board. The scientists often use the instrument time to finish off collaborative experiments. Even at the ILL quite a lot of beam time is reserved for internal use, and most people think this appropriate.
A. Carne	Q How much beam time does the HEP test beam get?
J. Carpenter	A It uses 1% of the beam which is scattered out continuously.
C. Potts	Comment - We expect 500 MeV operation to be just as reliable as 450 MeV.

J. M. Carpenter, D. L. Price, G. H. Lander

V. Stipp, A. W. Schulke, I. Bresof, F. J. Rotella

G. S. Bauer, K. L. Kliewer

A. Carne, C. W. Potts

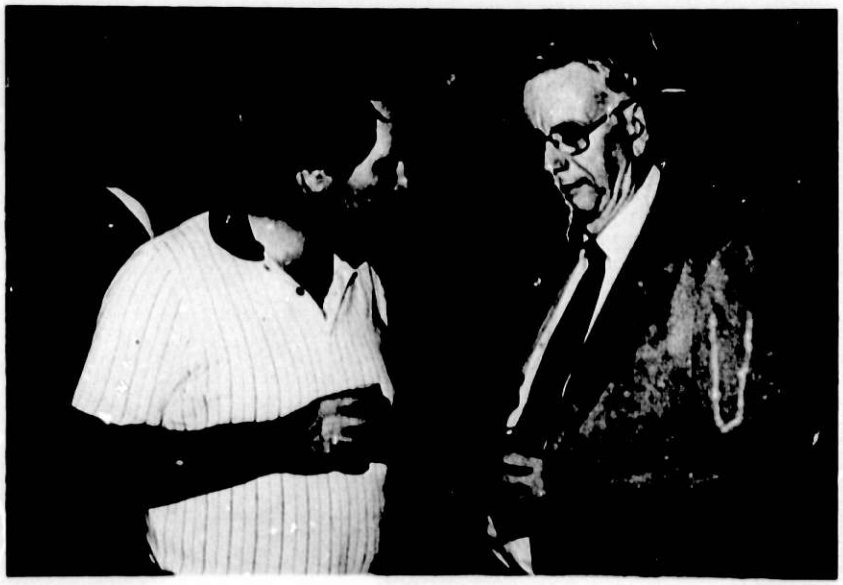

B. S. Brown, T. H. Blewitt

ELECTRONICALLY FOCUSED POWDER DIFFRACTOMETERS AT IPNS-I

J. D. Jorgensen and J. Faber
Argonne National Laboratory, Argonne, Illinois 60439

ABSTRACT

Two powder diffractometers have been operated at IPNS-I since August 1981. The diffractometers achieve high resolutioin with large detector solid angles for scattering angles from ± 12 to 157° by electronically focussing the events from individual detectors in an on-line microprocessor.

INTRODUCTION

During the operation of the ZING-P' prototype pulsed neutron source at Argonne National Laboratory (December 1977 to August 1980) considerable data were taken with a time-of-flight diffractometer known as the High Resolution Powder Diffractometer (HRPD).[1] The HRPD clearly demonstrated the high and nearly constant resolution which could be obtained by the time-of-flight technique at a pulsed neutron source, but suffered from one important limitation. The long incident and short scattered flight paths rendered mechanical time-focusing techniques impractical except in back scattering. (90° detectors were provided on the HRPD, but with a much smaller solid angle than at 160°.) For this reason, the HRPD was ineffective for studying magnetic structures and indexing unknown structures where complete data are required at large d-spacings.

The two powder diffractometers at IPNS-I, the General Purpose Powder Diffractometer (GPPD) and the Special Environment Powder Diffractometer (SEPD), achieve focusing, which allows events from separate detectors to be summed, by processing signals from a large number of individual detectors in a dedicated microprocessor before data histogrms are constructed. This technique allows detector arrays of large solid angle to be constructed at any desired scattering angle. Moreover, the focusing of the instrument can be software controlled which allows the detector configuration to be optimized for a particular experiment or the initial flight path to be changed to achieve a different overall resolution.

DIFFRACTOMETER DESIGN

The GPPD and SEPD are of identical basic design but are positioned on different initial flight paths and have different detector configurations. A schematic of the instrument is shown in Fig. 1. The instrument consists of a large octagonal shielded enclosure with the sample position at the center and available detector positions from ± 12° to ± 157° at a constant radius of 1.5 meters. Final collimation of the incident beam occurs just prior to entering the sample chamber. The final collimators are cast from boron carbide and epoxy resin and are supported in an iron "wheel" 61 cm. in diameter and 8.9 cm. thick which can be rotated to select three incident beam sizes up to a maximum of 2.5 × 7.6 cm. The nominal beam size which is used for routine powder diffraction and upon which the design calculations were made is 1.3 × 5.0 cm.

The sample chamber is an aluminum tank 61 cm. in diameter and 122 cm. long. The beam enters through a thin (0.4 mm) aluminum window which is located within the collimator shielding wedge where it is not viewed by any

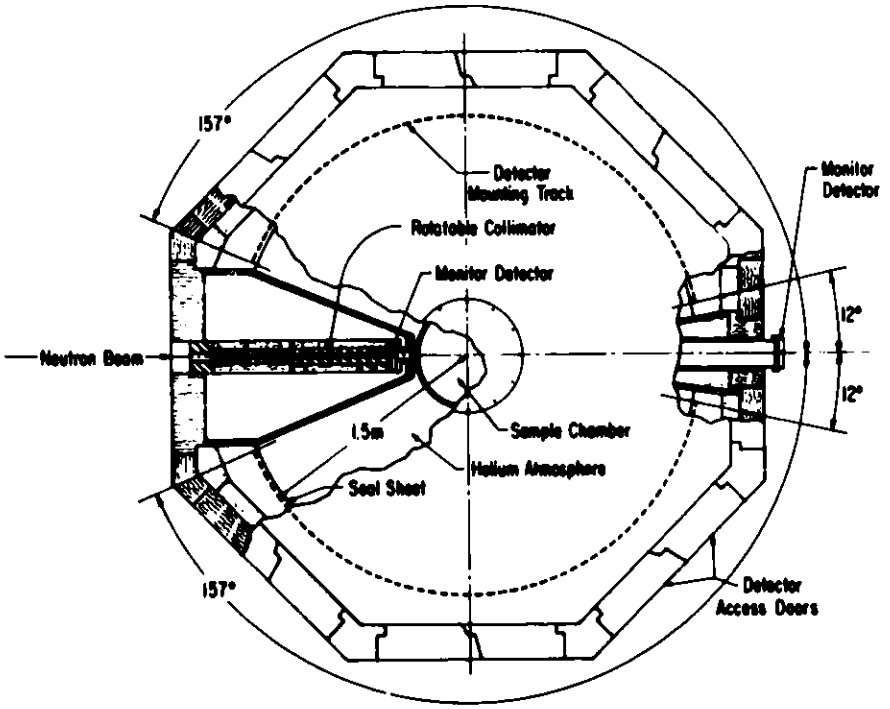

Fig. 1. Schematic layout of the General Purpose and Special Environment Powder Diffractometer.

of the detectors. The exit window is located outside the instrument shielding at the end of a 15 cm diameter pipe connected to the chamber. The sample chamber is evacuated throguh this exit pipe. The wall of the chamber has been thinned to 0.3 cm in the scattered neutron path leading to the detectors. Samples are mounted on an arm extending from the center of the top cover plate. Separate cover plates and adapters are available for mounting furnaces, cryostats, displex refrigerators and pressure cells.

Each instrument presently contains approximately 140 10-atmosphere ^3He proportional counters 1.27 cm. diameter and 38.1 cm. long. The detectors are grouped ito arrays centered around specific scattering angles as listed in Table I. The detectors and their individual preamps are supported in modules which clamp onto the constant radius detector mounting track. The

TABLE I

Performance parameters for the General Purpose and Special Environment Powder Diffractometers at IPNS-I. (May 1982).

GPPD

Incident flight path: 20 m
Useful thermal flux on sample: 2×10^5 n-cm^{-2}-sec^{-1}

2θ	d_{min}(A)	d_{max}(A)	Δd/d	Det. area (ster.)
152	0.2	2.9	0.0022	0.10
90	0.3	3.9	0.0040	0.086
60	0.4	5.5	0.0075	0.052
30	0.9	11	0.025	0.034

SEPD

Incident flight path: 14m
Useful thermal flux on sample: 4×10^5 n-cm^{-2}-sec^{-1}

2θ	d_{min}(A)	d_{max}(A)	Δd/d	Det. area (ster.)
145	0.2	4.0	0.0035	0.086
90	0.3	5.4	0.006	0.086
57	0.4	8.0	0.01	0.052
22	1	19	0.035	0.034

entire detector chamber is dehumidified to reduce electrical noise. Easy access to the detectors is obtained through the hinged, shielded access doors. Shielding is an integral part of the instrument structure and consists of polyethylene, borax, and boron carbide.

DATA ACQUISITION SYSTEM

Signals from the individual detectors are discriminated, time-encoded, and mapped into histograms in a data acquisition system built around a Z8000 microcomputer coupled to a PDP 11/34A minicomputer. (Fig. 2).[2] The Z8000

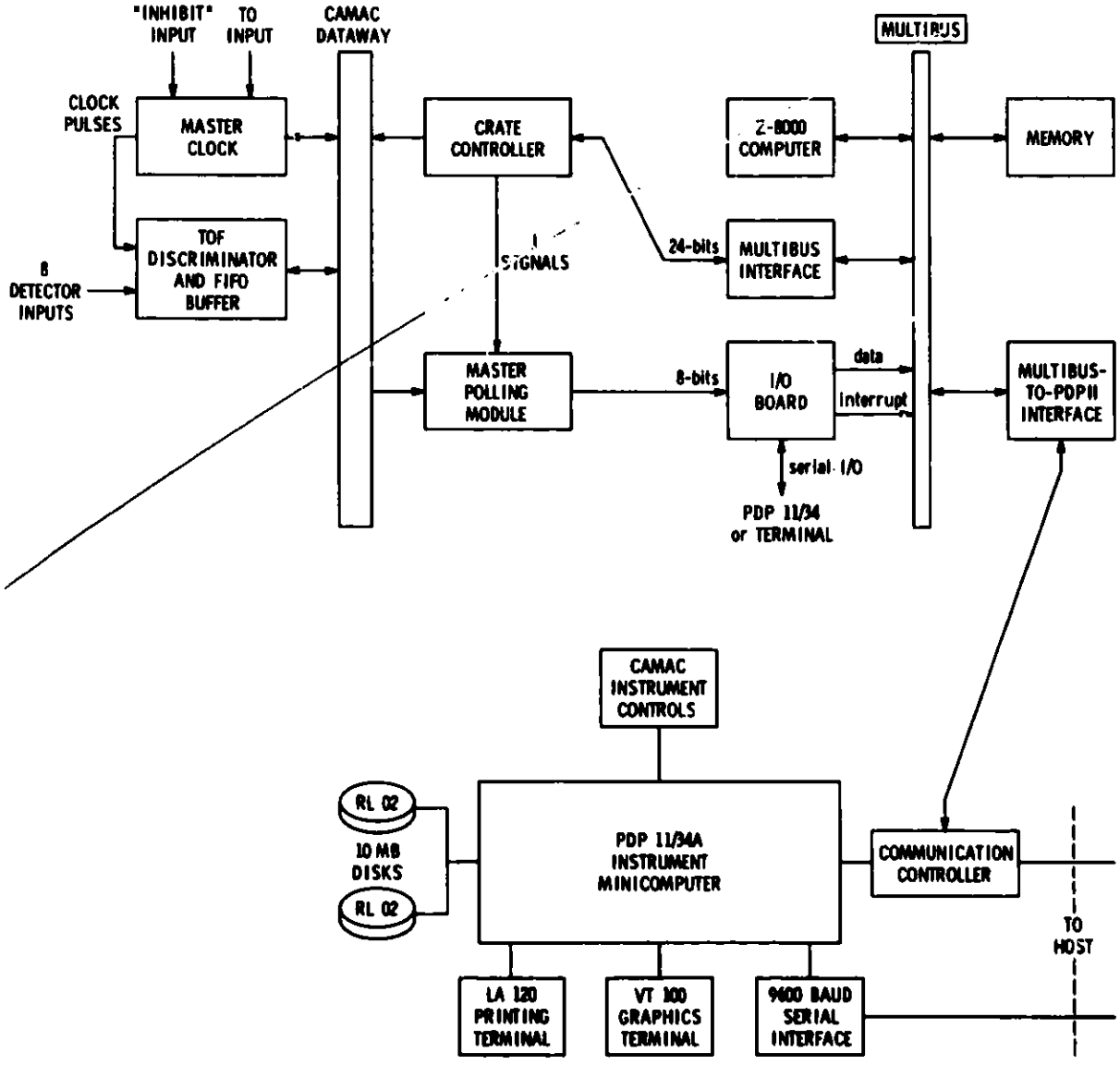

Fig. 2. Block diagram of the data acquisition system.

microcomputer is dedicated solely to data acquisition and histogram construction, and directly accesses semiconductor random accesses memory in which data histograms are stored. All other instrument functions, e.g., input, output and display of data, instrument control, etc., are handled by the PDP 11/34A minicomputer which also supervises the Z8000 microcomputer and has access to the histogram memory.

Discrimination and time-encoding occur in modules in a CAMAC system with 8 detector inputs per module. All of the time-of-flight discriminator modules are connected to a single 8 MHz master clock. Whenever one of the inputs of a TOF discriminator module receives an analog pulse within the discriminator window, a 20 bit time word (125 ns. resolution) is combined with 3 bits of input identification and loaded into a first-in-first-out (FIFO) buffer in the module. Each FIFO buffer can store sixteen 24-bit words (the 24th bit is used to indicate FIFO overflow). A polling module scans the FIFO buffers and identifies those which are over half full. The 8 bit addresses of FIFO buffers to be read are passed through a multibus interface to the Z8000 microcomputer which then reads the data from the buffer. Each event is then represented by a 32-bit word containing 20 bits of time information, 11 bits of detector identification and one overflow bit.

Before constructing histograms, the microcomputer performs the arithmetic operations on the raw time-of-flight data required to achieve time-focusing of detectors at different angles. The standard time-focusing algorithm mimics mechanical time-focusing where path length, ℓ, and scattering angle, θ, are constrained to achieve

$$\ell \sin \theta = \text{constant} ,$$

so that d-spacing becomes a linear function of time with a single contant, A, for an extended array:

$$d = \frac{\lambda}{2\sin\theta} = \frac{ht}{2m\ell\sin\theta} = A\,t \quad .$$

In the case of electronic time-focusing, a pseudotime, t^*, is calculated from the measured time-of-flight, t, in order to make each detector in an extended array appear as if it were at some reference scattering angle, θ_r, and path length, ℓ_r. The pseudotime, t^*, for the detector at angle θ_n and path length ℓ_n is

$$t^* = \frac{\ell_r \sin\theta_r}{\ell_n \sin\theta_n} t = K_n t \quad .$$

The constants K_n (one for each detector) are calculated by the PDP 11/34A minicomputer during the setup of a run and are stored in a lookup table in memory where they can be accessed by the microcomputer to perform the focusing calculations.

Since the time resolution prior to focusing is 125 ns, no significant contribution to overall resolution is introduced by the focusing calculation. Having calculated the pseudotime for each event, time channels of the desired length (typically 2-20 μs) can be constructed and data from different detectors can be summed into the same time fields in memory. System software is written so that more than one historgram may be constructed from the same data if desired. The maximum data processing rate of the Z8000 microcomputer is about 3 KHz.

INSTRUMENT PERFORMANCE

Instrument performance characteristics for the GPPD and SEPD in their present configurations are summarized in Table I. During the first year of operation, the two powder diffractometers have viewed opposite sides of a 10 × 10 × 5 cm thick polyethylene moderator poisoned at the center (2.5 cm) with 0.5 mm thick cadmium. The GPPD is located on a 20 meter and the SEPD on a 14 meter indident flight path. Time-averaged thermal neutron fluxes at the sample position given in Table I are based on Monte Carlo calculations of the target-moderator assembly and have been confirmed by gold foil activation. With the large detector area available on these instruments, typical data can be collected in 6 - 24 hours depending on the complexity of the structure under study and the type of information desired.

Comparisons of unfocused and focused data show that no significant peak broadening or change in peak shape is introduced by the focusing process except at small scattering angles where the resolution of a detector becomes a strong function of angle. Figure 3 shows raw data for the end detectors

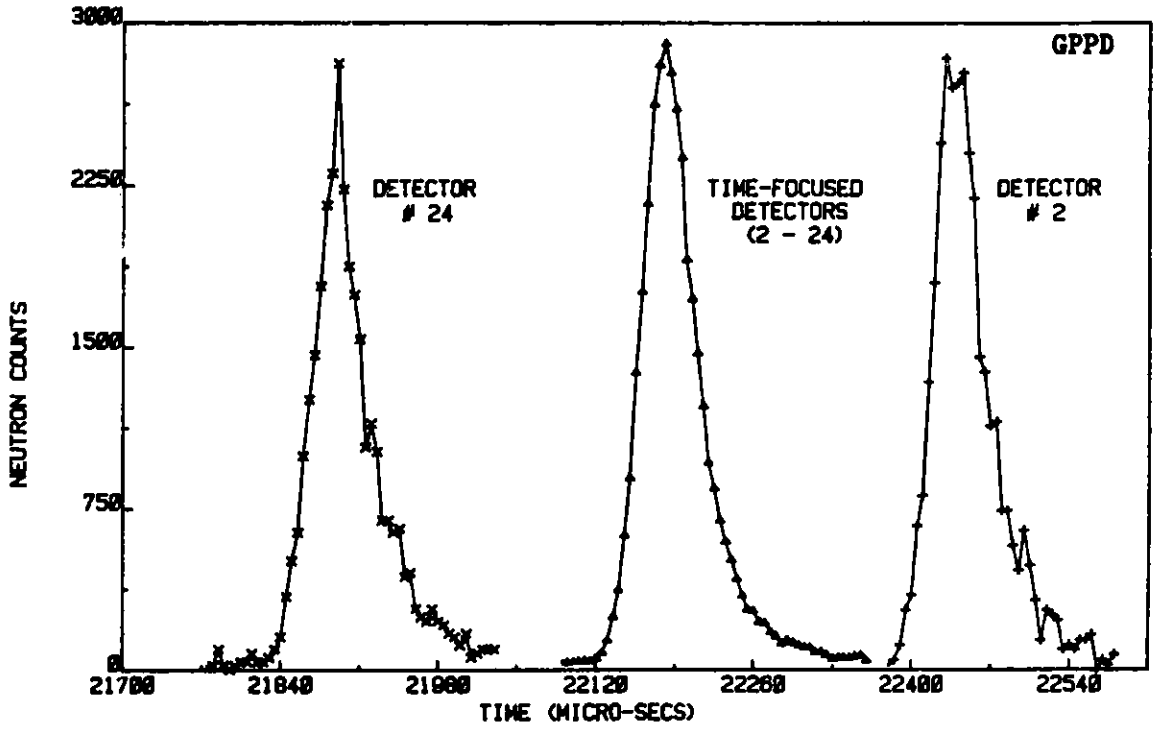

Fig. 3. Raw time-of-flight data for the first and last detectors of a 23 detector extended array on the GPPD and the electronically-focused sum for the array.

of an extended array of detectors along with the focused sum for the array.

A substantial number of data have been collected and analyzed on the GPPD and SEPD during the first year of operation at IPNS-I. Where detailed structural information is desired, the Rietveld refinement method has been used, usually concentrating on back scattering data where resolution is highest and the largest number of peaks are observed. The raw 152° data and Rietveld profile for a standard sample of Al_2O_3 run for 8 hours on the GPPD is shown in Fig. 4. The lower Q data obtained at smaller scattering angles have been successfully used to index unknown or hypothesized nuclear and magnetic structures and to extend the range of measurements on amorphous solids and liquids.

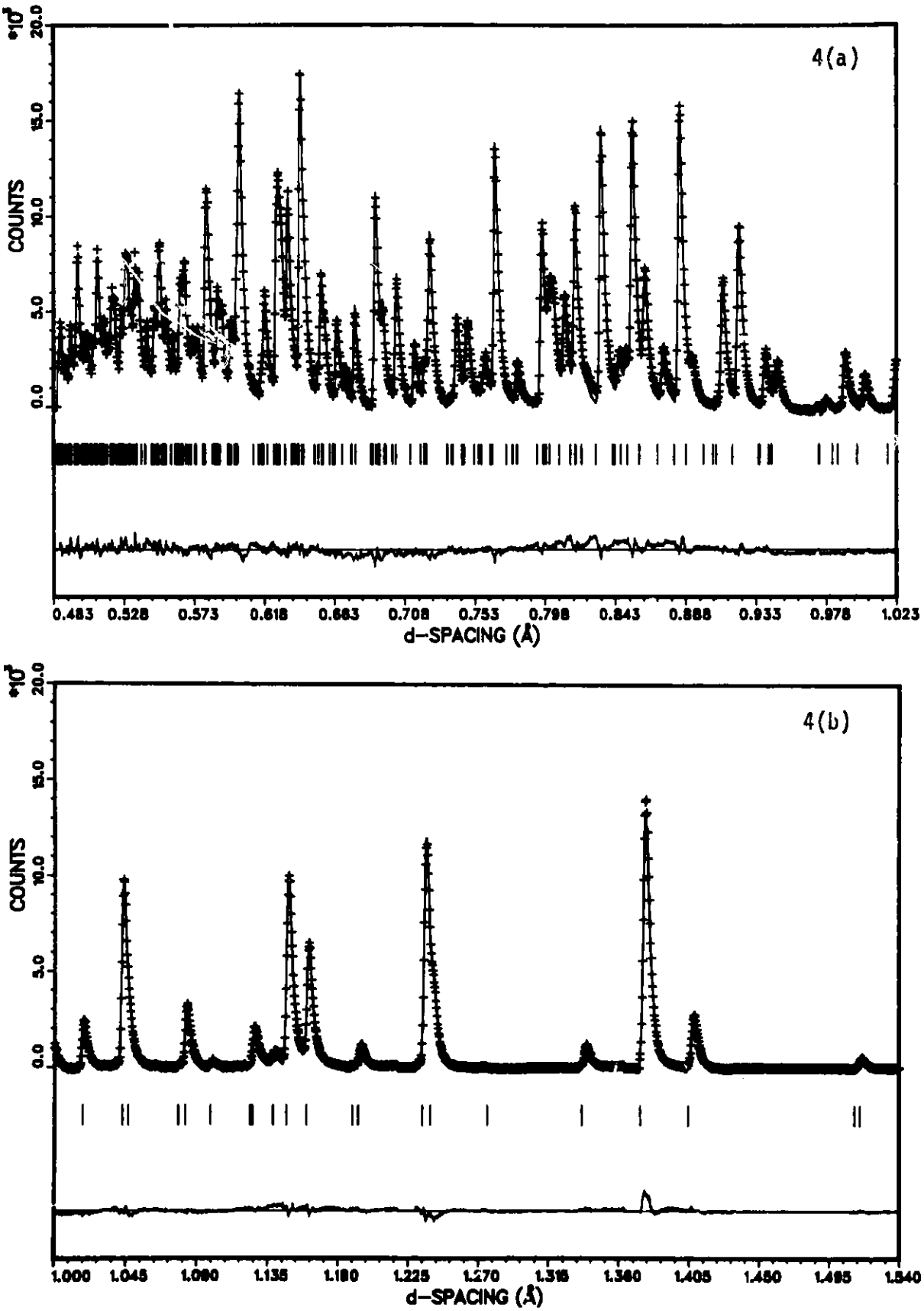

Fig. 4. Raw data (crosses) and calculated Rietveld profile (solid line) for Al_2O_3 taken at $2\theta = 152^\circ$ on the GPPD. Tick marks below the profile indicate positions of all allowed reflections. A difference plot (observed minus calculated) appears at the bottom. Background has been subtracted before plotting.

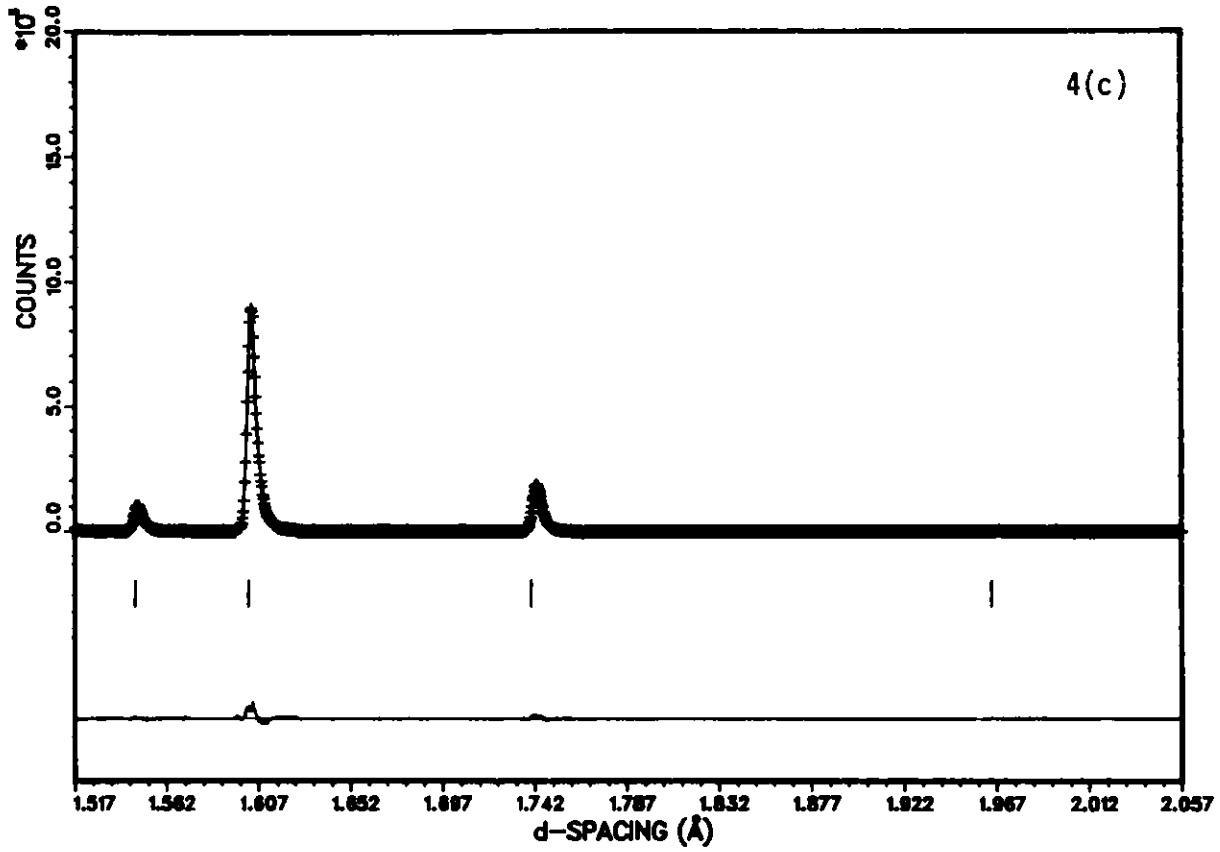
4(c)
COUNTS
*10³
20.0
15.0
10.0
5.0
0.0
1.517
1.562
1.607
1.652
1.697
1.742
1.787
1.832
1.877
1.922
1.967
2.012
2.057
d-SPACING (Å)

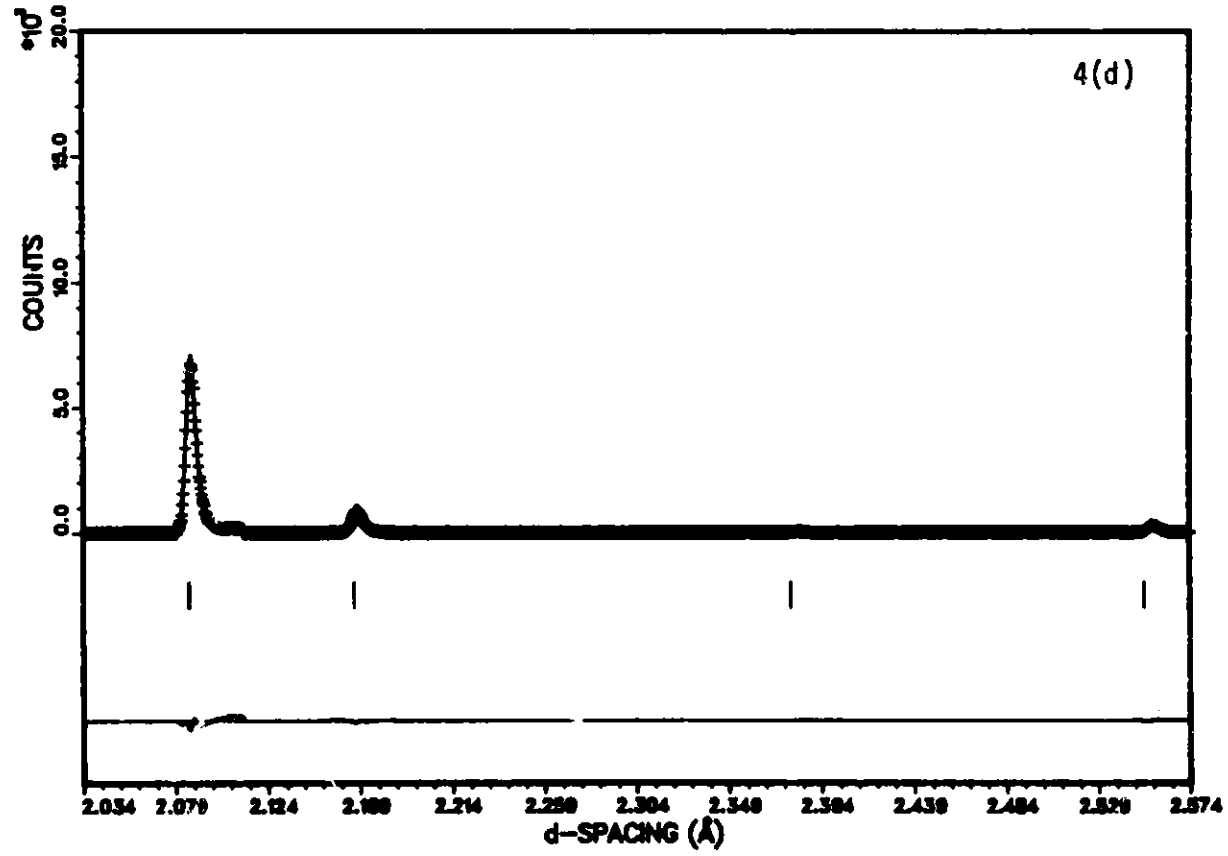
4(d)
COUNTS
*10³
20.0
15.0
10.0
5.0
0.0
2.034
2.079
2.124
2.169
2.214
2.259
2.304
2.348
2.394
2.439
2.484
2.529
2.574
d-SPACING (Å)

SUMMARY

The GPPD and SEPD at IPNS-I clearly show that electronic focusing techniques can be used to increase the Q range and flexibility of time-of-flight diffractometers. The two IPNS-I diffractometers do this focusing during data collection with a dedicated microcomputer. This allows high time resolution before focusing and on-line display of the composite histograms.

REFERENCES

1. J. D. Jorgensen and F. J. Rotella, J. Appl. Cryst. 15, 27 (1982).

2. R. K. Crawford, R. T. Daly, J. R. Haumann, R. L. Hitterman, C. B. Morgan, G. E. Ostrowski and T. G. Worlton, IEEE Trans. Nucl. Sci. NS-28, 3692 (1981).

ICANS-VI

INTERNATIONAL COLLABORATION ON ADVANCED NEUTRON SOURCES

June 27 - July 2, 1982

THE IPNS TIME-OF-FLIGHT SINGLE CRYSTAL DIFFRACTOMETER

A. J. Schultz, R. G. Teller and Jack M. Williams

Chemistry Division, Argonne National Laboratory
Argonne, Illinois 60435, U.S.A.

The single crystal diffractometer (SCD) at the Argonne Intense Pulsed Neutron Source (IPNS) utilizes the time-of-flight (TOF) Laue technique to provide a three-dimensional sampling of reciprocal space during each pulse. The instrument contains a unique neutron position-sensitive ^{6}Li-glass scintillation detector with an active area of 30x30 cm. The three-dimensional nature of the data is very useful for fast, efficient measurement of Bragg intensities and for the studies of superlattice and diffuse scattering. The instrument was designed to achieve a resolution of 2% or better ($R = \Delta Q/Q$) with $2\theta > 60°$ and $\lambda > 0.7\text{Å}$.

THE IPNS TIME-OF-FLIGHT SINGLE CRYSTAL DIFFRACTOMETER

A. J. Schultz, R. G. Teller and Jack M. Williams
Chemistry Division
Argonne National Laboratory
Argonne, Illinois 60435

I. INTRODUCTION

The single crystal diffractometer (SCD)[1,2] at the Argonne Intense Pulsed Neutron Source (IPNS) is designed to provide fast, efficient data collection over a large solid angle and a large $|Q|$ range in reciprocal space. The major component of the instrument is a neutron position sensitive ^{6}Li-glass scintillation detector with an active area of 30 x 30 cm.[3]

As shown in Figure 1, the area detector and multiwavelength incident neutron radiation provide a three-dimensional sampling of reciprocal space during each pulse. In combination with a high

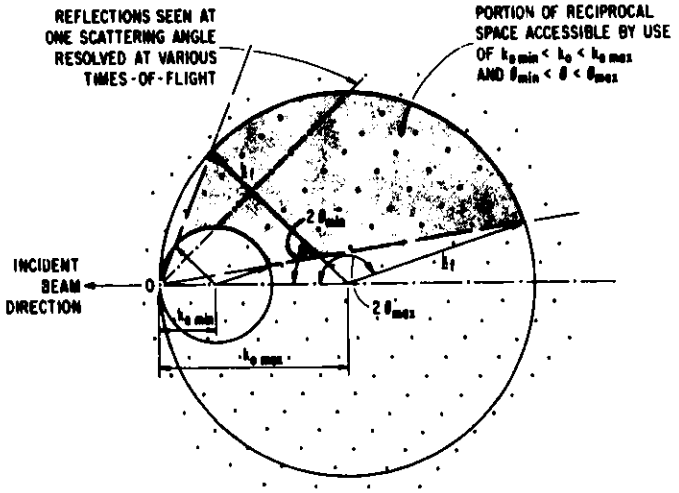

Fig. 1. Construction in reciprocal space to illustrate the use of multiwavelength radiation in single crystal diffraction. The circles with radii $k_{o\,max} = 1/\lambda_{min}$ and $k_{o\,min} = 1/\lambda_{max}$ are drawn through the origin. All reciprocal lattice points within the shaded area may be sampled by a large position-sensitive detector.

intensity pulsed source this can lead to higher data rates or the use of smaller crystals. The three-dimensional nature of the data can also be extremely useful in studying superlattice and scattering and diffuse scattering.

2. INSTRUMENT DESIGN[1,2]

The crystal and detector orienter incorporates all 4 circles which are normally found with conventional diffractometers (see Fig. 2). The detector is mounted on a 0.5 m. detector arm which permits sample-to-detector distances of 20 to 45 cm. and an accessible 2θ range of 20-160°. A Displex closed cycle helium refrigerator can be mounted on the diffractometer to permit sample temperatures in the range of 10-300 K. The sample is 663 cm. from the moderator surface, of which it "sees" a circular portion 8.8 cm in diameter. A low efficiency BF_3 counter is 30 cm. upstream from the sample and is used to monitor the incident neutron flux.

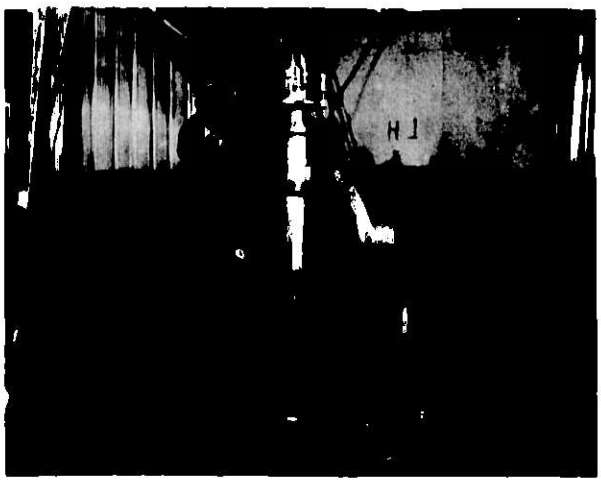

Fig. 2. Photograph of the Single Crystal diffractometer. The area detector is inside the shielded enclosure on the detector arm. A Displex helium refrigerator mounted on the goniostat permits sample temperatures of 10-300 K.

3. DETECTOR DESCRIPTION[3,4]

Over the past few years a program to develop a neutron position-sensitive detector, based on the Anger γ-ray camera principle, has been carried out at Argonne. The new detector has a number of important advantages relative to the conventional ^{3}He gas-filled multiwire proportional counter, as listed in Table I. Most important is higher efficiency at shorter wavelengths where the density of Bragg reflections is highest (Fig.3).

TABLE I. Inherent advantages of Scintillation Detector Vs. Proportional Counter

HIGHER DETECTION EFFICIENCY:	Particularly above 0.025 eV (Below 1.8 Å)
HIGHER COUNT-RATE CAPABILITIES:	No slow positive-ion collection
THINNER DETECTION MEDIUM:	Virtually parrallax free
THINNER WINDOW:	Virtually windowless
MORE FLEXIBLE CONFIGURATION:	No inherent shape or size limitations
MORE RUGGED:	No fragile anode, no microphonics, no gas leakage or contamination
GREATER CONSTRUCTION SIMPLICITY:	Requires no special fabrication facilities

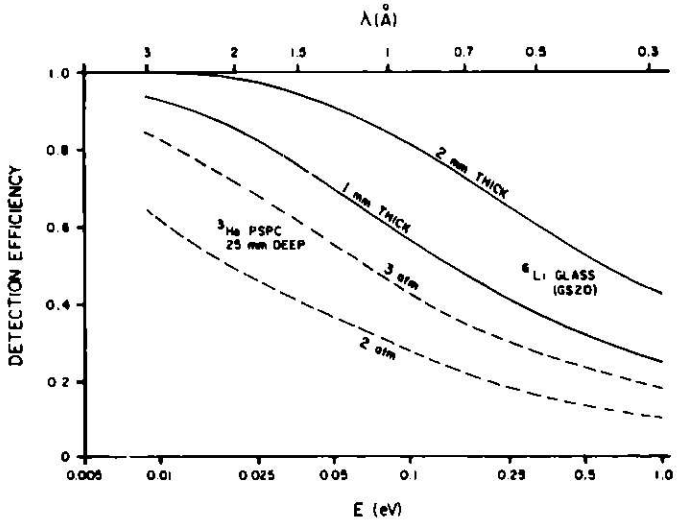

Fig. 3 Plots of neutron detector efficiency vs. wavelength for ^{3}He gas and ^{6}Li glass.

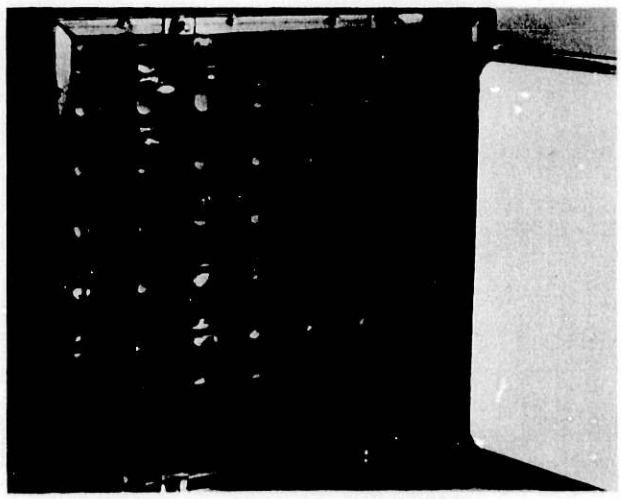

Fig. 4. Neutron-position scintillation detector consisting of a 7x7 array of square photomultiplier tubes, each 51x51 mm^2 and a 30x30 cm^2 ^{6}Li glass scintillator shown at the lower right removed from in front of the light disperser.

A photograph of the detector now in use on the SCD is shown in Figure 4, and a schematic drawing is shown in Figure 5. The detector contains a 2 mm. thick ^{6}Li-loaded, Ce-activated, glass scintillator, a 38 mm. thick light disperser consisting of Pyrex glass and plexiglass, and a 7x7 array of 2-inch square photomultiplier tubes (PMT's). A small air gap (0.1 mm.) between the scintillator glass and the light disperser provides a critical refraction angle of 40° which spreads the light over at least two PMT's in the horizontal and vertical directions. Incident light rays with angles greater than 40° are reflected and then scattered back by the layer of aluminum oxide on the opposite side of the scintillator.

The signal from each PMT is resistively weighted according to X and Y positions, respectively. The weighted sums for X and Y are divided by the unweighted sum to provide the centroid of the scintillation event. We estimate the intrinsic resolution of the detector is approximately 3.5 mm.

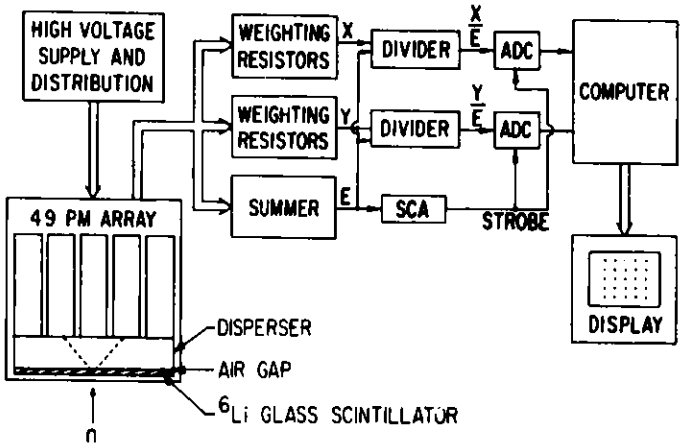

Fig. 5. Basic operation of neutron-position scintillation detector. The position of a neutron interaction in the ^{6}Li glass is determined by calculating the normalized centroids of scintillation X/E and Y/E using a resistor weighting scheme.

4. DATA ACQUISITION SYSTEM[5]

The data acquisition system (DAS) for the SCD consists of a PDP 11/34 computer with both a CRT and a printer terminal for user interaction, two 10-Mbyte RL02 disk drives, a magnetic tape drive, a color CRT graphics display terminal, and an interface to a CAMAC crate containing the motor controller for the goniostat. The PDP 11/34 is also interfaced to a multibus which links to a Z8001 microcomputer, 2.5 Mbytes of random access memory, and a second CAMAC crate used for data acquisi tion which contains a first-in-first-out (FIFO) buffer memory and the TOF clock. The digitized X and Y positions from the detector ADC are initially stored in the FIFO memory along with the digitized TOF. The Z8001 microcomputer histograms data from the FIFO memory in the random access memory using a user-generated look-up table. A typical histogram may have dimensions of 85x85x120, corresponding to X and Y on the detec-tor and TOF, respectively (Fig. 6).

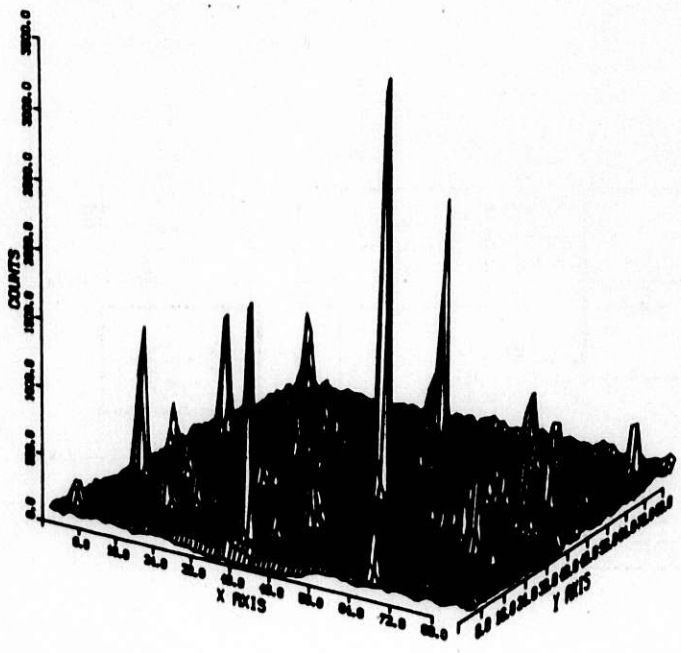

Fig. 6. A portion of a Laue pattern. The X and Y axes represent X and Y channel numbers corresponding to positions on the detector face. The counts for each X,Y bin have been summed over a wave-length range of 1-3 Å. Since there are 117 time, or wavelength channels, all of the Bragg peaks are easily resolved in the 3-D histogram.

5. DEADTIME LOSS

In addition to the three-dimensional histogram, a TOF spectrum is obtained from a low efficiency BF_3 proportional counter in the direct beam between the source and the crystal. As shown in Figure 7, whenever an event is obtained from the BF_3 monitor detector, the area detector is sampled to see if it is busy processing an event. If the 2-D detector is busy, the proper time channel of the deadtime loss histogram is incremented. The fractional deadtime loss for each time channel is then the number of lost events N_L divided by the number of monitor events N_T.

Since data rates may vary by a factor of 50 during each pulse, the data must be corrected for deadtime based on its TOF. Our experience at this time is that for a wavelength range of 0.7 to 3.5 Å (TOF = 1.2 to 6.1 msec.), depending on the sample, the percent deadtime loss may range from a maximum of 10-20% at the short wavelength end of the spectrum to 0% at the longest

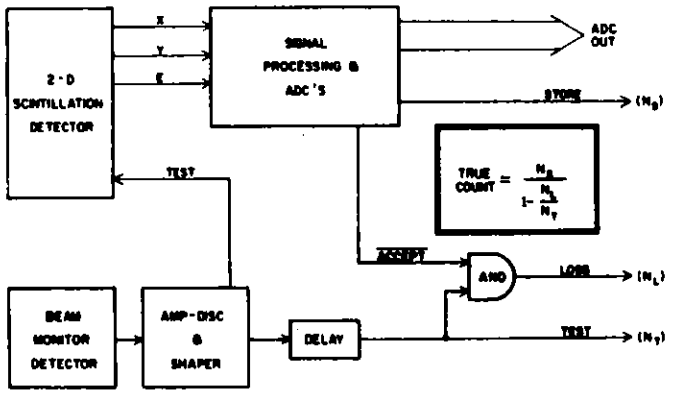

Fig. 7. Deadtime correction scheme. An event in the BF_3 beam monitor detector triggers a test pulse to the 2-D detector. If the test pulse is not accepted a deadtime loss event is added to the appropriate TOF histogram channel.

wavelength. From observed counting rates, we estimate this represents an average deadtime of approximately 7 μsec. This number includes the rejection of signals which do not fall within the pulse-height discriminator window (e. g., gamma-rays) or have been effected by pileup. Since the pulse risetime of the ^{6}Li glass is 0.5 μsec. (90% of final amplitude), improvements in shielding, background levels, signal shaping and position encoding could lead to a smaller deadtime.

6. RESOLUTION

The resolution function of the instrument is

$$R_S = \frac{\Delta S}{S} = [R_t^2 + R_L^2 + (\cot\theta \cdot \Delta\theta)^2]^{\frac{1}{2}}$$

where $S = \frac{2\sin\theta}{\lambda} = (2m/h)(L/t)\sin\theta$ and t is the time-of-flight, L is the neutron flight distance, θ is the Bragg angle, λ is the neutron wavelength, m is the neutron mass, and h is Planck's constant. Reasonable values for the variables in the resolution function are $R_t = 0.017$, $R_L = 0.0015$ and $\Delta\theta = 0.85°$. By varying the time channel width such that Δt/t is constant, these values are wavelength independent and R_S is 2θ dependent due to the cotθ function. However, above $2\theta = 60°$ the contribution to R_S becomes small, and R_S quickly approaches or falls below a value of 0.02. To resolve a 25 Å axis at the d-spacing of 1 Å only requires 4% resolution, such that the SCD resolution is sufficient for single crystal studies of mose molecular compounds with upwards of 100 independent atoms in the unit cell.

REFERENCES

[1]S. W. Peterson, A. H. Reis, Jr., A. J. Schultz and P. Day, Advances in Chemistry Series, No. 186, Solid State Chemistry: A Contemporary Overview, S. L. Holt, J. B. Milstern and M. Robbins, eds., American Chemical Society, 1970, pp. 75-91.

[2]A. J. Schultz, R. G. Teller, J. M. Williams, M. G. Strauss and R. Brenner, Trans, Am. Cryst. Assoc., Vol. 18, 1982, in press.

[3]A. J. Schultz, R. G. Teller, S. W. Peterson and J. M. Williams, Transactions of the Symposium on Neutron Scattering, Argonne National Laboratory, August 12-14, 1981, American Institute of Physics, J. Faber, ed., in press.

[4]M. G. Strauss, R. Brenner, F. J. Lynch and C. B. Morgan, IEEE Trans. Nucl. Sci., NS-28, 800 (1981).

[5]R. K. Crawford, R. T. Daly, J. R. Baumann, C. B. Morgan, G. E. Ostrowski and T. G. Worlton, IEEE Trans. Nucl. Sci., NS-28, 3692 (1981).

BERYLLIUM-BERYLLIUM OXIDE FILTER DIFFERENCE SPECTROMETER

by

J. A. Goldstone, J. Eckert, A. D. Taylor,
and E. J. Wood

Los Alamos National Laboratory
Los Alamos, NM 87545

1. INTRODUCTION

Inelastic neutron scattering is the most important technique for the study of elementary excitations in condensed matter over a wide range of energy and momentum transfers. However, intensity limitations do, in some instances, prevent the use of inelastic neutron scattering. Since some of the new pulsed neutron sources promise to reach higher neutron fluxes than currently available at reactor based sources, the development of optimal inelastic time-of-flight (TOF) neutron spectrometers is of considerable importance. Even at the present low to medium flux pulsed sources the spectrum in the epithermal region is more intense than at high flux reactors, particularly if a hot moderator is not used. Molecular vibrational spectroscopy using inelastic incoherent neutron scattering is a natural application for this energy range whose importance has increased greatly since the Be filter inelastic spectrometer IN-1B at the hot source of the reactor of the Institut Laue Langevin (ILL) became available. The instrument described in this paper is an optimized TOF analog of the ILL spectrometer for use at pulsed neutron sources.

For inelastic scattering by TOF techniques either the incident or final flight time of the neutrons scattered by the sample must be determined separately as only the total flight time is recorded. In the Be filter spectrometer the final energy of the neutrons reaching the detector is less than the polycrystalline cutoff (5.22 meV) which gives a wide bandpass of final flight times. The resulting count rates are therefore much higher than those of a crystal analyzer whose bandpass is defined by the crystal mosaic and the range of Bragg angles available to the scattered neutrons. Furthermore, since the final energy for a filter analyzer is small compared to the incident neutron energy for measurements of large energy transfers,

the momentum transfer Q does not vary much with scattering angle. A large solid angle can therefore be covered with adequate Q-resolution. This type of spectrometer is however most useful for the study of essentially dispersionless excitations, since it effectively allows only one cut through (Q,E) space.

A large improvement for the filter spectrometer is possible by taking the difference of spectra recorded with two different filter materials. The instrument described in this paper utilizes as the bandpass of final energies the difference between the cutoffs of Be and BeO of 1.5 meV. A schematic of the spectrometer is shown in Fig. 1. The filter sections are arranged in an alternating sequence of beryllium and beryllium oxide, five on each side covering a range of 90^{0} in scattering angle on each side. The physical dimensions of a section are: inner radius 90mm, outer radius 240mm, angular spread 18^{0} and height 100mm. The sample position is 13m from the target and the detectors are 0.28m from the sample. Each detector bank consists of six ^{3}He 10 atm detectors. The beam size is 25mm x 100mm at the sample position. Each bank is separately recorded, like filter material spectra summed, and the weighed difference taken.

We begin by giving a description of the data analysis for a simple filter analyzer, followed by a discussion of the difference method. The filter difference technique is then compared with the single material filter and the current Weapons Neutron Research (WNR) crystal analyzer. A brief survey of experiments conducted with the difference spectrometer is presented in section 4. Finally, the expected types of use of this instrument in future high intensity operation are discussed.

2. SINGLE FILTER MATERIAL

Before proceeding with taking the difference of two filter materials it is important to understand the lineshape and resolution of spectra taken with a single filter material. In a TOF experiment the bandpass of the polycrystalline filter material is measured on a time scale, not an energy scale as in a reactor experiment. The observed inelastic spectrum is a convolution of the instrumental resolution, the response function of the excitation being measured and the filter response function. First, the instrumental time resolution may be described by an effectively gaussian lineshape. Contributions to it include the moderator pulse width, the proton burst width, the sample size, and the width of the filter edge. The intrinsic lineshape from many types of excitations can be assumed to be a lorentzian in energy, for which a lorentzian in time is a reasonable approximation. Finally the filter transmission is not an ideal step function especially for a filter length sufficient to prevent leakage of neutrons above the filter edge. A finite cross section remaining for energies less than the filter edge attentuates the beam. The transmission function has the form

$$T \propto \left(\frac{t_e}{t}\right)^4 \exp\,(-\beta dt/L) \qquad (1)$$

where t_e is the time-of-flight from the sample to the detector for neutrons of the edge energy, β the absorption coefficient, d the filter length, L the distance from the sample to the detectors, and t the time-of-flight from the sample to the detector for a neutron of an energy less than the filter edge.

The lineshape resulting from the convolution of the three contributions is quite asymmetric with a steep rise on the short time side and a tail on the long time side (see figure 2a). The fit to the data shown in Fig. 2a

shows that this model for the filter lineshape yields reasonable parameters at least for isolated peaks. Not shown is the fit to the BeO spectrum, which is in excellent agreement with the fit to the Be spectrum. Thus we can consider spectra taken with a single material filter to be well understood.

These spectra, however, have some disadvantages which limit the usefulness of such a spectrometer. The relatively poor resolution makes deconvolution of overlapping peaks difficult, particularly if a broadened peak shows no obvious structure. A practical upper limit of three lorentzians in a convolution reduces the information obtainable from a complex spectrum such as that shown in figure 3a. The most disturbing aspect of the model is that the shift of the peak position resulting from the convolution is dependent on the intrinsic width of the mode being measured. The time-to-energy transformation is therefore very complex.

3. DIFFERENCE METHOD

Some of the complications and restrictions of the single filter spectra may be overcome by combining data using filters with two different cutoff energies such as Be and BeO. The bandpass is then restricted to the energies between the two cutoffs (3.76 to 5.22 meV). While this is important, the main improvement results from the elimination of the long low energy tail present with the single filter material.

The most important problem for the difference method is to subtract the two spectra correctly. For physical considerations the filters were selected to be the same length and the detectors all the same distance from the sample. In order to perform the difference, the transmission fractions for the two filters should be matched for energies below that of the BeO edge. Using Eq. 1 of section 2, we require that

$$\alpha\, T(Be) = \alpha'\, T(BeO)$$

or

$$\alpha\left(\frac{t_e}{t}\right)^4 \exp\,(-\beta dt/L) = \alpha'\left(\frac{t'_e}{t}\right)^4 \exp\,(-\beta' d' t/L')$$

where the primed values refer to the BeO. Since d and L are the same for both materials, then

$$\frac{\alpha'}{\alpha} = \left(\frac{t_e}{t'_e}\right)^4 \exp\,[-d(\beta-\beta')t/L]$$

giving $\alpha'/\alpha = 0.58$ at the Be edge. Although α'/α is still a function of t, its dependence over a peak is weak and may be replaced by a weighted mean $\overline{\alpha'/\alpha} = 0.60$. This is in excellent agreement with transmission measurements made on two sections at WNR which yielded a mean ratio of 0.60.

While taking the difference leads to a loss in statistical accuracy, the high throughput of the spectrometer nevertheless allows a few percent statistics to be collected in a reasonable amount of time. The advantages gained however are considerable. First, a symmetric lineshape (see Fig. 2b) is recovered because the bandpass between the two filter edges is nearly a square function. Second, the greatly improved resolution allows peaks which are not obvious in the undifferenced spectra to be discerned. An example is given in figures 3a and b where the Be filter spectrum and the difference spectrum of potassium hydrogen maleate are shown. Finally, the time to energy mapping is no longer dependent on the intrinsic width of the vibrational excitation. Fitting can now be performed outside the convolution, which is needed in the undifferenced case, and can be done on an energy rather than a time-of-flight scale.

The resolution of the filter difference spectrometer is compared (Fig 4.) with that of the crystal analyzer spectrometer currently in use at the WNR. At energy transfers greater than about 100 meV the resolution is similar to that of the crystal analyzer, but the count rate significantly is higher because of the larger solid angle covered and the wider bandpass of final energies.

4. EXPERIMENTAL PROGRAM

The present experimental program using the filter difference spectrometer at the WNR consists of the following areas.

(1) A principal application has been the study of localized hydrogen vibrations in metals, particularly the bcc hydrides such as Nb and Ta. In this case the aim is to relate vibrational energy levels to anharmonicity of the hydrogen potential. A program in cooperation with Sandia National Laboratories has been initiated on rare earth metal hydrides. The vibrational frequencies and relative occupation of tetrahedral and octahedral site hydrogen atoms have been measured for concentrations near the dihydride for lanthanum and yttrium (see Fig. 5). In addition, the hydrogen storage material FeTi was studied.

(2) The vibrational frequencies of H in extremely short intramolecular hydrogen bonds were determined for a number of such compounds in a collaboration with the University of Durham, U.K. (see, e.g. the spectrum of KH maleate, Fig. 3b). The resulting correlation of the out-of-plane bending mode γ(OHO) with the O-O distance is completely different than that found in many previous studies for the usually longer intermolecular hydrogen bonds.

(3) A series of experiments were conducted to study the coupling of torsional modes of NH_2 and NH_4 groups to other internal modes in

insensitive high explosives such as picrates, triaminotrinitrobenzene and related compounds (Fig. 6). Torsional modes could readily be identified, and pronounced frequency shifts were observed as a result of the intramolecular mode coupling.

(4) Catalytic reactions can be studied on large surface area materials owing to the penetrating power of neutrons in comparison to electrons or light. Preliminary experiments on organometallic compounds such as $Mn(CO)_5CH_3$ and $HCCo_3(CO)_9$ to observe C-H modes have been performed. Work is also in progress on ethylene on a supported platinum catalyst in collaboration with Brookhaven National Laboratory.

5. CONCLUSIONS

A successful experimental program has been initiated on the filter difference spectrometer. The instrument is most appropriate for energy transfers from about 50 to 600 meV when moderate energy resolution is sufficient and a high count rate of importance. The difference technique is well enough understood so that peak positions, line widths and integrated intensities can be determined from fairly complex spectra.

Several improvements to the instrument are in progress. An important change will be cooling of the sections which is expected to give approximately a factor of two increase in signal. The solid angle subtended by the detector banks will also be increased by a factor of 1.7 without significant degradation in resolution. With these improvements, much smaller samples can be examined in cases where material is unavailable in larger quantities, as well as samples with much small scattering cross sections.

The major improvement will come when the proton storage ring becomes operational in 1985. A total increase of approximately 100 in neutrons detected will allow much more difficult experiments to be performed on this instrument with still a fast turnover rate.

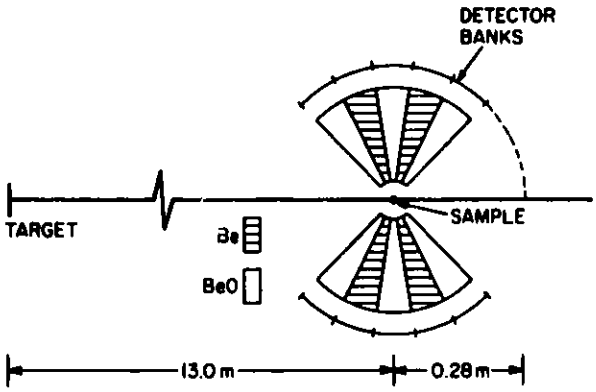

Fig. 1

A schematic of the filter difference spectrometer is shown. Filter sections are 150mm long, 100mm high and span 18 degrees. Each detector bank consists of six ^{3}He 10atm detectors.

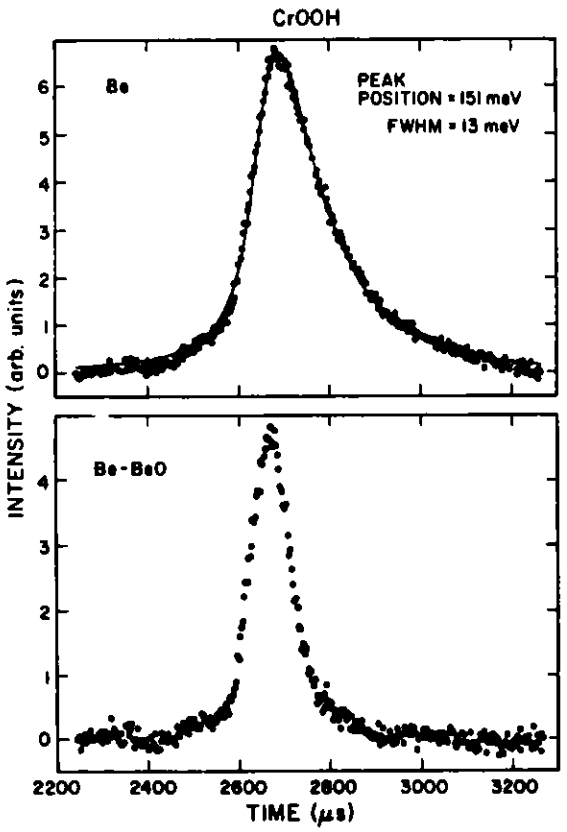

Fig. 2. (a) Chromous acid spectrum from the beryllium filter data and the fit given by the solid line. (b) Chromous acid difference spectrum. Notice the missing tail on the long time side of the peak.

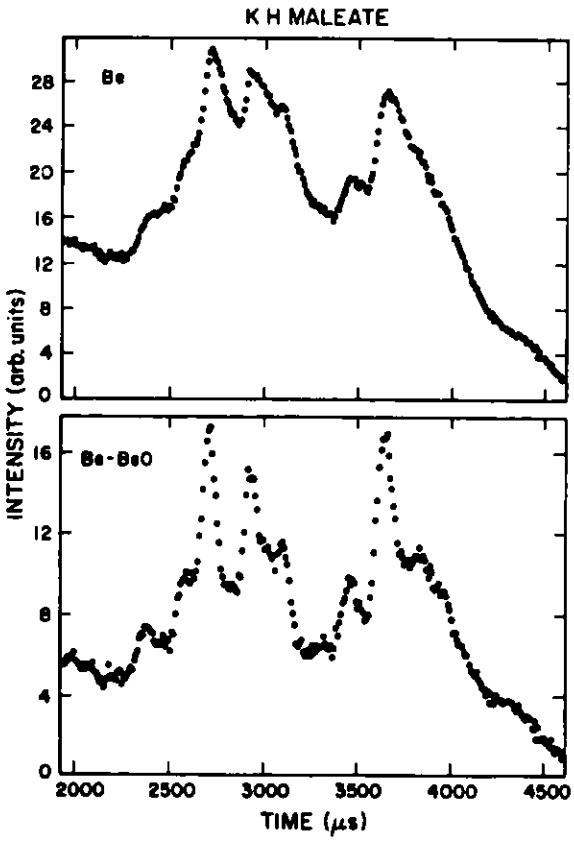

Fig. 3. (a) Beryllium filter spectrum of potassium hydrogen maleate. (b) Difference spectrum of potassium hydrogen maleate. The peak at 2,500 μs is γ(OHO) mode.

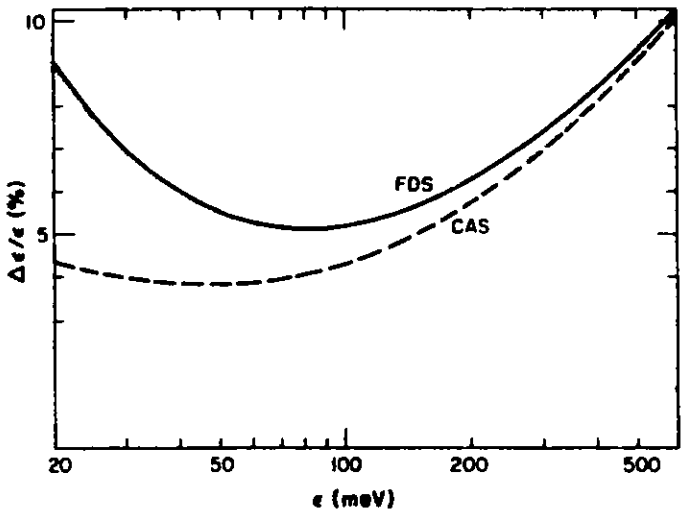

Fig. 4. Energy resolution (FWHM) of the filter difference spectrometer (FDS) and the WNR crystal analyzer spectrometer (CAS).

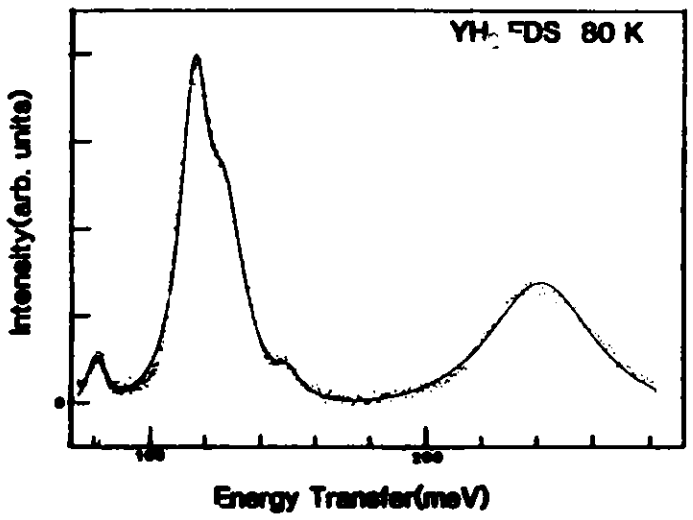

Fig. 5. Yttrium dihydride spectrum taken on the filter difference spectrometer. The peak near 80 meV is due to octahedral site hydrogen atoms while the one at 120 meV is due to tetrahedral site atoms.

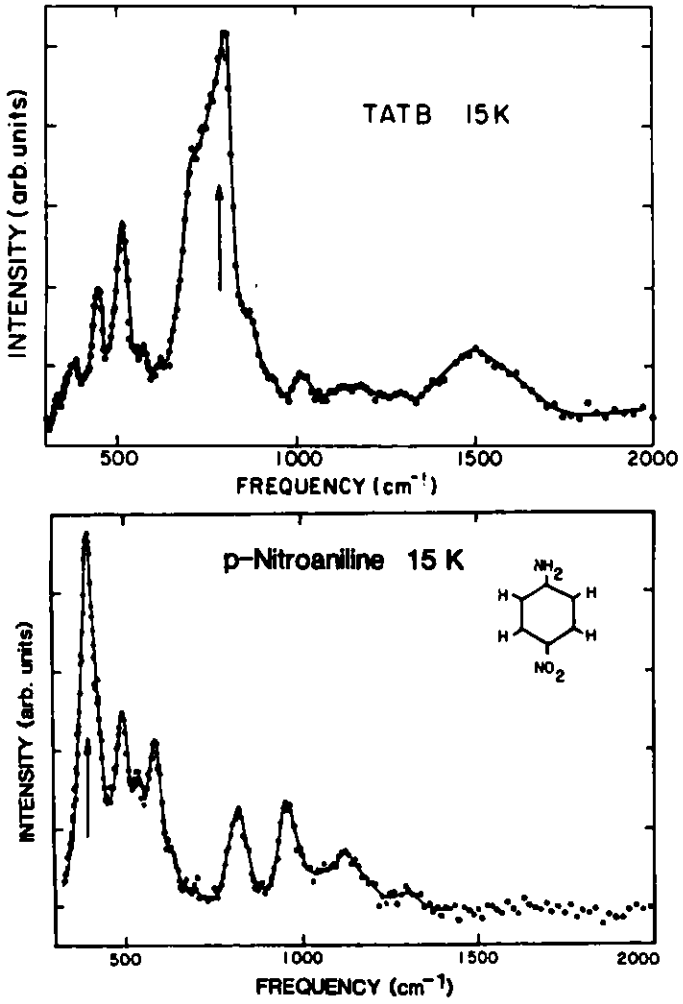

Fig. 6

1, 3, 5-triamino 2, 4, 6-trinitrobenzene(TATB) and para-nitro-aniline are shown. The NH_2 torsional frequency (arrows) is significantly higher in TATB where strong coupling to the NO_2 groups is suspected.

Fig. 7

Tricobalt-nonacarbonyl-methylidyne difference spectrum showing the H-C bending mode at 105 meV, a C-Co stretch at 86 meV and their harmonics at 172 and 210 meV. The modes between 50 and 70 meV are Co-C-O and Co-Co modes.

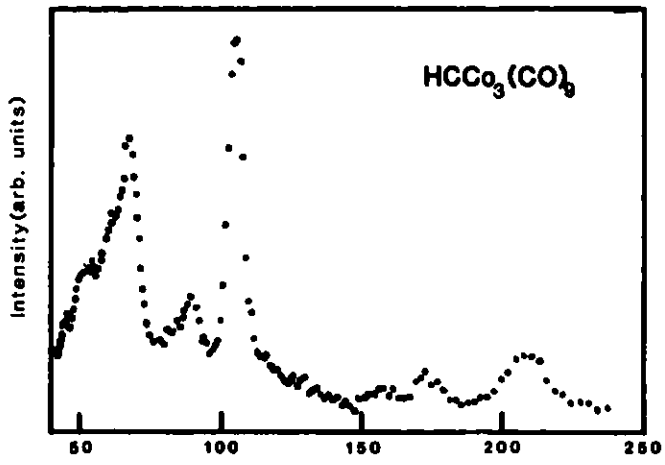

ICANS-VI

INTERNATIONAL COLLABORATION ON ADVANCED NEUTRON SOURCES

June 27 - July 2, 1982

A RESONANCE FILTERED BEAM SPECTROMETER

R.M. Brugger*, A.D. Taylor+, C.E. Olsen, J.A. Goldstone
and A.K. Soper

Physics Division
Los Alamos National Laboratory
Los Alamos, NM 87545

ABSTRACT

A new inelastic neutron scattering spectrometer which operates in the range 1 eV to 15 eV has been developed at the Los Alamos pulsed spallation source WNR. Based on a nuclear resonance filtering the beam, the concept has been tested in 'direct', 'inverted' and 'sample' geometries. A number of resonance filters have been tested to determine their effectiveness. The spectrometer is described and examples of data are presented.

*Permanent address: University of Missouri Research Reactor
University of Missouri
Columbia, MO

+Permanent address: Rutherford Appleton Laboratory
Chilton, Didcot
OXON OX11 0QX
United Kingdom

I. INTRODUCTION

The next generation of neutron sources, pulsed spallation sources, are now producing neutrons and scientific results[1]. These sources have a rich flux of epithermal neutrons which should open up unique research in the field of electron volt energy transfers. However, before this can be tested, spectrometers must be developed to explore this region. One such spectrometer, the resonance filtered beam spectrometer FBS is described in this paper[2,3].

II. PRINCIPLE OF OPERATION

The FBS uses a foil or filter with a strong nuclear resonance at E_R to define the energy of the incident (or scattered) neutrons. The scattered (or incident) energy is then found by time-of-flight TOF. The difference between TOF spectra taken without and with a filter in the beam gives the spectrum of scattered neutrons that would have had an incident (or final) energy corresponding to E_R. Thus the primary and secondary energies and momenta can be determined, and the conditions for performing an inelastic neutron scattering experiment are achieved. If the filter is in the incident beam, the geometry is called 'direct' while with the filter in the scattered beam, the geometry is called 'inverted.' A related arrangement, 'sample' geometry, where the system under investigation has a component with a nuclear scattering resonance has also beam tried, and is described.

III. RESOLUTION

The overall energy transfer resolution is a convolution of the contributions from the energy width of the resonance, incident and scattered flight path uncertainties and the moderated neutron pulse widths. These

contributions are, to a first approximation, for the direct geometry case, respectively

$$\Delta\epsilon^{(1)} = \left[1 + \frac{L_i}{L_f} \cdot \left(\frac{E_f}{E_i}\right)^{3/2}\right] \Delta E_R$$

$$\Delta\epsilon^{(2)} = 2 \cdot \frac{\Delta L_i}{L_f} \cdot \frac{E_f^{3/2}}{E_i^{1/2}}$$

$$\Delta\epsilon^{(3)} = 2 \cdot \frac{\Delta L_f}{L_f} \cdot E_f$$

$$\Delta\epsilon^{(4)} = 2 \cdot \frac{E_f^{3/2}}{2286\, L_f} \Delta t$$

The overall resolution is then

$$(\Delta\epsilon)^2 = \sum_i \left(\Delta\epsilon^{(i)}\right)^2 \quad .$$

In these equations, L_i and L_f are the incident and scattered flight paths and ΔL_i and ΔL_f their respective uncertainties. The energy width of the resonance filter's transmission is ΔE_R. The moderated neutron pulse width, Δt, is itself a convolution of contributions from neutron moderation Δt_m, and from the intrinsic width of the proton burst Δt_p where

$$\Delta t^2 = \Delta t_m^2 + \Delta t_p^2$$

or

$$\Delta t^2 \simeq \frac{4000}{E} + \Delta t_p^2$$

Lengths are measured in meters, energies in meV and time in μs. For the inverted geometry case, these expressions become

$$\Delta\epsilon^{(1)} = \left[1 + \frac{L_f}{L_i} \cdot \left(\frac{E_i}{E_f}\right)^{3/2}\right] \Delta E_R$$

$$\Delta\epsilon^{(2)} = 2 \cdot \frac{\Delta L_i}{L_i} \cdot E_i$$

$$\Delta\epsilon^{(3)} = 2 \cdot \frac{\Delta L_f}{L_i} \frac{E_i^{3/2}}{E_f^{1/2}}$$

$$\Delta\epsilon^{(4)} = 2 \cdot \frac{\Delta L_f}{L_i} \frac{E_i^{3/2}}{2286\, L_i} \Delta t$$

The above sets of equations indicate that the FBS in the direct geometry and inverted geometry are similar in resolution when flight paths can be optimized and energies are comparable. One practical consideration favoring the inverted geometry is that with the existing target shield it is quite difficult to make L_i short for the direct geometry while it is quite easy to make L_f short for the inverted geometry.

In addition to these explicit contributions to the energy transfer resolution, a defocusing effect is produced as the dispersion relationship for a given mass nucleus crossing the Q-ϵ locus for a resonance at a particular scattering angle. The effect may be seen in figure 1 (direct geometry) and figure 2 (inverted geometry). In these figures both the dispersion relation and the Q-ϵ loci which are illustrated as lines are, in reality, bands in Q-ϵ space.

IV. RESONANCE FILTERS

A search was made for nuclei with suitable resonances. Table I is a partial list of those which have been identified. It is important that the appropriate resonance is well separated from other resonances, that the resonant cross-section is high while the cross section beyond the resonance be relatively small. Also it is important that the resonance have a narrow natural width and a narrow Doppler width. Further criteria are that the material can be easily obtained elementally or isotopically and that it is easy to handle. The underlined cases in table I are those that have been, or are planned to be used at WNR. What is of importance in the measurement is not the cross-section but the transmission, so the resolution and intensity of a given resonance may be tuned by adjusting the filter thickness. As an example, ENDF/B-V cross-section data show the Doppler broadened widths of the 1.056 eV resonance of ^{240}Pu to be 58 meV at 300K and 43 meV at 77K. Such widths are only achievable in the limit of an infinitly thin absorber for which there would be no significant signal. Considerations of signal and resolution imply that at the resonance center an attenuation of about 0.75 is appropriate. Note that the optimum thickness for a given resonance is a function of the filter temperature. Figure 3 gives the variation of ΔE_R as a function of the filter thickness for ^{240}Pu. Data for Rh, Au and ^{238}U filters are given in figure 4. The solid points on the curves show the filter thicknesses at which the peak of the resonace gives 0.75 attentuation.

Table I shows that there are a number of available elements or isotopes that have narrow and isolated resonances. The limit to the resolution which can be achieved, set by the natural and Doppler widths of these resonances

is about 50 meV for 1 eV neutrons using a ^{240}Pu foil and 75 meV FWHM at 6.67 eV using a ^{238}U foil.

V. EXPERIMENTAL ARRANGEMENT

The three modes of this spectrometer have been developed and tested at WNR. Figure 5 shows the WNR target station and experimental area with the FBS set up in direct goemetry. On flight path 3 the incident flight path is about 5.5 m and the scattered neutrons are detected at about 5.5 m from the sample at an angle which may be varied between 0° and 120°. The unscattered beam is removed via the get lost pipe, thus reducing background.

Figure 6 shows the specta with the filter in and with the filter out when the sample was a thin slab of H_2O and a 0.002" thick sheet of Rh metal was the resonance filter. The scattering angle was 22°. At short times (less than 300μs) where the foil essentially attenuates no neutrons both spectra superimpose exactly. The dip in the foil in the spectrum at 700 μs corresponds to neutrons being absorbed from the primary beam at 1.257 eV by the Rh resonance. The difference between the two spectra, equivalent to scattering from an incident beam of 1.257 eV neutrons, is shown in figure 7.

The resolution function of this version of the spectrometer calculated for current WNR conditions using the equations of section III is given in figure 8 for a variety of resonance filters. It should be noted that the WNR proton pulse of about 4 μs (contribution $\Delta\epsilon^{(4)}$) dominates the ^{238}U resolution, is an equal contribution to the resolution when Au is the filter, but does not effect the resolution functions when either Rh or ^{240}Pu are the filters.

Figure 9 shows the FBS set up in its inverted geometry mode on flight path 11. In this configuration the incident flight path of about 30 m

provides excellent TOF resolution. The filter is placed in the scattered beam, thus defining the final energy. A short secondary flight path further improves the resolution. Detectors are time analyzed independently to improve Q resolution by limiting the angular resolution. The form of the resolution function for this spectrometer is given in figure 10.

An earlier trial version of the inverted geometry mode on flight path 3 used a 5.5 m incident flight path and a 1.4 m secondary flight path. The energy resolution of this configuration is given in figure 11. The large solid angle accepted by the ganged detectors in this case degraded the Q resolution. Figure 12 shows spectra obtained in this inverted geometry when the sample was 1mm of ZrH_2 and the filter was 0.002" of Rh. The top spectrum is for no filter in the final beam and the middle spectrum is the response with Au in the final beam. The bottom spectrum is the difference. One sees "elastic" scattering from the Zr at channel 1100 while the inelastic scattering from the H is near channel 800. Each spectrum was run for 20 μA-hr.

Figure 13 shows the FBS set up in the sample geometry. In this arrangement, the energy defining resonance is part of the sample and no additional filter is used. Figure 14 shows the scattering spectrum from a 0.001" thick sample of UO_2. Peaks from the 6.674 eV, 20.90 eV, 36.80 eV, 102.47 eV and 208.46 eV scattering resonances are observed on top of a background from the fast neutron burst. The resonances define an interaction energy while the energy after scattering is measured by TOF over the secondary flight path of 5.5 m. Thus information about the recoil energy and broadening of the resonance caused by binding effects can be determined.

The spectra presented in the proceeding paragraphs show the versatility of FBS and that it can operate in all three geometries.

VI. SCATTERING EXPERIMENTS

The goals of developing eV spectrometers are to study high energy excitations, excitations that show the ground state momentum distribution of particles, transitions between magnetic states of crystals, and transitions between electronic states of materials. Many of these experiments are difficult and beyond the initial capabilities of FBS or any other eV spectrometer. More accessable experiments were tried first to show the capability of an FBS.

An easy class of experiment is found by scattering from atoms of mass 1 amu, where the widths of the inelastic scattering are correspondingly greater. Scattering at high Q gives a direct observation of the ground state momentum distribution of the H atom and hence leads to the shape of the potential the proton experiences. Such measurements are clearly of importance in understanding, for example, hydrogen bonded systems.

As a preliminary experiment, the ground state momentum distribution of ZrH_2 was investigated where the potential is well described by a simple harmonic oscillator of frequency 140 meV. Figure 15 shows data for scattering from ZrH_2 at 90° using a 0.002" Rh foil. The sharp peak at channel 45 corresponds to recoil scattering from Zr atoms and the broad feature centered at channel 66 is due to scattering from H. The width of the Zr peak corresponds to the calculated resolution function. The dashed line corresponds to scattering from a simple harmonic oscillator of frequency 150 meV, evaluated along a constant scattering angle of 90°. The resolution

function for the Rh foil has been folded in. The actual position of the maximum in scattering from H is an artifact of the cut taken thru Q-ϵ space and the shape of $S(Q,\epsilon)$. This position is very sensitive to the width of the scattering function. Figure 16 shows an inverted geometry measurement made on the same system with a 0.002" Rh filter and the detectors at 60°, (using the short FP 3 configuration). These data have been transformed to an energy transfer scale. Again the sharp peak at $\epsilon = 0$ eV is Zr scattering and its width is in excellent agreement with the calculation shown in figure 11. The broad H mode centered at $\epsilon = 1.5$ eV is again consistent with a simple harmonic oscillator of frequency 150 meV. This time the peak does reflect a maximum in $S(Q,\epsilon)$. Detailed analysis of these data was not carried out due to the large ($\pm$ 6°) acceptance of the detector bank in the trial geometry.

Scattering at large Q requires large scattering angles, thus removing detector from regions of high background. The physics processes in the system of interest tend to broaden with Q and so energy and resolution requirements become less severe. Figure 17 shows the high Q scattering from a series of different mass nuclei. The FBS was in direct geometry with the scattering angle 117.5° and the foil was 0.003" of ^{238}U. In these data, shifts in peak position due to recoil, $\epsilon_R = \frac{\hbar^2 Q^2}{2M}$ are evident. The effect being greatest for the mass 4 amu case. Although for these particular run conditions the width of each peak was dominated by instrumental resolution, the effect of resolution is again least for He. By fitting the He data, a ground state momentum distribution of the struck particles (normal He) was obtained. The He peak has a width corresponding to an effective temperature of 13K, in agreement with previous measurements. The resolution, figure 8, of this geometry was, however, too poor to attempt to separate the condensate and noncondensate fractions for He below the lambda oint.

Two approaches are possible to improve the charactistics of the He experiment. By using the inverted geometry, with a long primary flight path and by using short proton burst (0.5 μs) all contributions to the resolution can be made small relative to the intrinsic energy width of the resonance. For a 30 m primary path and a 1 m secondary path, some 100 meV resolution may be achieved at a final energy of 6.67 eV corresponding to the ^{238}U resonance. The second device which may be employed to improve the experiment is, that by going to the inverted technique ($E_i > E_f = E_R$), Q can be increased since E_i is larger. This expands the characteristic widths of both distributions, which are proportional to Q, relative to the intrinsic resolution, which has a much weaker dependence on Q. Figure 18a, illustrates the cut taken thru Q-ϵ space and Figure 18b shows simulated data including a statistical variance appropriate to the subtraction technique for a 10% condensate fraction. A fit to these simulated data (solid and dashed lines) allows the two components of this lineshape to be extracted, recovering, within resonable errors, the simulated condensate fraction and the condensate and noncondensate widths.

Figure 19 gives an example of a sample geometry experiment. The two peaks correspond to scattering from the 6.674 eV resonance in U when the U atoms are bound in UO_2 and UF_4. Within the present resolution, the same recoil energy and widths are measured for both materials.

The above examples of data show that a certain class of experiments using eV neutrons on FBS are now possible. The results also provide encouragement to attempt the more difficult experiments such as observing magnetic

transitions for which Q must be $< 4\ \mathring{A}^{-1}$ while ϵ will be greater than 100 meV. Similar measurements to observe electronic excitations in molecules will require $Q < 4\ \mathring{A}^{-1}$.

VII. CONCLUSIONS

The results presented in the preceeding sections show that FBS works as an inelastic neutron spectrometer with eV neutrons. Its major disadvantages are: 1) that the statistical accuracy of each point is limited because FBS employs a difference to define an event and 2) the resolution is limited by the energy width of the nuclear resonance used as a filter.

The general advantages of FBS are: 1) it is relatively easy to assemble and use, 2) it can be used in all three geometries, 3) counting rates can be large which helps to overcome the difference disadvantage, 4) the subtraction technique removes fast neutron background, 5) a large number of resonances are available, 6) the foils are relatively easy to handle and cool, and 7) since only neutrons are detected, filters that are radioactive can be used.

Both the direct and inverted geometry configurations have their merits. In the direct geometry, the necessity of having a long secondary flight path may be capitalized on for low Q scattering where a reasonable radial separation between beam and detector may be achieved at small angle. A further advantage of the filter being in the primary beam is that only a small filter area is required and so smaller (and hence more esoteric) filters may be used. Cooling the filters to suppress Doppler broadening is also facilitated. The inverted geometry has the advantage that the long initial flight path fits well with the biological shielding requirement. In many cases, the direct and indirect geometries complement each other.

References

1. C. G. Windsor, Pulsed Neutron Scatttering, Taylor and Francis Ltd, London (1981).
2. R. M. Brugger, A. D. Taylor, C. E. Olsen and J. A. Goldstone, Bulletin of the APS, 27, #1, pp 13 (Jan 1982).
3. A. D. Taylor and R. M. Brugger, Bulletin of the APS, 27, #1, pp 14 (Jan 1982).

Acknowledgements

The authors appreciate the encourgement and helpful discussions of Richard Silver and the mechanical assistance of Rod Hardee.

TABLE I

Some Possible Resonances for FBS

Isotope	Natural Abundance (%)	E_R (eV)	Nuclear Width (meV)	Doppler-Broadened Width (meV)	Peak Cross Section (Temperature) (barns (K))
^{149}Sm	13.9	0.872	61		2790(300)
^{240}Pu	-	1.056	33.3	58	112000(300)
^{240}Pu	-	-	-	43	139000 (77)
^{103}Rh	100	1.257	156	178	4081(300)
^{193}Ir	62.7	1.303	87.3		5830(300)
^{115}In	95.7	1.457	75		29900(300)
^{185}Re	37.4	2.156	57.7		9300(300)
^{242}Pu	-	2.67	27		35200(300)
^{238}Pu	-	2.90	38		1020(300)
^{169}Tm	100	3.90	108		30100(300)
^{181}Ta	100	4.28	57		14100(300)
^{197}Au	100	4.906	139	180	30800(300)
^{234}U	-	5.19	29		27500(300)
^{236}U	-	5.45	27		15700(300)
^{238}U	99.3	6.674	27.5	104	7712(300)
^{238}U	-	-	-	54	12475 (77)
^{238}Pu	-	9.98	42		4200(300)
^{159}Tb	100	11.14	95		7140(300)
^{195}Pt	33.8	11.9	127		3120(300)
^{163}Dy	24.9	16.23	124		2070(300)
^{186}W	28.6	18.84	337		29800(300)
^{238}U	99.3	20.90	34	-	8510(300)

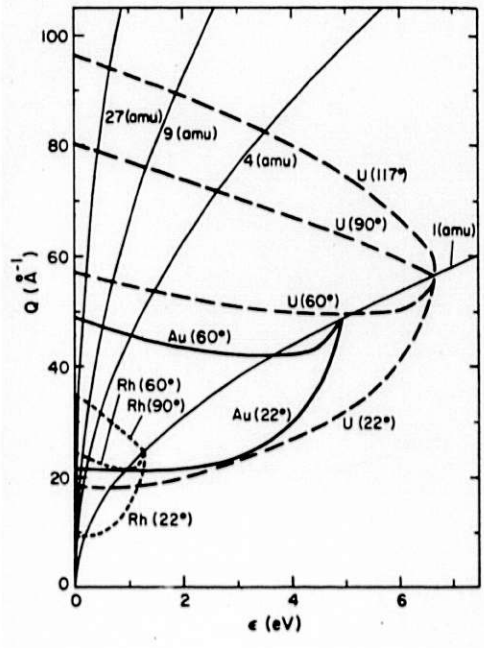

Fig. 1. For direct geometry, the cut in Q-ε space of inelastic scattering for particular incident energies (Rh, Au, U) at particular angles (22°, 60°, 90°, 117°) by particular mass particles (1, 4, 9, 27 amu).

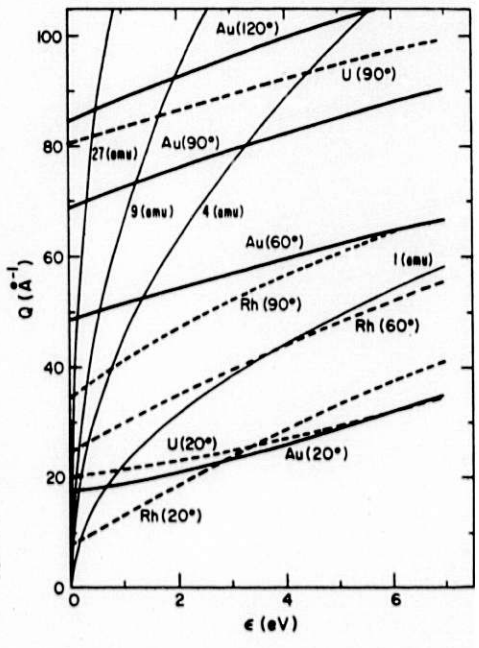

Fig. 2. For indirect geometry similar cuts in Q-ε space to Figure 1.

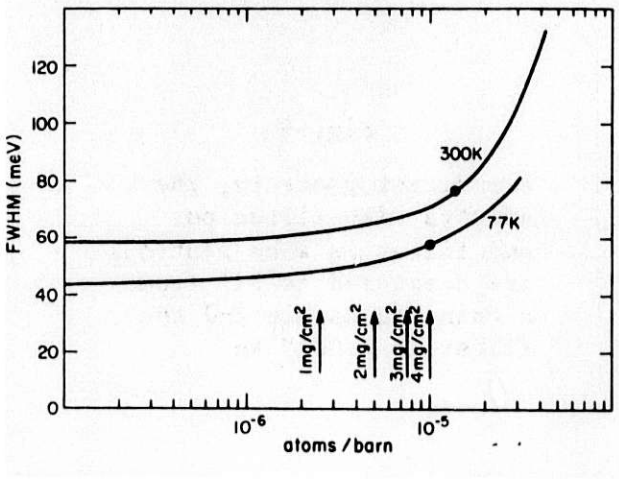

Fig. 3. For ^{240}Pu, the variation of the observed resonance width ΔE_R as a function of filter thickness. The solid points represent thicknesses that give 0.75 attenuation at the center of the resonance.

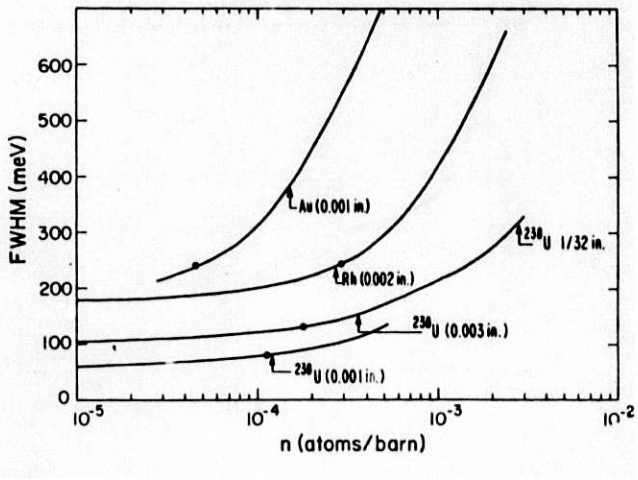

Fig. 4. For Rh, Au and U, the variation of the observed resonance width ΔE_R as a function of filter thickness. The solid points represent thicknesses that give 0.75 attenuation at the center of the resonance.

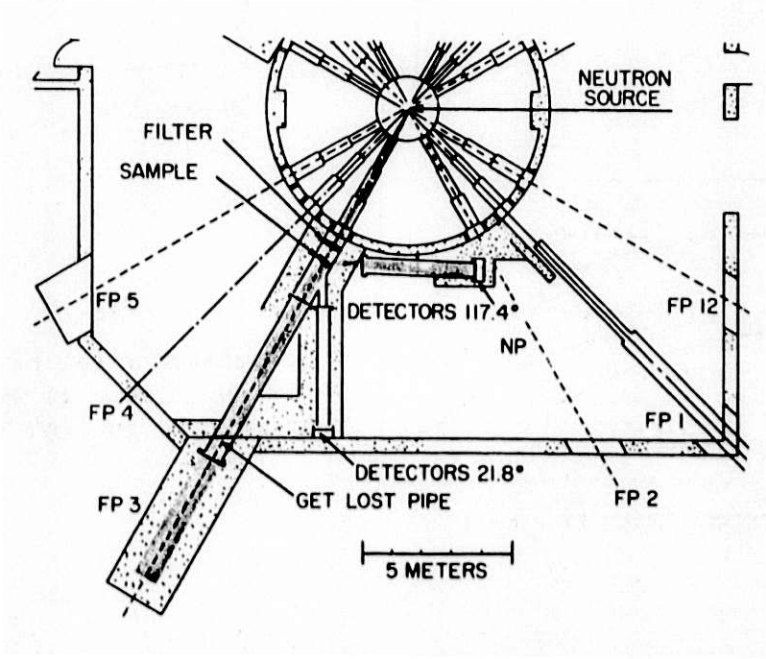

Fig. 5. The WNR target station and experimental area with the FBS in direct geometry at flight path 3.

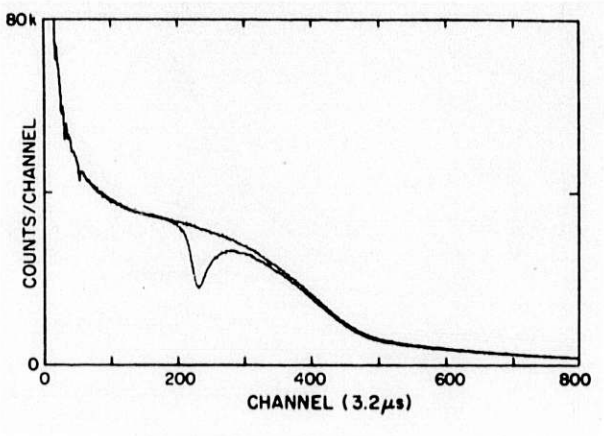

Fig. 6

For direct geometry, the spectra with filter out and filter in when neutrons are scattered at 22° from a thin H_2O sample and the filter is 0.002" Rh.

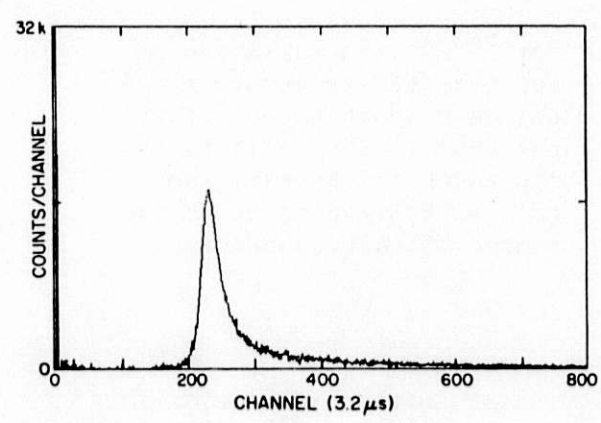

Fig. 7

The difference of the two spectra of Figure 6.

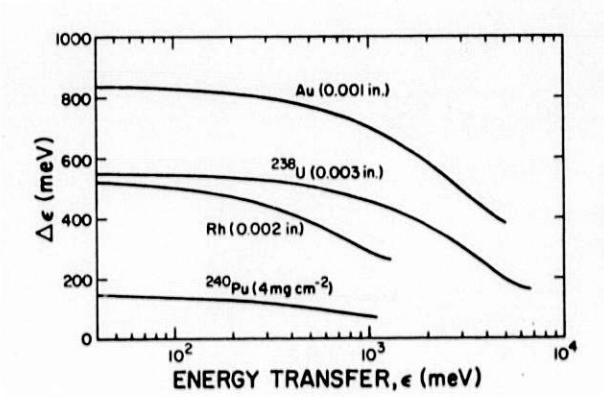

Fig. 8

Calculated resolution of the FBS for direct geometry as structured in Figure 5.

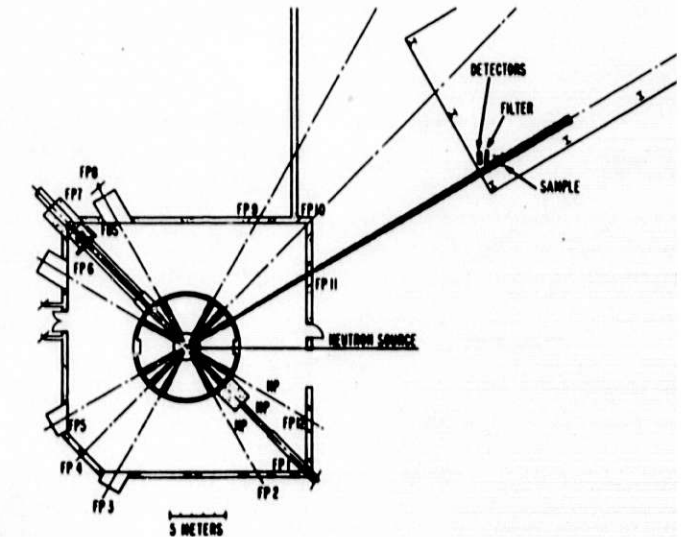

Fig. 9

The WNR target station and experimental area with the FBS in inverted geometry at flight path 11.

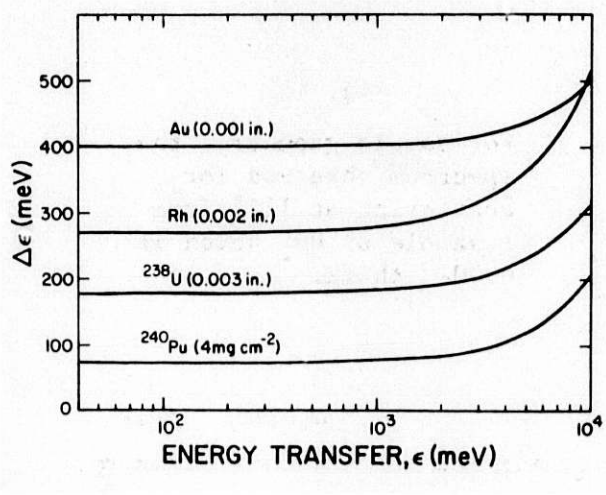

Fig. 10

Calculated resolution of FBS in inverted geometry as structured in Figure 9.

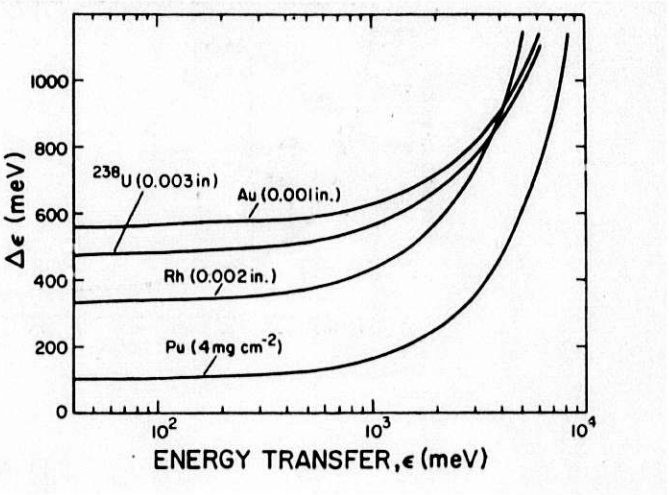

Fig. 11

Calculated resolution FBS in inverted geometry at flight path 3.

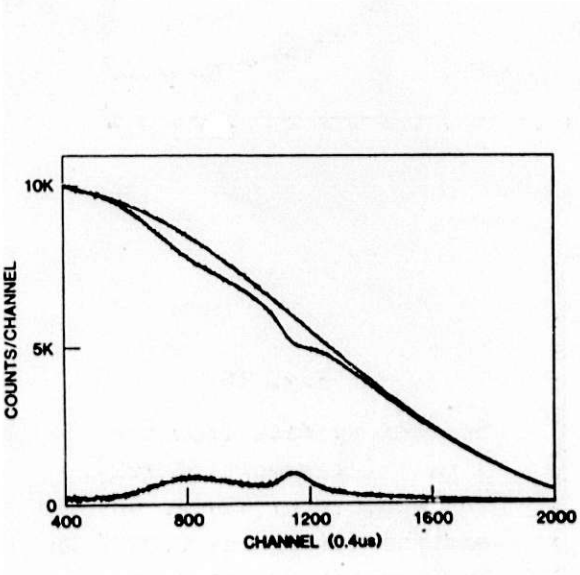

Fig. 12

For inverted geometry, the spectra taken at flight path 3 for a 1 mm thick sample of ZrH_2 and with a filter of 0.002" Rh. The detectors observed scattering at 60°.

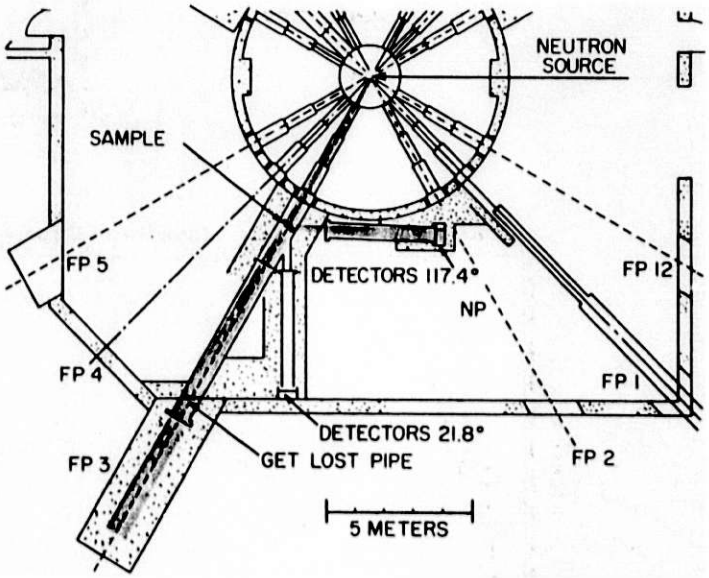

Fig. 13

The WNR target station and experimental area with the FBS in sample geometry at flight path 3.

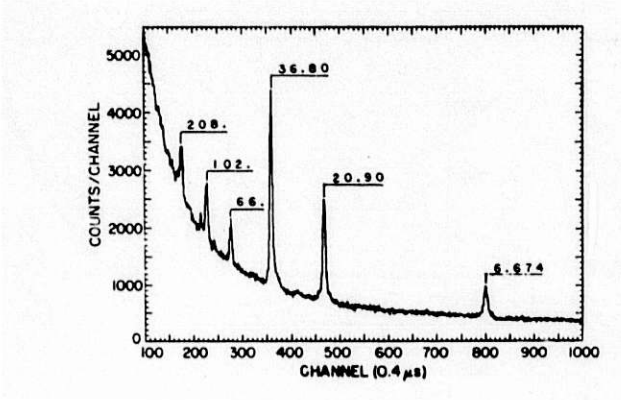

Fig. 14

For sample geometry, the spectrum observed for scattering at 117° from a sample of UO_2 which is 0.001" thick.

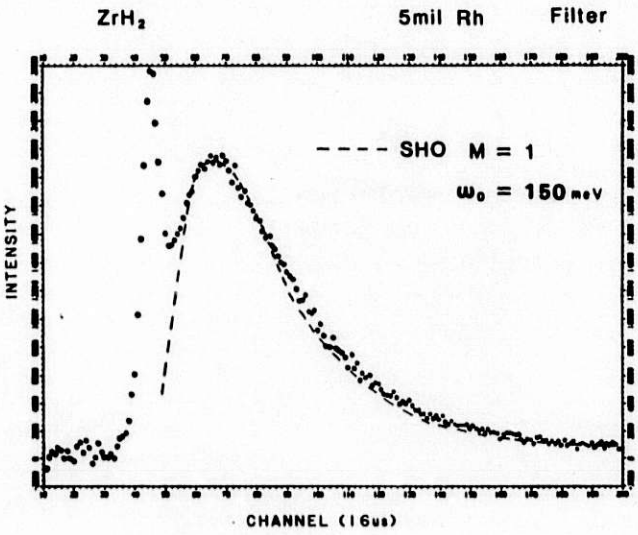

Fig. 15

Scattering data for a 1 mm thick sample of ZrH_2. The scattering was at 90° and the filter was 0.002" in direct geometry.

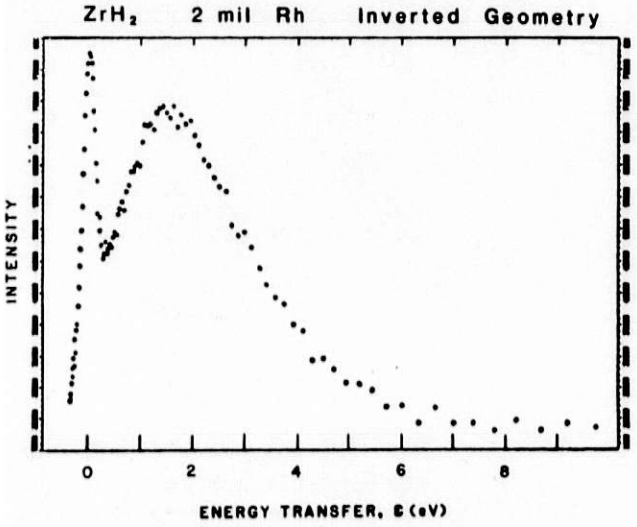

Fig. 16

Scattering data from the 1 mm thick sample of ZrH_2. The scattering was at 60° and the filter was 0.002" Rh in inverted geometry at flight path 3.

Fig. 17

Scattering data from samples of Pb, Al, liquid N_2 and liquid He. The scattering was at 117.5° and the filter was 0.003" ^{258}U in direct geometry.

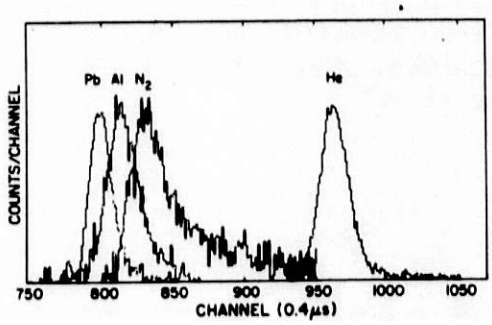

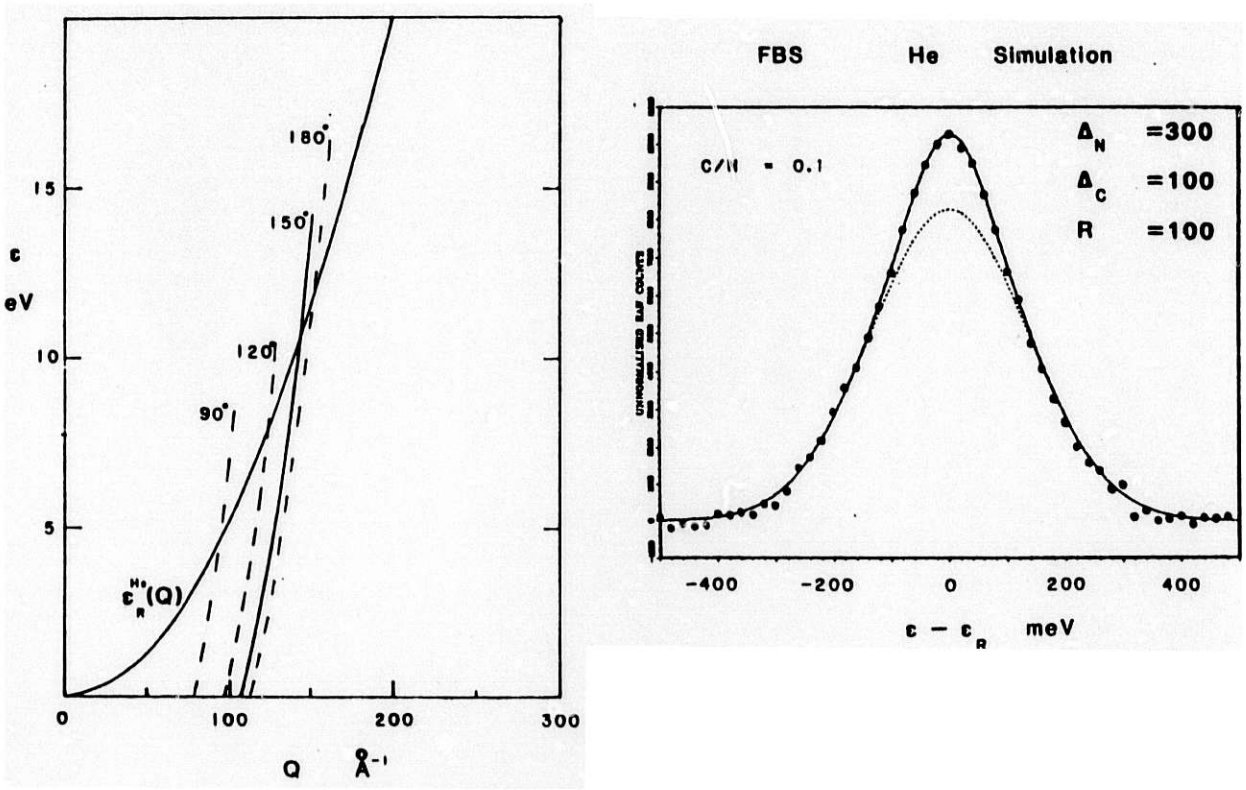

Fig. 18. a) The cut in Q-ε space for scattering from He. The filter is ^{238}U in inverted geometry. b) A simulated curve for scattering from He (90% normal and 10% condensed phase).

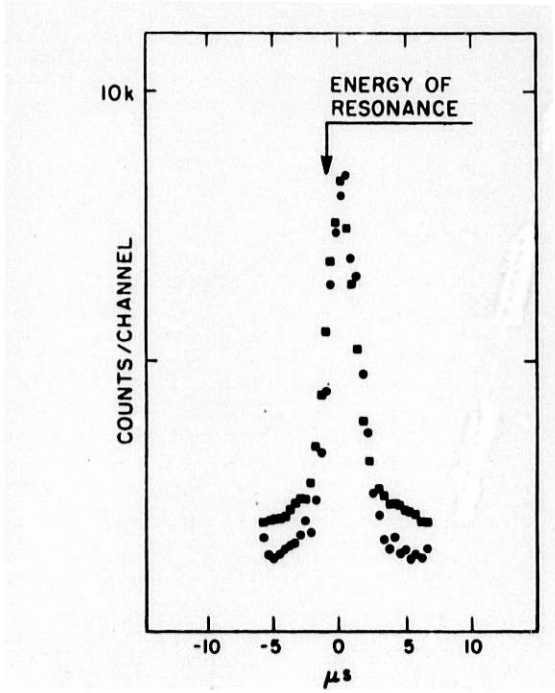

Fig. 19

Example of data for sample geometry. The samples were $^{238}UO_2$ and $^{238}UF_4$ about 0.001" thick. The scattering was at 117.5°. The squares are UO_2 and the circles are UF_4.

ICANS-VI
INTERNATIONAL COLLABORATION ON ADVANCED NEUTRON SOURCES
June 27 - July 2, 1982

eV NEUTRON SPECTROSCOPY USING RESONANCE ABSORPTION ENERGY SELECTION ON A PULSED SOURCE

W G Williams and J Penfold
Neutron Division, Rutherford Appleton Laboratory

ABSTRACT

A method is proposed for measuring excitation energies up to approx 1 eV by using an absorption foil difference technique in the inverse geometry. The discussion is restricted to using the ^{149}Sm resonance at an energy E_R = 0.873 eV and utilises other fixed absorption filters to improve the sensitivity of the method for inelastic measurements. Feasibility tests have been carried out on the LAD total scattering spectrometer at the Harwell Linac. By extrapolating from results obtained for ZrH_2 it is predicted that with more powerful sources such as the SNS it should be possible to observe high energy magnetic excitations.

eV NEUTRON SPECTROSCOPY USING RESONANCE ABSORPTION ENERGY SELECTION ON A PULSED SOURCE

W G Williams and J Penfold
Neutron Division, Rutherford Appleton Laboratory

1. INTRODUCTION

The new pulsed neutron sources provide much greater fluxes of epithermal neutrons than steady state sources and the importance of this characteristic to studies in condensed matter physics has been expounded by several authors eg Sinha[1]. In order to exploit this feature in dynamical studies we require effective monochromators at neutron energies $E \gtrsim 1eV$ and three methods of energy selection viz (i) crystal monochromators[2], (ii) phased Fermi choppers[3] and (iii) nuclear resonance absorption[4] may be considered. A detailed discussion of methods (i) and (ii) has been given in reference 2; they provide a means of performing high resolution measurements (energy transfer resolutions $\Delta\hbar\omega/\hbar\omega \sim 2\%$).

Two variations of method (iii) have been examined. In the first, the "resonance detector spectrometer"[4,5,6], an analysing foil placed after the scatterer captures neutrons resonantly over a narrow energy region and the emitted γ-rays are detected. This is an example of an inverse geometry instrument in which a large fraction of the incident white pulsed beam can be utilised. The second variation is a direct geometry instrument, the "filtered beam spectrometer"[7], where the absorbing foil is used to define the incident neutron energy and the difference TOF spectra of data collected with and without the foil gives the sample's response to the resonance energy incident neutrons.

This paper discusses the possibilities of using a Samarium-149 resonance absorber with a resonance energy E_R = 0.873 eV for inelastic experiments initially at the Harwell Linac and later on the SNS. The reason for confining the discussion to this resonance is two-fold: (i) it is possible to polarise the nucleus[8], so there is the potential eventually of extending the method to look at spin-dependent scattering processes, and (ii) the resonance has a conveniently small total width Γ = 60 meV[9]. It was decided first to examine the possibilities offered by the foil difference method, both in direct and inverse instrument geometries. In the latter case, in contrast to ref 7, the difference TOF spectra result from scattered neutrons at the resonance energy.

2. FOIL DIFFERENCE METHOD IN DIRECT AND INVERSE GEOMETRIES

Since the difference counts are always combined with the total TOF on a pulsed source spectrometer it is possible, at least in principle, to use the foil difference technique in either the direct or inverse geometry. The advantages and disadvantages of each method can only really be assessed by experiment, however for foils with $E_R \sim 1$ eV such as Sm, we favour using the inverse geometry approach. The need to carry out many measurements at the lowest possible momentum transfer $\hbar Q$ means that the scattered neutron wavevector k_2 (hence energy E_2) should be as high as possible; this is easiest with $E_2 = E_R$ for neutron down-scattering ie with an analyser foil after the scatterer.

Another important reason for choosing the inverse geometry is that it should in practice provide better energy resolution over much of the energy transfer range of interest ($0.2 < \hbar\omega(\text{eV}) < 1$). These resolutions are dominated by the term representing the energy width of the resonance peak and for direct (D) and inverse (I) geometry spectrometers on a pulse source may be approximated by:

$$\left[\frac{\Delta\hbar\omega}{\hbar\omega}\right]_I = \frac{\Delta E_R}{\hbar\omega}\left[1 + \frac{L_2}{L_1}\left(\frac{E_1}{E_R}\right)^{1.5}\right], \quad \text{and} \tag{2.1}$$

$$\left[\frac{\Delta\hbar\omega}{\hbar\omega}\right]_D = \frac{\Delta E_R}{\hbar\omega}\left[1 + \frac{L_1}{L_2}\left(\frac{E_2}{E_R}\right)^{1.5}\right] \tag{2.2}$$

where L_1 and L_2 represent the incident and scattered beam flight paths, and E_1 and E_2 the incident and scattered neutron energies. We now calculate these contributions to the energy resolutions for situations where the difference count rates (per unit energy transfer) in the direct and inverse geometry foil experiments are comparable. Matching of incident and scattered beam solid angles gives:

$$\left[\frac{A_m}{L_1^2} \cdot \frac{A_d}{L_2^2} \right]_D = \left[\frac{A_m}{L_1^2} \cdot \frac{A_d}{L_2^2} \right]_I \qquad (2.3)$$

where A_m and A_d are the moderator and total detector areas and if we assume that these are equal (it should for example be possible to cover a large part of the scattered beam solid angle by placing the absorbing foil close to the sample in case I) we obtain equivalent count rate differences with:

$$\begin{aligned} (L_1L_2)_D &= (L_1L_2)_I, \quad \text{or} \\ L_{1D}L_{2D} &= L_{1I}D_{2I} \end{aligned} \qquad (2.4)$$

The resolution equations require $L_{2I} \ll L_{1I}$ and $L_{2D} \gg L_{1D}$, and whereas the first condition is relatively easily met, the second is not. For the SNS L_{1D} must be greater than approx 6 m so that the sample extends beyond the biological shielding. We have calculated the energy resolutions for the following hypothetical (but practical) spectrometer case where equation (2.4) is fulfilled:

$$\begin{aligned} L_{1D} &= 6 \text{ m}; \quad L_{2D} = 3 \text{ m} \\ L_{1I} &= 18 \text{ m}; \quad L_{21} = 1 \text{ m} \\ \text{and } E_R &= 1 \text{ eV}; \quad \Delta E_R = 0.05 \text{ eV} \end{aligned}$$

The results are shown in Figure 1. It is concluded that the inverse geometry arrangement gives appreciably better resolutions for resonance energy foils with $E_R \sim 1$ eV and it was decided to carry out detailed calculations of the performance of a Sm analyser difference spectrometer on the Harwell Linac and SNS sources.

The equating of luminosities, as discussed above, neglects the effect of the incident and scattered beam divergencies on the Q resolution. This factor was considered, at least initially, to be less important than the optimisation of the intensity and energy transfer resolution. The beam divergence effect on the Q resolution can, in principle, be improved by reducing the area of detector elements while maintaining large total areas.

3. ENERGY SELECTION USING THE SAMARIUM RESONANCE AT $E_R = 0.873$ eV

The optimum resolutions and difference counts in resonance absorption difference spectrometers are obtained by optimising the thickness of the absorption foil. If the foil is too thin the difference counts are less than the optimum, whereas very thick foils cause a degradation in the energy transfer resolutions. The optimisation method described in this section was applied to the Sm resonance at $E_R = 0.873$ eV. It has been shown[10] that the absorption cross-section across this resonance peak can be described by the Breit Wigner expression:

$$\sigma(E) = \left(\frac{\sigma_o}{1 + 4(E-E_R)^2/\Gamma^2} \right) \left(\frac{E_R}{E} \right)^{\frac{1}{2}} \qquad (3.1)$$

where E is the neutron energy, Γ the total resonance width, and σ_o is the maximum cross-section at the resonance energy E_R. The foil attenuation A(E) across the absorption peak, which is proportional to the difference counts in these experiments, is then given by:

$$A(E) = 1 - \exp \left\{ \frac{-\sigma\, Nd}{1 + 4(E-E_R)^2/\Gamma^2} \left(\frac{E_R}{E} \right)^{\frac{1}{2}} \right\}, \qquad (3.2)$$

where Nd is the atomic thickness of the absorbing nucleus in the foil. This function was calculated for the Sm resonance using the recommended resonance parameters given in reference (9). The curves for different Sm thicknesses Nd are shown in Fig 2. The foil thickness optimisation uses a quality factor $A(E_R)/\Delta E_R^2$, where $A(E_R)$ is the attenuation factor at $E = E_R$ and ΔE_R is the FWHM of the attenuation peak. The variation of this quality factor with Sm foil thickness is also shown in Fig 2. We conclude that the optimum Sm thickness is Nd $\sim 3.5 \times 10^{20}$ at cm^{-2}. In the calculations to be presented and in the test experiments to be performed we shall use a Sm foil atomic thickness Nd $\sim 3.0 \times 10^{20}$ at cm^{-2} which corresponds to a physical thickness d $\sim$ 0.1 mm; this gives a peak attenuation $A(E_R) = 0.61$ and a resolution width $\Delta E_R = 0.075$ eV.

4. DESIGN OF RESONANCE FILTER DIFFERENCE SPECTROMETER IN THE INVERSE GEOMETRY

(a) Outline Description

Feasibility experiments on the resonance foil analyser method were carried out on the SNS total scattering spectrometer LAD[11] which is currently in operation at the Harwell Linac. This has convenient incident (L_1 = 10.5 m) and scattered (L_2 = 1 m) neutron flight paths to give a near optimum resolution in inverse geometry. Detectors at scattering angles $\phi = 5^o$, 10^o and 20^o were used and the detector apertures were opened up to approx 20 mm (wide) x 250 mm (high); these are considerably larger than that normally used in the high Q resolution mode. We were particularly interested in the performance of the instrument at small scattering angles since its application to magnetic scattering problems demands a low Q capability. Figure 3 shows a schematic diagram of the test instrument. The functions of the incident and scattered beam absorption filters are described in the following section.

(b) Incident and Scattered Beam Filters

The statistical errors in the filter difference method for measuring inelastic scattering processes can be considerably reduced by minimising the general background in the spectrometer as well as the counts due to elastic scattering. This is achieved in this spectrometer design by using two sets of absorbing filters, one in the incident beam and one in the scattered beam; these remain stationary in all measurements. The purpose of the incident beam filter (Filter A) is to selectively attenuate neutrons of energies E 1 eV and this contains Cd, Er and Sm absorbers. The Sm filter is the highest energy

absorber of these three and is made "thick" to ensure that no E = 0.873 eV neutrons are incident at the scatterer. This means that any 0.873 eV neutrons detected by the Sm foil analyser difference method must have been scattered inelastically, in fact by down-scattering. The thermal neutron absorbers (Cd and Sm) also serve to remove potential "frame overlap" slow neutrons from the incident beam. For example elastically scattered neutrons at energies 12 - 13 meV arising from the previous machine pulse would also appear in the same time channels as the main inelastic events of interest in the LAD test instrument. The second set of filters (Filter B) contains Hf, In and Rh foils and is placed in the scattered beam to reduce the counts detected due to elastic scattering at neutron energies between approx 1.1 eV and 1.6 eV. The compositions of filters A and B are given in Table 1 and their calculated transmittances at neutron energies up to 1.8 eV are illustrated in Fig 4. It is reiterated that their function is to reduce the number of counts that occur in the time channels where a difference count due to inelastic scattering can be expected ie they improve the sensitivity of the difference method but do not contribute to the difference count.

Filters		Atomic Thickness of Absorber (at cm^{-2})	Physical Thickness
Filter A	Cd	9.3×10^{21}	2 mm
	Er_2O_3 Powder	1.0×10^{22} (Er)	15 mm
	Sm_2O_3 Powder	9.2×10^{21} (Sm)	30 mm
Filter B	In foil	1.9×10^{21}	0.5 mm
	Rh foil	3.6×10^{20}	0.05 mm
	Hf foil	1.1×10^{21}	0.25 mm

Table 1 Incident and scattered beam filters used for Sm foil analyser instrument tests.

It is worthwhile expanding on the discrimination between elastic and inelastic events provided by the incident and scattered beam filters. The transmittance product $T_A\ T_B$ is shown as a function of total time-of-flight on the test instrument for both elastic and inelastic scattering in Fig 5. The difference counts are proportional to $T_A\ T_B$ (inel) whereas $T_A\ T_B$ (el) produces a constant "background" count in the two parts of the measurement. The elastic-inelastic discrimination is particularly good for energy transfers between 0.4 and 0.9 eV.

(c) Predicted Performance of Test Instrument

The expected performance of the test instrument was simulated using a computer code written by R M Richardson for the Beryllium Filter inverse geometry spectrometer on the SNS[12] which has been modified for resonance peak analysers. The code predicts the energy transfer and momentum transfer resolutions by including all the possible contributions due to uncertainties in lengths and times as well as the spread in the energy selection. It also gives the count rates where the scattering cross-section is well known or can be modelled.

Fig 6 shows the energy transfer resolution $\Delta\hbar\omega/\hbar\omega$, which is effectively determined by the absorption peak width ΔE_R = 0.075 eV, calculated for the test instrument as a function of the energy transfer. Fig 7 shows the (Q,ω) scans available on the test instrument for the three fixed angle detectors at $\phi = 5^o$, 10^o and 20^o. The Q difference offered by the three detector scans may be useful in distinguishing between nuclear and magnetic inelastic scattering, though this will probably require a smaller 5^o detector height (approx 100 mm) ie improved Q resolution. The figure also shows that it should be possible to observe magnetic excitations up to energies $\hbar\omega \sim 0.35$ eV with the 5^o detector ($Q < 4\text{Å}^{-1}$).

Figure 8 shows a simulation of the time of flight spectra with and without the analysing foil for an isotropic Einstein oscillator with unit effective mass (eg H in a metal) where the fundamental frequency is $\hbar\omega_o$ = 0.16 eV. The sample chosen was a 25% scatterer and the predicted count rates pertain only to the 5^o detector on the LAD test instrument where the inelastic cross-section for the fundamental mode was estimated to be $(d^2\sigma/d\Omega dE) \sim ?\ 3$ barns $sr^{-1}\ eV^{-1}$. The difference count rates are also shown in the figure and the integrated difference count rate over the fundamental peak is approx 10 cts/hr. The two most important features to notice are: (i) that the

difference count rates are always larger than a factor x 0.1 compared with the individually measured count rates over the major part of the energy transfer range of interest ($\hbar\omega$ 1 eV) and (ii) the difference counts at times of flight ~ 970 μsec correspond to elastically scattered neutrons at energies ~ 0.73 eV, where there is an increase in the transmittance of the incident beam filters (see T_A curve in Fig 4).

These count rate calculations were also substantiated using analytic expressions similar to those given by Allen et al[4] for the resonance detector spectrometer. The predicted count rates for the other two detectors were approximately x2 those shown for the 5° detector.

(d) Measurements with a ZrH_2 scatterer

The raw data T.O.F. difference spectra due to hydrogen vibrations in a zirconium hydride 25% scattering sample on the LAD Test spectrometer are shown in Figs 9(a-c). The fundamental mode at $\hbar\omega$ = 0.14 eV and the overtone modes are clearly observed, though they remain unresolved due largely to the Doppler broadening of the resonance absorption peak which was not included in the computer simulation. The variation in the peak intensities at different scattering angles has the expected Q-dependence. These preliminary results clearly demonstrate the feasibility of the experimental method.

5. SUMMARY

A discussion has been presented of the application of a resonance absorber difference method in an inverse geometry TOF spectrometer for measuring excitations over the energy transfer range $0.1 < \hbar\omega$ (eV) < 1. The feasibility of the technique was assessed using the LAD total scattering spectrometer at the Harwell Linac as a test instrument. It should prove possible to use the method to observe overtone modes in metal-hydrogen samples, and, particularly with more powerful sources such as the SNS, high energy magnetic excitations.

Finally it should be pointed out that significant improvements in these count rates are expected for any purpose-designed SNS instrument since:

(i) large improvements in the detector solid angle (x 10) should easily be possible, and

(ii) the SNS source strength at full intensity is approx x600 that used in above calculations and experiment.

It is therefore reasonable to expect any SNS instrument to be capable of measuring cross-sections at least three orders of magnitude lower than that given in the above example, and this brings with it the prospect of observing many magnetic excitations which have hitherto not been measureable.

ACKNOWLEDGEMENT

The authors acknowledge useful discussions with our colleagues Dr R Cywinski and Dr A D Taylor.

REFERENCES

1. S K Sinha. J Appl Phys 50 (1979) 1952

2. C J Carlile and W G Williams. ' Inelastic Neutron Scattering using a Crystal Spectrometer on a Pulsed Source'. Rutherford Appleton Laboratory Report RL-81-028 (1981)

3. B C Boland 'High Energy Inelastic Spectrometer'. Proc ICANS-IV KENS Report II (1981) 580

4. D R Allen, E W J Mitchell and R N Sinclair. J Phys E Sci Instrum 13 (1980) 639

5. R N Sinclair, M C Moxon and J M Carpenter. Bull Am Phys Soc 22 (1977) 101

6. L Cser, N Kroo, P Pacher, V G Simkin and E V Vasilyeva. Nucl Instrum Meth 179 (1981) 515

7. R M Brugger, A D Taylor, C E Olsen and J A Goldstone. Bull Am Phys Soc 27 (1982) 14

8. F F Freeman and W G Williams. J Phys E Sci Instrum 11 459 (1978)

9. 'Neutron Cross Sections'. BNL 325 Second Edition Supplement No: 2. August 1966 62-149-3

10. A W McReynolds and E Andersen Phys Rev 93 (1954) 195

11. W S Howells. 'A Diffractometer for Liquid and Amorphous Materials Research'. Rutherford Appleton Laboratory Report RL-80-017 (1980)

12. R M Richardson. 'A High Throughput Inelastic Neutron Scattering Spectrometer for the Harwell Linac and the Spallation Neutron Source'. Rutherford Appleton Laboratory Report RL-82-035 (1982).

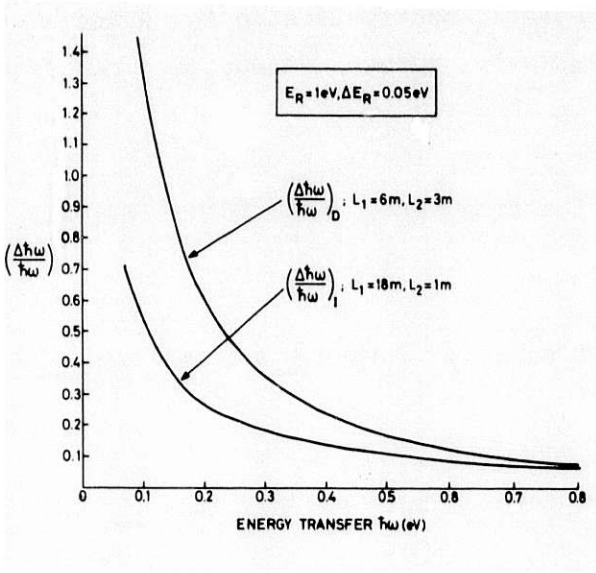

Fig. 1. Energy transfer resolutions in direct(D) and inverse(I) geometry resonance absorption spectrometers.

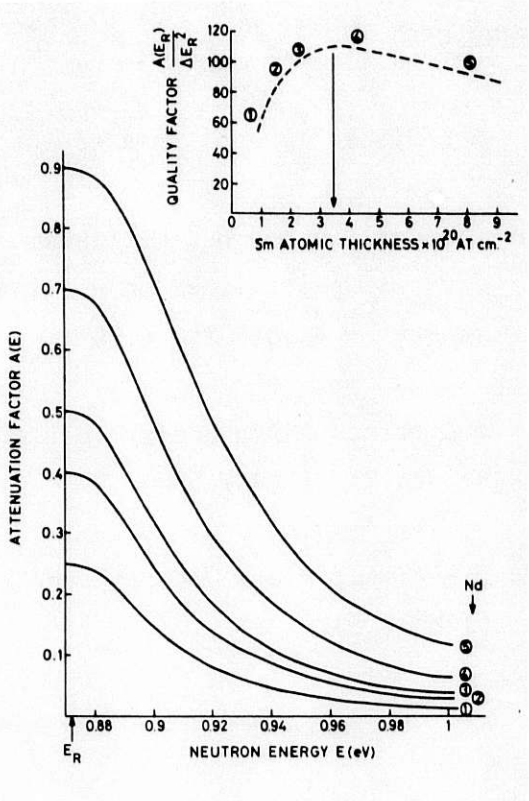

Fig. 2. Attenuation curves for different Sm atomic thicknesses around E_R = 0.873eV.

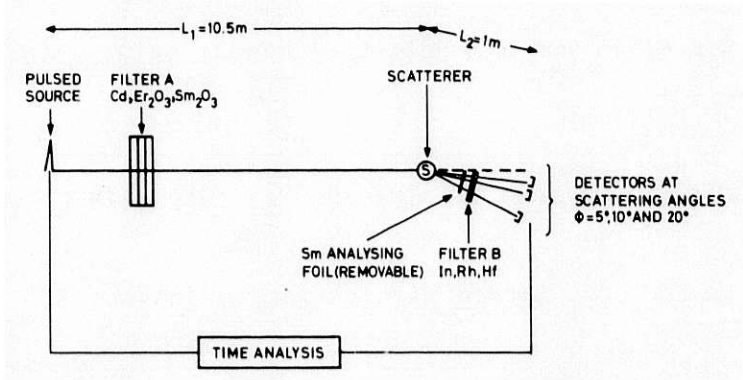

Fig. 3

Schematic diagram of resonance foil difference method in the inverse geometry on a pulsed source (the distances and detectors shown are those used in the Lad test experiments).

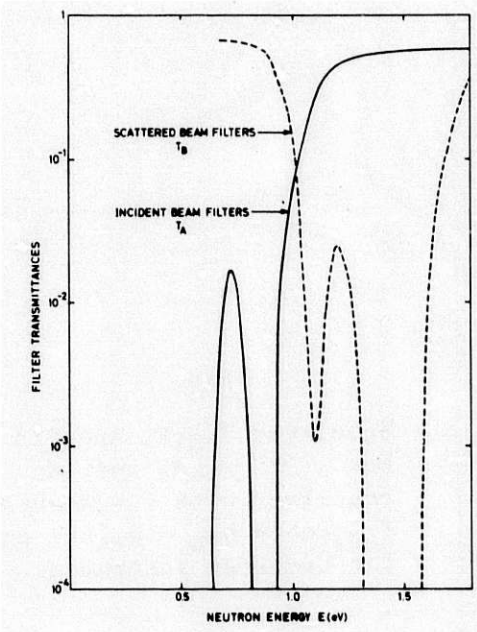

Fig. 4. Neutron energy dependences of the transmittances of the incident and scattered beam filters.

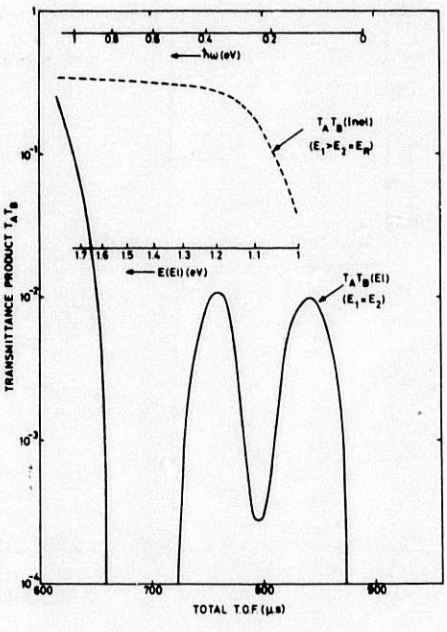

Fig. 5. Elastic-inelastic scattering discrimination provided by incident and scattered beam filters.

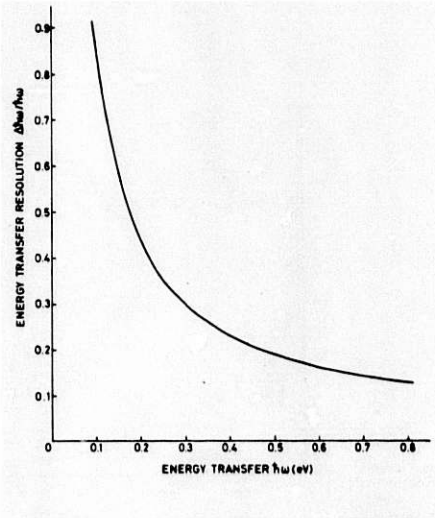

Fig. 6. Energy transfer resolution on Lad test instrument.

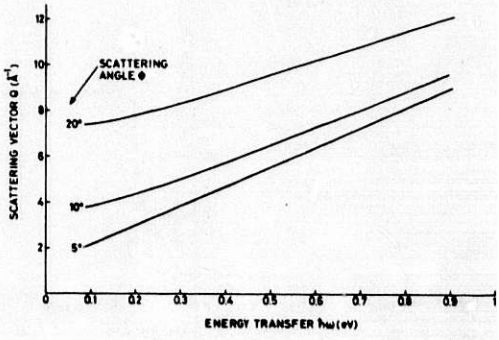

Fig. 7. (Q,ω) Scans on Lad test instrument for fixed angle detectors at ϕ = 5°, 10° and 20°.

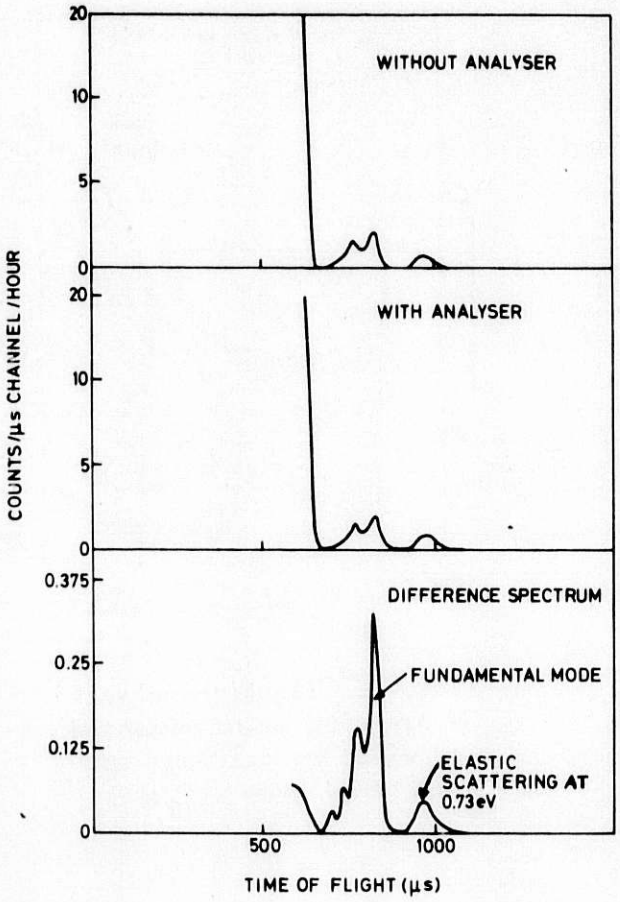

Fig. 8

Simulated T.O.F. spectra for a 25% metal hydride scatterer with fundamental frequency $\hbar\omega_0$ = 0.16eV on the Lad test instrument.

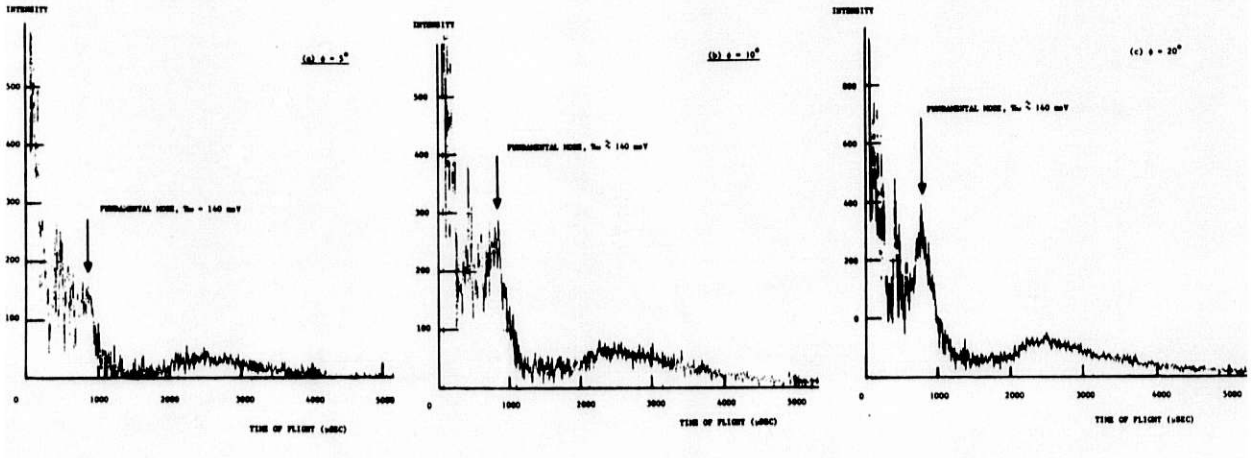

Fig. 9. T.O.F. difference spectra for a 25% ZrH_2 scatterer on the Lad test instrument.

ICANS - VI

INTERNATIONAL COLLABORATION ON ADVANCED NEUTRON SOURCES
June 27 - July 2, 1982

POLARIZED EPITHERMAL NEUTRON SPECTROMETER AT KENS

M. Kohgi
Department of Physics, Tohoku University, Sendai 980, Japan

ABSTRACT

A spectrometer employing a white, epithermal, polarized neutron beam is under construction at KENS. The neutron polarization is achieved by passage through a dynamically polarized proton filter (D.P.P.F). The results of the test experiments show that the D.P.P.F method is promising in obtaining polarized epithermal neutron beam. The basic design of the spectrometer is described.

POLARIZED EPITHERMAL NEUTRON SPECTROMETER AT KENS

M. Kohgi
Department of Physics, Tohoku University, Sendai 980, Japan

1. INTRODUCTION

A spectrometer employing a white, epithermal, polarized neutron beem is now under construction at KENS. The neutron polarization is planned to be achieved by passage through a dynamically polarized proton filter (D.P.P.F)[1]. This Polarized Epithermal Neutron Spectrometer (PEN) will be used for the wide purposes ; for example, the study of the process of the dynamical polarization of protons itself, the magnetic structure determination of the amorphous magnets, the observation of high energy magnetic excitations in the ferromagnets, as well as the nuclear physics problems.

Prior to the installation of the PEN spectrometer, we performed some test experiments (Pre - PEN experiments). The results are briefly summarized below. The basic design of the PEN spectrometer is shown in the last section.

2. PRE-PEN EXPERIMENTS

The aim of the Pre-PEN experiments was twofold. One was to establish the technique for cooling a large area filter by liquid ^{3}He and another was to examine the geometrical dependence of the neutron polarization cross section by polarizing longitudinally the neutron beams and comparing the results with those obtained by Hiramatsu et al.[1] and Lushchikov et al.[2] where the neutrons were polarized in the transverse directions.

The Pre-PEN machine consists of a horizontally mounted coaxial superconducting magnet with a ^{3}He cryostat in it[3], a Drabkin type spin flipper, a goniometer to install the Fe_8Co_{92} analyzer crystal and a detector rotating around the goniometer. Because of the testing nature of the Pre-PEN experiments, the

machine was constructed by assembling the existing apparatuses[3] which were not necessarily optimized for the present purpose. The neutron beam was tightly collimated to 15 x 15 mm^2 so that no neutrons bypassing the filter were monitored by the detector. The polarizing filter was made with a polycrystalline sample of ethylene glycol with stable Cr^V complex[1]. The filter was cooled to ca. 0.5 K in a cryostat by pumping on liquid ^3He. Since ^3He has a large neutron absorption cross section and the cryostat was mounted horizontally, a protection of neutron beam path from liquid ^3He constitutes the most difficult part of the experiment.

The protons of the filter were polarized by a dynamic method at a frequency of 70 GHz in a magnetic field of 25 KG applied in the direction of the neutron beams (longitudinal polarization). The proton polarization was detected by analyzing the height of NMR signal from the filter. The neutron polarization was determined by two methods ; either directly by Bragg reflection from a saturated Fe_8Co_{92} at discrete energies or indirectly by analyzing the intensity of the transmitted beams.

The filter configuration which was used in the early stage of the experiments is shown in Fig. 1(a). Using this type of filter (case (a)), the high enough polarization of neutrons was observed at the low energy side (for example, over 90% at 50 meV, 80% at 100 meV). However, it was found that in this configuration the leakage of unpolarized neutrons through the Cd shield was unavoidable at the high energy side because of the lowering of the liquid ^3H level.

The finally adopted filter configuration which made the bypass leakage of neutrons as small as possible is shown in Fig. 1(b) (case(b)). In this case, the beam size was significantly reduced and we were obliged to decrease the filter thickness to 10 mm in order to increase the counting statistics. The neutron polarization is, therefore, reduced in case (b) compared with the case (a), but the energy dependence of the polarization could be determined with less ambiguity.

The results of polarization of the white neutron beams with

the polarized proton filter of case (b) is shown in Fig. 2, where the polarization determined by Bragg reflection (open circles) are corrected for the efficiency of the spin flipper.

The neutron polarization, P_N, obtained after passage thgough a filter of proton polarization P_p is given by

$$P_N = \tanh (P_p \sigma_p Nt), \quad (1)$$

where σ_p is the polarization cross section ($=1/4(\sigma_s-\sigma_t)$),N the number of protons per cm^3 and t the filter thickness. The solid line in Fig. 2 is calculated by eq. (1) using the data for σ_p of Lushchikov et al.[2], while the closed circles are the results of analysis from the transmission intensity T. The transmission T is given by

$$T/T_o = \exp(P_p^2 \sigma_1 Nt) \cosh(P_p \sigma_p Nt),^{2)} \quad (2)$$

with T_o the transmission of the unpolarized target. σ_1 which is the cross section depending on the materials is assumed to be zero for the present analysis. The overall agreement among the values of polarization estimated by three different methods was obtained as shown in Fig. 2. Note that the neutron polarization determined by the transmission agrees well with that of Lushchikov et al. above 400 meV where σ_1 is expected to disappear.

Several important conclusions could be derived from the Pre-PEN experiments which are summarized below.

(i) The epithermal neutron beam with neutron energies extending beyond 10 eV could successfully be polarized by the polarized proton filter method.

(ii) In case of (a) (t=15mm, 45% proton polarization) an 80% polarization was achieved at typical neutron energy of 100 meV.

(iii) The longitudinal polarization has the same polarization cross section as the transverse one[1,2] within the accuracy of the experiments as was anticipated by Hoshizaki et al.[4].

(iv) The downward deviation of the open circles from the closed circles in Fig.2 in the high energy side is presumably due to the depolarization which would occur between the spin flipper and the analyzer. The distance between them was found not enough to satisfy the adiabatic condition.

(v) The upward deviation of the closed circles from the solid line can be attributed to σ_1 in eq. (2).

Further experiments would, however, be necessary before we conclude that σ_p in eq. (1) is completely the same for both LMN (Lushchikov et al.) and ethylene glycol (Pre-PEN).

3. DESIGN OF PEN SPECTROMETER

In contrast to the Pre-PEN machine, we adopted the transverse polarization scheme in PEN ; The He^3 cryostat is vertically inserted in the Helmholtz type superconducting magnet with the magnetic field in the vertical direction. This configuration was selected because of its advantage over the Pre-PEN machine for the neutron scattering experiments ; the neutron scattering experiments can be performed for the dynamically polarized material, the distance between the filter and sample can be made shorter, the level of liquid He^3 can be kept stable, the consumption of liquid He^4 can be significantly reduced, etc. The superconducting magnet was specially designed so as to produce 25 KG with a homogenuity of 5×10^{-5} over a dimension of 30 x 40 x 20 mm^3 and with no zero field in the neutron beam path. The magnet as well as the shield house to accomodate it have already been installed in H8 beam hole. The designing of the proton filter configuration is now in progress taking account of the results of the Pre-PEN experiments. The neutron detecting system of the PEN spectrometer is scheduled to be divided into three groups. The first is used for the observation of the scattering from the dynamically polarized materials or others set on the proton filter position. The scattered neutrons from the center of the proton filter system are observed through several small windows open on its shield. The ^3He detectors with their shield boxes are placed in front of the windows. The second group is used for the magnetic total scattering. An assembly of a sample table, ^3He detectors and their shield is placed just after the polarized neutron exit of the proton filter system. The position of the assembly is variable along the incident neutron path. A electric magnet can be

settled on the sample table. The third group is used for inelastic scattering (mainly magnetic). It is composed of a small detector bank and its shield. The detectors look the center of the second scattering assembly. The flight path between the sample table and the detector bank as well as the scattering angle is variable. This configuration was selected taking account of its flexibility for controlling the resolution and choosing the scattering condition.

The first part of the neutron detecting system described above has already been constructed. The final designing of the other parts is now in progress.

In conclusion,the D.P.P.F. method is promising in obtaining polarized epithermal neutron beams. Since the various factors will be optimized in designing PEN, including an effort to increase the total neutron intensity, PEN will become a powerful polarized epithermal neutron beam facility at KENS.

This paper is based on the work done by PEN-group at KENS ; Y. Ishikawa, M. Kohgi, T. Nakajima, M. Ishida, and J. M. Newsam : Tohoku University ; A. Masaike, S. Ishimoto, Y. Masuda, S. Isagawa and K. Morimoto : KEK.

References

1) S. Hiramatsu, S. Isagawa, S. Ishimoto, A. Masaike, K. Morimoto, S. Funahashi, Y. Hamaguchi, N.Minakawa and Y. Yamaguchi : J. Phys. Soc Jpn. 45 (1978) 949.
2) V. I. Lushchikov, Yu. V. Taran and F. L. Shapiro : Soviet J. Nucl. Phys. 10 (1970) 669.
3) S. Ishimoto : Proc. ICANS - IV (1981) 630
4) N. Hoshizaki and A. Masaike : KEK Report 81-22 (1981).

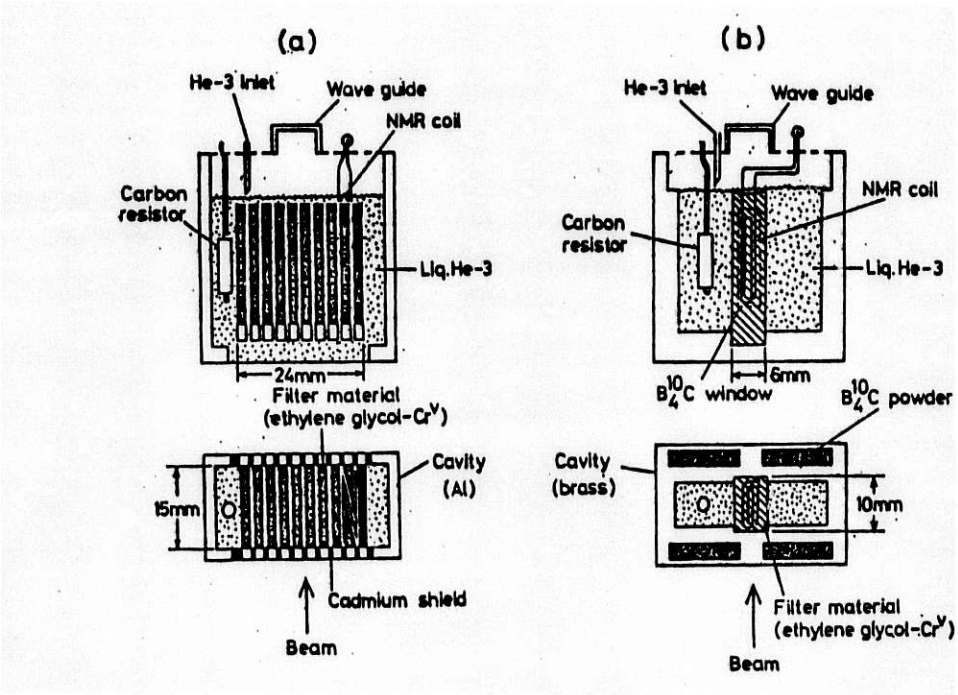

Fig.1 Proton filter configuration for Pre-PEN experiments

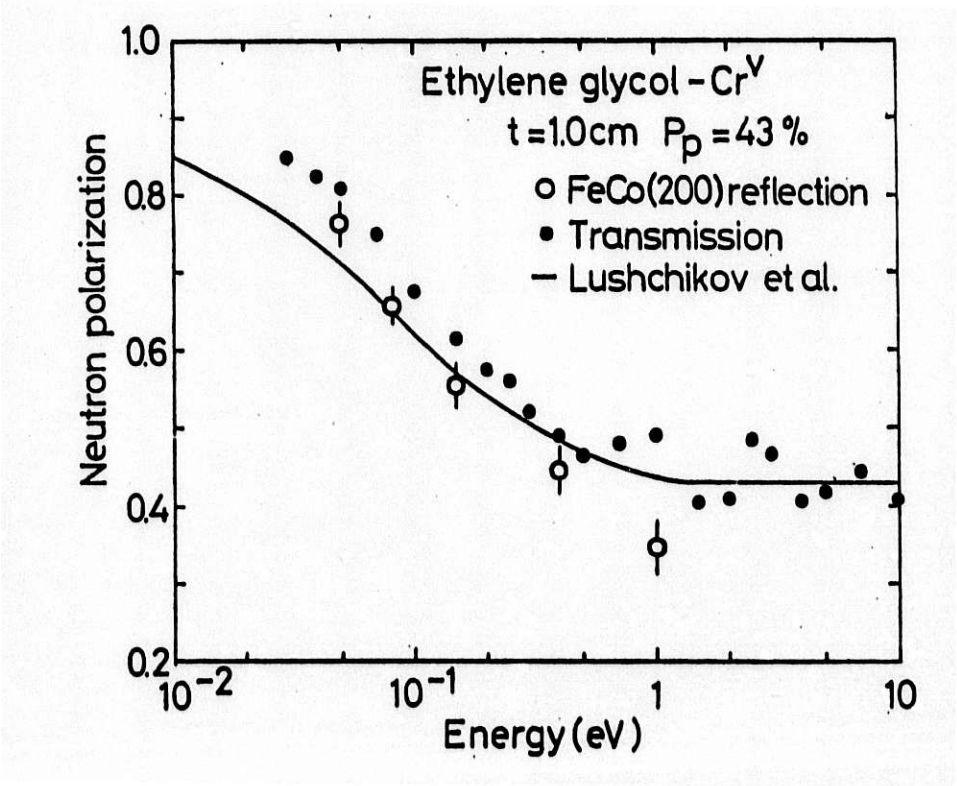

Fig.2 Neutron polarization by D.P.P.F with the configuration shown in Fig.1(b)

ICANS-VI

INTERNATIONAL COLLABORATION ON ADVANCED NEUTRON SOURCES
June 27 - July 2, 1982

POLARIZED NEUTRON TECHNIQUES AND APPLICATIONS*

G. P. Felcher
Argonne National Laboratory, Argonne, IL 60439

ABSTRACT

Among the possible uses of a polarized, polychromatic neutron beam emitted by a pulsed source is the study of medium and high energy excitations in solids and liquids with high energy resolution. This can be achieved with an instrument that combines the capabilities of the resonance detector spectrometer with those of the spin-precession analysis.[1] As first step toward the realization of such an insturment, a device has been constructed that filters the spins of a polychromatic neutron beam. The device consists in a polarized proton target, that selectively scatters away from the beam neutrons of one spin state only. The target is made of an hydrogenated crystal containing paramagnetic ytterbium; the polarization of the hydrogen nuclei is obtained indirectly, via the polarization of ytterbium, by a method called spin refrigeration.[2] The first neutron tests of the device at the Intense Pulsed Neutron Source at Argonne are quite promising.

---

*Work supported by the U.S. Department of Energy

[1] G. P. Felcher and J. M. Carpenter, Nuclear Insturments and Methods, 192, 513 (1982).

[2] J. Button-Shafer, R. Lichti and W. H. Potter, Phys. Rev. Letters, 39, 677 (1977).

ICANS-VI
INTERNATIONAL COLLABORATION ON ADVANCED NEUTRON SOURCES
June 27 - July 2, 1982

DYNAMIC RANGE ASPECTS OF PULSED SOURCE INSTRUMENTS

F. Mezei

Institut Laue-Langevin, 156X, 38042 Grenoble, France

ABSTRACT

In recent applications of neutron scattering the dynamic range is found to be an important aspect of instrument performance along with neutron flux and resolution. It is pointed out that due to the inherent use of a broad wavelength band, certain instruments, like small angle scattering and neutron spin echo spectrometers, provide better dynamic range capability on a pulsed source than on a continuous source.

DYNAMIC RANGE ASPECTS OF PULSED SOURCE INSTRUMENTS

F. Mezei

Institut Laue-Langevin, 156X, 38042 Grenoble, France

1. INTRODUCTION

Neutron scattering instruments are most often considered from the double point of view of resolution and neutron intensity only. The fundamental importance of a third parameter, dynamic range (DR), has only been recently realized. This is probably due to the fact that classical neutron scattering instruments have a rather small DR, typically between 1:20 and 1:50 (in what follows DR is characterized by the ratio of the smallest and biggest value of a parameter which can be measured by a given instrument in a single configuration). In recent small angle neutron scattering (SANS) and inelastic (mostly magnetic) studies it has been found, that in order to cover a range wide enough to produce a complete set of data, the same sample had to be investigated in a sequence of similar experiments with different resolutions. Practice has also shown that the wide DR, which was made available for the first time by the rather recent neutron spin echo (NSE) method (about 1:1000) is a most essential feature in some experiments.

In what follows I will discuss experimental examples in order to show that large DR can be crucial in obtaining model independent information, which is the major advantage of neutron scattering. It will also be pointed out that the use of a broad wavelength band on pulsed source instruments is instrumental for achieving an improved DR. This makes pulsed neutron sources particularly well adapted to SANS and quasielastic NSE experiments.

2. EXPERIMENTAL CONSIDERATIONS

The main advantage of neutron scattering with respect to other microscopic methods of probing atomic structure and dynamics is that neutrons can provide model independent information. The neutron scattering cross section

is directly related to the correlation function $S(\vec{q},\omega)$ and by neutrons we can explore both space and time via the largely independent experimental parameters $\vec{q}$ and ω. In magnetic problems neutrons present a further unique feature, viz. their direct coupling to the magnetization allows to single out unambiguously the magnetic scattering effects (eventually by the use of polarization analysis).

The a priori model independence of the neutron scattering data is just due to the fact that both parameters $\vec{q}$ and ω are kept track of. In experiments like NMR, ESR, μSR, etc. certain points or integrals in the $(\vec{q},\omega)$ parameter space are only explored. This is why in most cases these data can only be interpreted by fitting to specific models.

However, neutron scattering provides model independent information only if the experimental conditions are good enough that the data reduction does not imply deconvolution or heavy corrections (e.g. for inelasticity in diffraction work). In practice this means sufficient resolution and dynamic range. A parameter we wish to determine often varies substantially e.g. as a function of temperature or over the $(\vec{q},\omega)$ space. If we have to use several instruments to follow this variation, we might face very serious difficulties in patching together the bits of information. In particular, the comparison of absolute scattering intensities from one instrument to another is always a problem. Therefore it is preferable to use instruments with a wide DR in a single setting. This of course implies high resolution on the one end of the range. As a matter of fact, a roughly constant relative resolution ($\delta x/x$=const. over the range of the parameter x) is the best compatible with large DR.

To proceed let us consider a few typical experimental examples. In Fig. 1 the distribution of neutron intensity scattered by Southern beam mottle virus in H_2O solution is shown [1]. These data could not be obtained in a single scan using the D11 SANS instrument at the ILL, because too wide ranges had to be covered both in intensity and momentum transfer. In fact this figure has been assembled from results of several experiments made on different samples, at different neutron wavelengths and using different instrumental configurations. This procedure is tedious, takes longer time than a single scan and it is less reliable, of course.

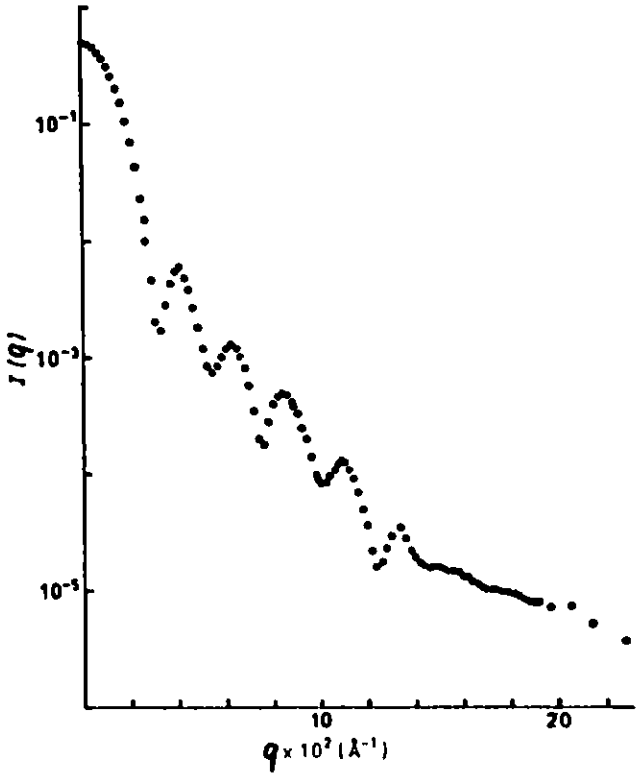

Fig. 1 Neutron intensity distribution scattered by Southern bean mottle virus in H_2O solution as a function of the momentum transfer [1].

The second example (Fig. 2) shows the q dependence of the inelastic Lorentzian line width Γ_q of the critical scattering of iron at the Curie point [2]. It is seen that the results follow the predicted power law $\Gamma_q \alpha q^z$ with $z \simeq 2.5$ over an impressive range of four orders of magnitude in ω. This is in constrast to the interpretation given to anomalies observed in hyperfine field experiments [3], according to which below $q \sim 0.05$ Å^{-1} a cross over should take place to the $\Gamma_q \alpha q^2$ behavior. Previous neutron scattering results [4,5] only covered q values above 0.05 Å^{-1}, and only recent high resolution time-of-flight (TOF) and NSE experiments [2] (made respectively on the IN5 and IN11 instruments at the ILL) allowed to rule out the hypothesis of a crossover, and to give another explanation for the hyperfine field anomalies. The value of the exponent z, however, could only be determined with a precision of ± 0.05 in view of the uncertainties of comparing data taken under different conditions and by different methods. In order to check finer details of theoretical predictions we should determine

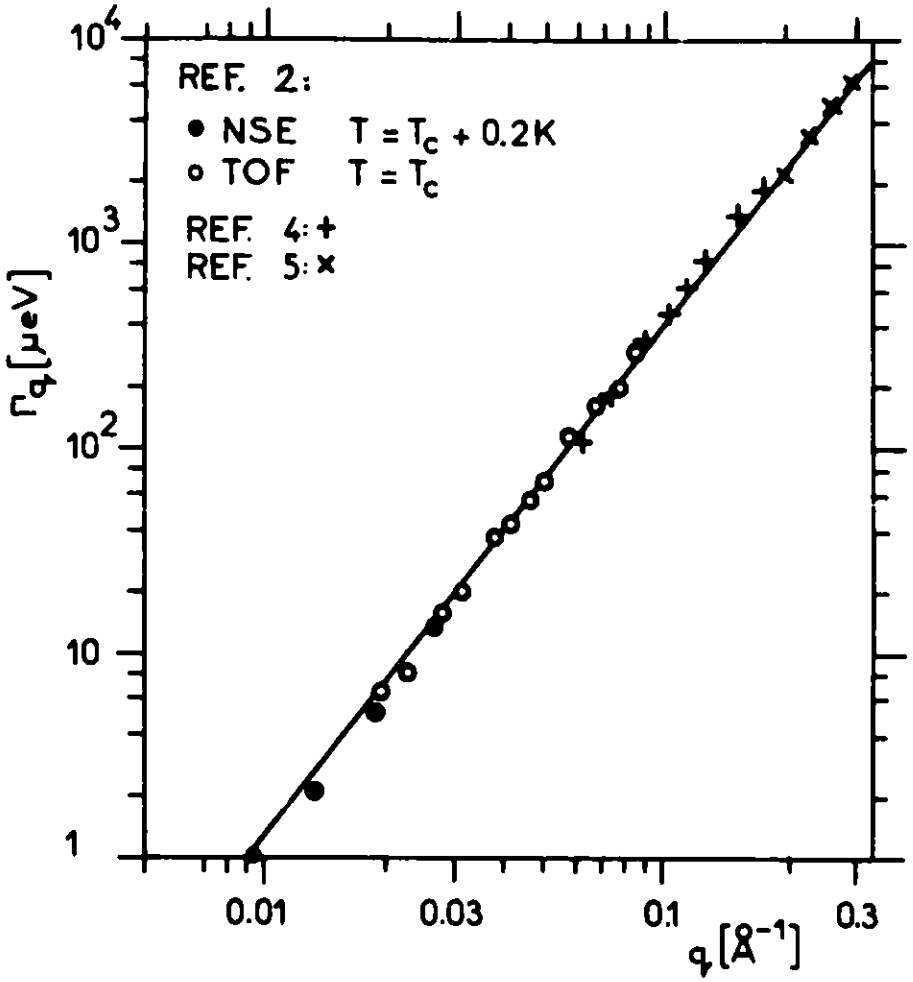

Fig. 2 Momentum dependence of the quasielastic linewidth of the critical scattering of Fe at the Curie point. The recent TOF and NSE results, Ref. [2] were obtained at the ILL, the previous results, Refs. [4] and [5], represent triple-axis data.

z with ± 0.02 precision, which could only be made in a single scan. This example illustrates that (a) the nature of certain physical phonomena makes wide DR experiments indispensable, (b) by using indirect probes (like hyperfine field interaction in this case) it is eventually possible to show if a model assumption works or not, but it is impossible to interpret unambiguously observed deviations from a model and (c) high resolution is necessary in order to achieve large DR.

One last example illustrates that single, large DR scans are indispensable in studying unknown lineshapes. The dynamics of spin relaxation in spin glasses is characterized by an anomalous decay of the spin correlations as a function of time, i.e. by deviations from the usual ext(-γt) form [which leads to the common Lorentzian line shape, $\gamma/(\gamma^2+\omega^2)$, by the $t \to \omega$

Fourier transformation]. This has been established in the pioneering work of Amir Murani [6], who patched together data taken on the IN4, IN5 and IN10 spectrometers at the ILL in order to cover the ω range of 1 μeV to 2 meV. However, this procedure did not allow to obtain quantitative results on the actual lineshape. This was only made possible by using the NSE method, which allowed to cover a 1:600 range in a single scan, incidentally, directly in the time domain [7]. The results [8] in Fig. 3 show that at some temperatures (viz. 30 and 36 K) the data are compatible with the predicted const - ℓn(t) shape (which would give straight lines in the log-scale figure), but not at other temperatures. In this particular case a.c. susceptibility data allowed to extend the results [10] over an improbable range of $1:10^{12}$, which revealed that there can be interesting details only apparent on such a large DR (e.g. the drop in the 26K curve between 10^{-8} and 10^{-5} sec). Note that the ESR and μSR experiments made on the same system were invariably evaluated under the obviously wrong assumption of exponential decay. This shows again the fundamental role of neutron scattering as model independent probe.

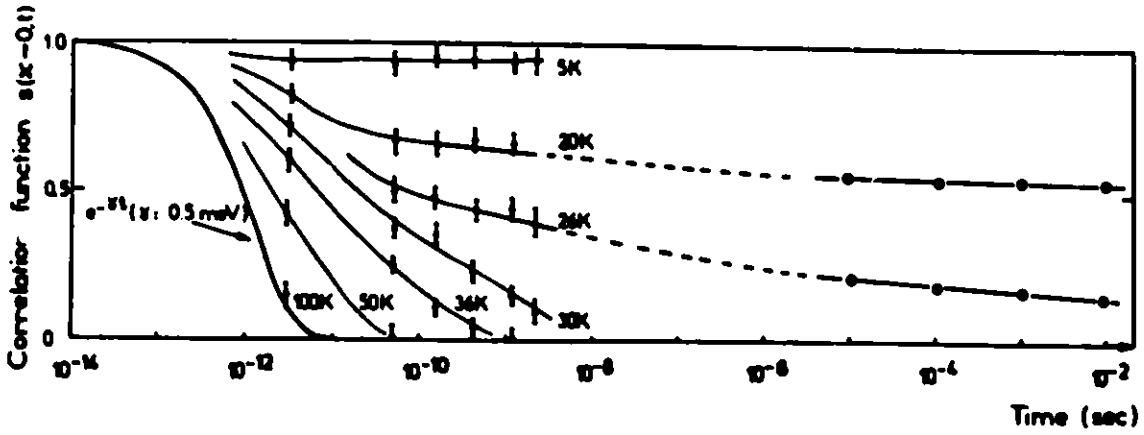

Fig. 3 Decay of the spin-spin correlations vs. time in Cu-5% Mn spin glass alloy. Dots with error bars represent NSE and polarization analysis data (Ref. [8]) measured at $q=0.1$ Å^{-1}. The open circles give values calculated from a.c. susceptibility data (Ref. [9])

3. DYNAMIC RANGE OF PULSED SOURCE INSTRUMENTS

There are basically two ways of making wide DR experiments:

a) use of very high resolution

b) use of several wavelengths

The only existing neutron scattering technique which provides large DR at fixed wavelength by its high resolution capability is NSE with a DR of about 1:1000. Further increase of the range in NSE, and achieving anything like 1:200 - 500 with the other methods requires the application of several wavelengths in a single experiment. This is exactly what pulsed source instruments do, and in what follows I will consider this aspect for SANS and NSE.

The resolution in SANS experiments is determined by the definition of the scattering angle and of the neutron wavelength λ. Since in cold moderators the neutron pulse length is roughly proportional to the wavelength, an approximately constant relative resolution $\delta\lambda/\lambda$ will be maintained in the most interesting part of the wavelength band between about 2 and 10 Å. Note that this resolution happens to be around 1-2%, which is considerably better than what is usually required and used in SANS experiments (viz. about 10%). At any given scattering angle, the smallest q information will be given by the $\lambda\sim$10 Å neutrons, while the shorter wavelength, higher flux portion of the spectrum provides information at higher q's, where the scattering cross section tends to be smaller (cf. Fig. 1). This intensity compensation effect is a very important feature, and it can make useful much of the data collected during the same time. In usual, fixed wavelength SANS experiments long wavelength is used to access the smallest q values, and thus the measuring time is determined by the low cross section higher q data, taken at the same lower incoming flux. Thus a SANS instrument not only covers a wider DR on a pulsed source than on a continuous one (typically 1:200 compared with 1:40), but also collects data more efficiently. At the final end the data rate at a pulsed source should be comparable to that at a continuous source with a flux about 20-50 times higher than the time averaged pulsed flux.

Many of the above considerations apply to the use of NSE on a pulsed source [11]. The DR could be extended to 1:10000 by using a wavelength band between 3 and 10 Å, which can be handled by supermirror neutron

polarizers. In experiments like the study of diffusion at small scattering angles, the above intensity compensation arguments also apply, and in addition a similar situation holds for the resolution. Shorter wavelength neutrons provide information at high q, where the quasielastic linewidth tends to be bigger (cf. Fig. 2), i.e. less resolution is required. In addition, shorter wavelength might even be necessary in order to keep the scattering triangle close to a constant q configuration. (e.g. in Fig. 2 the TOF data could not be extended to higher q values because the inelasticity would have become comparable to the incoming neutron energy of 0.8 meV). For the rate of data collection in NSE at a pulsed source the same figures should apply than those given above for SANS.

4. CONCLUSION

Recent experience shows that in some neutron scattering studies the dynamic range of the instrument used is as important as neutron intensity or resolution. This implies, that the same way as e.g. high flux can not make up for poor resolution, the use of several instruments with different ranges can not always replace a large DR scan in a single setting of a single instrument. Pulsed source instruments are bound to provide superior DR with respect to continuous source machines, due to the inherent use of a broad wavelength band. In particular this feature makes pulsed sources well adapted for small angle scattering and quasielastic neutron spin echo experiments. In these cases the data collection rate corresponds to that on a continuous source with 20-50 times the time averaged flux of the pulsed source, and no good time-of-flight resolution is required, i.e. cold neutron pulses of several 100 μsec length are perfectly acceptable.

REFERENCES

[1] See B. Jacrot Rep. Prog. Phys. 39, 911 (1976)

[2] F. Mezei, to be published.

[3] L. Chow, C. Hohenemser and R. M. Suter, Phys. Rev. Ltr. 45, 908 (1980)

[4] M. F. Collins et al., Phys. Rev. 179, 952 (1969)

[5] S. Boronkay and M. F. Collins, Int. J. Magn. 4, 205 (1973)

[6] See A. P. Murani, J. de Physique Suppl. Coll. 39, C6-1517 (1978)

[7] See Neutron Spin Echo, edited by F. Mezei, (Lecture Notes in Physics, Vol. 128, Springer Verlag, Heidelberg, 1980)

[8] F. Mezei and A. P. Murani, J. Magn. Magn. Mat, 14, 211 (1979)

[9] J. L. Tholence, Solid State Comm. 35, 113 (1980)

[10] F. Mezei, in "Recent Developments in Condensed Matter Physics", Y. T. Devreese, editors (Plenum Press, New York, 1981) pp. 679-694

[11] F. Mezei, Nucl. Inst. Meth., 164, 153 (1979)

A PHASED CHOPPER AT WNR**

by

V. Bolie*, R.M. Brugger+, R. N. Silver
Physics Division
Los Alamos National Laboratory
Los Alamos, NM 87545

ABSTRACT

At WNR, a proportional-integral-derivative PID control system has been developed to hold a neutron chopper within the 128 μsec wide window allowed by LAMPF. After achieving this control, LAMPF is triggered from the chopper to limit the phase jitter between the LAMPF produced burst of neutrons and the chopper opening. This PID system has been tested for phase control, phase jitter and neutron control using a chopper spinning at 14,400 RPM. The results to date, which are discussed, indicate that a chopper can be phased to the neutron pulses produced by LAMPF to ± 0.5 μsec..

*Permanent address: Department of Electrical and Computer Engineering
University of New Mexico
Albuquerque, NM

+Permanent address: University of Missouri Research Reactor
University of Missouri
Columbia, MO

** A paper presented at the VIth annual ICANS Meeting, ANL, June 28, 1982.

I. Introduction

Since the beginning of slow neutron spectroscropy, phased chopper-velocity selectors[1,2] have been important instruments for inelastic neutron scattering experiments. With the advent of the new pulsed spallation neutron sources, a chopper phased to the pulsed source [3,4,5,6] is again projected to be an important spectrometer. At the WNR pulsed source, the LAMPF proton accelerator produces the neutron bursts in phase with the 60 Hz wave form of the commercial power-line voltage. Since the power line frequency is not exact, it is a challenge to keep a chopper, with its required high moment of inertia, sufficiently in phase ($\pm$ 1/2 μsec) with the neutron bursts to achieve precise time-of-flight TOF resolution. Unfortunately, this problem will remain after completion of the Proton Storage Ring, PSR. Despite the PSR's anticipated capability to store protons for extraction, maximum current will be achieved by minimizing storage time to minimize beam spill. This paper presents the recent success in developing a control system for chopper phasing at the WNR. A discussion of the effort to solve a similar problem at the SNS at the Rutherford Laboratory was presented at the ICANS IV meeting.[8]

II. Statement of the Problem

Fig. 1 shows a schematic layout of the coupling of the LAMPF accelerator to a chopper at the WNR. With the switch U in the down position, LAMPF is triggered directly by the zero crossings of the commercial power line. The accelerator delivers proton bursts to a spallation target at the WNR to produce neutron bursts. To define the incident energy of the neutron beam impinging on the sample, the chopper must open at a fixed time delay after the neutron burst. To maintain this delay, a control system is required. Because the chopper mass, and hence moment of inertia, must be large in order for the chopper to be neutronically effective, it is impractical to control the phase of the chopper to the required accuracy of $\pm$ 1/2 μsec alignment with the zero crossings of the power-line voltage. Therefore, LAMPF allows a 128 μsec wide window around each zero

crossing of the line voltage during which a signal from one chopper at WNR can be sent to LAMPF to trigger the accelerator. This requires the switch U to be in the up position. The first challenge, then, is to maintain the chopper phase alignment to within + 64μsec of the power line phase.

Characteristics of the power line are shown in Figs. 2 and 3. A typical plot of the deviation of the period from 1/60 Hz is shown as a function of time in Fig. 2. Each point has been averaged over 10 seconds. One notes that there are long term trends as well as a great deal of statistical scatter. Similar behavior occurs regardless of the scale, even down to seconds. The limitation for control purposes is determined by the short time behavior. Fig. 3 is a plot of the autocorrelation function of the period as a function of time. There is above the top of the graph a white noise spike at zero time. The curve shows a characteristic time scale for the fall off of correlations of about 10 seconds. The power spectral density of the period deviations may be approximately represented by

$$(1)\quad \frac{d\sigma^2}{d\nu} = \frac{\sigma_1^2}{2\nu_1} \exp\left(-|\nu|/\nu_1\right)$$

with $\sigma_1 \simeq .011$ Hz and $\nu_1 \simeq .025$ Hz.

Consider a proportional-integral-derivative PID control system in which the feedback torque is applied to the chopper is a sum of terms proportional to the phase error, to its integral, and to its derivative. Then, ignoring the integral term,

$$(2)\quad JN\ddot{\varepsilon} + C\dot{\varepsilon} + K\varepsilon = JN\ddot{\theta},$$

where N is a multiple of the power line frequency, J is the moment of inertia of the armature plus the rotor, ε is the phase error, K is the stiffness coefficient of the system, and θ is the power line phase angle. In the limit of Butterworth damping, $C = \sqrt{2KNJ}$, one can show that the power spectral density of the phase-lag error is given by

$$(3)\quad \frac{d\Upsilon^2}{d\nu} = \left(\frac{T}{2\pi\nu_0}\right)^2 \frac{(\nu/\nu_0)^2}{1+(\nu/\nu_0)} \frac{d\sigma^2}{d\nu} \quad .$$

Here T is the period and $\nu_0 = (2)^{-1}\sqrt{K/NJ}$. For $\nu_1 << \nu_0$, one can then show that the RMS phase-lag error is

$$(4)\quad \Upsilon_{RMS} = \frac{2\pi\sqrt{2}\,NJ}{F_0 K}\,\sigma_1\nu_1$$

and the RMS control power is

$$(5)\quad P_{RMS} = 8\pi^3\sqrt{2}N^2F_0J\sigma_1\nu_1 \quad .$$

The available power must be must greater than (5) to keep the control system linear. If one estimates ten times (5), then, for a typical rotor of J = 500 kgcm^2 operating at 32,400 RPM, one obtains a control power requirement of 230 W. Additional power is required to overcome bearing drag.

III. Control System for 14,400 RPM Test

A PID control system was tested using one of the choppers from the MTR velocity selector[2]. Fig. 4 shows the control system in schematic form.

The input signal E_L is the train of 20 μsec pulses of 120 Hz nominal repetition rate, corresponding to the successive zero crossings of the powerline voltage waveform. The output is the advancing phase angle θ of the chopper shaft S, which rotates at the nominal speed of 2 X 120 = 240 Hz. Each revolution of the shaft is detected by a magnetic pickup Q which senses the passage of a slot in the iron disk D attached coaxially to the shaft (or equivalently an iron stud attached to the chopper rotor). The signal conditioner P squares up the rough pulse train from the pickup Q, and delivers (as a feedback signal E_R) a train of 20 μsec pulses of 120 Hz normal repetition rate.

The shaft S is driven by a 500 W, 2 phase, 4 pole induction motor M, which receives its stator excitation from a 2 phase, 240 ± 48 Hz, variable-frequency drive unit. Each phase of the drive unit is a 250 W solid state amplifier, connected to an 8-bit digital-to-analog converter which has its data input furnished by a 256-byte read-only-memory ROM. The phase one memory contains a cosine wave, and the phase-two memory contains a sine wave. The two ROM's are addressed simultaneously by the parallel outputs of an 8-bit binary counter, which is toggled by a voltage-controlled oscillator having a 61.4 ± 12.3 kHz output frequency which is linearly related to the input voltage V.

The function of the controller box B is to transform the line signal E_L and the rotor signal E_R into a control voltage V which will maintain phase lock within an acceptable phase tracking error. Early studies showed that the conventional rate generator in a standard PID controller is far too insensitive to detect the miniscule, but crucial, speed changes. Instead, a digital timing-and-computing scheme was devised to measure the relative phase lag and the duration of every revolution of the shaft S with an accuracy of ± 204 nsec, and to convert the resulting data streams into a phase error signal and "vernier speed error" signal needed to stabilize the associated phase loop.

In obtaining the experimental data reported here, the speed error gain setting was such that full scale correction ($-10 < V < +10$ volts) corresponded to a ±0.375 Hz speed error. The phase error gain was manually set to the highest value achievable without inducing overshoot oscillations. With the motor and chopper running in a one Torr vacuum, the four supporting bearings consumed an average drag power of ∿150 W.

IV. Phasing Experience

As a test of the PID control system, one of the surplused choppers from the MTR velocity selector[2] was reactivated. This chopper has a moment of inertia of about 200 $Kgcm^2$. The 500 W

motor was used to drive the chopper at speeds up to 14,400 RPM. A magnetic pickup was used to sense an iron stud on the chopper to record the chopper's relative angular position. Figure 5, which demonstrates the phase control, shows the spectrum of magnetic pickup events when the chopper is controlled to the line and the scan is triggered by the time of the zero crossing signal from LAMPF. The full width half maximum FWHM of this curve is 15 μsec, while the full width at the base FWB is 45 μsec. These times are both well within the window of 128 μsec in which LAMPF will allow for a trigger from the chopper to be sent back to trigger LAMPF.

Figure 6, which is a first demonstration of the jitter, shows the spectrum of magnetic pickup events when the chopper is controlled to the line and LAMPF is triggered by the chopper. The FWHM is 2.0 μsec while the FWB is 5.0 μsec, both approaching the conditions that will be satisfactory for a phased chopper.

Since the MTR chopper with its Ni shell and Ni + Cd shades in the foil package will not be satisfactory for chopping neutrons above 0.3 eV, a new chopper was made. This new chopper, which is shown in Figure 7, has a shell of Al and shades in the foil package of three pieces of Borsical[9,10], a composite of B fiber covered with Al. The radius of curvature of these slots is 130" to pass 0.5 eV neutrons when the chopper is spinning at 14,400 RPM. The moment of inertia of this chopper is 100 $Kgcm^2$.

Figure 8 shows an example of the phase control for the Al shell chopper while Figure 9 shows the jitter. The chopper was spinning at 14,400 RPM. Figure 8 shows that the control or phase lock of the chopper to the line that drives LAMPF was 50 μsec FWB, well within the 128 μsec window allowed by LAMPF. Figure 9 has a FWHM of 1.8 μsec and a FWB of 6 μsec, close but not as narrow as desired. Analysis of parts of the control system indicate that the adjustable delay #1 of Figure 1 has a jitter of ± 1 μsec while the adjustable delay #2 has a jitter of ± 0.5 μsec. These could account for much of the ± 1 μsec jitter of Figure 9. Inspection using an oscilloscope of the change in speed of the chopper as sensed by the magnetic

pickup signal indicates a short time jitter of only a few tenths of a μsec. This should represent the jitter that is achievable with the PID control system when the coarseness of the delay units is reduced.

A longer time hunting is observed in the speed of the chopper. This may cause some jitter and a longer time-integral control may need to be used in the control system.

IV. Neutron Experience

For neutron tests, the Al shelled chopper was placed at flight path 8 of WNR. A fluted beam was used which viewed the 10cm X 10cm source at the target through a 2cm X 0.13cm slot at the chopper. Neutron detectors were placed just before the chopper, and just after the chopper.

Figure 10 shows spectra of the flux of neutrons that were measured by the two detectors. The upper curve of Figure 10 is the typical WNR spectrum for a beam filtered only by Cd. The increase near channel 500 is the start of the thermal Maxwellian distribution. The dip near channel 900 indicates the Cd cut off. The lower curve of Figure 10 shows the bursts as sensed by the detector just after the chopper, for several different phase settings. Since the detector was near the chopper and in a high field of scattered neutrons, the backgrounds of the lower curve are not indicative of the true effectiveness of the chopper when closed. The envelope of the bursts of the lower curve show the coarse transmission of the chopper.

The bursts are sharp, even the first burst at channel 60 which is about 20 eV. The 4th burst is at about 0.4 eV, a little below the design target for maximum transmission for this chopper. The last burst at channel 950 is for about 80 meV neutrons which are so slow that they are mostly swept out by the nearly straight slots.

Figure 11 shows an expanded view of the 4th burst, the one for 0.4 eV neutrons. Its FWHM which is 10 μsec, is a composite of the 5.2 μsec FWHM of the chopper opening and closing, the 11.2 μsec FWB of the sweep of the chopper across the source and the 2 μsec FWHM of

the jitter of the chopper. The boron shades made of three thicknesses of Borsical seem to be effective for chopping neutrons even up to 20 eV. The background of Figure 11 is not significant because of the way these tests were run.

V. Conclusions

The control tests and neutronic tests presented in this paper demonstrate that the PID control system effectively holds a chopper within the time window allowed by LAMPF. The jitter measurements show that a chopper can trigger LAMPF to within $< \pm 0.5$ μsec once the electronic coarseness is refined. The neutronics measurements show that the boron fiber shades are effective neutron choppers.

Acknowledgements

The authors recognize and thank Harold Bowen for his many contributions and assistance in the construction and checkout of the PID control system. Rod Hardee was a great help in reassembling the MTR chopper. The authors also thank Joyce Goldstone, Phil Seeger and Don Crocker for valuable assistance during the course of this development.

References

1. R. A. Egelstaff, "Proceedings of the First International Conference on the Peaceful Uses of Atomic Energy", Geneve, Vol IV, p. 119, United Nations, New York, (1955).

2. R.M. Brugger and J.E. Evans, Nuclear Inst. and Meth., 12, 75, (1961).

3. W. D. Whittemore and H. R. Danner, "Neutron Inelastic Scattering," Vol 1, p. 273, IAEA, Vienna, (1963).

4. G. J. Kirouac, W. E. Moore, L. J. Esch, K. W. Seeman and M. L. Yeater. Thermalization of Reactor Spectra Vol 1, p. 389, IAEA, Vienna, (1968).

5. B. C. Boland, D. F. R. Mildner, G. C. Sterling, L. J. Bunce, R. N. Sinclair and C. G. Windsor, Nucl. Inst. and Meth. 154 349, (1978).

6. R. Kleb, C. A. Pelizzari and J. M. Carpenter, "Fermi Choppers for Epithermal Neutrons", (in preparation).

7. C. G. Windsor, Pulsed Neutron Scattering, pp. 296, Taylor and Francis LTD, London, (1981).

8. T. J. L. Jones and J. G. Parker, Proceedings of the IVth ICANS Meeting, KEK, TSUKUBA, Oct 20-24, (1980), KENS Report II, pp 499, (March 1981).

9. Composite Technology, Inc., 6 Mill Street, Broadbrook, Conn. 06016.

10. T. J. L. Jones, J. Penfold and W. G. Williams, Rutherford Laboratory Report RL-79-020, (March 1979).

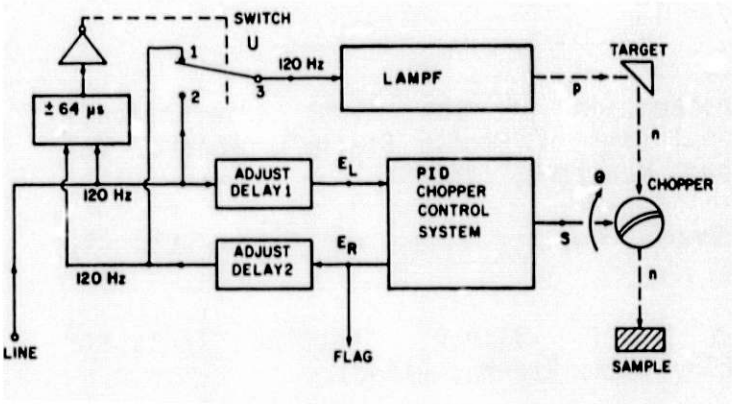

Fig. 1

Schematic layout of the coupling of a chopper at WNR to the LAMPF accelerator.

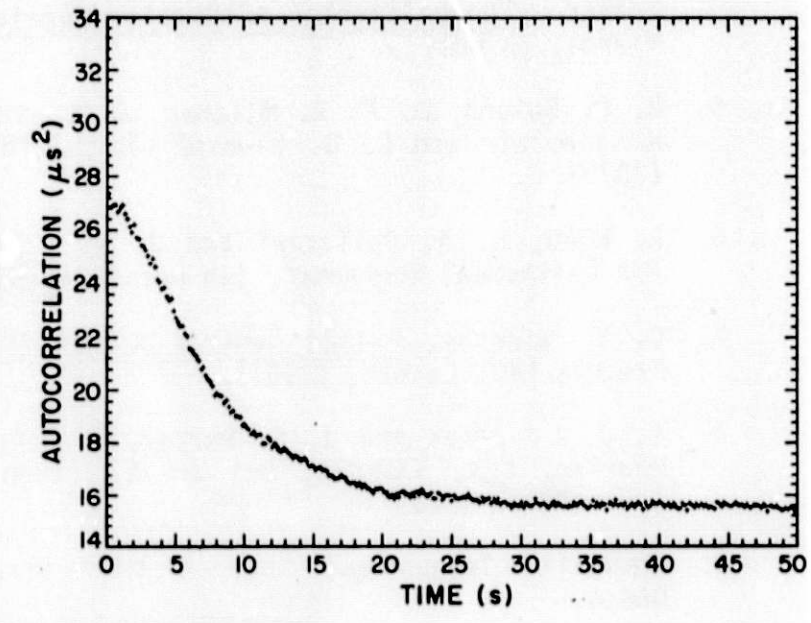

Fig. 2

Period deviation from 60 Hz versus time of the LAMPF commercial power line.

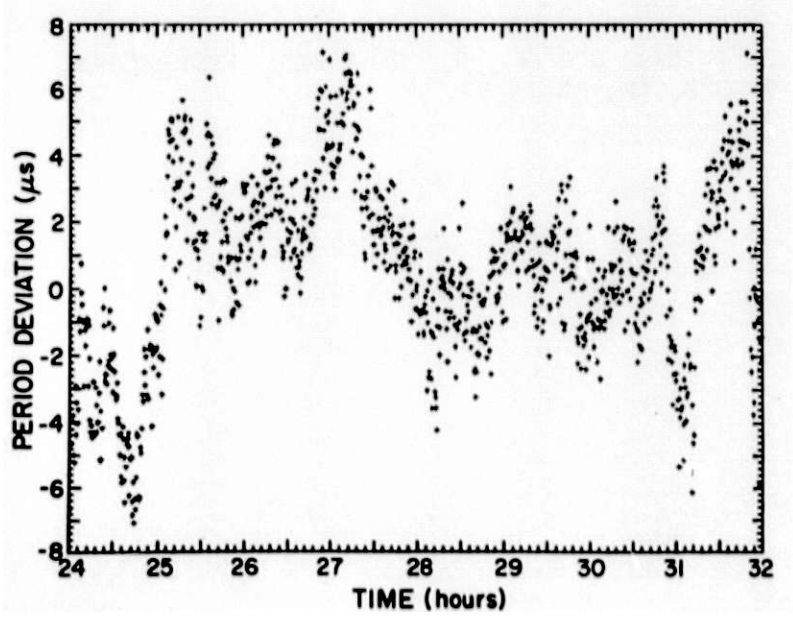

Fig. 3

Autocorrelation of the period deviations of Figure 2.

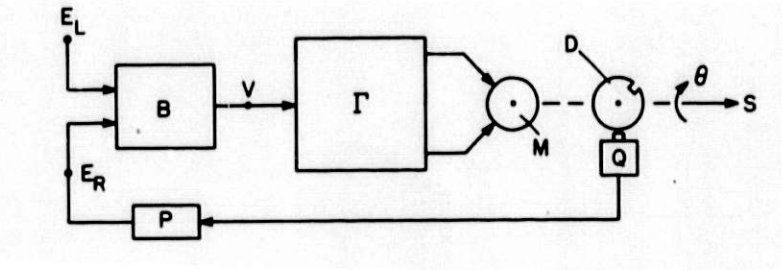

Fig. 4

The neutron chopper control system.

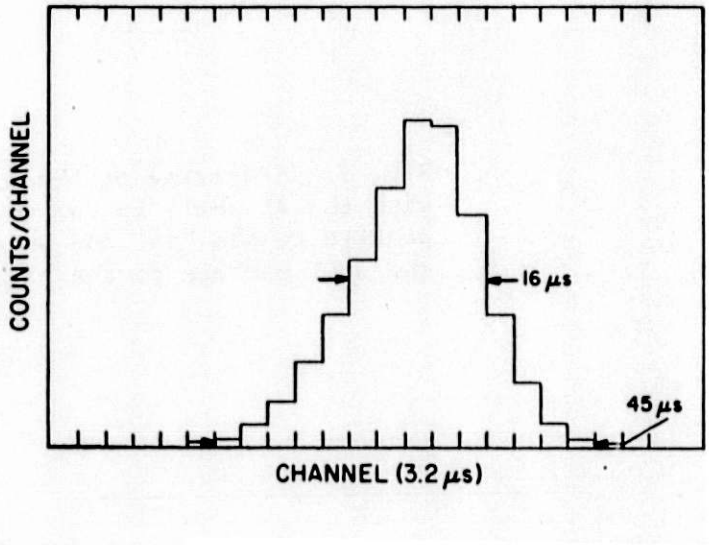

Fig. 5

The measured phase error distribution between the LAMPF power-line cross-over and the chopper angular position using the PID control system. The chopper had a nickel shell, a moment of inertia of 200 Kgcm^2 and was running at 14,400 RPM.

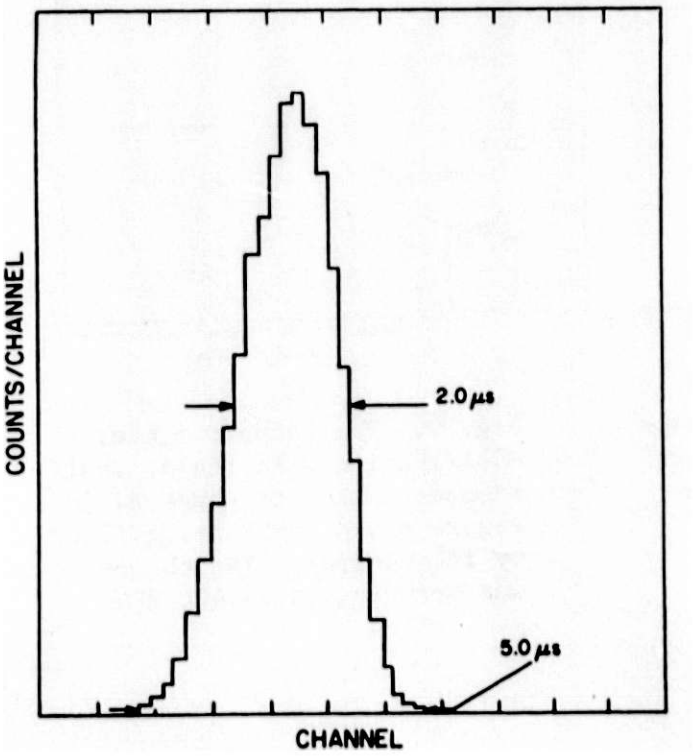

Fig. 6

The chopper jitter distribution when the chopper is phased to LAMPF as in Figure 5 and LAMPF is fired within the 128 μsec window. In this case, the chopper was spinning at 7,200 RPM.

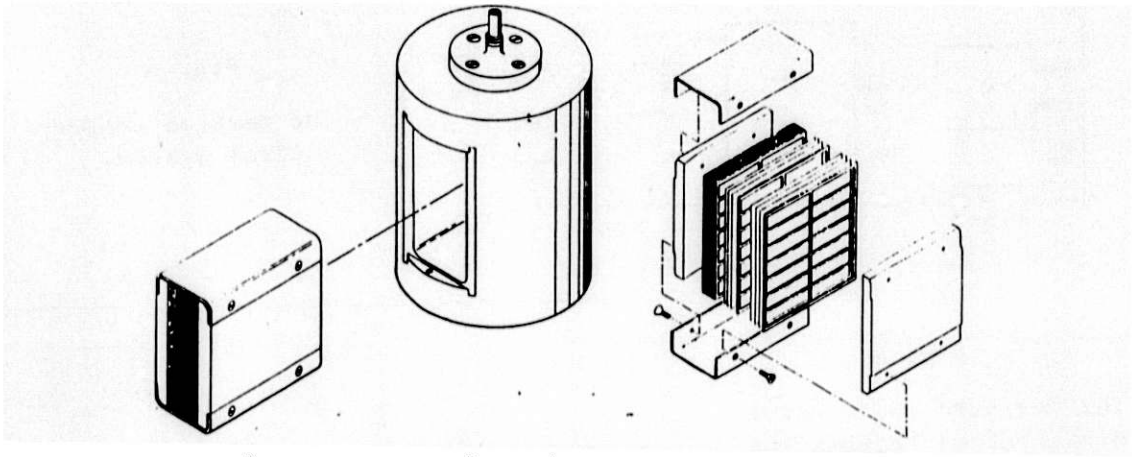

Fig. 7. A drawing of the Al shell chopper with the Al shell in the center, a foil package to the left and an exploded view of the foil package to the right.

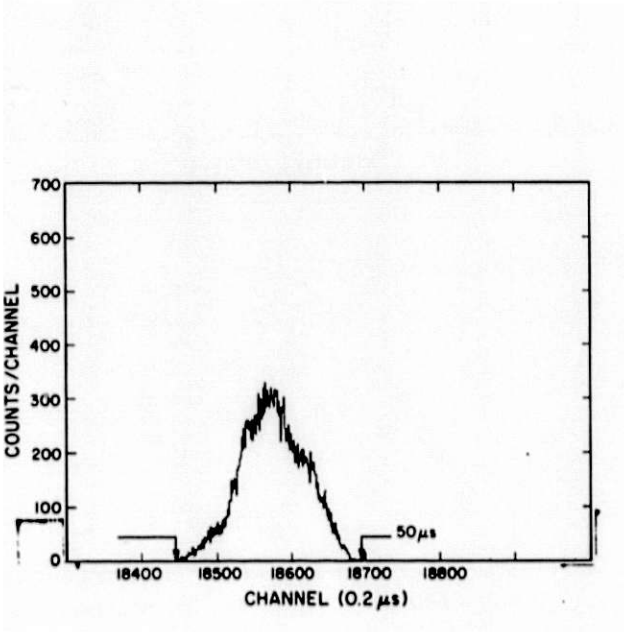

Fig. 8. The control or phase error distribution for the Al shell chopper with 100 Kgcm^2 spinning at 14,400 RPM.

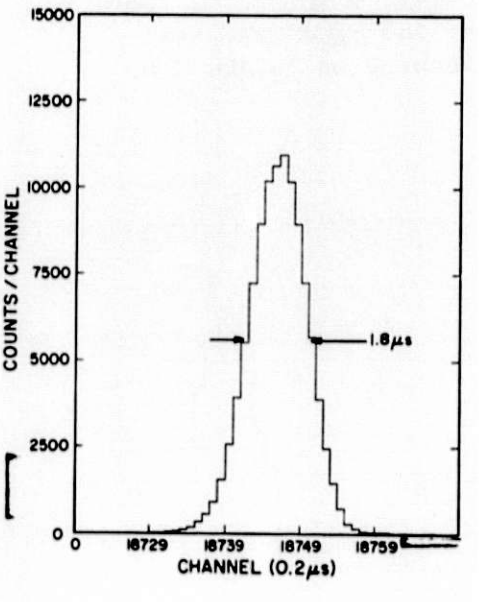

Fig. 9. The chopper jitter distribution with the Al shell chopper phased to LAMPF as in Figure 8 and LAMPF being fired by the chopper. The chopper was spinning at 14,400 RPM.

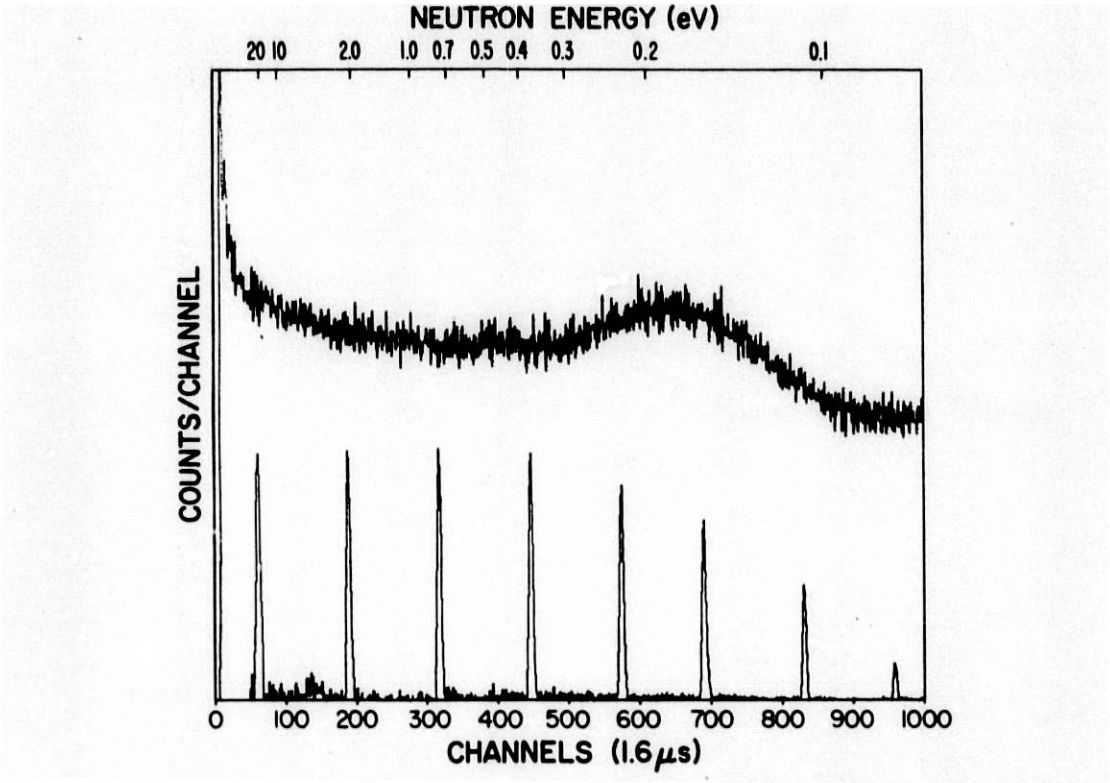

Fig. 10. Spectra of the flux of neutrons measured in flight path 8 by detectors just before and just after the chopper.

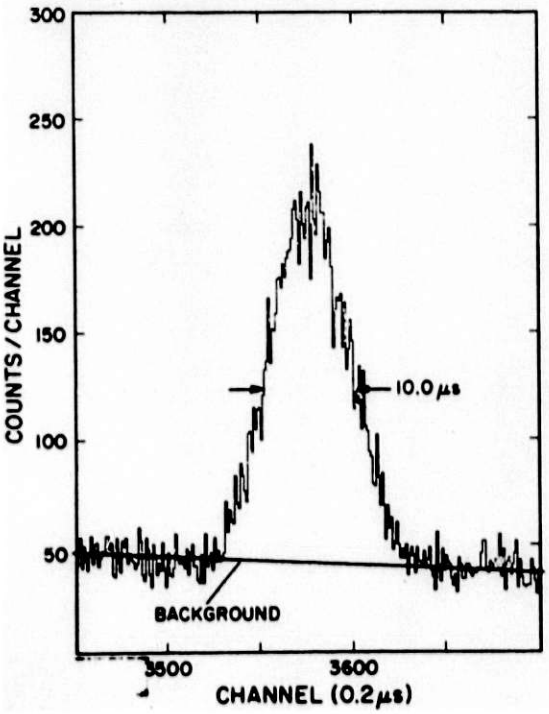

Fig. 11

An expanded view of the 4th burst from the left of Figure 10.

ICANS-VI

INTERNATIONAL COLLABORATION ON ADVANCED NEUTRON SOURCES

June 27 - July 2, 1982

THE IPNS-I CHOPPER SPECTROMETERS

D. L. Price, J. M. Carpenter, C. A. Pelizzari,
S. K. Sinha, I. Bresof and G. E. Ostrowski

Argonne National Laboratory, Argonne, Illinois 60439 U.S.A.

ABSTRACT

We briefly describe the layout and operation of the two chopper experiments at IPNS-I. The recent measurement on solid ^{4}He by Hilleke *et al.* provides examples of time-of-flight data from the Low Resolution Chopper Spectrometer.

THE IPNS-I CHOPPER SPECTROMETERS

D. L. Price, J. M. Carpenter, C. A. Pelizzari
S. K. Sinha, I. Bresof and G. E. Ostrowski

Argonne National Laboratory, Argonne, Illinois 60439 U.S.A.

The chopper spectrometers at IPNS-I enable measurements of inelastic scattering with energy transfers in the range 40-800 meV. Detectors placed at many different angles determine the scattering as a function of wave vector Q as well as energy transfer E. As an example, Fig. 1 shows the region of (Q,E) space opened up by the use of 500 meV neutrons compared with the region accessible to 100 meV neutrons, which are towards the upper end of the range available at reactors. The aim of the chopper spectrometers at IPNS-I is to explore the new scientific opportunities in this new (Q,E) region.

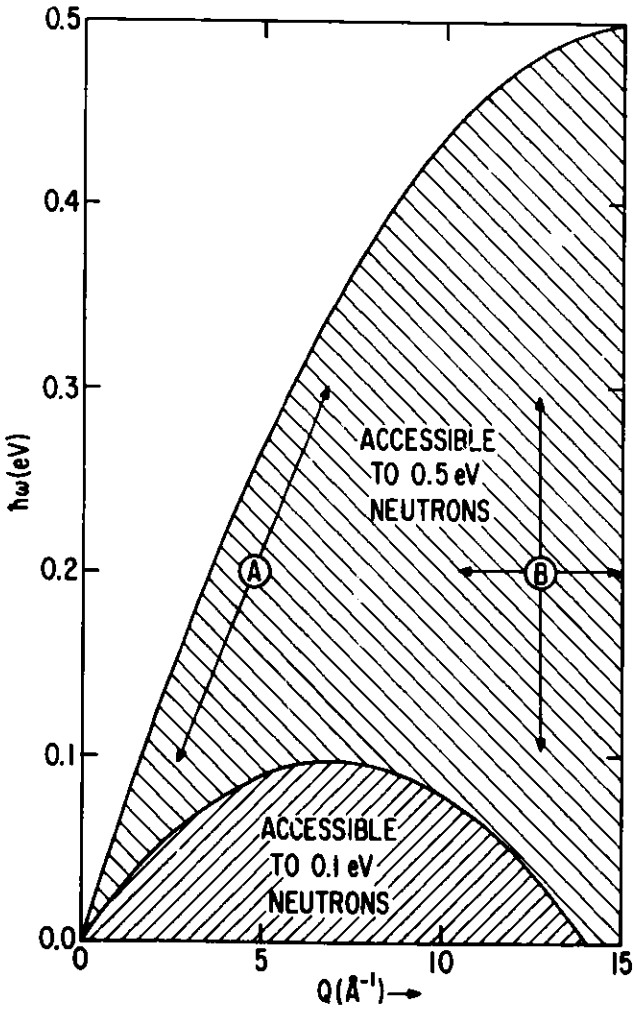

Fig. 1 Region of (Q, E) space opened up by 500 meV neutrons compared with 100 meV (E = ħω).

Fig. 2 shows a schematic of the layout for the two spectrometers now existing at IPNS-I. By increasing the distances d_1 and d_3 the resolution is improved but at the expense of intensity. The two machines, Low-Resolution Medium-Energy Spectrometer (LRMECS) and High-Resolution Medium-Energy Chopper Spectrometer (HRMECS) represent different compromise positions with respect to this trade-off. The dimensions for the two machines are given in the figure.

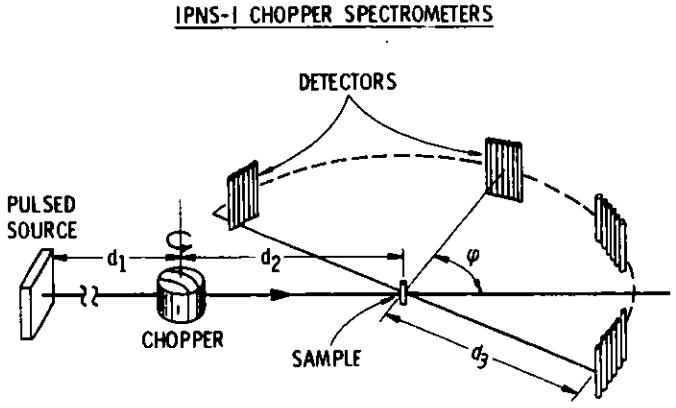

	d_1	d_2	d_3	$\Delta E/E_0$	φ
LRMECS	6.2 m	0.6 m	2.5 m	6-8%	-10° to +120°
HRMECS	12.8 m	1.1 m	4.0 m	3-4%	-20° to +20°

Fig. 2

Schematic of the layout and dimensions of the two chopper spectrometers at IPNS-I.

The chopper has a body of beryllium with aluminum end-caps; boron fiber/aluminum composite defines the slits; details are given elsewhere[1].

The system shown in Figure 3 maintains the choppers for these and other

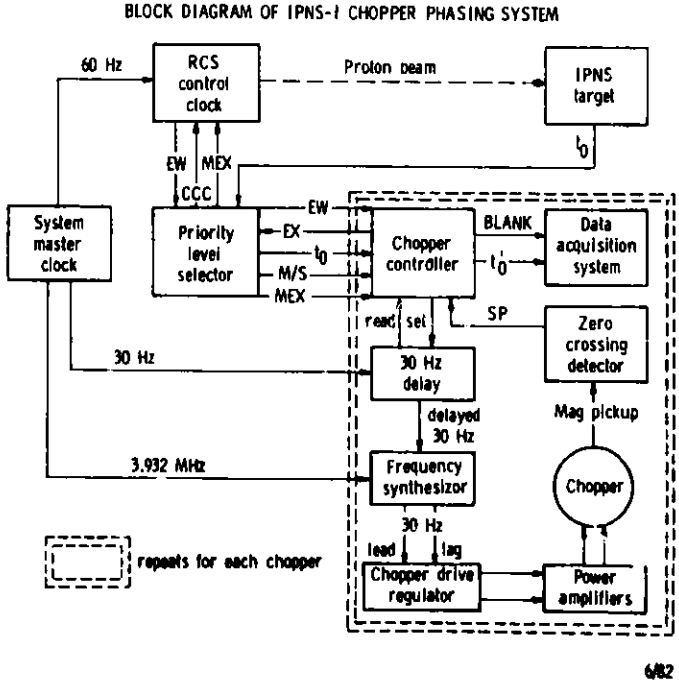

Fig. 3

Summary of the scheme for chopper phasing at IPNS-I.

machines in a fixed phase relation to the accelerator[2]. A key element is the system master clock, based on a crystal oscillator and sending synchronized driving pulses to the Rapid Cycling Synchrotron (RCS) and the choppers. Each chopper circuit (in the dashed-line box in Fig. 3) generates a signal demanding extraction from the accelerator, based on the t_0 signal from the target, the chopper period and a preset delay time. The priority level selector sends the highest priority (relative to a preassigned hierarchy) valid extraction signal to the RCS. The logic of the phasing mechanism is shown in detail in Fig. 4. The system performs excellently with the two choppers running simultaneously.

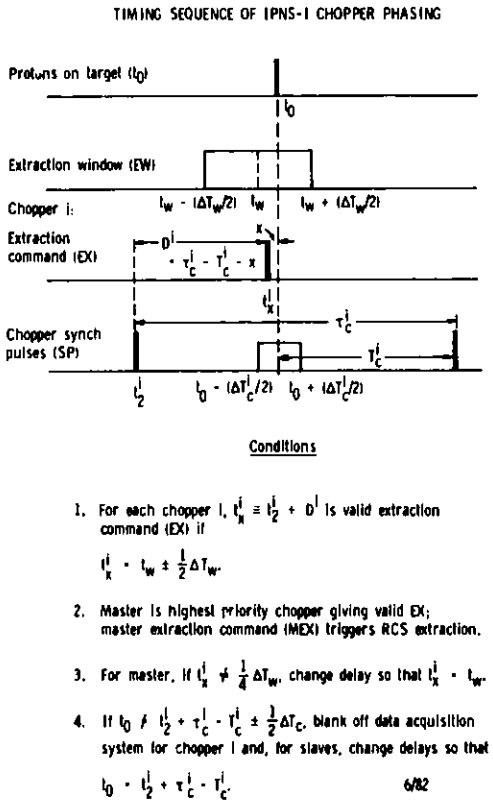

Fig. 4. Timing sequence and logic of the chopper phasing system.

Approximately 100 ^{3}He proportional counters in each instrument detect scattered neutrons. The signals run to the IPNS-I Data Acquisition System[3]; the software enables signals from individual detectors to be binned singly or together as a larger group. The data are analyzed on the VAX 11-780 using general purpose programs which have been developed[4]. Fig. 5 gives a summary of the scheme involved.

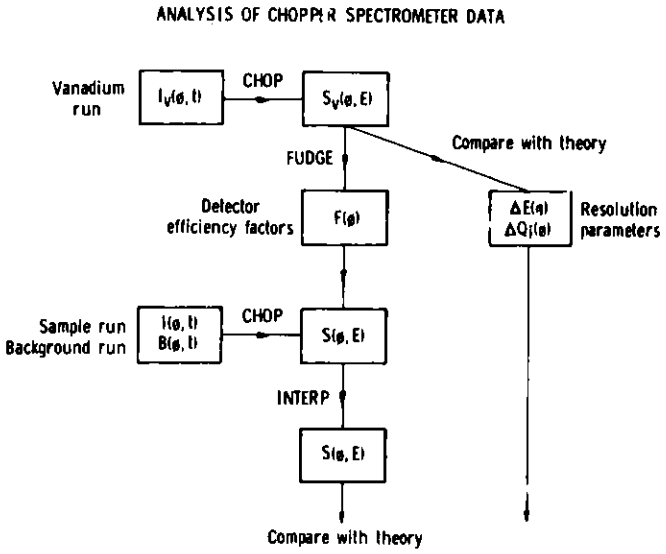

Fig. 5

Summary of the scheme for chopper data analysis.

Since HRMECS has only just become operational, we now limit our discussion to LRMECS. Table I lists the experiments recommended by the Program Committee for the first year of full operation. At the present time all experiments recommended for the first half-year have been run and are in various stages of data analysis. In some cases additional data are needed.

As an example, we show raw time-of-flight data for the solid ^{4}He experiment[5]. The data were taken with E_0 = 500 meV. The object was to determine the ground state momentum distribution in hcp solid ^{4}He.

Figure 6 shows the scans through (Q,E) space corresponding to a fixed detector as a function of angle. Peaks are expected at the points where the curve for the recoil energy

$$E_R = \frac{\hbar^2 Q^2}{2M}$$

crosses the (Q,E) scans (M = mass of scattering atom).

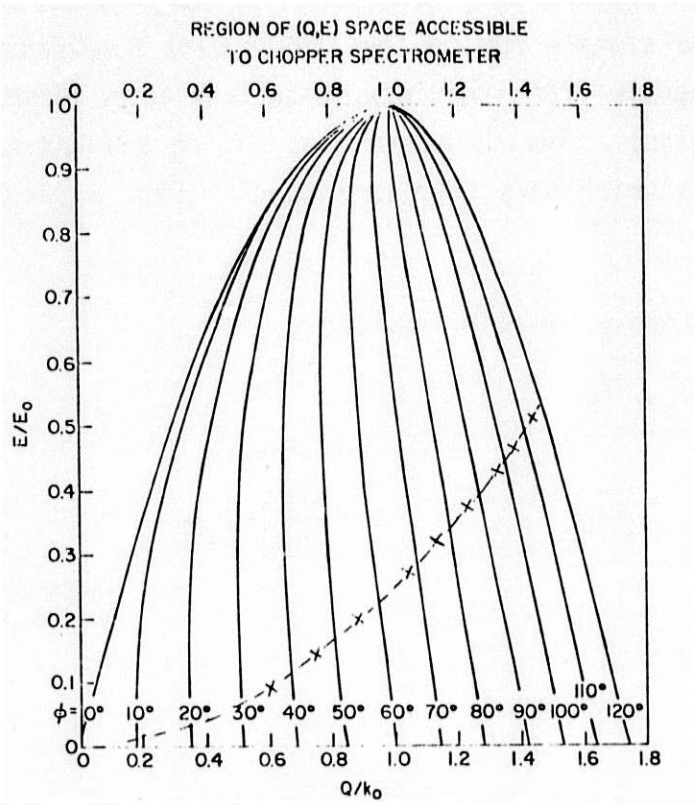

Fig. 6

(Q, E) conditions for the ^{4}He experiment. The solid curves are the loci through (Q, E) space scanned by detectors at the angles indicated. The dashed curve is the recoil energy for ^{4}He. The crosses indicate the peak positions in the measurement of Hilleke et al. (Ref. 5). E_0 = 505 meV, k_0 = 15.6 Å^{-1}.

The remaining figures show the count rate as a function of time for three angles. The circles represent the scattering with the container full and the lines the empty container scattering normalized by monitor counts to the full container run. Fig. 7 shows the helium peak at a small angle, ϕ = 7.5°, where the recoil energy is very small and the helium peak is superimposed on the scattering from the container.

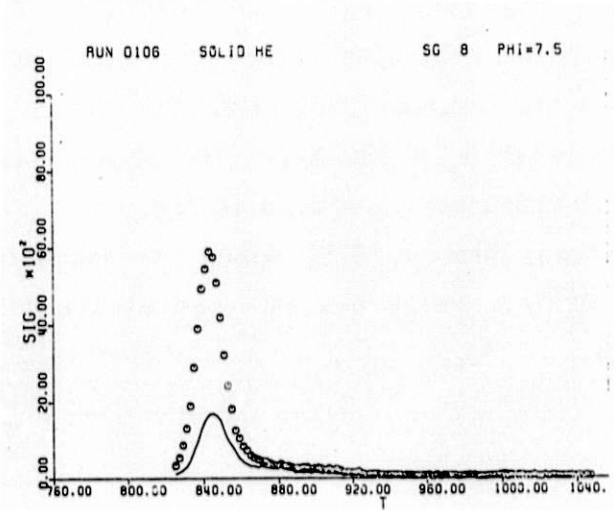

Fig. 7

Curve of scattering from ^{4}He (open circles) compared with that from the empty container (normalized to the sample run) at room temperature, ϕ = 7.5° (Hilleke et al., Ref. 5).

As the angle is increased the helium peak begins to move away from the container scattering ($\phi \sim 57°$, Fig. 8), and at larger angles it becomes well resolved ($\phi \sim 87°$, Fig. 9). The data for the signal run were accumulated in 40 hours with a current of 8 μA of 400 MeV protons. At the present time analysis is underway to provide the scattering function S(Q,E) to compare with theoretical calculations.

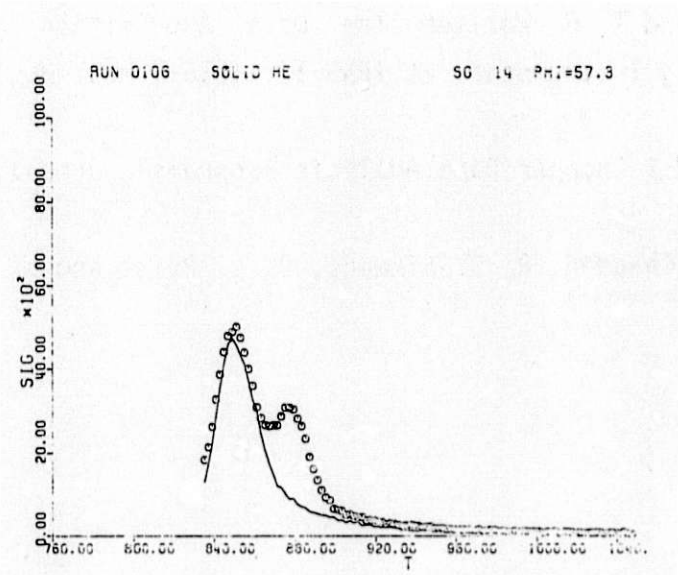

Fig. 8

Curve of scattering from ^{4}He (open circles) compared with that from the empty container (normalized to the sample run) at room temperature, ϕ = 57.3° (Hilleke et al., Ref. 5).

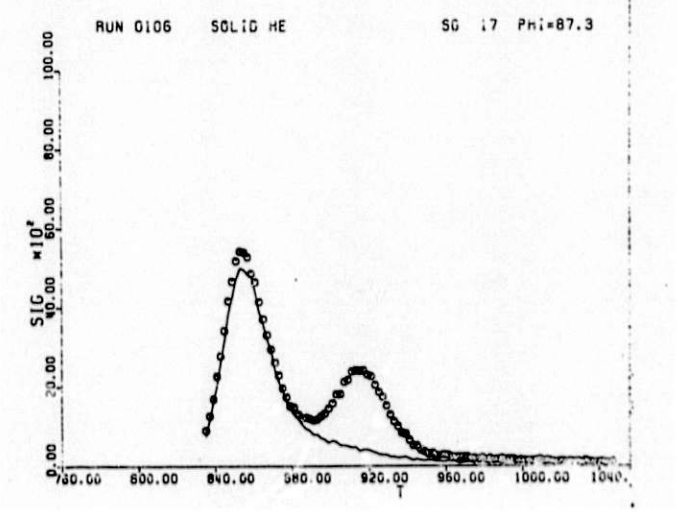

Fig. 9

Curve of scattering from ^{4}He (open circles) compared with that from the empty container (normalized to the sample run) at room temperature, ϕ = 87.3° (Hilleke et al., Ref. 5).

References

1. R. Kleb, C. A. Pelizzari and J. M. Carpenter "Fermi Choppers for Epithermal Neutron Beams", to be published.
2. W. Praeg, D. McGhee and G. Volk "Phase Lock of Rapidly Cycling Synchrotron and Neutron Choppers", IEEE Trans. Nucl. Sci. NS-28, 2171 (1981).
3. R. K. Crawford, R. T. Daly, J. R. Haumann, R. L. Hitterman, C. B. Morgan, G. E. Ostrowski and T. G. Worlton "The Data Acquisition System for the Nuclear Scattering Instruments at IPNS-I", IEEE Trans. Nucl. Sci. NS-28, 3692 (1981).
4. D. L. Price, "IPNS-I Chopper Data Analysis Programs", June 1, 1982 (unpublished).
5. R. O. Hilleke, P. Chaddah, R. O. Simmons, D. L. Price and S. K. Sinha (to be published).

TABLE 1. LIST OF EXPERIMENTS RECOMMENDED BY THE PROGRAM COMMITTEE FOR THE FIRST YEAR OF LRMECS

LOW-RESOLUTION MEDIUM-ENERGY CHOPPER SPECTROMETER

Accepted Proposals November 1981 - April 1982

6	S. A. Werner G. Shirane	U. of Missouri Brookhaven	High Energy Magnetic Excitations in Pure Chromium	7 days
71	R. O. Hilleke R. O. Simmons P. Chaddah S. K. Sinha	U. of Illinois U. of Illinois Bhabha At. En. Res. Cntr. Argonne	Momentum Density of HCP ^{4}He	10 days
43	J. M. Carpenter C. A. Pelizzari D. F. R. Mildner	Argonne Argonne U. of Missouri	Mapping the Scattering Law for Vitreous SiO_2	7 days
57	S. M. Shapiro S. K. Sinha	Brookhaven Argonne	Measurement of Spin Dynamics in the Mixed Valence Alloy $Ce_{1-x}Th_x$	7 days (with #65)
58	J. S. Lannin L. Pilione R. Magaña S. K. Sinha	Penn State U. Penn State U. Penn State U. Argonne	Time of Flight Study of the Phonon Density of Amorphous Phosphorus	7 days (Backup)
65	R. D. Parks S. Shapiro B. Grier S. K. Sinha	Polytechnic Inst. of New York Brookhaven Brookhaven Argonne	Quasielastic Neutron Scattering Study of $Ce_{0.9-x}La_xTh_{0.1}$	7 days (with #57)

Accepted Proposals May - October 1982

9	S-H. Chen D. L. Price	MIT Argonne	Proton Dynamics in Supercooled Water	2nd Backup
66	S. K. Sinha H. A. Mook B. Goodman	Argonne Oak Ridge U. of Cincinnati	Measurement of the Condensate Fraction of ^{4}He in Superfluid ^{4}He and ^{3}He-^{4}He Solutions	10 days
72	S. K. Sinha A. J. Arko D. L. Price R. M. Nicklow	Argonne Argonne Argonne Oak Ridge	Dynamical Response in the Exchange Enhanced Paramagnet U Al_2	10 x 1/2 days with #127
104	J. R. D. Copley W. S. Howells	McMaster Univ. Rutherford Lab.	Atomic Motion in Liquid Lithium and Selected Lithium Alloys	10 days
127	M. Loewenhaupt	Jülich	Magnetic Excitations in Cerium and Uranium Compounds	10 x 1/2 days with #72
136	P. Blanckenhagen	Karlsruhe	Spin Waves in Ordered Ni_3Mn	1st Backup

ICANS-VI

INTERNATIONAL COLLABORATION ON ADVANCED NEUTRON SOURCES

June 27 - July 2, 1982

A ROTATING CRYSTAL PULSE SHAPER FOR USE ON A PULSED NEUTRON SOURCE

J M Carpenter
Argonne, National Laboratory
Argonne, Illinois 60439
USA

C J Carlile
Rutherford Appleton Laboratory
Chilton, Oxfordshire OX11 0QX
England

ABSTRACT

A pulse shortening device is described for use on pulsed thermal neutron sources. The device employs rotating single crystals and has applications in the design of high resolution cold neutron spectrometers.

A ROTATING CRYSTAL PULSE SHAPER FOR USE ON A PULSED NEUTRON SOURCE

J M Carpenter
Argonne National Laboratory

C J Carlile
Rutherford Appleton Laboratory

1. Introduction

It is much more favourable to use white beam time of flight techniques on pulsed neutron sources than on continuous reactor-based neutron sources for reasons of neutron economy. However, from the moment of formation of the neutron burst in the moderator the white beam is correlated in wavelength and time unlike a beam on a continuous source and therefore neutrons of different wavelengths disperse as they travel from the moderator. This correlation provides the basis of the design of many pulsed source neutron spectrometers. In certain cases however it can be the cause of design constraints.

This is the case for the time of flight high resolution quasielastic spectrometer IRIS [1] to be built on the spallation neutron source SNS [2] at the Rutherford Appleton Laboratory. For this spectrometer a pulse of cold neutrons narrow in time but as wide as possible in wavelength is required. It is necessary therefore to reduce the moderator pulse width by chopping the beam as close to the moderator as possible in order to maintain an adequately wide incident neutron wavelength window. The distance of closest approach, and thus the wavelength window, is limited

however by the intense radiation field in which the chopper must operate. A rotating crystal monochromator can produce a wider wavelength window than a mechanical chopper at the same position by matching the time of arrival of neutrons of different wavelengths in the incident beam to the time dependent Bragg condition of the rotating crystal. This paper explores the feasibility of such a device.

2. The λ-t representation of the neutron pulse

In λ-t space, where t is the time of arrival of a particular neutron of wavelength λ at a given distance L from the moderator, the neutron pulse can be represented by a straight line passing through the origin as shown in figure 1. Wavelength and time of arrival are related through the de Broglie relationship

$$\lambda = \frac{h}{mL} \cdot t \equiv ct$$

Thus at a position close to the moderator this locus has a higher gradient, and far from the moderator a lower gradient reflecting the dispersion of the pulse with distance. For a given monochromatic neutron wavelength the time distribution of such neutrons is shown schematically in figure 2. A measure of the time width of the neutron pulse is given by the FWHM δt_M of this curve although this conceals the asymmetric shape of the pulse particularly the tail at long times. Nevertheless on the λ-t diagram the pulse width can be represented by separate traces for the leading and trailing edges of the pulse at the FWHM positions as indicated in figure 1. Note that the time distribution is independent of distance from the moderator and that δt_M is determined for the neutron pulse at the moment of its emission from the moderator surface and remains constant for each wavelength at all distances from the moderator. Consequently the principle

parameter with which to vary the resolution of a spectrometer is its distance from the moderator and, for high resolution instruments, the required distance can become untenable. In these circumstances δt_M can be reduced in order to achieve the desired resolution. δt_M is proportional to wavelength in the slowing down region of the spectrum ($\delta t_M \sim 7\lambda$ where λ is expressed in Angstroms and δt_M in microseconds). In the thermalised Maxwell-Boltzmann region of the spectrum the pulse broadens and the constant of proportionality rises to between 12 and 25 [2,4].

The pulse narrowing necessary to attain high resolution can be achieved by two methods:

- The moderator itself can be designed such as to provide the pulse structure required by a particular spectrometer. However, since a number of spectrometers, in general, view the same moderator there is a limited, but nevertheless important, scope for this option.

- The pulse itself can be tailored after formation by some mechanism. This can be achieved by the use of a mechanical chopper but, as its alternative name of velocity selector implies, this greatly reduces the wavelength distribution in the beam transmitted by the chopper. This can be seen in figure 3 where we restrict our attention to a relatively narrow range of wavelengths. In this case the neutron pulse at a fixed distance from the moderator can be represented by two approximately parallel lines in λ-t space.The action of the chopper, of burst time δt_C, restricts the wavelength component in the transmitted beam to a relatively narrow range $\Delta\lambda$, particularly when $\delta t_C < \delta t_M$. Thus one advantage of the pulsed source - its white beam - can be severely limited in the design of high resolution instruments.

An idealised pulsed shortening device would reduce the pulse in time whilst maintaining its full wavelength range. This ideal case is indicated by the dashed lines in figure 3. A rotating crystal assembly, as described in the following section, more nearly approaches this ideal than does a chopper.

3. The rotating crystal pulse shaper

3.1 The basic principle

Suppose we arrange a single crystal, rotating with a constant angular frequency ω, at a distance L from the moderator as shown in figure 4. Then as initially fast and later slow neutrons illuminate the crystal, the rotational motion adjusts the Bragg angle θ_B to reflect a continuous broad band of wavelengths whilst only remaining in the reflecting position for any particular wavelength for a time short compared to the intrinsic neutron pulse width δt_M from the moderator.

3.2 Phasing

Correct phasing of the crystal with respect to the time origin of the neutron pulse will enable the resulting sinusoidal locus of the beam reflected from the rotating crystal in λ-t space to form a tangent to the moderator neutron pulse locus as shown in figure 5. The crystal locus is given from Bragg's law as

$$\lambda(t) = 2d \sin \theta_B(t) \qquad (1)$$

where

$$\theta_B(t) = \omega\ (t - t_o^*)$$

and t^*_o is a time origin for the crystal (equivalent to the time when the crystal planes are parallel to the incident beam).

Its gradient is given by

$$\frac{d\lambda(t)}{dt} = 2d \cos \theta_B(t) \cdot \frac{d\theta_B(t)}{dt}$$

By setting this gradient at a particular wavelength equal to the gradient c of the pulse from the moderator we obtain an expression for the crystal frequency ω required to reflect a neutron wavelength λ^* at time $t^*(= \lambda^*/c)$.

Hence

$$\omega = \frac{d\theta_B(t)}{dt} = \frac{h}{mL\,[(2d)^2 - \lambda^{*2}]^{\frac{1}{2}}} \qquad (2)$$

3.3 The wavelength and time windows

Figure 6 illustrates the general case of the interaction of the rotating crystal pulse shaper with the moderator pulse in which the traces in λ-t space intersect. The half-height contours of the pulse are represented by the lines

$$\lambda = c(t \pm \delta t_M/2) \quad \text{where } c = \frac{h}{mL}$$

The rotating crystal, phased to be in reflecting orientation at time $t^* = \lambda^*/c$, reflects neutrons of wavelength λ at time t given to first order by

$$\lambda \simeq \lambda^* + c' (t-t^*)$$

$$= c' (t - t_o^*)$$

where c' is the gradient of the sine wave trace from the crystal and is given by

$$c' \equiv \omega [(2d)^2 - \lambda^{*2}]^{\frac{1}{2}}$$

$$= 2\omega d \cos \theta_B(t^*)$$

$\Delta\lambda_c$ is the wavelength band reflected at a particular Bragg angle and is given by $\Delta\lambda_c = 2d \cos\theta_B \Delta\theta$, where $\Delta\theta$ is the range of Bragg angles contributing to the reflection process and is a measure of the divergence of the reflected beam.

$\Delta\lambda_M$ $(= c\Delta t_M)$ is the wavelength band transmitted by the chopper whereas the overall wavelength band of neutrons selected by a rotating crystal can be seen from figure 6 to be

$$\Delta\lambda'_M = \Delta\lambda_M \frac{c'}{c' - c}$$

$c'/(c' - c)$ is the wavelength band gain factor of the crystal over the chopper and for $c' = c$ the selected band becomes very large but not arbitrarily so inasmuch as the arguments here are based on a linearized treatment. A numerical solution of the problem is presented in section 4 where a realistic value of the wavelength band reflected can be estimated for the case when the two curves are tangential.

3.4 The burst time of the rotating crystal

The burst time of the rotating crystal determines the resolution of the system and is equivalent to the chopper burst time in determining the overall resolution of a chopper spectrometer. The time width of the reflected neutron pulse for a particular wavelength, caused by the inherent divergences of the beam, is given by

$$\Delta t_c = \frac{\Delta \lambda_c}{c'}$$

This is dependent on the incident and exit collimations α_1 and α_2 and on the mosaic spread β of the crystal and is equal to $\Delta\theta/\omega$. This factor can be identified with the scan time contribution to the resolution of a reactor based rotating crystal spectrometer which is given in [5] as:

$$\Delta t_c = \frac{\Delta\theta}{\omega} = \frac{1}{\omega}\left[\frac{\alpha_1^2\,\beta^2 + \alpha_1^2\,\alpha_2^2 + \alpha_2^2\,\beta^2}{\alpha_1^2 + \alpha_2^2 + 4\beta^2}\right]^{\frac{1}{2}} \qquad (3)$$

The approach is only valid provided that the scan time is shorter than the moderator burst width, ie the pulsed source appears to be a continuous source for the duration of the reflection of a particular wavelength. In this case where cold neutrons are employed and collimations are $\sim 1^{\circ}$ then crystal rotational frequencies above 25 Hz ensure its validity.

The pulse formed by the rotating crystal pulse shaper does not appear to diverge from either the crystal or the moderator. Rather the pulse appears to have been formed at a distance $L = \frac{h}{m}\left(\frac{1}{c} - \frac{1}{c'}\right)$ downstream from the moderator, and at a time $t_o^* = \lambda * \left(\frac{1}{c} - \frac{1}{c'}\right)$ after the moderator pulse itself.

3.5 The Doppler Effect

Since the monochromator crystal is moving with respect to the incident neutron beam the presence of the Doppler effect on the reflection process must be assessed.

The Doppler effect serves, for a particular point in the rotating crystal, to vary (i) the Bragg angles of incidence and reflection in the laboratory frame (ii) the selected and reflected wavelengths and (iii) the point in time of the reflection, each with respect to the equivalent parameters for the case of a stationary monochromator [6]. Considering the whole volume of the crystal this causes a broadening of the wavelength band selected, the time of reflection and the divergence of the reflected neutron beam. However, in the plane denoted AA in figure 7 (a) which is perpendicular to the Bragg reflection planes and passes through the axis of rotation, the Doppler effect does not manifest itself. In this plane the direction of motion is perpendicular to the momentum transfer vector in the reflection process and therefore the Doppler effect becomes negligible. This can be achieved in practice by using plate crystals in Laue transmission geometry (figure 7 (b)).

The Doppler effect has been used to advantage in focussing rotating crystal spectrometers on continuous neutron sources [5,7] but it appears impossible to fulfill all these conditions on a pulsed source where the incident beam is already correlated in energy and time. In particular the focussing conditions employed in rotating crystal spectrometers require that the crystal be rotated in the opposite sense to that required for this application.

3.6 Practical Considerations

Because of geometrical and shielding constraints the tailored neutron beam should emerge from the neutron source radially.

This can be achieved with the set-up shown in figure 8 (a) where a second identical crystal is phased with the first to reflect the neutron beam into the primary drift path of the spectrometer. In practice there also requires to be a translation of one crystal with respect to the other in order to satisfy the Bragg conditions for all wavelengths.

A second method is for the two crystals to be mounted on a single rotating table either with the first crystal located centrally and the second eccentrically (figure 8 (b)) or with both crystals positioned symmetrically with respect to the axis of rotation of the rotating table (figure 8 (c)).

In all cases the motion of the two crystals approximates well the rotational and translational motions required to satisfy the conditions described previously without significant degradation by the Doppler effect.

4. A Numerical Solution

In order to assertain the possible gain of a rotating crystal over a chopper we will compare the performance of the two systems constrained to the design specifications of the IRIS quasielastic spectrometer to be installed on the SNS [1].

4.1 The IRIS spectrometer

IRIS is a high resolution (1 μeV) quasielastic spectrometer. It operates by defining a neutron pulse at 4.4 metres from the moderator, allowing this pulse to disperse 40 metres to the sample position, and analysing the scattered beam by back-scattering from an array of silicon analyser crystals. In the design of the IRIS spectrometer the beam definition is by a 12 μsec burst time chopper and the analysing wavelength of the silicon (111) reflections in backscattering is 6.28Å.

The wavelength window transmitted by the chopper, taking the half height positions as limits and a pulse width of 25 λ , is 0.14Å, corresponding to an equivalent energy band of 93 μeV. For comparison the backscattering spectrometer IN10 at the ILL, Grenoble has an energy band of ± 15 μeV (± 0.023Å) and a resolution of ∿ 1 μeV.

The rotating crystal device with which to replace the chopper must use monochromators with a Bragg cut off greater than 6.28Å. The obvious choice is graphite with a Bragg cut-off of 6.69Å and a reflectivity for cold neutrons approaching 100%.

4.2 The application of graphite crystals

The maximum useful wavelength window Δλ is reflected when the crystal locus and the pulse are tangential at 6.28Å. From equation 2 there is a reciprocal relation between crystal frequency and the distance of the crystal from the moderator. In order that periodic phasing occurs the crystal frequency must bear an integral relationship to the pulsed source frequency. For the SNS this frequency is 50Hz. Therefore one can define a series of distances each corresponding to a

particular crystal frequency. The times of arrival t* of 6.28Å neutrons (λ *) at these distances can thus be determined and, from equation 1, the values of t_o*, the time origin of the crystal rotation. Therefore one has a limited choice of distances at which to locate the crystal if one choses to reflect the maximum wavelength band. These distances are given in Table 1.

Crystal Frequency (Hz)	Moderator-crystal distance (metres)
25	10.92
50	5.46
75	3.64
100	2.73

Table 1 The relationship between crystal position and frequency

The intersection of a sine wave and a straight line has, surprisingly, no analytical solution and so the equations have been solved numerically using the data in Table 1.

A graphical solution for 50 Hz is shown in figure 9. The required scan time of the crystal is a factor of ten less than the moderator pulse width and therefore for convenience in the calculations of wavelength windows this width is assumed to be negligible. On an expanded scale in figure 10 it can be seen that one can increase the wavelength window substantially by

phasing the crystal to the leading edge of the pulse [figure 10 (b)] rather than its peak [figure 10 (a)]. The resulting wavelength windows are given in Table 2 together with the wavelength window which would be obtained from a chopper in the same position.

Crystal Frequency (Hz)	Wavelength Window (Å)		
	Crystal		Chopper
	Peak Centre	Leading Edge	
25	0.44	0.62	0.06
50	0.63	0.86	0.115
75	0.75	1.05	0.17
100	0.87	1.21	0.24

Table 2 The wavelength windows transmitted by a chopper and a rotating crystal assembly for the conditions given in table 1.

These values, converted to units of energy are shown in table 3 and plotted in figure 11 as a function of frequency and distance. For operation of the crystal at 50 Hz at a distance of 5.46 metres the energy window is estimated to be 567 μ eV

when phased to the leading edge of the pulse. This can be compared with the value of 76 μeV for the chopper at the same distance and the window of ± 15 μeV presently available on the backscattering spectrometer at Grenoble.

Crystal Frequency (Hz)	Energy Window (μeV)		
	Crystal		Chopper
	Peak Centre	Leading Edge	
25	290	409	40
50	415	567	76
75	494	692	112
100	574	798	158

Table 3 The energy windows transmitted by a chopper and a rotating crystal assembly for the conditions given in table 1.

This energy window does not exceed the overlap value for 40 metres which is ∿ 1 meV at 6.28Å.

4.3 The scan time

For a frequency of 50 Hz a burst time of 12 μ sec can be achieved by the choice of appropriate values of the collimation and mosaic spread. As an example by setting $\alpha_1 = \alpha_2 = \beta \equiv \alpha$ equation 3 reduces to

$$\Delta t_c = \frac{\alpha}{\sqrt{2}\omega}$$

and the value of the collimation and the crystal mosaic spread required for a burst time of 12 μsec is 18.3 minutes of arc which is acceptable.

5. Conclusions

Our assessment indicates that the selected wavelength band can be substantially increased and the source pulse significantly shortened by the use of a rotating crystal pulse shaper instead of a mechanical chopper. This method has applications in the design of high resolution cold neutron spectrometers and diffractometers on accelerator based pulsed neutron sources. It could also have applications for pulse shortening on pulsed reactors [8] and quasi-pulsed accelerator based neutron sources [9] where the intrinsically long pulse widths limit the resolution capabilities of the source. The concept is presently being tested experimentally [10] at the KENS pulsed neutron source in Japan.

The ultimate pulse shortening device would be represented by a crystal with a time varying angular velocity such that its trace in λ-t space would be a saw-tooth. This seems to be a practical possibility in view of the modest frequency requirements for a uniformly rotating crystal.

References

[1] Carlile C J. Rutherford Laboratory report (1982) RL-82-009

[2] Manning G. Contemporary Physics (1978) 19 505

[3] Windsor C G. Pulsed Neutron Scattering (1981) Taylor & Francis Ltd (London)

[4] Carpenter J M. Nucl Insts & Meths (1977) 145 91

[5] Carlile C J and Ross D K. J Appl Cryst (1975) 8 292

[6] Buras B and Giebultowicz T. Acta Cryst (1972) A28 151

[7] Meister H and Weckermann B. Inelastic Scattering of Neutrons in Solids & Liquids (1972) 713 IAEA (Vienna)

[8] Anan'ev V D et al. Instr & Exptl Techns (1977) 20 1245

[9] Bauer G S, Sebening H, Vetter J E and Willax H (1981) Joint Julich/Karlsruhe report Jul Spec 113/KfK 3175

[10] Carpenter J M and Watanabe N. Private communication

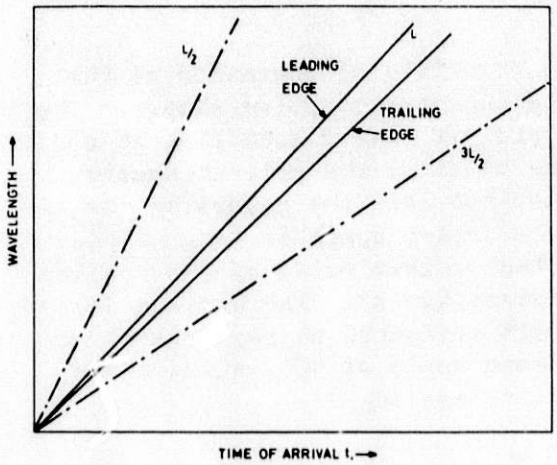

Fig. 1

The λ-t representation of a pulse from a pulsed neutron source at a given distance L from the moderator. At nearer or farther points the λ-t trace has a higher or lower gradient respectively as shown by the dashed lines.

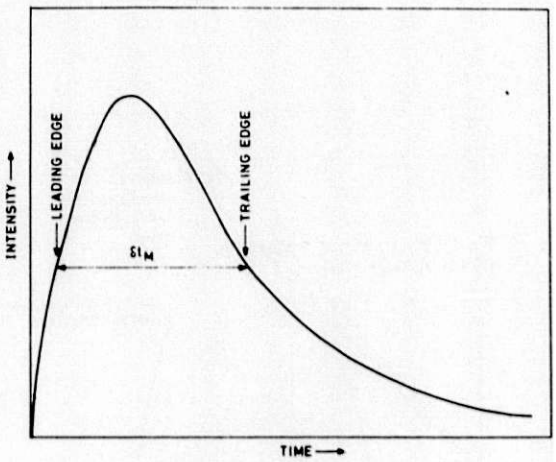

Fig. 2

A schematic representation of the time distribution of a particular wavelength emitted from the moderator. Once formed this distribution remains unchanged as the neutron pulse drifts from the moderator.

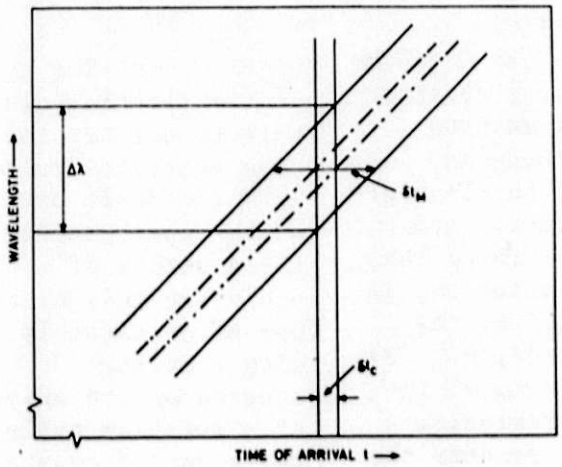

Fig. 3

A relatively narrow wavelength range in a neutron pulse where the leading and trailing edges are approximately parallel. A chopper of burst time δt_C much less than the moderator pulse width δt_M selects a restricted range of wavelengths $\Delta\lambda$ from the pulse. An idealised short time cut from the pulse is shown by the dashed lines.

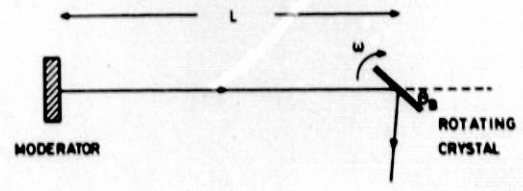

Fig. 4

A rotating crystal shaper at a distance L from the moderator and rotating with constant angular velocity.

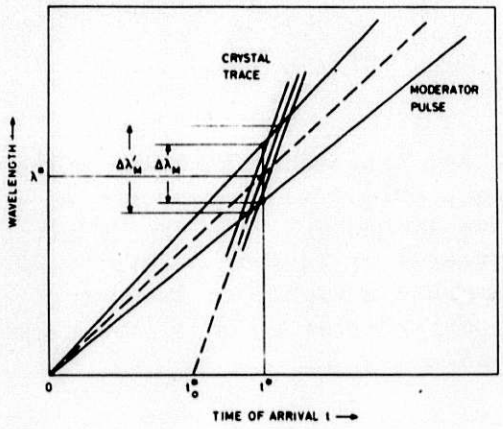

Fig. 5

The principle of operation of the rotating crystal pulse shaper. The crystal is phased such that at a time t* after the poly-chromatic pulse has left the moderator its trace in λ-t space is tangential to the neutron pulse at the desired wavelength. λ*. The maximum wavelength reflected by the crystal at a Bragg angle of 90° is twice the lattice spacing 2d.

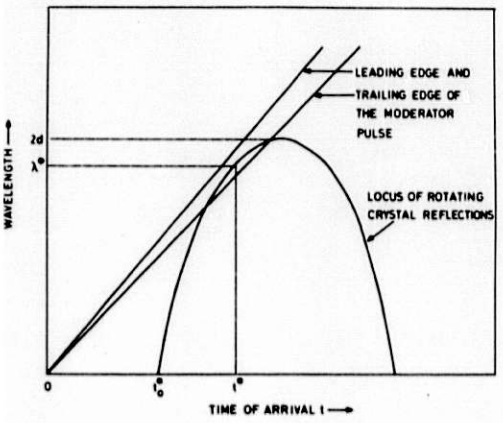

Fig. 6. The general case of the interaction of the rotating crystal pulse shaper with the moderator pulse in which the traces in λ-t space intersect.

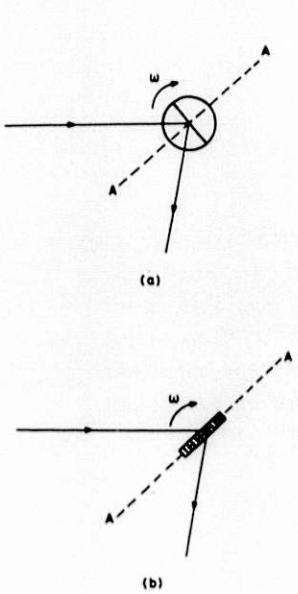

Fig. 7. (a) A cylindrical crystal rotating in a neutron beam. Plane AA, parallel to the scattering vector and passing through the axis of rotation, is unaffected by the Doppler effect. (b) A plate crystal in Laue transmission geometry renders the Doppler effect negligible.

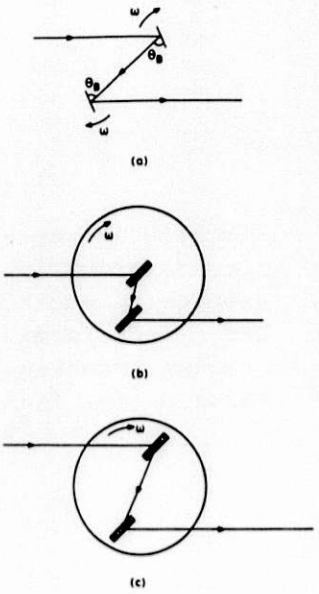

Fig. 8. (a) The use of two rotating crystals to deflect the time-shortened pulse into the drift path of the spectrometer. (b) A method of achieving this by the use of an assembly with a crystal mounted on the axis of a rotating table and a second crystal mounted eccentrically. (c) As in (b) but with both crystals mounted eccentrically and symmetric with respect to the table axis.

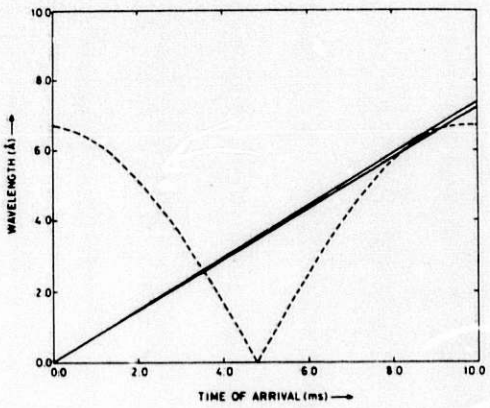

Fig. 9

A graphical solution using a graphite crystal at 5.46 m from the moderator, rotating at 50 Hz and reflecting a wavelength of 6.28Å.

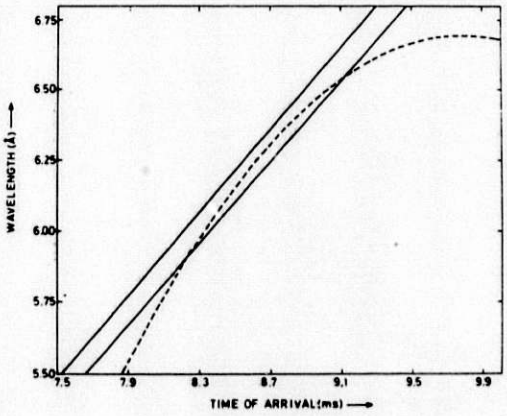

Fig. 10. (a) As for figure 9 but with the wavelength region around 6.28Å.

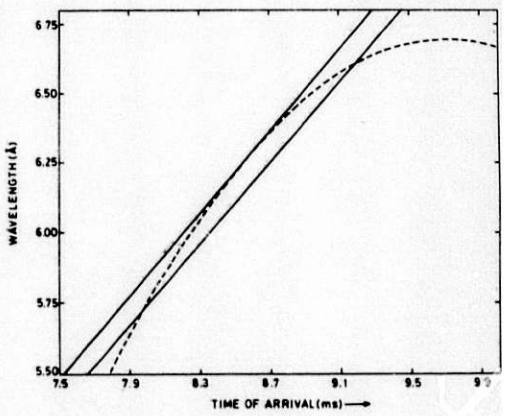

(b) As for (a) but with the crystal phased to be tangential to the leading edge of the pulse substantially increasing the wavelength band reflected.

Fig. 11

The energy window reflected by a rotating graphite crystal as a function of crystal frequency and distance from the moderator. Separate curves are shown for phasing to the peak maximum and to the leading edge. For comparison purposes the energy band passed by a chopper at the same distances from the moderator as the crystal is shown.

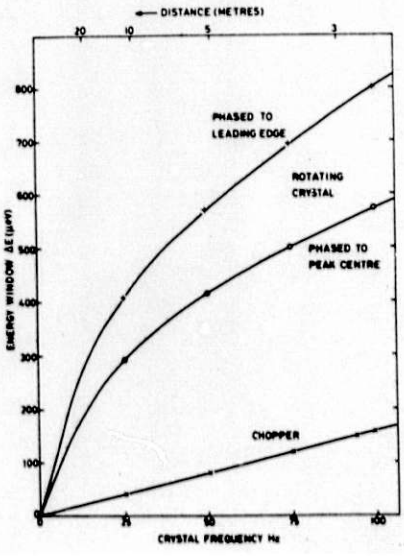

ICANS-VI

INTERNATIONAL COLLABORATION ON ADVANCED NEUTRON SOURCE

June 27 - July 2, 1982

A LINEAR POSITION SENSITIVE NEUTRON DETECTOR USING FIBRE OPTIC ENCODED SCINTILLATORS

P L Davidson and H Wroe
Neutron Division, Rutherford Appleton Laboratory

ABSTRACT

A linear position sensitive slow neutron detector with 3 mm resolution is described. It uses the fibre optic coding principle in which the resolution elements are separate pieces of lithium loaded glass scintillator each coupled by means of flexible polymer optical fibres to a unique combination of 3 photo multipliers (PM's) out of a bank of 12. A decoder circuit responds to a triple coincidence between PM outputs and generates a 12 bit word which identifies the scintillator element which stopped the incident neutron. Some details of the construction and decoding electronics are given together with test results obtained using a laboratory isotope neutron source and a monochomated, collimated neutron beam from a reactor. The count rate in the absence of neutron sources is 2-3 c min^{-1} per element; the element to element variation in response to a uniform flux is a few percent for 95% of the elements; the resolution as measured by a 1 mm wide prode neutron beam is 3 mm; the relative long term stability is about 0.1% over 3 days and the detection efficiency measured by comparison with an end windowed, high pressure gas counter is about 65% at a neutron wavelength of 0.9A^{o}.

A LINEAR POSITION SENSITIVE NEUTRON DETECTOR USING FIBRE OPTIC ENCODED SCINTILLATORS

P L Davidson and H Wroe
Rutherford Appleton Laboratory
Chilton, Didcot, Oxon, UK

1. INTRODUCTION

The principle of fibre optic encoded neutron detectors has been described elsewhere[1][2]. This paper describes the properties of a linear detector module made to meet a specification for a 1600 element, high count rate detector for the proposed D20 powder diffractometer at ILL. The geometry and method of construction are briefly given together with measurements of uniformity of response, stability, intrinsic background, resolution and detection efficiency which were made using a laboratory neutron source and a collimated, monochromated neutron beam on the PANDA diffractometer at the Harwell PLUTO reactor.

2. GEOMETRY AND CONSTRUCTION

The basic geometry required for D20 is a linear array of 1600 resolution elements 3 mm wide by 150 mm high arranged as a "banana" detector on a radius of 1800 mm. A 100 element module with this geometry has been built, as shown in Fig.1, using the fibre optic encoding principle, in which each element is optically coupled to a unique combination of 3 photomultipliers (PM's) out of a bank of 12. The fibres are 1 mm diameter coated polymer type FP supplied in the UK by Optronic Fort Ltd of Cambridge. These have a numerical aperture of 0.5 (acceptance angle from air $\sim 30^{\circ}$) and a transmission of about 75% per metre at the wavelength of the light emitted by the scintillator which is lithium glass in this case (NE 905). Each resolution element is in the form of three pieces of scintillator 3 mm x 50 mm, with 3 fibres coupling to the end of each, as shown in Fig.1. Self absorption in the scintillator glass prevents the use of elements longer than about 50 mm. Each element is also a double layer giving a total thickness of 2 mm. These two layers are coded as separate elements, ie the module has really 200 elements. The reason for this is to afford a degree of γ discrimination because a Compton recoil electron from a γ absorption event is likely to

penetrate more than one element and the electronic decoder rejects simultaneous counts from 2 elements. The dead space between elements is 0.1 mm.

In this arrangement a neutron event is identified by a triple coincidence in a bank of 12 PM's. These are EMI type 9843A, a low cost, 38 mm diameter end-windowed tube with a good single photoelectron pulse height distribution but moderate gain, and a typical operating voltage of 900 v. The PM's are optically coupled to the bundles of fibres at an angle of 25° to minimise the possibility of light being reflected from the PM back up the fibres, an effect which is believed to cause an undesirable form of cross-talk between elements. The number of elements coupled to each PM and to each combination of 3 PM's are 55 and 136 respectively.

The whole assembly is contained in an aluminium alloy light-tight box with the dimensions shown in Fig.1 which illustrates the compact nature of the design, allowing shielding to be placed close to the scintillator.

3. ELECTRONICS

The principle of the decoder is illustrated in Fig.2[3]. The number of the elements, A, can have a value between 1 and 200. X, Y and Z are the numbers of the particular PM's in the triple coincidence which codes for A. With the code used, for every pair of values of X and Y there is a number D such that D = A-Z as shown in Fig.2 for the first few values of A. This property is used in the circuit shown schematically in Fig.3. Each PM output is passed to a Le Croy MVL100 amplifier/discriminator chip where pulse height discrimination takes place at a level of about 1 mV. Logic pulses from these chips are passed to a circuit which produces an output, the validity signal, if 3 or more inputs are present within a time window of 200 ns. This output starts the sequence controller. For a "good" event 3 and only 3 input lines will have signals. These are presented simultaneously, by a special circuit, to a 16 bit pattern register. The sequence is stopped if the number of bits latched is more than 3. Next a priority encoder reads, in turn, the positions of the 3 set bits (X, Y and Z) and encodes them as 4 bit numbers in 3 registers, as shown. X and Y address a Read Only Memory which contains the values of D. This process is performed in parallel with

the transfer of the third bit into the Z register. Finally, D is added to Z to produce a 12 bit position descriptor. The decoder is capable of handling 16 PM's (ie 560 elements) but only 12 are used for the D20 module. The time to decode is at present 400 ns but this time is being reduced to $\sim$ 100 ns using faster circuits.

4. PERFORMANCE MEASUREMENTS

4.1 Uniformity of Response

The detector was exposed to a 5 curie Pu/Be laboratory neutron source with a polyethylene moderator. The neutron flux at the detector position is roughly 5 n cm^{-2} s^{-1}. Fig.4 shows the result of a 6 h count. The general shape of the plot is due to the distribution of flux from the source which is not quite uniform. This is shown by the fact that if the detector is moved the same shape appears on a different set of elements. The element to element variation is a few per cent with one or two exceptions. The low count on the first element is because this one has only 5 pieces of scintillator rather than 6.

4.2 Intrinsic Background

The detector was placed about 10 m from the laboratory source and completely shielded by 30 cm of B_4C loaded plastic blocks. On an overnight run the average count recorded was 0.5 c min^{-1} cm^{-2}. The count per element varied between 2 and 3 c min^{-1}. This compares to about 10 c h^{-1} per element for an equivalent high pressure gas counter.

4.3 Stability

The relative long term stability from element to element was measured using the laboratory source over a period of 3 days 6 h. A million counts were accumulated in one particular element and the counts in all other elements recorded at that time. The average counts in 10 elements near the centre of the detector was found and used to

normalise all subsequent counts which were taken every 2½ hours. This procedure does not reveal identical systematic changes in all the elements. The results are shown in Fig.5 and are about what would be expected from statistical variations. Subsequent absolute measurements (simply recording the counts in a given time) show small systematic changes in all elements which may be temperature effects. The room in which these measurements are made has large temperature variations. It may be that a simple temperature stabilising system is needed for the very best stability to be achieved.

4.4 Resolution

Measurements of the spatial resolution were carried out on the PANDA powder diffractometer at the Harwell PLUTO reactor using the normal specimen arm to move the D20 module behind a fixed vertical slit which defined the test neutron beam. The "slit" was made up from boron loaded resin shielding blocks, 30 cm high separated by thin spacers. To obtain a reasonable beam intensity, the full height of the PANDA beam was used, viz about 40 mm, though the vertical intensity distribution was highly non-uniform being sharply peaked. For scanning this slit beam across the elements the detector module was mounted in the normal orientation and to scan along the 150 mm dimension it was turned through 90^{o}.

Fig.6 shows the results of a scan across a few elements in the centre of the detector. The full width at half height is 3 mm as expected. The level of the wings on either side of the response curves for each element was reduced in later mesurements by reducing the intensity in the beam with an extra lead collimator. (These measurements were all done in the direct beam from the PANDA monochromator where the radiation level measured by a β-γ monitor was 2r h^{-1}).

Fig.7 shows the results of a scan along the 150 mm dimension of an element. The small gaps between the three sections can be seen. The detection efficiency falls slightly near the end of the scintillator remote from the fibres due to attentuation of the light intensity in

the scintillator itself. It also falls at the fibre end because for a small fraction of the neutron absorption events which occur very close to one fibre light cannot enter the other two fibres directly since the line of sight is outside the acceptance angle. These events may not be counted. The latter effect could be eliminated by interposing a short length of non-scintillating "stand-off" light guide between the fibres and the scintillator, at the cost of increased complexity during assembly.

4.5 Detection Efficiency

The detection efficiency was measured by comparing the response of the detector to a 10 mm diameter beam with that of an end-windowed ^3He detector to the same beam. The ^3He detector was an LMT type 43NH10/-5AX, 10 cm long with a 4 mm thick alumina window. Summing the counts on these elements exposed to the beam, the total was 67% of the count on the ^3He detector with neutrons of wavelength 0.9 Å. The stopping power of 10 cm of ^3He at 5 atmospheres is 97%. Losses in the ceramic window are approximately the same as those in the aluminium window of the PSD plus the losses due to dead space between the elements. An estimate of the absolute efficiency of the scintillator itself is thus 67 x .97 = 65%. The theoretical stopping power of 2 mm of NE905 scintillator for neutrons of wavelength 0.9 Å is 78%, so there may be some electronic losses. The efficiency scaled to a neutron wavelength of 1 Å is 69%.

5. CONCLUSIONS

The edge coupled fibre optic coded PSD using lithium glass sintillator has been demonstrated. It has good detection efficiency, stability and resolution. The module has proved reliable and has been moved many times to different neutron sources with no problems. The maximum countrate capability has not yet been measured due to lack of an intense neutron beam but is expected to meet the specificaion for the proposed D20 instrument at ILL, viz: maximum countrte for one element - 10^5 c s^{-1} with 10% dead time losses and 5 x 10^6 c s^{-1} for the whole 1600 element detector.

The countrate in the absence of neutrons is 2-3 c min^{-1} per element, considerably higher than the equivalent gas counter but adequately low for high countrate applications or for use on pulsed sources such as the SNS.

The constructional techniques are straightforward though tedious, the time consuming element being the fixing of the scintillator tiles not making the fibre optic encoder. The compact design allows large area detectors to be made by stacking modules without the containment problems associated with high pressure gas detectors.

ACKNOWLEDGEMENTS

The authors would like to thank Mr C Moreton-Smith, Mr E M Mott and Mr J C Sutherland for their work on various aspects of the fibre optic coded detector development.

REFERENCES

1. Rutherford Laboratory Annual Report 1977, p.53.

2. Position Sensitive Slow Neutron Detectors Using Fibre Optic Encoding, P L Davidson and H Wroe, Proc ICANS IV, Oct 1980. (KENS Report II, March 1981, pp.642-649).

3. SNS Time-of-Flight Electronics, P Wilde and R G Milborrow, Internal RAL Memorandum, June 1978.

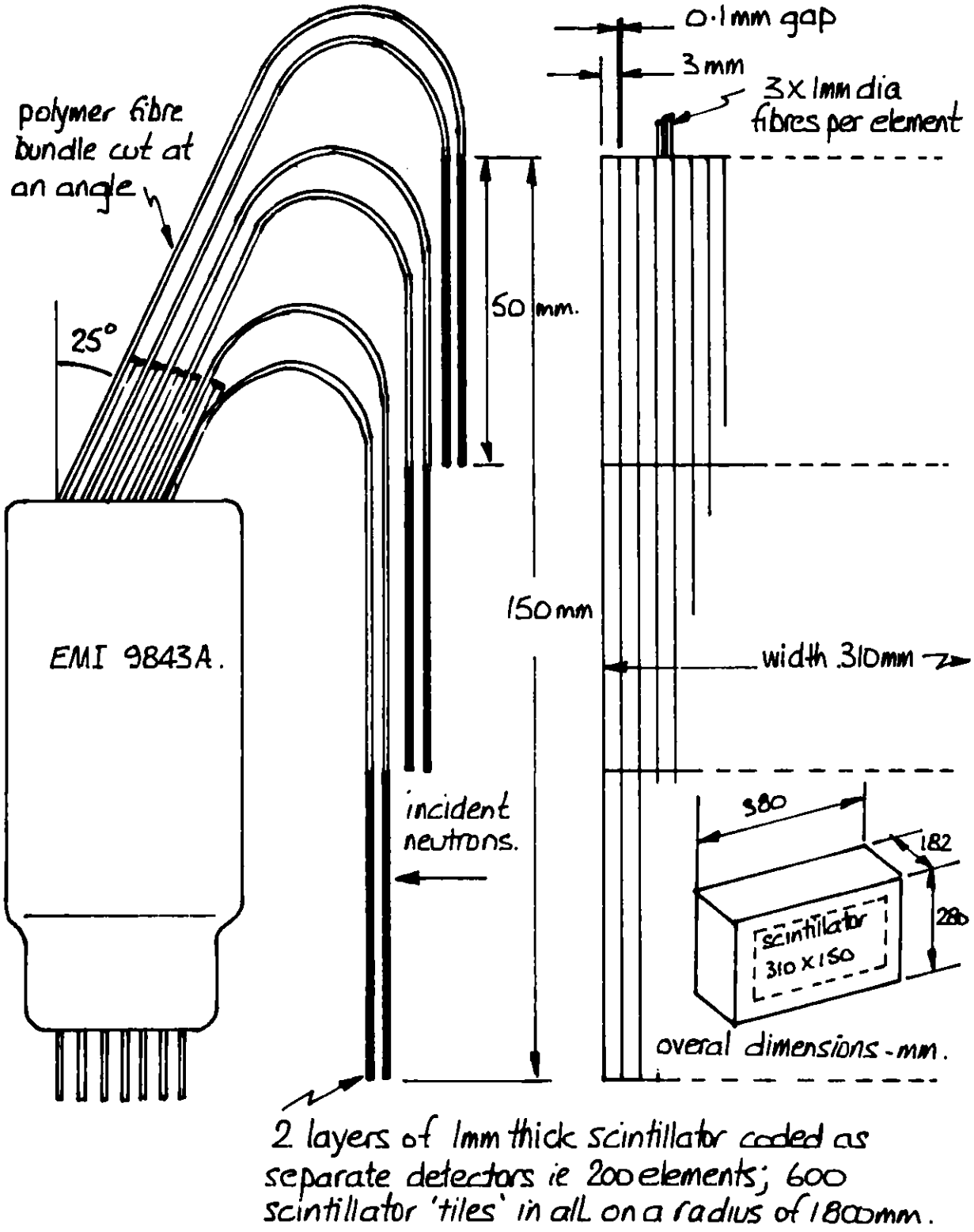

Fig. 1. Schematic arrangement of detector showing main dimensions.

Element No. A	Photomultiplier No. 1	2	3	4	5	6	7	8	9	10	11	12	13	14	15	16	X	Y	Z	D= A-Z
1	x	x	x														1	2	3	-2
2	x	x		x													1	2	4	-2
3	x	x			x												1	2	5	-2
4	x	x				x											1	2	6	-2
5	x	x					x										1	2	7	-2
6	x	x						x									1	2	8	-2
7	x	x							x								1	2	9	-2
8	x	x								x							1	2	10	-2
15		x	x	x													2	3	4	+11
16		x	x		x												2	3	5	+11
17		x	x			x											2	3	6	+11
18		x	x				x										2	3	7	+11

Fig. 2

Illustrating the code and parameters used in decoding

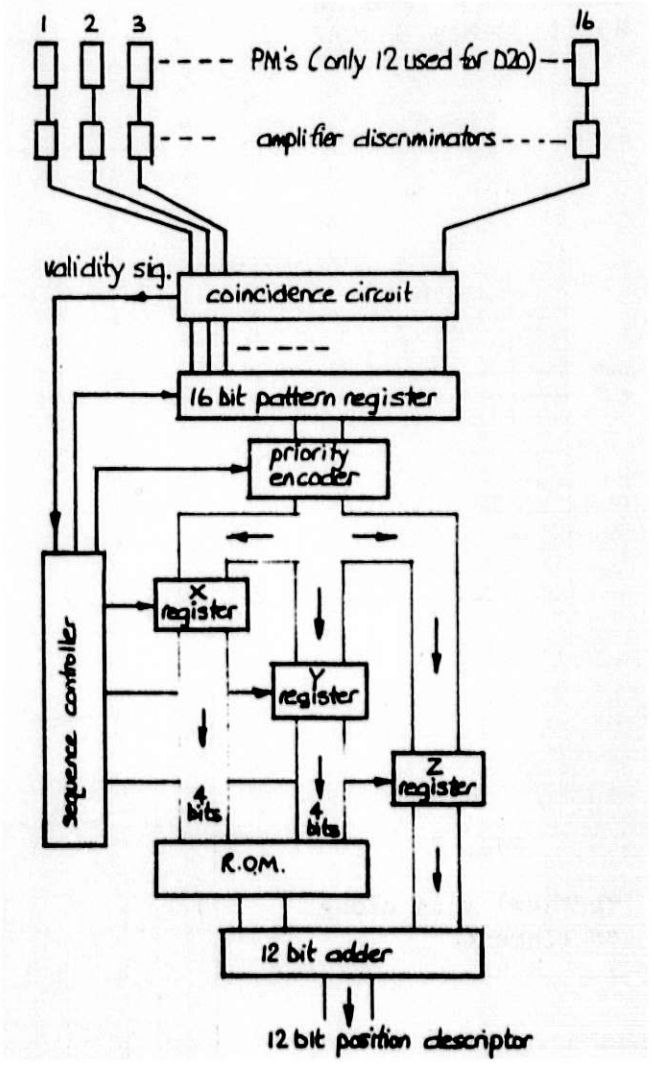

Fig. 3

Schematic of decoder

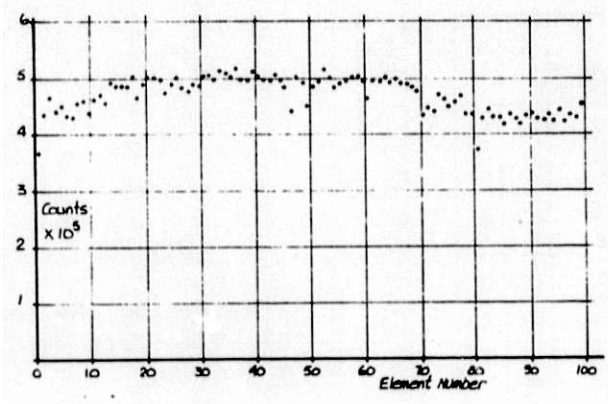

Fig. 4

Response to Laboratory Neutron Source.

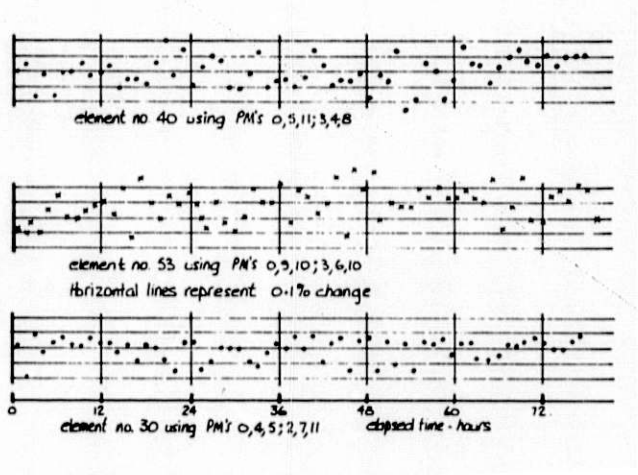

Fig. 5

Relative stability on laboratory source; April 30-May 3 1982.

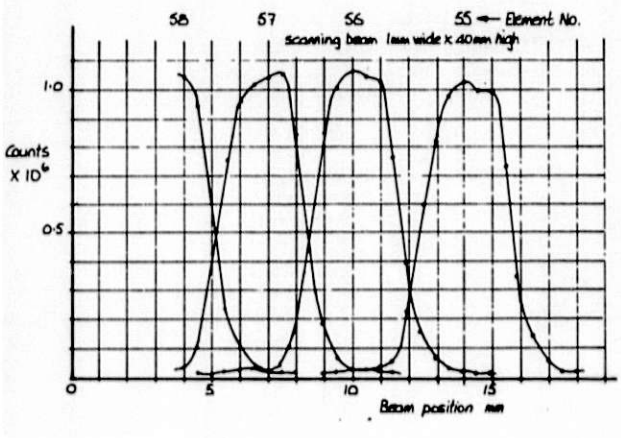

Fig. 6

Horizontal scan across centre of elements.

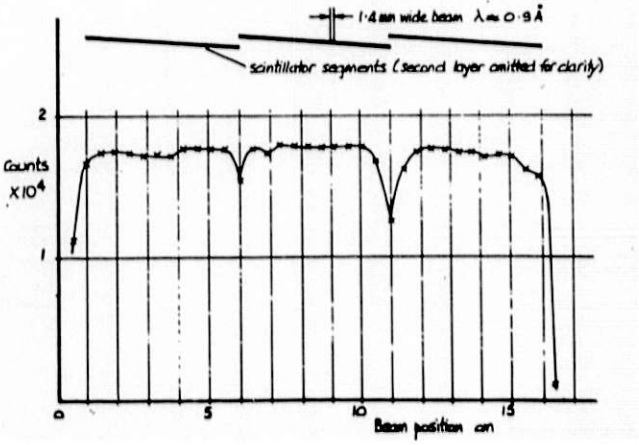

Fig. 7

Vertical scan along an element.

ICANS-VI

INTERNATIONAL COLLABORATION ON ADVANCED NEUTRON SOURCES

June 27 - July 2, 1982

THE IPNS DATA ACQUISITION SYSTEM

T. G. Worlton, R. K. Crawford,

J.R. Haumann, and R. Daly

Argonne National Laboratory

ABSTRACT

The IPNS Data Acquisition System (DAS) was designed to be reliable, flexible, and easy to use. It provides unique methods of acquiring Time-of-Flight neutron scattering data and allows collection, storage, display, and analysis of very large data arrays with a minimum of user input. Data can be collected from normal detectors, linear position-sensitive detectors, and/or area detectors. The data can be corrected for time-delays and can be time-focussed before being binned. Corrections to be made to the data and selection of inputs to be summed are entirely software controlled, as are the time ranges and resolutions for each detector element. Each system can be configured to collect data into millions of channels. Maximum continuous data rates are greater than 2000 counts/sec with full corrections, or 16000 counts/sec for the simpler binning scheme used with area detectors. Live displays of the data may be made as a function of time, wavevector, wavelength, lattice spacing, or energy. In most cases the complete data analysis can be done on the DAS host computer. The IPNS DAS became operational for four neutron scattering instruments in 1981 and has since been expanded to seven instruments.

1.0 INTRODUCTION

Scientific requirements for the Data Acquisition System for IPNS neutron scattering instruments were extensively analyzed in 1978-79 before the DAS was designed. The first section below summarizes our assessment of the requirements at that time. This is followed by a section outlining the DAS design selected and detailing specific hardware and software implementations. The third section summarizes our experience with the DAS since Summer, 1981 when it became operational. In this latter section we discuss current performance levels and the extent to which the initial requirements have been met, and comment on the extent to which our initial assessment of requirements is still valid.

2.0 DESIGN REQUIREMENTS

2.1 Data Acquisition Requirements

Although physically the time-of-flight instruments vary considerably, they all involve qualitatively similar data acquisition and control requirements. Each of the instruments appears to the data acquisition system as a collection of detectors or detector elements, from which data are received concurrently. Each event detected must be identified with a space and time descriptor. The spatial descriptor corresponds to the physical location of the detector, or detector element in the case of position sensitive detectors, in the instrument. The time descriptor corresponds to the time of arrival of the event at the detector with respect to the time of arrival of the protons at the heavy metal target. The energy range and flight length needed for some instruments mandate a time descriptor with a magnitude up to 0.1 seconds, while the precision desired for calculational purposes for some instruments requires the time descriptor to resolve 1/8 microsecond time increments. Table I lists the expected data rates, histogram sizes, etc., estimated in 1978 for the various instruments then being planned for initial construction. Since not all of the instruments were then defined, the hardware and software for the DAS had to be designed with sufficient flexibility so that future expansion to include additional instruments would not require a major redesign effort. Future expansion of the number of detector elements or of the data rates in existing instruments should also be easily incorporated into the DAS. Also since only limited manpower was available to implement the DAS within the allotted time and to maintain it when it became operational, the system had to be designed with the intent of purchasing as much of the equipment as possible from commercial vendors.

2.1.1 Grouping And/or "Electronic-Time-Focussing" - The numbers derived for n, the histogram size, in Table I represent an immense amount of data for the user to handle for a single experiment. In many cases this degree of spatial resolution is not required and the user would prefer to have a considerably condensed data set with which to work. In particular, in many cases the outputs from a number of detectors could be combined after suitable manipulation, so that a single set of time channels would represent that entire group of detectors. Thus it was required that the DAS be capable of providing such suitable manipulations "on-the-fly" on the raw data to allow such "grouping" of detectors. This concept has sometimes been referred to as "electronic time-focussing". Since the grouping desired differs from instrument to instrument (see below), and may differ from experiment to experiment on a given instrument, the selected grouping scheme must be very flexible. Changing of the grouping must also be a relatively simple task. Any such grouping should not cause a degradation of the resolution as far as the variable of interest is concerned.

In the case of the powder diffractometers the desired grouping would combine detectors in such a way that events corresponding to the same d-spacing between crystalline planes in the sample would be binned in the same channel. This diffraction by the sample is governed by Bragg's law W = 2d sin THETA, where W is the neutron wavelength and THETA is one half the scattering angle, and for the time-of-flight case this reduces to

$$d = (h/2m)\,(1/L \sin THETA)\,(t - t0)$$

Here L is the total source-sample-detector path length, t is the time of detection of the neutron, and t0 is the average time of emission of the neutron from the source. This grouping to combine events with the same values of d is best done before histogramming the data, as this calculation should be carried out with a high degree of precision in t if the overall resolution of the instrument is not to be degraded by the grouping process.

In the case of the chopper spectrometers, the desired grouping would combine events corresponding to the same scattered neutron energy Es. This is given by

$$Es = m\,Ls^{**}2/2(t - t1)^{**}2$$

where Ls is the sample-detector distance, t is the time of detection of the neutron, and t1 is the time the neutron was at the sample. (t1 is determined by the chopper open time and is the same for all detectors.) For some IPNS instruments, detectors are located at several values of Ls, so events with the same (t - t1)/Ls must be combined.

2.2 Other Requirements

IPNS is a "user-oriented" facility with major emphasis placed on satisfying the needs of an outside user community, many of whom are only occasionally involved in neutron scattering. Thus the DAS must be designed to interface with such "non-expert" users, and to minimize the amount of user input required to carry out routine operations. In order to support the fairly rigid scheduling inherent in a "user-oriented" facility, the DAS must be highly reliable, and must be reasonably immune to user errors. In particular, a user error or other failure on one instrument should not affect the operation of another instrument.

Display of live data is essential for each instrument if the users are to interact effectively with their experiments. Effective displays of both area-detector and non-area-detector data are also important if "non-expert" users are to be able to interpret the unfamiliar time-of-flight data. Hard-copy plotting capabilities should be readily accessible to each instrument.

It should be possible for the outside user to complete at least a preliminary data reduction, and preferrably a final data reduction, while at the IPNS facility. This is particularly important because the immense quantities of raw histogram data and the form in which the data appear in the histogram often make it difficult to ascertain the quality of the data or the appropriate course for further measurements until after the data reduction has been completed. An estimate of the computing power required to provide this analysis capability was made by scaling from previous experience with time-of-flight instruments. This estimate indicated that the analysis of data from a full complement of 12 instruments would require the equivalent of 2-3 hours of computing time on the IBM 370/195 system at the Argonne Central Computer Facility, per day of operation of the IPNS facility. Sufficient on-line disk storage must be available to handle all the data sets currently involved in analysis for each instrument. The histogram size and time/data-set data in Table I were used in estimating storage requirements. With the exception of the SCD, these requirements amount to a few Mbytes per instrument.

Requirements for control and monitoring which can be foreseen include monitoring and/or control of chopper-source phasing, driving of stepping motors to change sample or detector orientations, and monitoring and/or control of experimental environment parameters (eg - temperature, pressure, magnetic field, etc.).

3.0 IPNS DAS DESIGN AND IMPLEMENTATIONS

To fulfill the DAS requirements it was decided to provide each instrument with a number of processors dedicated to specific tasks. The tasks were divided into five main categories:

1. Data acquisition and histogramming
2. User interface and instrument control
3. Video display of data
4. Data analysis and bulk storage
5. Communication between the various processors

Figure 1 contains a block diagram of the distributed processor configuration used for the data acquisition system at IPNS. The separate subsystems are discussed in turn below.

3.1 Data Acquisition

3.1.1 CAMAC Hardware - CAMAC was chosen to provide a flexible, modular, standardized system in which to implement the special-purpose modules required to encode the data. The CAMAC system developed for the IPNS instruments is shown in block form in Figure 2. The time-of-flight discriminator modules used in the system have the common feature of interfacing to the CAMAC dataway through a First-In First-Out (FIFO) buffer memory. The function of these FIFO's is to acquire data at high instantaneous rates and to allow faster transfer of the data from the CAMAC system to the Multibus system by the use of Direct Memory Access (DMA) block transfers of the data.

In addition to the crate controller and time-of-flight discriminator module(s), two specialized modules are required in each system. These are the Polling module and the Clock module. This leaves 20 slots free for discriminator modules in each crate.

The Polling module scans the L lines from the discriminator modules within a given CAMAC crate to determine which modules contain data in their FIFO buffers. When a module is found which contains data the polling module passes an 8-bit byte to a parallel I/O port on the Multibus. This port in turn interrupts the Z8001 microcomputer and supplies it with the 8-bit byte, three bits identifying the crate and five bits indicating the module number within the crate. For some of the instruments it is necessary to have more than one CAMAC crate filled with discriminator modules. For this reason the polling module is designed to fill the role of either master or slave. As a slave unit the module will scan only its crate, while in the master mode it also scans the slave units in other crates.

Only one master clock module is used for each instrument computer system. This module generates an 8 MHz clock, which will result in a clock start time uncertainty of 125 ns, and will produce digitized times in 125 ns increments. Upon receipt of a t0 pulse (pulse indicating neutron production at the source) the module produces a 'SYNC' pulse which is used by the discriminator modules as a time digitizer reset pulse. The number of t0 pulses received while data acquisition is active are counted by a 24 bit counter. Upon command from the CAMAC controller, or from external hardware command, the clock module issues an 'INHIBIT' signal, synchronized to the t0 pulse. Upon receipt of the 'INHIBIT' signal all discriminator modules stop data acquisition. The clock module also has provisions for allowing data acquisition only within a programmable time window after each t0 pulse.

The CAMAC Time-of-Flight Discriminator Modules which are used for standard and linear position sensitive detectors produce output formats which are the same for both types of detectors, although the detector signal is digitized differently for each detector type. For the standard detectors, each discriminator module can handle inputs from 8 independent detectors. Each input has its own programmable lower discriminator level, and all 8 have a common, programmable upper discriminator level. When an analog pulse on one of the inputs falls within the discriminator levels, a 20-bit time word is combined with 3 bits of input identification, and the resulting 23 bits is loaded into a FIFO buffer in the module. The buffer can store sixteen 24-bit words. When this FIFO contains 8 data words, the module sets a CAMAC LAM indicating that the module requires service. The 24th bit in these words is used to indicate FIFO overflow. Data acquisition can be gated on or off at all modules by an 'INHIBIT' signal generated in the clock module.

The discriminator modules for linear-position-sensitive detectors produce a 20-bit time word, and 1 bit to indicate FIFO overflow. The 3-bit input identification now contains detector position information. This module also has a programmable window discriminator. In addition, it has position encoding circuitry which enables it to digitize the position information for one or two linear-position-sensitive detectors depending upon the resolution desired. The resolution is selectable to either 1 part in 4 or 1 part in 8. With the lower resolution, two detectors can be serviced, with the upper bit of the 3-bit position code indicating from which detector the data originated.

For area-position-sensitive detectors (initially present only on the SCD instrument) the role of the discriminator module is filled in part by an x-y position digitizer at the detector, in part by a time digitizer module, and in part by one or more 256 word x 16 bit commercial CAMAC FIFO modules (see Figure 2). The x-y position digitizer provides 8 bits of x and 8 bits of y position in digital form. The time digitizer module latches the x-y position data, produces a 16-bit time word, and multiplexes

and strobes these into the FIFO module. The FIFO module(s) also set a CAMAC LAM when they are filled to a selected level.

3.1.2 Multibus Hardware - The MULTIBUS (Trademark of Intel Corp.) was chosen as the system bus for the data acquisition computer because of the large array of support products available for this bus structure. The data acquisition Multibus system is made up of a Multibus crate containing four boards plus memory. The four boards are:

1. A Z8001-based single board computer
2. An interface to the CAMAC controller
3. An interface to the communications processor
4. An I/O board containing both serial and parallel I/O ports

The communications interface board is discussed below as part of the PDP-11 to Multibus link. The two interface boards, along with the CAMAC modules noted above, are the only custom designed hardware in the system. Memory boards with capacities of 128 Kbytes and 512 Kbytes are used, with the amount of memory contained in each system being dependent on the instrument. Each Multibus system has at least 128 Kbytes of this RAM memory, which is used for both program and data storage.

The data acquisition computer uses a 16-bit Z8001 microprocessor. This microprocessor was chosen mainly for its ability to directly access the large amounts of memory needed for building the space-time histograms which can contain several million elements. The data acquisition computer is a Multibus compatible product built by Central Data Corporation. This computer board provides 24 memory address lines to allow addressing of up to 16 Mbytes of memory, which is sufficient for all instruments currently envisioned. It also contains a 2K word PROM monitor which on power-up is written into and executed from RAM. This monitor provides on-line debug capabilities for the data acquisition programs.

3.1.3 Software And Data Flow - The data acquisition programs for the Z8001 are written and assembled using the PDP-11 user interface computer as a program development system. The histogramming programs are basically table-driven routines to allow flexibility in the formatting of the histograms. These tables are generated by routines on the PDP-11 when the user sets up the run, and are then down loaded to the Z8001 at run time.

During a data acquisition run, the Z8001 works on histogramming the data except when the CAMAC Polling module causes an interrupt. Upon receipt of this interrupt, the Z8001 programs the CAMAC controller for a DMA transfer of the data from

the FIFO in the Discriminator module requesting service to a 2K byte software-controlled circular buffer in the processor data memory. This block of data is then given a header containing the number of bytes in the block and the crate and slot number of the module from which the data was read. After this the Z8001 goes back to building histograms from this data.

Most of the instruments utilize only standard and/or linear-position-sensitive detectors. The algorithm developed for histogramming in this case emphasizes flexibility, since data-rate considerations indicate that speed is not of overriding importance. In this algorithm the fields are organized as 'time fields', each of which contains the histogram locations to hold the data from one group of detectors for one histogram. The histogram structure is controlled by four binning tables (DMAP, TTYPE, TSHIFT, TSCALE) which contain the information required by the Z8001 algorithm in order for it to properly histogram the data.

In this case the raw data stored in a block in the raw data circular buffer is organized as 24 bit words which contain 3 bits of input ID along with the time information. These 3 bits are combined with the crate and module number stored in the block header to make up the detector element identification number ID. A detector mapping table DMAP is used to determine which histograms an event with a given ID should be binned in, and for each such histogram DMAP will map ID to a memory address TSTRT for the start of the corresponding time field in histogram memory. Mapping more than one detector to the same time field results in 'grouping' of detectors.

The fundamental time coordinate is the elapsed time T in 0.125 microsecond clock cycles, which is encoded as a 20-bit number within the 24-bit raw data word. When "electronic-time-focussing" is desired, a pseudotime T* is calculated from T using the algorithm

$$T^* = (T - CD - ED) + KSC*(T - CD - ED)/2^{**}15$$

and this T* is then used in determining the mapping within this time field. The parameter CD is a constant time shift parameter, while ED is a time shift parameter which is a function of T only. The parameter KSC is found in the TSCALE table (addressed using ID) while the parameter ED is found in the TSHIFT table (addressed using a scaled T). This format for T* permits accommodation to the grouping equations simply by changing the contents of the TSCALE and TSHIFT tables.

The DMAP table also links each ID to an index ITYPE which points to a location in the TTYPE table. This table contains the descriptors which determine how each time field is organized (eg - range of pseudotime values included, parameters to determine channel widths, etc.). If ITYPE = 0 input from that detector ID will not be binned, so any given detector can be easily "turned

off" by software.

In this way a completed histogram is a two-dimensional array of the form I(p,t), where "p" is the position of the detector and "t" is the time of arrival of the event at that position. This software also has the unique capability of storing a given event more than once. This is equivalent to having parallel time-of-flight analyzers. This multiple histogramming allows the data to be collected with and without scaling or shifting corrections. It also permits collection of high-resolution data over special time regions. This histogramming software is designed so that various options in time scaling and limit checking can be eliminated to allow acquisition of data at higher average rates.

A second algorithm was developed to histogram data from area-position-sensitive detectors (initially used only for the SCD). In this case the CAMAC modules encode each event as 16 time-bits and 16 position-bits. The algorithm developed for this case emphasizes histogramming speed rather than flexibility, since data rates are high and the expected uses of the data do not require wide variations in histogram mapping. This algorithm is also table-driven, but the tables used in this case are much larger and provide a direct mapping of the 16-bit raw-time word and the 16-bit raw-position word. The histogram is organized in 'position fields' rather than time fields, as this format is better matched to the data display and analysis requirements.

The 16-bit time word is used in addressing a look-up table (192 Kbytes long) which maps to the 24-bit address PSTRT for the start of the corresponding position field. The 16-bit position word is used in addressing a word look-up table (128 Kbytes long) to find the 16-bit offset from PSTRT to the channel for this event. In the initial implementation the position and time look-up tables are independent and each event can be binned in only one histogram. Also, at least initially, position mapping is taken to be uniform over the face of the detector, although this is not a fundamental requirement.

The software is designed so that both types of detectors can be handled (using both algorithms and both types of parameter tables) concurrently by the Z8001. This permits, for example, the operation of standard beam monitor detectors concurrently with an area-position-sensitive detector.

3.2 User Interface

The user interface computer is a DEC PDP 11/34 containing 256 Kbytes of memory, two RL-02 10 Mbyte disk drives, a VT-100 raster scan video terminal, and an LA-120 hard copy terminal. This computer runs under DEC's RSX 11/M multi-tasking operating system. It also contains an a direct Unibus interface to a

second CAMAC controller which is used to control various devices associated with the instrument, such as stepping motors, sample changers, or shutters.

The instrument computer system configuration chosen, with the Z8001 microcomputer dedicated to data acquisition, provides a system capable of executing a variety of data-histogramming algorithms while leaving the PDP 11/34 minicomputer free to serve as a powerful and flexible interface to the user. All communication between the user and the data acquisition system takes place through the PDP-11 computer via the VT-100 terminal. The commands are executed under control of the RSX Monitor Console Routine (MCR) or a special command interpreter (PNS).

All data collection is organized around the concept of a run. All parameters defining a particular run, including the histogramming tables discussed above, are set up by the PDP-11 in a run file header, and the histogrammed data is later appended to this header to make a complete run file which contains the information necessary for subsequent data analysis. User commands have been implemented on the PDP-11 to set up histogramming tables tailored to a specific experiment; to schedule, start, and stop data acquisition for a run or a series of runs; and to print or display data or other run information in various formats on the graphics display terminal. Additional commands are available for diagnostic and maintenance purposes.

Set up of the run file headers has been kept as simple as possible consistent with the wide flexibility offered. As much of this information as possible is obtained automatically. If the method of data collection is the same as in a previous run, the previous run may be used as a "Default Run" which furnishes all information except the title and user name. Even if no "Default Run" is used to set up histogramming, default values of all input except the input numbers of the detectors to be binned are supplied. However the user has the option of selecting minimum and maximum times of interest and the resolution desired, as well as time-focussing parameters for each detector. If desired, the channel width may be doubled after a given number of channels to allow compression of the lower energy portion of the spectrum where there are not many peaks.

When a run is started, the histogramming algorithm is downloaded to the Multibus system and the tables from the selected run file are then downloaded to that system as well. The PDP-11 then issues a 'start' command to the Z8001 to initiate independent data acquisition. The layout of Multibus Memory after loading the data acquisition program and the histogramming tables is illustrated for instruments without area detectors in Fig. 3. An area of Multibus Memory has been set aside for the raw data table, and other areas have been reserved for FIFO overflows and for channel count overflows. When the count in a channel exceeds the maximum for a 16 bit word (65535) the acquisition program automatically stores the address of the

overflowing channel in the overflow buffer and these channel counts are corrected in the analysis phase.

In addition to the setup of histogramming tables, the PDP-11 is also used extensively for graphics displays (see Display section below), for backing up the data to disk, for user initiated data printouts, for monitoring the progress of the data acquisition process, etc.

3.3 PDP-11 To Multibus Link

The PDP-11 to Multibus link is implemented with two boards, a Unibus Micro Controller (UMC) board from Associated Computer Consultants on the PDP-11 Unibus, and a custom Multibus interface board on each Multibus. The UMC board can control seven Multibus interfaces, thus allowing each PDP-11 computer to link with up to seven independent Multibus systems.

The UMC provides a Z80 micro-computer with compatible Z80 peripheral chips together with Unibus DMA circuitry, 32 single-byte registers accessible from the Z80 and PDP-11, and a programmable PDP-11 interrupt vector. The local Z80 bus from the UMC is extended via a flat cable to interface boards in each linked Multibus. Each Multibus interface provides a bidirectional 64 word FIFO thru which data flows asynchronously between the local Z80 bus and the Multibus, DMA control logic and addressing registers for Multibus to FIFO transfers, 2 single-byte registers accessible as I/O ports from the Z80 and Multibus, and controls to reset the Multibus and generate a low priority interrupt on the Multibus.

Each new 24-bit Multibus address is generated by hardware addition of a 24-bit increment register and a 24-bit address register. This addressing scheme allows the DMA transfer of non-contiguous data and is used, for instance, to transfer time slices through space-time descriptor organized histograms. The data path for large block transfers between Multibus and UNIBUS is, MULTIBUS to FIFO to Z80-DMA to UNIBUS, and is handled entirely in hardware. The Z80 CPU is used mainly to accept I/O parameters from the PDP-11 in order to set up MULTIBUS and UNIBUS address registers and to program the Z80-DMA. The Z80 CPU also uses shared registers and interrupts as mechanisms to handle DMA initiations and completion sequences.

Besides transferring large data blocks directly between the Unibus and Multibus the communication processor system also passes short command blocks to the Z8001 from PDP-11 tasks. The command and the parameters needed to complete the command are located in the Subfunction byte and 6 Parameter words which are included in every PDP-11 RSX I/O request (i.e. - the QIO executive directive). The Z80 passes these command blocks to fixed Multibus locations and interrupts the Z8001 at a low

priority. The PDP-11 I/O completion then awaits the interpretation and implementation of this command block by the Z8001. The communication processor can handle up to 32 separate PDP-11 I/O channels. Since the PDP-11 needs only one channel per Multibus for sending a command block, all Multibus systems attached to the PDP-11 may be executing commands simultaneously.

3.4 Display

The display processor is a VS11 bit slice processor produced by the Computer Special systems group of DEC, which provides for raster graphics display with a resolution of 512 x 512 pixels with up to 16 colors or intensities.

Instructions and graphic data are placed in a "display file" in the PDP-11 memory, where they are accessed in a DMA operation by the VS11 image processor. Programming of graphic displays consists of setting up the appropriate display file which can be updated concurrently with its access by the VS11 image processor. The VS11 operation is synchronized to the PDP-11 software, where necessary, by the appropriate use of "start" and "stop" commands to the VS11. Otherwise the VS11 and PDP-11 operations are asynchronous.

The existence of the "point" and "vector" graphic modes makes it relatively simple to interface the VS11 to standard "pen-plotting" graphics software packages. We have interfaced the VS11 instruction set to such a pen-plotting software graphics package, and this package is used for display of histogram files stored on disk. However "live" data updating is programmed directly with the VS11 instruction set to achieve greater plotting speed. The "bitmap" graphic plotting mode is used for "density plot" representations of two-dimensional slices through histograms.

The display of "live" histogram data being accumulated in the Multibus memory involves the concurrent and asynchronous operation of the four front end processors. The PDP-11 determines, on the basis of user input, which portion of the histogram is to be displayed. The communication processor supervises the transferring of the histogram data to a static common region in the PDP-11 memory several times per second. Continuous-loop applications software operates on the data in this static common, performing scaling, change of units, etc., and then places this data in proper format in a display file. The display processor in the VS11 cycles through the display file and converts the data to pixel information and stores it in its image memory. This software produces rapid display updates which provide a good sense of the "live" nature of the data, as it is being histogrammed by the Z8001.

3.5 Data Analysis

A DEC VAX 11/780 is used for complex data analysis and shared I/O with all instrument systems. This data analysis computer includes 2 Mbytes of RAM memory, a Floating Point Accelerator, a 516 Mbyte disk (RP07), a 67 Mbyte disk (RM03), two 10 Mbyte (RL02) disks, a 800/1600 bpi magnetic tape drive, a Versatec printer-plotter, a 300 lpm Printronix line printer, modems, a number of VT-100 display terminals, and a VS11 graphics display processor with a color monitor.

This data analysis computer is meant to receive data from the various instrument computers via the communication interface or by transferring RL02 disk packs from the front-end computers. The data is then either stored or analyzed by routines provided by the user. After reduction the data can be plotted and/or printed by the various output devices connected to the VAX or it can be shipped back to the instrument system for display or further manipulation.

3.6 PDP 11/34-VAX Link

A serial high speed synchronous link is being developed between the PDP-11 front end computers and the VAX. Its main function will be to move large data files between the two processors. Its operation is not essential to data acquisition but will be useful in transferring data to the VAX for analysis. This transport is currently accomplished by moving the RL02 data disk from the front-end computer to the VAX. A low-speed serial link allows users to call up the VAX and log on to their front-end computer to check on the status of their experiment. The hardware for the high-speed serial link is in place and the software is now under development.

4.0 PERFORMANCE SUMMARY

The IPNS DAS became operational for four of the first five instruments in Summer, 1981. Construction of the fifth of the proposed initial instruments was completed in 1982, and it and two other instruments have been added to the DAS since it first became operational. Our experience with some of the various aspects of the system is outlined in the separate sections below.

4.1 Expansion

During 1981-82, the software on the PDP-11 computers and in the PDP-11 to Multibus interface computer (Z80) was modified to allow each PDP-11 computer to serve more than one instrument. In this implementation, each instrument still has its own independent CAMAC-Multibus Data Acquisition system, but shares the user interface, disk backup, graphics display, and link to host, with one or more additional instruments. In this manner the original five PDP-11 computer systems and VS11 graphics systems now support seven instruments, with an eighth soon to be added. The ease with which this expansion was performed indicates that the goals of flexibility and expandability have been well met. However, although this sharing of PDP-11 computers has resulted in significant cost savings, it has somewhat compromized the initial goal of complete independence of instruments. It is thus not as satisfactory a means of expansion as would be a simple expansion by including more of the independent complete instrument computer systems.

4.2 Data Rates

The initially established goals for instantaneous data rates have been achieved. The pulse-pair resolution for pulses in the same discriminator module is approximately 2 microseconds, while there is no interference whatsoever between pulses in different discriminator modules. This seems to be quite adequate for all data acquisition situations seen to date. However, for the area detectors where position encoding is done as part of the detector rather than as part of the DAS, pulse-pair resolution is of the order of 7 microseconds, and this does cause a dead-time problem.

The initially established goals for time-averaged data rates have been exceeded. The DAS can handle rates as high as 3000 events per second for non-area-detector instruments, and rates of up to 16,000 events per second for area-detector instruments. This time-averaged rate has so far proved adequate for area-detectors. However, in the case of non-area-detector instruments the users immediately found it to be "essential" to make full use of the very large time-of-flight range permitted by the system. This has caused the data rates from these instruments (particularly powder diffractometers) to be much higher than was anticipated on the basis of previous experience with similar earlier instruments (which were typically restricted to under 10,000 channels total for data). Data rates for these instruments are thus pressing against the limits imposed by the DAS. To alleviate this problem, a faster single-board-computer based on the Z8001 microprocessor is being designed. The use of multiple Z8001 processors on each Multibus is another possibility which was included in the original system architecture, and this is contemplated as a possible longer-term solution. With both these improvements a factor of ten increase in time-averaged data

rate should be achievable while still using the same flexible histogramming algorithm.

4.3 Histogram Sizes

The non-area-detector instruments currently have approximately 150 detectors each. In the initial calibration and testing of these instruments extensive use was made of the ability to concurrently collect and histogram data from each detector separately. The multiple-histogram option was also used extensively in this calibration/testing phase, and has been used to a lesser extent in more recent applications. Histograms (or multiple histograms) in excess of 200,000 channels have been collected on some of the non-area-detector instruments. (Multibus memory boards have on occasion been shifted between instruments to allow larger-than-originally-anticipated histograms. This is a simple process requiring only a few minutes.) In routine operation these instruments typically use 20,000 to 100,000 channels per run. The Single Crystal Diffractometer, which uses an area-detector, routinely collects histograms of about 800,000 channels.

4.4 Electronic Time-Focussing

This concept has worked extremely well. The flexibility inherent in the use of the table-driven focussing algorithm was most vividly demonstrated when the chopper was removed from one of the chopper spectrometers and a time-focussed powder diffraction spectrum was collected in that instrument from the same sample that was used in the inelastic scattering measurements. This required only the setup of a new run with the proper focussing parameters. In other tests on the powder diffractometers, detector banks at various angles (including angles down to about 15 degrees) have been focussed with no difficulty.

4.5 Display

The VS11 display has worked very well for our purposes. Especially important has been the speed of this display, which makes possible "live" updates of 4000 point histograms. Equally, if not more, important has been the density plotting capability which has been extremely useful for representing area-detector data.

4.6 Data Analysis

The presence and availability of the VAX host computer as part of the DAS has been extremely important, especially insofar as the experiments for outside users are concerned. Extensive data analysis software for the various instruments has veen developed for the VAX by the Instrument Scientists, and this has enabled outside users to begin data analysis immediately after they have completed data acquisition, and to leave Argonne with data that have already been at least partially analyzed. This computer is quite heavily used, although the CPU is not yet saturated. It appears that our initial estimate that this computer would be nearly saturated when a full complement of approximately 12 instruments was operational at IPNS is still valid.

Table 1

Instrument[a]	GPPD	SEPD	SCD	LRMECS	HRMECS
Detectors[b]					
SD	~160	~120	2	~150	~200
LPSD(Res)	~20(8)			~100(4)	~200(4)
APSD(Res)			1(256x256)		
n_d	~320	~120	~65000	~550	~1000
n_t[c]	8000	8000	256	500	1000
$n = n_d * n_t$	2.6M	1M	16M	0.3M	1M
$I^{tot}_{time-avg}$(cts/sec)[c]	~1500	~1000	~20000	~3000	~1000
$I^{tot}_{instantaneous}$(cts/sec)[c]	~10^5	~10^5	~10^6	~10^6	~10^5
Typical time[d] to obtain one histogram	1 day	1 day	4 hrs.	5 days	10 days

[a] GPPD = General Purpose Powder Diffractometer; SEPD = Special Environment Powder Diffractometer; SCD = Single Crystal Diffractometer; LRMECS = Low Resolution Medium Energy Chopper Spectrometer; HRMECS = High Resolution Medium Energy Chopper Spectrometer.

[b] SD = Standard ^{3}He-filled gas proportional counters; SPSD = ^{3}He filled linear position-sensitive gas proportional counters; APSD = area position-sensitive detector (^{3}He proportional counter or scintillation counter); Res = number of detector elements per detector.

[c] Worst case estimate.

[d] Estimated from experience - includes experiment setup time.

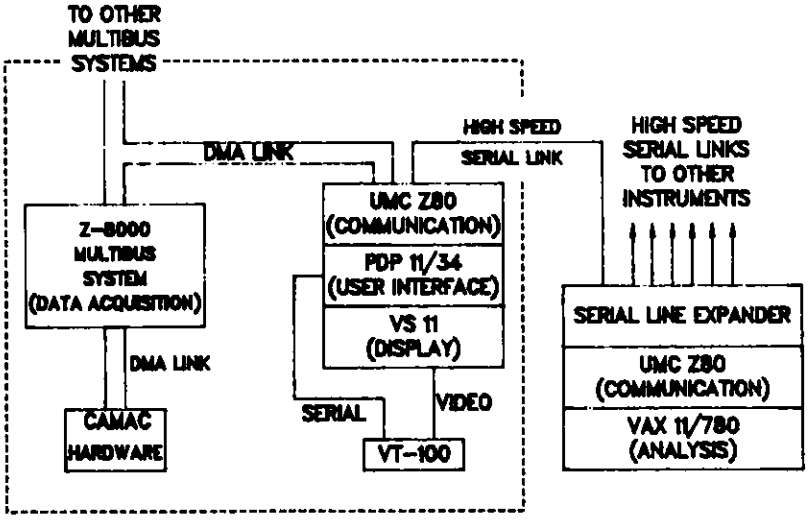

Fig. 1. A block diagram showing one instrument computer system (within dotted lines) and its link to the analysis computer.

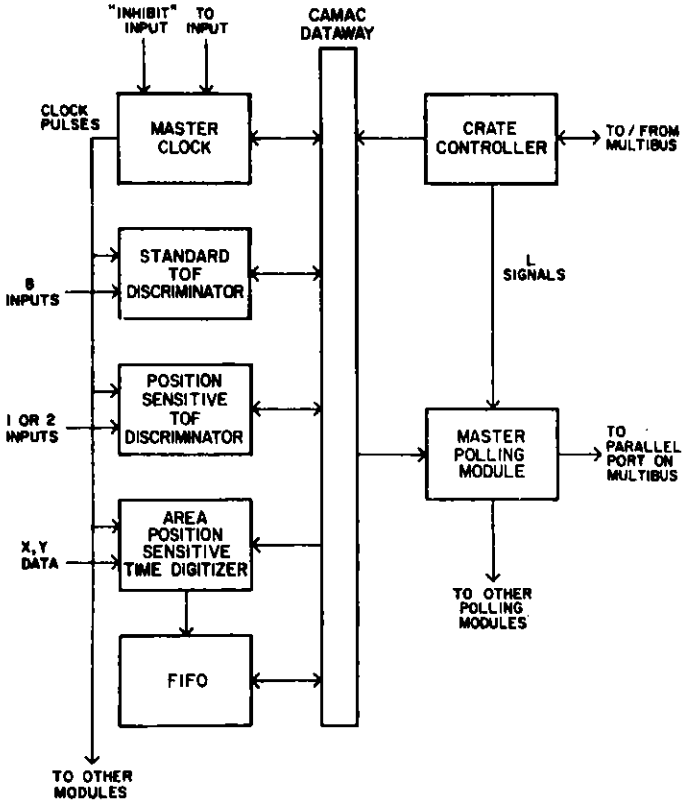

Fig. 2

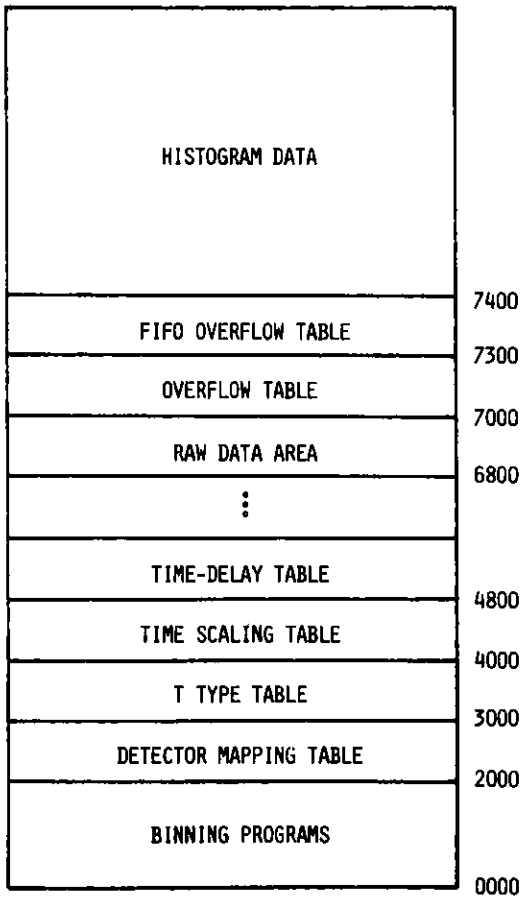

Fig. 3

Multibus memory map.

ICANS-VI

INTERNATIONAL COLLABORATION ON ADVANCED NEUTRON SOURCES

June 27 - July 2, 1982

TESTS OF A RESONANCE DETECTOR SPECTROMETER FOR ELECTRON-VOLT SPECTROSCOPY

J. M. Carpenter*
N. Watanabe
S. Ikeda
Y. Masuda
S. Sato

Japanese Laboratory for High Energy Physics (KEK),
Oho-Machi, Tsukuba-Gun, Ibaraki-Ken, 305 Japan

ABSTRACT

We have tested a resonance detector spectometer at the KENS neutron source, using ^{181}Ta, ^{121}Sb and ^{149}Sm absorbers and bismuth germanate (BGO), NaI and plastic scintillators. In the process we uncovered and solved numerous background problems, and discovered a time-focussing principle. We measured the scattering from a number of materials and so far have analyzed and present results for bismuth and graphite. Tests of cooled absorbers have indicated that resolution of 70 meV is possible with ^{181}Ta.

* Permanent address: Argonne National Laboratory, Argonne, Illinois, 60439, U.S.A.

TESTS OF A RESONANCE DETECTOR SPECTROMETER FOR ELECTRON-VOLT SPECTROSCOPY

J. M. Carpenter
N. Watanabe
S. Ikeda
Y. Masuda
S. Sato

Japanese Laboratory for High Energy Physics (KEK),
Oho-Machi, Tsukuba-Gun, Ibaraki-Ken, 305 Japan

1. INTRODUCTION

Spectroscopy using neutrons in the range 1-10 eV opens the prospect for several new kinds of measurements exploiting the short pulses and high intensity of epithermal neutrons produced by pulsed sources. Allen, Mitchell and Sinclair[1] have recently reviewed the principles and applications of these spectrometers, examples of which are in measurements of struck-particle momentum distributions, high frequency, low-wavevector excitations and molecular spectroscopy.

Heavy elements exhibit narrow nuclear resonances in the range of a few electron volts. These make possible spectrometers based on filter-difference methods or on detection of secondary capture products. We chose to develop a resonance detector spectrometer (RDS) based on detecting prompt capture gamma rays. This class of spectrometer gives the prospect of statistically cleaner results, as opposed to filter-difference spectrometers, particularly where the scattering function is small compared to its average value. Figure 1 schematically shows the resonance detector spectrometer. Scattered neutrons captured resonantly (at known energy E_f) by the absorber produce a cascade of gamma rays which register as pulses in the scintillation detector. The time-of-flight spectrum gives the incident energy dependence of the scattering probability.

(1) D. A. Allen, E. W. J. Mitchell and R. N. Sinclair, J. Phys. E: Sci. Instrum. 13 (1980) 639

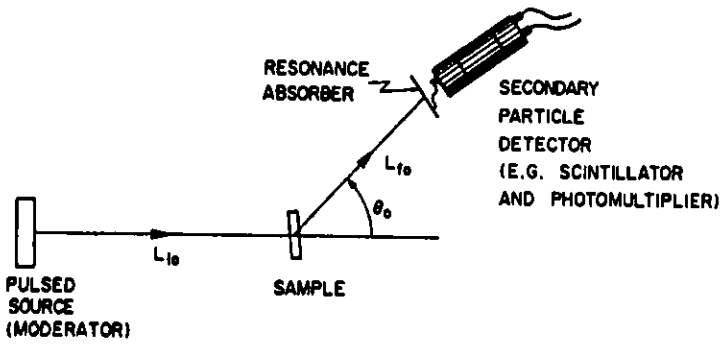

Fig. 1 Schematic diagram of a resonance detector spectrometer

The table shows some of the most-attractive resonances.

Table I Some Attractive Capture Resonances

Isotope	E_f, eV	Γ, meV
^{238}U	6.67	22.
^{181}Ta	4.28	57.
^{121}Sb	6.24	88.
^{149}Sm	.87	60.

We chose the 4.28 eV ^{181}Ta resonance for most of our tests because it has reasonably good resolution, lies in the range of energies of interest, and the material is readily available in appropriate thickness. Figure 2 shows the time-of-flight distribution of the capture gamma ray intensity from a 300 K, 12 μm foil of ^{181}Ta placed at the sample position of the spectrometer. The interval between 4.28 eV and the next-highest resonance at 10.34 eV is available for spectroscopy.

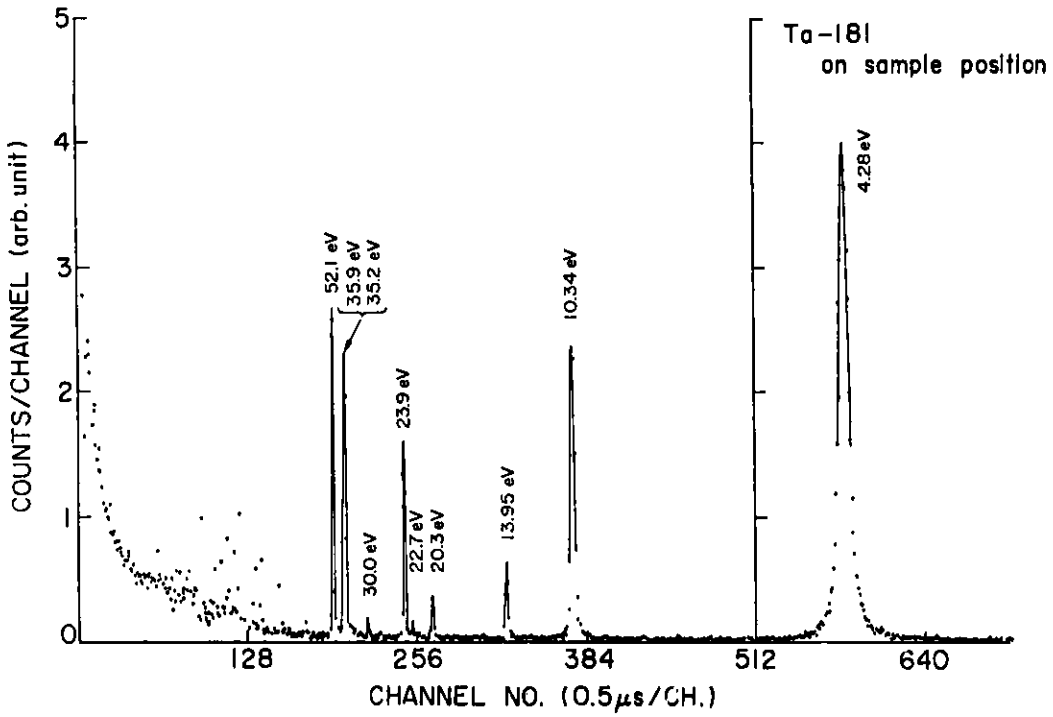

Fig. 2 Capture gamma ray intensity vs. neutron time-of-flight, for 12 μm Ta foil at the sample position (8.21 m, 0.5 μs/ch)

Figure 3 shows the 4.28 eV resonance in detail; the points are measurements, the solid line a first-principles calculation of the spectrometer response. The distance from moderator to absorber was 8.21 m for this test. The calculation includes the effect of geometry as well as self-shielding, Doppler broadening, and the intrinsic resonance width. We have performed a similar measurement and analysis of the 6.24 eV ^{121}Sb resonance and obtained similar agreement with a first principles calculation.

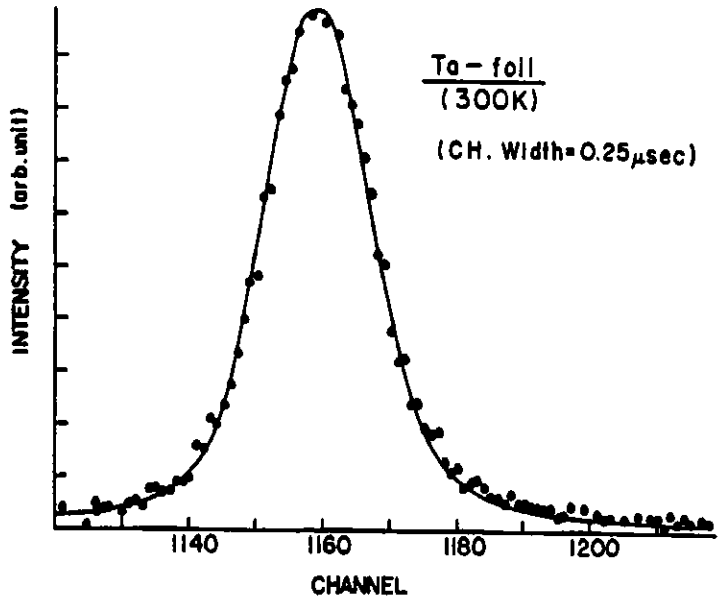

Fig. 3 The 4.28 eV ^{181}Ta resonance. Points, data of Fig. 2. Line, first-principles calculation, see text.

2. SHIELDING AND BACKGROUND

After extensive tests to identify sources of background and find corrective measures, we arrived at some general principles and some specific understandings which guided our development. Both neutron and gamma ray shielding emits capture gamma rays which can be detected by the scintillator. Both act as neutron traps, storing neutrons for several hundred microseconds. There is the possibility that some more-or-less short-lived (10-1,000 microseconds) isomers are produced in shielding and other components due to high energy neutron interactions, which decay during measuring time to produce detectable gamma rays. About 10 cm of lead is needed around the entire spectrometer to attenuate gamma rays from the surrounding concrete and steel. Beyond this, about 10 cm of hydrogenous material is needed to stop neutrons from outside. Polyethylene is inappropriate because of the 150 μs decay time of thermal neutrons in this medium; the thermal neutrons emit capture gamma rays (2.2 MeV) upon capture in hydrogen, and a 7 MeV cascade when they are captured in the adjacent lead. Boron loaded resin material works well.

B_4C shielding inside the spectrometer seems like a good idea. We tried configurations both with and without it, and at our levels of background, did not observe significant differences in the background. High energy neutrons accompany slow neutrons from the source, appearing in a difficult-to-stop halo around the beam. We finally found that very tight, massive collimation (lead, about 1 meter long, 40 cm dia.) around the indicent beam is required to deal with these neutrons. With this collimation, including B_4C and hydrogenous material, we were able to operate the detector within 10 cm of the center of the 4 cm wide beam.

We have tested various scintillators for gamma ray detection. Scintillator materials capture neutrons both resonantly and continuously; the resulting capture and decay gammas are detected with high efficiency. The traditional NaI detector is especially bad this way. We adopted bismuth germanate (BGO) ($Bi_4Ge_3O_{12}$) scintillators, which seem quite good in this application. Plastic scintillators have rather too low efficiency for the energetic gamma rays we must detect.

We measured the response of the BGO detector without a resonance absorber, and with a Pb scatterer. Most of the resonances are those of germanium. The spectrum is smooth, and the counting rate small for times longer than the arrival time of 40. eV neutrons.

Neutrons captured in the samples produce a sample-dependent capture gamma ray background in some cases. The vanadium 1/v cross section is large enough to be troublesome, giving a large constant background in the TOF spectrum. The vanadium sample contained a small amount of tantalum impurity, even though it is some of the highest-purity, zone-refined material. Since we were using the 4.28 eV resonance of tantalum as our monochromator, this interfered with measurement of the scattering. We made an antimony absorber, with which we satisfactorily measured the scattering from vanadium. The problem of 1/v capture in the important case of hydrogen is not so severe, since the ratio of scattering to capture is higher than in vanadium.

Some photomultiplier components contain materials having resonances in the neighborhood of those we want to use as monochromators. Gamma ray cascades from captures there are detected with high efficiency by the nearby scintillator, and may interfere with measurements as a structured background.

A persistent feature in the measured scattered neutron spectra was due to ^{121}Sb capture (6.24 eV). Since this moved (in time) according to detector position, we suspected it to be due to capture in some component of the detector assembly. We measured the capture gamma ray spectra of black dielectric tape, mu-metal and the photomultiplier dynode and photocathode regions, respectively used as light tight assembly material, magnetic shield and scintillation counter, irradiated in the sample position. Figure 4 shows the results.

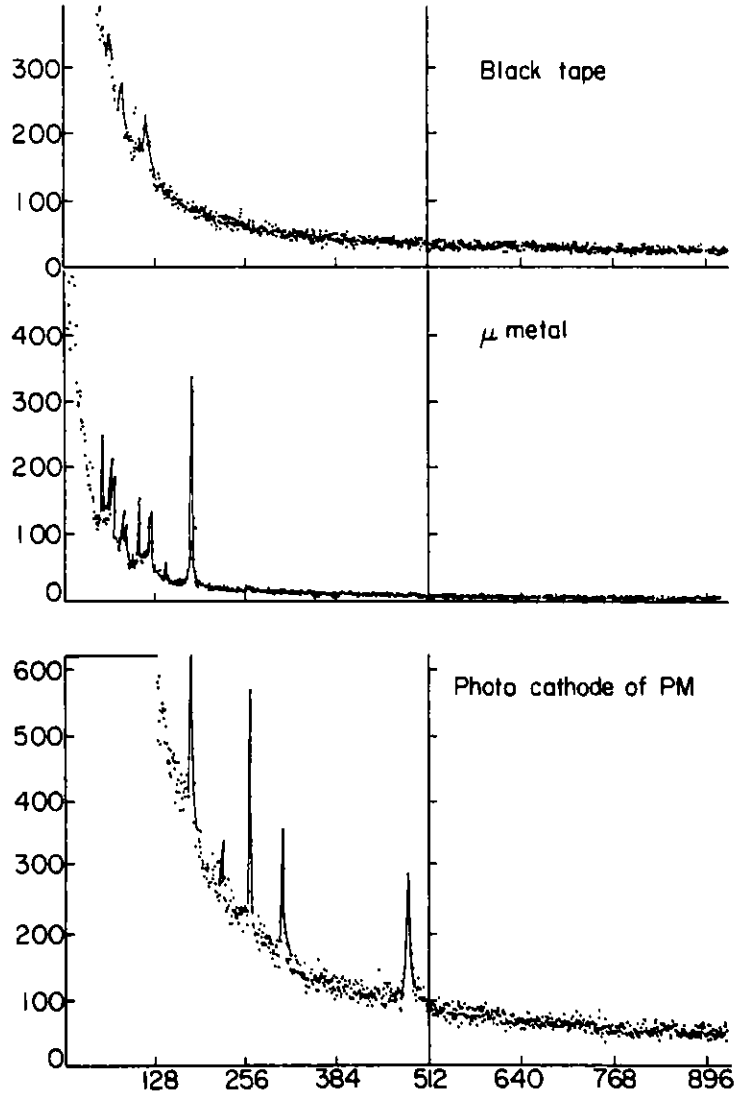

Fig. 4 Capture gamma ray intensity vs. time, for photomultiplier components irradiated at the sample position.

Even though the photocathode is so thin as to to be transparent, the troublesome 6.24 eV ^{121}Sb capture peak was evident only in the spectrum of the photocathode. Subsequently, we prepared a 1. mm thick shield of ^{10}B bound in epoxy resin; placed between the resonance absorber and the scintillator and photocathode, this reduced the spurious peak, and also reduced the background due to neutron capture in the scintillator.

Important in all this is that capture gammas appear after only about 10% of the captures in boron, moreover, their energy is low enough that we can electronically discriminate against them. Thus we have been able to freely use boron in the shielding.

3. RESOLUTION AND DEAD TIMES

The resolution accomplished so far is only modest, around 100 meV, limited by the fact that absorbers have been subject to room-temperature Doppler broadening, as well as by the lack of a uranium-238 absorber (which has the narrowest resonance we are aware of). Counting rates have enabled measurements to be completed in between a few hours and about ½ day.

We discovered a geometric focussing effect on the resolution, which comes about due to the joint effects of varying flight paths and scattering angles according to emission and interaction positions at the source, sample and detector. The recoil shift of the incident energy varies according to scattering angle, and times-of-flight vary according to incident energy and flight path length. The result is the subject of a separate paper.

We have examined a fast and a slow electronics for this application and found that the fast system worked well, having a dead time of about 100 nsec, while the slow one gave serious dead time problems in the TOF spectra.

4. SCATTERING MEASUREMENTS

We made test measurements on samples of Bi metal, V metal, graphite and H_2 gas. Figure 5 shows the results for 90° scattering from Bi, along with a

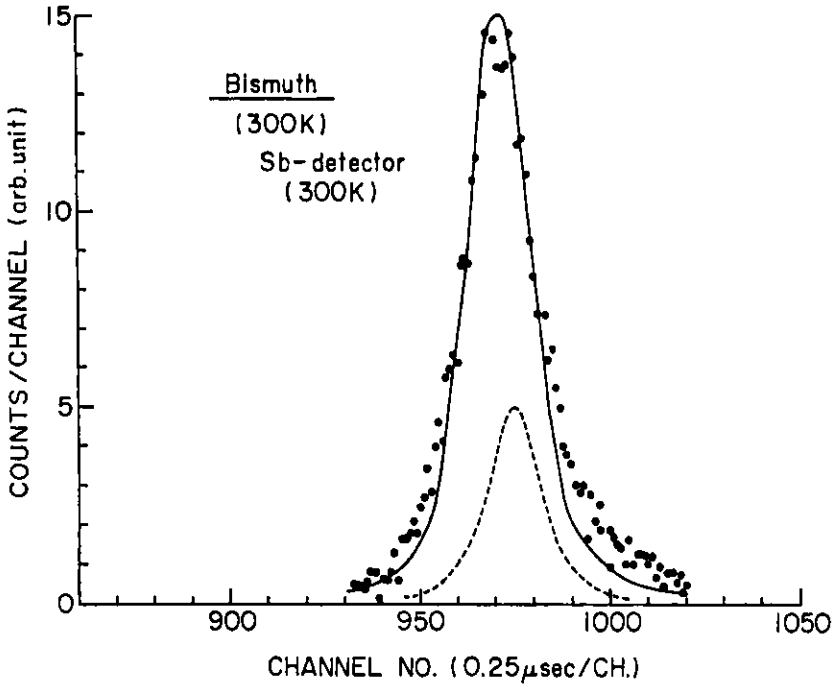

Fig. 5 The scattering from bismuth at 90°, observed at E_f = 6.24 eV with the ^{121}Sb detector. The line is a first-principles calculation, (see text). Dashed line-detector resolution.

first-principles calculation based on the Doppler-broadened scattered neutron profile calculated in Gaussian approximation, on Doppler-broadened and self-shielded resonance capture in the Sb foil, and instrument and source parameters. The agreement indicates that the instrument is well understood.

Tests with vanadium scattering at 90° reveal some potential complications in this type of measurement. Figure 6b shows the result of measurement with the Ta resonance absorber. The two peaks near channel 600 are both due to ^{181}Ta capture - the earlier peak due to capture in Ta, present as impurity in the V sample, the later, broader peak due to capture of scattered neutrons in the resonance absorber foil. By using a ^{121}Sb detector, (E=6.24 eV) we separated the scattered neutron peak from the Ta impurity peak, as shown in Figure 6a. Continuous, 1/v capture in V gives the constant high background in these measurements.

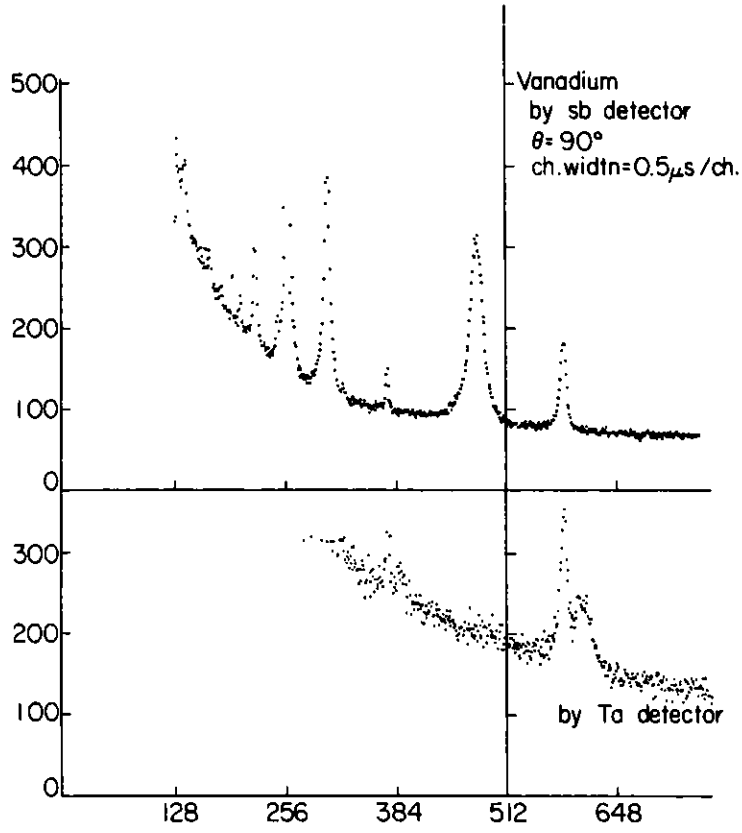

Figs. 6a&b The scattering from vanadium at 90° observed (a) at E_f = 6.24 eV with ^{121}Sb and (b) at E_f = 4.28 eV with ^{181}Ta absorbers.

We measured the scattering from graphite at 90° scattering angle. The data suffered from a substantial background, including the ^{121}Sb peak, presumably because our ^{10}B scintillator and photocathode shield had slipped out of place. The spectrum obtained by removing the Ta absorber proved to be a good measure of the background. Figure 7 shows the net scattering after subtraction of this background, with a first-principles calculation of the scattering to 4.28 eV.

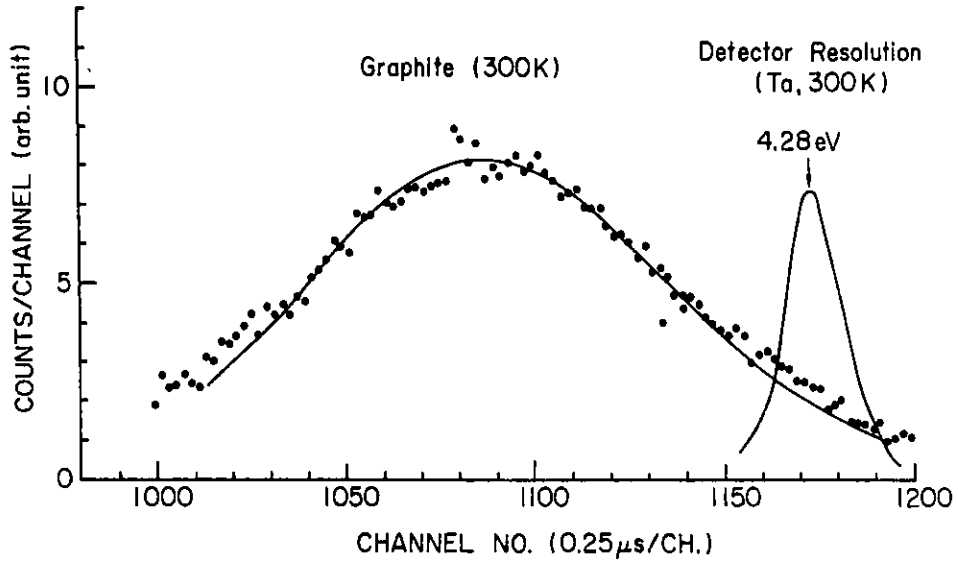

Fig. 7 The scattering from graphite at 90°, observed at E_f = 4.28 eV with ^{181}Ta absorber. The line is a first-principles calculation, modeling the graphite scattering with a gaussian scattering law with an effective temperature of 1097°K.

Satisfactory agreement could only be obtained by calculation using the mean kinetic energy of the struck carbon atoms, near 1100 K, substantially higher than that derived from any of the densities of states that we consulted. The table gives two energy moments of several densities of states which have been presented by different authors. γ_o is the coefficient of the Debye-Waller factor $e^{-\gamma_o Q^2}$. T_{eff} is the effective temperature in the Gaussian scattering model $S(Q,E) \alpha \exp[-(\varepsilon-\hbar^2Q^2/2M)^2 / (4\ \hbar^2Q^2/2M)\ k_B T_{eff})]$. Spectra of graphite cannot be successfully predicted using the handbook Debye temperature θ_D=420 K, for which T_{eff} = 325 K. Measurements at 22° scattering angle show a recoilless component, and a low component due to one-phonon scattering. The results have not yet been analyzed.

Table 2 Energy Moments of the Densities of States of Graphite

Density of states	$\gamma_o eV^{-1}$	$\bar{E} = 3/2 k_B T_{eff}, eV$ / T_{eff}, K
Young and Koppel[a)]	28.02	0.0920 / 712
Carvalho[b)]	24.70	0.0925 / 716
Page and Haywood[c)]	16.04	0.1033 / 799
Wilson[d)]	29.65	0.0977 / 756
Nicklow Wakabayashi, and Smith[e)]	33.95	0.0983 / 760

a) J. A. Young and J. U. Koppel, J. Chem. Phys. 42, 357 (1965)

b) F. Carvalho, Nucl. Sci. and Eng. 34, 224 (1968)

c) D. I. Page and B. C. Haywood, Atomic Energy Research Establishment (Harwell) Report AERE-R-5778 (1968)

d) J. V. Wilson, Oak Ridge National Laboratory Report ORNL-P-585 (1964)

e) R. Nicklow, N. Wakabayashi and H. G. Smith, Phys. Rev. B 5, 4951 (1972)

We measured the scattering from 300K H_2 gas at 22° scattering angle. Results have not yet been analyzed.

We tested ^{149}Sm and ^{181}Ta absorbers cooled to low temperature, by observing the capture gamma rays produced by the absorber in the sample position. Figure 8 shows the expected narrowing. Both absorbers suffer significant broadening due to self-shielding, and we compute that a 7μm-thick ^{181}Ta foil would provide 70 meV resolution at 50K.

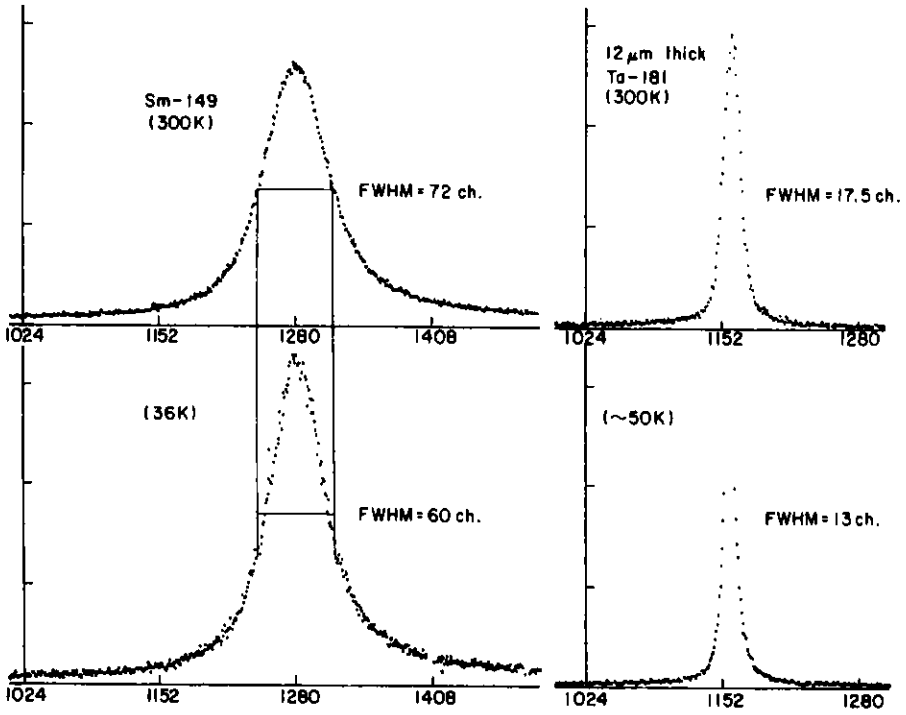

Fig. 8 Measurements with room temperature and cold ^{149}Sm and ^{181}Ta absorbers. On the left are the results for the .87 eV ^{149}Sm resonance (.5 μs/ch), on the right, those for the 4.28 eV ^{181}Ta resonance (.25 μs/ch).

5. CONCLUSIONS

We have solved many of the shielding problems related to resonance detector spectrometers, and measured spectra which are in agreement with calculated expectations. Resolution was in the neighborhood of 100 meV. By use of cooled absorbers of appropriate thickness, resolution can be reduced to about 70 meV, with ^{181}Ta. Further improvements in resolution are possible by use of ^{238}U (E=6.67 eV, Γ=22 meV). Use of a method in which spectra for thick and thin absorbers are subtracted, to eliminate the wings of the resolution function, may provide further improvement.

ICANS-VI

INTERNATIONAL COLLABORATION ON ADVANCED NEUTRON SOURCES

June 27 - July 2, 1982

CRYSTAL ANALYZER TOF SPECTROMETER (CAT) FOR HIGH ENERGY INCOHERENT NEUTRON SCATTERING

Noboru Watanabe and Susumu Ikeda

National Laboratory for High Energy Physics
Oho-machi, Tsukuba-gun, Ibaraki-ken, 305, Japan

Kenzo Kai

The Research Institute for Iron, Steel and Other Metals
Tohoku University, Sendai, 980, Japan

ABSTRACT

This paper reports the design and performances of a high resolution crystal analyzer spectrometer which has been built and operated at KENS. Energy resolution of the instrument is $\Delta\varepsilon/\varepsilon = 0.02 \sim 0.03$ in the range of energy transfer $\varepsilon = 0.05 \sim 1$ eV. With this spectrometer, local mode of hydrogens in various metallic hydrides have been measured. In case of TiH_2 or ZrH_x, higher harmonics of the optical peaks have been detected up to 5th orders with their fine structures. Higher order peaks of $TaH_{0.5}$ have also been detected. Optical mode in hydrogenated metallic glass of $NiTiH_{0.5}$ has been measured and compared with that in crystalline sample.

CRYSTAL ANALYZER TOF SPECTROMETER (CAT) FOR HIGH ENERGY INCOHERENT NEUTRON SCATTERING

Noboru Watanabe and Susumu Ikeda
National Laboratory for High Energy Physics
Oho-machi, Tsukuba-gun, Ibaraki-ken, 305, Japan

Kenzo Kai
The Research Institute for Iron, Steel and Other Metals
Tohoku University, Sendai, 980, Japan

1. INSTRUMENT

A high resolution crystal spectrometer has been built and operated at KENS. The instrument makes possible the measurement of incoherent neutron scattering with large energy transfer in the range $\varepsilon = 0.05 \sim 1$ eV, with resolution of about $\Delta\varepsilon/\varepsilon = 0.02 \sim 0.03$ in the entire range of energy transfer[1]. The instrument is an inverted geometry type; the scattered neutrons are detected at a fixed energy by a large analyzer crystal, while the incident neutron energy is determined from the measured total time of flight, t, using the following relation,

$$t = \frac{L_i}{V_i} + \frac{L_f}{V_f} , \qquad (1)$$

where L_i, L_f, V_i, and V_f are incident (i) and scattered (f) flight paths lengths and neutron velocities, respectively.

In this type of spectrometer, generally speaking, uncertainty in the second term becomes large due to the finite extent of sample, analyzer, and detector. This reflects on the first term through the relation in equation (1) and results in the poor definition of the incident energy. If we put the sample and the detector on a plane, and set the analyzer parallel to this plane as shown in Fig. 1(a), then two dimensional focussing is realized in time of flight between sample and detector. This focussing geometry make it possible to improve the energy resolution without sacrificing the geometric counting efficiency. A prototype spectrometer of this type was developed and operated at Tohoku linac[2-4]. In the new machine at KENS, signal to background ratio has been largely increased with an improved energy resolution[1]. Momentum transfer, Q,

is rapidly increased with energy transfer, ε, due to the low final energy, but the spectrometer will be useful for the measurements of the local mode of hydrogens in metalic hydrides, for the molecular spectroscopy, etc., where the value of Q is not crucial and the Q-dependence is not so important. Similar instruments were operated also at the pulsed neutron facilities of Harwell linac[5], ZING-P' at Argonne[6], and WNR, at Los Alamos[7].

Figure 1(b) shows the spectrometer configuration. The instrument has been installed at H-7 beam hole which views the surface of a moderator (polyethylene slab at room temp.) perpendicularly. Maximum beam size at sample position is 7 cm^W x 7 cm^H. In order to minimize the ambiguity of the incident flight path length, a plane sample is set perpendicularly to the beam at L_1 = 5.299 m. The analyzer crystal is a 10 cm x 10 cm pyrographite (mosaic spread 1.2°). Bragg angle of $\theta_B \sim 43°$ is used, and 002 reflection corresponds to E_f = 4 meV. Eight He-3 proportional counters, 1/2 inches in diam. and 12 inches in active length filled to 20 atoms pressure, are set in horizontal direction to form a detector plane. In the present configuration, center line distance between sample and analyzer, and that between analyzer and detector are 36 cm respecively which correspond to inter plane distance a = 24.2 cm. A beryllium filter (9.5 cm^H x 12 cm^W x 15 cm^L) cooled to liquid nitrogen temperature is used between analyzer and detector with a post cross collimator made of cadmium, in order to eliminate neutrons due to higher order reflections. Sample-analyzer-detector system is buried in a shield box of 2 cm thick B_4C and 25 cm thick borated resin wall.

2. ENERGY RESOLUTION

Extensive studies of the energy resolution were performed by a Monte Carlo computer simulation for sample-analyzer-filter detector system. Figure 2(a) shows the effect of the mosaic spread, β, in the analyzer crystal on the time distribution of the scattered neutrons. This indicates that mismatch in time focussing due to the finite value in β is not significant in this spectrometer. The most probable value

of t_f is determined to be t_f = 821 μsec from this result.

Figure 2(b) shows the calculated energy spectrum of the scattered neutrons. The width is fairly wide which is consistent with measurement, and from this distribution, mean value of E_f is determined to be $\bar{E}_f$ = 3.9 meV.

The effect of the finite size and circular cross section of the detector was also studied. Even with 1/2" diam. counter, the effect seems significant, and if necessary we can improve the resolution by placing a proper cadmium mask, with a sacrifice in counting efficiency by about 30 %. Calculated values of the total and partial resolution are shown in Fig. 3 as a function of energy transfer.

3. PERFORMANCE

In order to test the performance of the spectrometer, local vibration mode of hydrogens in various metalic hydride samples has been measured[1),8)]. In Fig. 4(a) is shown a typical raw data of TOF spectrum obtained from TiH_2 at room temperature which demonstrates the extremely low background level compared to the results obtained at other laboratories. Even at the time corresponding to $\epsilon = \infty$, background is low enough to observe a small step increase in the spectrum. Figure 4(b) shows the energy spectrum which demonstrates the higher resolution of the instrument. Higher harmonics are clearly observed up to 5th order with their fine structures.

$ZrH_{1.41}$ and $ZrH_{1.93}$ have been measured and the results are shown in Fig. 5. The locations of the peaks are listed in Table 1 with those obtained for TiH_2 and $TaH_{0.5}$. It is obvious that the frequencies for higher harmonics are shifted by appreciable amounts from the respective harmonic positions, and from these frequency shifts we can determine the anharmonicity parameters of the hydrogen potential. The striking feature of the fine structures in the higher harmonics is that the separation or the split of the subpeaks in the respective orders becomes more pronounced

at higher harmonics. In the fundamental peak of $ZrH_{1.93}$, there are two sub-peaks at about 138 meV and 145 meV with a shoulder at about 154 meV. The results is consistent with the reported values by Couch, et al.[9] There exists a distinct difference between the fine structures of $ZrH_{1.41}$ (cubic) and those of $ZrH_{1.93}$ (tetragonal), especially in the 2nd harmonics.

Table 1 Peak Positions of Localized Modes

	1st (meV)	2nd (meV)	3rd (meV)	4th (meV)	5th (meV)
$ZrH_{1.93}$ (300 K)	138 145 154	257 274 293	389 415	500 531	644 677
$ZrH_{1.41}$ (300 K)	137 141 146	260 274 297	394 433	493 531 565	644 666
TiH_2 (300 K)	139 148 154 171	263 280 304	394 405 433	523 565	678 740
$TaH_{0.5}$ (300 K)	122 130 162 167	233 236 277 318			
$TaH_{0.5}$ (30 K)	124 130 161	225 239 277			

Figure 6 shows the results of $TaH_{0.5}$. In $TaH_{0.5}$ at room temperature, the lower fundamental peak ($\sim$ 120 meV) has a shoulder at about 130 meV, and the higher fundamental ($\sim$ 160 meV) splits into two peaks. Hempelmann, et al.[10] have measured $TaH_{0.08}$ and fitted the higher fundamental peak by two Gaussians. The present results are qualitatively consistent with theirs. They have found the second harmonics of the lower fundamental at about 227 meV which may correspond to our peak at 223 meV. In the present spectrum, many extra peaks are observed above this energy. Some of them may be attributed to the multi-phonon contribution of the fundamentals. Assignement of the peaks are now in progress. The results at low temperature are also shown in the figure.

Hydrogenated metallic glass of $NiTi_2H_{0.5}$ has also been investigated[11], in which hydrogen atoms reside in the central hole of polyhedral unit structures of metallic atoms. The results are shown in Fig. 7 where the measured spectra of TiH_2, $NiTi_2H_{0.9}$ and $NiTi_2H_{0.5}$ crystals are also displayed for comparison. The striking new result is the observation of well defined higher harmonics of the local mode in glassy metallic hydride. Higher harmonics in the glassy sample are clearly observed up to 4th or 5th order at low temperature as in crystalline sample, while a rapidly damping occurs beyond 3rd harmonics at room temperature.

Table 2 Locations and Line Widths of 1st, 2nd and 3rd Harmonics

	1st level		2nd level		3rd level	
	$\hbar\omega$	FWHM	$\hbar\omega$	FWHM	$\hbar\omega$	FWHM
a-$(NiTi_2)H_{0.5}$	143±2	74±5	275±3	106±10		
c-$(NiTi_2)H_{0.5}$	150±2	36±5	286±3	67±10	410±8	90±20
c-$(NiTi_2)H_{0.9}$	144±2 155±2	47±5	286±3	90±10	412±8	140±20
TiH_2		31±1	264±3 285±3	55±5	394±8 428±8	96±10

unit: meV

The location and width of the optic peaks are summarised in Table 2. Note that the low-energy shoulder appearing at $\hbar\omega \lesssim 100$ meV in the crystalline $NiTi_2H_{0.5}$ is also found in the glassy state. This shoulder seems to be contributed from hydrogen atoms in the possible octahedral site as in crystalline state.[1] Details will be given in separate a rticles.

References

1) S. Ikeda, N. Watanabe, K. Kai and S. Yamaguchi, KENS Report III, KEK Internal (1982).

2) N. Watanabe, M. Furusaka and M. Misawa, Research Rep't. Lab. Nucl. Sci., Tohoku Univ. 12 (1979) 72 (in Japanese).

3) M. Furusaka, N. Watanabe and H. Asano, ibid. 12 (1979) 83 (in Japanese).

4) N. Watanabe and M. Furusaka, KENS Report I, KEK Internal 80-1 (1980) 181.

5) D. H. Day and R. N. Sinclair, J. Chem. Phys. 55 (1971) 2870.

6) K. Sköld, K. Crawford and H. Chen, Nucl. Instrum. Methods 145 (1977) 117.

7) J. Eckert, R. N. Silver, A. Soper, P. J. Vergamini, J. Goldstone, A. Larson, P. A. Seeger and J. Yarnell, Proc. ICANS-IV (1981) 434.

8) S. Ikeda, N. Watanabe and K. Kai, Kens Report III, KEK Internal (1982).

9) J. G. Couch, O. K. Harling and L. C. Clune, Phys. Rev. B 4 (1981) 159.

10) R. Hempelmann and D. Richter, Z. Phys. B - Condensed Matter 44 (1981) 159.

11) K. Kai, S. Ikeda, N. Watanabe and K. Suzuki, KENS Report III, KEK Internal (1982).

12) H. Buchner, M. A. Gutijar, K-D. Beccu and H. Säufferer, Z. Metalkd. 63 (1972) 497.

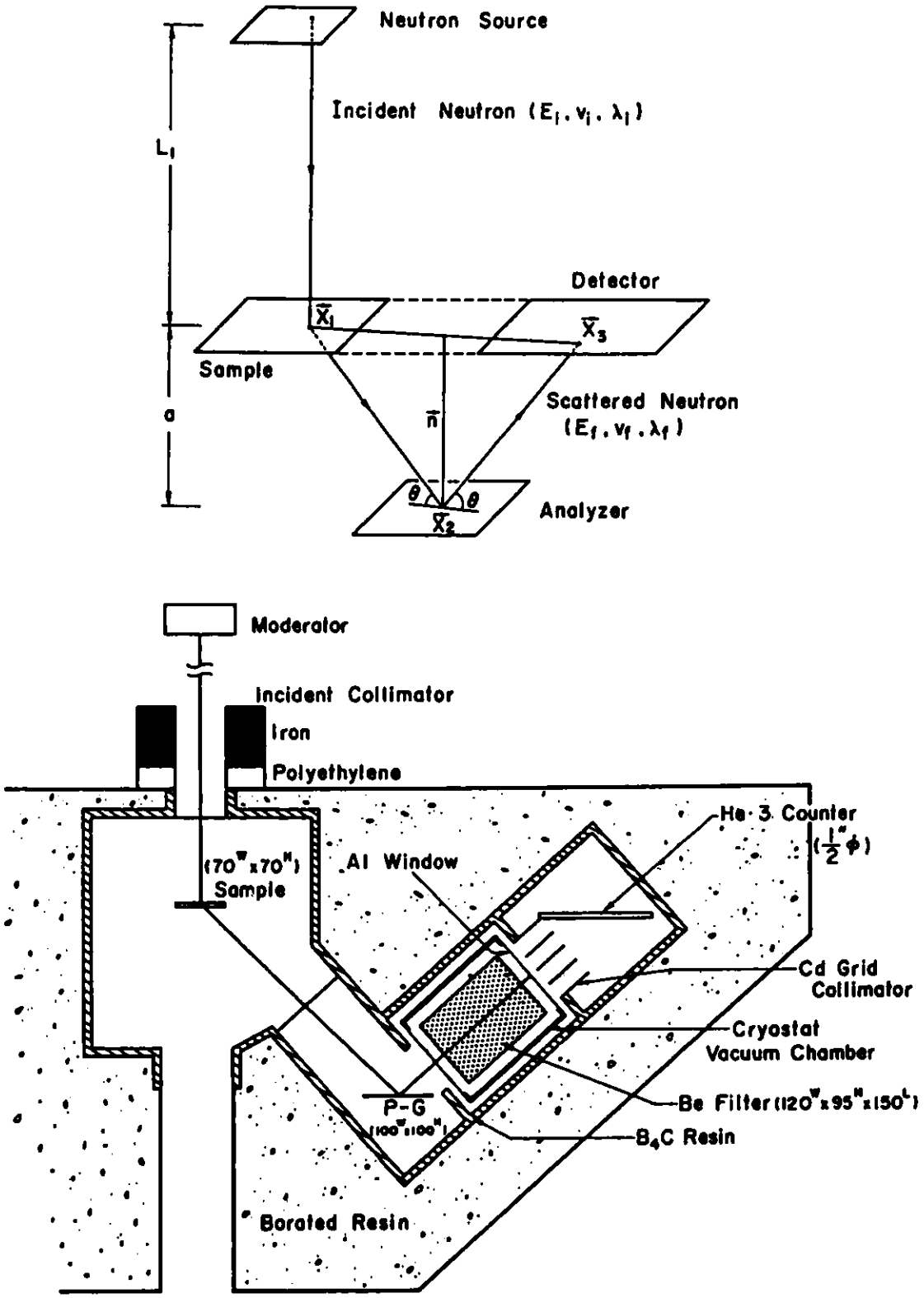

Fig. 1 Principle (a) and configuration (b) of the spectrometer

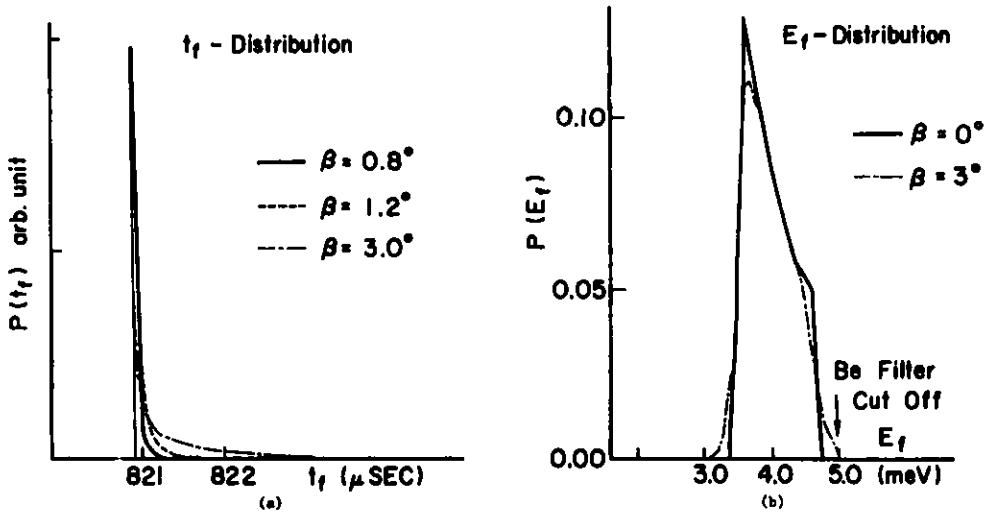

Fig. 2. Time distribution of detected neutrons due to finite mosaic spread of analyzer crystal (a) and energy distribution of detected neutrons.

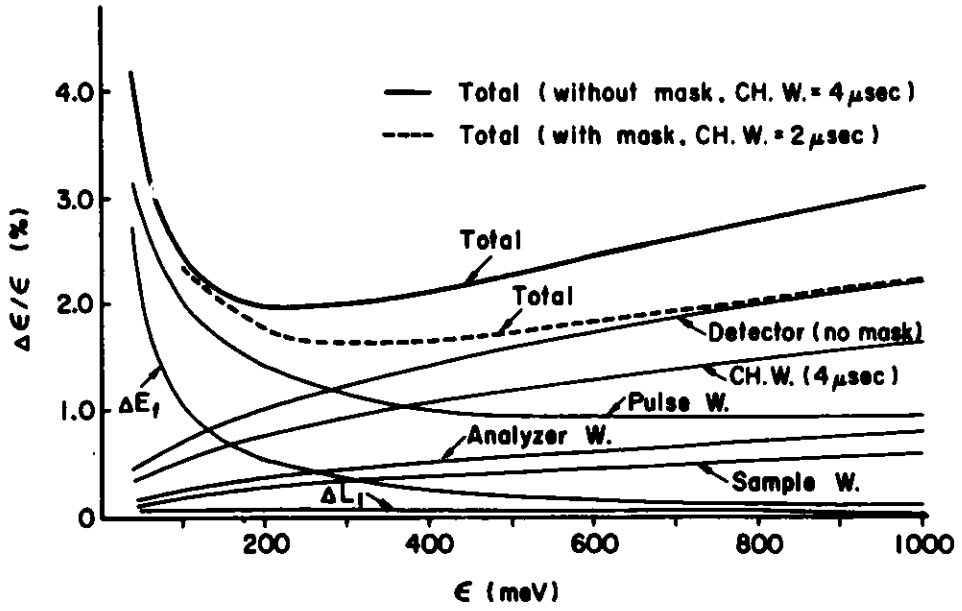

Fig. 3. Total and partial energy resolution.

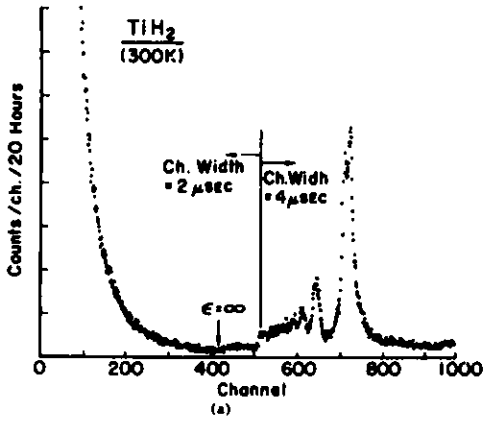

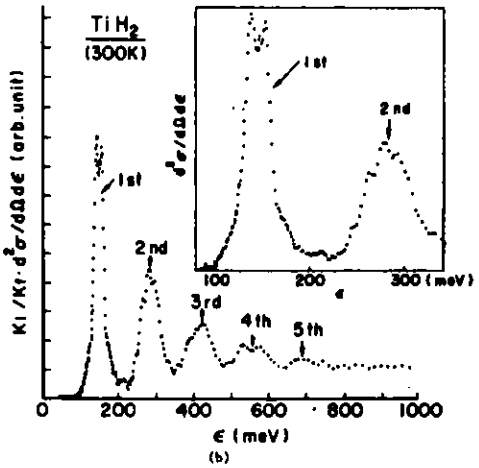

Fig. 4

Raw TOF spectrum (a) and double differential cross section (b) of TiH_2.

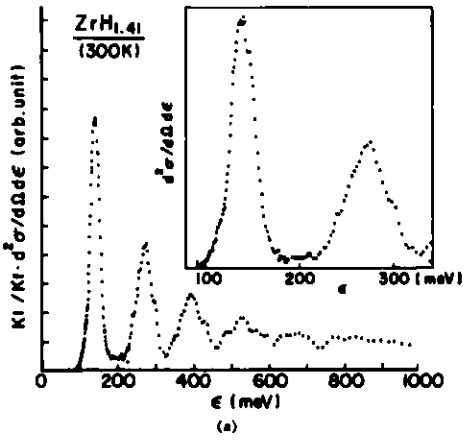

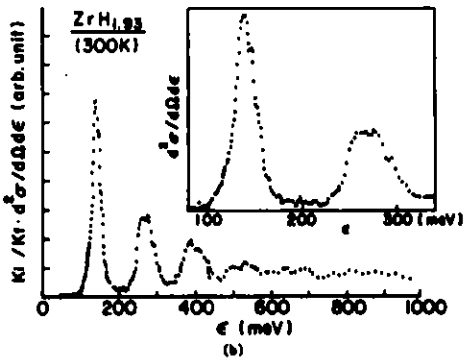

Fig. 5

Double differential cross section of $ZrH_{1.41}$ (a) and $ZrH_{1.93}$ (b)

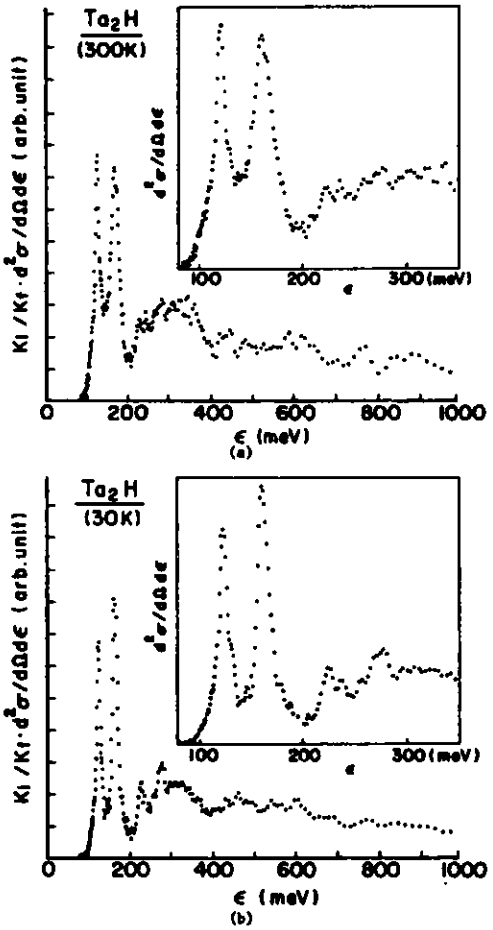

Fig. 6

Double differential cross section of Ta_2H at room temperature (a) and at 30 K (b).

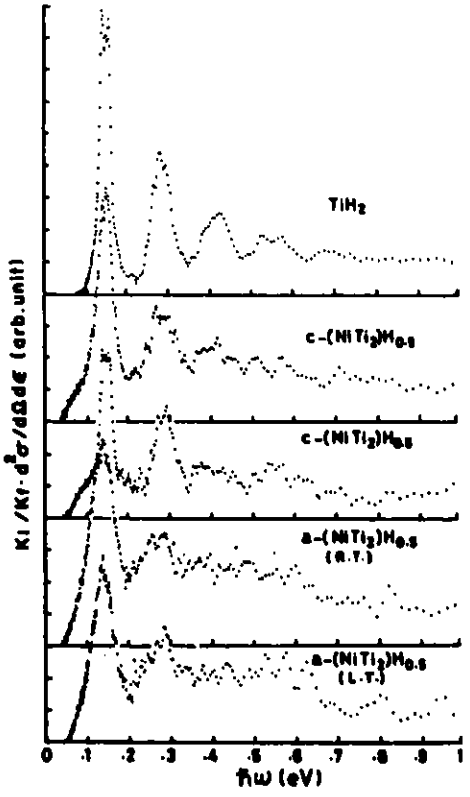

Fig. 7

Double differential cross section of amorphous $Ni_{0.33}Ti_{0.67}H_{0.5}$ compared with those of $Ni_{0.33}Ti_{0.67}H_{0.5}$, $NiTi_2H_{0.9}$ and TiH_2 crystals.

THE INELASTIC ROTOR SPECTROMETER AT THE HARWELL LINAC

B C Boland
Neutron Division
Rutherford Appleton Laboratory

1. INSTRUMENT DESCRIPTION

The Harwell Linac has been operating routinely for approximately 6 months at 25 Kw power and 75 Hz into a tantalum target. During this period a number of test experiments has been carried out and a period set aside for university user experiments

The instrument viewed a water moderator in slab geometry at 25° to the normal. The moderator was 4.4 cm thick with gadolinium poisoning 13 mm below the surface. No decoupler was present. The measured coupling efficiency is 5×10^{-4} n(1 eV)/n_f/ster.

The spectrometer is designed to measure energy transfers from 50 meV to 400 meV covering a range of Q values from 1-15 $\AA^{-1}$. Particular emphasis has been placed on the low Q counter banks where measurements at low Q reduce multiphonon contributions in vibrational spectra, diffusional broadening in liquids and allow measurements to be made on magnetic excitations(1). The spectrometer consists of a Nimonic rotor, rotating at 600 Hz, accurately phased to the linac with a jitter of less than $\pm$ ½ μs, placed at 6.4 metres from the moderator. Incident energy (E_o) selection is made by varying the phase of the rotor with respect to the linac. E_o can be varied from 150 meV to 500 meV. The selected neutrons are allowed to fall on the sample placed 1 metre downstream in an evacuated chamber. Sample temperature can be controlled from 20K to room temperature. Low angle counter banks are placed between 4°-11° either side of the main beam at 2.5 metres. In addition, counter banks are placed every 10° between 24°-94° at 1.62 metres. The counters are 1" diameter He^3 10 atmosphere and 4 atmosphere respectively. The region of (Q,ω) space covered for two values of E_o is shown in Figure 1 together with that covered by a beryllium filter spectrometer operating at these energy transfers. The energy resolution is estimated to be 7 meV at an energy transfer of 150 meV (4.7%). The intensity at the sample was measured using vanadium scattering to be 1100 n/s over 2" x 1" beam at 450 meV E_o.

2. EXPERIMENTAL RESULTS

Figure 2 shows the measured spectra for a sample of sodium bifluoride $NaHF_2$. The sample was ∿ 13% scatterer 3 mm thick inclined at 45° to the beam and kept at 90K. $NaHF_2$ in the pure salt form has been investigated before with neutrons but only at high Q values and relatively poor energy resolution using the beryllium filter technique (2). The bifluoride ion has a sharp bending mode ν_2 at 156 meV and an antisymmetric stretch ν_3 at ∿ 177 meV. The two modes are separated in the pure salt by IR measurement (3) but are both broad due to interactions with near ions. In a dilute sample of HF_2 ions in KCl the modes are seen as extremely narrow peaks in the IR spectrum. The modes have not been separated before in a neutron scattering experiment from the pure salt. In Figure 2 the two modes as seen by the low Q counter bank of the IRS are seen to be clearly separated (the ordinate, S, is proportional to $S(Q,\omega)$); the insert shows the comparable spectrum measured on the beryllium filter spectrometer IN1 at ILL. In addition, in collaboration with Durham Univer-sity(4), the sodium bifluoride was run at a higher incident energy E_o = 450 meV in order to collect data on the second harmonic at ∿ 300 meV. In a run of length 78 hours, data were collected over a wide Q range. Figures 3 and 4 show the raw data from the low angle (7°) counter and the 24° counter. Under these conditions the resolution is not good enough to separate the bend and stretch modes.

In a collaboration with the Universities of Munster and Birmingham (5) data were taken on samples of vanadium, and vanadium titanium, hydrides. With little multiphonon broadening of the optical mode, data from the high angle counter banks can be summed with little or no loss of resolution. Figures 5 and 6 show reduced data ($S(Q,\omega)$ against $\hbar\omega$) for the twosamples with the optical mode clearly split.

3. CONCLUSION

All indications are that the energy resolution is as predicted and is certainly twice as good as that of any other spectrometer presently available to the UK users at these energy transfers. Backgrounds on the high angle banks 24°–94° are excellent but at the low angles are too high at present for anything but hydrogenous samples. Tests have shown that much of this background comes from the main beam in the area of the collimation between the chopper and the sample, and steps are being taken to improve this area.

References

(1) Boland B C, Mildner D F R, Stirling G C, Bunce L J, Sinclair R N, Windsor C G, Nuclear Instruments and Methods 154 (1978) 349.

(2) Waddington T C, Howard J, Brierley K P and Tomkinson J, J Chem Phys 64 (1982) 193.

(3) Salthouse J A and Waddington T C, J Chem Phys 48 (1968) 5274.

(4) Howard J, Tomkinson J, Boland B C, to be published.

(5) Severin H, Wilson S K P, Wicke E, Ross D K, Carlile C J, to be published.

IRS Instrument Parameters

Moderator	5 cm thick water - Cd poisoned Slab geometry Viewed at 25^{o} to normal Area $\sim$ 170 cm^2 No decoupler
Chopper	At 6.4 metres 12 slot Nimonic operating at 600 Hz Beam size 2" x 1" Peak transmission at 300 meV Phased to better than $\pm$ ½ μs
Sample	At 7.4 metres In evacuated chamber Room temperature to 20^{o}K Displex type cryostats
Detector	Low angle 4^{o}-11^{o} either side of main beam 2 x 12 10 atmosphere He^3 counters at 2.5 metres 8 banks 24^{o}-94^{o} each 2 x 18" 4 atmosphere He^3 at 1.6 metres
T.O.F.	1024 channels channel width 1 μs variable start delay
Flux on sample	$\sim$ 4 x 10^3 n/s at full power at E_o = 450 meV.

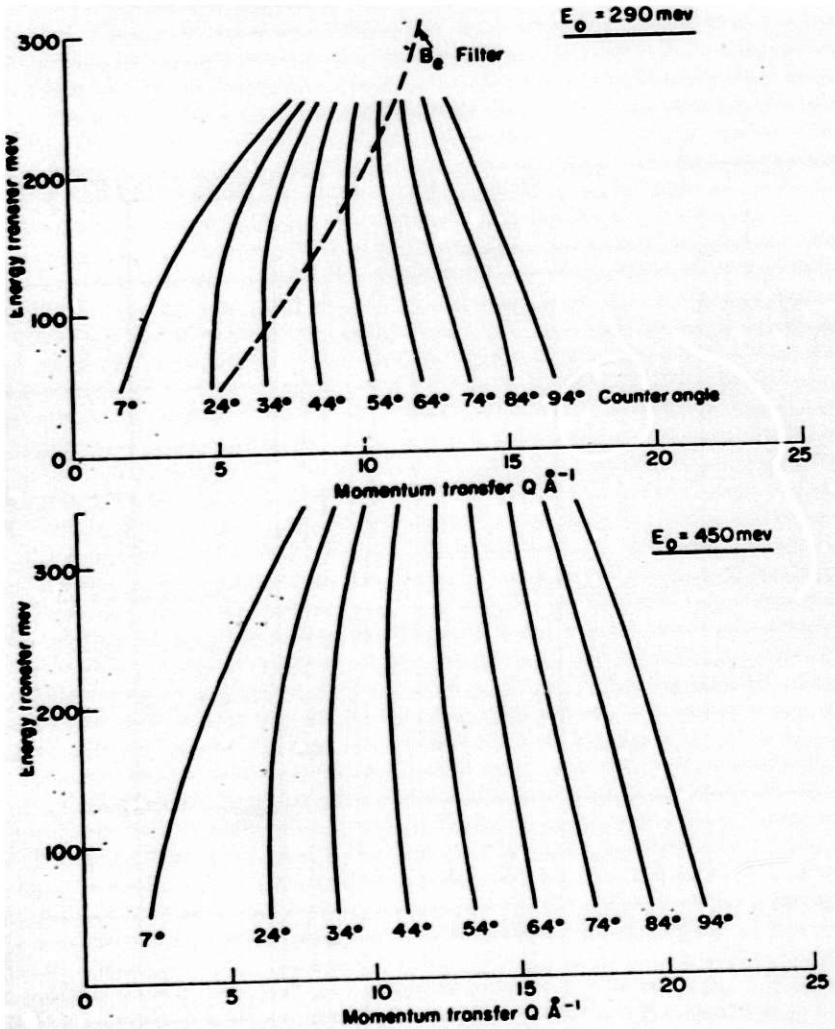

Fig. 1. Inelastic rotor spectrometer.

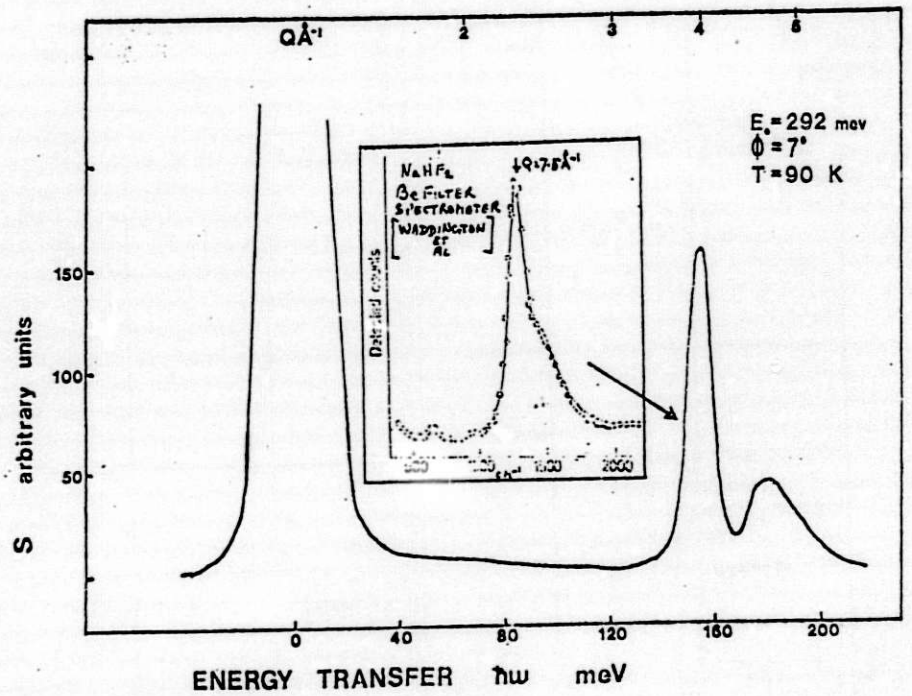

Fig. 2

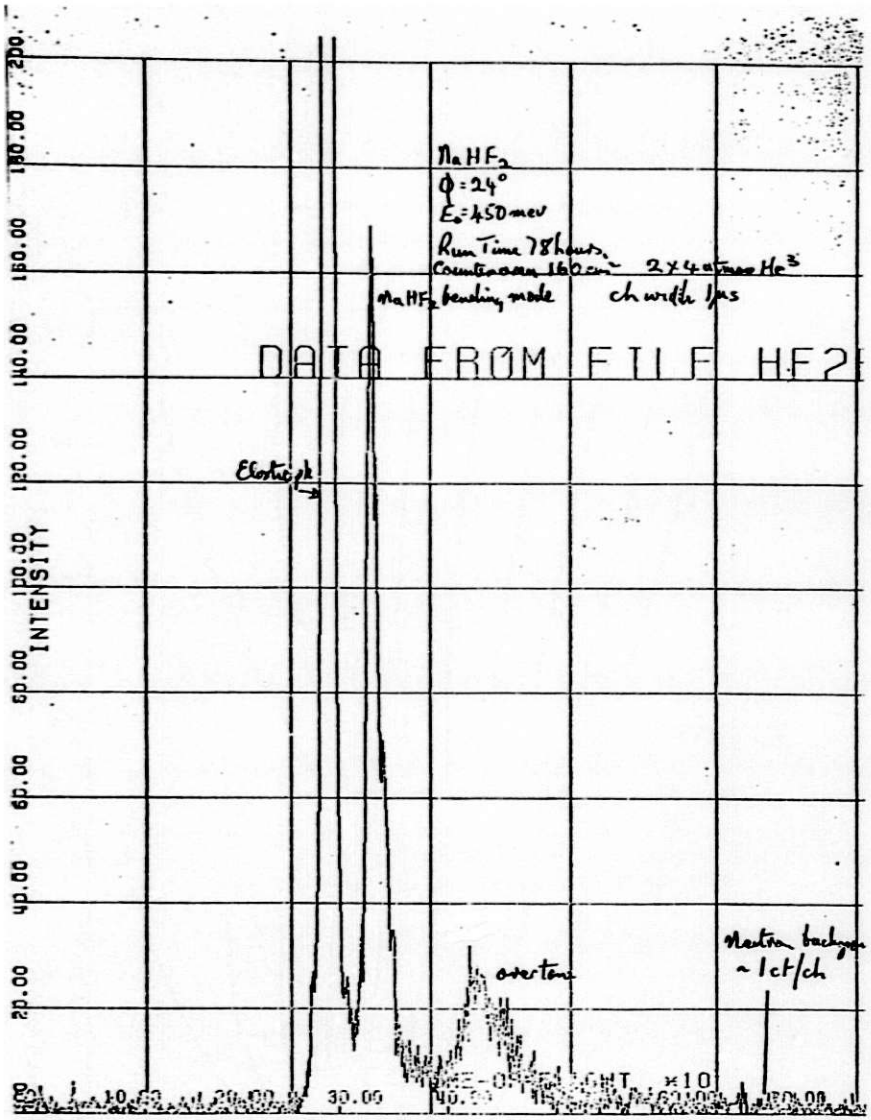
NaHF2
θ = 24°
E0 = 450 mev
Run Time 78 hours
Counter area 160 cm²
2 x 4 atm He³
NaHF2 bending mode
ch width 1 μs
DATA FROM FILE HF2
Elastic pk
INTENSITY
overtone
Neutron background
~ 1 ct/ch
TIME

Fig. 3

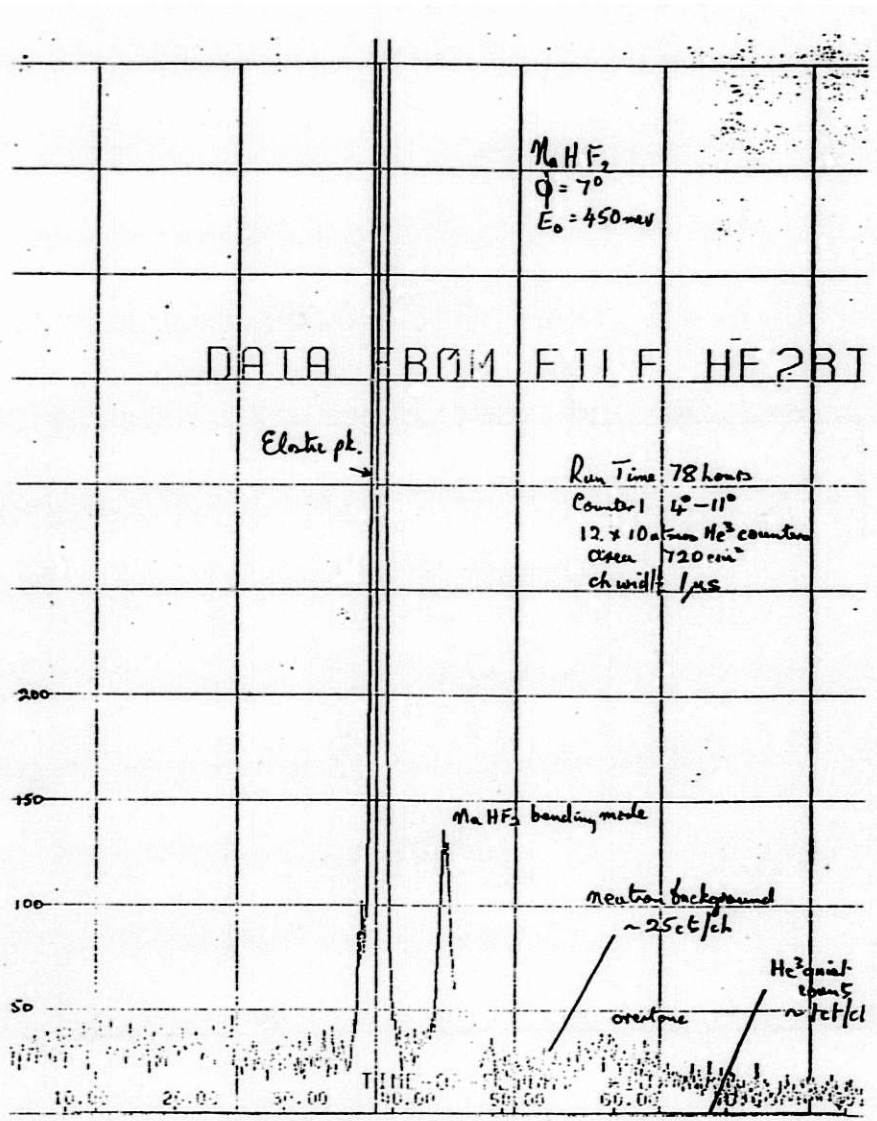
NaHF2
θ = 7°
E0 = 450 mev
DATA FROM FILE HF2RT
Elastic pk.
Run Time 78 hours
Counter 1 4° – 11°
12 x 10 atm He³ counters
Area 720 cm²
ch width 1 μs
NaHF2 bending mode
neutron background
~ 25 ct/ch
overtone
TIME

Fig. 4

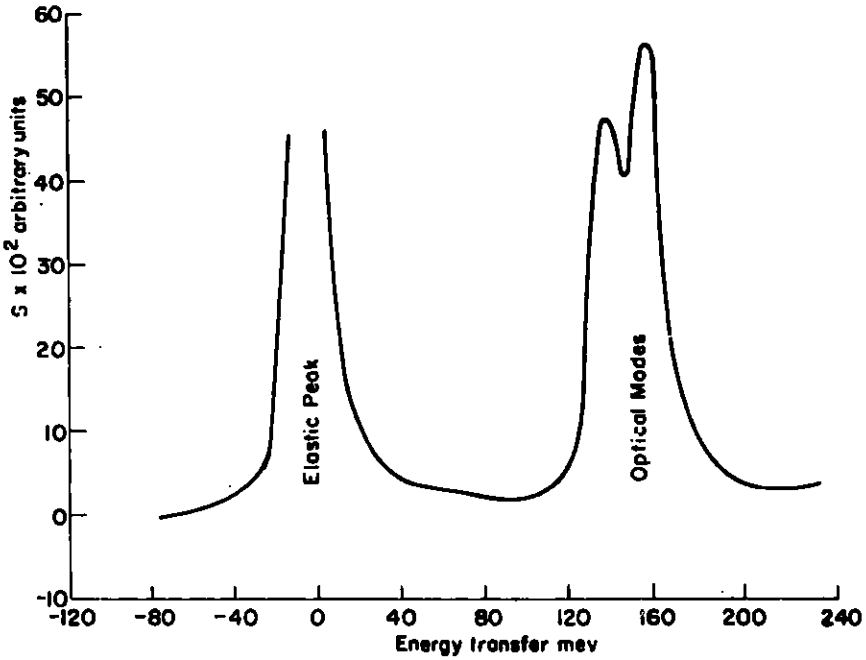

Vanadium Hydride

Run time — 48 hours

Fig. 5

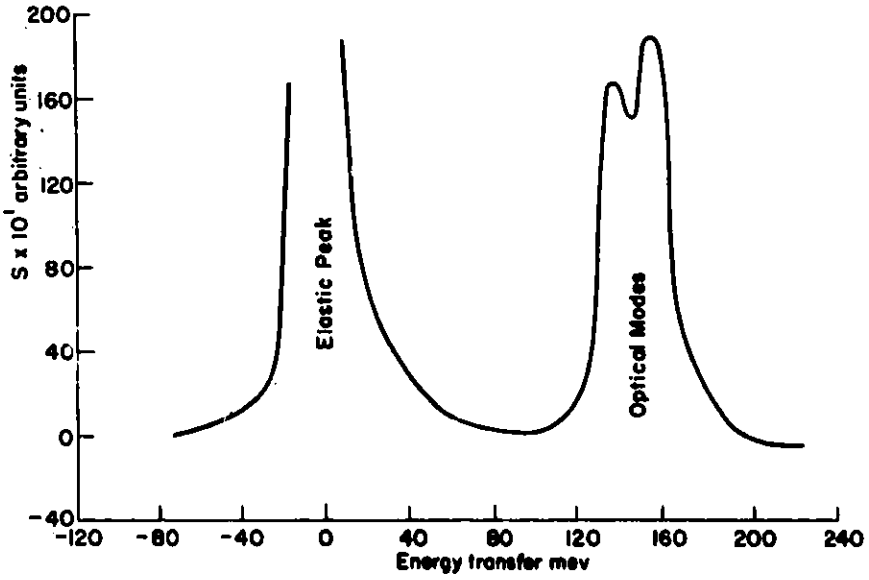

Vanadium Titanium Hydride

Run time — 48 hours

Fig. 6

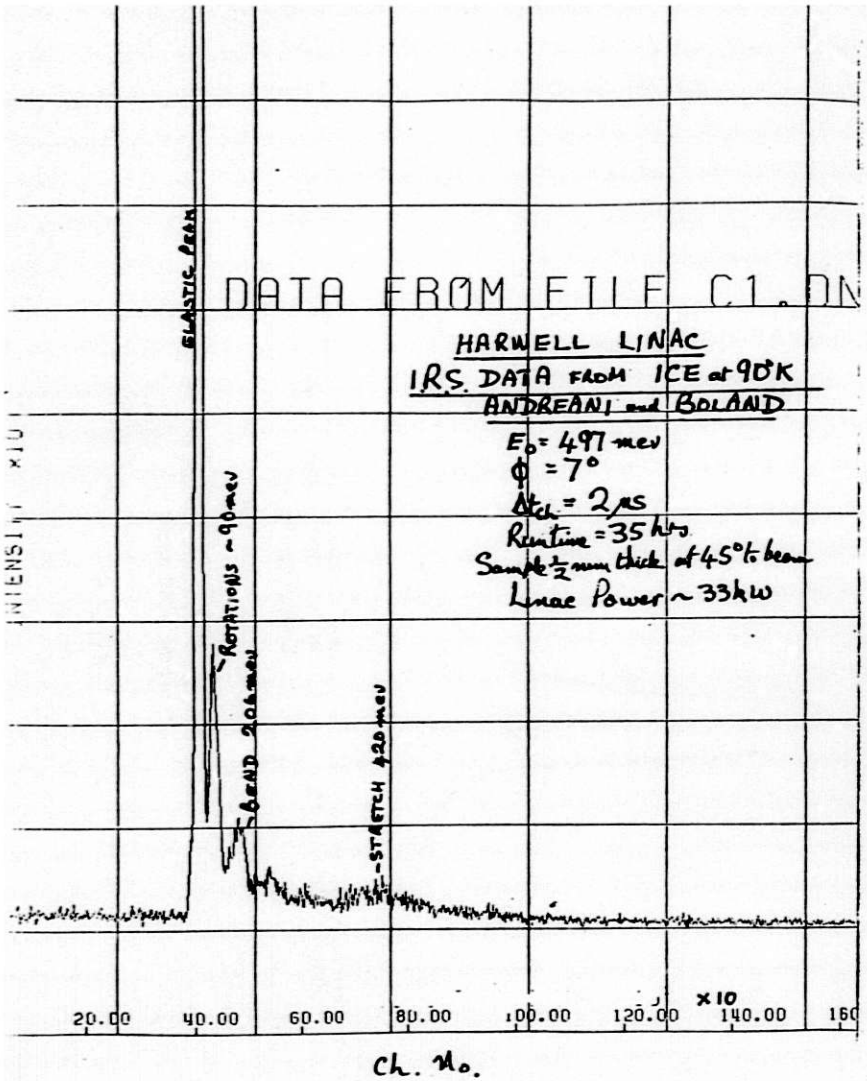
DATA FROM FILE C1.DN
HARWELL LINAC
IRS DATA FROM ICE at 90K
ANDREANI and BOLAND
E_0 = 497 mev
ϕ = 7°
Δtch = 2 μs
Runtime = 35 hrs
Sample ½ mm thick at 45° to beam
Linac Power ~ 33kw
ELASTIC PEAK
ROTATIONS ~ 90 mev
BEND 204 mev
STRETCH 420 mev
INTENSITY X10
20.00
40.00
60.00
80.00
100.00
120.00
140.00
x10
Ch. No.

Fig. 7

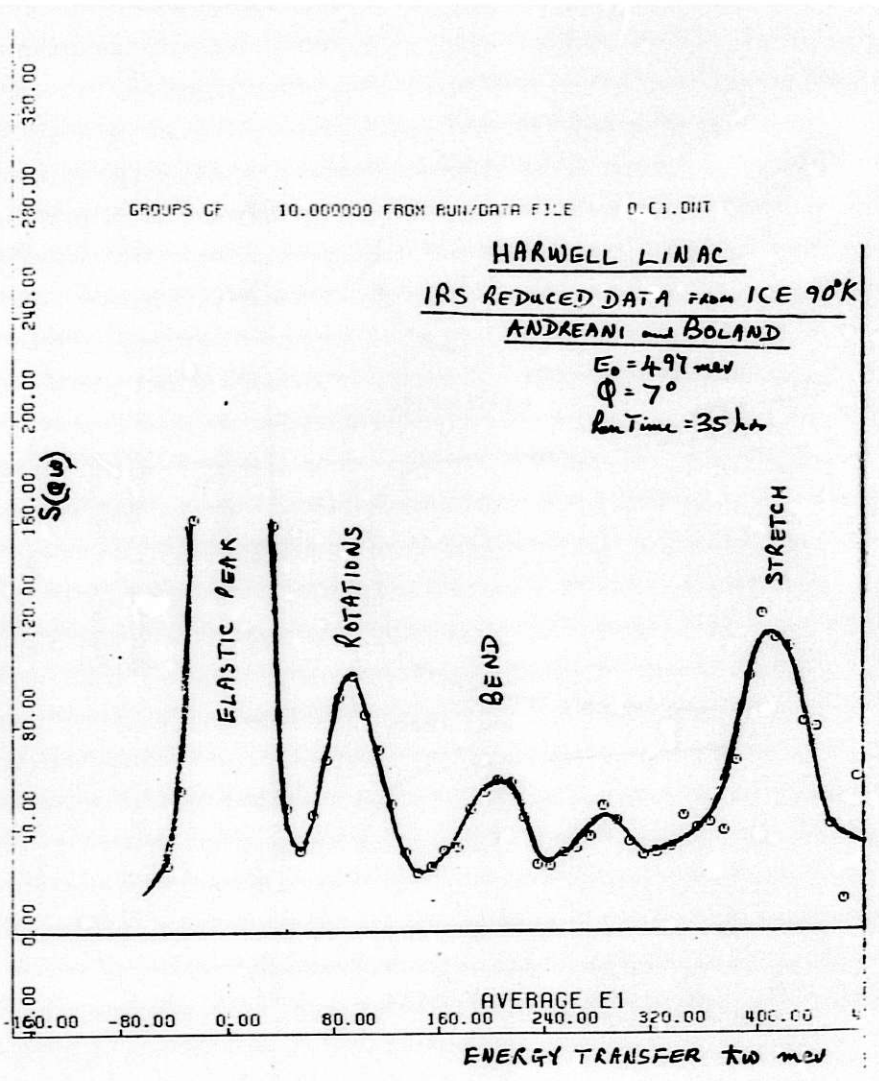
GROUPS OF 10.000000 FROM RUN/DATA FILE 0.C1.DNT
HARWELL LINAC
IRS REDUCED DATA FROM ICE 90°K
ANDREANI and BOLAND
E_0 = 497 mev
ϕ = 7°
Run Time = 35 hrs
S(ω)
ELASTIC PEAK
ROTATIONS
BEND
STRETCH
320.00
280.00
240.00
200.00
160.00
120.00
80.00
40.00
0.00
-160.00
-80.00
0.00
80.00
160.00
240.00
320.00
400.00
AVERAGE E1
ENERGY TRANSFER two mev

Fig. 8

Instrumentation - Summary of Contributed Paper and Discussion Sessions

R. K. Crawford

The contributed paper session included papers on the following major topics: Powder Diffractometers, Single Crystal Diffractometers, Small Angle Diffractometers, Inverted Geometry Spectrometers, Spectrometers for the Electron-Volt Energy Range, Choppers and Chopper Spectrometers, Polarized Neutron Instrumentation, Detectors, and Data Acquisition. There was also a general paper on the importance of the large dynamic range provided by most time-of-flight instruments. In the discussion sessions, additional material was presented on Inverted Geometry Spectrometers, Spectrometers for the Electron-Volt Energy Range, Choppers and Chopper Spectrometers, and Polarized Neutron Instrumentation. The summaries below combine material from the contributed paper session and discussion sessions under these major topic headings.

I. Diffractometers

Jim Jorgensen reported on the ANL powder diffractometers. His basic message was that these two instruments work extremely well. These instruments both use on-the-fly software time-focussing of the detectors, and this technique has been very successful. The high resolution provided by these instruments is being utilized by a number of powder diffraction users. These instruments have also proved to be quite good for obtaining high Q data from amorphous samples.

Art Schultz reported on the single-crystal diffractometer at ANL. This instrument uses an area-detector of the Anger type. The instrument, and its associated data analysis software, are now in routine use for crystal structure problems. Initial experiments also indicate the power of the area-detector-based time-of-flight Laue technique for finding low-intensity features such as diffuse scattering or satellite peaks between the Bragg peaks.

Ernest Epperson reported on the small angle diffractometer at ANL, and Masahumi Kohgi reported on the KENS small angle diffractometer. The KENS instrument is on a cold neutron guide and uses only the long-wavelength portion of the spectrum. It uses an area-detector made up of

an array of linear-position-sensitive detectors. The ANL instrument uses a gas-proportional-counter area-detector, and is designed to use epithermal neutrons as well as cold neutrons. The KENS instrument is now routinely taking data. The ANL instrument has cleared up most background and collimation problems but is not yet routinely taking data. It is not clear that data reduction techniques are entirely satisfactory for either of the instruments yet.

II. Inverted Geometry Spectrometers

Joyce Goldstone reported on the Be-BeO filter-difference spectrometer, and crystal analyzer spectrometer, in operation at LANL. Torben Brun reported on the ANL crystal analyzer spectrometer, and Noboru Watanabe reported on the high-energy crystal analyzer spectrometer at KENS. Both the ANL and KENS instruments have resolutions of ~ 2% at 100 meV. The KENS instrument uses a planar time-focussing geometry, so its resolution remains at nearly 2% over the entire range from 100 meV to 1 eV. The ANL instrument uses a curved array of crystals which gives resolutions better than the KENS instrument at energies below 100 meV, but its resolution falls off to about 7% at 1 eV. The LANL crystal analyzer spectrometer also uses a curved array of crystals but has a resolution of about 5% at 100 meV. The LANL Be-BeO filter difference spectrometer (which is in a production mode) also has a resolution of about 5% at 100 meV and sufficient intensity to give adequate statistics, even after taking the difference, in about 12 hours. She contrasted its performance with the Los Alamos crystal analyzer which has slightly better resolution but a significantly lower count rate. This latter instrument will be replaced in the fall by a constant-Q inverted geometry spectrometer. Approximate parameters of the LANL filter difference spectrometer and the ANL and KENS crystal analyzer spectrometers are summarized below.

	Filter Diff. LANL	Crystal Analyzer ANL	KENS
Sample area max. = A_s (cm^2)	2.5 x 10	2 x 5	7 x 7
Source-sample dist. = L_i (cm)	1300	1000	530
Sample-det. dist. = L_s (cm)	28	100	72
Analyzer solid angle = $\Delta\Omega$ (ster)	1.1	0.12	.017***
Analyzer reflectivity = R	-	0.8	0.8
Filter transmission = T	0.4†	0.8	0.8
Analyzer bandwidth = B (meV)	1.46	0.33	1.0
Relative counting eff.* = R1	9.5**	0.25	1.9
= R2	3.8**	0.025	0.039
Resolution = ΔE (meV)			
at E_f = 5 meV	1.5	0.5	1.0
100 meV	5	2.6	2.6
1000 meV	110	70	25

† at 300K

* $R2 = 10^6 \cdot \Delta\Omega \cdot R \cdot T \cdot B/L_i^2$; $R1 = A_s \cdot R2$
Use R1 if large samples are available, R2 if not.

** Suffers from statistics and background problems due to difference technique.

*** Geometric solid angle is 0.05 ster., but effective solid angle is 0.017 ster., due to θ_B-E_f correlation.

III. Electron-Volt Spectrometers

Bob Brugger and Andrew Taylor reported on the direct and inverted geometry resonance filter difference spectrometer prototype measurements at LANL, Gavin Williams reported on the inverted geometry resonance filter difference spectrometer prototype measurements underway by RAL at the Harwell Linac, and Jack Carpenter reported on the extensive development (in which he participated) of a resonance detector spectrometer at KENS. A general conclusion of the discussion was that the inverted geometry instruments were greatly superior to any practical direct geometry resonance filter difference instruments.

The filter difference techniques have the large advantage that the instrumentation is quite simple, involving only a resonance absorbing foil and standard neutron detectors. The difference method also means that background does not appear in the final results. However the difference method involves the subtraction of two large numbers and so has inherently large statistical errors. Thus it does not seem useful for measuring weak inelastic scattering. (However, Gavin Wlliams discussed the use of additional broadband filters in the incident and scattered beams as a technique to cut out most of the unwanted neutrons and hence greatly reduce this statistical problem. This technique will be tested on the Harwell Linac. This technique also suffers from the relative inefficiency of neutron detectors at these energies.

The resonance detector spectrometer also uses a resonant neutron foil, but in this case it is used as an energy-selective detector rather than as a filter. The capture gamma rays from the resonance of interest are detected by standard gamma techniques. This has the advantage of being a direct neutron detector technique, and so does not suffer from the bad statistics due to subtraction of large numbers inherent in the filter-difference techniques. However, shielding is much more complicated because the detector must be shielded from both gammas and unwanted neutrons.

Resolutions of about 70 meV (in a final resonance energy of several eV) are currently achievable.

IV. Choppers and Chopper Spectrometers

David Price reported on the chopper phasing techniques developed at ANL and on the results with the two chopper spectrometers there, Richard

Silver and Bob Brugger reported on current LANL attempts to phase a chopper to the LAMPF accelerator, and Spencer Howells reported on recent results on the chopper spectrometer operated by Brian Boland at the Harwell linac. ANL has solved its chopper phasing problems by running both the choppers and the accelerator from a fixed frequency crystal oscillator. A further refinement allows one "master" chopper to control extraction from the accelerator, thus effectively eliminating any effects of hunting oscillations for this chopper. Additional choppers can also operate as "slaves", in which case they cannot control extraction and so must follow the extraction frequency as best they can. At present the master can stay in phase within 1-2 microseconds while the single slave chopper currently operating is in phase within about 7 microseconds over 95% of the time.

LANL can control the LAMPF pulse within a 64 microsecond window which follows the line frequency. They are attempting to do this by using a relatively large permanent-magnet motor to provide sufficient torque to drive the chopper to follow the required rapidly-varying smoothed live frequency. Preliminary tests indicate the chopper can follow this frequency fairly well, although details about hunting oscillations, chopper heating and long-term ability to remain in phase were still sketchy.

The Harwell linac is phased to a crystal oscillator, so there is no major phasing problem for the RAL chopper spectrometer there.

Results on the ANL and RAL chopper spectrometers have mostly been aimed at the epithermal part of the spectrum. Both have used incident beams of about 500 meV. Background problems at these energies, although difficult, have been tractable in both cases. Progress is being made in understanding the resolution functions of these instruments.

Jack Carpenter discussed the use of Bragg reflection from a rotating crystal as an alternative to choppers for providing pulse-shaping in some cases for pulsed source instruments. In particular, this can provide a narrow time pulse with a wide energy band, which is difficult to do with choppers outside the biological shield. No plans are currently underway to build or test such a device, however.

V. Polarized Neutron Instrumentation

Masahumi Kohgi reported on the cold polarized neutron spectrometer and on tests performed on a polarized proton polarizer at KENS, Gian Felcher reported on progress on the spin refrigerator polarizer at ANL, on a proposed neutron spin precession technique for enhancing resolution in eV spectrometers, and on the current ANL efforts with cold polarized neutrons, and Gavin Williams reported on the RAL efforts using resonance absorption polarizers, including the prototype instrument being tested at the Harwell linac. The main effort continues to be directed toward developing efficient broad-band polarizers for thermal and epithermal neutrons. This work is technically very demanding and although some progress has been made the optimum solution has not yet been achieved.

The polarizing filter method based on the spin-dependent scattering of neutrons by polarized protons in a dynamically polarized ethylene glycol target is being pursued at KENS. A proton polarization of 43% has been achieved in a 1 cm thick target. Workers at KENS are now building an instrument based on a filter of this type. The spin refrigerator principle, which is an alternative method for polarizing protons, is currently being tested at ANL. It uses a crystal of Yttrium Ethyl Sulphate doped with Yb^{3+}, which is rotated in a magnetic field of 1.3 T. The apparatus is much simpler and more compact, and has much simpler cryogenic and field-homogeniety requirements, than the dynamic polarization method. A proton polarization of 30% has so far been achieved in preliminary measurements. Considerably higher proton polarization will be needed in both types of filter. These polarized proton filter techniques are extremely important to the future of polarized beam research at pulsed neutron sources, since this is the only known technique which provides white beam neutron polarization over a broad energy range up to KeV energies.

RAL is investigating the filter method using selective absorption by polarized nuclear resonances. Several statically polarizable nuclei have been identified as potentially useful neutron polarizing filters in the epithermal and lower eV energy range. ^{151}Eu is particularly interesting since it has a broad-band polarizing capability extending up to 0.6 eV. A new application using neutron resonances for combined energy and spin analysis (eg. for inelastic polarization measurements)

was also described. These techniques will be extensively tested at the Harwell linac.

Cold neutron polarizers based on mirror reflections are easy to make, and many experiments have been performed on the TOP spectrometer at KENS. A novel application of the critical reflection of polarized cold neutrons from magnetized surfaces, is being used at ANL to probe the penetration of a magnetic field into the surface of a superconductor. Time-of-flight polarized beam measurements are particularly appropriate in this case, since a wide range of wavelengths can be covered with the sample set at a fixed reflection angle.

Gian Felcher discussed his proposed use of polarized neutrons in a spin precession technique which could yield energy resolutions of about 30 meV in the lower eV energy range. However, any tests of this technique await the development of a satisfactory white-beam neutron polarizer.

VI. Detector Development

There has been significant progress since the last ICANS in the use of scintillator detectors at pulse sources. The 30 cm square, 49 tube Anger Camera using square photomultipliers has been brought into service at the single crystal diffractometer at IPNS. The effects of the intrinsic backgrounds in the Li glass scintillator and its sensitivity to γ radiation have not so far proved troublesome though care is taken to minimize the amount of γ producing shielding material such as Cd or B. Work is proceeding on the difficult problems of reduction of data from PSD's used in diffraction studies. Powerful FEM computers with large memory are needed. Detailed studies of the properties of the detector such as long term stability and uniformity of detection efficiency over the scintillator area have not yet been made.

A coded scintillator detector using solid glass light guides rather than optical fibers was tried on the constant Q spectrometer at the Harwell linac but proved to have too high a background for that low count rate instrument. An alternative arrangement of individual scintillator elements and coupled to ½" photomultipliers was much more successful yielding background levels in use which were slightly lower than an 8 atmosphere 9mm diameter ^{3}He counter, with the advantage of higher efficiency and lower cost. The best results were obtained with 2 layers

of scintillator 1mm thick separated by a layer of lead (3mm thick) to absorb the secondary electrons from γ capture events. Significant reductions in intrinsic background can be made by using a separate plastic scintillator to veto cosmic ray events in the glass scintillator.

In discussion of the origins of the intrinsic background in ^{6}Li-loaded glass scintillators, Tom Holden referring to CRNL work by Aslam Lone, pointed out that this may be due to reactions induced by the triton recoiling from the $^{6}Li(n,\alpha)$ T reaction; triton decay itself is not a problem. The most likely candidate reaction is

$$T + {}^{16}O \rightarrow {}^{19}F \rightarrow {}^{18}F + n$$

$$^{18}F \xrightarrow{109.\ min.} {}^{18}O + \beta^{+}\ (.633\ MeV)$$

The Coulomb barrier is 2.4 MeV, while the triton energy is 2.7 MeV. Other possibilities are

$$T + {}^{29}Si \rightarrow {}^{32}P + \gamma \quad \text{and} \quad T + {}^{30}Si \rightarrow {}^{32}P + n,$$

$$^{32}P \xrightarrow{14.3\ d} {}^{32}S + \beta^{-}\ (1.71\ MeV)$$

The Coulomb barrier is 3.8 MeV. The key to diagnosing the background problem is probably to measure the decay time of the background, following neutron irradiation. Neutron activation of other isotopes in the scintillator may also account for the "cooling off" effect seen when a detector is removed from a neutron field.

Good lithium-loaded scintillating glass is now being produced in Japan by Nikon. There is enough difference in the pulse shape for neutron and γ interactions to enable pulse shape discrimination to be used. There was no evidence of α activity in the pulse height spectrum. Work is also going on in Japan on fibre optic coupling.

VII. Data Acquisition

There have been no significant conceptual developments in data acquisition systems for neutron scattering instruments since the last ICANS meeting. However, since then the IPNS data acquisition has been brought on line. Tom Worlton reported on the performance of this system which is quite satisfactory. RAL has just placed the initial order for VAX computers for the SNS neutron scattering data acquisition system.

VIII. Importance of Dynamic Range

Ferei Mezei discussed the importance of providing instrumentation which covers a wide dynamic range, noting that many experiments at ILL must be done on several different instruments in order to cover a sufficient dynamic range. He also cited several examples of experiments which led to the wrong conclusions because the experiments did not span a sufficient dynamic range. He noted that this makes pulsed source instruments potentially very attractive, since the wide dynamic range is an inherent feature of most time-of-flight instruments.

IX. Standard Samples

There was a general discussion of the adoption of a standard sample material for the intercomparison of inelastic spectrometers. It was decided to adopt as a standard the material sodium bifluoride ($NaHF_2$). Sodium bifluoride has a sharp peak (~ 11 meV wide) at 159 meV, and has a much broader peak at 179 meV. Some peaks at higher energies have also been observed.

Measurements are to be made at low temperatures (20-30K) using sample geometries optimized for the instrument on which the measurements are made. Results of these measurements are to be distributed informally among the ICANS laboratories by the experimentalists involved.

Summary of Discussions of Electron Volt Spectroscopy

A. D. Taylor, LANL
N. Watanabe, KEK
J. M. Carpenter, ANL

For purposes of discussion, we define these spectrometers to be those which use sharp nuclear resonances to define the neutron energy before or after scattering. We heard descriptions of tests of two types of these spectrometers, the Resonance Filter Beam Spectrometer (RFBS) (Brugger & Taylor, these proceedings) and the Resonance Detector Spectrometer (RDS) (Carpenter and Watanabe, these proceedings).

The diagram shows the general plan of these spectrometers; letters designate the position of the resonance device.

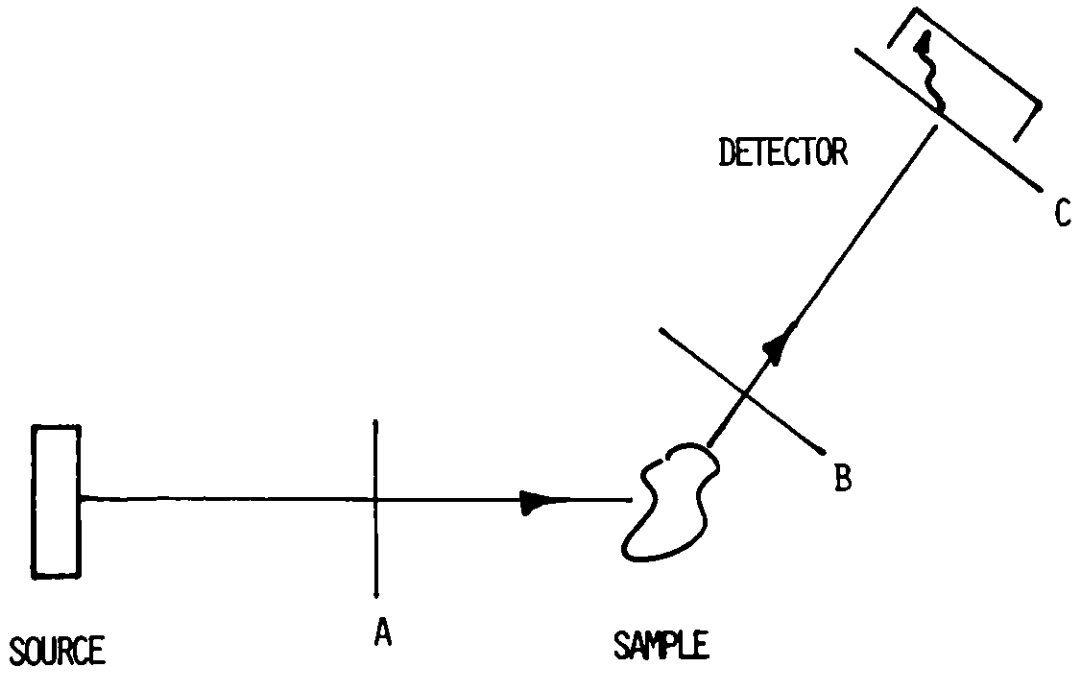

Fig. 1 Schematic diagram of Electron Volt Spectrometers.

The table summarizes the distinctions between the two methods, and introduces a third, prospect, that of the Resonance Filter Detector Spectrometer (RFDS), which has been prototyped (Brugger and Taylor; Williams and Penfold, these proceedings).

Methods of Electron-Volt Spectroscopy

Statistical Method \ Particle Detected	Neutron	Secondary (γ)
Difference	RFBS (A) and RFDS (B)	
Direct		RDS (C)

In the RFBS resonance interactions remove neutrons of definite energy from the incident beam and the distribution of scattered neutron energies is determined by time of flight. The difference between spectra measured with and without the filter gives the net scattered intensity distribution for fixed initial energy. In the RFDS, resonance interactions remove neutrons of definite energy from the scattered beam, and the distribution of incident neutron energies is determined by time of flight. The difference between spectra with and without the filter gives the net scattering for fixed final energy. In the RDS, resonant interactions in an absorber are detected through the prompt secondary particles produced, and the incident neutron energy distribution is determined by time of flight. The measured spectrum is directly proportional to the desired intensity distribution.

We tabulated the following characteristics of these spectrometers.

Characteristics of Electron-Volt Spectrometers

Resonance Filter-Beam Spectrometer	Resonance Filter-Detector Spectrometer	Resonance Detector Spectrometer
Detects neutrons - (a) Simple detector system and simplified shield design if gas proportional counters are used; then efficiency is limited to about 20%, at 5 eV where detector thickness contributes to resolution approximately as the source pulse; dead time and electronic jitter are about 1 μs. (b) ^{6}Li Glass scintillators may be used, with high efficiency, with dead times about 100 nsec, and smaller electronic jitter. Shield design is then made more complex and a sample-dependent background may exist due to capture-gammas seen by the detector, generated in the sample or filter.		Detects gamma rays or other secondaries. This is fast but more complex than neutron counting, in the case of gamma counting, necessitates design of shielding effective for both neutrons and gammas. Dead times and electronic jitter are less than about 100 nsec. Efficiency is on the order of 50% but depends on the choice of absorber.
Difference spectroscopy automatically accounts for sample-independent backgrounds. Separate, sample-out measurement for sample-dependent background.		Separate background measurement necessary without absorber.
Difference spectroscopy introduces large statistical errors for all energies - favors measurements where scattering is near maximum.		Direct measurement gives small statistical errors where scattering is small.
Long incident path necessitated by shielding amplifies resonance resolution broadening.	Long incident path useful for resolution, short scattered-neutron path allows larger solid angles with fixed detector size.	
Resolution ~ 200 meV demonstrated - can be improved.		Resolution ~ 70 meV demonstrated - can be improved.
Polarization possible in all cases.		
Capture, scattering, fission resonances all useful.		Restricted to capture and fission resonances.
Resonance filter small, $\lesssim$ size of incident beam.		Resonance absorber area proportional to detector solid angle.

Resonance Filter-Beam Spectrometer	Resonance Filter-Detector Spectrometer	Resonance Detector Spectrometer
Detector far from sample, so small detector solid angle.	Detector close to sample, so large detector solid angle.	Sample - detector distance 10cm accomplished.
Filter independent of detector simplifies cooling to reduce Doppler broadening contribution to resolution.		Cooling of absorber probably requires cooling of secondary-particle detector.
Pulse shape rejection of gamma ray background possible with use of ^{6}Li scintillators.		Backgrounds can be reduced by coincidence counting or spectroscopy of secondaries at sacrifice of efficiency.

We find the RFBS, and the less-tested RFDS to be apparently simple devices, notably useful for testing methods. The RDS requires more complex detector technology, but for statistical reasons will probably be best especially for problems in which the scattering of interest is small compared to the average scattering from the sample, the most-common case.

So far tests have been mostly in measurements characterizable as those of struck-particle momentum distributions. Richard Silver showed that these can include some interestingly-structured, but easily-resolvable features. Much more exploration of magnetic, molecular and electronic excitations is needed, as well as tests of the RFDS, which can be done in more-or-less simple adaptations of TOF diffractometers.

The technique using the difference spectra obtained using resonance devices of two different thicknesses of absorber should be tested. Here, the absorption $(1 - e^{-n\sigma(E)})$ is proportional to $n\sigma(E)$ in the wings of the resonance, but due to self-shielding in the thick case, is less sharp near the peak than in the thin case. The difference spectrum can be made sharper than that in the thin-absorber case. The technique would be applicable to any of the spectrometers discussed here.

Gavin Williams described the potential advantages, particularly for low Q scattering, of using thick composite filters which have strong resonance absorbtion regions on either side of the energy range of interest. When placed in the direct beam, these filters suppress background and greatly enhance signal to noise.

D. A. Gray, C. W. Potts

H. Conrad, B. Diplock, M. Meier, C. Tschalär

A. W. Armstrong, D. Filges

J. Goldstone, W. S. Howells, H. Wroe, M. H. Mueller

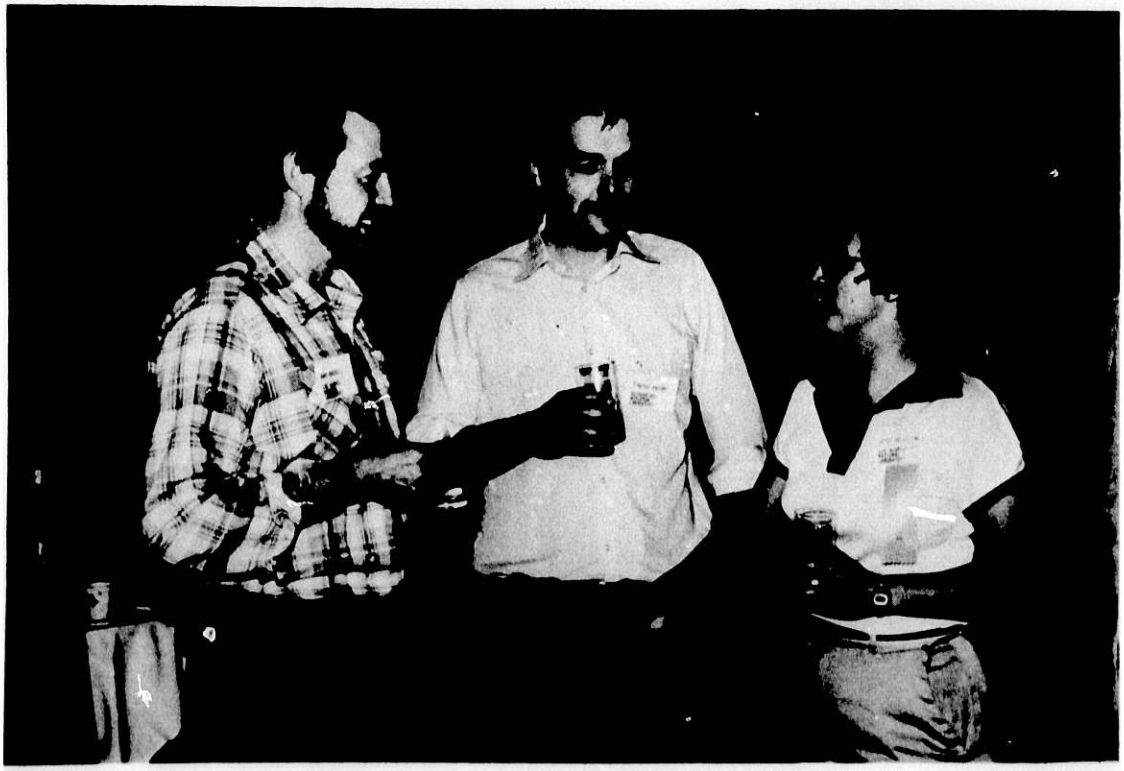

G. J. Russell, T. A. Broome, J. Goldstone

ICANS-VI ANL

INTERNATIONAL COLLABORATION ON ADVANCED NEUTRON SOURCES

June 27 - July 2, 1982

PROGRESS ON THE SNS TARGET STATION

A Carne
Rutherford Appleton Laboratory
Chilton, Didcot, Oxon, UK.

1 Introduction

This progress report is a continuation of reports given in the previous ICANS meetings. In particular, the report given at ICANS IV (1) was a definitive statement of the overall Target Station, containing the expected performance parameters. This review gives progress and modifications covering the last eighteen months, under the five broad areas of Target, Target Assembly, Control System, Bulk Shield and Remote Handling. Finally a discussion of additional facilities to the SNS is presented.

2 Target

(i) The general description of the target was given at the ICANS IV meeting. Since that time a full description of the theoretical study on the whole target assembly, based on a modified HETC code package, has been produced (2).

A study of the cooling tests on target plate models has shown that the cooling is mainly forced convective and that the expected uranium centreline temperatures would be as low as 290°C. Accordingly new uranium thicknesses have been obtained based on a centreline temperature of 380°C and assuming a reduction of up to 10% in thermal conductivity due to uranium burn-up. The choice of temperature allows a greater

mechanical strength and a margin of error in reduction of beam size (~ 10%) or in beam intensity (~ 20%) whilst keeping below the cavitational swelling regime of radiation damage. The new target will have 23 plates in 4 batches of uranium thickness 7.7mm (8), 9.7mm (8), 16.8mm (4) and 26.2mm (3), as shown in the schematic diagram, figure 1.

(ii) Fabrication of the zircaloy-2 clad uranium plates has been under development with the Fulmer Research Institute in the UK. The HIP bonding technique is used in which the assembly of uranium disk and zircaloy cover plates are subjected to an isostatic pressure of 2000 bars in an argon atmosphere furnace at 800°C for 3 hours. Two successful test plates have been obtained with complete bonding; however, β-quenching to refine grain size resulted in some small areas of de-bond at the corners. This problem is being investigated, along with mounting of thermocouple wells.

3 Target Assembly

(i) The four moderators discussed in reference (1) have been confirmed and their basic geometries fixed, as shown in Table 1. Of the two lower, cryogenic, moderators one will be liquid methane at 95 - 97K and the second will be para-hydrogen at 25K. The moderators will be single phase to give uniform density and flow, requiring operating pressures of 4 atmospheres (ie. subcooled with T_B ~ 131K) for methane and 15 atmosphere (ie. supercritical) for hydrogen. New estimates of the total energy deposition in the moderators indicate values of about 665W for the methane and 520W hydrogen moderators for an assumed 200μA on target. These new figures have been based on references (3) and (4) and are about two times the previous estimates. Further details of the moderators are given elsewhere in this meeting (5).

(ii) The moderators will be surrounded on all but the exit faces by decoupler using a boron loaded laminate containing 35% of natural B_4C, to give an effective decoupling energy of about 3eV. No decoupler is proposed for the hydrogen moderator, high intensity of the long wavelength neutrons being required rather than pulse shape. The beam ports through the reflector will also contain decoupler of the same type. The total energy desposition is expected to be about 4KW, to be removed through thermal contact with the reflector vessels.

4 Control System

The target station control system has three tasks: to set up and monitor the operation of the plant, to provide an interlock system to ensure safe operation and to provide an emergency shutdown system whilst maintaining cooling of the target at all times. The system itself is composed of 4 parts; (i) a Minicomputer Control System (MINICS) using a GEC 4070 minicomputer to provide the overall control function and to carry out routine monitoring, (ii) a Microcomputer Control System (MCS), using an Intel iSBC microprocessor, to monitor the vital parameters related to the condition and safety of the target station components (eg. target temperatures, coolant presssures and flow) and to provide the facility for a software-generated beam trip under monitored faults, (iii) a Target Beam Trip (TBT) to provide a hard-wired interlock operating independently of the computers, (iv) Coolant Control Logic (CCL) to ensure adequate cooling to the target in the event of plant or computer failure. Each of the first three parts is capable of turning off the proton beam in the event of a fault thus providing a three-fold heirarchy of safety monitoring and operation: the last part ensures continued target safety under all circumstances, eg. against decay heating which has a maximum value of about 9KW. The CCL is implemented using programmed logic controllers (PLCs) in a triple redundant configuration such that a single failure within a PLC will not cause CCL malfunction.

Sensors (eg. temperature, pressure, position) are standard radiation-hard commercial devices connected to standard panel meters which interface directly to the data acquisition system. Modular design is maintained to allow rapid servicing and simple alignment and calibration. This basically simple system is designed to make commissioning and trouble shooting as straight forward as possible and to enhance reliability.

The system is designed so that the target station, once set-up, can be left unattended during normal operation with monitoring and control exercised remotely via the main SNS control system.

5 Bulk Shield

Major components of the bulk shield have been designed and have been delivered or are under construction.

The shielding inserts provide local supports into which the collimated neutron beams and their shielding are placed. The arrangement makes the mounting of the neutron beams independent of the bulk shield and so allows flexibility in any future instrument layouts. The inserts, in 6 modules, have been delivered and figure 2 shows the mounting of a set of three in the bulk shield. The second set will be mounted in July/August of this year. The datum base plates and the central pillar, acting as the target station central datum and the eventual emergency drain pipe, can also be seen in this figure.

The shutter "vessels" contain triangular shielding wedges and the neutron beam shutters. The shielding wedges are in production, with completion expected by the end of November 1982. The shutters themselves are designed and the order for manufacture will be placed in September 1982. The centre section of the shutter incorporates a cast-lead collimator with its own helium atmosphere.

The target void vessel provides a contained atmosphere of helium, at 4.5mbar below ambient, around the target assembly. The helium gas performs several functions: at 95% concentration it guarantees there is no risk of burning or detonation with complete leakage of either or both cryogenic moderators; when circulated it provides cooling for the 5KW energy deposition in the vessel walls; it serves as a low attenuation transport medium for thermal neutrons. The void vessel is some 3.2m diameter and 3.2m high. Its walls contain eighteen neutron beam double windows each of size 190 x 190mm^2 of 2 x 0.5mm thick aluminium. Pressure cycling tests of a single 0.5mm sheet from ambient to vacuum to ambient, with 207mbar on the other side, have shown a distortion of less than 10mm over a 1000 cycles without failure. The number of cycles is an order of magnitude greater than ever likely in operation. The vessel has been designed, is being constructed under the ASME III category 'A' regulations and is due for delivery in April 1983.

Figure 3 shows the void vessel. In this figure can also be seen the tubes for the proposed Fusion Materials Irradiation Test Facility, which will sample the backward flux of fast and high energy neutrons escaping from the target assembly. At the location shown, fluxes of $4 \times 10^{11} ncm^{-2} sec^{-1}$ for En $\geq$ 1 MeV and $4 \times 10^{10} ncm^{-2} sec^{-1}$ for En $\geq$ 10MeV are expected for a 200μA input proton beam.

6 Remote Handling

The dimensions of the remote handling cell have been fixed at 3.3m (L) by 4m (W) by 5.5m (H). The walls and roof are respectively 1.6m and 1m thick. The wall thickness will reduce the radiation dose rate at the outside of the shielding to less than 10μSv/hr and so allow prolonged use of the manipulators. Detail design is underway for installation, together with the rail and drainage systems, in the second half of this year. The overall ventilation system has been specified according to the appropriate UK codes of practice.

A full scale mock-up remote handling cell has been built to start the testing and development of the tools and techniques for handling all the components of the Target Assembly. The major task is removal and replacement of the target. The alignment and lifting frames and the mechanism for rotating the target from horizontal to vertical prior to placing it in the storage wells have been built. The overall operation of removing a (dummy) target, rotating it and placing it ready for storage takes about 1¼ hours. Various fasteners for the target flange have been examined, with captive swing bolts appearing to be the best. Coolant seals for this flange (and others) have also been studied, with silver-plated stainless steel ("Corruseals") giving the best seals with minimum corrosion.

Figure 4 shows part of the target removal operation showing the lifting frames around the dummy target. More details of remote handling are given elsewhere in this meeting (6).

7 Other Facilities

The use of an irradiation test facility in the target station has already been mentioned: there are further major facilities additional to the SNS based on an intermediate transmission target located in the extracted proton beam some 20m upstream of the main SNS target. These facilities consist of a negative pion beam for medical applications and a surface μ^+ beam for studies in solid state and chemistry using the μSR technique. The pion beam will rely on the high intensity of the proton beam and will complement the existing facilities at SIN, LANL and TRIUMF. The surface muon beam will be unique in that it will be pulsed, give useful μ^+ stopping rates up to 100 times greater than existing facilities and give wide flexibility in available operating modes. Figure 5 shows a general layout of the Experimental Hall with the intermediate target station, pion and muon beams.

(i) The target itself will have a variety of geometries with graphite thicknesses up to 50mm in the proton beam direction, resulting in a reduction of thermal neutron flux from the main SNS target of up to about 16%. Various tunes of the proton beam are available to produce different waist sizes (horizontal and vertical) at the target as required by the pion and muon beams whilst still satisfying the main optics requirement of transmitting good beam onto the neutron production target. Local steel shielding will be installed around the target to reduce the external radiation dose rate to the same value as elsewhere for the EPB shielding, ie. less than 7μSv/hr. Further shielding may be added as necessary to ensure low time-independent backgrounds for the neutron instruments.

(ii) The biomedical pion beam will be a conventional low momentum (up to 210 MeV/c) negative pion beam of large acceptance (285 msr %Δp/p), which combined with the 200μA incident proton beam will generate dose rates in the pion stopping region (volume 120 x 80 x 70mm^3, 0.67 litres, depth 285 - 375mm in tissue) of 0.11 Gy/min (10.9 Rads/min). The primary task of this beam will be radiological experiments and eventually radiotherapy on human patients. A comprehensive programme of research with this beam has been proposed by groups from UK universities and medical institutions.

(iii) The 28MeV/c pulsed surface muon beam facility will be one of the only two pulsed μ^+ sources in existence, the other being the low current (I_p = 2μA) source at KEK. The advantages of a pulsed μ^+ source will be combined with those of a surface muon beam to achieve increases of up to a factor 100 of the useful μ^+ stopping rates for μSR studies. The beam will incorporate two fast kicker magnets, the first separates the individual muon bursts generated by the intrinsic pulse structure of the SNS proton beam (2 x 100ns bursts separated by 230ns, repeated at 50Hz) and the second to shorten each pulse down to ~10ns FWHM when required. The use of Soller-type collimators before the second kicker might allow a decrease of the final pulse width down to 1 - 2ns. Beam intensities of $10^7\,\mu^+$/s total, ie. $10^5\,\mu^+$/burst will be available with the full time width of each burst. This intensity decreases linearly with pulse width down to the 1 - 2ns available. The beam will include a crossed-field electrostatic velocity selector which, at 10% rating, will eliminate electron contamination, and at full rating (E = 5MV/m, B = 6.5 x 10^{-2}T, L = 2.3m) will rotate the muon polarisation from 100% longitudinal to 100% transverse.

The beam can also be operated with the pulse separation facility for cloud muons of both charge signs of momentum up to 50MeV/c and as a conventional high momentum pion beam ($\pi^{\pm}$) up to 200MeV/c.

The principal use of this beam will be for μSR, channeling experiments in solid state and a wide spectrum of pure research with pions and muons.

The status of this work is that funds have been provided to allow the modification of the EPB for the future implementation of these proposals. The proton beam line has been redesigned and includes the use of large aperture quadrupoles (which already exist); the mechanical support systems for the quadrupoles and a rail system have been designed to overcome the restricted access due to the presence of the intermediate target; the EPB shielding has been modified to allow the installation of either or both beams; detail work is starting on the intermediate target itself. No further committment has yet been made on the biomedical beam; but for the μSR beam work is going ahead to prepare a full proposal for presentation at the end of this year with the possibility of installation ready for SNS "Day One" in 1984.

8 Acknowledgements

This report gratefully acknowledges the work of the members of the SNS Target and Utilisation Group, in particular Tim Broome, Dave Clarke, Brian Diplock, Gordon Eaton, John Hogston, Mike Holding, Bernard Poulten, Ken Moye, Ken Roberts and Eddie Fitzharris and Colin Thomas, also the collaboration with members of Neutron Division.

9 References

(1) A Carne, "Review of SNS Target Station". Proceedings of ICANS IV, KEK Tsukuba, Japan, October 1980.

(2) F Atchison, "A Theoretical Study of a Target Reflector and Moderator Assembly for SNS". Report RL-81-006, April 1981.

(3) N Watanabe and K Boning, "Summary of Energy Deposition and Cryogenic Equipment". Proceedings of ICANS V, Julich, West Germany, June 1981.

(4) E Karls, K Hain, W Leiling, "Technisches Konzept einer Kalten Neutronen-Quelle fur die SNQ". SNQ Study Teil III KfA Julich/Karlsruhe, June 1981.

(5) B R Diplock, "Cryogenic Moderator Design". This Conference.

(6) B H Poulten, "Remote Handling Equipment For SNS". This Conference.

TABLE 1

SNS Moderators

A	B	C	D
H_2O	CH_4	$p\text{-}H_2$	H_2O
316 K ± 1 K	95 - 97 K ± 1 K	25 K ± 1 K	316 K ± 1 K
High Intensity at expense of resolution	High Resolution slowing down spectrum	Long wavelength	(as required)
dimensions of moderator material, mm			
w 120 h 120 d 15, 30 } 45	120 115 45 (at centre)	110 120 80 (at centre)	120 120 22.5, 22.5 } 45
Poison: 0.05mm Gd. Clad	Poison: provision for future incorporation	Poison: None	Poison: 0.05 mm Gd. Clad
Decoupler: 6mm boron loaded laminate, 35% natural B_4C	Decoupler: 6mm boron loaded laminate, 35% natural B_4C	Decoupler: None	Decoupler: As 'A'
Void Liner: As for decoupler (shared with 'D')	Void Liner: As decoupler preferred (shared with 'C')	Void Liner: 1mm Cd preferred (shared with 'B')	Void Liner: As for decoupler (shared with 'A')

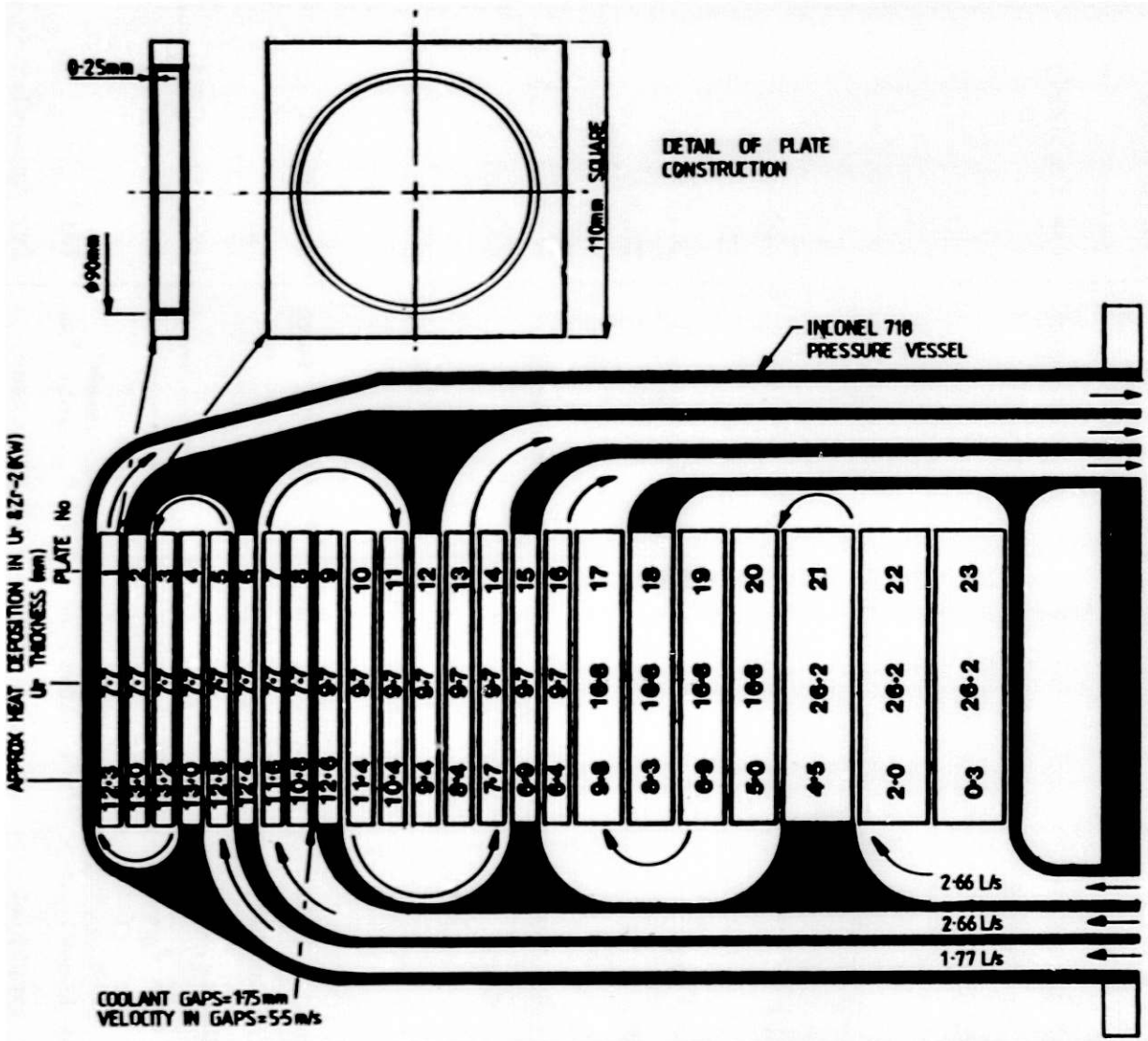

T_{ct} (max) = 380°C

W max = 300 W cm^{-2}

T (Zr) ~ 120°C

BULK OUTLET TEMPERATURE 50°C

OUTLET PRESSURE 3·4 BARS

HEAT DEPOSITED IN TARGET	KW
a) In ^{238}U including decay	209
b) In Zircaloy-2 cladding	6
c) In Inconel Vessel including Window	7
d) In Heavy Water Coolant	5
TOTAL	227

INLET PRESSURE 4·76 BARS

HEAVY WATER COOLANT

AT 43°C

FIG:1 TARGET COOLING PARAMETERS AND TEMPERATURE DISTRIBUTION (FULL INTENSITY PROTON BEAM)

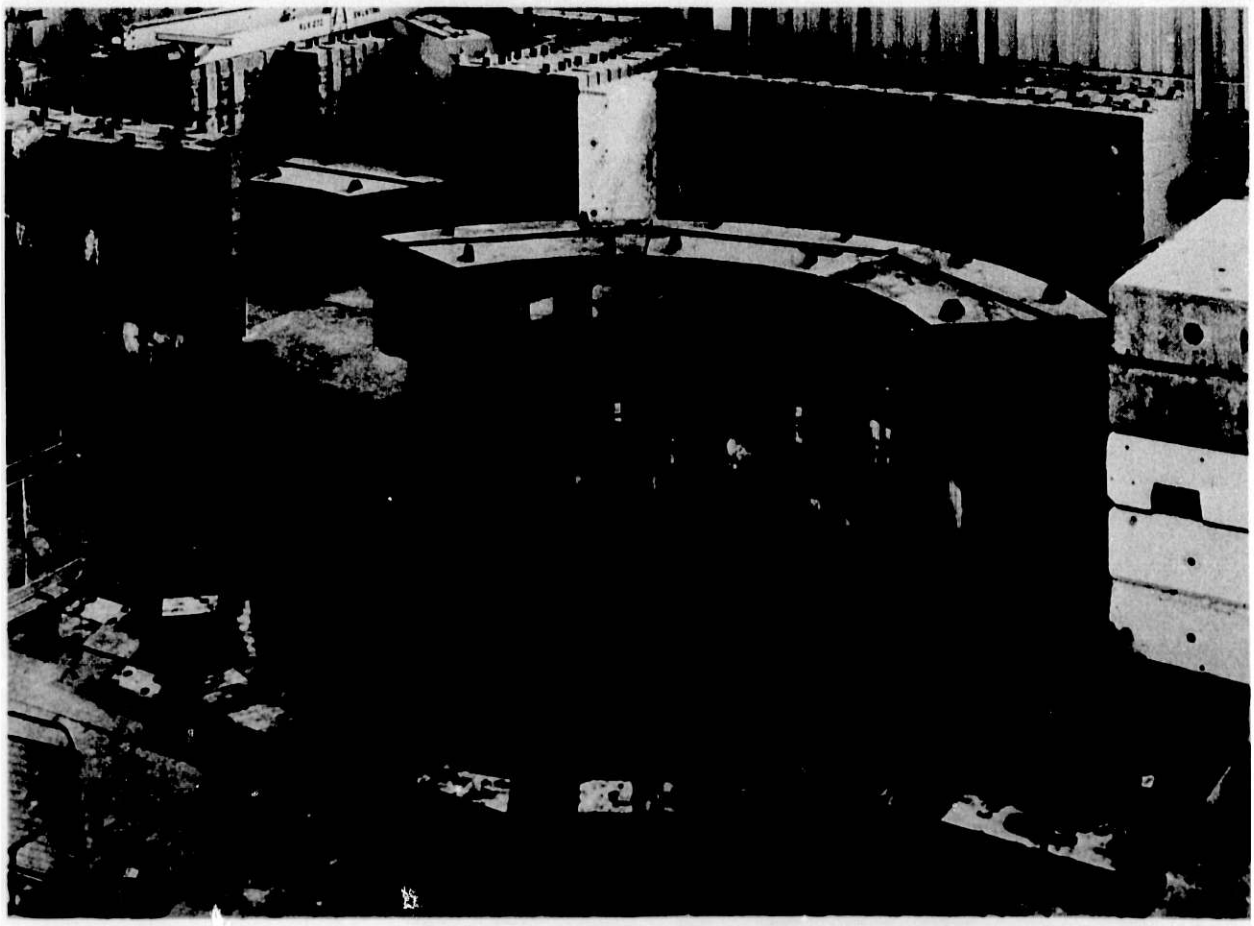

Fig. 2. Installation of first set of shielding inserts.

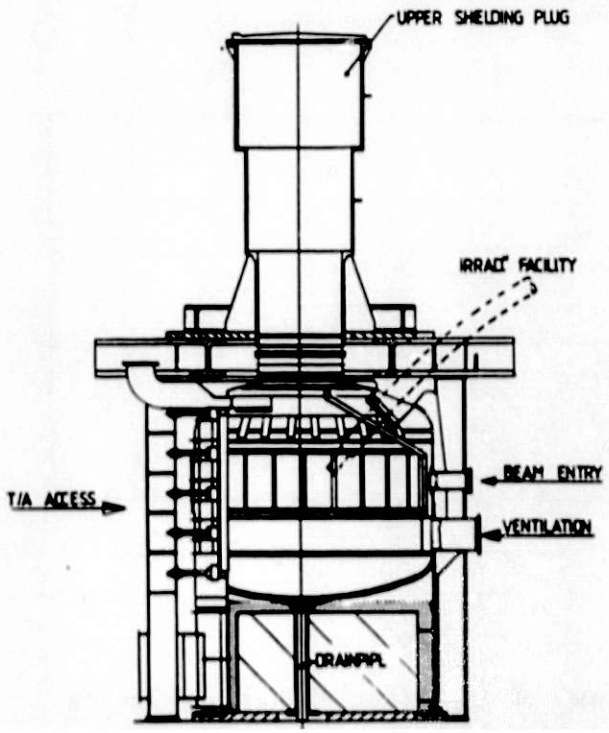

Fig. 3

Target station void vessel (vertical section)

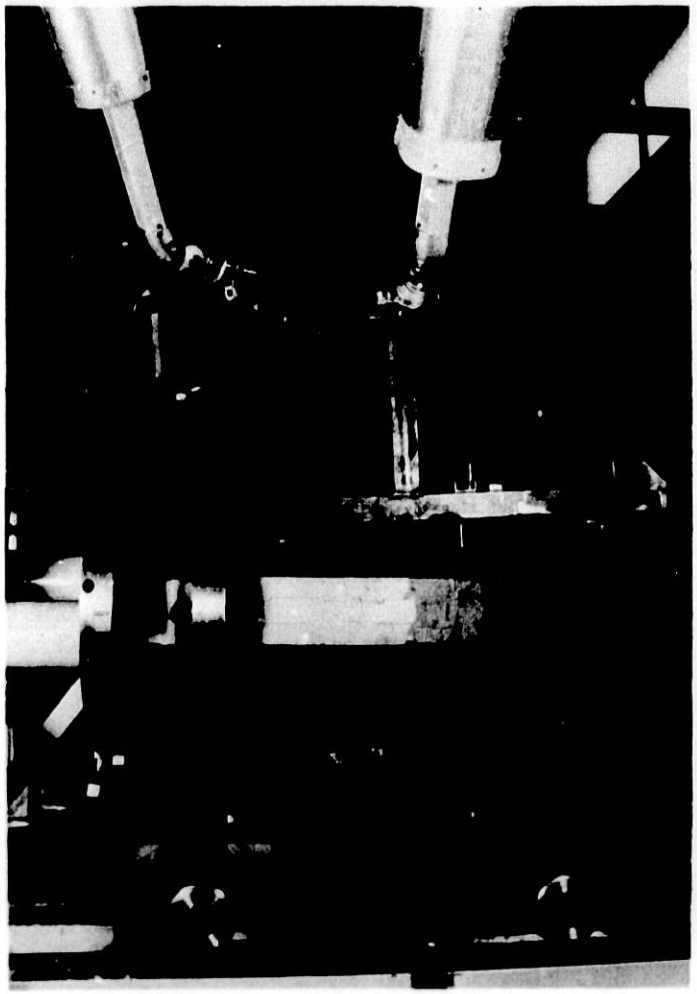

Fig. 4

Target removal operation in mock-up RHC.

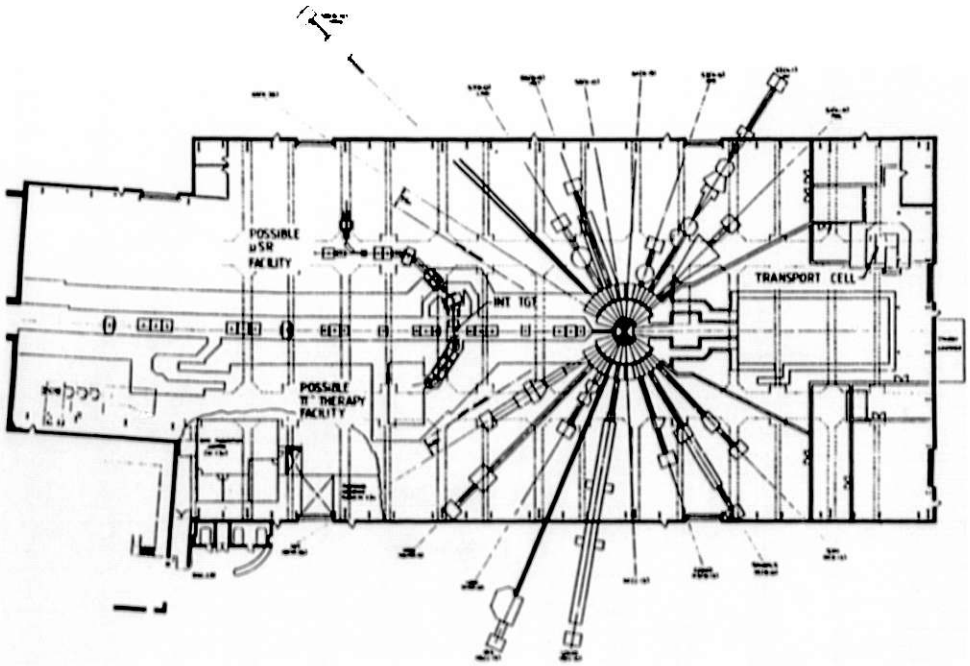

Fig. 5. General layout of experimental hall including intermediate target, pion and muon beams.

ICANS-VI

INTERNATIONAL COLLABORATION ON ADVANCED NEUTRON SOURCES

June 27 - July 2, 1982

CRYOGENIC MODERATOR DESIGN

B R Diplock
Rutherford Appleton Laboratory
Chilton, Didcot, Oxon, United Kingdom

ABSTRACT

This paper describes the present design of the two cold moderators to be built for the Spallation Neutron Source. It discusses the reasons behind a number of the design features and highlights several problem areas requiring solutions before a final design can be constructed.

ICANS-VI

INTERNATIONAL COLLABORATION ON ADVANCED NEUTRON SOURCES

June 27 - July 2, 1982

CRYOGENIC MODERATOR DESIGN

B R Diplock
Rutherford Appleton Laboratory
Chilton, Didcot, Oxon, United Kingdom

1. INTRODUCTION

This paper is intended to be a report on the current position of the two cold moderators being designed for the SNS. It is not meant to indicate how cold moderators should be designed, but rather to indicate the author's present thinking in the hope that it will stimulate discussion.

2. TARGET/MODERATOR ASSEMBLY

The position of the four moderators with respect to the target is shown in Fig 1, two ambient temperature moderators above the target, and two cryogenic moderators below. The physics requirements for the four moderators is shown in Table 1.

The forward lower moderator contains liquid methane (CH_4) at a temperature in the range 95-97K controlled to ± 1K, and the rearword lower moderator contains supercritical hydrogen (H_2) at a temperature of 25 ± 1K.

The methane is at a pressure of 4 atmospheres so that the boiling point (131.4K) is well away from the operating temperature to minimise the formation of bubbles which would give unacceptable density variations.

The hydrogen is at a pressure of 15 atmospheres, ie. above the critical pressure, to again avoid the risk of large variations in density.

3. MODERATOR VESSEL DESIGN (FIGS 2 AND 3)

Since the moderating fluids are at elevated pressures, both vessels need to be designed as pressure vessels, and a compromise needs to be reached between wall flatness and thickness. Ideally, for maximum coupling to the target, the walls should be completely flat and for minimum wall interactions, should have zero thickness.

To a first approximation, the ratio of wall radius of curvature to thickness is constant for a given stress level. It is possible, therefore, to vary one of the parameters, provided the other is varied simultaneously. Thus a flat wall requires to be thick, or alternatively, a thin wall needs a small radius of curvature.

A spherical radius of 250 mm has been chosen for both vessels coupled with a wall thickness of 3 mm for the CH_4 vessel, and 5 mm for the H_2 vessel. The material for both vessels is a 3.5% Mg aluminium alloy, since it has good mechanical properties at cryogenic temperatures and is easily welded.

The hydrogen moderator design has triple containment, the space between the outer wall and the vacuum vessel being filled with pure helium gas at a slight pressure above the outside volume. This latter volume is the target void vessel containing a minimum of 95% helium, the remainder being air. If no triple containment were provided, any leak through the vacuum vessel would allow the 5% air to cryopump on to the cold moderator vessel. Under irradiation ozone and various oxides of nitrogen would be formed which could explode spontaneously possibly causing a major failure of the moderator and target assembly. The pure helium blanket around the vacuum vessel provides a guarantee that air can never reach and cryopump on to the cold vessel.

4. HEAT LOAD

The heat load on the moderators arises from several sources. The vast majority of the energy input is due to nuclear heating within the moderating fluid itself, and this is very large compared with the heat input due to

thermal radiation. As a result, there is little penalty in deleting the thermal radiation shield on the hydrogen moderator that is customary for cryogenic vessels that operate at temperatures below 80 K. Deletion of this shield reduces both the complication and also the material in the neutron beam.

A summary of the estimated heat loads from the various sources is shown in Tables 2 and 3 together with the moderator flow rates required to keep the temperature rise to the values stated.

The magnitude of the energy deposition in the moderator due to nuclear heating causes great concern, since the accuracy of the estimate appears to be poor. Under-estimation results in too little refrigeration capacity being available with the result that the operating temperature will not be attained, and over-estimation means that large amounts of money are needlessly used to provide over-size refrigeration.

The estimates that have been made for SNS have been based on information given at ICANS V[1] and from SNQ[2]. This information has been extrapolated in the best possible way to the proton beam power of SNS.

It is very necessary for further experimental and theoretical work to be done to corroborate these estimates.

5. HEAT REMOVAL

Early calculations indicated that it was not possible to remove the heat from a static volume of moderator without unacceptable temperature variations due to the limitations of natural convection and conduction.

It was decided therefore that there remained two alternatives:-

a) Design a local circulation system for the moderator and transfer the heat via a heat exchanger to cold helium gas flowing through a long transfer line from the refrigerator.

b) Circulate the moderator through the long transfer line to the refrigerator.

Option a) reduces to a minimum the areas where hazardous gases are present, but requires a circulation fan to be placed in a high radiation environment, and the extra heat exchanger requires an operating temperature drop that reduces the operating temperature of the refrigerator.

Option b) is a simpler system but has a considerably larger region containing hazardous fluids.

After careful consideration, it was decided to opt for the second alternative, largely to avoid the problem of breakdown of the circulating fan in the high radiation area and its subsequent replacement using remote handling techniques.

6. LAYOUT OF CRYOGENIC SYSTEM

The general layout of the cold moderator system is shown in Fig 4. The target, moderator, transfer lines, refrigerators and shielding plugs are all mounted on a number of trollies making up a train. The whole assembly is designed to move horizontally on rails a distance of about 8 m to place the target assembly in the remote handling cell for maintenance work, target change, etc.

As can be seen, the transfer lines pass through the primary and secondary shielding plugs and have an overall length of about 16 m. As a result, it is very difficult, if not impossible, to design a removable transfer line without dis-assembling the shielding plugs. It is proposed therefore to design the transfer lines that are installed in the shielding plugs to be permanent and of maximum possible reliability. This means that they will have a minimum number of joints which will be fully welded and of high integrity.

To allow changes in moderator design to be accommodated, a demountable joint will be incorporated between the primary shielding plug and the moderator.

Due to the extremely intense radiation in this region, this joint will be designed for breaking and re-making using remote handling techniques, thus posing a major design problem.

As the refrigerators are mounted on a trolley in a restricted area, emphasis will be placed on using a design which is as compact and integrated as possible. It is hoped that an inert working fluid can be used, and that fans for circulating the moderating fluids will be incorporated in the refrigerators. The basic requirements for the refrigerators are shown in Table 4.

7. IRRADIATION EFFECTS ON METHANE

It is expected that a partial breakdown of the methane moderator will occur under irradiation and the products will be hydrogen gas and higher hydrocarbons, such as ethane, propane, etc.

The hydrogen gas can be removed fairly easily by a gas eliminater, but the higher hydrocarbons pose more of a problem. Some of the radiation products may have a freezing point above the operating temperature of 95 K so there is a finite risk of partial or complete blockage of the circuit, particularly in the refrigerator area.

To avoid this it is proposed to continuously remove a small percentage of the fluid, replacing it with fresh methane. It is anticipated that this will maintain the levels of the higher hydrocarbons at a sufficiently low level to avoid the risk of blockage. The amount of fluid to be removed has not yet been established, but it is hoped that it will be considerably less than 1% of the total flow.

A schematic layout of the methane circuit, Fig 5, shows this outgoing methane bleed cooling the make up gas in a regenerative heat exchanger.

8. OUTSTANDING PROBLEMS

As was said in the introduction, this paper is a report on the author's thinking on cold moderator design and it is clear that a number of problems still exist which should be resolved before the two moderators are built and commissioned. These can be summarised as follows:-

a. Temperature Variations in Moderator

The present design has a simple "in and out" flow system. Will this be good enough to maintain the temperature variation within ± 1 K, or must a more sophisticated design of flow channels be incorporated?

b. Temperature Excursions Due to Variations of Proton Beam Intensity (including On/Off transients)

What magnitude of excursions will occur and what time interval is there before temperatures settle down to within the acceptable limits?

c. Design of Remote Handled Transfer Line Joint

How simple, or difficult, will it be to design a reliable leak tight joint using remote handling techniques?

d. Risk of Methane Freezing in the Refrigerator

Is it reasonable to operate the moderator at 95 K (4.5 K above the freezing point) without the risk of local freezing in the refrigerator heat exchanger?

e. Triple Containment for H_2 Moderator

Is the risk of air cryopumping on the hydrogen moderator vessel sufficiently real to warrant incorporating a pure helium atmosphere in a triple containment?

f. Radiation Breakdown of Methane

What is the magnitude of the build-up of higher freezing point radiation products and how can they best be eliminated?

Answers to the above questions are not easy to obtain, but are necessary in order to design and build cold moderators having a high degree of reliability

and safety.

9. ACKNOWLEDGEMENTS

The author gratefully acknowledges the help of various members of the SNS Target and Utilisation Group in discussions on cold moderators, and to Rob Hambleton, Graham Toplis and Elaine Wright for producing the illustrations.

10. REFERENCES

1. N WATANABE and K BONING. "Summary of Energy Deposition and Cryogenic Equipment". Proceedings of ICANS V, Jülich, West Germany, June 1981.

2. E KARLS, K HAIN, W LEILING. "Technisches Konzept einer Kalten Neutronen Quelle für die SNQ". SNS Study Teil III, Jülich/Karlsruhe, June 1981.

TABLE 1

SNS Moderators

A	B	C	D
H_2O	CH_4	$p\text{-}H_2$	H_2O
316 K ± 1 K	95 - 97 K ± 1 K	25 K ± 1 K	316 K ± 1 K
High Intensity at expense of resolution	High Resolution slowing down spectrum	Long wavelength	(as required)
dimensions of moderator material, mm			
w 120 h 120 d 15, 30 } 45	120 115 45 (at centre)	110 120 80 (at centre)	120 120 22.5, 22.5 } 45
Poison: 0.05mm Gd. Clad	Poison: provision for future incorporation	Poison: None	Poison: 0.05 mm Gd. Clad
Decoupler: 6mm boron loaded laminate, 35% natural B_4C	Decoupler: 6mm boron loaded laminate, 35% natural B_4C	Decoupler: None	Decoupler: As 'A'
Void Liner: As for decoupler (shared with 'D')	Void Liner: As decoupler preferred (shared with 'C')	Void Liner: 1mm Cd preferred (shared with 'B')	Void Liner: As for decoupler (shared with 'A')

TABLE 2

25K MODERATOR (PARA-HYDROGEN)

Max. Dimensions:	12 cm H, 11 cm W, 8 cm D,	
Volume:	≈ 1 litre	
Heat Input:	Nuclear in H_2	454 W*
	Nuclear in Aluminium	30 W†
	Thermal into Moderator	35 W
		519 W
	Transfer line (80K→25K)	6 W
	Circulating Fan	60 W
	TOTAL REFRIGERATION	585 W

Temperature Rise Across Moderator ∿ 1.3°C
H_2 flow rate: ∿ 33g/sec. (500 cm³/sec)
H_2 pressure: 15 atm abs. (supercritical)

* based on 1.2 mW/cm³ - μA for 500 MeV beam (ref ICANS V)
† based on 2.4 W/G for aluminium and 5mA beam (ref SNQ data)

TABLE 3

95K MODERATOR (METHANE)

Max. Dimensions:	11.5 cm H, 12 cm W, 4.5 cm D.	
Volume:	≈ 0.6 litres	
Heat Input:	Nuclear in CH_4	625 W*
	Nuclear in Aluminium	13 W†
	Thermal into Moderator	26 W
		664 W
	Transfer line	60 W
	Circulating Fan	60 W
	TOTAL REFRIGERATION	784 W

Temperature Rise Across Moderator ∿ 2°C
CH_4 flow rate: ∿ 98g/sec (220 cm³/sec)
CH_4 pressure: 4 atm abs
Boiling Point: 131.4K

* based on 2.6A mW/cm³ - μA for 500 MeV beam (ref ICANS V)
† based on 2.4 W/G for aluminium and 5 mA beam (ref SNQ data)

TABLE 4

REFRIGERATORS

HYDROGEN

∿ 600 W at 25K
+ ∿ 150 W at 80K for radiation shield.

Working Fluid:	High Pressure Helium Gas.
Transfer Fluid:	Supercritical Hydrogen.
Flow Rate:	500 cm³/sec. (33g/sec)
Pipe Bore:	15 mm.
Circuit Resistance:	40 m.
Fan Power:	60 W into Transfer Fluid.

METHANE

∿ 800 W at 95K

Working Fluid:	High Pressure Helium Gas.
Transfer Fluid:	Liquid Methane.
Flow Rate:	220 cm³/sec. (98 g/sec).
Pipe Bore:	15 mm.
Circuit Resistance:	30 m.
Fan Power:	60 W into Transfer Fluid.

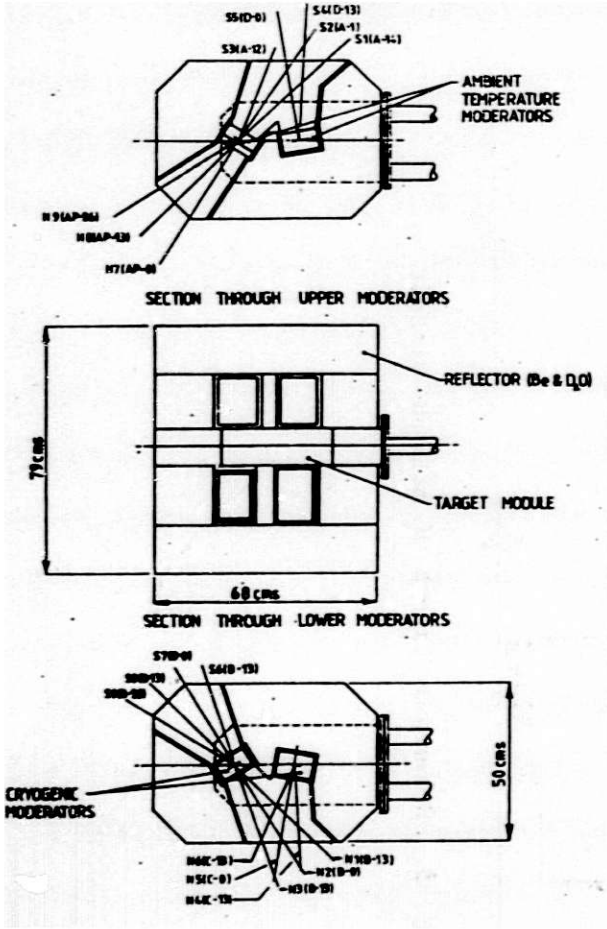

Fig. 1. Target/moderator/ reflector assembly

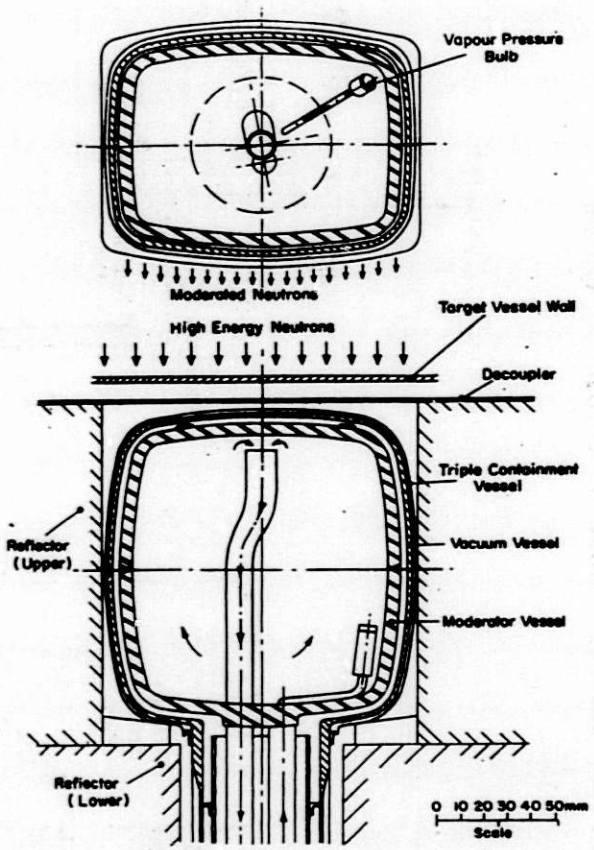

Fig. 2. Hydrogen Moderator (25°K)

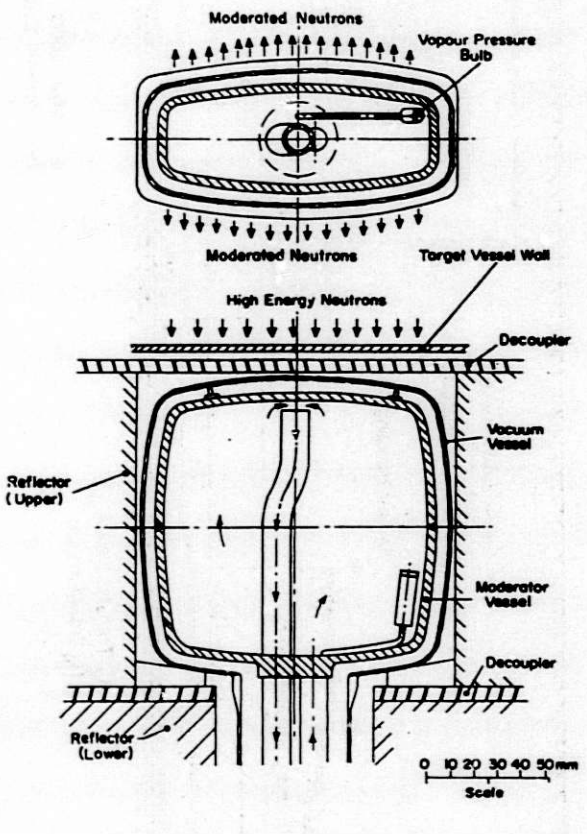

Fig. 3. Methane Moderator (95°K)

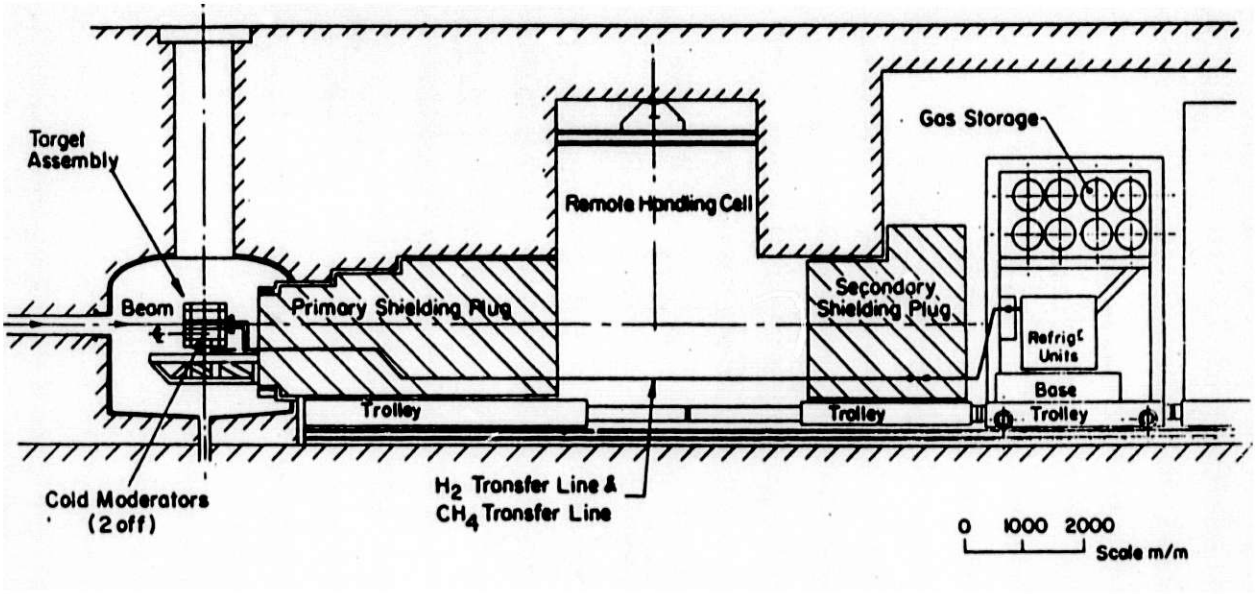

Fig. 4. General layout of cryogenic system

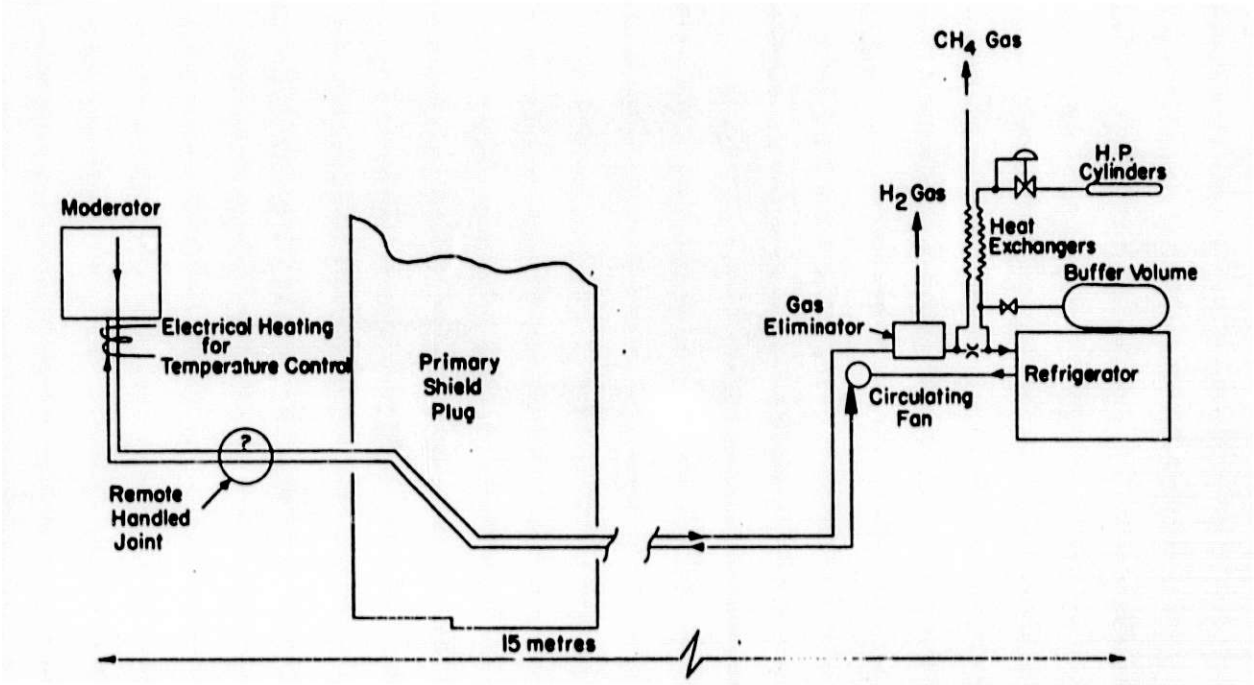

Fig. 5. Schematic layout of methane circuit

ICANS-VI

INTERNATIONAL COLLABORATION ON ADVANCED NEUTRON SOURCES

June 27 - July 2, 1982

REMOTE HANDLING EQUIPMENT FOR SNS

B H Poulten
Rutherford Appleton Laboratory
Chilton, Didcot, Oxon, United Kingdom

1. INTRODUCTION

This report gives information on the areas of the SNS facility which become highly radioactive preventing "hands-on" maintenance. Levels of activity are sufficiently high in the Target Station Area of the SNS, especially under fault conditions, to warrant reactor technology to be used in the design of the water, drainage and ventilation systems. These problems, together with the type of remote handling equipment required in the SNS are discussed.

2. DESIGN OF THE SNS FACILITY

The SNS facility is being built in the old "Nimrod" accelerator buildings, some existing "Nimrod" equipment is being utilised wherever possible in order to save costs. This fact restricts the design parameters when consideration has to be given to remote handling as neither the buildings nor the Nimrod equipment was designed with remote handling in mind.

This has not deterred the designers from considering the problems of remote handling. All equipment has been designed to cater for quick release of the water, electrical and vacuum connections. The majority of accelerator components are in modular form; a module, once disconnected, can be slid or lifted out of its position and a new modular unit fitted. The old unit is then taken to an active handling area in Hall 1 where maintenance can be undertaken. "Nimrod" magnets have also been set in modular units down the EPB line.

When designing an SNS type accelerator the ventilation, water and drainage systems have to be considered for active and remote handling. Systems have to be designed to cope with a target failure however low the probability of this type of incident occurring. If such a failure should occur, the ventilation and filters in the water circuit should be capable of being renewed by remote handling techniques. Radioactive material spilt on the floor must be able to be washed down to a recovery tank in the drainage area.

There have been very few problems in designing these basic requirements into the systems as standard Atomic Energy Codes of practice, proven over the years, have been used. The main codes of practice used, especially in the Target Station area, are listed in Table 1.

3. REMOTE HANDLING AREAS

Fig 1 shows the SNS facility with the Ion Source, pre-injector and linac in the foreground. It is envisaged that these items should be able to be maintained with normal "hands-on" maintenance. Special handling equipment has been devised to handle the steering magnets and chopper vessel installed after the linac(Ref 1). This equipment (modified fork lift trucks) will aid in keeping time spent by the maintenance crews in a high radiation area down to a minimum.

All other areas shown in figure 1 require some form of remote handling equipment to undertake maintenance tasks around the facility. They are:-

Area 1 Synchrotron Hall.
Area 2 The Extracted Proton Beam Line running from the Synchrotron Hall to the Target Station.
Area 3 The Target Station in Building R55.
Area 4 Transfer Tunnel and Cell.

4. REMOTE HANDLING EQUIPMENT

4.1 Area 1 Synchrotron Hall

As yet no firm decision has been made as to the type of equipment to purchase for work in the area. It is thought that radiation will not reach a level that will prevent "hands-on" maintenance until two years after the start-up date.

To keep radiation levels as low as possible in this area, it is proposed to encase the accelerator in a shielding wall. All electrical and water connections to the synchrotron will be outside the wall to enable "hands-on" maintenance methods to be applied, vacuum vee band clamps are to be disconnected by long rods or by over-the-wall type manipulators.

Some special components, eg. scrapers, will be handled by some form of remote handling from very early on. The main purpose of the shield wall is to minimise activation of the building itself and to contain the activity of "hot" items so allowing freer access elsewhere. The shield will be added gradually as and when needed. We must be careful that the extra time needed for access to the enclosed units does not result in greater doses to the people involved.

Long term plans are to install a mobile remote manipulator aided by remote manipulators mounted from one of the cranes. This type of equipment has been proven at LAMPF, Fermi and CERN labs. Consideration is also being given to purchase a Marauder type vehicle(Ref 2).

Cranes will be radio-controlled in this area; special techniques are being devised to determine the position of a crane to aid remote handling. So that "hands-on" maintenance can be undertaken on the cranes, they will be parked in special shielded areas when the accelerator is operating.

Viewing will be via television cameras. TV cameras are to be mounted on cranes and specially designed track vehicles(Ref 2). Lighting intensity will be as that proposed for the HEF mock-up at Los Alamos(Ref 3).

4.2 Area 2 The Extracted Proton Beam Line

This is the most difficult area of the accelerator to maintain, for not only are the radiation levels high but the area available for remote handling work is extremely restricted. Also the major part of the equipment is ex-Nimrod stock. Vacuum, electrical and water connections are to be disconnected by a mobile manipulator. The modular units are mounted on rails, once released from their supplies they are then motored down the tunnel to an area where they can be removed.

Viewing equipment will be the same as that used for Area 1 in the Synchrotron Hall.

4.3 Area 3 Target Station

The target which contains 33 kg of Uranium 238 becomes highly radioactive under irradiation by the 800 MeV 200 μA proton beam. Because of this high level of radioactivity, a specially designed remote handling cell is being installed where the target can be removed safely (see figs 2, 3 and 4). The cell has been designed using four commercial through the wall type manipulators, two either side of the target, and two standard zinc bromide windows for viewing purposes. A one tonne remotely operated crane is used for lifting purposes, entry into the cell is via the transfer tunnel and then through the floor of the cell. See fig 5.

To ensure accurate fitting of the target to the water cooling flanges and to prevent the mating flanges from being damaged, a special lifting frame for the target has been produced. The target in the lifting frame is first swung into position on the rail system with the mating flanges 150 mm apart, the target is then pushed forward on a small trolley. Alignment, if required, is achieved by using the alignment screws on the lifting frame.

The target is supplied to the cell in a vertical mode and is stored after irradiation in storage wells in the same position.

In order to turn the target into the horizontal position (and back to vertical) a special turning frame has been designed.

The flanges are tightened by a pneumatic nut runner which is supported by a balancer mounted on a swinging jib.

There are three storage wells in the cell, each target is stored in a well for approximately one year before its removal. The storage wells are fitted with a separate cooling circuit to remove the decay heating in the targets. Before a target is removed from its working position, the storage well cooling circuit is coupled to a secondary cooling circuit of the target. Whilst the target is being moved and stored, the target is cooled at all times.

The reflector and cold moderators have yet to be finalised in design(Ref 4) but it is envisaged that special handling equipment will be made to help maintain the moderators in service. To give adequate viewing of these components, TV cameras are being placed in the cell.

4.4 Area 4 Transfer Tunnel and Transport Cell

The Transport Cell is similar to the Remote Handling Cell but contains only two sets of through-the-wall manipulators. Facilities for installing zinc bromide windows will be made but they will only be installed if it is proven that TV viewing is not adequate. The main function of the Transport Cell is to handle the target into its Transport Flask but it will also be used as a general remote handling workshop.

Radioactive material is received from the remote handling cell via the transfer tunnel and through the cell floor. The material is then placed in suitable radioactive containers and dispatched through a large shielded door at floor level.

To transport the radioactive material between the remote handling cell and the transport cell, a remotely operated transport trolley has been designed. The transport trolley has a cask with 100 mm lead walls to carry the active

material. This thickness of lead gives sufficient protection for a person to work hands on for a few minutes on the transport trolley in the event of a breakdown. Viewing of the transport trolley in the tunnel will be undertaken with TV cameras.

5. TARGET FLANGE DESIGN

Several flange designs have been tried in the mock-up remote handling cell. See figs 6, 7, 8 and 9. The Vee Clamp performed well but it cannot be incorporated into the design as it fouled the cold moderator system. At least 10 clamps would be required to obtain the correct closing force on the seal. The lever clamp assembly and the standard nut and bolt were not as easily fitted with remote manipulators as the other two systems.

The swing or eyebolt gave some problems in the cell but worked well once the spring loaded ball was fitted. This enabled the bolt to be placed in the required position whilst the runner was fitted. A firm decision has been taken to use this bolting arrangement.

6. DRAINAGE AND VENTILATION SYSTEMS

If a target failure occurs all the activity is contained within the target station area. To ensure complete encapsulation, the drainage and ventilation systems are being designed to the latest AECP standards.

The drainage system, see fig 10 has been designed to be double sealed throughout the complex. Where pipework goes outside the complex, the pipework is double contained. All inner pipework is stainless steel but to reduce costs the outer pipes may be painted or zinc coated mild steel if they are in a rust free area.

The Synchrotron Room had a drainage and ventilation system installed for Nimrod. The low level active drainage network has been modified and checked. Extra filters are being added to the ventilation plant to ensure that the

system is suitable for the SNS.

For the Target Station area a complete new ventilation system is being designed, see fig 11. Several important factors have had to be taken into consideration. They are:

a. The activated air in the target shutter vessels.
b. The helium in the target void vessel.
c. The air in the remote handling cell, the services area, the transfer tunnel and transport cell.
d. The hydrogen and methane plants in the services area.

The major activity in the shutter void vessel is ^{41}Ar (half life 1.8 hr), ^{11}C (half life 20.5 min) and ^{13}N (half life 10 min), see Ref 5. Air from the shutter void vessel is routed via the EPB line and then the Synchrotron Room, the air takes two hours to pass this route thus ensuring at least one half life decay period has occurred. The air from the shutter void vessel is also used for removing 13 kW of heat from the shielding and target void vessel, this heat is removed before it is sent down the EPB line.

To keep a safe atmosphere in the Target Void Vessel, because of the presence of hydrogen and methane, the target void vessel is run at a higher pressure than the surrounding ventilation systems, ie. the target shutter vessels and the remote handling cell. However, to ensure no activity ever escapes from the target void vessel to the surrounding atmosphere, the target void vessel is run at a negative atmospheric pressure. In operation, the target shutter vessel and the remote handling cell will be at -55 mm WG and the target void vessel at -45 mm WG.

The filters in the Target Void Vessel will be the new Harwell circular type, see Ref 6.

The air systems in the remote handling cell and the services area all have HEPA filters (99.95% Eff) to remove particles. Charcoal filters are fitted to remove ^{131}I.

The hydrogen and methane plant ventilation systems have sufficient capacity to remove the total air volume in the plant area in one minute.

7. CONCLUSION

When designing a complex such as the SNS, certain areas of the plant are closer to reactor technology than accelerator technology and have to be designed accordingly. Although this increases the design load, no new technology is required as drainage, ventilation and remote handling techniques for highly radioactive components are well known in the nuclear industry.

8. ACKNOWLEDGEMENTS

The author gratefully acknowledges John Hogston who has carried out design work both on the remote handling cell and the drainage system, Graham Toplis for producing the illustrations and Claire Cheesmore for typing the report.

REFERENCES

Ref 1 70 MeV Injector Component Handling in the HEDS Tunnel. P Gregory. Internal SNS Report No. SNS/AMM/P8/81.

Ref 2 Manufactured by Morfax Ltd, Mitcham, England.

Ref 3 HEF Mock-up at Los Alamos. Paper No. LA-UK-82-1393.

Ref 4 Cryogenic Moderator Design. B R Diplock. This conference.

Ref 5 Activation of Air in Shutter Vessels. T Broome. Internal SNS Report No. SNS/ENV/M6/80 Amend 1.

Ref 6 Development of Filters and Housing for Active Plant. S Hackney and R Platt. AERE UKAEA. 17 DOE Nuclear Air Cleaning Conference.

Table 1. Summary of the UKAEA Atomic Energy Codes of Practice & Standards used in the Design, Construction and Testing of Components of the Remote Handling and Transport Cells

COMPONENT	SUBJECT OF CONTROL	CODE OF PRACTICE OR STANDARD
Ventilation Systems	Design, construction and testing	AECP 1054
Drainage	" " "	AECP 1058
Interior lighting	" " "	AECP 1019
Interior painting	" " "	AECP 1002
Lifting equipment	" " "	AECP 17
Electrical equipment	" " "	AECP 1039
Compressed air systems	" " "	AECP 1033
Zinc Bromide windows (optical grade)	" " "	AESS 10886
Fire prevention	" " "	AECP(W) 152
Coatings for decontamination	" " "	AECP 1057

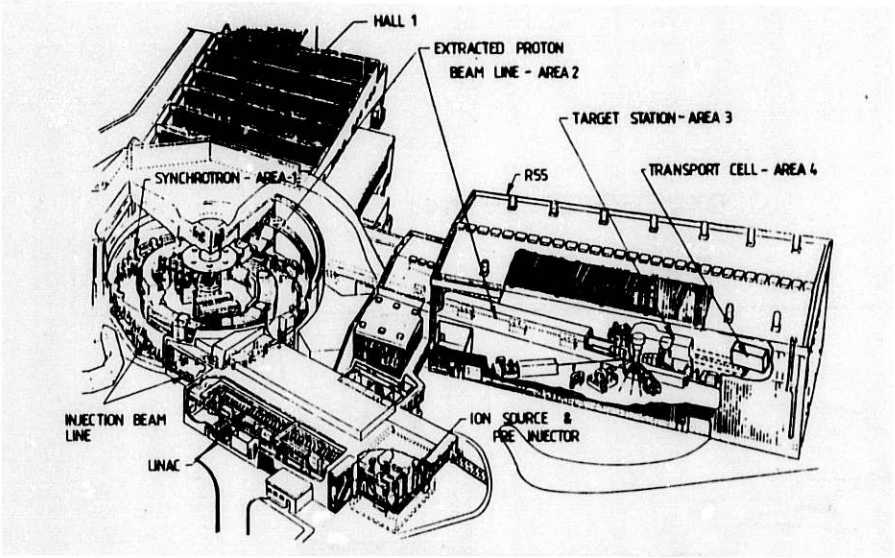

Fig. 1. The overall SNS facility

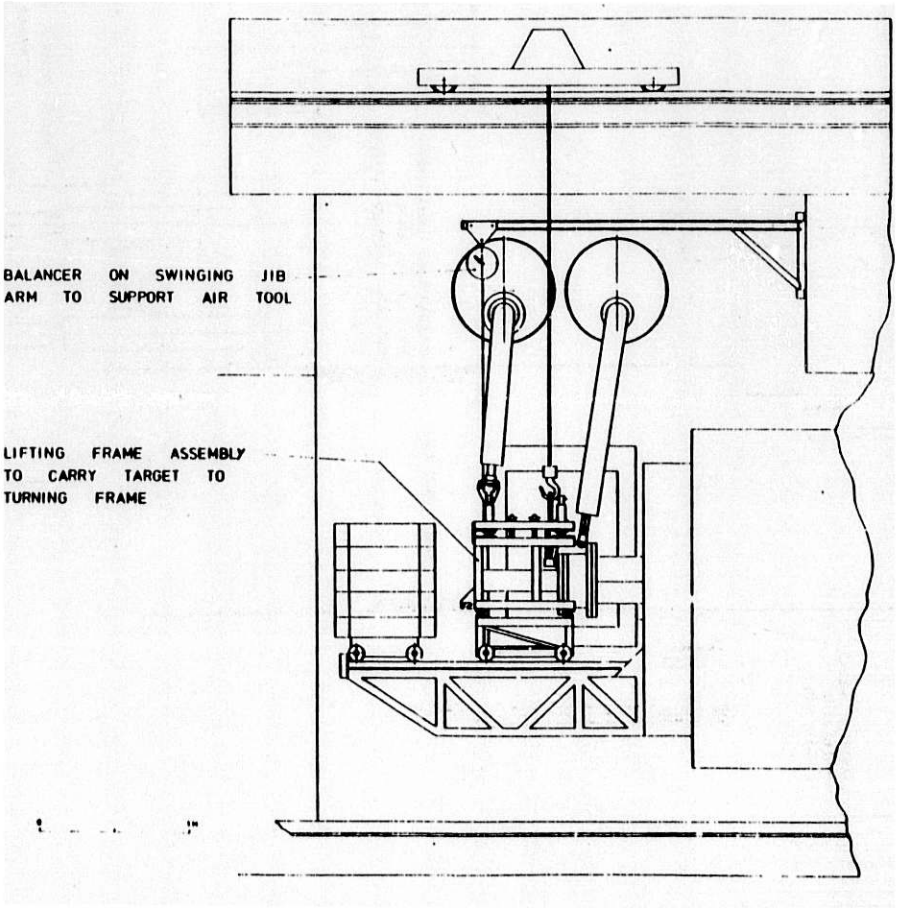

Fig. 2. Remote handling cell (side view)

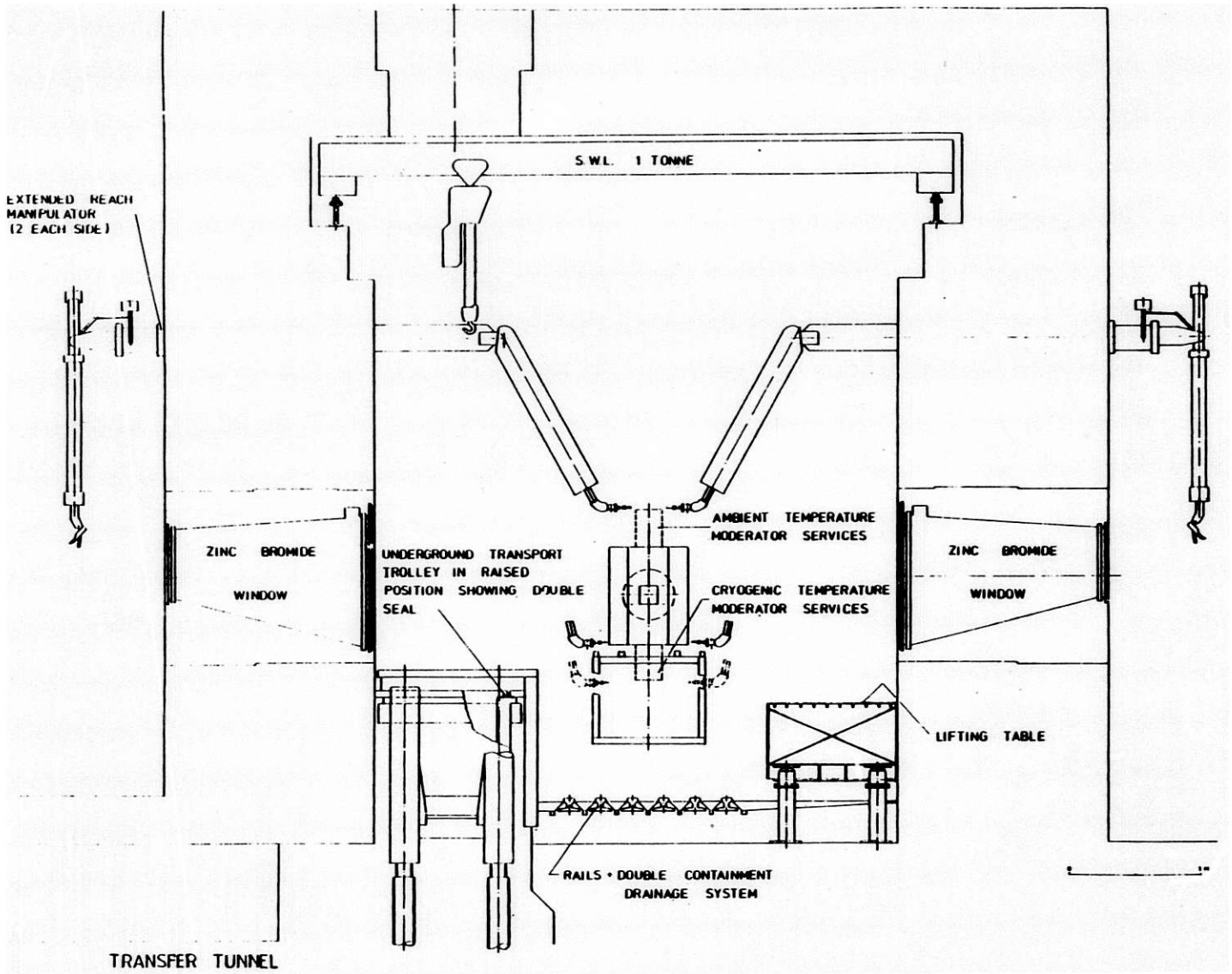

Fig. 3. SNS remote handling cell (end view)

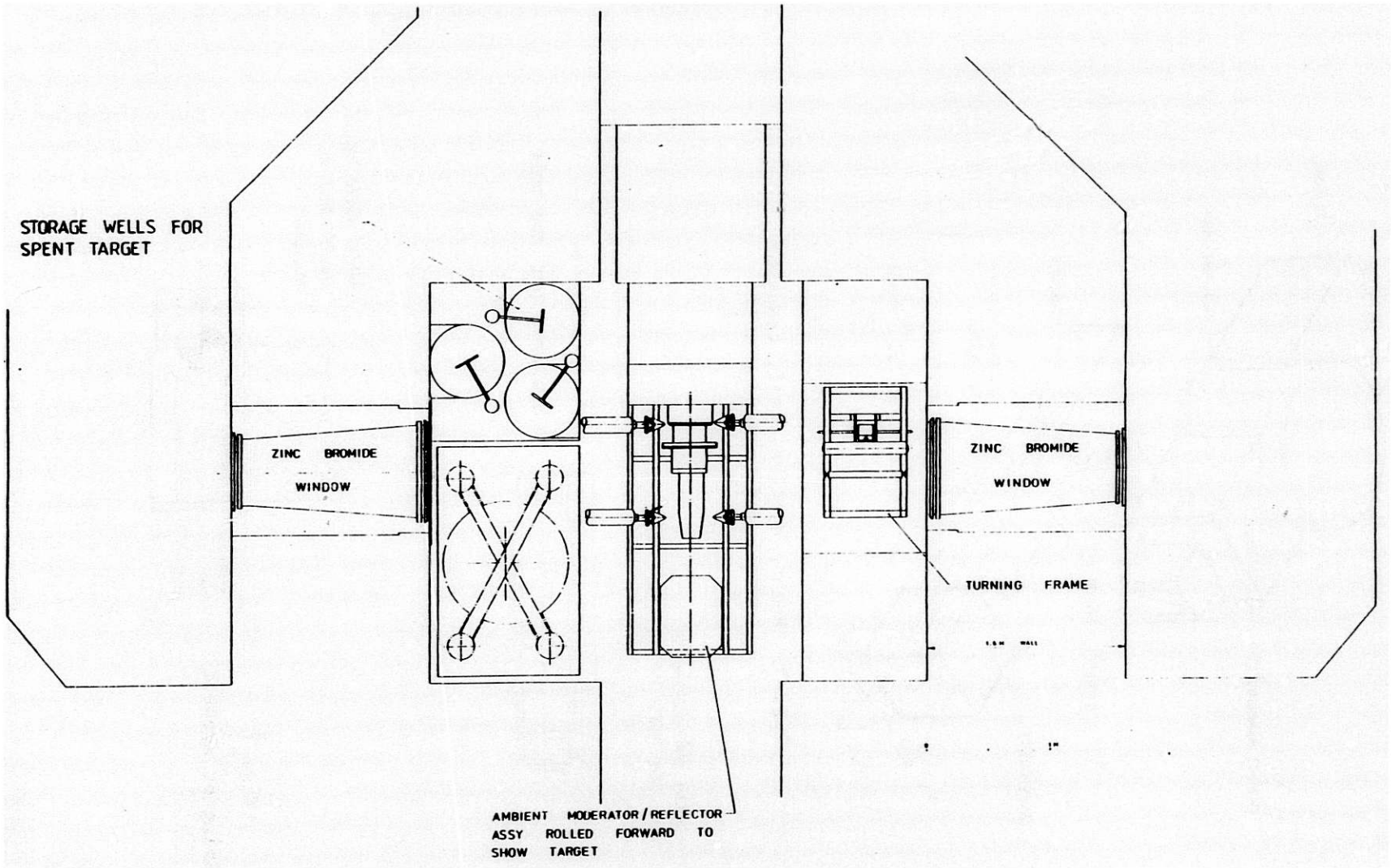

Fig. 4. SNS remote handling cell (plan view)

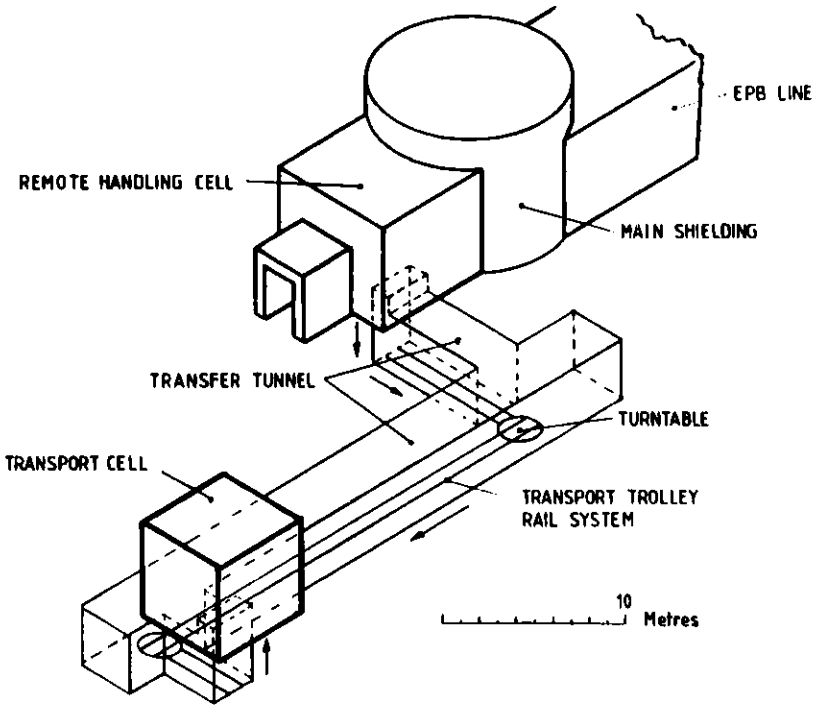

Fig. 5. Remote handling cell, transfer tunnel, and transport cell.

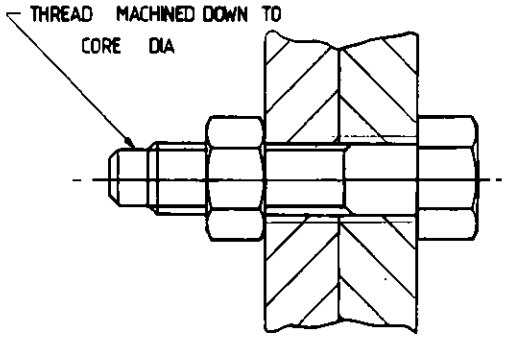

Fig. 6
Standard nut and bolt

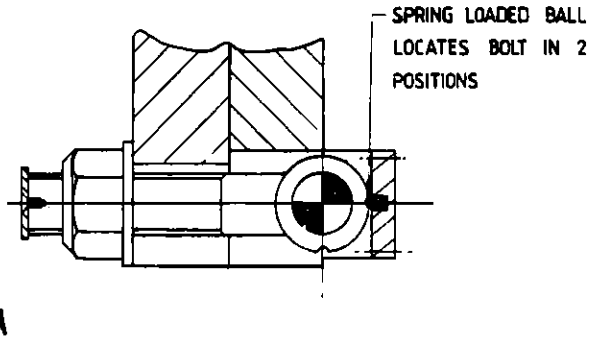

Fig. 7
Swing or eyebolt

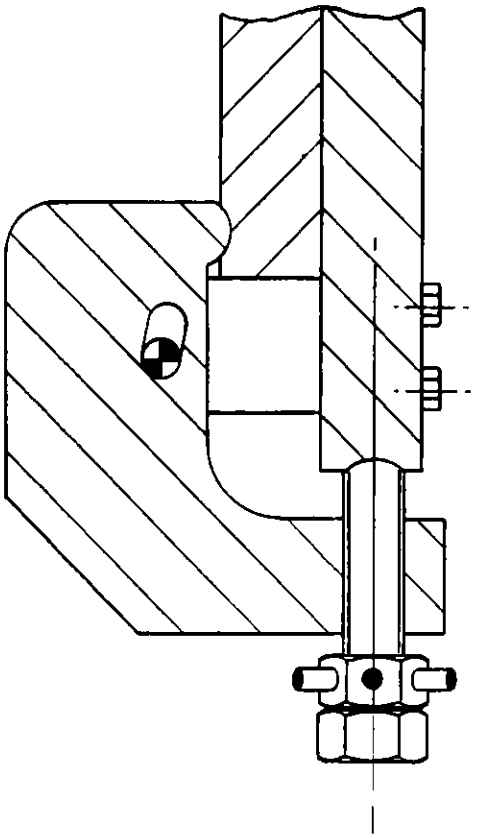

Fig. 8
Lever clamp assembly

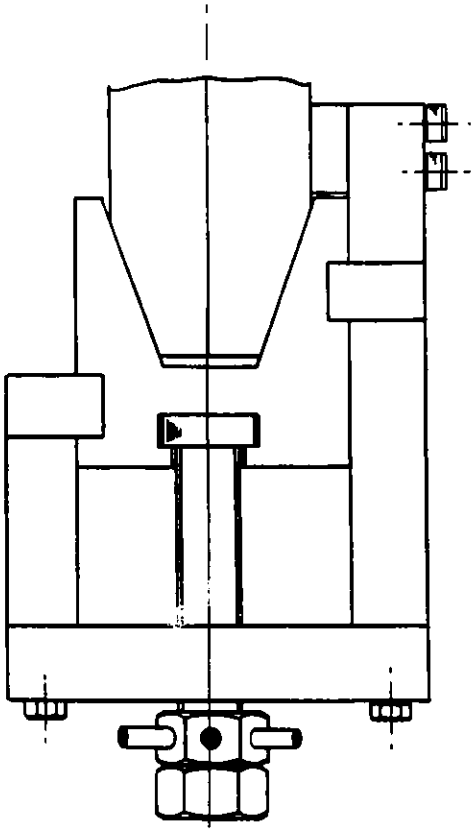

Fig. 9
Vee clamp

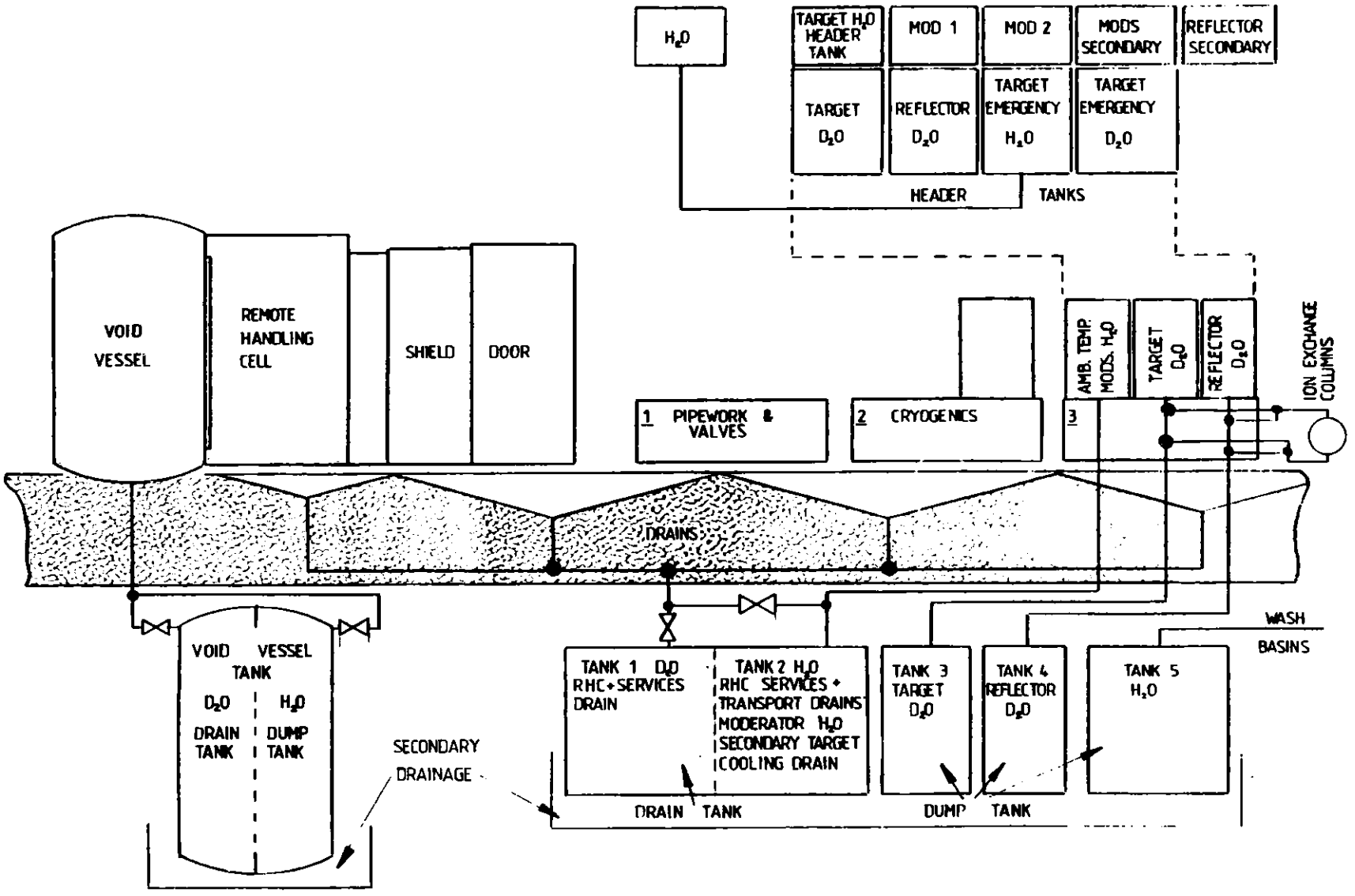

Fig. 10. Drainage system for SNS target station

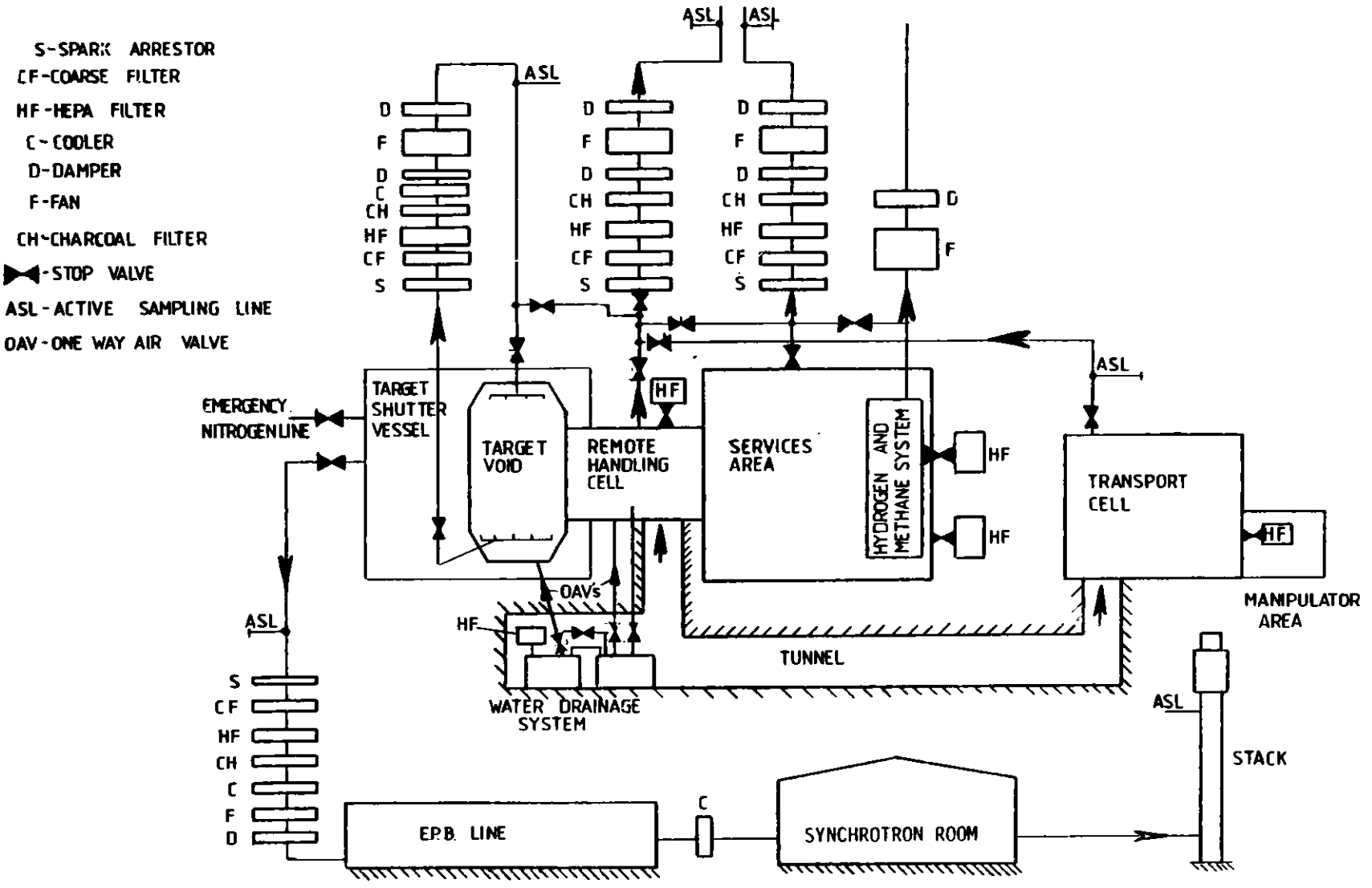

Fig. 11. Ventilation system for target station

ICANS-VI

INTERNATIONAL COLLABORATION ON ADVANCED NEUTRON SOURCES

June 27 - July 2, 1982

THERMOFLUID DYNAMICS OF THE L[illegible] LEAD-BISMUTH TARGET FOR THE SPALLATION NE[illegible]URCE AT SIN

Y. Takeda
Schweizerisches Institut für Nuklearforschung
CH-5234 Villigen, Switzerland

ABSTRACT

Natural convection of liquid Lead-Bismuth Eutectics (LBE) has been numerically simulated and thermal-fluid behaviours of a target were studied. The calculation was based on the Boussinesq approximation and made for a simple geometry of a vertical cylindrical container with a distributed internal heat generation. Studies have been made of the effects of the target height, beam power and adiabatic side wall. They showed that the natural convection is effective for transporting heat and the vertical cylindrical target is practicable.

THERMOFLUID DYNAMICS OF THE LIQUID LEAD-BISMUTH TARGET FOR THE SPALLATION NEUTRON SOURCE AT SIN

Y. Takeda
Schweizerisches Institut für Nuklearforschung
CH-5234 Villigen, Switzerland

1. INTRODUCTION

The spallation neutron source at SIN is planning to use Lead-Bismuth Eutectics (LBE) in a liquid state as a target material [1]. Since the proton beam power is quite high (MW level), the choice of a liquid target seems attractive from the standpoint of heat removal. Furthermore it is planned to have a vertical target with beam entry from the bottom. The principle of this idea is to utilize the natural convection of LBE to transport the heat deposited by the beam in the lower part of the target, to a heat exchanger at the top. In spite of the attractions of a liquid target for high current beams from accelerators, hydrodynamic investigations are not plentiful. In the German project [2], pumped liquid metal was an alternative candidate for the target, and experimental and theoretical investigations were carried out. At TRIUMF, the lead target is in a partially molten state during operation. Calculations including natural convection were done [3] for this horizontal cylindrical target, and this seems to be the only thermofluid dynamical analysis of natural convection in a liquid target.

The principal difficulties of the problem are as follows:

(i) natural convection is in a completely confined space which allows no use of boundary layer theory,
(ii) the very low Prandtl number of liquid metal,
(iii) a difficulty in defining the Grashof number because of the distributed internal heat generation,
(iv) a fairly large aspect ratio (height/radius) which may lead to hydrodynamic instability,
(v) high power deposition.

A further result of the difficulties is that they can lead the flow regime into the turbulent region. For turbulent flow, it is very difficult to obtain an analytical prediction for an optimal design of the target. There exist a very limited number of reports of experimental work for turbulent natural convection of liquid metal.

In the present work, the numerical simulation was performed for natural convection of LBE in a vertical cylindrical container of finite length, in order to examine the general thermofluid behaviours.

2. CALCULATIONAL METHOD

2.1 Assumptions

In formulating the problem, the following assumptions were adopted:

(i) All the physical phenomena are axis-symmetric, and the beam profile does not change during irradiation, so that the problem is treated in a two-dimensional system.
(ii) The flow is laminar.
(iii) The Boussinesq approximation is valid, that is, all the physical properties are constant except for those affecting the buoyancy force.
(iv) The LBE is always molten so as to avoid the moving boundary problem.

The coordinate system used is shown in Fig. 1. Only the half plane of the vertical cross section is shown.

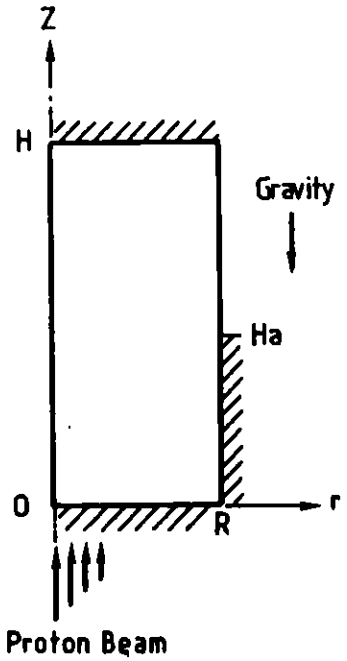

Fig. 1
Schematic of target and coordinate system.

2.2 Basic equations

The basic equations are the coupled partial differential equations of continuity, momentum and energy. However, in this work, these were transformed to equations of vorticity by applying the ROT-operation and introducing the stream function. They are then expressed in dimensionless form by normalization (see appendix) to give:

$$\frac{\partial\Omega}{\partial t} + \gamma V_r \frac{\partial\Omega}{\partial r} + \gamma V_z \frac{\partial\Omega}{\partial z} - \gamma V_r \frac{\Omega}{r}$$

$$= Pr \left[-\gamma \frac{\Omega}{r^2} + \frac{\gamma}{r}\frac{\partial\Omega}{\partial r} + \gamma \frac{\partial^2\Omega}{\partial r^2} + \frac{1}{\gamma}\frac{\partial^2\Omega}{\partial z^2}\right] - Pr^2 Gr \frac{\partial T}{\partial r} \qquad (1)$$

$$\frac{\partial T}{\partial t} + \gamma V_r \frac{\partial T}{\partial r} + \gamma V_z \frac{\partial T}{\partial z} = \frac{\gamma}{r}\frac{\partial T}{\partial r} + \gamma \frac{\partial^2 T}{\partial r^2} + \frac{1}{\gamma}\frac{\partial^2 T}{\partial z^2} + \Phi \qquad (2)$$

$$\Omega = \frac{\gamma^2}{r^2}\frac{\partial\Psi}{\partial r} - \frac{\gamma^2}{r}\frac{\partial^2\Psi}{\partial r^2} - \frac{1}{r}\frac{\partial^2\Psi}{\partial z^2} \qquad (3)$$

where Pr is the Prandtl number ($= \nu/\alpha$), and Gr the Grashof number ($= g\beta T_o L^2 d/\nu^2$).

The stream function is related to the fluid velocities by

$$V_z = \frac{1}{r}\frac{\partial\Psi}{\partial r} \quad , \qquad V_r = -\frac{1}{r}\frac{\partial\Psi}{\partial z} \qquad (4)$$

Through this relationship the continuity equation is automatically satisfied.

2.3 Boundary and initial conditions

Boundary conditions for the stream function are taken as

$$\Psi = \frac{\partial \Psi}{\partial z} = 0 \quad ; z = 0\&1 \quad 0 < r < 1 \tag{5}$$

$$\Psi = \frac{\partial \Psi}{\partial \Psi} = 0 \quad ; r = 0\&1 \quad 0 < z < 1 \tag{6}$$

$$\frac{\partial T}{\partial r} = 0 \quad ; r = 0 \quad 0 < z < 1$$
$$r = 1 \quad 0 < z < Ha \tag{7}$$

and the thermal boundary conditions are

$$T = 0 \quad ; r = 1 \quad Ha < z < 1 \tag{8}$$

$$\frac{\partial T}{\partial z} = 0 \quad ; z = 0\&1 \quad 0 < r < 1 \tag{9}$$

where Ha is the length of the adiabatic surface as defined in Fig. 1.

Since vorticity boundary conditions cannot be given, they are approximated with the values at the next inside grid points and corrected by iteration.

Initial conditions were determined from the assumption of having a quiescent liquid with a uniform temperature (the melting temperature of LBE)

$$V_r = V_z = \Psi = \Omega = T = 0 \text{ at } t = 0 \tag{10}$$

Most of the calculations were carried out with a boundary condition of the full length of the side wall at a constant temperature (conducting wall, Ha = 0).

2.4 Profile of heat generation

As the driving force for the fluid motion of the target liquid is only the buoyancy force due to the internal heat generation, and no external temperature difference is applied to the system, the

profile of heat generation needs to be approximated fairly well. For these calculations the empirical formula for the volumetric energy deposition [4] was used. The formula is expressed as:

$$q(r,z) = \frac{5.7 \times 10^6 \times I}{(\sigma_o + 0.04\ z)^2}\ e^{-\left(\frac{r}{\sigma_o + 0.04\ z}\right)^2}\ e^{-\frac{z}{30}} \qquad (11)$$

where r and z are position variables in cm unit, I beam current in Ampères and σ_o is a parameter which was determined experimentally as 1.6 cm.

2.5 Numerical calculation

For solving the time dependent equations, (1) to (3) above, the finite difference technique was used. The normal centred differencing formula was mainly used, but the so-called upwind difference scheme was used for the inertial terms in equations (1) and (2). The vorticity and temperature equations were solved by the Alternating Directional Implicit (ADI) method and the stream function equation by the Successive Over Relaxation method (SOR). The schematic flow diagram for the calculational procedure is illustrated in Fig. 2. Since all the boundary values cannot be given at some time level simultaneously, the values of results at the preceding time level were used; to correct this approximation, some internal iterations were carried out (II1 to II3 in Fig. 2). Furthermore, to take account of the nonlinearity and coupling of the basic equations, another iteration (II4) was performed. These internal iterations were terminated when maximum changes of values decreased to 0.1 %. The total iteration with respect to time was terminated when the maximum change of stream function decreased to 0.1 % of the value at the preceding time level.

Since the limit of numerical stability of the ADI method has not yet been formulated in a general manner, the time step cannot be determined from a stability condition. From the author's experiences for the present problem, it was found to be quite dependent on the beam power; the higher the beam power, the smaller the time mesh required, otherwise numerical divergence occurred. The time step was kept constant in any one computational run and varied from 1×10^{-5} to 1×10^{-6} (dimensionless).

The number of grid points also cannot be determined from stability analysis. For some cases of target height and beam current, there was no divergence of computation but some apparently false physical solution were obtained. In order to determine the number of grid points several trial computations were performed for the highest beam power and the largest aspect ratio, using grid points of 20 x 20, 40 x 40 and 80 x 80. The results showed sufficiently similar profiles of transient temperature

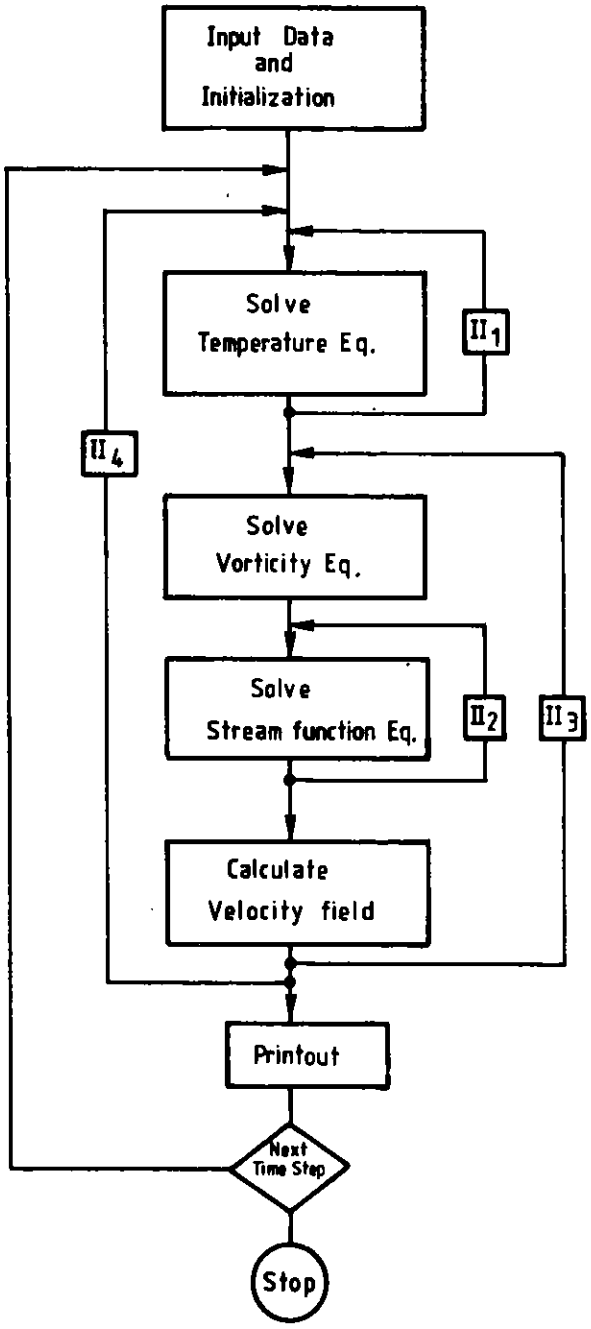

Fig. 2
Flow diagram of numerical calculation

field and stream lines for 40 x 40 and 80 x 80, that 40 x 40 was used in the series of computations.

All the computations were carried out on the SIN VAX-11 computer.

3. RESULTS AND DISCUSSIONS

For most of the computations, the following values are common: a target radius of 15 cm and a beam current of 0.1 mA. The majority of the results are presented as contour maps of stream function and temperature. The contour lines of stream function represent the path of flow of an elemental fluid particle. The outermost contour for both temperature and stream function, correspond to the lowest values (= dT and dΨ), and these values are also used as the interval between the lines. Explicit values of dT and dΨ are given in the figure captions.

3.1 Transient behaviours

3.1.1 Streamline field and temperature profile

Figure 3 shows the transient temperature distributions and streamline fields for a 150 cm high target with side wall cooling.

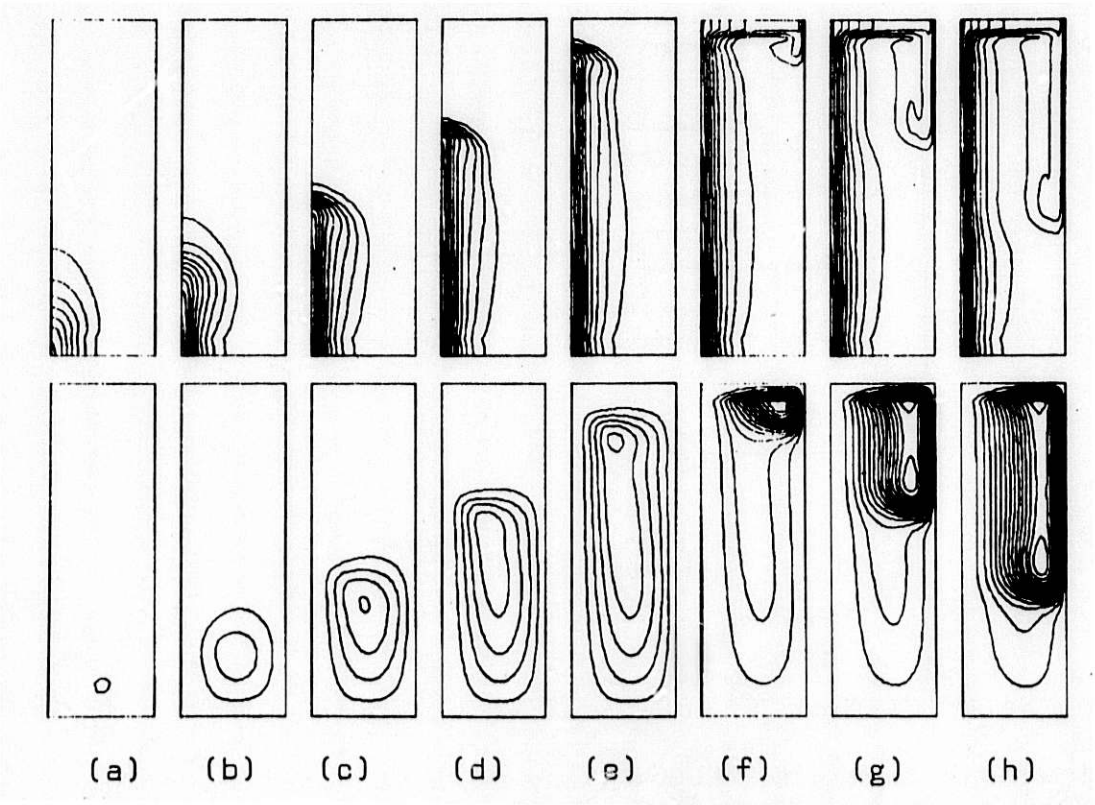

Fig. 3
Transient behaviour for a 150 cm high target. Beam current is 0.1 mA. Contour lines are for dT = 0.05 (6.3 ^{o}C) for temperature in (a) to (m), 0.025 (3.1 ^{o}C) in (n) to (p), and with dΨ = 10 for streamline. (a) is at 1.2×10^{-4} (3.8 sec) and the time interval is 8×10^{-5} (2.5 sec).

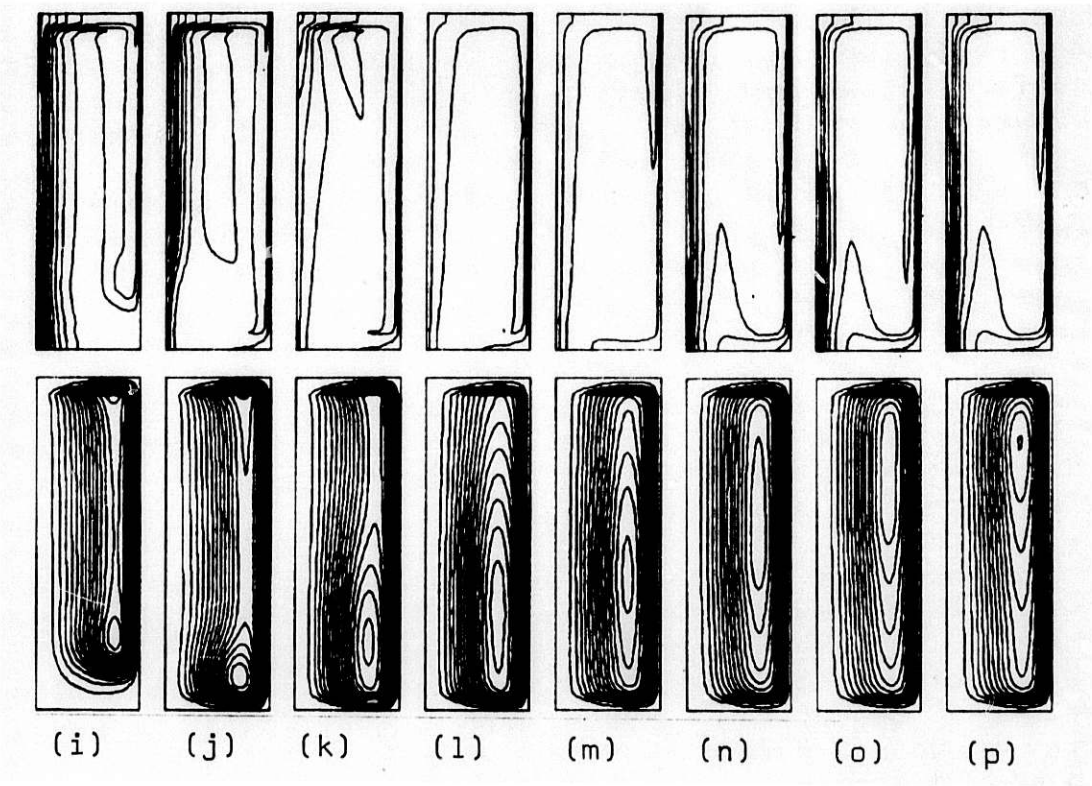

Fig. 3 (continued)
(i) is at 7.6×10^{-4} (24.2 sec) and interval is also 8×10^{-5} (2.5 sec).

It shows clearly the process of generation and growth of circulation (a - h). At (a - b), a clockwise circulation starts in the lower portion of the container where most of the energy is deposited. As time proceeds, the circulation grows (the number of contour lines increases) and the centre of the roll rises. When this roll reaches the top, it grows rapidly. A second roll appears (g), grows and moves downwards elongating the total circulation (g - j). The coexistence of these two rolls lasts until the second reaches the bottom, when they both merge into the total circulation (j - m), giving a stable laminar flow by time step (n).

The distribution of temperature follows the above mentioned changes of streamline fields. At first the flow is so small that the temperature distribution is similar to the profile of internal heat generation. But at (b), the bottom part of the distribution shrinks, since cold liquid flows inward due to the circulation. As time proceeds, this shrinkage spreads upwards, following the rise of the roll, resulting in a vertical hot column around the centre line (vertical and parallel contour lines). The presence of a very weak secondary roll leads to the slight distortion of the temperature distribution (c - e).

A stronger effect can be seen from the first roll in figures (f) - (h). At the top of the container the strong local circulation makes the isothermal lines horizontal transporting heat from the central region to the periphery. Following the downward motion of the second roll, the hot liquid column (which is partially cooled at the surface) flows down, leaving the intermediate region (core) between the central hot column and surface at low temperature (g - i). When the second roll reaches the bottom (j), this core becomes an island of lower temperature. During the time when the two rolls are merging and the total circulation is growing, the central hot column is washed away and the position of the temperature maximum moves from the bottom centre to the top centre (j - l), and a relatively uniform temperature distribution is formed (l - m). However, once the total circulation is established, the heat is accumulated around the centre line and forms the central hot column again (n - p). The maximum temperature is also at the bottom centre. The high temperature gradient due to the side-wall cooling can also be seen.

This general aspect of temperature profile and streamline field agrees well with the experimental and numerical investigation by Torrance et al. [5]. Their work was done for natural convection of air in a cylindrical container of unit aspect ratio (but with local heating at the bottom surface) and, in particular, showed the "vortex shedding" during the transient phase for a high Grashof number system.

3.1.2 Time change of temperature

Figure 4 shows the change of temperature with time for a 150 cm high target. T_{max} is the maximum temperature in the system while the others are at fixed points. The total length of time is 1.68×10^{-3}. The maximum temperature increases very quickly to about 75 ^{o}C above the melting temperature. It then drops, reaching a stable value of 26 ^{o}C after some weak oscillations. The position of the maximum temperature is mainly located at the bottom centre of the target, but during the drop, it moves up the centre line.

Temperatures at the fixed points show a similar behaviour to that of the maximum; an increase followed by a decrease with a somewhat flat "plateau" inbetween. The starting time of the temperature increase is earlier and its "plateau" value is larger, the closer the point is to the bottom centre. This behaviour of the temperature can be understood as follows: At first, the hot fluid heated by the beam flows up and increases the temperature at these points, and then, as the flow is being established cold fluid is carried in from the peripheral regions to decrease the temperature. For the lower portion of the target, the small overshoot at the start of the "plateau" might be caused by the devel-

opment of the flow; this indicates that it may be possible to monitor the degree of development of the main flow by observing the temperature change at points in the lower part of the target.

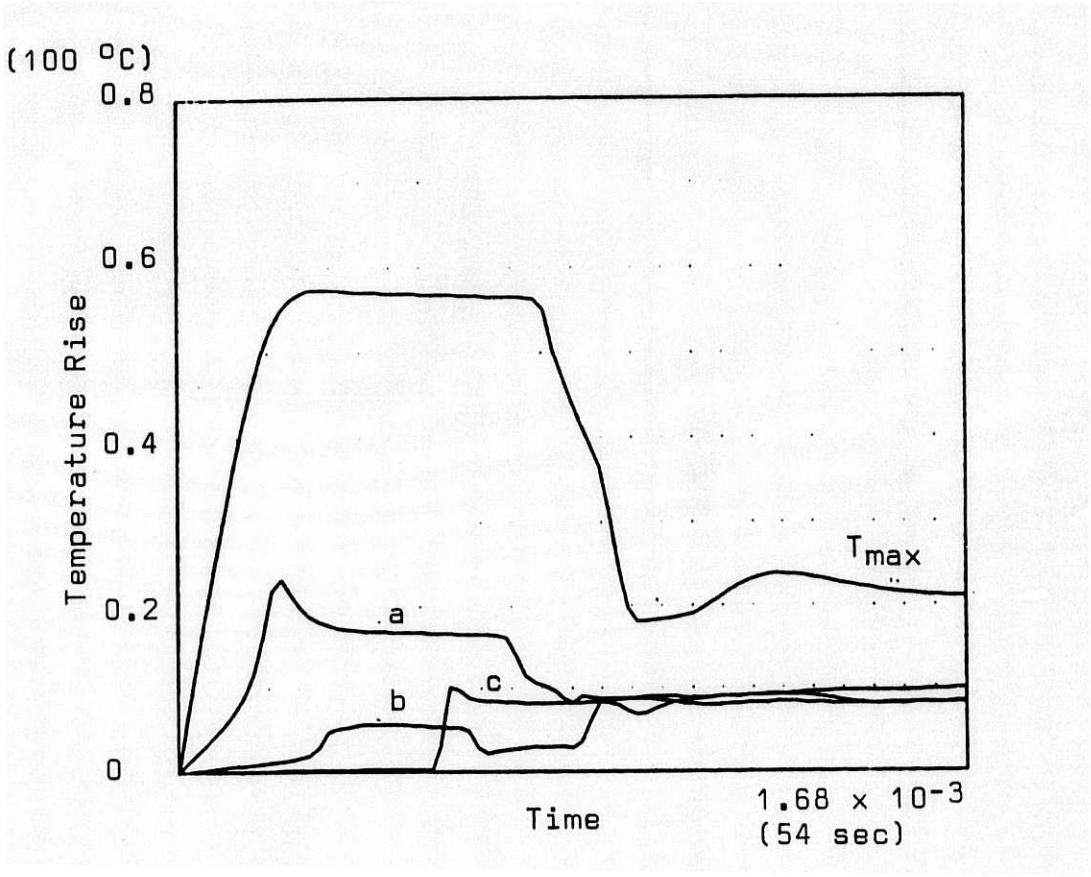

Fig. 4
Change of temperature with time.
T_{max}: maximum temperature in the whole system.
(a): Temperature is at the fixed point
r = z = 0.25; (b) at r = z = 0.5; (c) at
r = z = 0.75. The time range is from 0 to
1.68×10^{-3} (54 sec)

3.1.3 Energy flow

Figure 5 is a vectorial representation of energy flux shortly after the start of heating:
Fig. 5 (a) shows the contribution from heat conduction,
(b) convection and,
(c) the total energy flux.

The main contribution to the energy flow from the heated region comes from convection, even at this early stage, as is illustrated by the similarity of Fig. 5 (b) and Fig. 5 (c). Convection completely dominates conduction at later stages. Figure 6 shows the change of

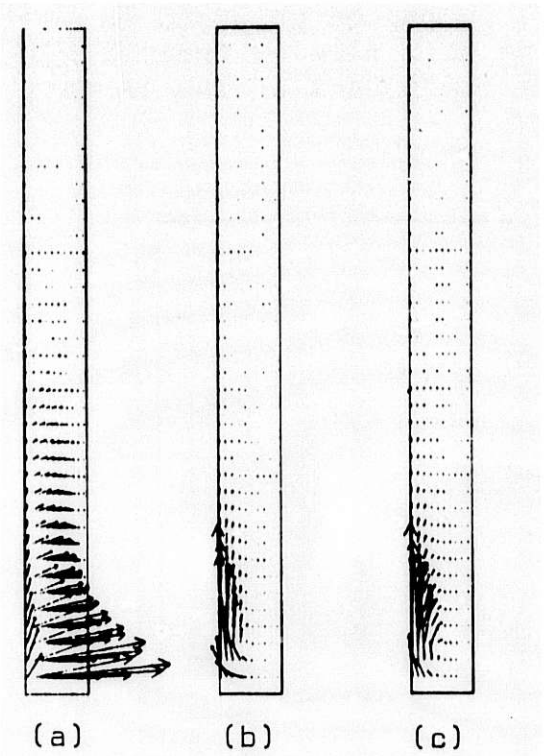

Fig. 5

Vectorial energy flux for 150 cm high target, current = 0.1 mA and at time = 2×10^{-5} (0.64 sec)
(a) conduction
(b) convection
(c) total
These figures are normalized in each frame independently, and there is no relationship in length of arrows between the three.

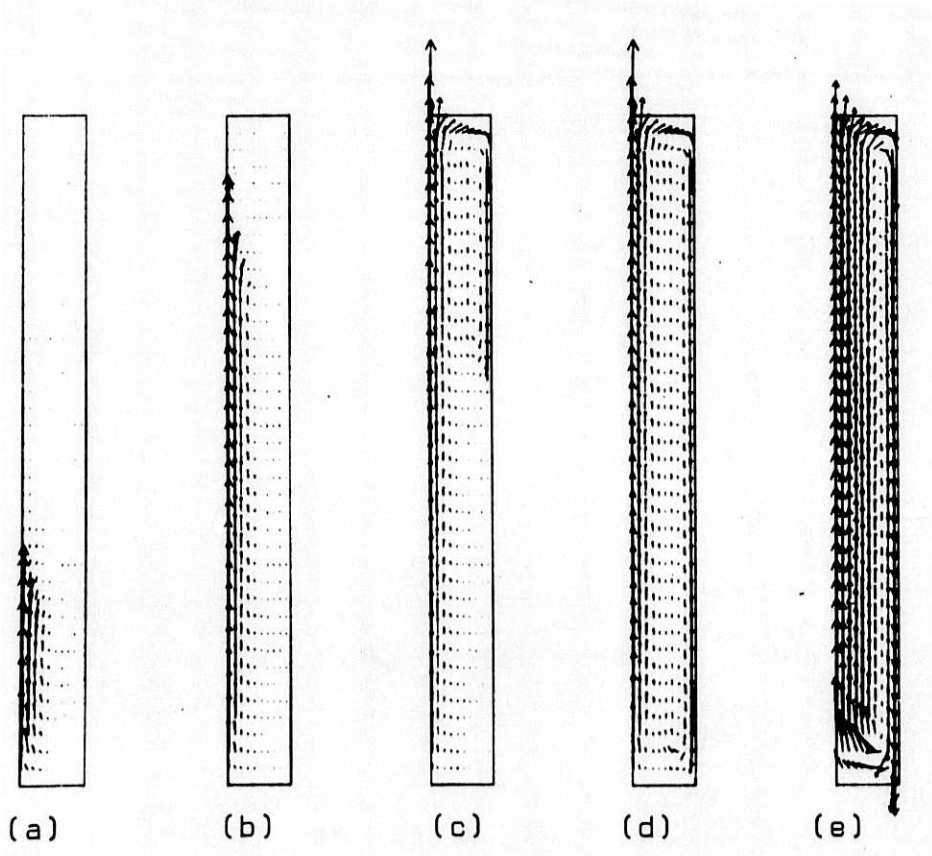

Fig. 6
Change of vectorial energy flux. Calculational parameters are the same as in Fig. 5. (a) is at 2×10^{-4} (6.4 sec), and the time interval between successive diagrams is 2×10^{-4} (6.4 sec).

the total energy flux with time. The change of the energy flow is fairly large, and follows the development of the liquid flow. When the flow is established, the energy flows towards the centre line in the bottom regions of the target and towards the periphery at the top. In the middle region of the target, the energy flows vertically upward in a central column transporting the deposited energy to the top. This heat is then transferred to the cooled wall during the downwards flow in the outer region of the target.

3.2 The effects of physical conditions

3.2.1 Target height

Figure 7 gives a comparison of the profiles of temperature distribution and streamline fields for various target heights at one fixed dimensionless time (1.6×10^{-3}). By this time, the total circulation is well established for all three cases. The value of stream function is largest for the shortest target. The general features of the temperature distribution are the vertical isotherms in the central and peripheral regions, horizontal isotherms in the top region, and a fairly uniform temperature distribution in the intermediate core. Inversion layers are generated by the total circulation at the top centre and the bottom periphery, indicating some possibility of the appearance of the stagnation at the bottom corner. From this general behaviour, (but bearing in mind the fundamental limitations in the calculation), we could expect that in the main part of the container a stable laminar flow develops, which is part of a total circulation throughout the target and is effective for energy transport.

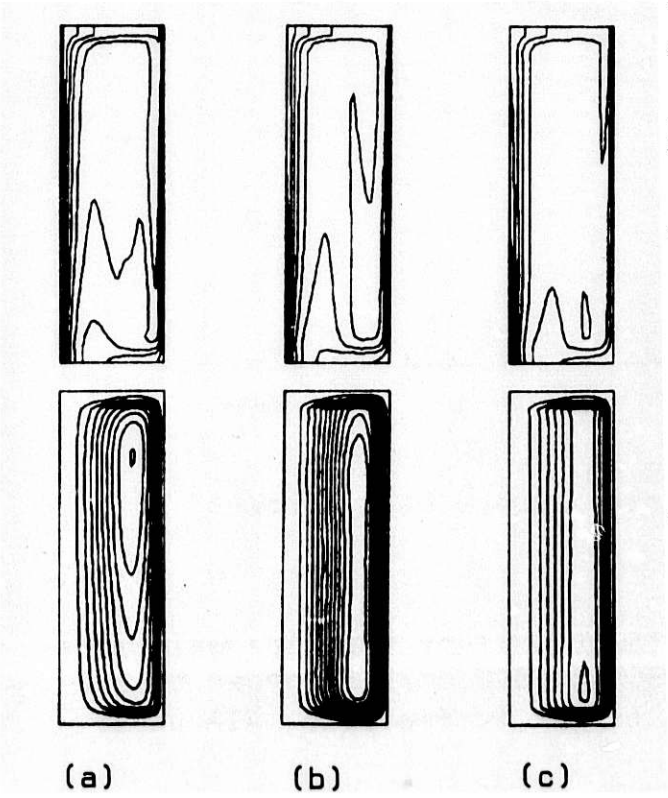

Fig. 7
Change of temperature (top) and flow (bottom) profiles with target height;
radius = 15 cm
current = 0.1 mA
(a) 75 cm at 26.1 sec
(b) 150 cm at 52.2 sec
(c) 300 cm at 104.5 sec
(1.64×10^{-3} for all)
Contour lines are with
$dT = 0.025$ (3.1 °C) and
$d\Psi = 10$

3.2.2 Beam power

Calculations were performed with various beam currents for a target height of 150 cm. Beam currents of 0.1, 0.5 and 1 mA were used. Profiles for temperature and streamlines are very similar although the absolute values of these are different. The significant difference is that the speed of rising of the roll is somewhat larger for higher beam currents. This is caused by the larger buoyancy forces due to the higher temperature difference. The highest temperatures in the container were found at the bottom centre for all three cases, and the values are plotted as a function of beam current in Fig. 8. A power law relationship between maximum temperature rise and beam current was found, and an estimate of the exponent is 0.68, which is in very good agreement with the value of 2/3 given by a simple one-dimensional analysis [6]. This relationship is helpful in estimating the maximum temperature for other beam currents.

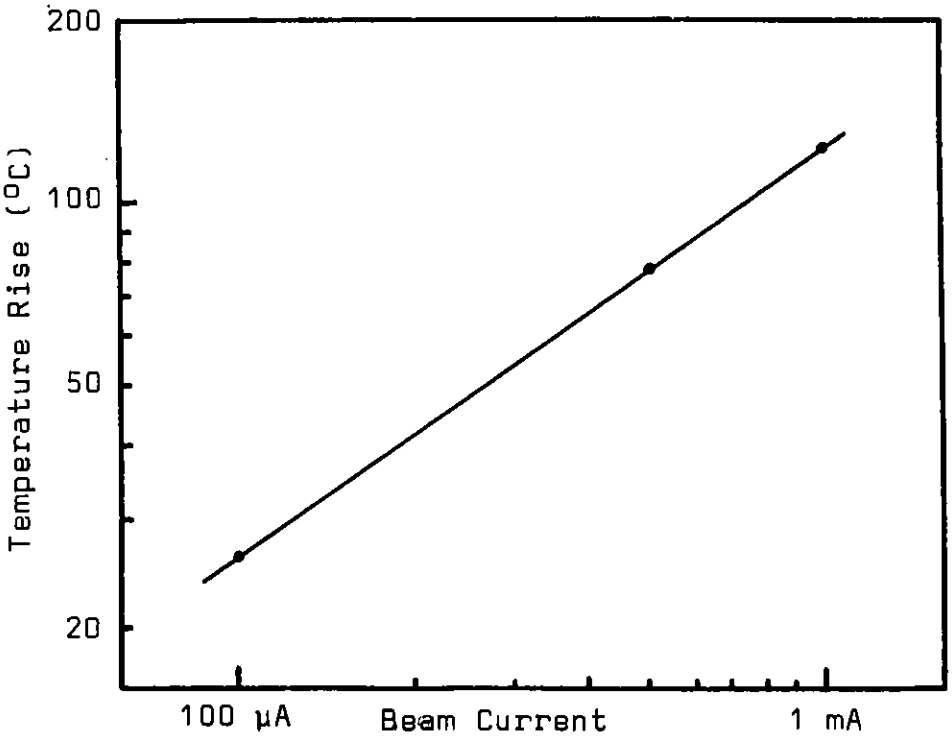

Fig. 8
Maximum temperature rise versus beam current

3.2.3 Adiabatic side wall

Calculations were done with the lower half of the side wall adiabatic, for two target heights (150 and 300 cm), in order to see if a simpler arrangement for the target is feasible. All other

conditions and parameter values are the same as for the case with a conducting side wall. The temperature distribution and streamline field are shown in Fig. 9. The general structure of the flow

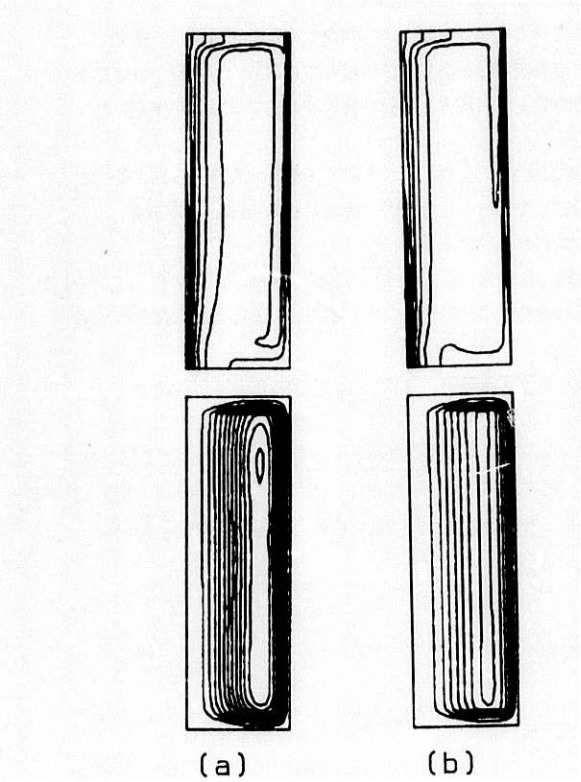

Fig. 9
Temperature (top) and flow (bottom) profile for adiabatic side wall condition;
(a) Ha = 75 cm
(b) = 150 cm
Physical parameters are all the same as in Fig. 7.
Contour lines are with
$d\Theta = 0.025$ (3.1 ^{o}C) and
$d\Psi = 10$

patterns are very similar to the cooled side wall cases (see Fig. 7), with the absolute values of stream function larger in the upper region implying a stronger circulation. The temperature distributions show more significant differences. The temperature gradients are smaller beside the adiabatic surface, which is obviously from the difference of boundary condition, and also leads to the simpler temperature profile in the lower peripheral and core regions. Because the area of heat transfer out of the target is reduced, the temperature in the central column is higher. At the end of the calculations the maximum temperature rises above the melting point were 35.9^{o}C for 150 cm target and 32.8^{o}C for 300 cm, whereas they are 26.0^{o}C and 25.2^{o}C respectively, for conducting walls.

4. CONCLUSIONS

Numerical investigations have been made for the natural convection in a liquid lead-bismuth target based on the conventional Boussinesq approximation. Geometrical configurations were restricted to vertical cylinders of various lengths. A distributed internal heat generation was taken into account and is the only driving force for liquid motion. The following conclusions are made:

1) In the transient phase, the flow bifurcated but did not lead to a hydrodynamic instability.
2) Following the initial transient phase, a stable total circulation is established in all the cases examined.
3) The temperature profile shows that there is a hot column of liquid about the centre line and a steep gradient at the surface. In the intermediate core region, the temperature variation is small.
4) The position of the maximum temperature in a target is at the bottom centre, i.e. at the middle of the beam entry window, except for a short period in the transient.
5) This maximum temperature rise in the transient is several times higher, depending on the systems, than that of the stationary value.
6) The maximum temperature rise in the system is directly proportional to (beam power)$^{0.68}$.
7) Calculations with an adiabatic side wall of half the length of the target show the accumulation of small amounts of heat in the insulated region of the system, resulting in a higher maximum temperature at the bottom center.

ACKNOWLEDGEMENT

The author is grateful to Dr. W.E. Fischer, F. Atchison and Dr. Ch. Tschalär for their helpful discussions and encouragements.

REFERENCES

[1] W.E. Fischer, Status Report on the SIN Neutron Source, These proceedings
[2] H. Hoffmann, Proceedings ICANS-V, Jülich
[3] Y. Takeda, to be published
[4] L. Buth and H. Werle, INR-996, Kernforschungszentrum Karlsruhe (1980)
[5] K.E. Torrance and J.A. Rocket, J.Fluid Mech., Vol. 36 (1969) p. 21 and 33
[6] Ch. Tschalär, Proceedings ICANS-V, Jülich

NOMENCLATURE

H	: Target height	z	: Axial coordinate
Ha	: Height of adiabatic wall	γ	: Aspect ratio (= H/R)
R	: Target radius	Ω	: Vorticity
r	: Radial coordinate	Ψ	: Stream function
t	: Time	ϕ	: Internal heat generation
T	: Temperature	Gr	: Grashof number
V_r	: Radial velocity	Pr	: Prandtl number
V_z	: Axial velocity	β	: Thermal volume expansion coefficient

APPENDIX

The physical variables (shown with *) were normalized in the following way:

t	$= \alpha t^*/HR$	V_z	$= R^2 V_z^*/H\alpha$
Ψ	$= \Psi^*/H\alpha$	z	$= z^*/H$
V_r	$= RV_r^*/\alpha$	T	$= (T^*-T_o)/T_o$
r	$= r^*/R$	Φ	$= HRq/(\alpha T_o\ \rho C_p)$
Ω	$= HR\ \Omega^*/\alpha$		

where α is the thermal diffusivity and T_o the melting temperature, ρ the density, C_p the specific heat of LBE and q the power density.

ICANS-VI

INTERNATIONAL COLLABORATION ON ADVANCED NEUTRON SOURCES

June 27 - July 2, 1982

DEVELOPING AN OPTIMUM TARGET DESIGN FOR A HIGH ENERGY SPALLATION NEUTRON SOURCE WITH RESPECT TO MECHANICAL AND THERMAL CONSTRAINTS

J.F.Stelzer

KFA Jülich

ABSTRACT

On the search for a suited target design different variants have been systematically been studied with respect to their temperature and rigidity behaviour. The calculations dealt with the temperatures and stresses in the maximally loaded parts and were carried out using the finite element method. The final solution is a rotating, internally water-cooled wheel of 2.5 m outer diameter, carrying about 9000 rods filled with lead. There are three highly loaded areas: the outer housing, the beam window and the lead-filled target rods. The construction of the mathematical models is shown. The results are introduced and discussed. The design satisfies the mechanical demands.

DEVELOPING AN OPTIMUM TARGET DESIGN FOR A HIGH ENERGY SPALLATION NEUTRON SOURCE WITH RESPECT TO MECHANICAL AND THERMAL CONSTRAINTS

J.F.Stelzer
KFA Jülich

1. THE SEARCH FOR A SUITED TARGET DESIGN

When our work on the target station started there existed two competing ideas how the problems arising with the extremly high heat deposition could be solved: 1) using a liquid metal circuit, and 2) using a rotating target wheel similarly like a rotating anode.

One of the most severe reasons speaking against the liquid metal circuit was the impossibility to find a acceptable window located between the pressurized liquid metal and the vacuum of the proton accelerating region. There is a certain thickness of the window necessary to withstand the fluid pressure, but the thicker the window the longer are the heat flux paths to the cooled surface and, consquently, the higher the temperatures and the thermal stresses. The appropriate relationships for a window consisting of graphite are exhibited in figure 1. Also windows of Molybdenum were examined as is reported in ref./1/ and /2/.

A concentration followed on Bauer's concept of a rotating target. The first proposal consisted in a compact lead target which was only cooled from its surfaces/3/. However, our finite element calculations of the temperature and stress distribution showed that the temperatures in the hottest region rose approximately to the melting temperature of lead, and the thermal stresses attained values beyond the tensile strength.

From this experience we learned that 1) the length of the heat flux paths from the region of the heat scurces to the water-cooled surfaces need to be short, and 2) the lead volume should not be large and compact but distributed in several smaller sections to decrease the thermal stresses.

Consequently, a rotating target was proposed with evolvent-shaped lead sections with cooling water in the intermediate gaps, see ref./4/. A schematic picture of this design shows figure 2, and, addidionally, a scheme of the marching heat sources as considered in the calculations. However, an evaluation of the results showed that the maximal temperatures at the hot spots were still rather high, unless the evolvent width was small (<2 cm), and the thermal stresses could not yet be tolerated. The experience we gained from this was that the changing over from a compact 3-d-structure to a strip shape, a 2-d-structure, did not bring sufficient relief. The consequence was now to turn to a 1-d-configuration, where the target material is distributed in some thousand single rods which is the present concept. But before this design was studied for a certain time a compact target (also rotating) was examined where a partly melting of the lead was allowed.

Figure 3 gives an impression of the melting target concept. The beam enters with a flat angle and hits the inner surface. This design, however, cannot be realized because of the too high stresses in the housing. As material for the housing we proposed molybdenum or niobium since the intermediate temperatures in the hottest spot arise up to 1100 ^{o}C, but the thermal stresses increased to intolerable high values.

The described history of the Juelich target station shows the advantages resulting from a cowork between physicists who create always new proposals and ideas and engineers, in this case especially finite element analysts, who check in rather quick and not very expensive mathematical models the realisation possibilities. In this way by a chain of varied and stepwise improved designs an optimum can be found, or at least a compromise to live with.

As already mentioned, a provisionally final design exists. In this design some thousand single rods are fixed in a housing, as figure 4 displays. In the following the behaviour of this target wheel under thermal and mechanical loads is reported.

2. THE ANTICIPATED TARGET WHEEL DESIGN

A target wheel was chosen consisting of a slowly rotating, internally water-cooled wheel. With this concept it is possible to control the extremely high heat deposition (120 kW/cm^3 in a proton pulse peak) in such a way that neither the local temperatures nor the stresses exceed conventional limits, as will be shown. The calculations, throughout executed using the finite element analysis method, are concerned with those parts of the target which are subjected to the highest loads. These are

1) the rather weak housing which comprises the water-cooled, cylindrically-shaped target elements and which is mainly stressed by the water pressure,
2) that part of the housing which serves as the proton window and is exposed to intensive and intermittently acting thermal loads,
3) the target elements themselves which are stressed for a short time by a very intensive heat deposition resulting from the interaction between protons and matter. Some of these lead-filled cylinders have an additional task, working as tie-rods between the housing lid and the bottom and are thus additionally stressed.

The calculations were carried out using the FEABL2 programme. This programme was developed by A.Sievers, J.F.Stelzer and R.Welzel at the KFA Juelich, based on a software package developed by Orringer /6/. An advantage of this program is to calculate simultaneously temperature fields, structural deformations and stresses. Some routines had been adjusted to the special requirements of the task, as e.g. allowance for the pulsing character of the heat deposition by an accordingly fine incrementation of the time axis. The accompanying thermal stresses result for each time step from the momentary temperature distribution. Dynamic stress wave effects depending on a very rapid heating of the material as reported by P.Sievers /7/ were neglected in the calculations because this influence is very small under our operating conditions with pulse widths of 0.5 milliseconds.

Physical parameters. The heat sources in the exposed matter last for 0.5 milliseconds followed by a break of 10 milliseconds without heat deposition. The proton beam penetrates with a circular cross section. The corresponding heat sources form a Gaussian distribution across this area. The intensity decreases exponentially as it progresses through the target material. The relationships are shown schematically in Figure 5. Some data of the target wheel are given in table 1.

Table 1: Some target wheel data

outside diameter	250 cm
height of the target material (lead)	10 cm

depth of the area filled with target material in beam direction	70 cm
peripheral speed	4 m/s
speed of rotation	30.56 min^{-1}
angular velocity	3.2 s^{-1}

Our remarks concerning the three hard loaded design parts now begin with an examination of the stress behaviour of the target housing.

Rigidity analysis of the target housing. The outer casing of the water-cooled zone is made of AlMg3. It contains the lead filled, Al-clad target rods of approximately 24 mm outside diameter and 100 mm length, see figure 6. The casing houses about 9000 such rods. The casing bottom is thus stressed by the corresponding gravitational load. The main load, however, results from the coolant pressure. There are still other, but smaller loads resulting e.g. from the centrifugal forces acting in the water and the stagnation pressure at the outside wall. Because of its material and geometry the housing is not very rigid and its deformations become intolerable if all the rods are fixed according to figure 6.

The mathematical model. Figure 7 shows the calculation model. It is represented by 324 finite elements with 672 nodal points. Figure 8 gives some dimensions and the pressure distribution. In the actual structure the rods are located on 37 radii designated R1 to R37, from the largest radius to the smaller ones in the proton flight direction. The model has fewer opposite pairs of nodal points than rods. Therefore, with the connecting rods calculation a certain number of them is presumed to be combined at these locations.

Calculation results. Figure 9 shows the housing deformation if no special measures are undertaken. The maximum displacements of lid and bottom have approximately opposite positions and open a clearance of 2.13 mm. If target rods in this region are firmly connected to the opposite sheets, a considerable stiffening of the casing results. Figure 10 displays the deformation pattern with every second rod being fastened on the radii R16 and R18. In this way 272 rods act as traverses. The next two figures, 11 and 12, illustrate the reference stress distributions in the lid for both cases. The stresses remain tolerably low. The problem of the number and location of the traverses was the subject of an optimization procedure, see reference /8/.
The connecting rods altogether carry a total load of approximately 70 tons. The tensile stress in the rods will be superimposed by the thermal stress in a process described below. The same is true of the beam window which is also under tensile stress from the water pressure.

Rigidity analysis of the beam window. In addition to the mechanical load described, the beam window is also subjected to thermal stress by the proton beam. The protons arrive intermittently since the beam is pulsed. When the next proton flash enters the wheel has rotated further over a distance of one beam radius, see figure 13. This relationship establishs the context between the target wheel geometry and its rotating speed.

The mathematical model. This reproduces a part of the peripheral vertical sheet, see figure 14. The curvature is not taken into consideration with regard to the rather large radius. The following data are used, table 2.

Table 2 Data of the beam window

Material	Al Mg3
sheet thickness	5 mm

proton beam radius 40 mm
maximum heat deposition 47 kW/cm^3
water cooling from the rear with 1 W/(cm^{2}K)
water temperature 30 ^{o}C.

Cooling is only effected from the rear since the front is surrounded by vacuum. For the calculation it is assumed that an appropriate angular range of the window stays in the beam for 0.5 milliseconds. After 10 milliseconds the next spot is hit, the centre of which is one radius distant from the former one. The same cross section is once again immersed in the heat deposition area after 2 seconds. Cooling is continuously maintained. For reasons of symmetry only the hatched half of the window needs to be taken into consideration. The transient temperature field calculation takes the moving heat sources into consideration in the manner mentioned. The initial temperature is 30 ^{o}C.The results from the casing calculation must also be introduced. This is performed by including the found radial and axial displacements as constraints in the window calculation, as is shown diagrammatically in figure 15.

Results. The calculation reveals that the quasi steady-state relationships are attained after 6 target wheel revolutions. The temperature distribution occuring immediately before heat deposition is illustrated in figure 15. The proton shot then causes the temperatures which are given in figure 16. The maximum temperature rise amounts to about 11 K. The stresses (here: the reference stresses) in the element centres can be seen in figure 18. An evaluation of the stresses is made at the end of the paper.

Temperatures and stresses in the target elements. A target rod has a cylindrical shape, is filled with lead and clad with AlMg3. Similarly to the beam window, every rod stays for a short time in the proton beam before it is carried away by the rotating wheel. Thus, from shot to shot hitting the same spot a rather long cooling period occurs.

The calculations deal with target rods in different positions. The highest thermal load is induced in the rods on the largest radius (R1). The calculations also take the rods on the radii R16 and R18 into consideration. There is only a reduced thermal stress here since the incoming proton energy is already weakened by the 30 cm path through an energy absorbing zone. On the other hand, these rods must bear the tensile load due to their function as through-bolts discussed above. Some variants with different cladding thicknesses were calculated since the cladding must take over the main part of the tensile load because of the weakness of the lead.

The mathematical model. This is shown in figure 19. For reasons of symmetry only one quarter needs to be simulated. The subdivision into finite elements is accomplished in three storeys. The limiting planes between them where the nodal points are situated are designated Z0 to Z3. Each storey is subdivided into 126 finite elements as can be seen in figure 20. On the outer surface of the model a heat transfer coefficient of 1 W/(cm^{2}K) is assumed. At the beginning of the transient temperature field calculation the whole rod is at the temperature of the cooling water. During the calculation a constant ambient fluid temperature is assumed.

Heat deposition. The pulsing heat deposition is again observed with 5 ms heating followed by 2 s cooling time. The Gaussian distribution of the heat deposition over the beam radius and the exponential axial decrease are taken into account. However, the heat source decrease across one rod does not

amount to more than 10 %.

Pre-stressing. The case was also considered in which the lead kernel is undercooled before being inserted into the AlMg3 cladding to prevent a gap between the kernel and the cover. The tangential initial stress of 50 N/mm^2 is appropriate. But there is little danger that such a gap and an associated temperature rise will occur since the lead shows a larger thermal expansion (about 20 %) than the AlMg3. An axial pre-stress appears in the rods acting as traverses. This load is induced by constrained displacements resulting from the casing analysis.

Results. Temperatures. Let us first consider a rod on the largest radius. The time dependent temperature development is exhibited in figure 21 for the hottest point of a rod. After about 10 s or 5 wheel revolutions a stable state is reached. The rise between the temperature extremes amounts to 42 K. A survey of all nodal point temperatures is given in figure 22. The temperature exceeding that of the cooling water in the centre of the rod middle plane (Z3) varies between 21 and 63 K. The outer AlMg3 jacket is 15 K above the coolant temperature. The leaving heat flux density amounts to 15 W/cm^2. This means a very large interval between subcooled boiling (which is not dangerous at all), not to speak of the dangerous film boiling which would not appear before 300 W/cm^2. Despite the rather low melting point of lead (327 ^oC) no melting will take place. With a coolant temperature of for example 60 ^oC the highest lead temperature will be at 123 ^oC.

Stresses are calculated in the geometrical centres of the finite elements. In the non-prestressed rods the stresses are only a consequence of the temperature gradients and the impeded thermal expansion of the lead restrained by the influence of the AlMg3. Tangential and axial stress components predominate. Figure 23 illustrates the reference stress distribution in the layer with the highest load which is located between the planes Z2 and Z3. The maximum reference stress appears in the AlMg3 jacket and amounts to 75 N/mm^2. In the case of pre-stressing by shrinking, the maximum stress rises to 109 N/mm^2.

A hypothetical operating disturbance. Some problems could perhaps arise if the coolant flow were partly blocked e.g. by distorted or disconnected target rods. It may be assumed that then the heat transfer along half of the target rod surface decreases to one tenth, to 0.1 $W/(cm^2K)$. In the central plane of the rod temperatures then occur as shown in figure 24. The highest overtemperatures above the coolant now vary between 72 and 112 K. It can be seen that even such a severe deterioration of local cooling does not provoke a dangerous temperature increase.

Temperatures and stresses in the through-bolt rods. These rods are located in the radii R16 and R18. The proton beam only deposits about one quarter of the heat sources here compared to the radius R1. The maximum temperature variations range between 5 and 15 K above the coolant temperature. The stresses were calculated for jacket thicknesses of 0.5 and 1 mm and thermal and tensile load. The tangential pre-stress caused by a shrunken jacket was also taken into account. The results are listed in the following table 3.

Table 3: Maximum stresses in the cladding of a rod on R18, layer between the planes Z2 and Z3, in N/mm^2

Cladding thickness (mm)	tangential pre-stress	tensile load	σ_r	σ_ϕ	σ_z	σ_{ref}
0.5	no	no	0.04	12.4	12.8	12.7

0.5	yes	no	-0.9	57	15.2	51.8
0.5	yes	yes	-0.9	57.3	21.6	50.9
1	no	no				11
1	yes	no				47
1	yes	yes				47

It can be seen that the stress reduction by a doubling of the cladding thickness is insignificant. A tangential pre-stress is responsible for a high stress increase. The maximum reference stress in the lead is 5.9 N/mm^2.

3. FINAL EVALUATION OF THE RESULTS

As has been shown, in the design the temperatures remain at low and non-critical values at all locations. In order to evaluate the stresses we must refer to the appropriate tolerable stresses. Because of continuous cyclic loading the fatigue stress should preferably be taken into consideration. AlMg3 in a soft, annealed state is in this respect superior to hard, cold-formed material. The following values are given in ref. /9/, table 4.

Table 4: Fatigue strength of AlMg3 in N/mm^2 under cyclic loading with alternating tensile and compressive stress

state	lower limit	upper limit
soft	72	126
semihard	58	115
hard	52	78 .

At two locations on the target the lower limit of the soft material is slightly exceeded: in the centre of the beam window (stress equals 75 N/mm^2) and in the rod jacket of a rod on the outer radius (also 75 N/mm^2). We see that it is not advisable to shrink the jackets on the rods since then the stress will increase to the intolerable value of 109 N/mm^2.

It can thus be seen from the results that an arbitrarily long lifetime of the target assembly cannot be expected. This would undoubtedly be the case if the maximum stress were to remain everywhere below the lower fatigue strength limit. However, from the engineer's point of view it can be stated that the thermal and mechanical loads occuring in the target wheel do not exceed tolerable and commonly accepted limits.

References

/1/ SNQ Realisationsstudie zur Spallations-Neutronenquelle, ed.G.S. Bauer, H.Sebening, J.Vetter, H.Willax, Jül-Spez-113, Jülich, 1981, 3 volumes

/2/ Seitz, L., A.Sievers, J.F.Stelzer: Strahlfenster unter thermischer und mechanischer Belastung, chapter 42 in vol.3 of /1/

/3/ Stelzer, J.F.: Heat dissipation and thermal stress in solid targets, paper at the Meeting on Targets for Neutron Beam Spallation sources, Juelich, 11-12 June 1979

/4/ Emmerich, R., L.Seitz, J.F.Stelzer: Temperatures and thermal stresses in a spallation target from lead, evolvent target, chapter 41 in vol.3 of /1/

/5/ Seitz, L., A.Sievers, J.F.Stelzer: A rotating target from lead with phase change solid-liquid, chapter 40 in vol.3 of /1/

/6/ Orringer, O., S.E.French: FEABL finite element analysis basis library, AFOSR TR, ASRLTR 162-2, MIT, Cambridge, Mass., 1972

/7/ Sievers, P.: Elastic stress waves in matter due to rapid heating by an intense high-energy particle beam, European Organization for Nuclear Research, paper LAB II/BT/74-2, Geneva, 1974

/8/ Stelzer, J.F.: Two applications of optimum structural design in the field of nuclear technique, Proc. Int.Symp. on Optimum Structural Design, ed. R.H.Gallagher, E.Atrek, A.J.Morris e.a., University of Arizona, Tucson, 1981, pp.1-23 to 1-29

/9/ Sass,F. and Ch.Bouché, editors: Dubbels Taschenbuch für den Maschinenbau, 11th ed., Springer, Berlin, 1958, pp.540-542

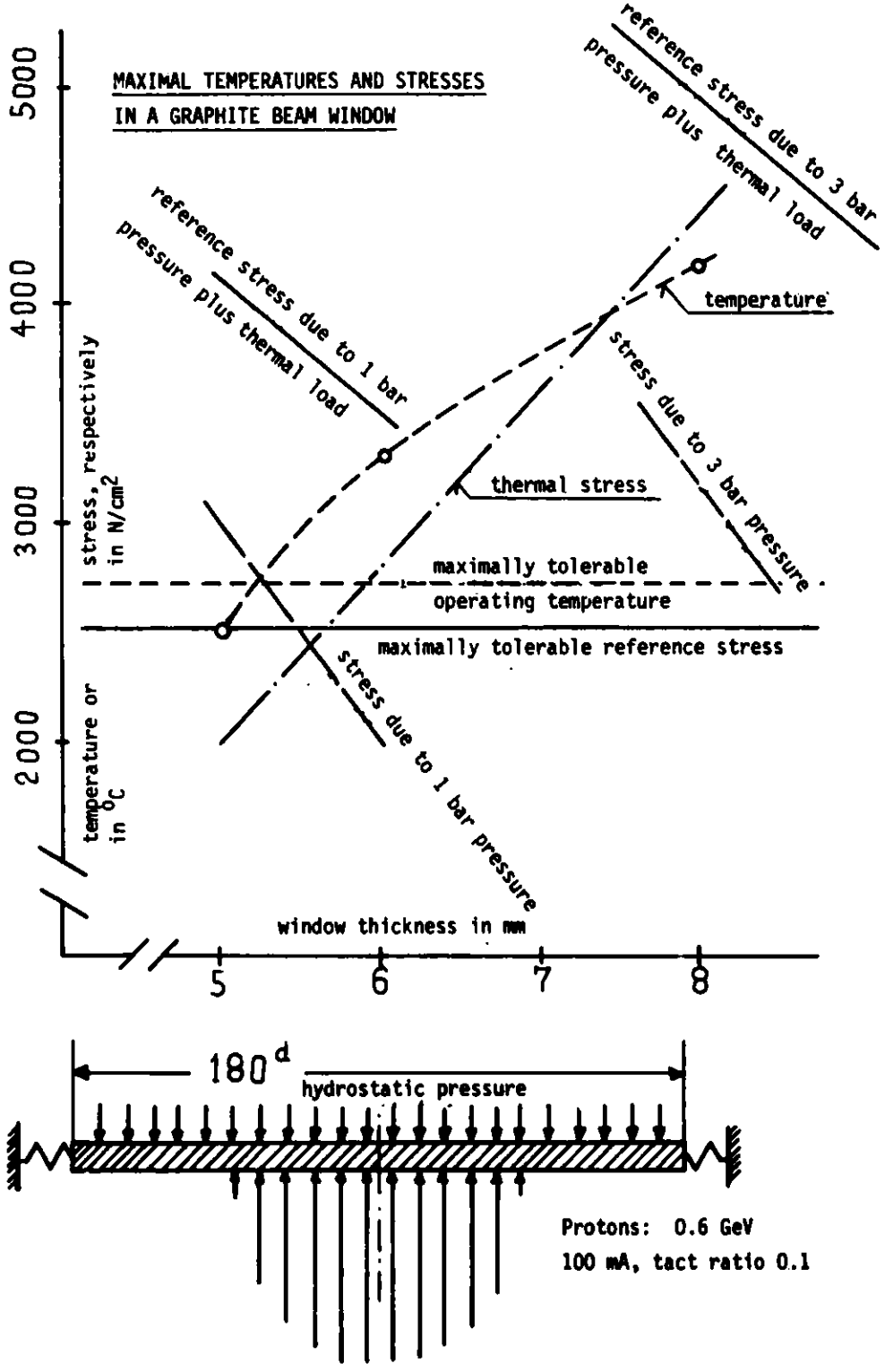

Fig. 1. Maximum temperatures and stresses vs. window thickness in a beam window of graphite. Heat deposition according to the anticipated Juelich spallation source.

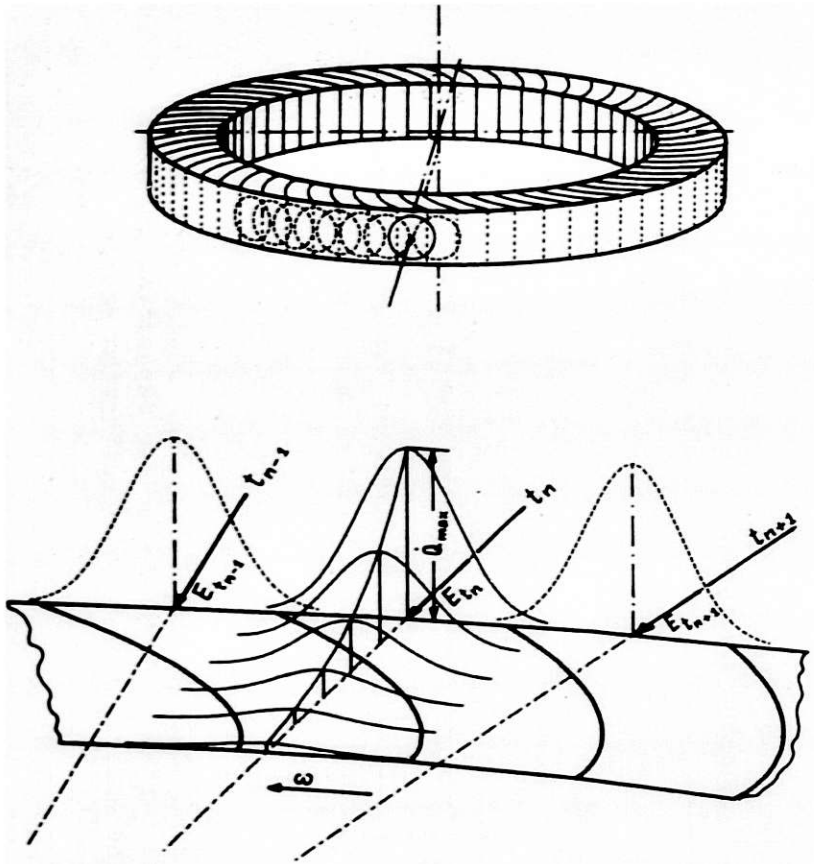

Fig. 2. Scheme of the evolvent-shaped target wheel (above) and of the marching heat sources (below)

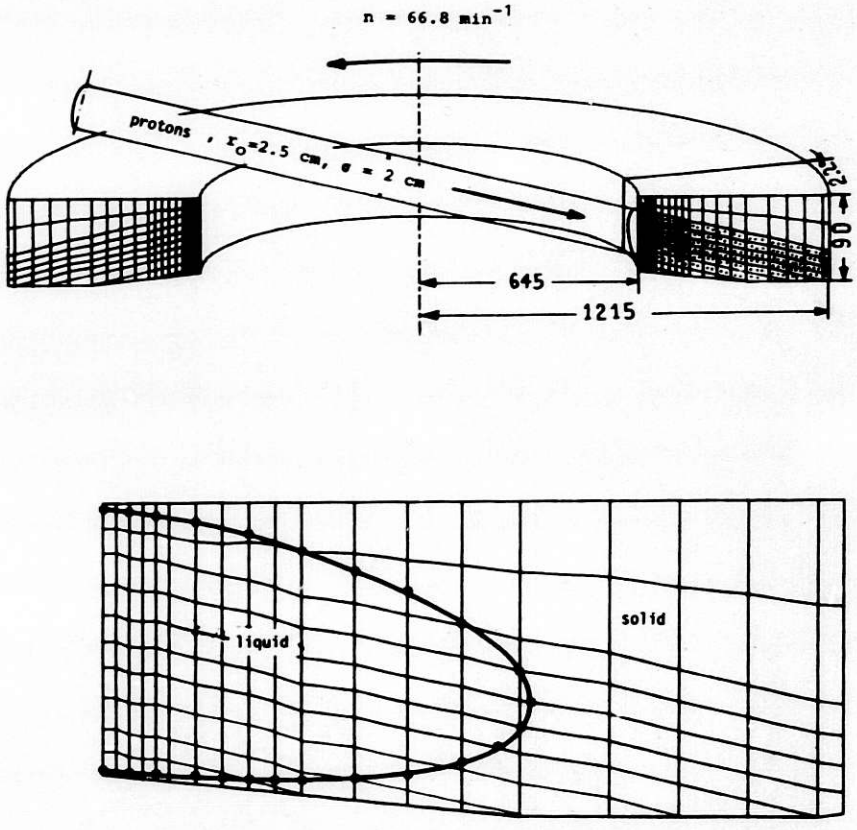

Fig. 3. Melting target with the finite element subdivision (above). Calculated areas of molten and solid lead after 80 target wheel revolutions, quasi-steady-state (below).

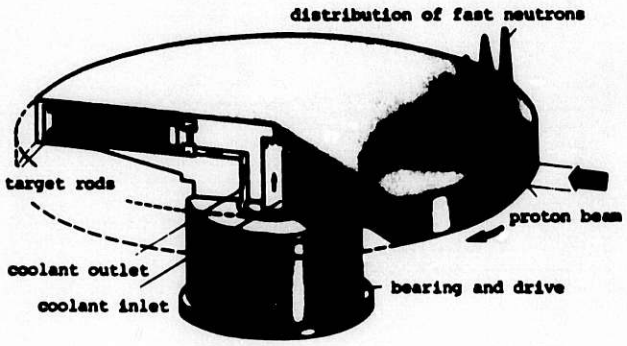

Fig. 4. Survey of the target wheel which suits all thermal and mechanical demands

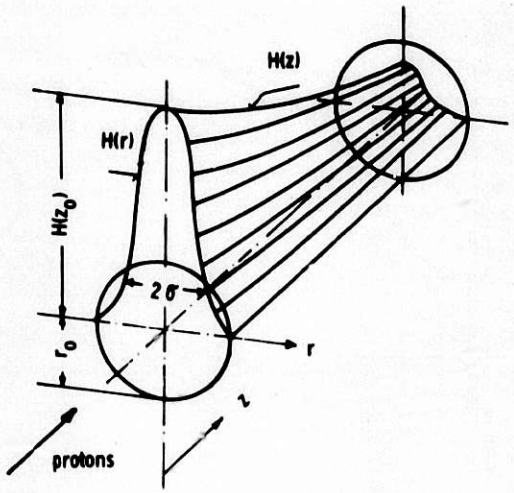

Fig. 5. Distribution of the induced heat deposition in a solid body by proton bombardment

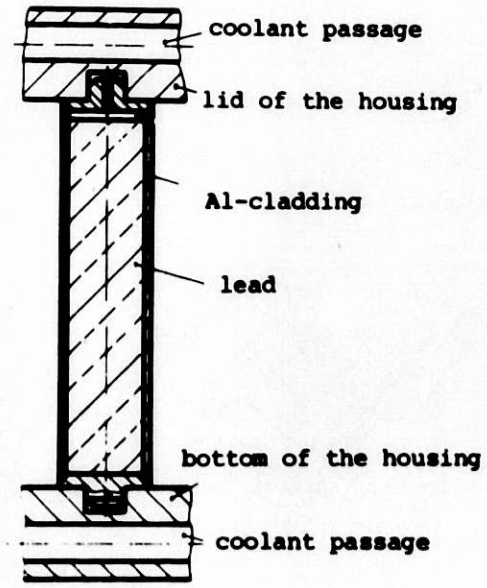

Fig. 6. A single target rod. It is situated in the wheel housing with plugs at both ends. It can expand independently of the ambient rods.

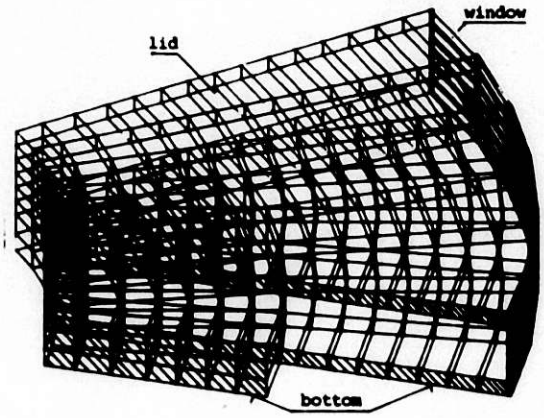

Fig. 7. Projected view of the calculation model

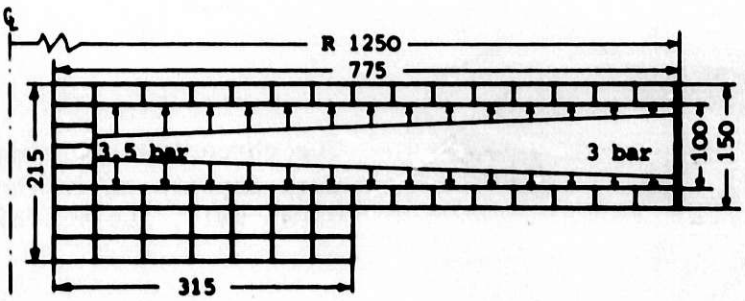

Fig. 8. A model cross section

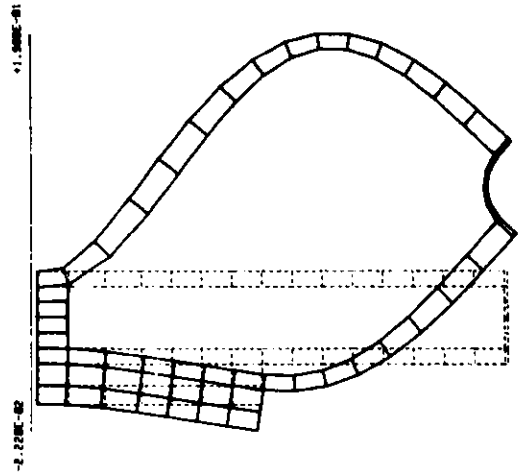

Fig. 9. Deformation of the housing if no traverses are present. Deformation enhancement by a factor of 200.

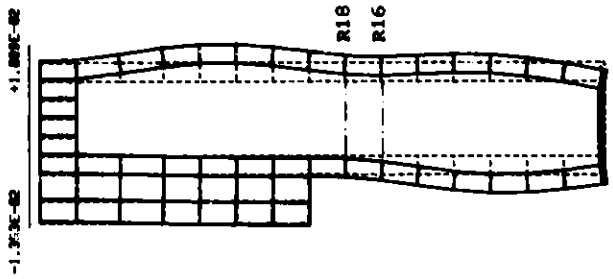

Fig. 10. Deformation of the housing with traverses at the radii R16 and R18. Deformation enhancement by a factor of 200.

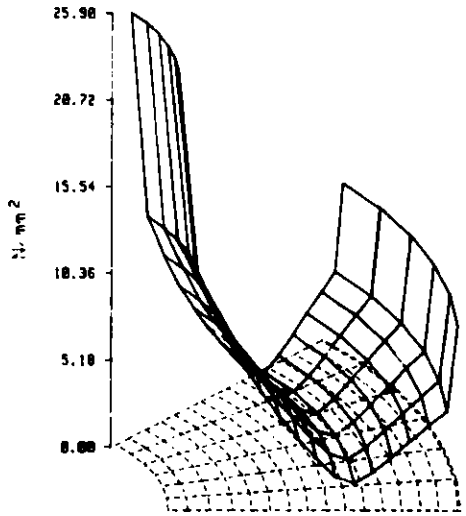

Fig. 11. Distribution of the reference stresses in the lid of the housing if no traverses are present

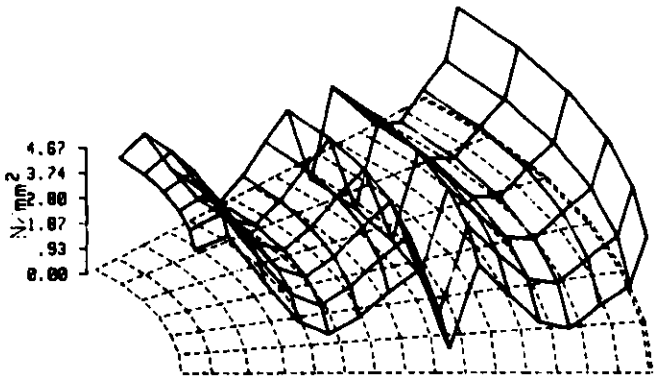

Fig. 12. Reference stress distribution in the lid of the housing with traverses in the radii R16 and R18

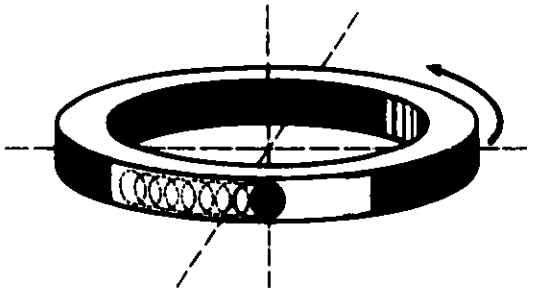

Fig. 13

The chronological order of energy deposition in the outer wheel wall, the window

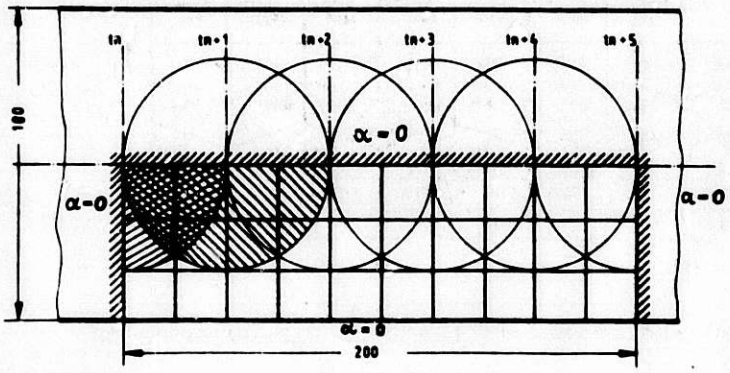

Fig. 14

Mathematical model of the beam window

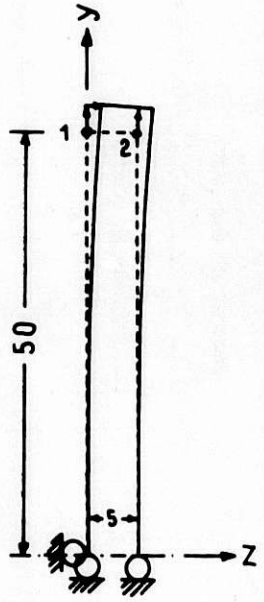

Fig. 15

Displacement constraints of a window cross section

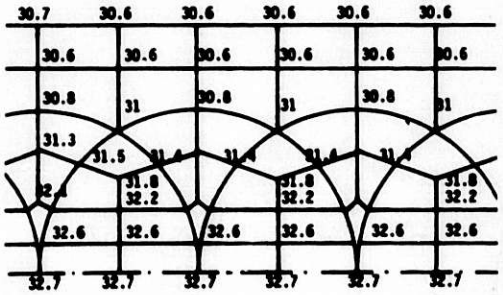

Fig. 16. Temperature distribution in the window after 2 s cooling shortly before heat deposition, quasi-steady-state, in centigrade

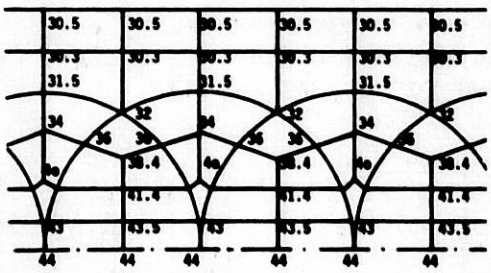

Fig. 17. Temperature distribution in centigrade in the window immediately after heat deposition

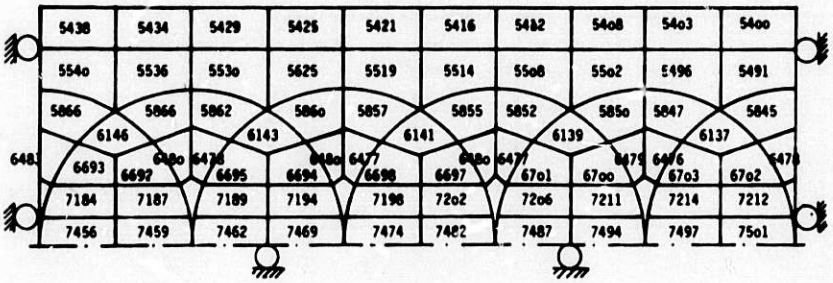

Fig. 18. Reference stresses in the beam window in N/cm^2

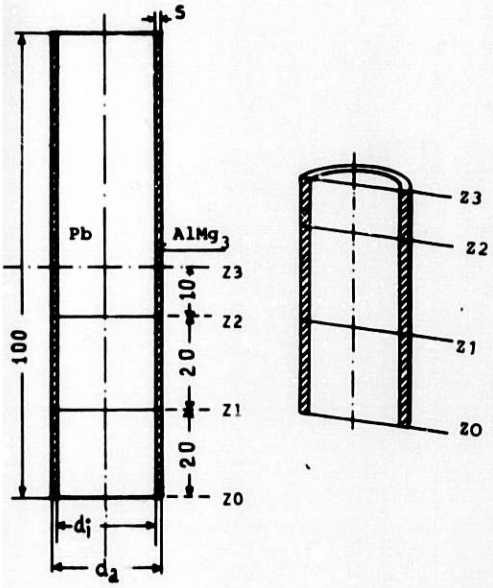

Fig. 19

Mathematical model of the target rod. It consists of three finite element storeys. The intermediate planes are designated Z0, Z1, Z2 and Z3.

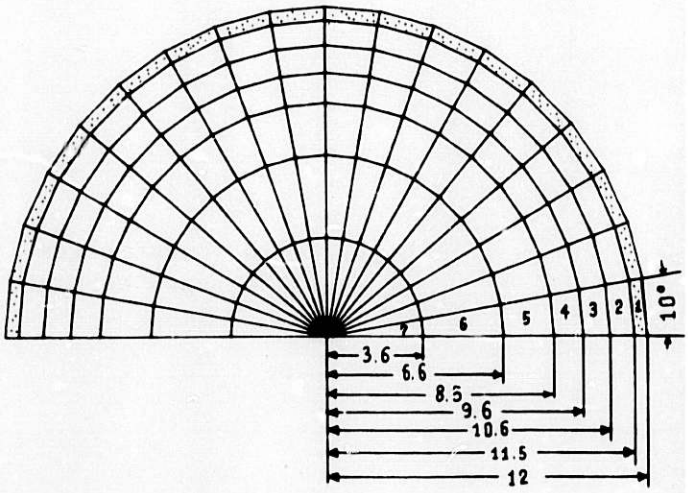

Fig. 20

Plane with nodal point

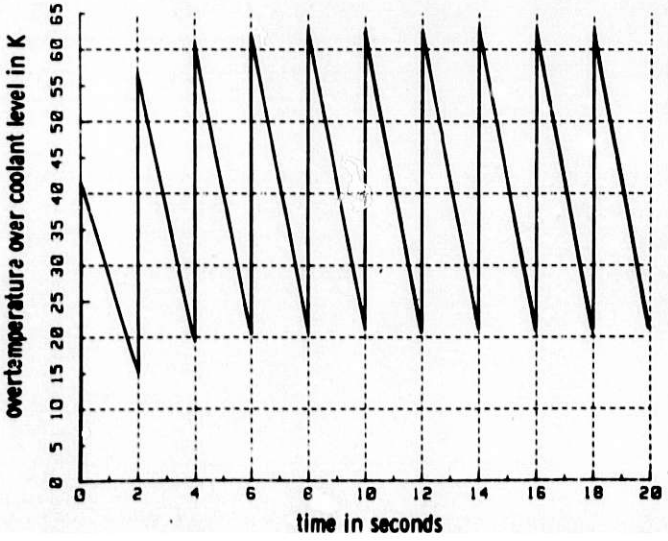

Fig. 21

Time-dependent development of the temperature at the hottest spot of a target rod on the largest radius

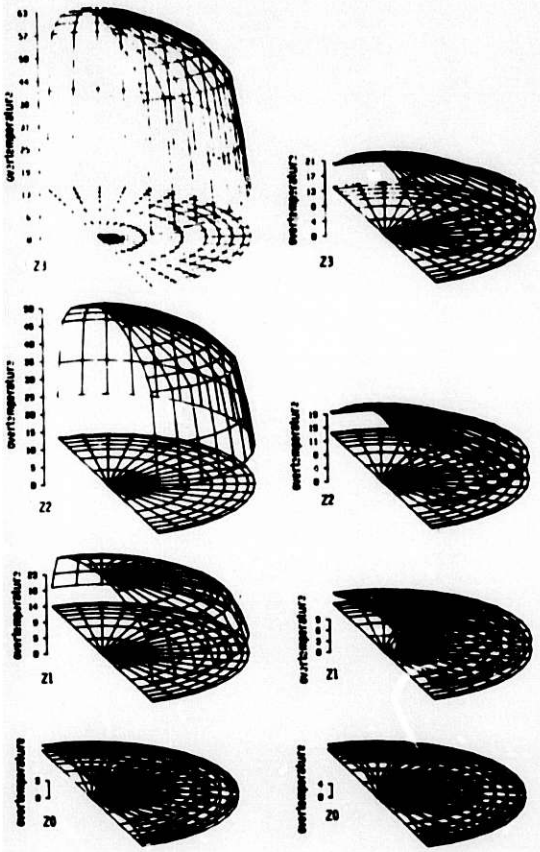

Fig. 22

Temperatures in the four planes of the target rod. Left column: immediately after energy deposition, right column: after an intermediate cooling time of 2 s.

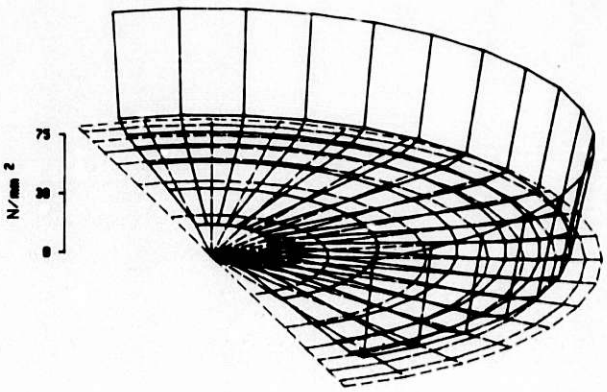

Fig. 23

Distribution of the reference stresses in the target rod in the region of the highest load

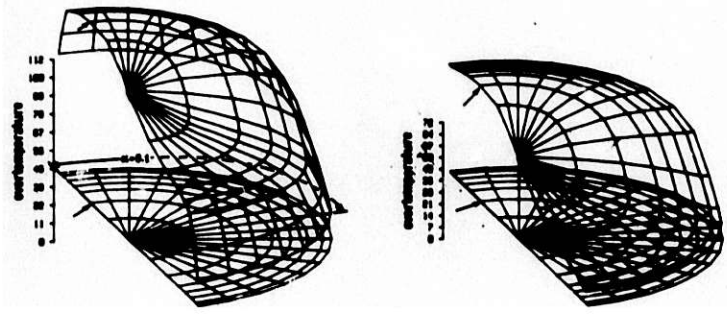

Fig. 24

Temperatures in a target rod, plane with the maximum temperatures in the context of a coolant flow disturbance. Left: after the shot, right: after 2 s cooling.

GROOVED COLD MODERATOR TESTS

K. Inoue, Y. Kiyanagi, H. Iwasa
Department of Nuclear Engineering, Hokkaido University

N. Watanabe, S. Ikeda
National Laboratory for High Energy Physics

J. M. Carpenter
Argonne National Laboratory

and Y. Ishikawa
Physics Department, Tohoku University

ABSTRACT

We performed some grooved cold moderator experiments for methane at 20 K by using the Hokkaido University linac to obtain information to be used in the planning of the KENS-I' project. Cold neutron gains, spatial distribution of emitted beams and time distribution of the neutrons in the grooved cold moderator were measured. Furthermore, we assessed the effects of the grooved cold moderator on the performances of the spectrometers presently installed at the KENS-I cold source. We concluded that the grooved cold moderator benefited appreciably the performances of the spectrometers.

GROOVED COLD MODERATOR TESTS

K. Inoue, Y. Kiyanagi, H. Iwasa
Department of Nuclear Engineering, Hokkaido University

N. Watanabe, S. Ikeda
National Laboratory for High Energy Physics

J. M. Carpenter
Argonne National Laboratory

and Y. Ishikawa
Physics Department, Tohoku University

1. INTRODUCTION

From the results of our experiments and laboratory experiences using the Hokkaido University cold source and the KENS source over a period of several years, we have concluded that the accelerator-based cold neutron source using a 20 K methane moderator is a safe, reliable and highly efficient device which can be applied as both a photo neutron source and a spallation neutron source[1-4]. Current operations of the KENS cold source have proved to be satisfactory, and it has been useful in many studies embracing various fields since fiscal year 1980.

The KENS-I' project is designed to increase the intensity of the present KENS-I source. This endeavor will require several sophisticated techniques[4] among which is the optimum design and use of a grooved cold moderator chamber which will be feasible and economical. Several authors investigated the grooved moderator for thermal neutrons, but no work on the grooved cold moderator has been done as yet[5,6]. Current plans call for the installation of the new chamber in the presently in use fast neutron reflector under its limited space and restricted design conditions. In order to decide the appropriate dimensions and to get quantitative data of the pulse shape which will be needed to assess its influence on the performance of the spectrometers,

we performed some preliminary experiments on the 20 K methane grooved moderator by using the cold source facility at Hokkaido University. Some of the results of the experiments and an assessment of the grooved cold moderators are reported in this presentation.

2. EXPERIMENTAL METHOD

The techniques used in the present experiments took advantage of the ordinary neutron time-of-flight technique and cryogenic facilities for the cold moderator. The experimental arrangement, shown in Fig. 1, has already been described in some detail in connection with the Hokkaido University cold source[2].

The grooved moderator chamber and a new flat one of the same dimensions as the KENS cold source replaced the commonly used cold moderator chamber. We purchased both a grooved chamber and a flat one made of aluminum, the dimensions of which are shown in Fig. 2, and attached them to the bottom of the heat exchanger of the cold source facility instead of to the actual moderator chamber. Because of the occurence of clogging of the methane at the entrance of the gas inlet tube, we had to replace the inlet tube with a wider one.

For the measurements of spatial dependence of the neutrons emitted from the grooved surface of the chamber, we utilized a movable, remotely controlled slit plate which was made of cadmium. The size of the slit was 4 mm in height and 100 mm in width, and the slit was placed parallel to the grooves and at the outside of the Dewar chamber as shown in Fig. 1. The measurements of the time dependence of the neutron pulse emitted from the chamber were performed by using the time-of-flight technique and a mica monochrometer.

3. EXPERIMENTAL RESULTS

A. Time-of-flight spectra

Emitting neutrons from a methane moderator at 20 K, the grooved and flat moderators had unique time-of-flight spectra as shown in Fig. 3. Both spectra were normalized for the fast neutron intensities emitted from the target. Relative fast neutron intensities were determined by measuring the β-activity induced by the (n,p) reaction of aluminum. A large enhancement of the time-of-flight spectra took place in the cold neutrons, resulting in an approximately doubled neutron gain.

B. Spatial dependence of emitted beams

Considerably irregular spatial distribution of the emitted neutron beam from the grooved surface was expected. We measured the dependence of the beam along the vertical direction of the grooved chamber by using the movable cadmium slit described above. Figs. 4 and 5 show the measured data for neutrons of energies 2, 5 and 50 meV respectively.

Although the overall spatial dependence in the grooved moderator was similar to the one in the flat moderator, the ratio of the intensities of the beams emitted from the bottom and the top of the grooves was cosiderably high. As seen from the figures, the ratio became larger as the neutron energy decreased.

C. Time dependence of pulses

We next measured the time dependence of the pulses by using a mica monochrometer with Bragg angle of 85°. Figs. 6 and 7(a) show the pulse spectra of 5.26 meV neutrons emitted from the tops and the bottoms of the grooves and from the whole grooved surface, which were all normalized to the peak height.

Fig. 7(b) shows a comparison of the three pulse spectra from the grooved moderator and a spectrum from the flat moderator. As is clearly recognized, the shapes of the pulses from the top and the bottom of the grooves are very similar but the starting time of the sharp rise in the latter one has a time delay of about 40 μs compared to the former one. This time delay approximately corresponds to the time-of-flight of the groove height for 5 meV neutrons. Thus the shape of the pulse spectra from the whole surface of the grooved moderator is apparently distorted as compared to the one from the flat moderator; moreover, the effective width is appreciably longer than that of the flat moderator.

4. EFFECTS OF PULSE SHAPE DISTORTION ON PERFORMANCE OF SPECTROMETERS

We report in this section our assessment of the effects of pulse shape distortion on the performance of the spectrometers. There are three spectrometers installed at the KENS' cold neutron source: SAN: a small angle scattering spectrometer, TOP: a polarized neutron spectrometer and LAM: a quasielastic spectrometer.

The former two spectrometers are equipped with 20 m long neutron guide tubes which provide sufficient time-of-flight length of incident neutrons. Thus pulse shape distortion is not a problem in the case of the former two. Furthermore, the increase of total intensity benefits primarily their performances.

In the case of the LAM, which is a conventional energy resolution quasielastic spectrometer, the pulse shape distortion affects the resolution to some extent. To assess this effect we calculated the elastically scattered neutron spectra from both the grooved and the flat moderators. The measured intensity distribution, $y(t)$, on the time analyser is related to the neutron cross section $\sigma(E_1 \to E_2)$ and various instrumental conditions[7],

$$y(t) = \text{const.} \iint \eta(E_1) Z(t - \frac{l_1}{\sqrt{2E_1/m}} - \frac{l_2}{\sqrt{2E_2/m}}) \sigma(E_1 \to E_2) R(E_2) dE_1 dE_2$$

where $\eta(E_1)$ is the energy spectrum of neutrons emitted from the moderator, $Z(\tau)$ is the time distribution of the pulse, τ is the emission time, $R(E_2)$ is the resolution function of the analyser for the scattered neutrons and l_1 and l_2 are the first and second flight path lengths respectively.

Fig. 8 shows the calculated results of y(t) in the cases of the grooved and the flat moderators in which the cross section was assumed to be elastic and synthesized time distributions were used as shown in Fig. 9. As seen from Fig. 8, the effective pulse width in the case of the grooved moderator is about 15 percent longer than that obtained from the flat moderator. However, there is no appreciable difference in the pulse shape on the rising side. In the case of the LAM, intrinsic resolution is determined by the pulse shape on the rising side. Therefore, it was proved that the grooved cold moderator operates efficiently without diminishing resolution performance.

References

1) K. Inoue, et al.: J. Nucl. Sci. Tech., 13(1976)389.
2) K. Inoue, et al.: Nucl. Instr. Meth., 192(1982)129.
3) Y. Ishikawa, et al.: Proc. 4th Int. Collaboration on Advanced Neutron Source(ICANS), Tsukuba, Japan(Oct.1980).
4) N. Watanabe, et al.: Proc. 6th Int. Collaboration on Advanced Neutron Source(ICANS), Argonne, USA(June 1982).
5) J. M. Carpenter: Proc. 4th Int. Collaboration on Advanced Neutron Source(ICANS), Tsukuba, Japan(Oct.1980).
6) G. S. Bauer: ibid.
7) K. Inoue, et al.: Nucl. Instr. Meth., 178(1980)459.

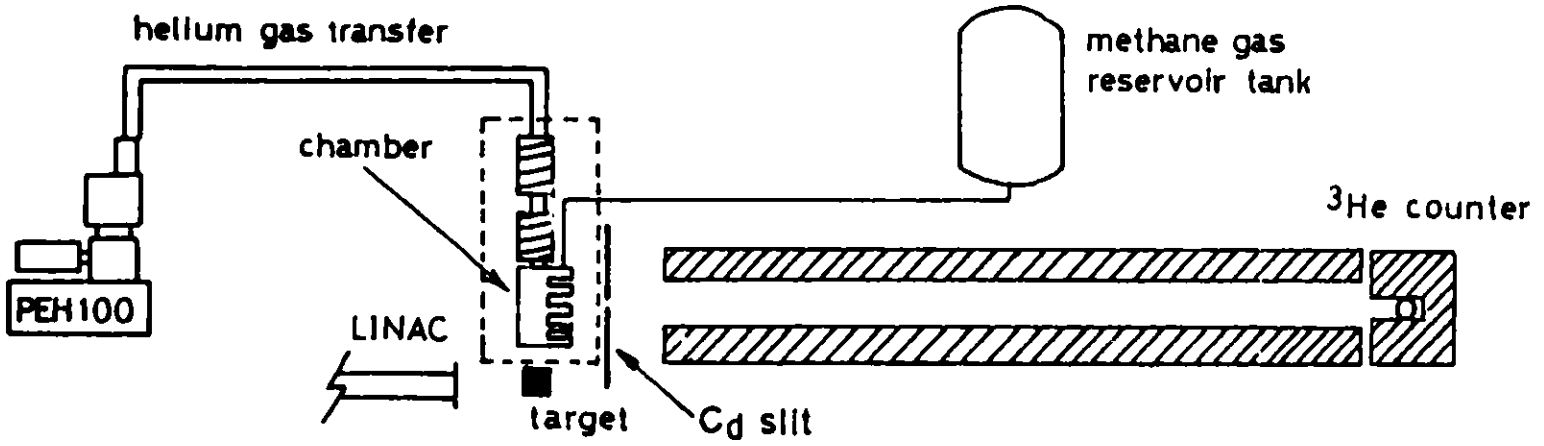

Fig. 1 Layout of the experimental facilities.

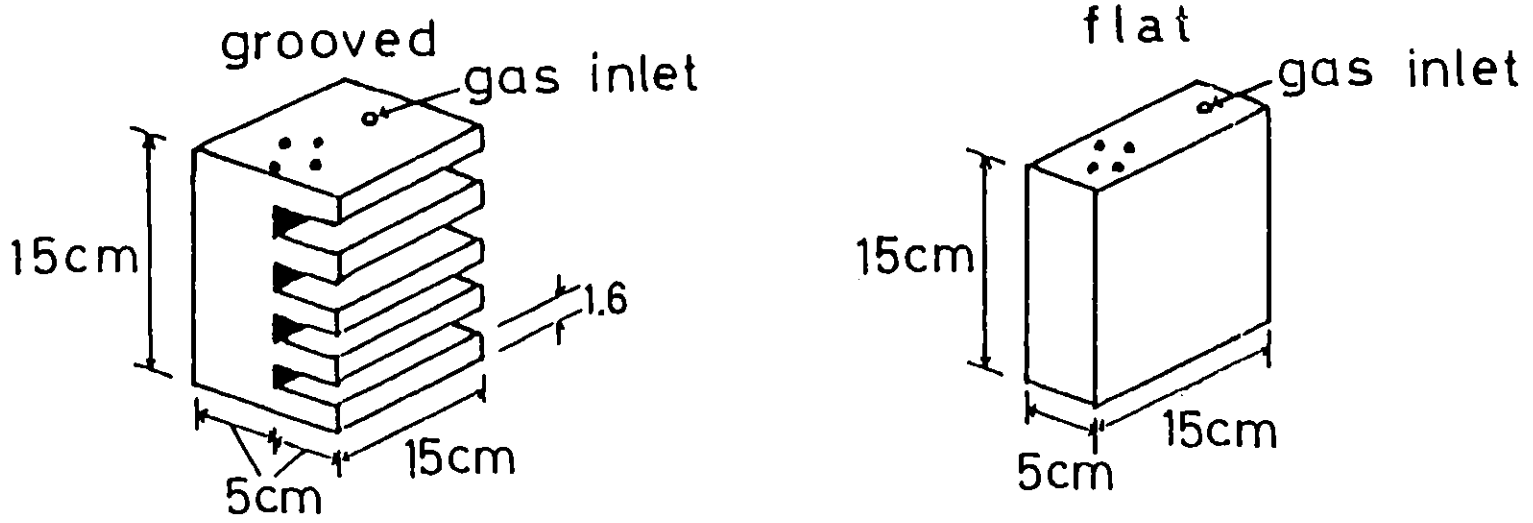

Fig. 2 Grooved and flat methane chambers.

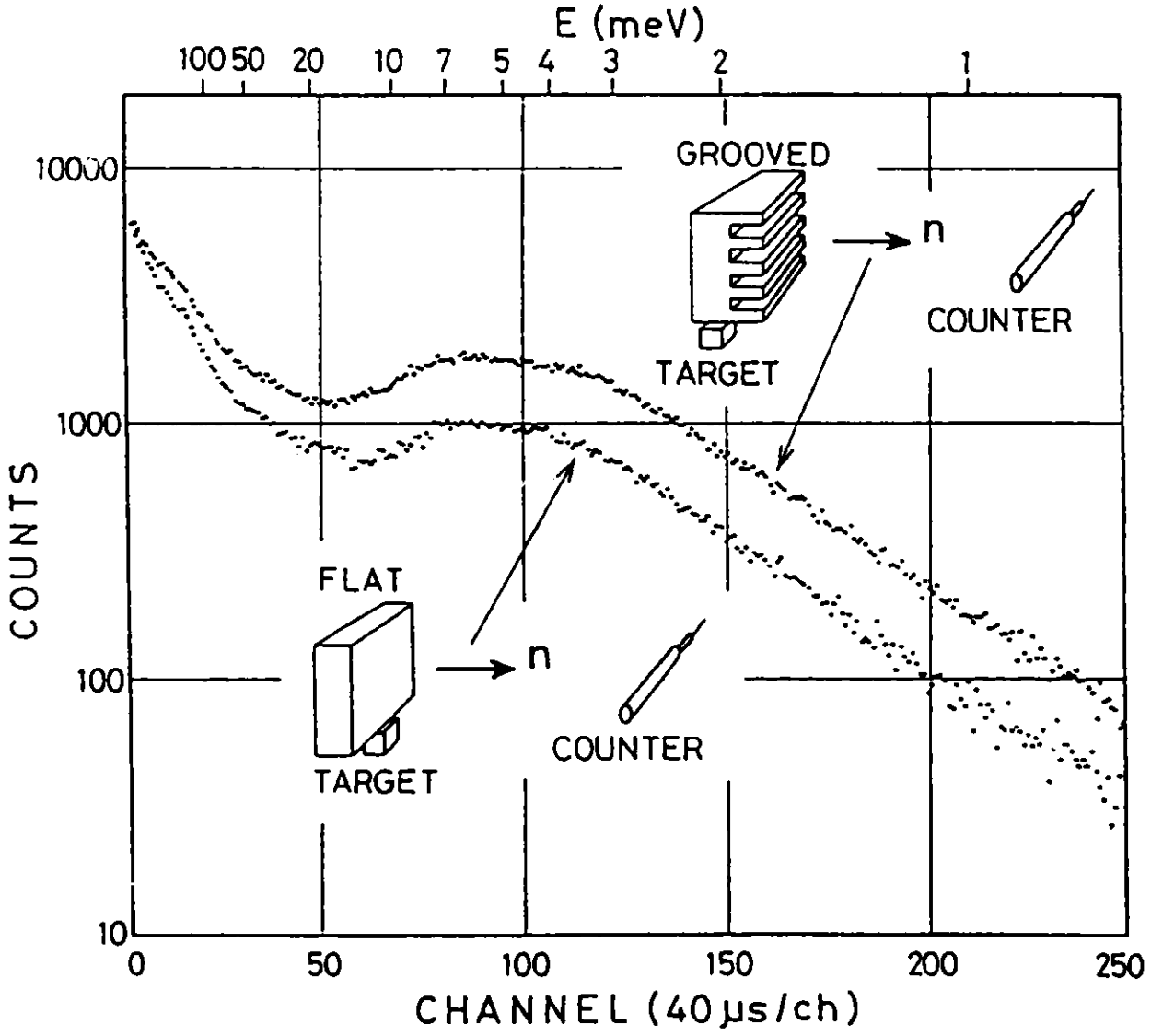

Fig. 3 Time-of-flight neutron spectra from grooved and flat moderators.

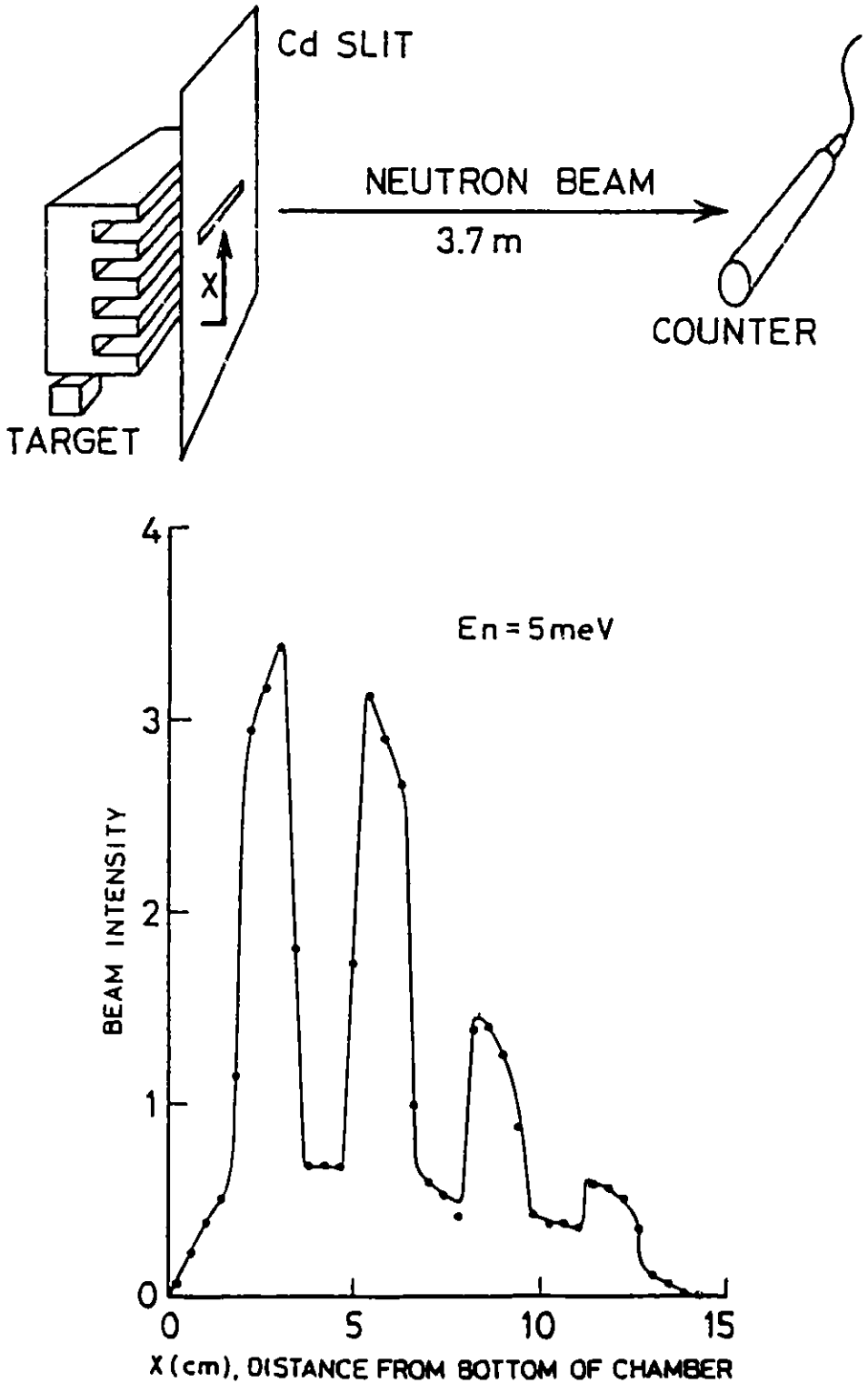

Fig. 4 Spatial dependence of emitted neutron beam with energy 5 meV.

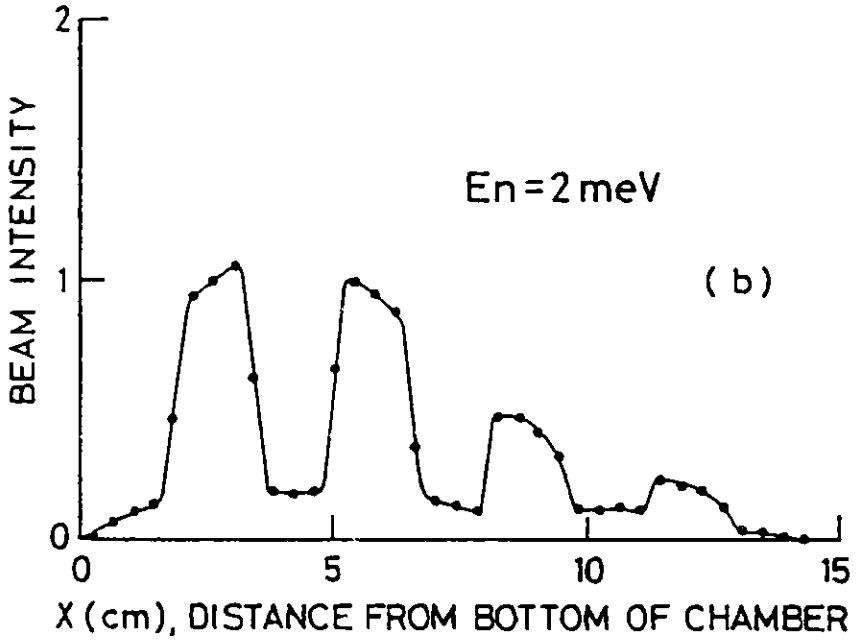

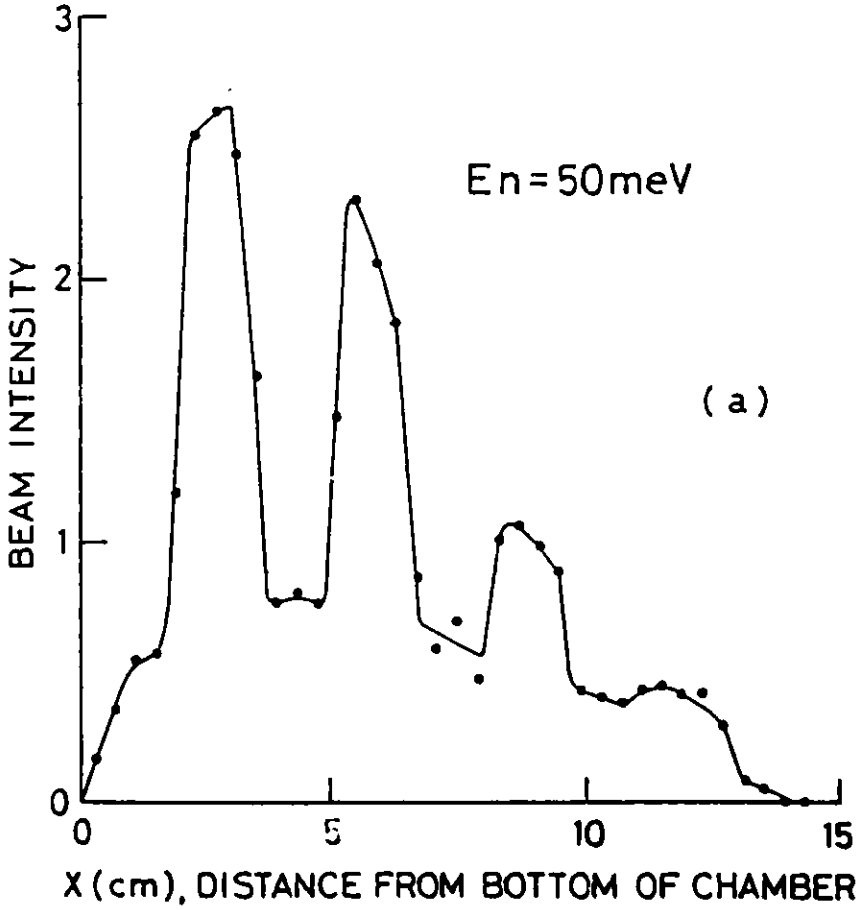

Fig. 5 Spatial dependences of emitted neutron beams with energies 50 meV:(a) and 2 meV:(b).

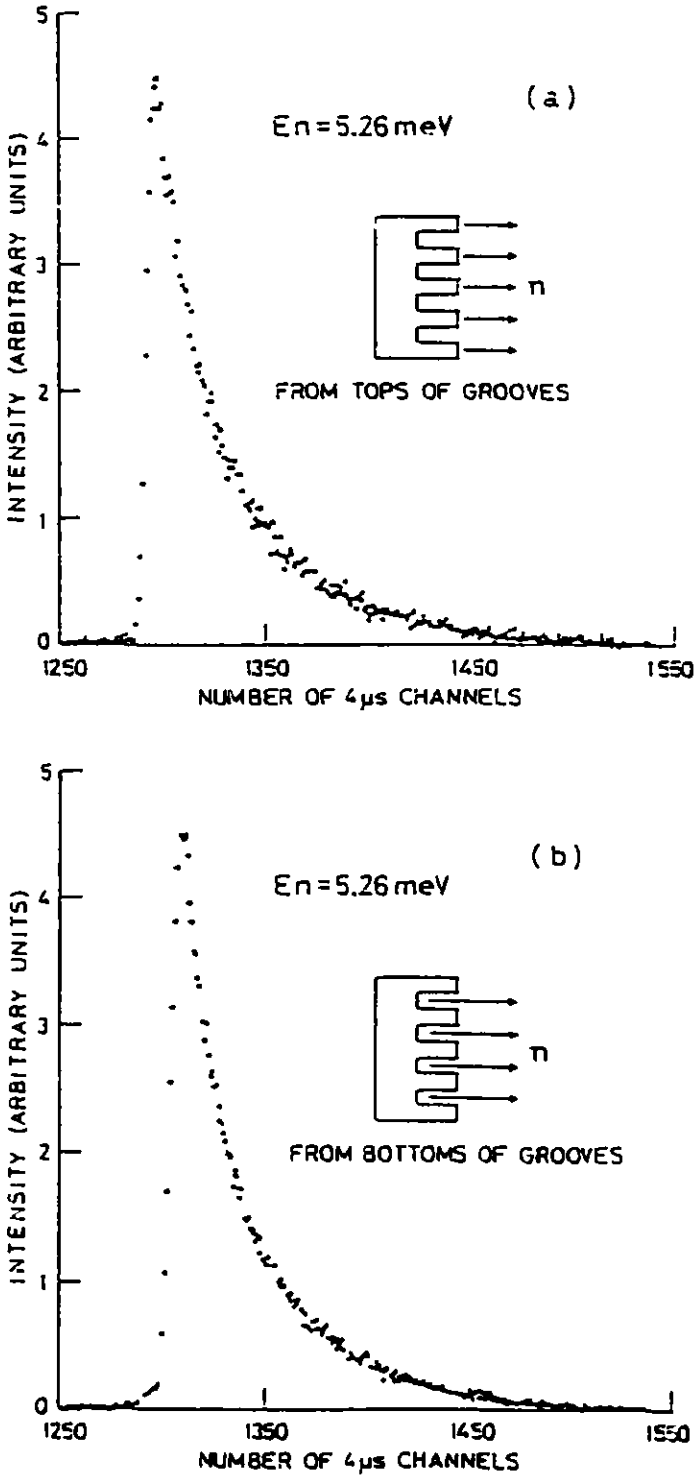

Fig. 6 (a) Time distribution of the pulse of neutrons emitted from the tops of the grooves. (b) Time distribution of the pulse of neutrons emitted from the bottoms of the grooves.

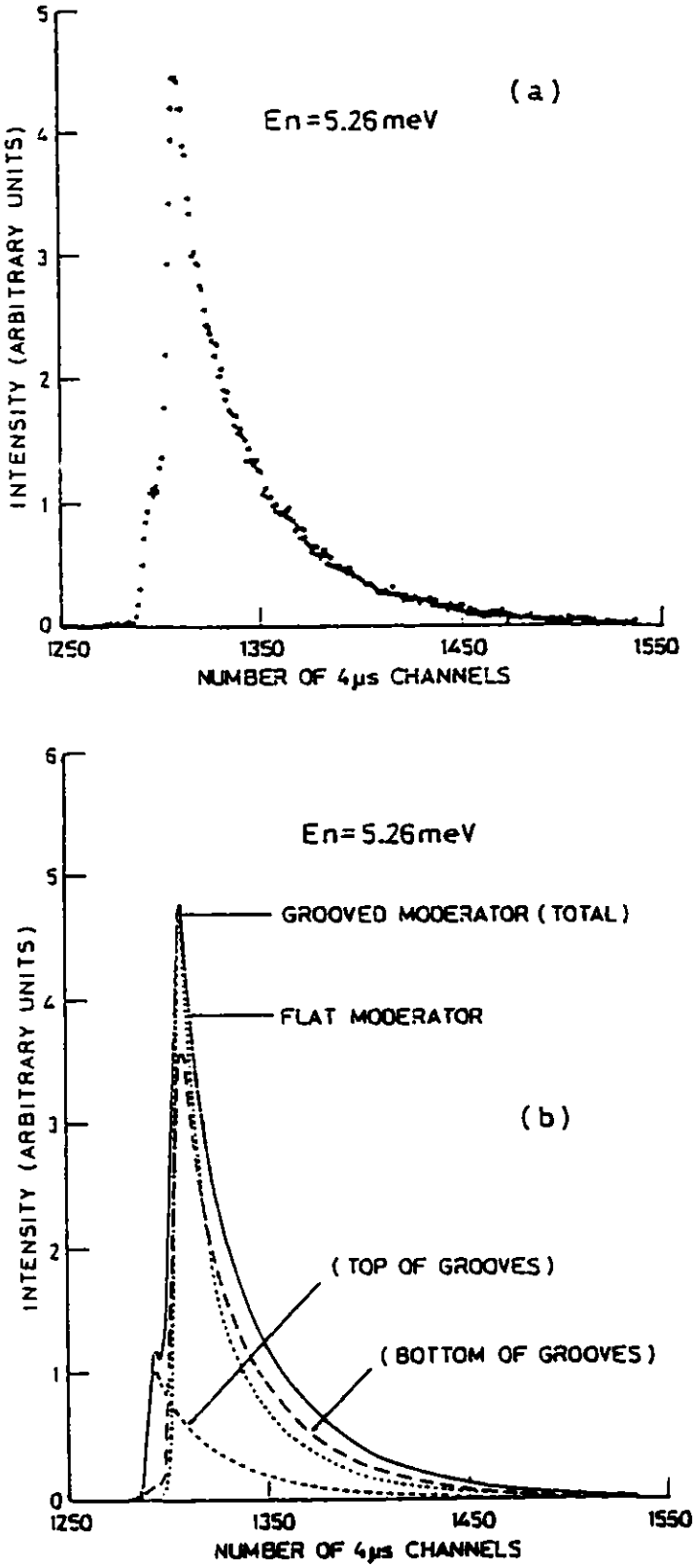

Fig. 7 (a) Time distribution of the pusle of neutrons emitted from the whole surface of the grooved chamber. (b) Comparison of the three pulses emitted from the tops and the bottoms of the grooves and the whole surface, and the pulse emitted from the flat chamber.

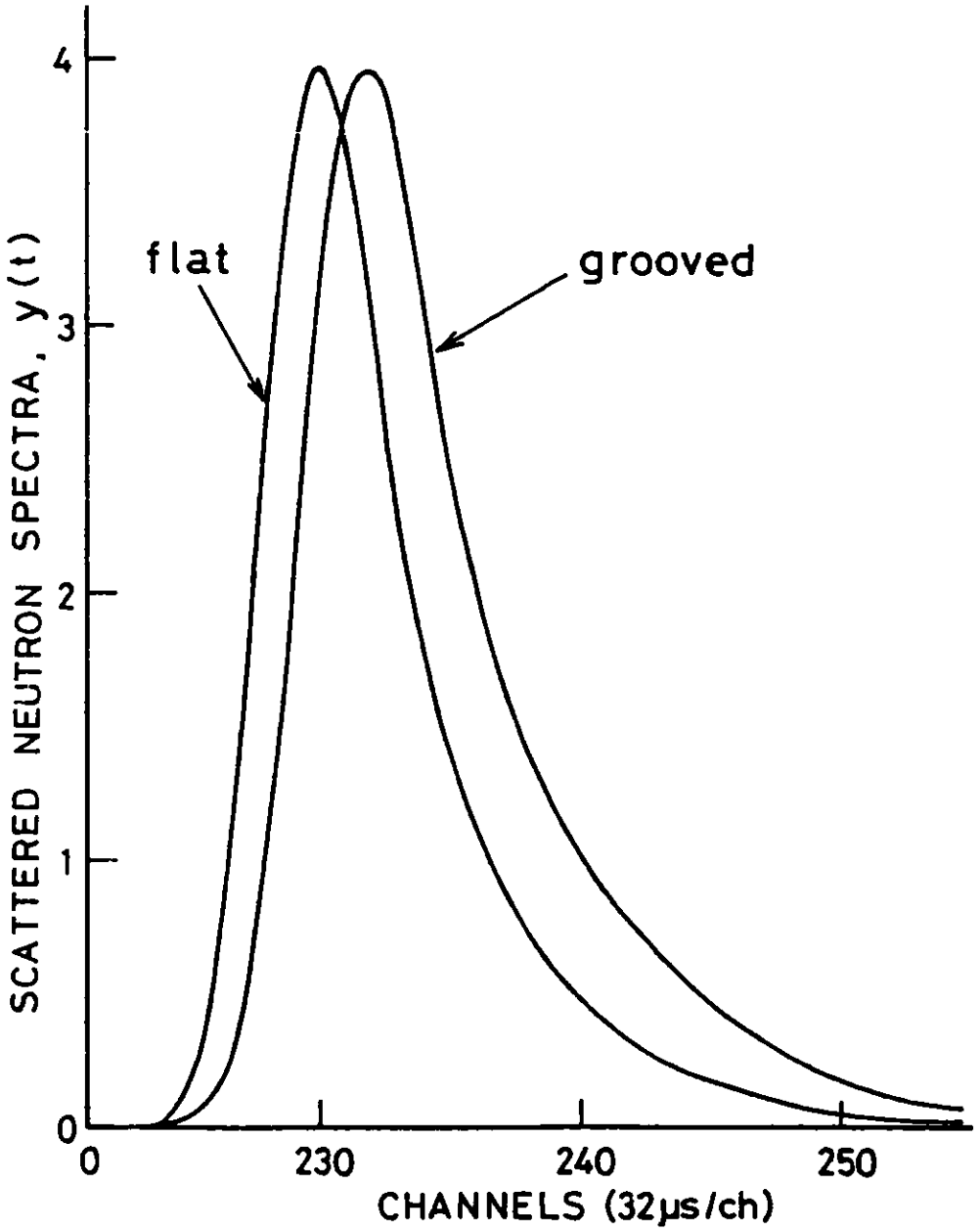

Fig. 8 Calculated scattered spectra for the grooved and the flat moderators using an elastic scatterer. These data exhibited effective resolutions.

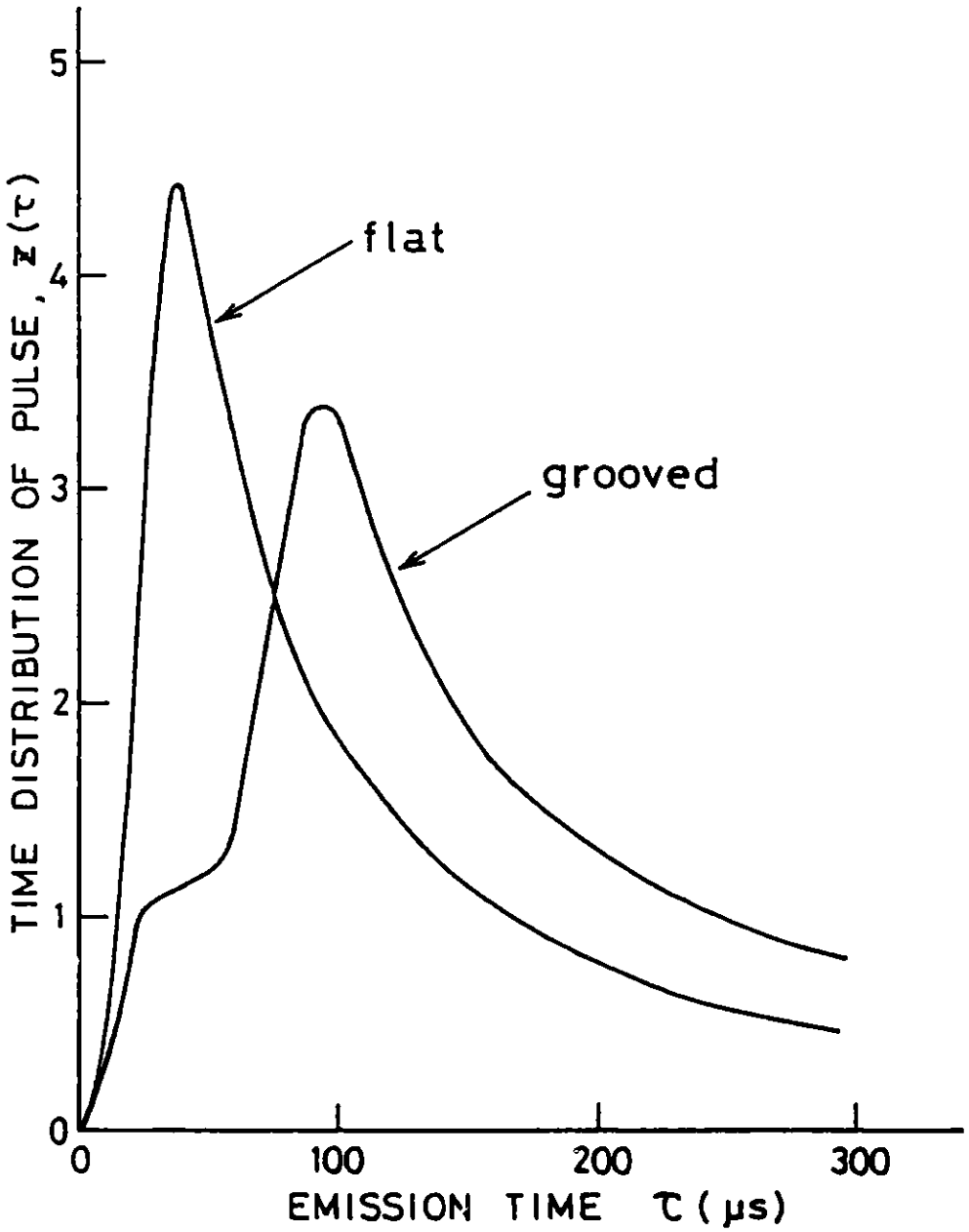

Fig. 9 Synthesized time distributions of the pulses used in the spectral calculation.

MEASUREMENT OF NEUTRON SPECTRA AND FLUXES AT THE IPNS RADIATION EFFECTS FACILITY

R. C. Birtcher, M. A. Kirk, T. H. Blewitt and L. R. Greenwood

Argonne National Laboratory
Argonne, Illinois 60439

ABSTRACT

We have measured the neutron spectra, fluxes, and flux distributions produced by nuclear spallation resulting from 478-MeV proton bombardment of tantalum and depleted uranium targets surrounded by a thick lead neutron reflector. The configuration was chosen to simulate a radiation effects facility at a spallation-neutron source. The method of multiple foil activation with spectrum unfolding by the STAYSL computer code was used to measure the neutron spectra. The experimental results are compared in detail with the results of computer calculations on the same configuration of targets and reflector. The neutron production and transport codes HETC and VIM were employed in these calculations.

Based on these measurements, the Radiation Effects Facility (REF) was designed and constructed at the IPNS. Using simular activation techniques the neutron spectra, fluxes and flux distributions have been determined for the REF.

1. INTRODUCTION

The Development of nuclear reactors as energy sources has required and will continue to require the study of the effects of neutron irradiations upon materials. This has lead to the need for a Radiation Effects Facility (REF) at the IPNS [1].The study of radiation effects requires well-controlled intense fluxes of high-energy neutrons without contamination by secondary particles. Further, access to these neutrons must be direct and allow precise environment and temperature control. Many basic studies also require

irradiation at liquid helium temperatures to arrest defect migration. These requirements have placed several restrictions upon the design of the REF. The proton target should generate the largest number of neutrons per proton with the minimum of neutron-energy moderation and minimum γ flux. This led to the minimization of the target cooling water and target diameter consistant with acceptable target temperatures. Both Ta and ^{238}U were considered as target materials. To further minimize the neutron energy loss and increase the neutron flux, the target should be surrounded by a high density reflector material consisting of atoms with a high atomic number. These considerations lead to the testing of several target/reflector systems by computer modeling and finally by a full scale experimental mock-up [2].

2. Experimental Details

2.1 Mock-up.

A simplified schematic of the experimental arrangement for the REF mock-up is shown in Fig. 1. The targets were solid cylinders of Ta, 8.2 cm in diameter and 13.2 cm long, and of Zircaloy-clad ^{238}U, 8.3 cm in diameter and 14.6 cm long. Each target was irradiated separately while centrally located in a cylindrical Pb cask. The Pb cask surrounded the target with 25 cm of reflector material, and held the neutron-dosimetry assemblies. The perpendicular neutron dosimetry assembly was located in a hole that passed within 1 cm of the ID surface of the cask. The target was located so that this hole was at the calculated peak neutron flux position along the target axis. The principal neutron dosimetry package was also located within the hole, and adjacent to the target. The parallel neutron dosimetry assembly was located in an Al tube suspended between the Pb cask and the target. An additional 46 cm of Pb was placed above and on one side of the Pb cask for radiation shielding of the environment. The entire target and cask were electrically isolated to provide a Faraday-cup measurement of incident-proton current. This and another Faraday-cup beam stop were used to monitor beam alignment on target during the irradiation, but proved to be substantially in error for an absolute measurement of integrated proton current over the entire irradiation period. Instead, the integrated proton flux was measured with Al monitor foils, as described in the next subsection.

Both targets were water cooled with a flow of ~0.6 l/sec. Temperatures were monitored by thermocouples during irradiations by 478-MeV protons at

typical time-averaged currents of ~1 μA. The temperature increased by ~2°C

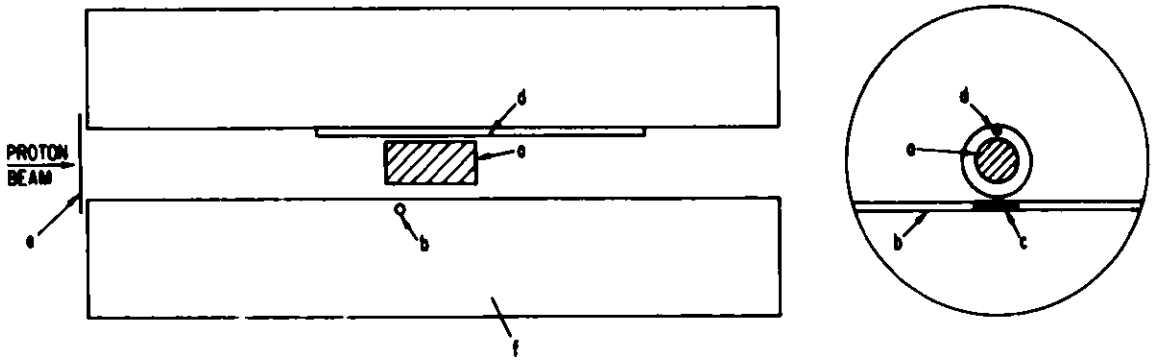

Figure 1. Schematic of target, reflector, and dosimetry positions. (a) Ta or ^{238}U target; (b) hole for perpendicular neutron dosimetry assembly; (c) principal neutron dosimetry site; (d) tube for parallel neutron dosimetry assembly; (e) proton dosimetry foils; and (f) Pd reflector.

above the coolant temperature (35°C) on the surface of the Ta target at the calculated axial position of maximum energy deposition (5 cm from the front face of the target). There was a ~35°C rise in the centerline temperature at a similar axial position in the ^{238}U target.

The 478-MeV proton beam was supplied to the mock-up experiment by the ANL Rapid Cycling Synchrotron (RCS, formerly called Booster II [3] when associated with the ZGS accelerator). The protons were obtained by stripping the electrons from a 50-MeV H^- beam supplied by a linear accelerator (Linac), which also served to inject the ZGS during these experiments. As a result of the sharing of the Linac system with the ZGS, the RCS was operated in a "burst mode", consisting of approximately 2.7 seconds of beam extraction at 15-Hz repetition, followed by 1.3 seconds without beam. This mode of operation had no effect on the operation of the experiment or the results. The number of protons per pulse on target averaged ~7 x 10^{11} with an effective frequency of ~10 Hz as a result of the burst-mode operation, yielding an average beam current on target of about 1 μA during normal operation of the accelerator. "Abnormal" accelerator operation consisted of complete shutdowns due to equipment failures. Details of the accelerator operation were recorded for each irradiation, and used to correct the corresponding neutron dosimetry data.

Integral dosimetry of the 478-MeV proton beam was accomplished by monitoring the ^{27}Al (p,x) ^{22}Na reaction in aluminum foils placed at the entrance to the Pb reflector (Fig. 1). A cross section of 17.8 mb (±15%) was

used for the ^{27}Al (p,x) ^{22}Na reaction at the proton energy of 478 MeV. This cross section is the value recommended by the CEA (France) in their 1971 compilation of nuclear monitor reactions [4]. The error represents the spread of the various experimental data at this energy. The uncertainty in the value of this cross section is the predominant source of possible error in the absolute number of protons on target. To compensate for the loss of energetic spallation products at the surfaces of the Al foil, a high-purity Al foil 0.025 mm thick was sandwiched between two ordinary Al foils 0.012 mm thick. These foil thicknesses proved adequate to compensate for loss of the ^{22}Na product, but inadequate for the lighter ^{7}Be product. For this reason, and because the cross section for its production is not as well established, the ^{7}Be activity was not used for dosimetry purposes. The proton spallation reaction yielding ^{24}Na was not used for proton dosimetry because ^{24}Na is produced by neutron absorption in Al and because of the short ^{24}Na half-life (15 hr).

The Al dosimetry foils were also used to obtain autoradiographs of the integrated intensity distribution of the proton beam for each target irradiation. Microphotodensitometry data were obtained from the autoradiographs to generate the experimental beam profiles (linearity with fluence was assumed), which were then averaged about the cylindrical axes of the targets. These averaged radial beam profiles were used as input parameters to the computer programs that calculated the spallation-neutron production with which the experimental results will be compared. The proton beam for irradiation of the ^{233}U target was intentionally broadened somewhat to lower the target centerline temperature.

2.2 Computer Model Calculations.

Spallation-neutron production and neutron transport were calculated by two Monte Carlo-based three-dimensional computer codes, HETC [5] and VIM [6]. The High Energy Transport Code (HETC) employs nuclear models to calculate high-energy-cascade and evaporation particles caused by the incident protons. Spallation neutrons with energies from 500 MeV down to 15 MeV were transported by this code to the volumes in which the experimental measurements were made. Neutrons with E_n < 15 MeV were subsequently transported by the VIM code. Neutron-produced fission in the ^{238}U target was included in the VIM

calculations, but not in the NETC calculations.

The detailed geometry and material composition of the target, cooling system, and reflector were taken into account in the calculations of the mock-up experiment. Neutron spectra, integrated flux, and spatial flux distributions were obtained for each target by averaging three independent calculations, each involving 2000 incident 500 MeV protons distributed on the target face according to the experimental beam profile. The results of these calculations will be displayed and compared with the experimental dosimetry results in section.

2.3 Radiation Effects Facility

The REF, shown in Fig. 2, consists of the ^{238}U target, two vertical irradiation thimbles, and a horizontal irradiation thimble, all surrounded by a Pb neutron reflector. Based on the results of the mock-up experiment, the target material was chosen to maximize the conversion of protons to neutrons. There is some gamma production associated with the fission process in ^{238}U, although much less than in a reactor-based facility where all neutrons are produced by fission. Should the gamma flux pose an experimental problem, it is possible to change to a Ta target, from which there would be a greatly reduced gamma flux. Lead was chosen as the reflector material based on the results of the mock-up experiment. The Pb reflector alongside the target is in the form of removable sections 10 cm on a side and 45 cm long in cladding. For specialized needs, reflector sections can be removed to increase the irradiation volume or to allow replacement with a different reflector material. Such a change in reflector or target material could change the energy distribution of the neutrons within the irradiation facilities.

The two vertical irradiation thimbles, located on either side of the target at the positions of maximum flux, contain liquid helium cryostats (5 cm inner diameter) that can operate at temperatures between 4 and 1000 K. The liquid helium is supplied by a single 400-W refrigerator (CTI model 2800 R). The two cryostats have separate vacuum systems, which allow the temperature to be controlled independently in each cryostat. The horizontal irradiation thimble (2 cm inner diameter) is located on an axis parallel to and directly below the target. The majority of the ^{238}U target-cooling water is between

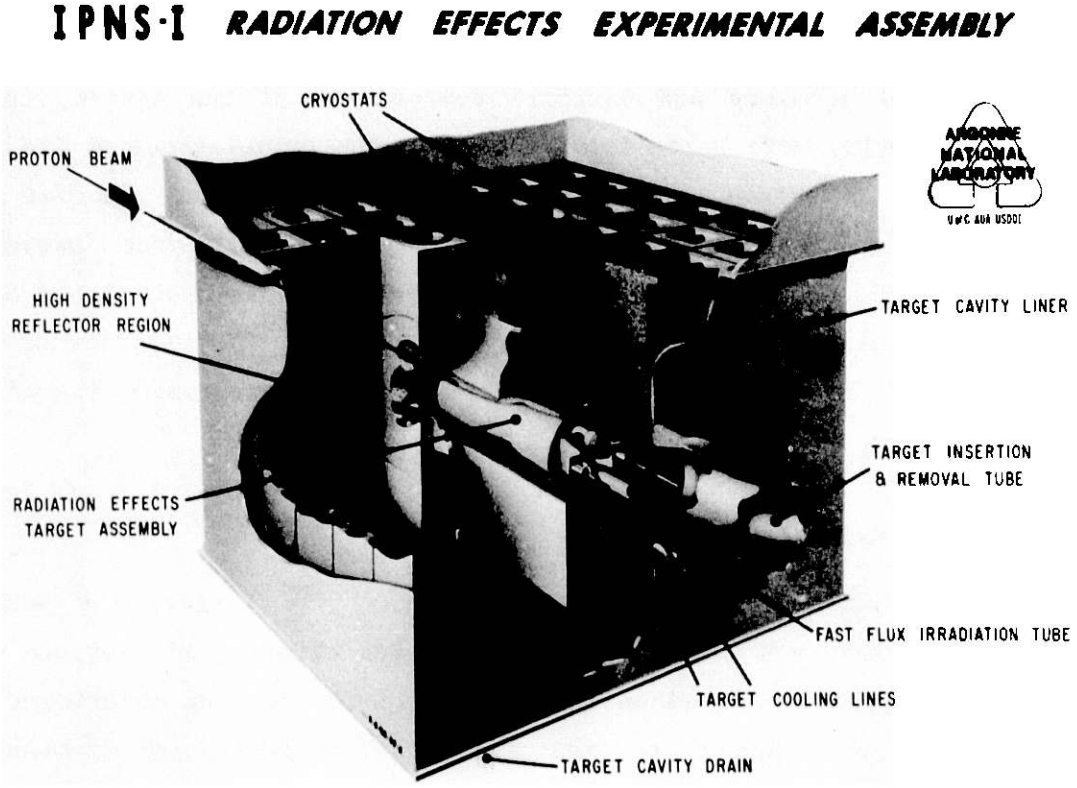

Figure 2. IPNS-I radiation effects assembly.

the target and this thimble. The horizontal thimble operates at ambient temperature and is designed to permit short irradiations with sample removal while neutrons are being produced. The REF differs from the mock-up experiment in the large voids near the target.

2.4 Neutron Scattering Facility

The ^{238}U target in the NSF is surrounded by C and Be reflectors which are penetrated by 12 neutron beam lines. Moderators for producing the thermal-neutron beams are located directly above and below the target. Two unused horizontal beam lines have been modified to contain irradiation thimbles (~1 cm diameter). These two thimbles radially approach within 4 cm of the target axis at the position of maximum neutron flux along this. The majority of target-cooling water is between the target and these thimbles. Both NSF irradiation thimbles operate a ambient temperature.

Protons for the IPNS were supplied by the RCS at 500 MeV [7]. The protons were ~100 ns long pulses at a repetition rate of 30 Hz. The proton flux incident upon the ^{238}U targets was determined from the current induced in

a toroid located 3.5 m upstream from the target. This measurement is uncertain by 5 percent. The protons had an energy of 500 MeV.

2.5 Neutron Dosimetry.

A multiple-foil-activation method was used to determine the neutron fluxes and energy spectra for the Ta and ^{238}U irradiations at the principal dosimetry site in the mock-up experiment (Fig. 1) and at the primary irradiation positions in the irradiation facilities. The STAYSL computer code [8] was used to find the most probable neutron spectra from the foil acitivies, using a least-squares technique. The input spectra were taken from the computer-model calculations of neutron production and transport to the principal dosimetry site for each target and reflector system.

The Dosimetry Group and the Analytical Chemistry Laboratory at ANL measured foil activities with Ge(Li) detectors over several γ-decay half-lives for each of the 28 reactions listed in Table 1. Peak integrations and Compton-background subtractions were done by means of computer programs in routine use by the Dosimetry Group [9]. Prior to spectrum unfolding, activation corrections for neutron and gamma self-shielding, cover foils, and decay during and after irradiation were made for foil geometries in an isotropic flux. The STAYSL program compared the calculated activities with the measured activities. It then adjusted the differential neutron spectrum (100 energy groups), using a least-squares procedure. The energy-dependent cross sections were taken from ENDF/B-IV [10]. For those reactions sensitive to neutron energies $\gtrsim$ 30 MeV, the energy-dependent cross sections have been extrapolated [11] to 44 MeV and integrally tested in a well-defined Be (d,n) neutron spectra [12].

The output of the STAYSL code includes a complete covariance-error matrix for the neutron-flux spectra. Errors and covariances in the measured acitivities, cross sections, and input spectra were estimated from the available nuclear data. The integral activities typically had errors of ±2%, whereas cross-section and flux errors varied from 5 to 50% depending on the estimated reliability of nuclear data. Flux and cross-section self-covariances were specified by a Gaussian function assuming that nearby groups are highly correlated and widely separated groups uncorrelated. This procedure also guarantees a smooth output spectra, avoiding sharp peaks and

Table 1. Neutron dosimetry reactions

Material	Reaction	Half-life (days)	Cd Cover[a]
^{235}U	$(n,f)^{95}Zr$, ^{103}Ru, ^{140}Ba	64.1,39.4,12.8	+[a]
^{237}Np	$(n,f)^{95}Zr$, ^{103}Ru, ^{140}Ba[b]	64.1,39.4,12.8	+
	$(n,\gamma)^{238}Np$[b]	2.1	+
^{238}U	$(n,f)^{95}Zr$, ^{103}Ru, ^{140}Ba	64.1,39.4,12.8	-
	$(n,\gamma)^{239}Np$	2.36	+
	$(n,2n)^{237}U$	6.75	-
Ni	$^{58}Ni(n,p)^{58}Co$	70.85	-
	$(n,2n)^{57}Ni$	1.5	-
Fe	$^{54}Fe(n,p)^{54}Mn$[b]	312.5	-
	$(n,\alpha)^{51}Cr$[b]	27.7	-
	$^{58}Fe(n,\gamma)^{59}Fe$	44.60	+[b]
Au	$^{197}Au(n,\gamma)^{198}Au$[c]	2.7	+
	$(n,2n)^{196}Au$	6.1	-
	$(n,3n)^{195}Au$	184	-
Co	$^{59}Co(n,\gamma)^{60}Co$	1925	+
	$(n,p)^{59}Fe$	44.6	-
	$(n,2n)^{58}Co$	70.85	-
	$(n,3n)^{57}Co$	271	-
	$(n,4n)^{56}Co$[b]	78.5	-
Ti	$^{46}Ti(n,p)^{46}Sc$[b]	88.9	-
	$^{47}Ti(n,p)^{47}Sc$[b]	3.4	-
	$^{48}Ti(n,p)^{48}Sc$	1.8	-
Sc	$^{45}Sc(n,\gamma)^{46}Sc$	88.9	+
	$(n,2n)^{44m}Sc$	2.44	-
Al	$^{27}Al(n,\alpha)^{24}Na$	0.63	-
Nb	$^{93}Nb(n,2n)^{92m}Nb$	10.1	-

[a]"+" means both covered and uncovered samples were included.

[b]Not used for spectral analysis — cross section uncertain.

[c]Both thick and dilute alloy foils.

Proton dosimetry reactions

Material	Reaction	Half-life (days)
Cu	$^{65}Cu(p,n)^{65}Zn$	244
V	$^{51}V(p,n)^{51}Cr$	27.7
LiF	$^{7}Li(p,n)^{7}Be$	53.3

dips at known neutron resonances. The output covariance-error matrix was used to compute broad group flux errors (Table 2) and can be used for errors in derived quantities such as nuclear displacements or gas production in irradiated materials.

In addition, the spatial flux distribution was determined for the two other neutron-dosimetry locations of the mock-up shown in Fig. 1 and in the vertical thimble of the REF, using 50-cm-long dosimetry wires of Fe, Ni, Ti, and Co. After irradiation, the wires were cut into 2.5-cm segments. The neutron spectrum in each segment was calculated by means of STAYSL to fit the activities produced by eight reactions in the wires; the spectrum measured at the corresponding principal disometry site was used as an input spectrum, Integral fluxes (E > 1.0 MeV) of the resultant spectra were determined along the length of these two dosimetry locations, but with less accuracy than at the principal site, since fewer neutron reactions were available.

Secondary-proton dosimetry was also performed in a position near the principal neutron dosimetry site. The proton reactions listed in Table 1 for Cu, V, and LiF were used to obtain an approximate estimate of secondary-protron flux and crude energy distribution.

3. Neutron Spectra and Fluxes

3.1 Mock-up

The neutron spectra obtained at the principal dosimetry site of the mock-up experiment are shown in Figs. 3 and 4 for the Ta and ^{238}U targets, respectively. In these two figures, the solid lines are the theoretical calculations (HETC and VIM) and the dotted lines are the results of fitting the experimental foil activities of Table 1 with the STAYSL code, using the calculated spectra as input. In Figs. 3 and 4, the experimental determinations extend to 44 MeV, and the calculated spectra are not displayed above this energy.

For both targets, the agreement between calculated and experimental neutron spectra, is seen to be reasonably good. However, the experimental data tend to yield more neutrons in the energy range between about 10^{-2} and 10^{-1} MeV, and fewer neutrons below 10^{-3} MeV, than one finds in the calculated spectra for the two targets. The remaining differences above 10^{-1} MeV are close to, or within, the experimental error. The experimental error is least

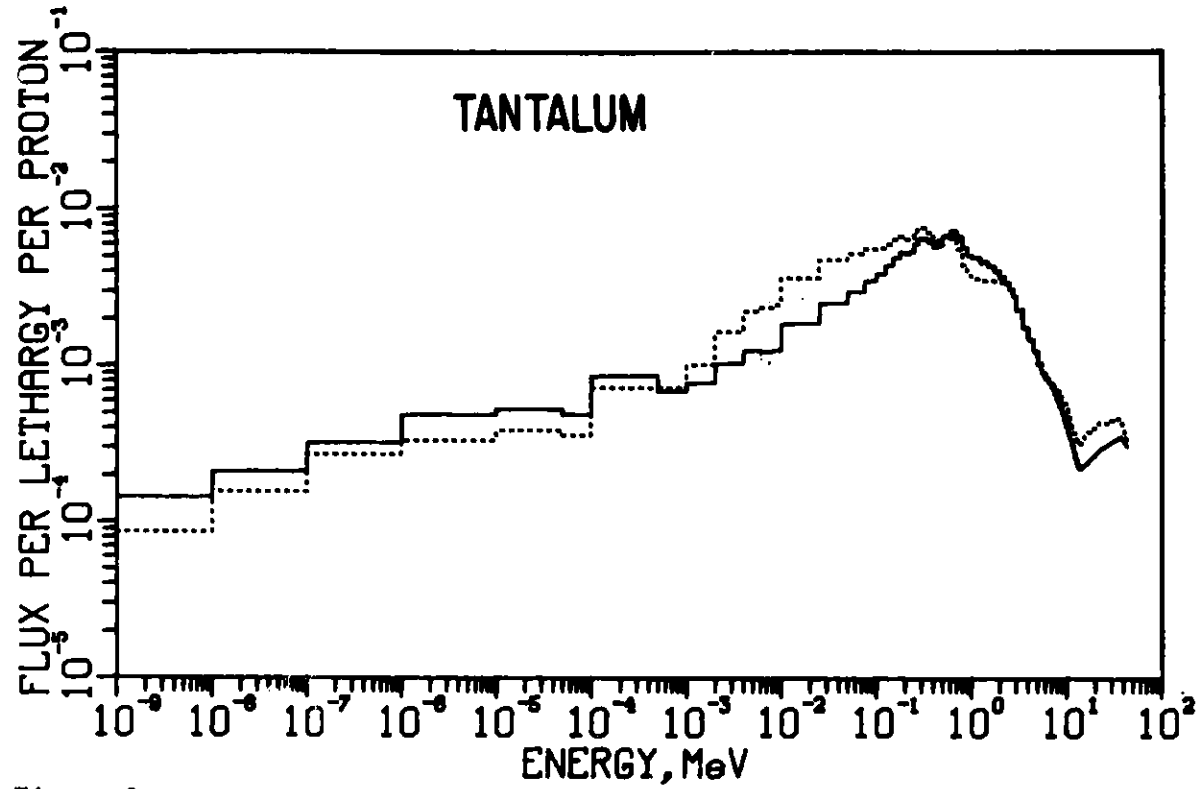

Figure 3. Spallation neutron spectra produced in the mock-up experiment by irradiation of the tantalum target.. The solid line is calculated and the dotted line is experimental.

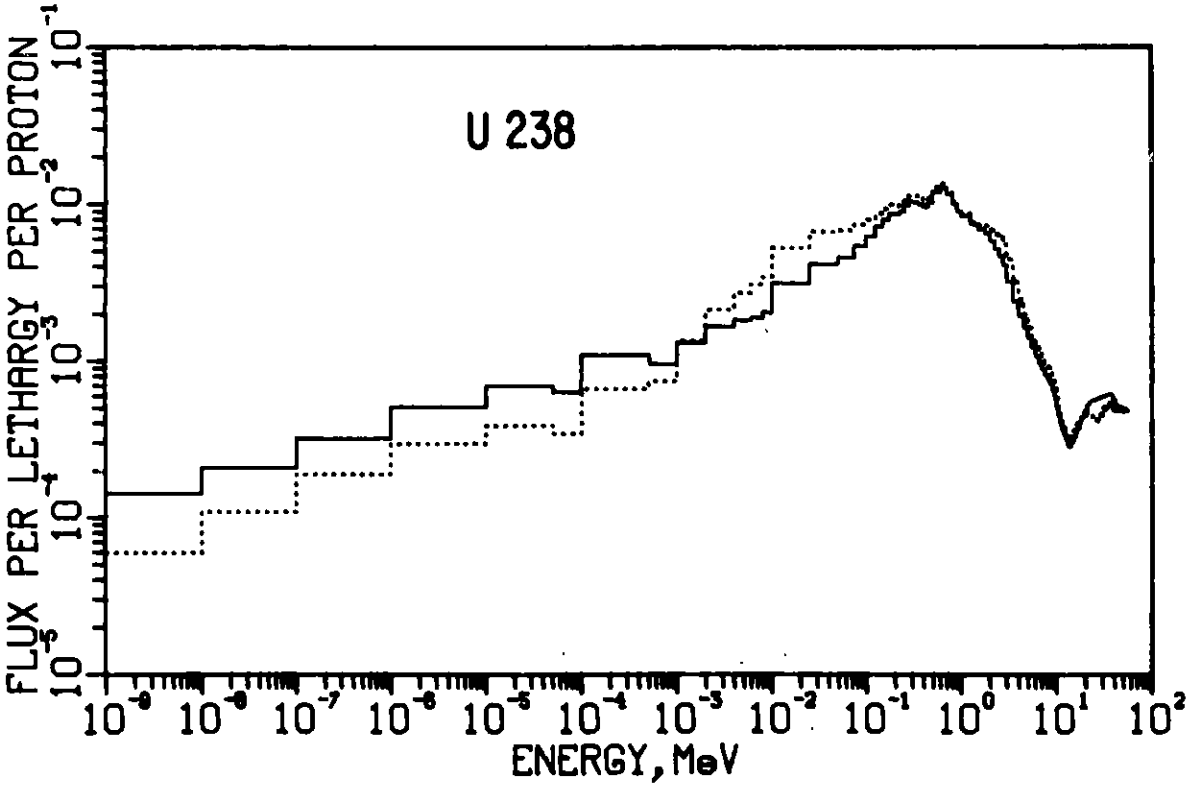

Figure 4. Spallation neutron spectra produced in the mock-up experiment by irradiation of the depleted uranium target. The solid line is calculated and the dotted line is experimental.

where the number of nuclear reactions and the magnitude of the cross sections used in this study are greatest, namely, for neutron energies less than 10^{-3} MeV and between 2 and 10 MeV. However, owing to the strong covariance effects between different neutron-energy groups, reducing the error in energy regions that are well covered by reactions helps to establish the neutron spectrum in the difficult region between 10^{-2} and 2 MeV, and integral errors in fluxes or derived quantities are less than might be expected.

Above 10 MeV, an unexpected bump appears in both calculated and experimental spectra for both target materials. The sharpness of these bumps is due to the method of plotting the flux per unit lethargy ($d\phi/d\ln E$, or equivalently, $E\, d\phi/dE$), which tends to accentuate high-energy features. In a linear differential plot, $d\phi/dE$, this feature becomes a marked change in slope and is also revealed in the calculations of Fullwood et al. [13] In the calculated spectra, this change of slope in the differential plot is the beginning of the high-energy tail of spallation neutrons with energies up to the incident proton energy, or 478 MeV in the present experiment.

The calculated neutron flux falls rapidly above 30 MeV. The neutron flux in the 44-500 MeV energy region was ignored in the spectral measurements, since adequate activation cross sections are not available. However, this omission does not have any significant effect on the output flux solutions, since the flux is falling rapidly with energy and the flux above 44 MeV is less than 1% of the total. In particular, the rise in the lethargy spectra above 14 MeV is not caused by omitting neutrons above 44 MeV, since the reactions which have large cross sections between 10 and 30 MeV have negligible cross sections above 44 MeV. Only the $^{59}Co(n,3n)$ reaction would be significantly affected, probably lowering the flux in the last few energy groups (> 40 MeV) where the uncertainty is already very large.

Only the spectrum for neutron energies > 0.1 MeV is of importance to most radiation-damage phenomena; however, the entire spectrum and neutron yield is of concern for slow neutron scattering studies. Some values of integral flux determined at the principal dosimetry site are displayed in Table 2 for both target systems. The integral flux values for neutrons in several energy ranges are shown, along with the one-standard-deviation error, and are compared with the calculated results for neutron energies > 0.1 MeV and > 1.0 MeV. As a best estimate and for completeness, the calculated flux for neutron

Table 2. Integral neutron fluxes per incident 500 MeV proton

Neutron Energy (MeV)	Neutrons (n/m^2 per proton)						
	Mock-up Ta Target		Mock-up ^{238}U Target		REF Vertical thimble (Center)	REF horizontal thimble	NSF horizontal thimble
	Exp.	Calc.	Exp.	Calc.			
Total	383(±15%)		579(±13%)		311	203	194
Thermal	8.31(±16%)		4.51(±16%)		2.4	1.7	44
> 0.1	209(±21%)	200	362(±17%)	310	199	122	55
> 1.0	60.1(±11%)	63	114(±13%)	93	66	36	13
Secondary Proton Energy (MeV)	Secondary Protons (P/m^2 per proton)						
20-40	~0.3		~0.3		~0.7	~0.2	~0.2

energies > 44 MeV has been added to the experimental determinations of integral fluxes for all lower energy limits. The consequences of this assumption, or any other reasonable assumption for the flux above 44 MeV, are quite small for the total, thermal E_n > 0.1 MeV, and E_n > 1 MeV integral fluxes. The standard-deviation errors for the integral fluxes reflect the uncertainties in the neutron-spectrum determinations. They do not, however, include an overall 15% uncertainty due to possible error in the ^{27}Al (p,x) ^{22}Na cross section (17.8 mb) used to ^{238}U targets, but not to the realtive error between the Ta and ^{238}U results.

It should be noted that the agreement between experimental and calculated values of integrated flux for neutrons with energies > 0.1 MeV is somewhat fortuitous for Ta. With reference to Fig. 3, it can be seen that the integrals of the calculated and experimental curves are equal only if the lower-energy limit is about 0.1 MeV. Other lower-energy limits of integration will result in significant differences between calculated and experimental integrated fluxes.

Also displayed in Table 2 are the results of an attempt to measure the secondary-proton flux present at the principal neutron dosimetry site. The spallation reaction ^{27}Al (p,x) ^{22}Na is of only limited use, owing to probably interference by a similar neutron spallation reaction, ^{27}Al (n,x) ^{22}Na, of unknown cross section. This interference will only take place at the neutron-dosimetry sites that are near the target. The primary-proton dosimetry foils at the front of the Pb reflector (Fig. 1) will not be exposed to a comparable flux of very high-energy neutrons ($\phi_n << \phi_p$). The results of the reactions listed in Table 2 indicate a secondary-proton flux of roughly 0.3 p/m^2 per incident 478-MeV proton, with energy values in the range of 20-40 MeV. The ^{22}Na production can be accounted for by assuming the calculated neutron flux for E_n > 40 MeV and a high-energy neutron cross section for ^{22}Na production equal to the cross section for high-energy protons. The estimate of the secondary-proton flux could be improved considerably through knowledge of the spallation cross section for high-energy neutrons in aluminum. The secondary-proton flux is assumed to be predominantly above 20 MeV, since the cross sections for the proton reactions with Cu, V, and Li all rise steeply below 20 MeV. We would thus expect to observe much greater activation if there were a significant proton flux below 20 MeV. Furthermore, all three activation rates

can be simultaneously fit, assuming most protons are in the 20-40 MeV energy region. In any case, this weak secondary-proton flux does not appear to be significant in terms of either radiation damage in materials or interference with the neutron dosimetry [e.g., the (p,d) reaction is indistinguishable from (n,2n), etc.].

3.2 Radiation Effects Facility

The energy distribution of the neutrons at the position of maximum flux along the center of the REF vertical thimble is shown in Fig. 5 along with the energy distribution for fission neutrons. The neutron flux measurements were made with 1 atm of He gas in the irradiation thimble, and only minor changes are expected if the cryostats contain liquid helium. The REF neutron spectrum can be characterized as a degraded fission spectrum with a high-energy component. The flux of neutrons with E > 0.1 MeV is 199 $(n/m^2)/p$, and the ratio of thermal to "fast" (E > 0.1 MeV) neutrons is 0.012 for 500-MeV protons incident upon the ^{238}U target. The secondary proton flux is estimated to be 0.7 ± 0.5 $(p/m^2)/p$ or 0.4% of the flux of neutrons with E > 0.1 MeV. Radiation of LiF thermal luminescence dosimeters has placed an upper limit on the γ flux of 15% of the total dose in Rads.

The neutron energy distribution for the REF horizontal thimble is also shown in Fig. 5. This spectrum is very similar to the spectrum for the vertical thimble, and the minor differences are likely due to the increased target-cooling water near the horizontal thimble. In the horizontal thimble the flux of neutrons with E > 0.1 MeV is 122 $(n/m^2)p$, and the ratio of thermal to "fast" (E > 0.1 MeV) neutrons is 0.014 for 400-MeV protons incident upon the ^{238}U target. The lower number of neutrons per proton for the horizontal thimble is due in part to the differences in the distance from the target axis to the horizontal thimble and the vertical irradiation thimbles. The proton flux in the horizontal thimble is estimated to be 0.20 ± 0.15 $(p/m^2)/p$ or 0.2% of the flux of neutrons with E > 0.1 MeV. The neutron and proton fluxes at the principle dosimetry sites in the REF are listed in Table 2.

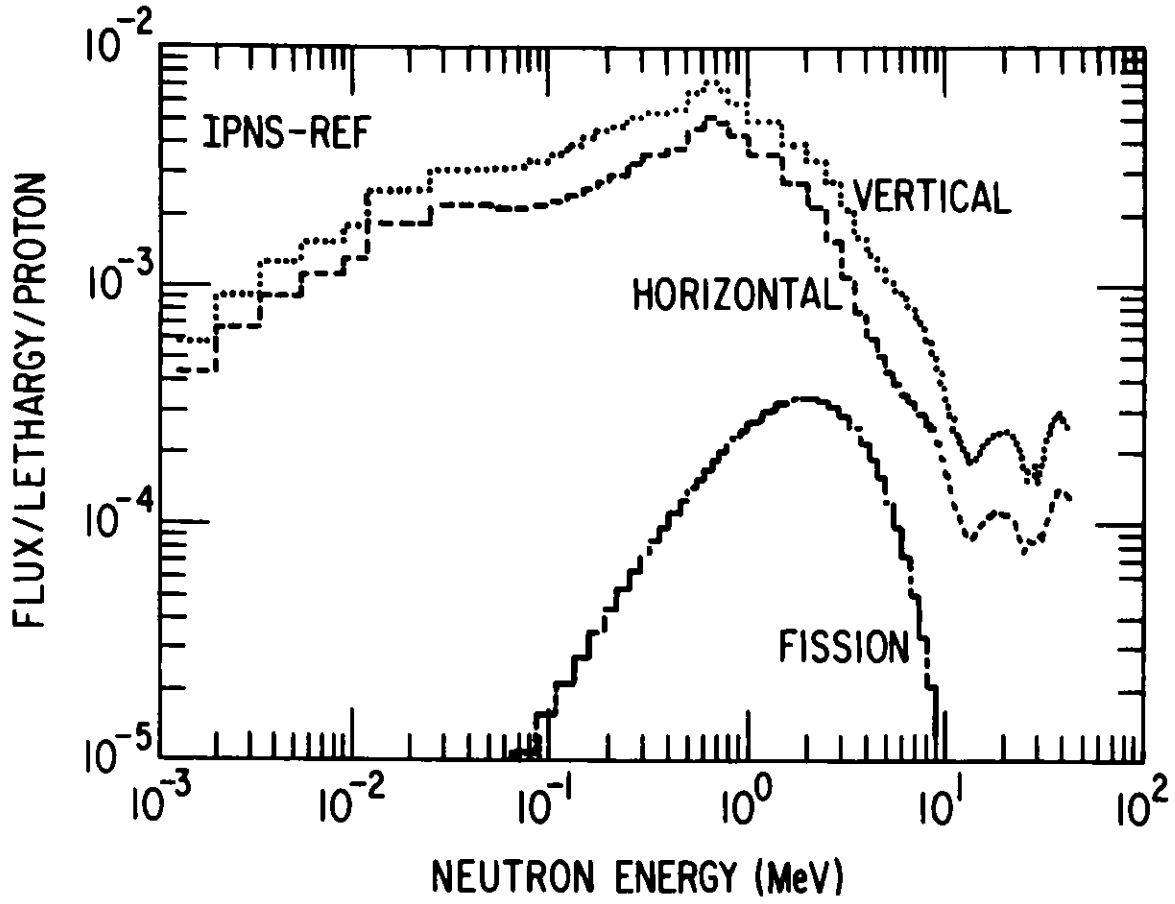

Figure 5. Neutron spectra produced in the vertical and horizontal thimbles of the REF by 500-MeV protons incident upon the ^{238}U target; a pure fission neutron spectrum is shown for comparison.

3.3 Neutron Scattering Facility

Figure 6 shows the neutron energy spectrum for one of the horizontal thimbles in the NSF, the REF vertical thimble, and a pure fission spectrum. The neutron energy distribution for the NSF and REF are quite different, particularly at low neutron energies. The additional low-energy neutrons are produced by (n,2n) reactions and down-scattering in the C and Be. The flux of neutrons with E > 0.1 MeV is 55 $(n/m^2)/p$, and the ratio of thermal to "fast" (E > 0.1 MeV) neutrons is 0.80 for 500-MeV protons incident upon the ^{238}U target. The neutron fluxes available in the NSF are listed in Table 2.

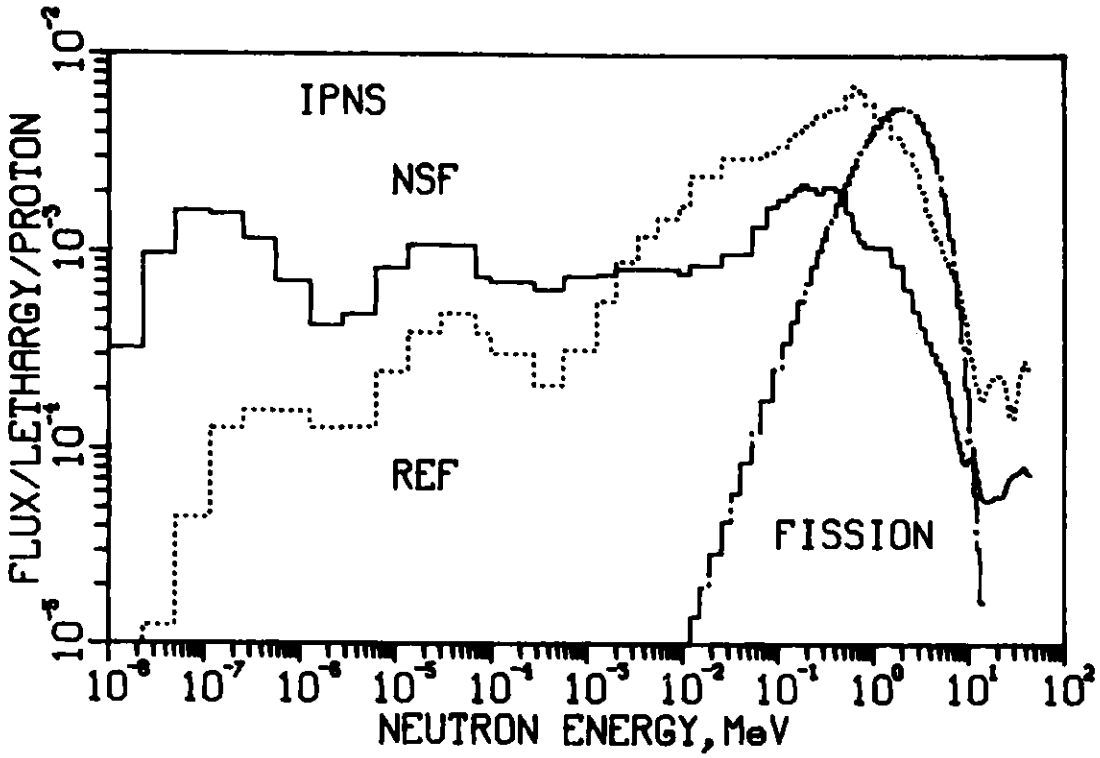

Figure 6. Neutron spectra produced in the REF vertical thimble and NSF horizontal thimble by 500-MeV protons incident upon the ^{238}U targets; a pure fission spectrum is shown for comparison.

4. Spatial Distribution of Neutron Flux

4.1 Mock-up.

All of the above results have been obtained from the complete set of reactions listed in Table 1, determined at the principal dosimetry sites; however, additional data were obtained at the other neutron dosimetry locations shown in Fig. 1, using only eight reactions. Integrated-spatial flux distributions were obtained in directions perpendicular and parallel to the target cylinder axis, though not to the same degree of accuracy as was possible at the principal dosimetry site. Figure 7 shows the experimental and calculated integrated flux for neutron energies greater than 1.0 MeV, for both Ta and ^{238}U irradiations in the direction perpendicular to the target axis (see Fig 1.). The perpendicular dosimetry hole was located ~4 cm from the front face of the target, a position chosen to coincide with the maximum flux along the target axis as calculated prior to these experiments. The calculated position of the flux peak is confirmed in Fig. 8, which shows the experimental and calculated flux distributions (E_n > 1.0 MeV) along the parallel dosimetry direction.

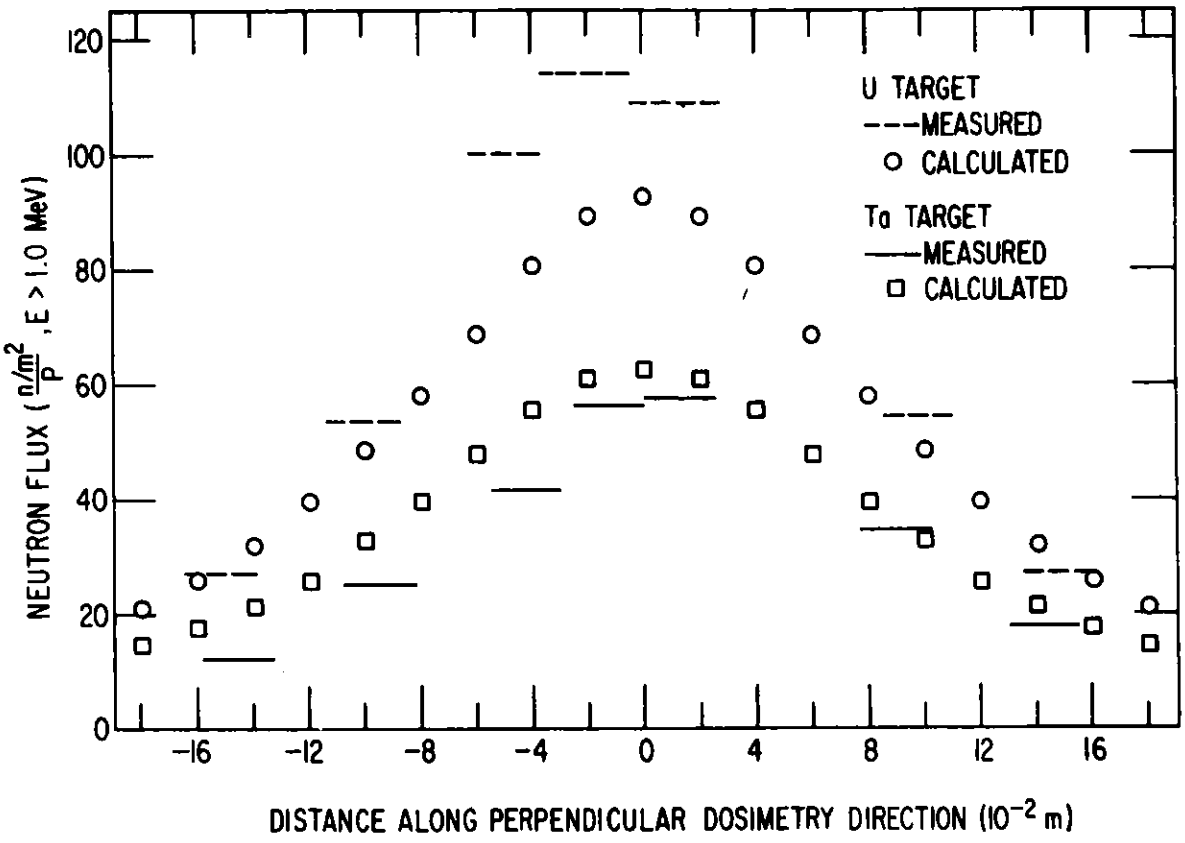

Figure 7. Flux distribution (E_n> 1.0 MeV) along the perpendicular dosimetry direction in the mock-up experiment.

As mentioned above, the fluxes in Figs. 7 and 8 are for neutron energies > 1.0 MeV. The measured peak values of Fig. 7 are the same as those of the principal dosimetry site and have an uncertainty of 11 to 13% (Table 2). The remaining measurements shown in Fig. 7 and all measurements in Fig. 8 were obtained from eight neutron reactions which were fit at each measurement position with the STAYSL computer code, using the neutron spectra obtained at the principal dosimetry site as the input spectra. The resultant neutron spectra and the integrated flux (E_n>1.0 MeV) at each position are uncertain by approximately ±30%. Since the neutron reaction thresholds are above 1 MeV, the uncertainty of integrated flux values for E_n greater than 0.1 MeV in these positions is considerably greater. However, the agreement between measured and calculated fluxes in Fig. 7 and 8 is reasonably good, especially for the Ta target irradiation. The rather larger disagreement in Fig. 8 between experimental and calculated peak flux values for the ^{238}U target must be viewed cautiously, as the uncertainty is larger for these experimental flux values than for the peak values of Fig. 7.

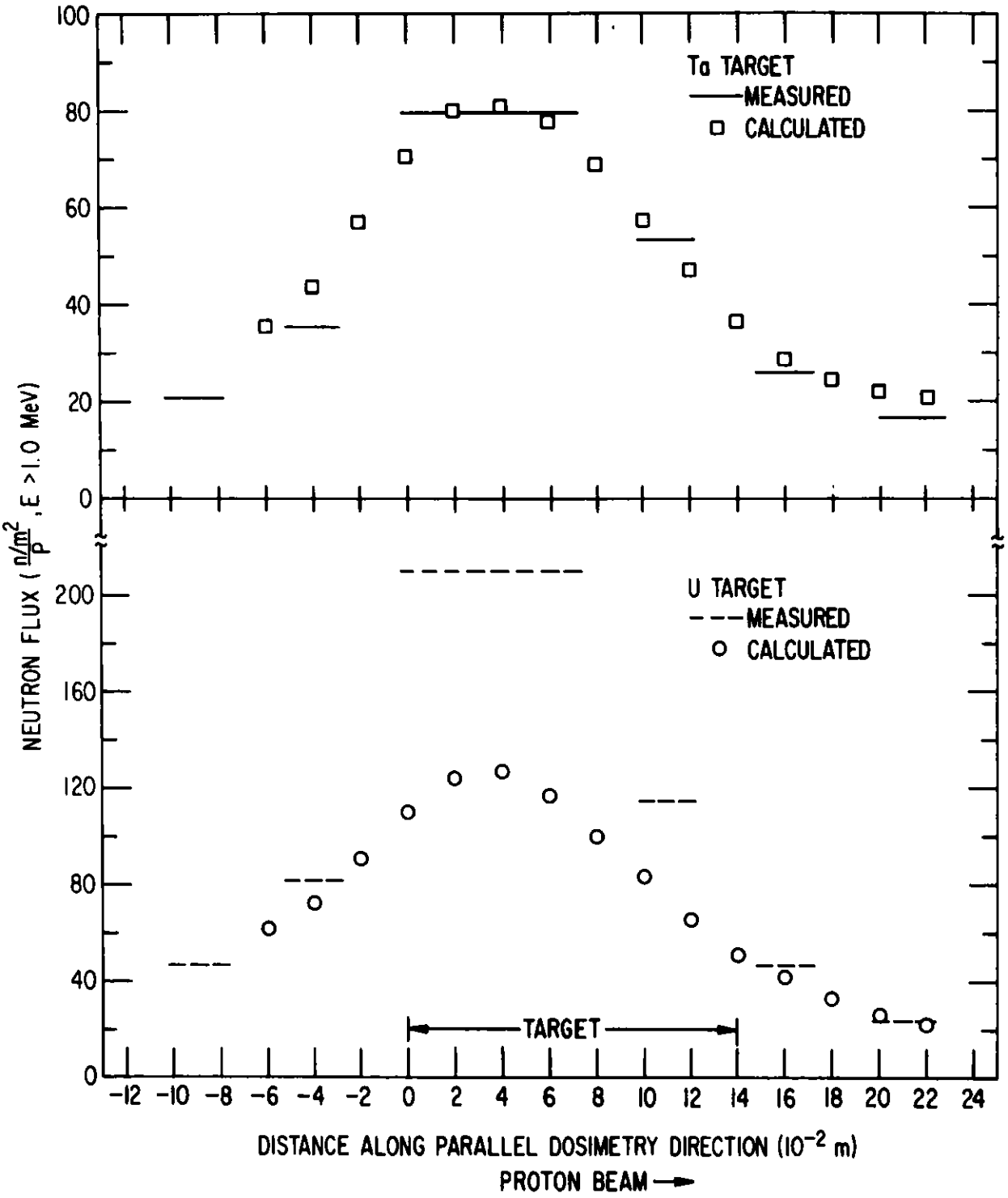

Figure 8. Flux distribution (E_n > 1.0 MeV) along the parallel dosimetry direction in the mock-up experiment.

The accuracy of the spectra above 1.0 MeV is sufficient to make some qualitative statements concerning the variation of these spectra along the two directions. In the perpendicular direction, which is nearly radial, the neutron spectrum above 1.0 MeV softens slightly with increasing distance from either target; the ratio of neutrons above 10 MeV to those above 1.0 MeV is ~30% lower at a location 20 cm out from the primary dosimetry site. In this direction the thermal-neutron flux decreases less sharply than the flux for E_n > 1.0 MeV.

The spectral changes above 1.0 MeV are slight along the direction parallel to the target axis and between the target and reflector. Above 1.0 MeV, the spectrum hardens somewhat with increasing distance behind the front face of the target; the ratio of neutrons above 10 MeV to those above 1.0 MeV is ~20% higher 20 cm from the peak flux position. However, the thermal-neutron flux, measured in front of and behind the target, falls less sharply than the flux for E > 1.0 MeV. This is probably due to the target-cooling systems, since slightly larger volumes of water are located immediately in front of and behind the targets than along their sides.

4.2 REF.

The spatial variation of neutrons with E > 0.1 MeV within the REF thimbles has been determined from the activation of Ni dosimeter wires [^{58}Ni (n,p)^{58}Co]. The fluxes were determined by comparing the measured activities with those measured at the positions of the full spectral dosimetry packages. Any changes in the neutron energy spectrum have been ingnored.

Figure 9 shows the variagion of the neutron flux (E > 0.1 MeV) within the REF vertical thimble. The surfaces of constant neutron flux within the thimble can be approximated by cylinders centered on the ^{238}U target axis. The maximum flux is 311 (n/ m^2)/p at the position nearest the target. The flux decrease within the crystal in a direction perpendicular to the target axis is nearly linear. The 50% decrease across the vertical thimble is larger than the ~30% decrease expected in a solid Pb reflector but the same as the decrease expected in a solid Ta reflector. The difference between these two reflector materials is due to the additional neutron generation in Pb by multiple neutron reactions.

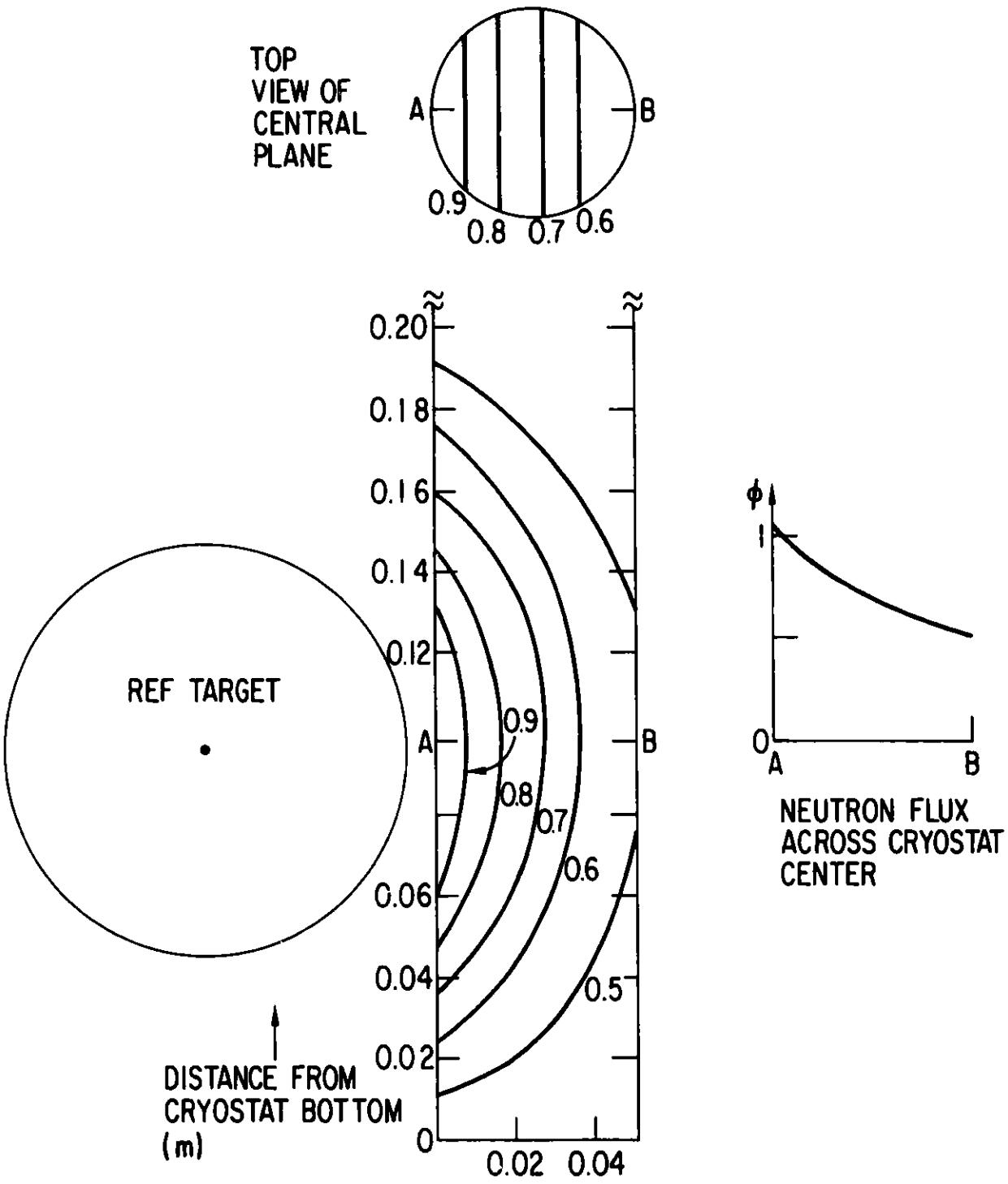

Figure 9. Spatial variation of the neutron flux (E_n > 0.1 MeV) within the REF vertical thimble.

Figure 10 shows the variation of the neutron flux (E > 0.1 MeV) along the length of the REF horizontal thimble located below the ^{238}U target. The neutron flux is a maximum at a position 4-5 cm behind the front face of the ^{238}U target, in agreement with previous calculations. This measurement was made along the bottom of the horizontal thimble. At the top of the horizontal thimble (1.5 cm closer to the target), the flux is 30% higher.

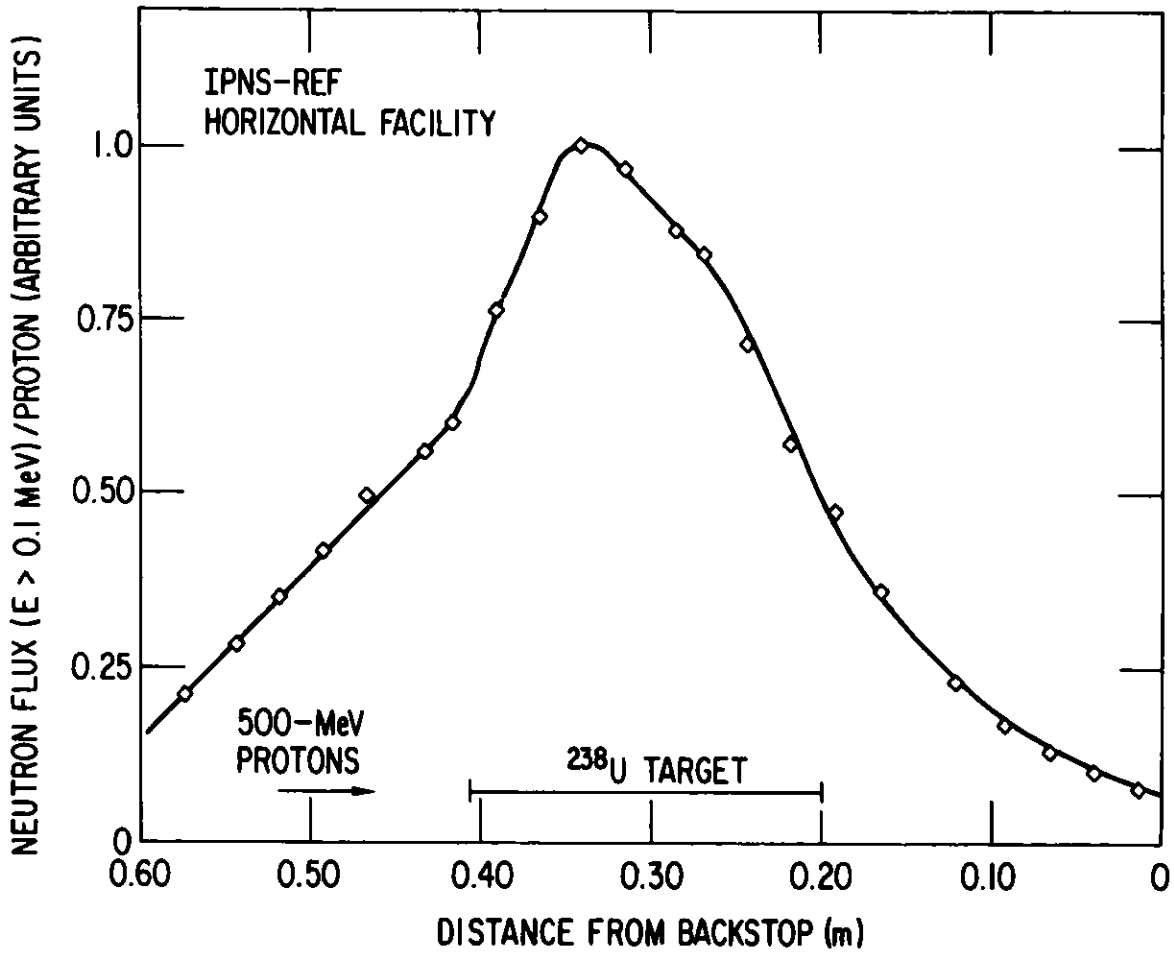

Figure 10. Spatial variation of the neutron flux (E_n > 0.1 MeV) within the REF horizontal thimble.

In the case of the NSF horizontal thimbles, which are nearly radial to the target axis, the neutron flux decreases rapidly with increasing distance from the target. The rate of flux decrease is the same as in the midplane of the REF vertical thimble (Fig. 9).

7. Summary

The neutron spectra, flux and flux spatial distribution for a spallation neturon source have been determined for a simplified system who's geometry allowed computer modeling of the neutron generation. Based on these results, a new neutron source, the IPNS, has recently been constructed at Argonne National Laboratory. This source is a national facility for radiation effects and condensed matter research. The Radiation Effects Facility (REF) has two cryogenic irradiation thimbles and one ambient-temperature irradiation thimble, and the Neutron Scattering Facility has two ambient-temperature irradiation thimbles. The neutron spectra, flux and flux spatial distribution has been determined for each of these thimbles. The large, well-controlled and -instrumented irradiation volume, the well-characterized neutron spectrum and flux, and the dedication to radiation effects studies make the REF ideally suited for both basic and applied research.

Acknowledgments

The authors would like to thank the operators and other personnel associated with the RCS accelerator for their assistance with the irradiations.

References

1.) R. C. Britcher, T. H. Blewitt, M. A. Kirk, T. L. Scott, B. S. Brown and L. R. Greenwood, J. Nucl. Mater. To be published.

2.) M. A. Kirk, R. C. Birtcher, T. H. Blewitt, L. R. Greenwood, R. J. Popek and R. R. Neinrich, J. Nucl. Mater. 96 (1981) 37.

3.) E. A. Crosbie, M. H. Foss, T. K. Khoc and J. D. Simpson, IEEE Trans. Nucl. Sci. NS-22(3) 1975, 1056.

4.) J. Tobailem, C. H. Lassus-St. Genies and L. Leveque, Commissariat a l'Energie Atomique (France) Report No. CEA-N-1446 (1971).

5.) K. C. Chandler and T. W. Armstrong, Oak Ridge National Laboratory Report ORNL-4744 (1972).

6.) F. M. Gelbard and R. E. Prael, Argonne National Laboratory Report ANL-75-2 (1974).

7.) C. W. Potts, IEEE Trans. Nucl. Sci., NS-28 (1981) 2104.

8.) F. G. Perey, Oak Ridge National Laboratory Report ORNL/TM-6062 (1977) as modified by L. R. Greenwood.

9.) R. Malewicki, R. R. Heinrich and R. J. Popek, Proc. 23rd Conf. on Analytical Chemistry in Energy Technology, Radioelement Analysis-Progress and Problems, Gatlinburg, Tnn., Oct. 9-11, (1979) 155.

10.) ENDF/B-IV Dosimetry File, Brookhaven National Laboratory Report BLN-NCS-50446 (1975).

11.) L. R. Greenwood, Argonne National Laboratory Report ANL-FPP/TM-115 (1978).

12.) L. R. Greenwood, R. R. Heinrich, M. J. Saltmarsh and C. B. Fulmer, Nucl. Sci. Eng. 72 (1979) 175.

13.) R. R. Fullwood, J. D. Cramer, R. A. Haarman, R. F. Forrest, Jr., and R. G. Schrandt, Los Alamos Scientific Laboratory Report LA-4789 (1972).

ICANS-VI
INTERNATIONAL COLLABORATION ON ADVANCED NEUTRON SOURCES
June 27 - July 2, 1982

TIME-STRUCTURE OF THERMAL NEUTRON LEAKAGE FROM FAST AND SLOW MODERATORS FOR SPALLATION NEUTRON SOURCES

G.S. Bauer, H.M. Conrad, K. Grünhagen and H. Spitzer
Institut für Festkörperforschung der KFA Jülich GmbH
W.Germany

F. Gompf and W. Reichardt
Kernforschungszentrum Karlsruhe
Institut für Angewandte Kernphysik
W.Germany

W.E. Fischer
Schweizerisches Institut für Nuklearforschung
Villigen, Switzerland

ABSTRACT

The dwell-times of neutrons slowed down either in small polyethylene moderators or a large D_2O volume have been measured. The fast neutrons have been produced by bombarding lead, lead-bismuth, depleted uranium and tungsten targets of slab or cylindrical shape with short pulses of 590 MeV protons. Lead and beryllium reflectors have been employed for the rectangular shaped grooved polyethylene moderators. The geometry-adapted (jagged) polyethylene moderators used with the cylindrical target have been measured only in "D_2O-reflected" configuration. The essential result of the numerical analysis of about 40 target-moderator-reflector configurations tested is that for the "fast" (light hydrogen) moderators the most intense flux component decays in 100 μs or less.

TIME-STRUCTURE OF THERMAL NEUTRON LEAKAGE FROM FAST AND SLOW MODERATORS FOR SPALLATION NEUTRON SOURCES

G.S. Bauer, H.M. Conrad, K. Grünhagen and H. Spitzer
Institut für Festkörperforschung der KFA Jülich GmbH
W.Germany

F. Gompf and W. Reichardt
Kernforschungszentrum Karlsruhe
Institut für Angewandte Kernphysik
W.Germany

W.E. Fischer
Schweizerisches Institut für Nuklearforschung
Villigen, Switzerland

1. INTRODUCTION

The main advantage of the latest type of high intensity neutron source is the nearly unrestricted time structure which can be imposed on the primary fast neutron flux. The width of the thermal neutron peak flux is, however, governed both by the proton pulse width and the dwell time of the thermalized neutrons in the moderator. In other words, even an infinitely short proton pulse would result in a thermal neutron peak decaying with a finite half-width determined by geometry and material of the moderator. Besides short neutron pulses necessary for time-of-flight spectroscopy the designer of a spallation source is interested in obtaining as high peak and average fluxes as possible. In order to optimize pulse width, peak flux and average flux the precise dwell times of thermalized neutrons in different moderators have to be measured. The experimental analysis of moderator characteristics is quite difficult, if the proton pulse on the target is inadequately broad. Therefore we repeated and extended our previous investigations /Bauer et al. 1981a/ at the Swiss proton cyclotron (SIN) with a considerably improved proton chopper.

2. EXPERIMENTAL

This improved proton chopper of the Fermi type was machined from a solid cylinder of aluminum (instead of a hollow cylinder as the one used in the previous experiment). The resulting proton pulse shape was a single triangle of 200 µs FWHM. The measurements have been performed at the Swiss Institute for Nuclear Research (SIN) with its 590 MeV proton beam from the isochronous cyclotron pulsed at 200 Hz using the chopper just mentionned. The target-moderator-reflector set-up was the same as described in a previous report /Bauer 1981a/ and is outlined in figure 1.

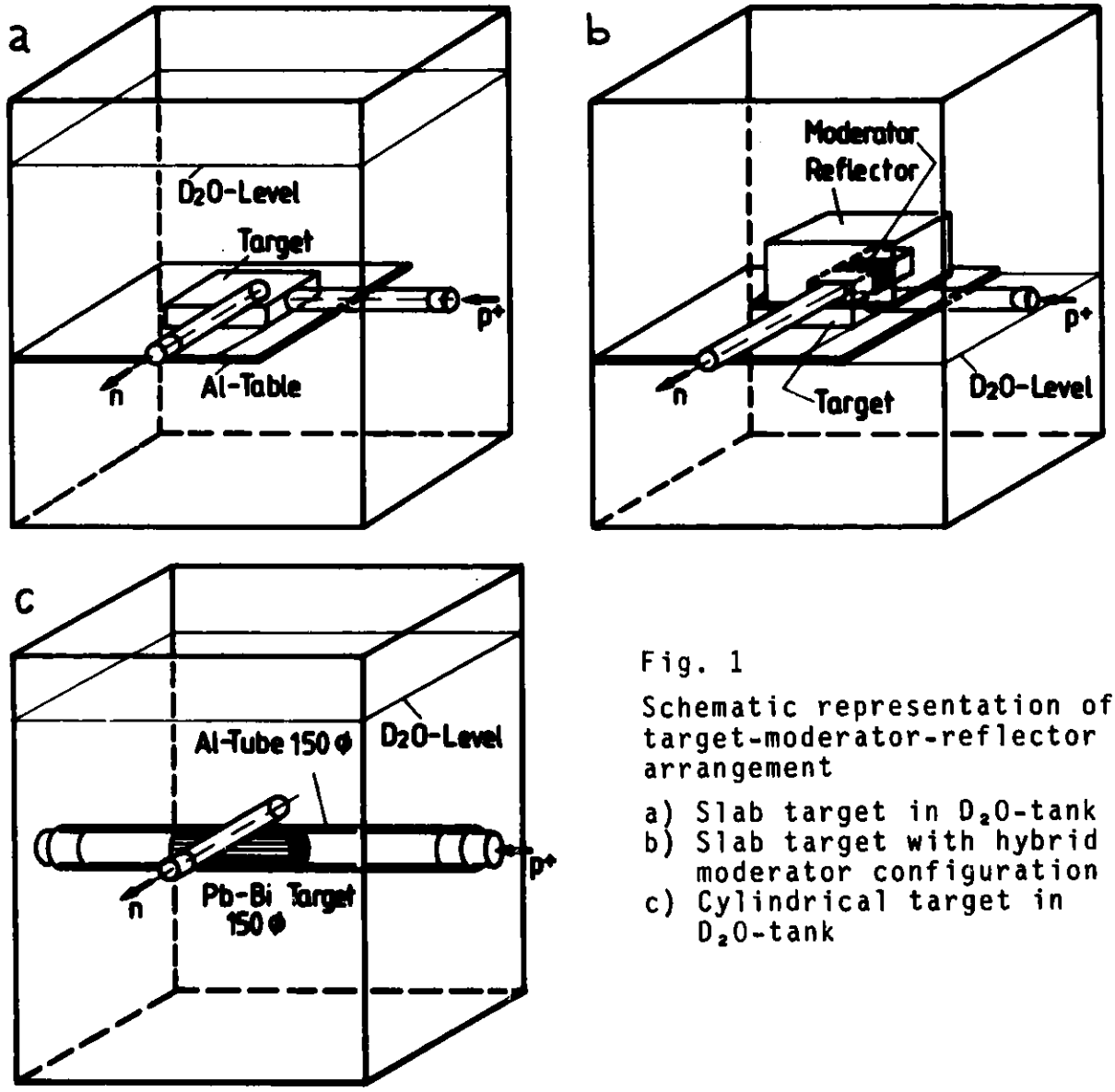

Fig. 1

Schematic representation of target-moderator-reflector arrangement

a) Slab target in D_2O-tank
b) Slab target with hybrid moderator configuration
c) Cylindrical target in D_2O-tank

Two types of arrangements have been investigated: the slab target geometry representing the lay-out of the proposed German spallation source SNQ and a cylindrical target configuration simulating the liquid metal target proposed for the Swiss project.

In the case of the cylindrical target jagged polyethylene moderators of sixfold rotational symmetry, both with and without grooves, have been employed. This new moderator is shown in figure 2.

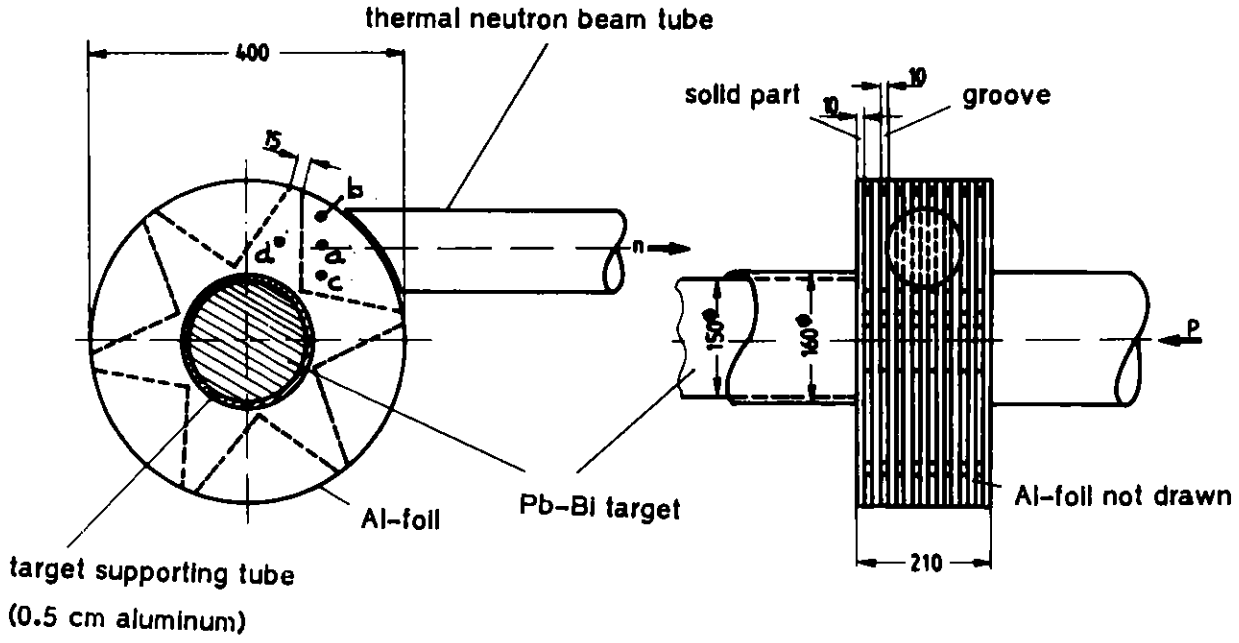

Fig. 2
The jagged moderator for cylindrical targets

In order to more realistically simulate the flux depression by beam holes, additional aluminum tubes not shown in figure 1 viewing the moderators have been mounted.

The time structure of the thermal neutron field in the polyethylene moderator and in the D_2O tank have been measured inserting a small, low-efficiency BF_3 counter (0.6 cm diameter, 3 cm long) into holes in the polyethylene moderators. The neutron intensities measured as a function of time as well as the primary proton

distribution were stored in a small computer with time-of-flight interface. The time channel width was 25 μs. The primary proton time distribution (triangle!) was measured with a scintillator telescope viewing a carbon scatterer in the direct beam.

3. DATA EVALUATION AND RESULTS

In order to extract the neutron dwell times from the measured intensity distributions we assumed a mathematical expression for the neutron field decay of the form

$$f(t) = f_1 \cdot \exp(-t/\tau_1) + f_2 \cdot \exp(-t/\tau_2),$$

since we found that two time constants τ_1 and τ_2 were sufficient for a proper description of our data. This above expression was convoluted numerically with the measured triangular-shaped primary proton distribution and the resulting convolution fitted to the experimental data varying the four parameters f_1, f_2, τ_1 and τ_2. In a series of cases (mainly with the fast moderator and lead reflector) it was found that only two parameters (f_1 and τ_1) were necessary for a perfect fit. In figure 3 is given an example of the experimental data and the resulting fitted curve.

3.1 Results for slab targets

Three different target materials have been used in slab geometry simulating the target wheel of the German spallation project: a lead target of 10x75x60 cm^3 (height x depth x width), a tungsten target of 10x30x21 cm^3 and a target of depleted uranium of 10x50x45 cm^3. The grooved polyethylene moderator was placed at the maximum of the fast neutron flux emerging from the targets. Table 1 shows selected results from the numerical fitting calculations mentioned above. Besides the proper fitting parameters derived quantities like the integrated intensity and the standard deviation of the distribution are listed.

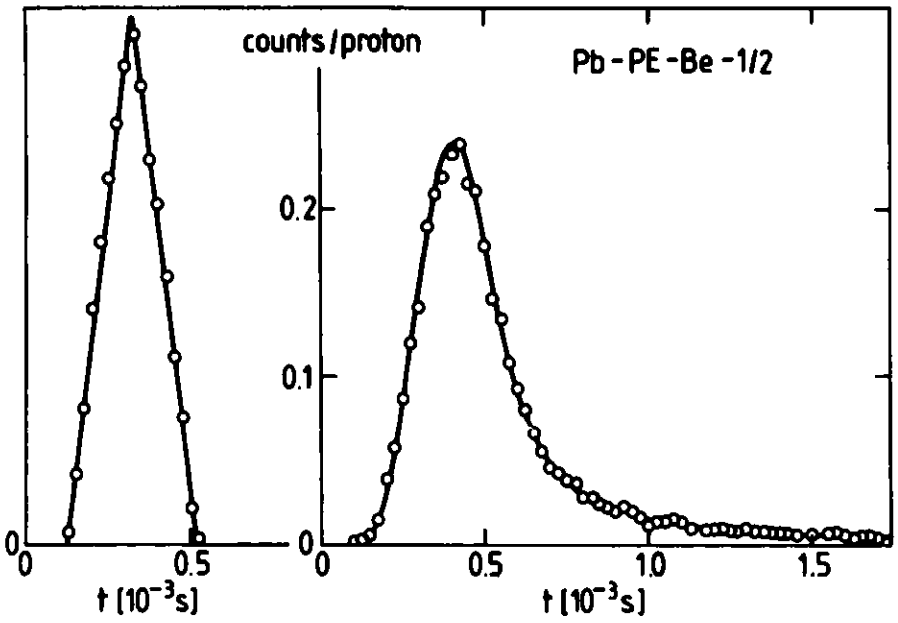

Fig. 3
Shape of the proton signal (left), example of a measured intensity distribution in the polyethylene moderator and the theoretical curve fitting the experimental data.

From the data listed in Table 1 it can be seen that the time structure of the thermal neutron peaks emerging from the grooved polyethylene moderator may be characterized by a single decay time if a lead reflector is used. This was already found in energy-selective measurements previously performed /Bauer et al. 1981b/. In the cases, where two time constants were necessary for data fitting, the dominating, i.e. high intensity component also decayed in times comparable with that of the single component neutron fields. These times range from 80 µs to 128 µs being thus significantly shorter than the 200 µs found before /Bauer et al. 1981a/.

configuration T - M - R - D_2O	τ_1 10^{-6}s	f_1 x 10^5	τ_2 10^{-6}s	f_2 x 10^5	integr. intensity I	standard deviations 10^{-6}s
Pb-PE-Pb-1/2	124	4.4	-	-	54.7	175
Pb-PE-Pb- 1	117	7.1	1680	0.79	215.5	1866
Pb-PE-Pb- 1 decoupled	93	6.0	-	-	56.9	132
Pb-PE-Be-1/2	80	4.9	289	1.30	95.2	370
Pb-PE-Be- 1	137	6.7	996	0.70	162.2	935
Pb-PE-Be- 1 decoupled	85	7.2	389	0.20	67.2	203
Pb-PE-Be-1/2 decoupled	92	5.4	-	-	49.6	130
Pb-PE-Be- 0 decoupled	100	4.7	-	-	47.4	141
Pb-PE-Be-1/2 *	104	5.3	588	0.40	80.9	485
W -PE-Pb-1/2	115	4.6	-	-	53.1	163
U -PE-Pb-1/2	128	7.9	-	-	100.5	181

Table 1

Dwell times τ, scale factors f, integrated intensities and standard deviations for selected slab target-moderator-reflector configurations.
Symbols and definitions: T = target; M = moderator; R = reflector; D_2O = level of tank filling; i.e.: 0 = empty, 1/2 = up to the target, 1 = full; PE = polyethylene; $I = \int f(t)dt = f_1\tau_1+f_2\tau_2$
$S = \sqrt{\sigma^2}$, where σ^2 is given by: $\sigma^2 = 2(f_1\tau_1^3 + f_2\tau_2^3)/(f_1\tau_1 + f_2\tau_2)$
* 4 cm of Be between PE moderator surface and beam tube

3.2 Results for cylindrical target with jagged polyethylene moderator

An eutectic lead-bismuth target of 15 cm in diameter and 60 cm length was inserted in the through tube of the D_2O tank (compare figure 1). The jagged polyethylene moderator was placed at the maximum of the fast neutron flux. The arrangement can be seen in figure 2. Two moderators have been tested, one with grooves in the gap between the jags and another one with empty gaps. In

both cases the moderator was cased with an aluminum foil to prevent D_2O to enter the space between the jags. The time structure of the thermal neutron pulses has been measured inserting the BF_3 counter into different bore holes in both the jags and the gaps. In all but one cases the tank was completely filled with D_2O. Both decoupled (Cd casing of the moderator) and coupled moderators have been investigated. A compilation of the results from the fitting computations is given in table 2.

configuration Pb/Bl - PE ✳$_i$ - D_2O grooved		τ_1 10^{-6}s	f_1 x 10^5	τ_2 10^{-6}s	f_2 x 10^5	integr. intensity I	standard deviation S [10^{-6}s]
l = a	0	143	3.7	-	-	53.0	202
no PE	1	125	0.9	3170	0.9	306.2	4406
l = a	1	131	5.5	2330	0.4	172.6	2520
l = b	1	170	2.3	2370	0.3	100.2	2604
l = c	1	150	6.5	2250	0.2	141.2	1795
l = d	1	110	11.2	2360	0.3	190.1	1983
l = a decoupled	1	126	5.5	1760	0.2	96.0	1318
l = b decoupled	1	148	2.9	-	-	42.5	209
l = d decoupled	1	102	12.2	1480	0.2	157.2	961
l = a (no grooves)	1	263	2.0	2240	0.5	167.4	2635
l = d (no grooves)	1	86	11.3	1550	0.5	167.6	1420

Table 2

Dwell times τ, scale factors f, integrated intensities and standard deviations of the cylindrical target-moderator-reflector arrangement. The configuration was the same in all but the first case listed, where the D_2O tank was empty. The index i at the symbol ✳ denotes the position, where the neutron counter has been inserted (see figure 2). The remaining symbols have been defined in the caption of table 1.

4. CONCLUSIONS

In the case of the grooved fast moderator for slab targets the neutron peaks were found to be shorter than deduced from previous measurements. A dwell time of 80...120 μs is considerably shorter than the proton pulses of 500 μs of the SNQ linac. Thus the maximum possible peak flux will not be reached. As compared to previous estimates based on decay times of 200 μs the peak flux would only increase by 8 % due to the reduction of the dwell time to 100 μs. Shortening, for instance, the proton pulse to 250 μs would yield a gain of 100 % with a dwell time of 100 μs, whereas a gain of 55 % only would result, if the dwell time was 200 μs. Thus there is a big incentive to try to increase the pulse proton current to 200 mA and shorten the pulse to 250 μs.

For the cylindrical target (in liquid state), which shall be employed for the Swiss spallation source, the above considerations may be of no importance, as it was proposed to operate that source continuously. Besides that, the D_2O moderator would dominate the time structure. Thereby the proton pulse length is no important parameter.

REFERENCES

G.S. Bauer, W.E. Fischer, F. Gompf, M. Küchle, W. Reichardt, and H. Spitzer (1981 a)
"Thermal Neutron Leakage and Time Structure Measured for Various Target-Moderator-Reflector Configurations for a Spallation Neutron Source"
paper D2-4 in "ICANS V" pp. 445-474, G.S. Bauer and D. Filges, eds., report Jül-Conf-45, Kernforschungsanlage Jülich

G.S. Bauer, H.M. Conrad, H. Spitzer, K. Friedrich, and G. Milleret (1981 b)
"Measurement of Time Structure and Thermal Neutron Spectra for Various Target-Moderator-Reflector Configurations of an Intensity-Modulated Spallation Neutron Source"
paper D2-5 in "ICANS V" pp. 475-488, G.S. Bauer and D. Filges, eds., report Jül-Conf-45, Kernforschungsanlage Jülich

ICANS-VI

INTERNATIONAL COLLABORATION ON ADVANCED NEUTRON SOURCES

June 27 - July 2, 1982

SOME ASPECTS OF THE NEUTRONICS OF THE SIN NEUTRON SOURCE

F. Atchison and W.E. Fischer
Schweizerisches Institut für Nuklearforschung
CH-5234 Villigen, Switzerland

and

B. Sigg
Institut für Reaktortechnik, ETHZ
CH-5303 Würenlingen, Switzerland

ABSTRACT

Some results from both experiment and calculation, obtained as part of the optimisation study for the SIN neutron source are presented.

SOME ASPECTS OF THE NEUTRONICS OF THE SIN NEUTRON SOURCE

F. Atchison and W.E. Fischer
Schweizerisches Institut für Nuklearforschung
CH-5234 Villigen, Switzerland

and

B. Sigg
Institut für Reaktortechnik, ETHZ
CH-5303 Würenlingen, Switzerland

1. INTRODUCTION

The current state of the SIN neutron source project is described elsewhere in these proceedings [1]. In this report we present some results, from both experiment and calculation, obtained as part of our detailed design study.

The overall source optimization is a several-year program and has, as its (usual) goal, the production of the best neutron source with the available resources. The major areas of study are:

(i) The neutronic optimization of the source: reconciliation of conflicting neutronic requirements of beam guides and thermal tubes, production of adequately low backgrounds, etc.

(ii) The thermofluid dynamics of the target.

(iii) The practical aspects of producing an operable source: radiological safety, choice of satisfactory materials, etc.

Calculations using both computer codes and "hand built" physics are presented; a brief résumé of the principal computer codes presently available to our project is given in Table I.

2. THE PRODUCTION TARGET

The target material is an eutectic mixture, 55 % Bi, 45 % Pb, of density 10 g/cc. A vertical cylinder of diameter between 10 and 11 cm and of length in excess of 1 m is envisaged, with natural convection in the liquid metal to provide the primary heat transfer mechanism. A major part of our study will be the reconciliation of neutronic and thermofluid-dynamic requirements, to obtain an optimum set of dimensions. The thermofluid dynamics of the

Table I

The principle computer codes available

CODE	COMPUTER	BRIEF DESCIPTION	AREAS OF APPLICATION
HET [1]	VAX-11	Analogue Monte- arlo nucleon-meson transport code.	- Primary production for fast neutrons in target - Energy deposition by the high-energy cascade - Nuclide production by HE spallation reactions - High energy backgrounds for the source
O5RSIN	VAX-11	Monte-carlo neutron transport code An extensively modified version of O5R [2]	- Sub-15 Mev neutron effects in the target - Neutronics of the moderator including thermalisation.
EGS [3]	VAX-11	Monte-carlo electromagnetic cascade code.	- Gamma transport throughout the neutron source
DOT-3 [4]	CYBER 170 SERIES	Discrete ordinates neutron transport code	- Shield design
RSYST [5]	CYBER 170 SERIES	One-dimensional transport (Sn) and two-dimensional diffusion code.	- Moderator optimisation studies
ORIHET	VAX-11	Isotope production and decay. A modified version of ORIGEN [6]	- Activation studies throughout the neutron source.

References for Table 1

[1] W.A. COLEMAN & T.W. ARMSTRONG ORNL-4606 (1970)
[2] R.R. COVEYOU et. al. ORNL-3622 (1965)
[3] R.L. FORD & W.R. NELSON SLAC-210 (1978)
[4] W.A. RHOADES & F.R. MYNATT ORNL-TM-4280 (1973)
[5] R. RUEHLE IKE-Ber. 4-12 (1973)
[6] M.J. BELL ORNL-4628 (1973)

HET & O5R are part of the RSIC computer code collection number CCC-178 and ORIGEN is CCC-217.

target are discussed in a separate report in these proceedings (Takeda [2]).

2.1 Neutronic performance

The general neutronic performance, as the target radius is varied, has been calculated using HET. The results are summarized in Fig. 1. The calculation was made using a 530 MeV proton beam in a 2 cm variance Gaussian truncated to 10 cm diameter. As should be expected, fast neutron production increases only slowly once the target radius exceeds that of the beam; similarly for the component of the power dissipation from the high energy cascade.

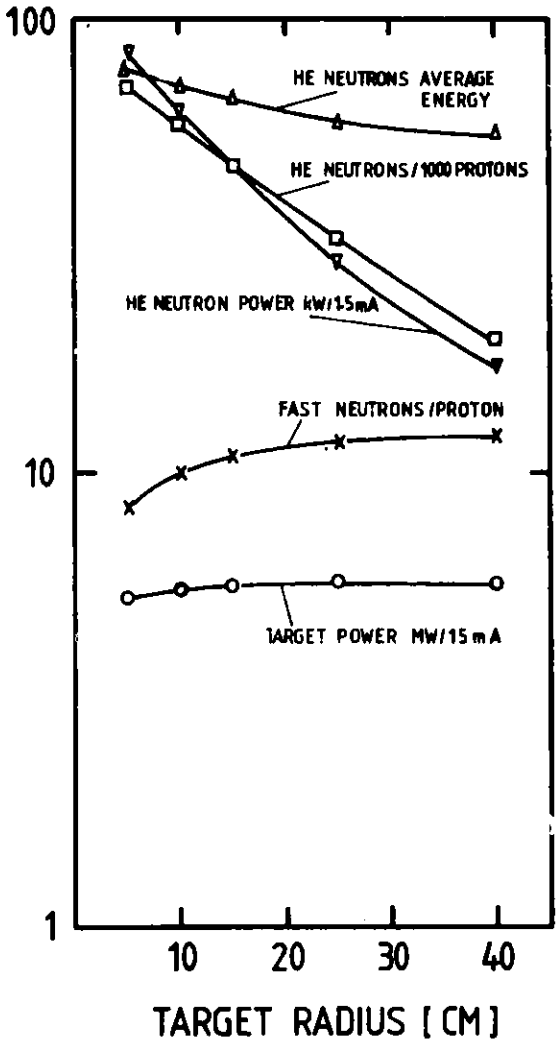

Fig. 1
Variation, with target radius, of target power, fast neutron production and HE neutron production rate, average power and escape power. Calculation for a Pb/Bi target using HET.

A major consideration in the design of the source is the background in thermal beam tubes. The shielding effect of the Pb/Bi is shown by the decrease of both the flux and average energy for the high energy neutron escapes.

2.2 Power dissipation

This is estimated to be approximately 73 % of the incident proton beam power from all sources, with the main contribution coming from ionization loss. The cooling system will have to remove somewhat under 1 MW. A further 17 % of the beam power is used to liberate the neutrons from the target nuclei. The remaining 10 % is deposited in the rest of the source (mainly in the moderator).

2.3 Target activation

The contribution from the residual nuclei of spallation reactions has been calculated using ORIHET. The build-up of activity as a fraction of continuous irradiation time at 1.5 mA, and the decay of activation after a 1 year irradiation are shown in Fig. 2. The target activation should be somewhat less than 1 MCi during normal operation. The power dissipation from these decays is 3 kW, including a 2.6 kW contribution from decay gammas.

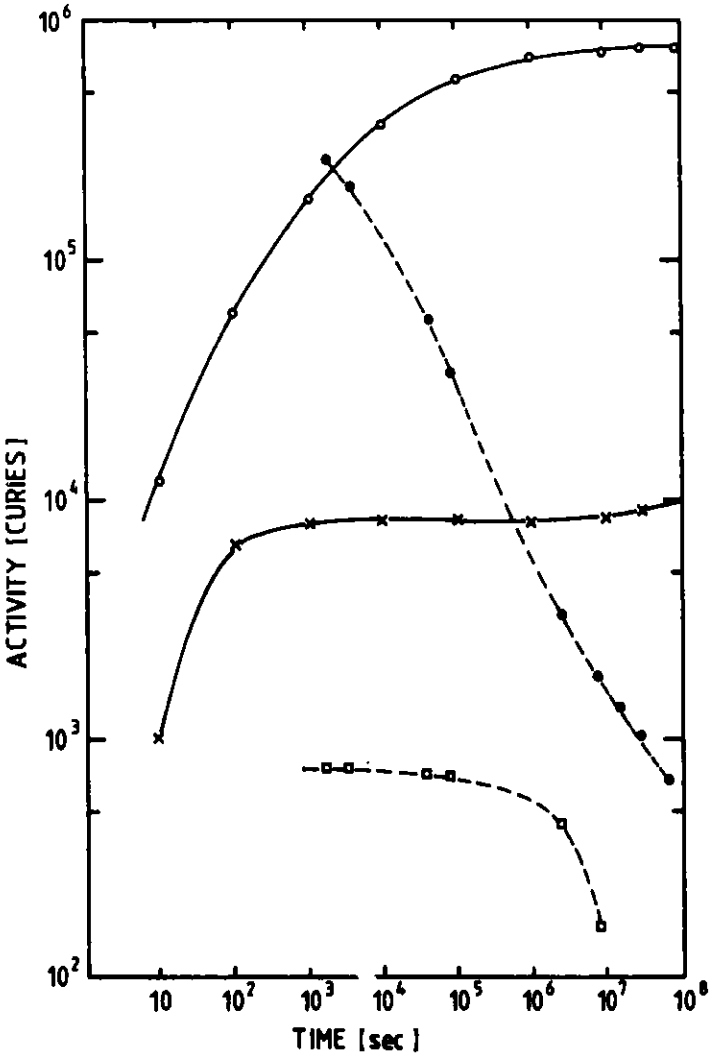

Fig. 2
Build-up and decay of activation for a Pb/Bi target at 1.5 mA and 530 MeV protons. (i) Buildup of total activity (-o-o-o-); (ii) Buildup of α-activity (-x-x-x-); (iii) Decay of total activity (-•-•-•-); (iv) Decay of α-activity (-□-□-□-). Decay curves are for time periods following 1 year irradiation.

For the fast and thermal neutrons, the principal product is Po-210; this is estimated to have an equilibrium activity of about 13 kCi, and corresponds to approximately 3 g weight.

2.4 Escape particles

HETC calculations for a 10 cm radius target give an escape evaporation-neutron intensity of 10.4/proton, with an average energy of 1.7 MeV. The calculated distribution of surface brightness is shown in Fig. 3 together with the measured values from ref. [3].

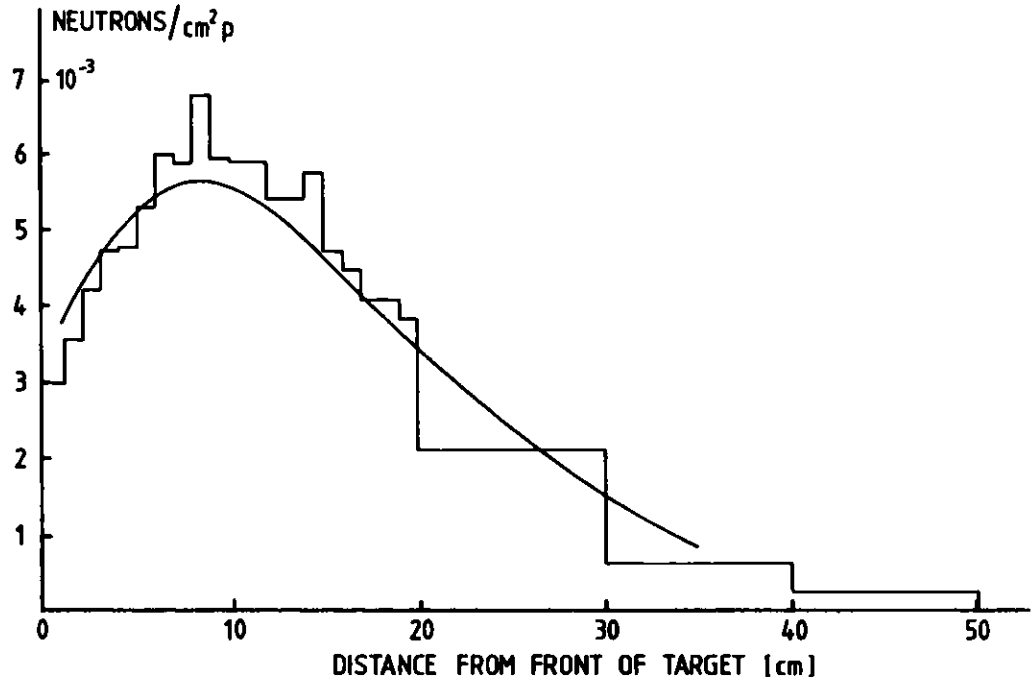

Fig. 3
Surface brightness for fast neutron escapes from a 10 cm radius Pb/Bi target. Histogram - calculation: Solid line - experiment [3].

The high energy particle escapes per incident proton calculated, are:

Neutrons	0.59	of mean energy	71 MeV
Protons	0.008	of mean energy	100 MeV
PI+	0.002	of mean energy	54 MeV
PI-	0.0006	of mean energy	46 MeV

2.5 Gamma Fluxes

A calculation for a 5 cm radius Pb target has been made using the EGS code. The source terms are as follows:

1. Prompt nuclear gammas: 1.2 per incident proton on the basis of the residual excitation being dissipated by emission of a single gamma. The source energy distribution is shown in Fig. 4. The source strength at 1.5 mA proton current is $1.2 \cdot 10^{16}$ photons/sec and 8 kW.

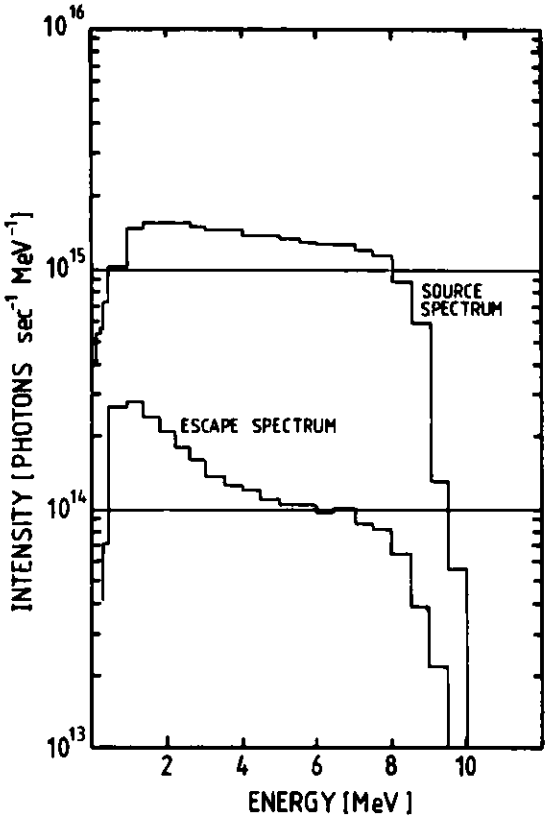

Fig. 4
Integrated source and surface-escape spectra for prompt nuclear gammas

2. π^0 decay: 0.024 are produced in the target per incident proton with an energy spectrum approximated by:

$$P(E_{\pi^0})dE_{\pi^0} = 0.0025\ E_{\pi^0} EXP[-(0.05\ E_{\pi^0})]dE_{\pi^0}$$

Isotropic decay in the CMS system at the production point is used to generate the source gammas. The gamma spectrum is shown in Fig. 5. The source strength at 1.5 mA is $4.5 \cdot 10^{14}$ photons/sec and 6.3 kW.

3. Decay gamma's: The Darmstadt gamma ray atlas [4]has been built into the ORIHET code. The spectrum after a 1 year irradiation at 1.5 mA is used and is shown in Fig. 6. The source strength is $2.9 \cdot 10^{16}$ photons/sec and 3.2 kW. The source is assumed uniformly distributed in a 1 m long target.

The source strength distributed throughout the target is $4 \cdot 10^{16}$ photons/sec and 17.5 kW. The calculated escape spectra after transport through the target are shown in Figs. 4, 5 and 6, with

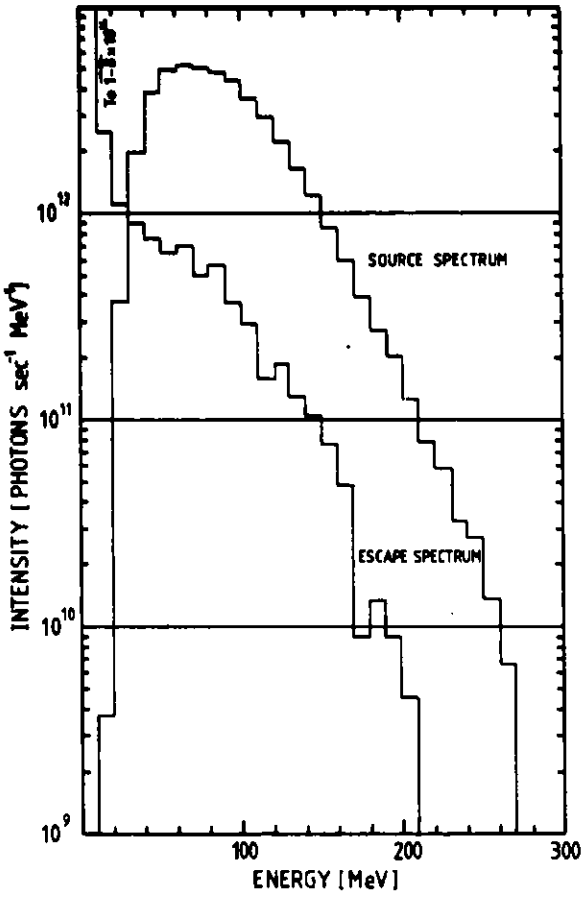

Fig. 5
Integrated source and surface-escape spectra for gammas from π^0 decay

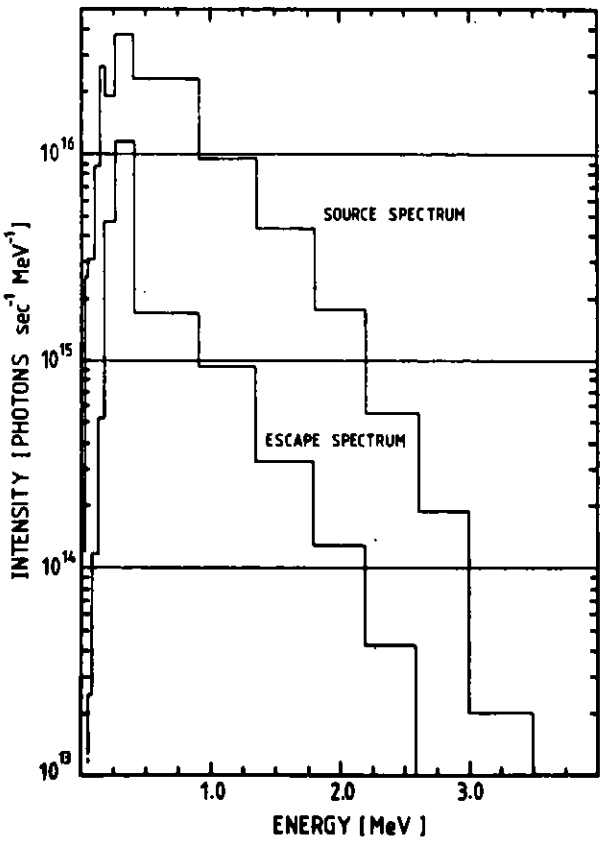

Fig. 6
Integrated source and surface-escape spectra for decay gammas

their source spectra. The overall escapes correspond to $8.5 \cdot 10^{15}$/sec and 3.9 kW, which is approximately 20 % of the source strength.

There are also $9.4 \cdot 10^{13}$/sec of electrons and positrons with mean energy 23 MeV (0.34 kW) escaping the target.

The distributions of escape-gamma intensity and power along the target are shown in Fig. 7. The localized π^0 and nuclear gamma ray production leads to the asymmetric distribution.

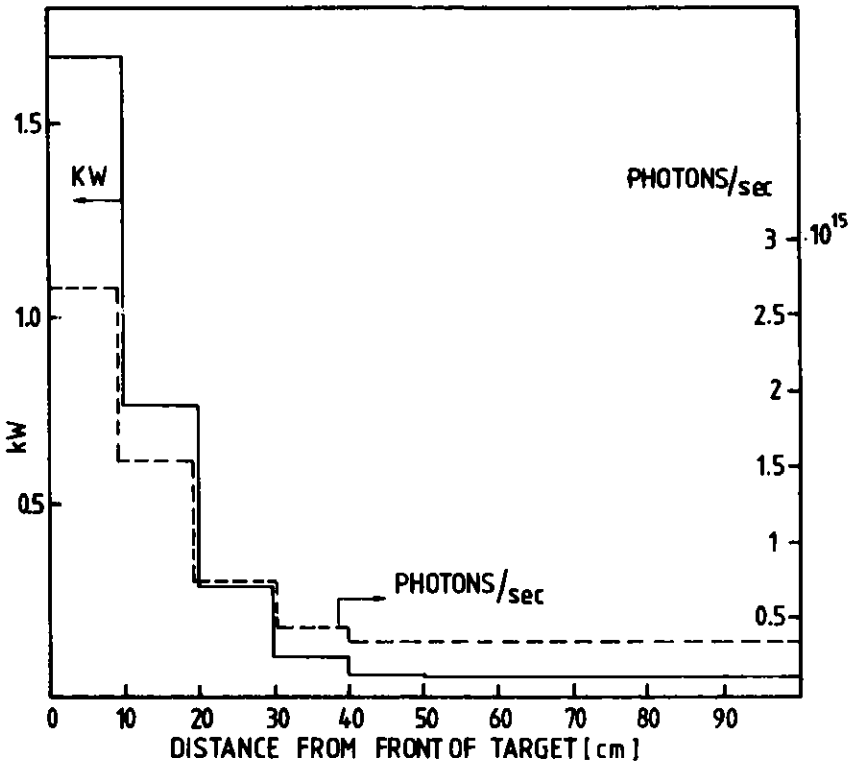

Fig. 7
Calculated distribution of surface-escape gamma flux and power for a 5 cm radius Pb/Bi target

3. THE MODERATOR

The outline design incorporates a 1 to 1.5 m radius D_2O tank of height 2 to 2.5 m. A cold source viewed by beam guides is to be incorporated. Tangential thermal neutron tubes and thermal neutron guides are also planned. The design study has as main aims, to find an optimum moderator volume and the best positions for:

(a) the thermal beam tubes, subject to obtaining an adequately low background;

(b) the cold source, taking into consideration a realistic thermal load on the refrigerator system.

3.1 Thermal Fluxes

Measurements of thermal neutron fluxes in a realistic model of our neutron source have been carried out as part of the SIN/KFA-Jülich collaboration. Some of these measurements have already been reported [5].

The following configurations are of particular interest, both from the point of view of thermal neutron flux maximization and also for consideration of the target/moderator interface design. A general layout of the measured system is shown in Fig. 8; further details of the experiment may be found in reference [5].

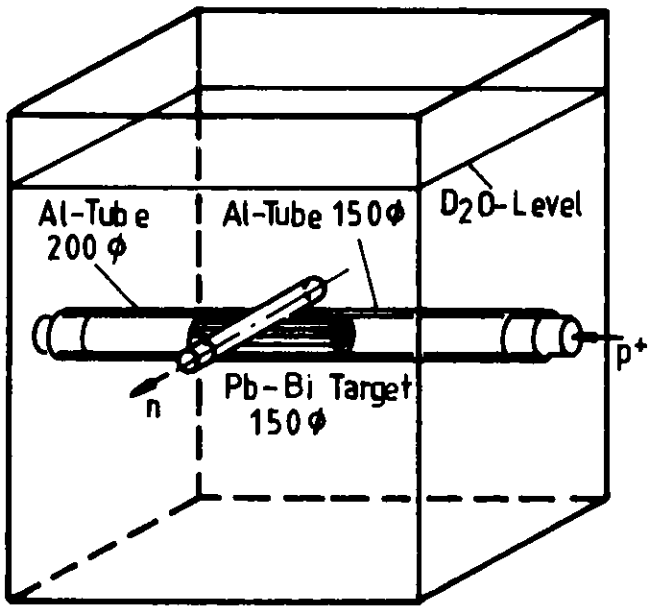

Fig. 8
General arrangement for thermal neutron flux measurements

The results from four configurations are considered:

A) Pb/Bi target + D_2O moderator
B) Pb/Bi target + 3 cm air gap (void) + D_2O moderator
C) Pb/Bi target + 5 cm Be + D_2O moderator
D) Dep.U target + 5 cm Be + D_2O moderator

For the purpose of discussion, A) is taken as a reference system. The thermal flux as a function of radius for two axial distances along the target is shown in Fig. 9 for systems A), B) and C): For further comparison, the flux-maps for cases A) and C) are shown in Fig. 10.

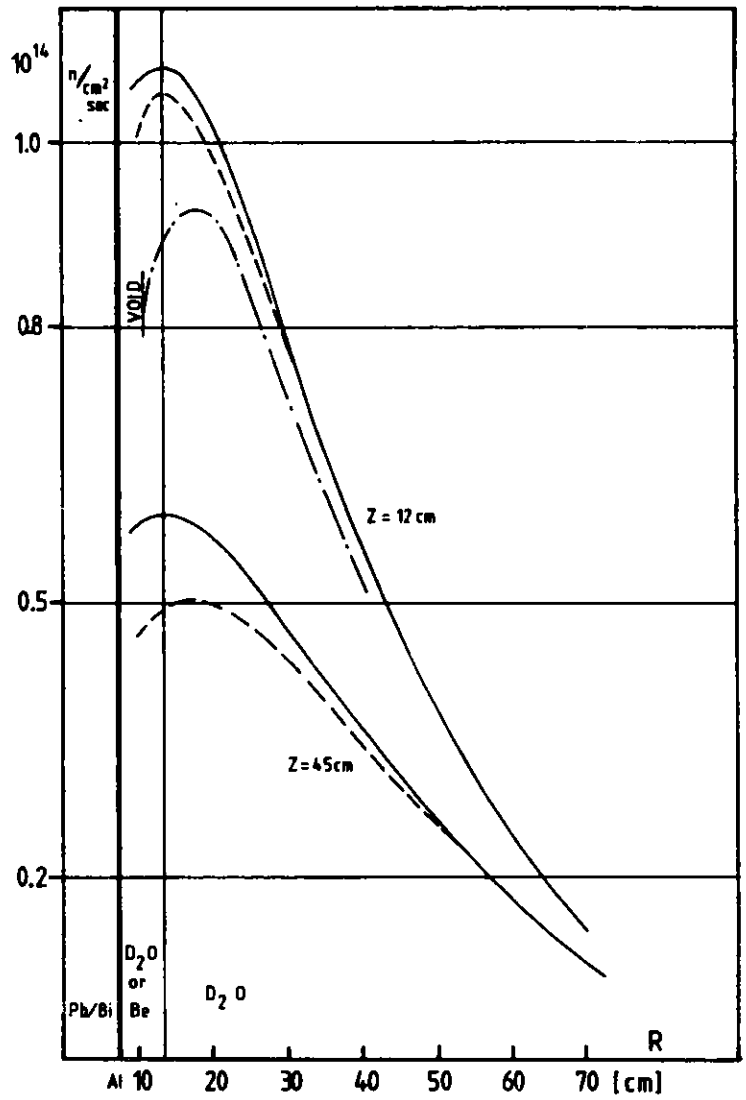

Fig. 9
Measured variation of thermal neutron flux in a D_2O moderator as a function of radial distance from the target axis. Z is measured from the front surface of the target.
(———) case A)
(-·-·-·-) case B)
(------) case C)

The 3 cm void of case B) leads to a peak thermal flux depression of 15 %, with an outward shift of approximately 5 cm. At larger radii, the flux penalty is of the order of 8 %. The effect of the void is to create an additional leakage path for neutrons.

Case C) has produced the most surprising result; although the peak thermal neutron flux is reduced by approximately 2 %, at large radii the fluxes are identical. There seems to be no overall neutron gain with a Be sleeve. In the axial direction the flux decrease with the Be sleeve is somewhat faster, as may be seen in Fig. 10. The gain factor, as estimated from the measured spectra of Cierjacks et al. [6] and published Be(n,2n) cross-section values [7], was approximately 14 %. The measurements indicate the increased absorption by the Be should reduce this

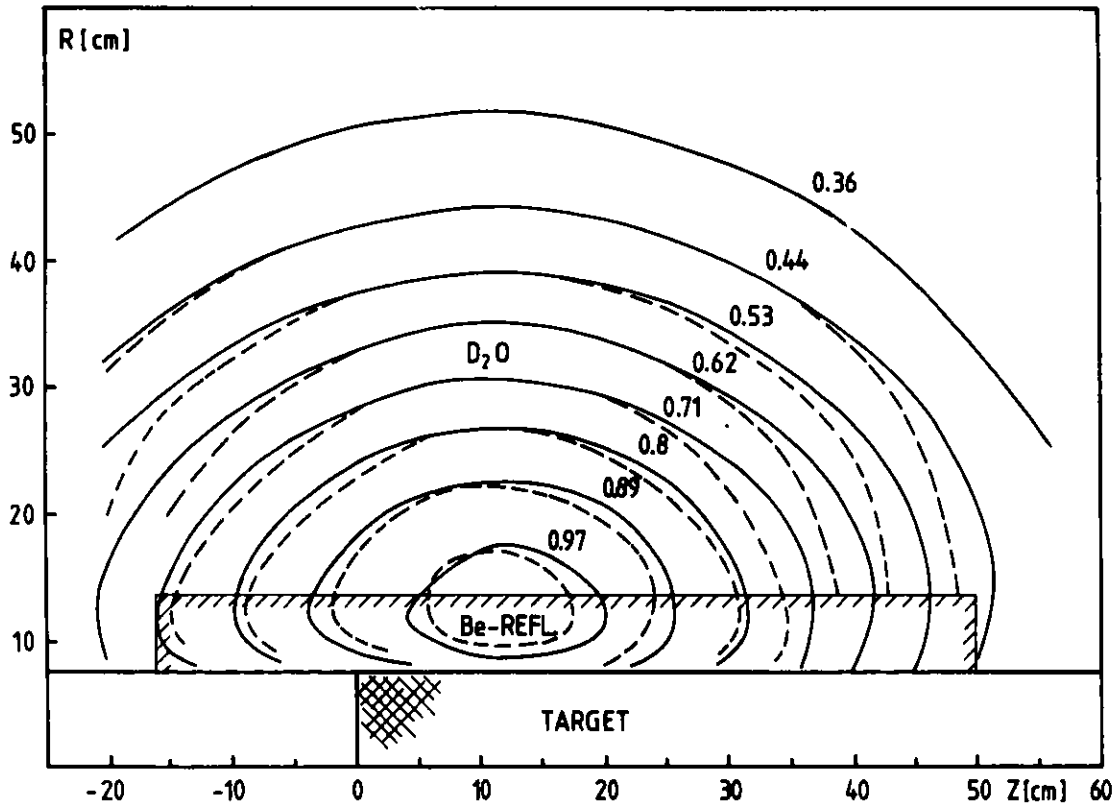

Fig. 10
Measured thermal-neutron flux map in a D_2O moderator. The curves are marked with intensity as a fraction of peak flux.
(———) case A)
(- - - - -) case B)

gain factor to about 9 %. This is a significant over-estimate; of the several possibilities, we believe the most probable cause to be, that the neutron spectrum used in the calculation is too hard. Further examination of this question is in progress.

These experimental measurements give us valuable results for code verification. Both diffusion theory and Monte-Carlo [8] give reasonable agreement with experiment. The discrepancy noted in reference [8]may arise from an overestimate for the absorption in the target; this is currently under investigation.

Further indications from these results are:

(i) Any void (for example a vacuum jacket) around the target should be kept to the smallest practicable width.
(ii) Beryllium could be a candidate for a target container material.

Case D) has been included to give an evaluation of depleted uranium as a target material. The thermal neutron flux at the peak was increased by 70 %, which should be compared to the source strength gain of 2.8 compared to Pb/Bi as measured by Bauer et al. [5]. The flux depression of 40 % is caused by the absorption of neutrons in the uranium. The peak flux position is shifted outwards by approximately 4 cm, a definite advantage for installation of beam tubes.

The model target, being solid, was highly unrealistic, lacking for instance any cooling medium and cladding. The considerable uranium density decrease in a technologically feasible target will lead to a further reduction of flux, which has been estimated to be at least 20 %.

The flux increase using depleted uranium would not seem to justify overcoming the prodigious technological problems its use would require.

3.2 Moderator Optimisation. I - D_2O Shield Interface

The moderator flux in the D_2O is affected by (among other things) the choice of material outside the tank. In contrast to the simplest system where the shielding iron starts immediately after the D_2O tank, a layer of material of one of the following two classes could be included:

(i) Combining good reflection and shielding properties, e.g. Pb, Bi.
(ii) Thin layer reflectors, e.g. H_2O, Be.

In both cases a reduction of both the radius of the D_2O tank and the outer shield are possible. An analytic method is used.

Case 1: A Pb reflector

To calculate the optimum thickness for the layer, the overall shielding effect of Pb plus iron is maximized subject to a constant thermal neutron flux in the moderator. Referring to Fig. 11, the thermal flux will be unchanged if $\hat{R}$ (=[R_{D_2O} + ℓ], R_{D_2O} the D_2O tank radius) is kept constant. The extrapolation length ℓ.

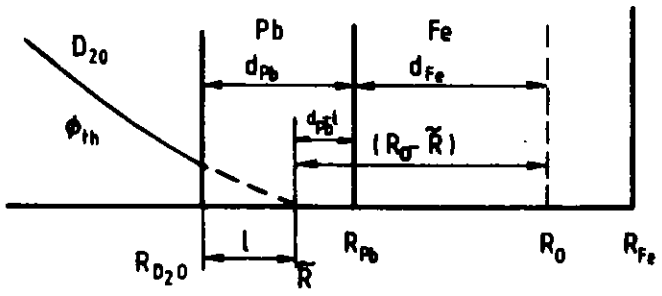

Fig. 11
Explanation of the symbols for calculation, of optimum Pb reflector thickness.

is a function of the thickness of the Pb layer, d_{Pb}, and will be longer for Pb than Fe. The marginally inferior shielding ability of Pb will be offset by it, in part, replacing some of the outer layer of D_2O.

The dose from the high energy neutrons at some radius R_o within the Fe shield may be considered in terms of a shielding function f, given by:

$$f = EXP\ -[\Sigma_{Pb}d_{Pb} + \Sigma_{Fe}d_{Fe}]$$

where Σ_{Pb} (= 0.058/cm) and Σ_{Fe} (= 0.062/cm) are the macroscopic shielding cross-sections. Using the dimensional relationships shown in Fig. 11 the function f may be rewritten as:

$$f = EXP\ -[\Sigma_{Fe}(R_o-\tilde{R})]\cdot EXP\ -[\Sigma_{Pb}d_{Pb}-\Sigma_{Fe}(d_{Pb}-\ell)]$$

$$= EXP\ -[\Sigma_{Fe}(R_o-\tilde{R})].f^*$$

As $(R_o-\tilde{R})$ is a constant, the minimum high energy flux may be found from the condition,

$$\frac{df^*}{d(d_{Pb})} = 0$$

The relationship between ℓ and d_{Pb} may be represented by the Albedo formula for thermal neutrons in the diffusion approximation:

$$\ell = \frac{D_{D_2O}}{D_{Pb}\cdot X_{Pb}}\ TANH\ [X_{Pb}(d_{Pb}+\ell_{Pb})] \qquad (1)$$

where D_{D_2O} (= 0.818 cm) and D_{Pb} (= 0.907 cm) are the diffusion coefficients, $X_{Pb} = \sqrt{\Sigma_{abs}/D_{Pb}}$, Σ_{abs} (= 0.00483 cm) is the macroscopic absorption cross-section for Pb and ℓ_{Pb} (= 3.58 cm) is the diffusion theory extrapolation length for a Pb/Fe interface.

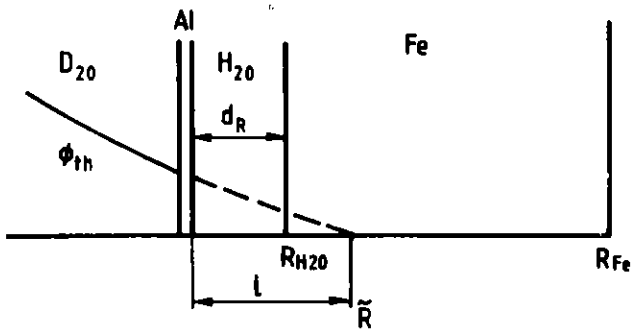

Fig. 12
Explanation of the symbols for calculation, of optimum H_2O reflector layer thickness.

The optimum Pb layer thickness is 23.45 cm and the corresponding extrapolation length 11.88 cm. The diffusion theory extrapolation length for a D_2O/Fe interface is 3.22 cm, hence for $\tilde{R}$ constant and constant flux in the moderator, 8.66 cm of the Pb layer replaces D_2O. The other 14.79 cm of Pb replaces Fe, but as the Pb layer is equivalent to $(\Sigma_{Pb}/\Sigma_{Fe})^*$ 23.45 = 21.88 cm of Fe, then the effective thickness of the shield is increased by 7.09 cm of Fe, which may be removed. (We note that the distance factor in the shielding allows us to take only a large fraction of these 7.09 cm.)

Case 2: A H_2O layer

In this case there is no strong shielding effect to consider, and the problem is to find the H_2O width, d_R, which minimised the iron shield radius R_{Fe} (see Fig. 12) that is:

$$\frac{d(\ell - d_R)}{d(d_R)} = 0$$

The extrapolation length ℓ is related by equation (1) on the previous page, with the appropriate changes due to the different materials and leads to optimum d_R and ℓ given by:

$$D_R = \frac{1}{X_{H_2O}} \text{ ACOSH } \sqrt{\frac{D_{D_2O}}{D_{H_2O}}} - \ell_R$$

$$\ell = \frac{1}{X_{H_2O}} \sqrt{\frac{D_{D_2O}}{D_{H_2O}} \left(\frac{D_{D_2O}}{D_{H_2O}} - 1\right)}$$

Taking ℓ_R for the H_2O/Fe interface = 0.6 cm, D_{H_2O} = 0.1532 cm and Σ_{abs} for H_2O as 0.0188 cm, then d_R = 3.62 cm and ℓ = 13.72.

The D_2O tank radius may be reduced by 10.5 cm and the outer shield radius is reduced by 6.88 cm.

The reduction of shielding and D_2O material quantities in the case of H_2O and Pb reflectors are comparable. For the D_2O, a 10 cm reduction of tank radius is significant, whilst the shielding thickness change in the case of Pb is small compared to the error involved in estimating the required thickness. It is likely that the innermost layers of shielding will require cooling; a light water cooling channel of about 3.6 cm width would be a neutronic optimum.

3.3 Moderator optimization. II - Physical dimensions

The size of the D_2O moderator affects the thermal neutron flux. Two different criteria apply:

(i) for beam tubes the maximum neutron current at the monochromator;
(ii) for guides and the cold source, the maximum flux of the moderator.

In this section, the optimisation for beam tubes is considered. The neutron current, I, at a monochromator is determined by the flux at the beam tube tip, ϕ, and the length from tip to monochromator L. The length L is determined principally by the radius of D_2O tank and the thickness of the bulk shield; reduction of L can only come from reduction of the D_2O tank radius for a properly shielded source.

Taking as a reference system, a 145 cm long by 15 cm diameter target in a 130 cm radius by 260 cm high D_2O tank (see Fig. 13), the thermal neutron flux distributions in the moderator, with three thicknesses of the whole peripheral layer of D_2O replaced by Pb, have been calculated using the DIFF-2D code of RSYST. Calculated axial and radial flux distributions are shown in Figs. 14 and 15.

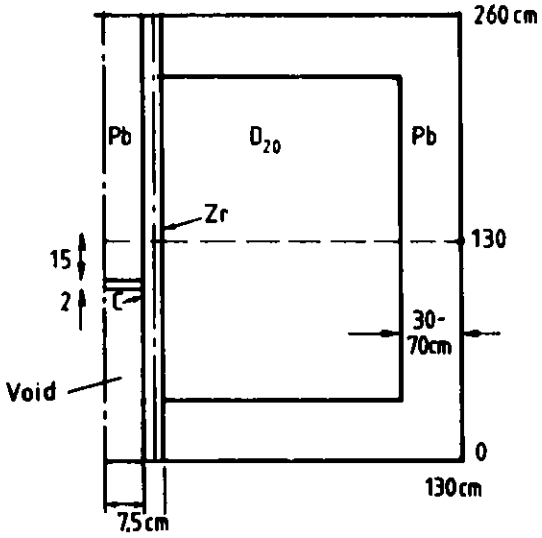

Fig. 13
Arrangement of target/ moderator/reflector assembly for calculation of optimum D_2O tank radius in section 3.3.

The figure of merit η for examining the performance is:

$$\eta = \frac{I}{I_{Ref}} = \frac{\phi}{\phi_{Ref}} \left(\frac{L_{Ref}}{L}\right)^2$$

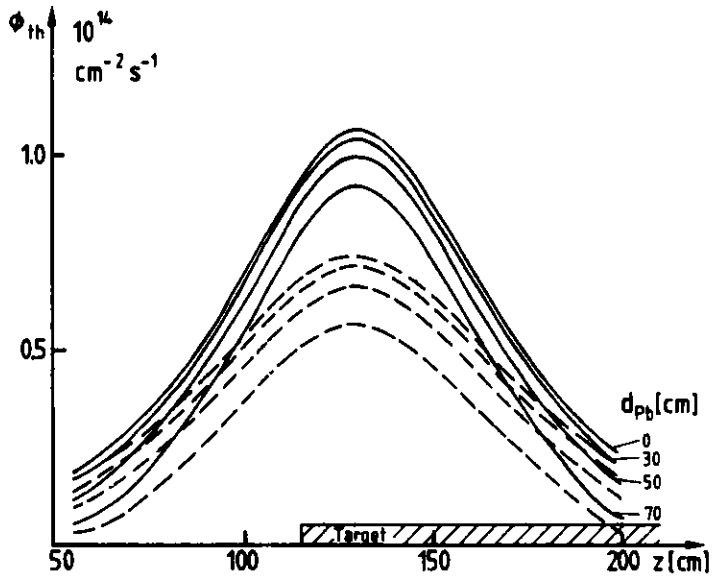

Fig. 14
Variation of neutron flux at radial distances of 16.25 cm (———) and 36.25 cm (- - - - -), from the target axis in the target axial direction. Calculation by diffusion theory for 0, 30, 50 and 70 cm of D_2O replaced by Pb.

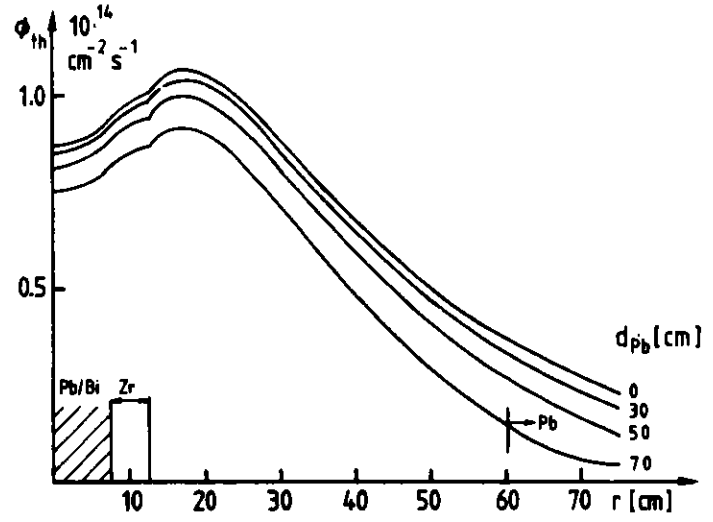

Fig. 15
Radial distribution of neutron flux in plane of the flux maximum from diffusion theory calculation. Curves are for 0, 30, 50 and 70 cm of D_2O replaced by Pb.

In Table II are shown values of η and ϕ for the reference system and three other 'effective' D_2O tank radii, at three different radii, r, in the D_2O. Taking r = 31.25 as a representative case, an effective D_2O tank radius of approximately 100 cm seems optimal. Using the extrapolation length for the H_2O layer of the previous section, this corresponds to a physical radius of approximately 90 cm.

Table II

Fluxes and figure of merit η for various D_2O tank effective radii

$\tilde{R}$(cm)	L(cm)	r = 16.25 cm		r = 31.25 cm		r = 42.5 cm	
		$\phi\ 10^{14}$ cm^{-2} sec^{-1}	η	φ	η	φ	η
131.6	600.0	1.027	1.0	0.826	1.0	0.606	1.0
112.0	580.4	1.002	1.043	0.798	1.032	0.575	1.014
92.3	560.6	0.959	1.070	0.748	1.036	0.520	0.984
72.3	540.7	0.881	1.057	0.655	0.977	0.419	0.851

3.4 Energy Deposition

The energy deposition by the fast neutrons during thermalisation has been calculated, but at present only an upper bound estimate for the other contributions is available. The following contributions to the total energy have been calculated for a 1 mA current:

1. High energy neutrons	42.0	kW (UL)
2. High energy protons	0.8	kW (UL)
3. Charged pions	0.14	kW (UL)
4. During thermalisation	18.2	kW (C)
5. Gammas (from target)	2.6	kW (UL)
6. Electrons (from target)	0.23	kW (UL)
7. Gammas (from D[n,γ]T)	2.7	kW (C)

where the qualifiers UL stand for Upper Limit and C for Calculated.

This gives an upper limit of approximately 67 kW/mA.

The distribution of energy deposition by the neutrons during thermalisation indicates that 50 % of their power contribution is deposited in approximately the first 6 cm of the D_2O and 90 % in the first 22 cm. The peak energy density for this contribution is 1.0 W/cc at 1 mA.

3.5 Moderator Activation

The tritium build-up has been estimated from the thermal flux distribution in the D_2O, using a macroscopic capture cross-section of 0.000034/cm. Averaging over the flux, the capture rate is estimated at $2.7 \cdot 10^{15}$/sec/mA. This corresponds to an equilibrium

activation of approximately 70 kCi. For a total D_2O volume of 4850 litres, this is an equilibrium specific activity, with mixing, of 14.4 Ci/ℓ.

The values during the build-up are 0.8 Ci/ℓ at 1 year, 1.5 Ci/ℓ at 2 years and 2.3 Ci/ℓ at 3 years.

REFERENCES

[1] W.E. Fischer, Status Report on the SIN Neutron Source, These proceedings
[2] Y. Takeda, Thermofluid Dynamics of the Liquid Lead-Bismuth Target for the Spallation Neutron Source at SIN, These proceedings
[3] W. Litzow et al., Paper 4, SNQ-Report, part III, A2 (1981)
[4] U. Reus, W. Westmeier, I. Warnecke, GSI-Report 79-2 (1979)
[5] G. Bauer et al., Contribution ICANS V (Jülich) p. 445 (1981)
[6] S. Cierjacks et al., Contribution ICANS IV (Tsukuba (1980)
[7] **Много групповые методы расчета защиты от неитронов Б.Р. Бергельсон, А.П. Суворов, Б.З.Торлин** (1970)
[8] F. Atchison et al., SIN Newsletter 14, p.NL5 (1982)

ICANS-VI
INTERNATIONAL COLLABORATION ON ADVANCED NEUTRON SOURCES
June 27 - July 2, 1982

STUDIES OF A LEAD REFLECTOR FOR A PULSED NEUTRON SOURCE

by

A. D. Taylor, G. J. Russell, M. M. Meier and H. Robinson
Physics Division
Los Alamos National Laboratory
Los Alamos, NM 87545

1. INTRODUCTION

Many of the new generation of accelerator based neutron sources have adopted a target-moderator geometry in which the neutron beam is tangential to the target (wing geometry). Such an arrangement significantly reduces the high energy (up to several hundred MeV) neutron background compared with the radial configuration (slab geometry). This improvement in background is accompanied by a severe reduction in solid angle between target and moderator, thus reducing the neutronic coupling. Some compensation may be achieved by using a fast neutron reflector [1]. These reflectors fall into two classes: moderating reflectors such as water, polyethylene, heavy water, graphite and beryllium; and non-moderating reflectors such as iron, copper, nickel and lead. Both experiment and Monte Carlo simulation show beryllium to be the superior moderating reflector. In this paper, we examine the consequences of adopting a non-moderating reflector and compare its performance to that of beryllium.

Reflector studies on a time modulated source [2] have shown lead to be an excellent reflector, maintaining the structure of the long time pulse (500 μs) marginally better than beryllium and with a slightly superior yield. Engineering, fabrication and cost factors as well as improved gamma and fast neutron shielding properties further favour lead as a reflector for these sources. Even for truly pulsed sources which rely primarily on time of flight for energy selection, Monte Carlo studies have shown that a lead reflector maintains an excellent time structure in hydrogenous moderators in the slowing down region [3]. In this paper, we describe the experimental comparison of lead and beryllium reflectors for the case of a pulsed spallation source. The target-moderator-reflector configuration used was a mock-up of the Rutherford Appleton Laboratory's SNS geometry. The experiments were performed in the low current target area of the Los Alamos National Laboratory's spallation source, the WNR. This work was complemented by Monte Carlo calculations using the TIMOC code[4].

2. EXPERIMENTAL MEASUREMENTS AT THE WNR

The capabilities of the low current target area of the WNR for time structure and spectral measurements on the neutron beams produced by pulsed spallation target-moderator-reflector assemblies have been described previously [5]. In this study, the normal WNR reflected 'T' configuration, figure 1a, was modified to simulate the geometry of the SNS assembly [6], figure 1b. Only one moderator was used and it was open on both faces. The decoupler and void liner (which was removable) were

cadmium; and a neutronic approximation to SNS's heavy water cooling wings was incorporated. The reflector, which could be either lead or beryllium, formed a 40 cm cube around the system. Both ^{238}U and Pb targets were used to study the effect of the harder spectrum from the small Pb target.

Using the pyrolytic graphite crystal analyser arm, the time structure of moderated neutron pulses from a lead reflected and a beryllium reflected moderator were compared. The 100 ns long proton pulses used make a negligible contribution to these data and the 0.4% resolution of the spectrometer is small in comparison with the observed widths. Semi-logarithmic plots of these data (unnormalized) are shown in figures 2a and 2b. In both cases, there was a cadmium decoupler between moderator and reflector and a cadmium void liner in the neutron beam port through the reflector. The FWHM of the time pulses were found, within experimental error, to be identical. Further, it was possible to superimpose the time pulses from both reflectors over two orders of magnitude showing that the shape was the same.

The overall efficiency of the two reflectors was compared by measuring the spectral distribution by time of flight over a 5.58 m flight path. Each data set was normalized, corrected for detector efficiency and attenuation factors and converted to an energy distribution (see [5] for details). The overall spectrum is then described by a maxwellian region:

$$\phi_{max}(E) = \phi_m \frac{E}{T^2} \exp(-E/T)$$

and an epithermal region

$$\phi_{epi}(E) = \frac{\phi e}{E^{\gamma}}$$

joined together by a switch function

$$\Delta(E) = \left[1 + \exp\left(\frac{W_1}{\sqrt{E}} - W_2\right)\right]^{-1}$$

thus

$$\phi(E) = \phi_{max}(E) + \Delta(E)\,\phi_{epi}(E)$$

In these equations, ϕ_m is the integrated maxwellian intensity, T is the effective neutron temperature, ϕ_e is the differential intensity at 1 eV, γ is a measure of the leakage of the system and W_1 and W_2 parameterize the switch from slowing down to thermalization behavior. Using ϕ_m, T, ϕ_e, γ, W_1 and W_2 as parameters, a fit is made to the data*. A typical fit is shown in figure 3. The results of this analysis are summarized in Table I for studies with a Pb target and in Table II for studies with the ^{238}U target. The latter table contains data from coupled as well as decoupled systems. The yield parameters ϕ_m and ϕ_e indicate that although a lead reflector performs well, it is not as efficient as a beryllium reflector. At this point the question of reflector dimensions must be raised: although both reflectors were physically identical in size, their neutronic dimensions were not the same. A 40 cm beryllium reflector is close to its optimum size [3]; the Monte Carlo technique was employed to establish the optimum size of a lead reflector.

*NOTE: The values of $\gamma > 1.0$ indicate that a high energy background has not been accounted for. This background is less then 7% at 1.257 eV (the rhodium resonance) and may be large at high energies. In the thermal region, it is negligible.

3. MONTE CARLO OPTIMIZATION

Variation of the reflector cube dimensions experimentally would have been costly in time and effort, difficult to achieve because of the experimental set up and hazardous to personnel involved because of the radiation levels around the target. A very good estimate of the functional dependence of performance on cube size is readily achieved by Monte Carlo simulation. Such an optimization has already been described for the case of a beryllium reflector. We now report results for a lead and a heavy water reflector. The geometry used to optimize the reflector dimensions is shown in figure 4. A 10 x 10 x 5 cm^3 moderator is located centrally in a cube of reflector of side 2L and decoupled by a variable density B^{10} layer. An isotropic point source is located below the moderator. The coupling efficiency, as measured by neutrons leaking down the beam tube, is determined for a variety of dimensions, 2L. These data are given in figure 5 for beryllium, lead and heavy water reflectors. We observe that a 40 cm beryllium reflector (L = 20 cm) is within a factor 1.08 of the saturation value whereas the performance of a 40 cm lead reflector may be enhanced by up to a factor 1.3.

We note that the absolute performance of beryllium in this simple geometry (figure 4) is significantly better than that of lead or heavy water. Calculations on realistic geometries (with a target source rather than a point source) do not support this result. It would appear to be an artifact of the extremely tight source to moderator coupling employed. The saturation of the coupling with increasing moderator size is, however, quantitatively supported by realistic calculations and by experiment [5].

Using the information of figure 5 to scale the experimental data on a 40 cm cube reflector to a reflector of optimal size gives 11.4 and 3.9 for the thermal and epithermal coupling parameters when lead is the reflector (Pb target) and 11.5 and 3.8 for a beryllium reflector (Pb target). With the softer spectrum from a U^{238} target the thermal and epithermal parameters become 24.1 and 8.46 with a lead reflector and 25.3 and 8.45 with a beryllium reflector.

We may conclude that for pulsed neutron moderators a lead reflector is as efficient as a beryllium reflector. On the question of decoupler, some differences appear. As expected a coupled beryllium system has an effective neutron temperature of 25 meV, indicating the highly moderated nature of the spectrum, in comparison with some 34 meV when decoupled. It is known from other work that this increase in moderation is accompanied by a degradation in time structure. In the case of the lead reflector, some lowering in the neutron temperature did occur for the coupled case. No time measurement was made on the coupled lead reflector but it is reasonable to infer that some pulse degradation has occured and that even a non-moderating reflector such as lead may need to be decoupled for use in a truly pulsed source.

Two secondary aspects of the reflector's performance should be discussed, namely the fast neutron shielding effect and the distribution of energy within the moderator-reflector system.

4. FAST NEUTRON SHIELDING

For a tightly coupled target-moderator system in wing geometry, the collimation is usually set such that no neutron may leak out of the target directly into the experimental area. Table III summarizes the high energy attenuation lengths for some common shielding materials. For very high energy neutrons some rays exist with only a few mean free paths of attenuation [7], see figure 5. Such a problem may be eased (at the expense of flux) by increasing the target-moderator distance, by minimizing the collimator void or by adding additional shielding external to the bulk shield or internal to the target crypt. The reflector is the first material that such neutrons encounter and it is highly desirable to maximize their attenuation within the bulk shield. We see from Table III that lead is far superior in this aspect to beryllium.

5. NEUTRONIC HEATING

A disturbing feature of non-moderating reflectors is the redistribution of neutronic heating in the target-moderator-reflector assembly. As neutrons moderate in the reflector, they deposit energy which might otherwise be added to the moderator's heat load. In a non-moderating reflector neutrons entering the moderator after several collisions in the reflector still carry a large fraction of their initial energy. Figure 6 shows the Monte Carlo results for the fraction of the total energy available in the test geometry that was deposited in the moderator and reeflector as a function of the size of reflector, for all three reflector materials. Both heavy water and beryllium reflectors absorb substantial fractions of this energy (~80%) whereas even the largest size of lead reflector takes up less than 40%. The result is a factor 2 increase in heat deposited in the moderator. This calculation is idealized and the presence of a target is expected to reduce the effect. Although such a factor may not be significant for ambient or 90°K moderators, a substantial financial penalty would be incurred in the case of a liquid hydrogen moderator operating at 20°K. In such a case, a composite reflector[9] with a beryllium blanket (or other moderating reflector) surrounding the cryogenic moderator would be desirable.

6. CONCLUSION

This study illustrates the complementarity of experiment and Monte Carlo simulation. Neither technique on its own would have been able to answer the questions raised; for example, thermal pulse shapes from a reflected configuration are extremely difficult to compute and heat loads in the reflector and moderators impossible to measure at currents which are low enough to keep induced radiation at a level which would allow the experiment to be performed. There are many practical advantages to using a lead reflector. We find no degradation in the quality or intensity of moderated neutron pulses. The shielding advantage may be somewhat offset by the higher moderator heat loads, especially if cryogenic moderators are used.

References

[1] J. M. Carpenter, "Pulsed Spallation Neutron Sources for Slow Neutron Scattering," Nucl. Instr. and Meth. 145 (1977) 91-113.

[2] G. S. Bauer, H. M. Conrad, H. Spitzer, K. Friedrich and G. Milleret, "Measurement of Time Structure and Thermal Neutron Spectra for Various Target-Moderator-Reflector Configurations of an Intensity-Moderated Spallation Source," Proceedings of the 5th Meeting of the International Collaboration on Advanced Neutron Sources, Jül-Conf-45, ISSN 0344-5789 Jülich (1981) 475-488.

[3] A. D. Taylor, "Monte Carlo Reflector Studies for a Pulsed Neutron Source," Proceedings of the 5th Meeting of the International Collaboration on Advanced Neutron Sources, Jül-Conf-45, ISSN -344-5789 Jülich (1981) 377-388.

[4] H. Kschwendt and H. Reif, "TIMOC--A General Purpose Monte Carlo Code for Stationary and Time Dependent Neutron Transport," Euration Report EUR 4915e (1970).

[5] G. J. Russell, M. M. Meier, H. Robinson and A. D. Taylor, "Preliminary Neutronics of a Reflected 'T' - Shape Premoderator/Moderator for the Weapons Neutron Research Facility," Proceedings of the 5th Meeting of the International Collaboration of Advanced Neutron Sources, Jül-Conf-45, ISSN 0344-5789 Julich (1981) 389-416.

[6] A. D. Taylor, "Neutron Transport from Targets to Moderators," Rutherford and Appleton Laboratory Report, RL-81-057.

[7] J. M. Carpenter, private communication.

[8] M. Barbier, "Shielding and Activation Study for the Intense Pulsed Neutron Source of Argonne National Laboratory". Mitre Technical Report MTR-6998 (1975).

[9] G. J. Russell, these proceedings.

Table I

Pb TARGET

Reflector	Decoupler	ϕ_e	ϕ_m	T	γ	W_1	W_2
Be	Cd	3.54	10.7	33.6	1.05	90	8.5
Pb	Cd	3.01	8.8	33.8	0.99	97	9.3

Table II

U TARGET

Reflector	Decoupler	ϕ_e	ϕ_m	T	γ	W_1	W_2
Be	Cd	7.82	23.4	34.0	1.05	91	8.5
Pb	Cd	6.51	18.5	33.9	1.00	93	8.9
Be	--	8.08	35.4	25.0	1.07	132	14.6
Pb	--	6.88	24.7	28.6	1.02	118	12.4

Table III

High Energy Neutron Nuclear Mean Free Paths (MFP) [8].

Material	Be	H_2O	Concrete	Fe	Cu	W	Pb	U
MFP(cm)	50.0	90.3	46.1	17.3	15.8	10.1	17.8	11.1

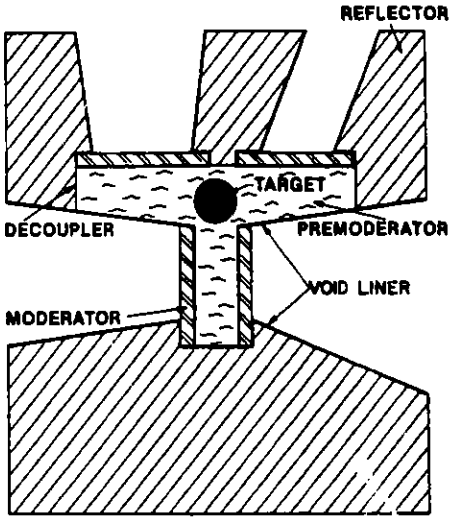

Fig. 1a

Section through the standard reflected 'T' shape moderator/ premoderator configuration used at the WNR.

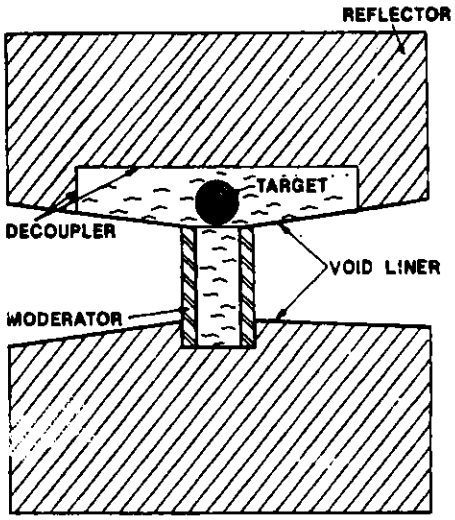

Fig. 1b

Section through the modified configuration simulating a single moderator SNS wing geometry.

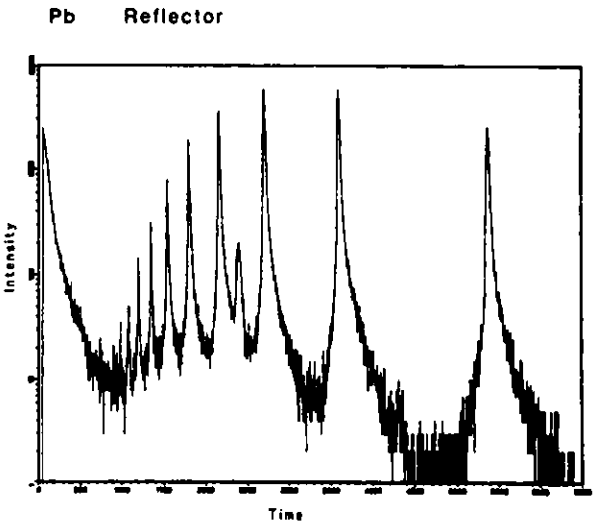

Fig. 2a

Semi-logarithmic plot the moderated pulse shapes of a lead reflected system. The moderator was cadmium decoupled polyethylene, poisoned at a depth of 1.27 cm by 0.025 mm of gadolinium. The peak at 5500 μs is the 004 reflection from pyrolitic graphite. The spurious peak at 2400 μs is the 002 reflection, viewed in frame overlap.

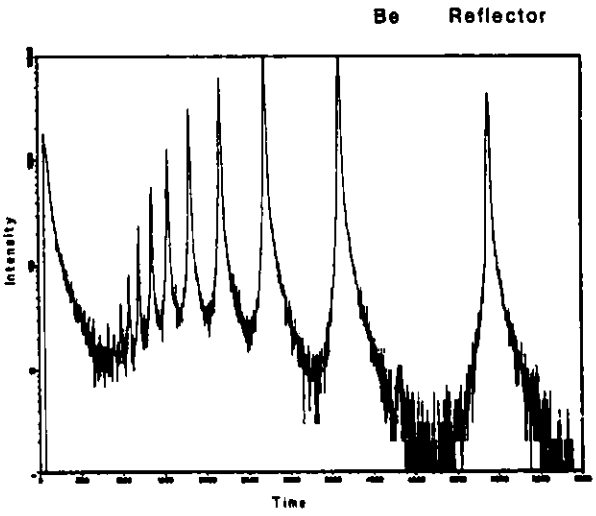

Fig. 2b

The corresponding data to figure 2a with beryllium as reflector. These data were taken at 60 Hz, thus eliminating the frame overlap problem.

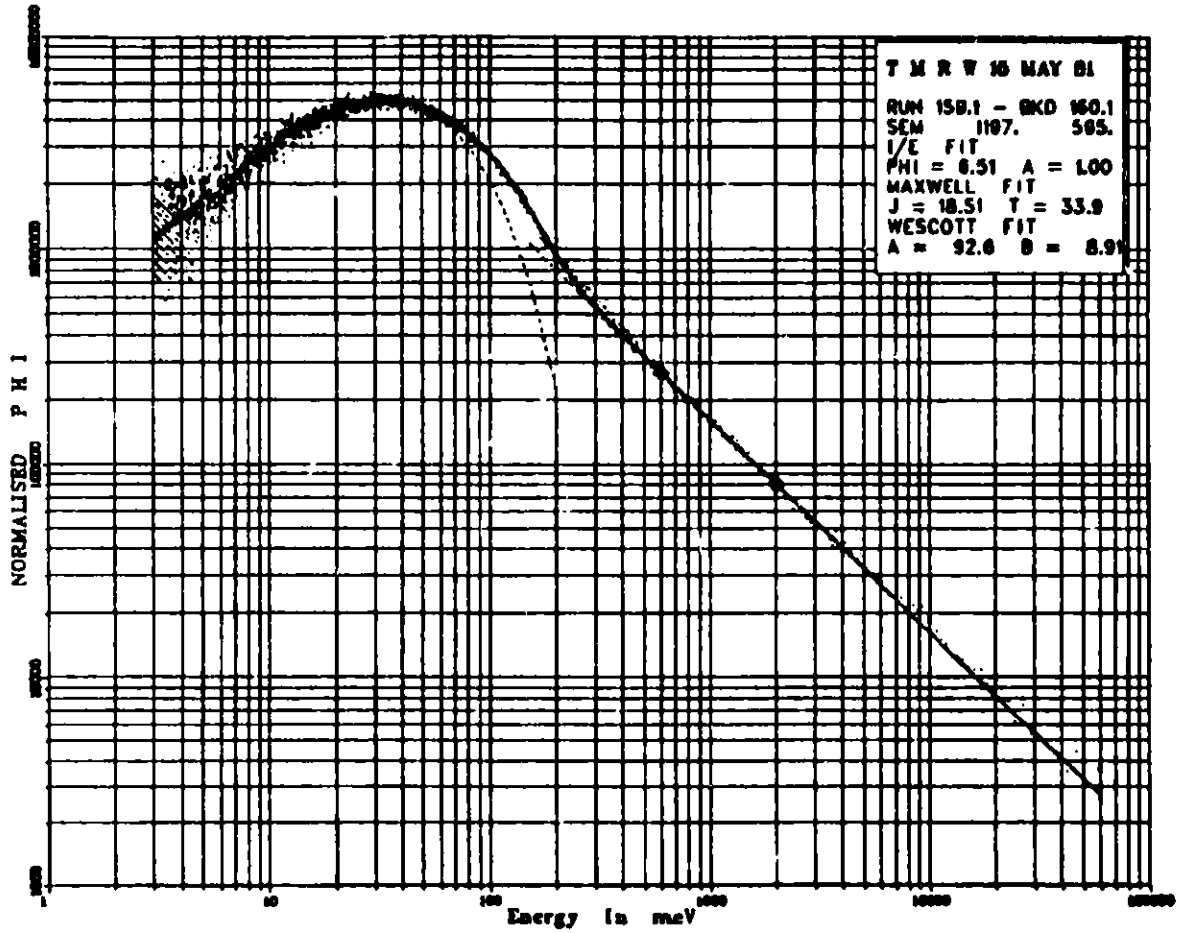

Fig. 3. A fit of a spectral measurement to the function described in the text. The dashed lines are independent fits to the maxwellian and slowing down regions. The solid line is the overall six parameter fit using the switch function.

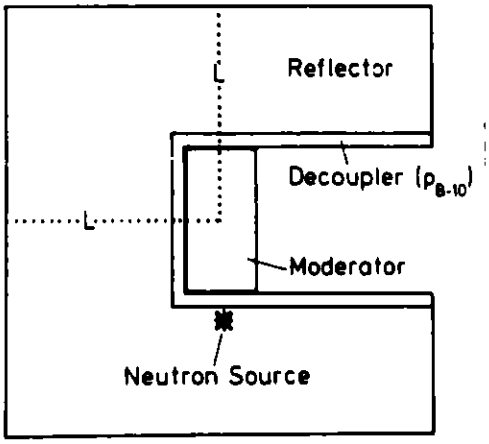

Fig. 4

The Monte Carlo geometry used to optimize the reflector dimension, L. The decoupler density for these studies was fixed at 0.5 eV(1/e).

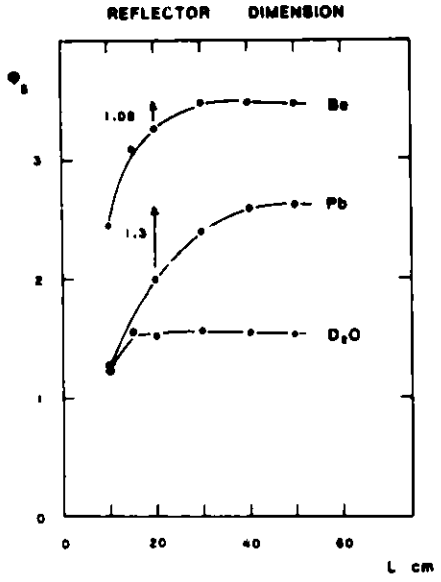

Fig. 5

The two steradian average of the surface flux from the moderator as a function of reflector dimension for beryllium, lead and heavy water reflectors. The numbers shown are the scaling factors required to convert a 40 cm cube of reflector to the asymptotic performance.

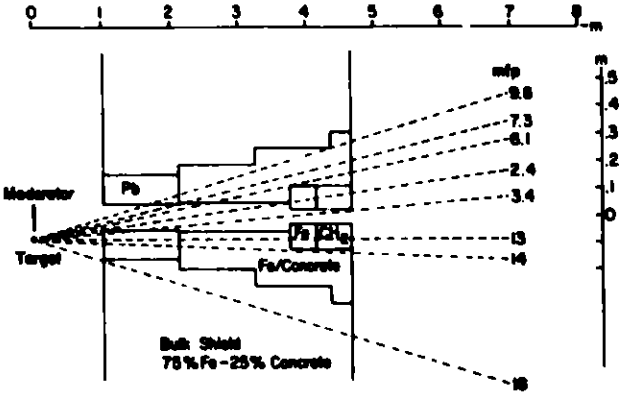

Fig. 6

The ray diagram for fast neutron collimation for a typical beam. The numbers opposite each ray correspond to the number of mean free paths seen by a 100 MeV neutron. Calculations [8] indicate that some 14 mean free paths are required to shield a 5 μA, 800 MeV source.

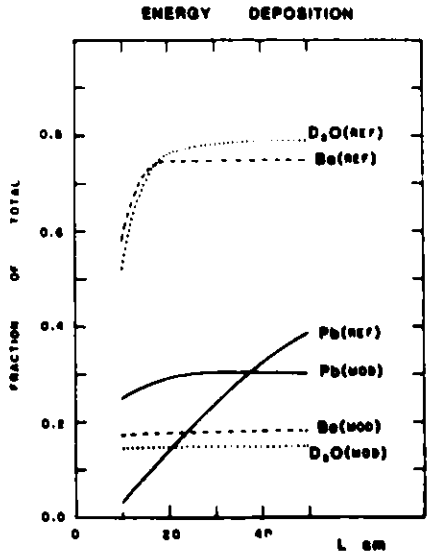

Fig. 7

The fraction of initial neutron energy deposited in the reflector and moderator of Figure 4 for beryllium, lead and heavy water reflectors.

ICANS-VI

INTERNATIONAL COLLABORATION OF ADVANCED NEUTRON SOURCES

June 28 - July 2, 1982

MODERATED NEUTRON PULSE SHAPES

A. D. Taylor
Physics Division
Los Alamos National Laboratory
Los Alamos, NM 87545

I. INTRODUCTION

The time dependence of the neutron pulse from hydrogeneous moderators is well known in the slowing down region. The full width at half maximum, Δt_{50}, behaves as $2/\sqrt{E}$ when time is measured in μs and energy in eV. The shape of the pulse throughout the slowing down region is a universal function of vt, $\phi(v,t) = (\Sigma_s vt)^2 \exp(-\Sigma_s vt)$. In this equation, v is the neutron velocity, Σ_s the macroscopic cross section of the moderating material and t is time. This infinite medium result is found to hold well even for small hydrogeneous moderators [1] and departures from this behaviour for reflected moderations are understood. Measurements of the time dependence have been made in the thermal region but no specific parameterization has been given. An empirical description is used in powder profile refinement [2] but this has no physical basis. The time behaviour depends strongly on the material and size of the moderator, the reflector and decoupler. Figure 1 shows the wavelength dependence of Δt_{50} in the thermal range for a series of possible moderator configurations, measured at the WNR [3]. Monte Carlo calculations have given some information on pulse shape [4], but are dependent on details of the scattering kernels used and are difficult to

perform for other than simple moderators. As condensed matter experiments on pulsed neutron sources become more sophisticated, information will be needed on the shape of the thermal pulse in addition to Δt_{50}. In this paper, we attempt to find some guidelines to the time behaviour of moderated neutron spectra in the thermal region.

2. TIME DEPENDENT DIFFUSION THEORY [5]

The long time dependence of the moderated neutron pulse shape is, in time dependent diffusion theory, given by

$$\phi(t) = \exp - t/\tau$$

where

$$\tau^{-1} = \alpha_0 + DB^2 - CB^4 + \ldots$$

In these equations, α_0 is the absorption probability, D the diffusion coefficient, C the diffusion cooling constant and B^2 the geometric buckling. For a rectangular moderator of dimension, $L_1 \times L_2 \times L_3$

$$B^2 = \pi^2 \sum_i^3 L_i^{-2}$$

We must correct the physical dimension of the moderator by the extrapolation length, $d = 0.71\lambda_{tr}$, where λ_{tr} is the transport mean free path. Thus

$$B^2 = \pi^2 \sum_i^3 \left(L_i + 2d\right)^{-2}$$

Table I gives the parameters α_0, D, C and λ_{tr} for four common moderating materials. With these parameters, we can anticipate the long time decay of neutron pulses from large moderators. Although not

strictly applicable, we will proceed to use this theory as a guide to the behaviour of quite small moderator ($B^2 \sim 1\ cm^{-2}$).

3. EXPERIMENTAL PROCEDURE

In this paper, we re-analyze two sets of data: time dependent measurements from a pyrolitic graphite crystal analyzer on a mock up spallation source at the CERN PS booster [6] and unpublished data taken with a similar analyzing system at the low current target area of the WNR [3]. An exponential is fitted to the long time decay portion of each reflection. At long wavelengths, this decay is found to be independent of reflection, although the intensity associated with the mode increases as energy decreases. In some cases, for example at small buckling, this mode totally dominates the peak shape. The fitted τ values and a description of the configuration are given in Table I.

4. COUPLED AND DECOUPLED SYSTEMS

All the data presented in Table II were taken on reflected systems. Only two of the runs had direct neutronic coupling between the moderator and the reflector. In Figure 2, we plot the τ vs B^2 prediction for beryllium, heavy water, light water and polyethylene using the diffusion parameters of Table I. The coupled run (CERN N) had a 10 X 20 X 7 cm^3 polyethylene moderator coupled with the beryllium reflector. The τ value of 500 μs from this moderator is totally consistent with the mode expected from beryllium with a volume equal to that of the reflector used, and not with the decay expected from the polyethylene moderator. When the same reflector was decoupled (CERN B_4C and CERN Cd), the decay is well described by the moderator mode. An intermediate case is the partially coupled dataset, WNR 184. In this run two strongly separated modes from the moderator were observed, a fast mode corresponding to the moderator decay and a slow mode of 300 μs (containing twice the intensity) resulting from the reflector decay. The system was decoupled, but no void liner was used. The WNR reflector, Figure 3, has a complex shape making the buckling difficult to calculate. However, reversing the analysis, for the 300 μs mode to result from beryllium would require $B^2 = 0.025\ cm^{-2}$, corresponding to a cube of side 36 cm. This is in good agreement with the physical size of the WNR reflector.

For the case of polyethylene moderators we now extend the comparison of diffusion theory to our data to very large values of buckling. In Figure 4 the solid line is the result obtained using the diffusion parameters of Table I. The open triangles and circle are results for decoupled, homogeneous moderators. The closed symbols are decoupled heterogeneously poisoned moderators. In these cases, the moderator dimension is taken to be that on the beam side of the 0.025 mm gadolinium poison which neutronically isolates the moderator from the premoderator for energies less than 150 meV. Both these sets of data are seen to be in excellent agreement with the diffusion result even at values of B^2 as large as 3.36 cm^{-2}.

The open square of Figure 3 (WNR 265) is, however, anomalously high. This configuration had a void liner but no decoupler between the moderator and the beryllium reflector. The 100 μs decay time is dramatically lower than the 300 μs expected from the reflector. This obvious effect of omitting the decoupler must be contrasted with our study of the effect of decoupler and void liner on the full width at half maximum of the pulse, Figure 5. These data show only a 3 μs degradation in Δt_{50} compared with the 30 μs increase in decay time. The slow mode does not appear to dominate the peak in these coupled and weakly decoupled systems but does significantly change the shape at levels lower than the half height. Often considerable intensity is to be found in these tails. Simple spectral measurements which indicate a gain in intensity at a particular energy may, therefore, be an erroneous guide to the most effective moderator.

6. CRYOGENIC MODERATORS

An extension of this approach to cryogenic moderators may be of some value, particularly since one application of these moderators is the production of pulses of long wavelength neutrons, where the exponential decay may be expected to dominate. Cryogenic materials of interest are liquid and solid methane and liquid hydrogen. The behaviour of methane should be similar to that of polyethylene with good agreement expected, with the appropriate diffusion parameters, even for small systems.

The equilibrium form of hydrogen at 20°K is para-hydrogen. A substantial decrease in its cross-section occurs for neutrons unable to excite the lowest level rotational transition (14 meV). Below 14 meV para-hydrogen is virtually transparent to neutrons. It is for this reason that para-hydrogen moderators should not show the gain reported for reentrant grooved methane and polyethylene moderators [7,8].

The diffusion parameters for various ortho-para mixtures have been measured at Los Alamos by G. Hansen [9], Figure 6. Unlike previous measurements [10], these data give consistent values of the absorbtion probability between the two spin states of hydrogen. Hansen found that the extrapolation length for 99.8 % para-hydrogen was approximately 12.5 cm, i.e., larger than the physical dimension of a liquid hydrogen moderator for a pulsed source. The conclusion is that for such tiny moderators, no fundamental mode will exist.

7. CONCLUSION

Simple diffusion theory may be used to describe some aspects of the behaviour of small hydrogeneous moderators in the thermal region. The measurement of diffusion parameters for methane, both liquid and solid, would be valuable. Unfortunately, such a general description does not seem applicable to parahydrogen.

References

[1] A. D. Taylor, "Neutron Transport from Targets to Moderators", Rutherford and Appleton Laboratory Report, RL-81-057 (1981).

[2] R. von Dreele, to be published.

[3] G. J. Russell, M. M. Meier, H Robinson and A. D. Taylor "Preliminary Neutronics of a Reflected 'T'-Shape Premoderator/Moderator for the Weapons Neutron Research Facility", Proceedings of the 5th Meeting of the International Collaboration of Advanced Neutron Sources, Jul-Conf-45, Julich (1981) 389-416.

[4] D. J. Picton, Ph. D. Thesis, University of Brimingham (1981).

[5] K. H. Beckurts and K. Wirtz, Neutron Physics, Springer-Verlag (1964).

[6] G. S. Bauer, J. P. Delahaye, H. Spiter, A. D. Taylor and K. Werner, "Relative Intensities and Time Structure of Thermal Neutron Leakage from Various Moderator-Decoupler Systems for a Spallation Neutron Source", Proceedings of the 5th Meeting of the International Collaboration on Advanced Neutron Sources. Jul-Conf-45. Julich (1981) 417-444.

[7] K. Inoue, Y. Kiyanagi, H. Iwasa, N. Watanbe, S, Ikeda, J. M. Carpenter and Y. Ishikawa, "Grooved Cold Moderator Tests", these proceedings.

[8] G. S. Bauer, "Summary on a Discussion on Moderators with Grooved Surfaces", Proceedings of the 4th Meeting of the International Collaboration on Advanced Neutron Sources, KENS Report II, Tsukuba (1981).

[9] G. Hansen, private communication.

[10] T. A. Bryan and A. W. Waltner, "Diffusion Parameters of Liquid Hydrogen", Phys. Lett. 17 (1965), pp 129-130.

Table I

Diffusion Parameters [5]

Moderator	α_o	D	C	λ_{tr}
	(S^{-1})	$(cm^2S^{-1}$	(cm^4S^{-1})	(cm)
CH_2	5,900	26,600	2,600	0.35
H_2O	4,800	36,900	5,100	0.43
D_2O	19	$2.0\ 10^5$	$5.3\ 10^5$	2.43
Be	285	$1.2\ 10^5$	$2.8\ 10^5$	1.48

Table II

Long Time Decay Modes

Data Set	Moderator	Poison	Decoupler		τ	B^2
	cm^3		Premod	Mod	μs	cm-2
WNR 63	10 X 10 X 1.27	Cd	--	Cd	14 ± 3	3.36
WNR 62	10 X 10 X 1.27	Gd	--	Cd	19 ± 3	3.36
WNR 326	8.7 X 8.7 X 1.27	Gd	B	B*	16 ± 3	3.38
WNR 325	10 X 10 X 1.27	Gd	Cd	Cd*	15 ± 3	3.36
WNR 323	10 X 10 X 1.27	Gd	Cd	Cd	17 ± 3	3.36
WNR 324	10 X 10 X 1.27	Gd	--	Cd	19 ± 3	3.36
WNR 322	10 X 10 X 1.59	--	Cd	--	17 ± 3	2.46
WNR 145	10 X 10 X 1.91	Gd	--	Cd	25 ± 3	1.90
CERN B_4C(Gd)	18 X 8 X 2.00	Gd	B	B	30 ± 5	1.74
CERN Cd(Gd)	20 X 10 X 2.00	Gd	Cd	Cd	30 ± 5	1.69
WNR 64	10 X 10 X 2.54	Gd	--	Cd	33 ± 3	1.25
CERN B_4C	18 X 8 X 7.00	--	B	--	72 ± 5	0.34
WNR 265	10 X 10 X 7.62	--	--	--	100 ± 5	0.33
CERN Cd	20 X 10 X 7.00	--	Cd	--	80 ± 5	0.29
CERN N	60 X 75 X 40 (Be)	--	--	--	500 ± 50	0.0107
WNR 184	--	Gd	--	Cd	300 ± 50	--

*Boral Void Liner. All others have a Cd void liner.

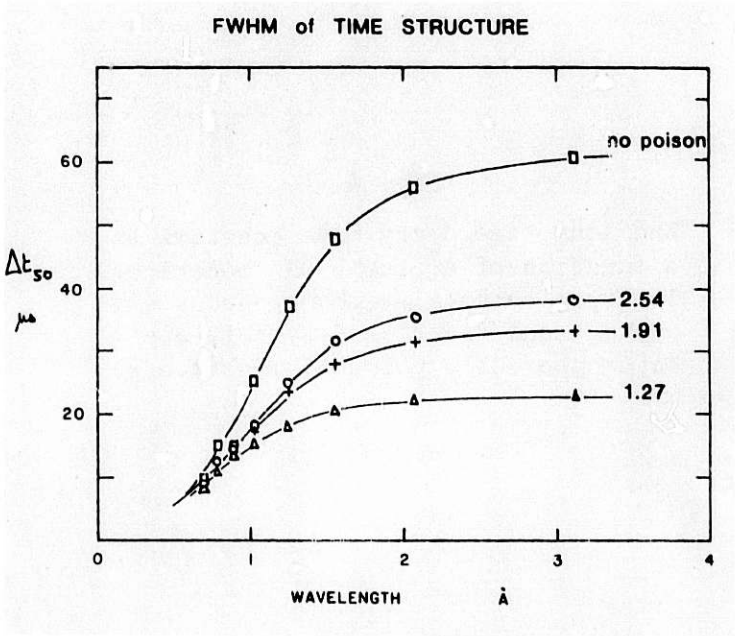

Fig. 1

The energy dependence of the full width at half maximum (FWHM) of the time structure from moderators poisoned at a depth of 1.27 cm, 1.91 cm and 2.54 cm by 0.025 mm of gadolinium. The no poison case, where the premoderator is viewed directly, is also shown.

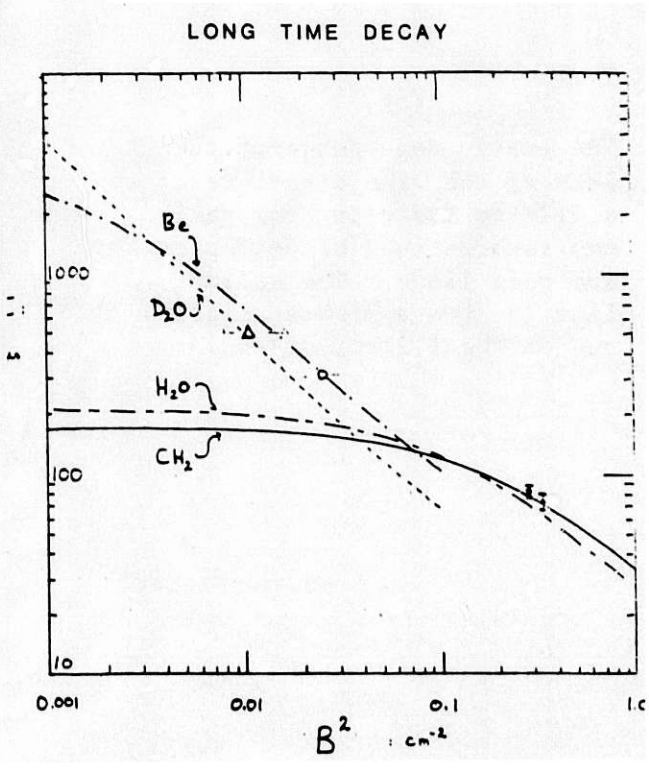

Fig. 2

The long time decay mode constant as a function of B^2 for Be, D_2O, H_2O and CH_2 moderators. The open triangle is the mode from CERN N and the open circle the mode from WNR 184. The solid triangles refer to decoupled CH_2 moderators.

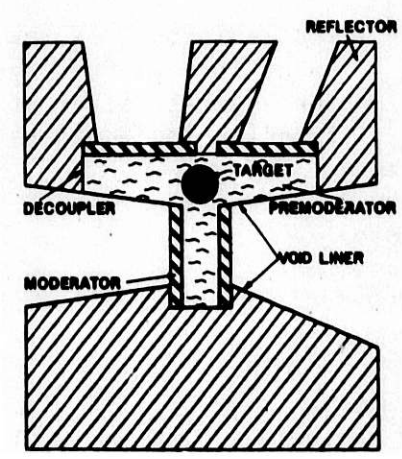

Fig. 3

A cross-section through the reflected 'T'-shaped moderator used at the WNR.

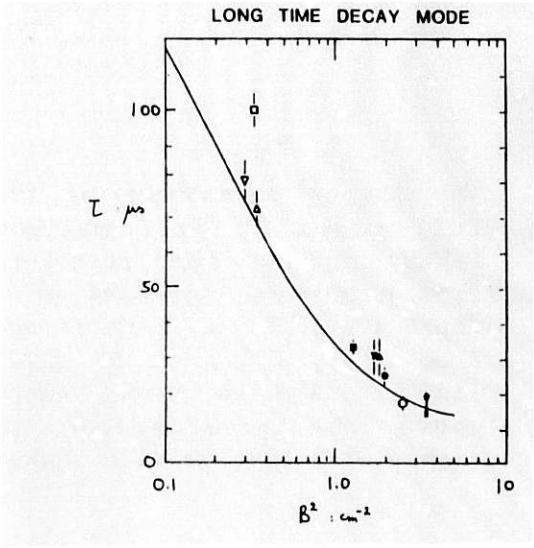

Fig. 4

The long time decay mode constant as a function of B^2 for a CH_2 moderator. The open symbols are homogeneous moderators and the closed symbols are heterogeneously poisoned moderators.

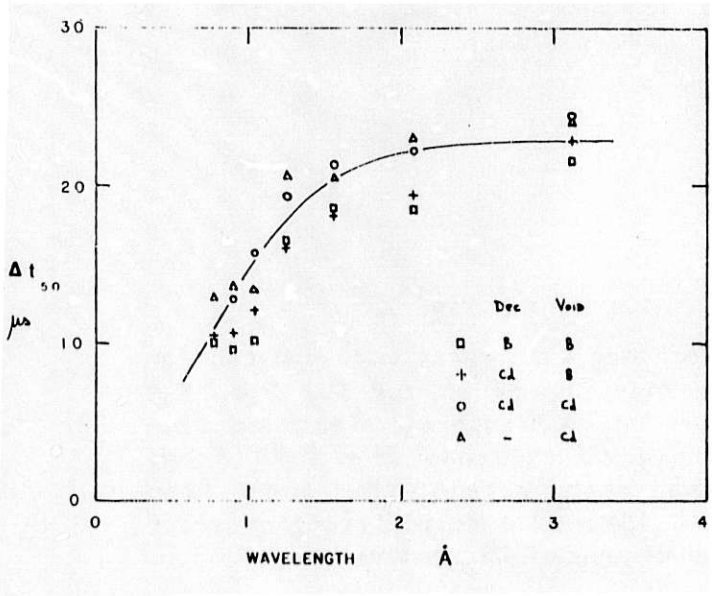

Fig. 5

The energy dependence of the FWHM of the time structure of a 1.27 cm moderator for various combinations of decoupler and void liner. The solid line is from a high statistics run on the 1.27 cm case.

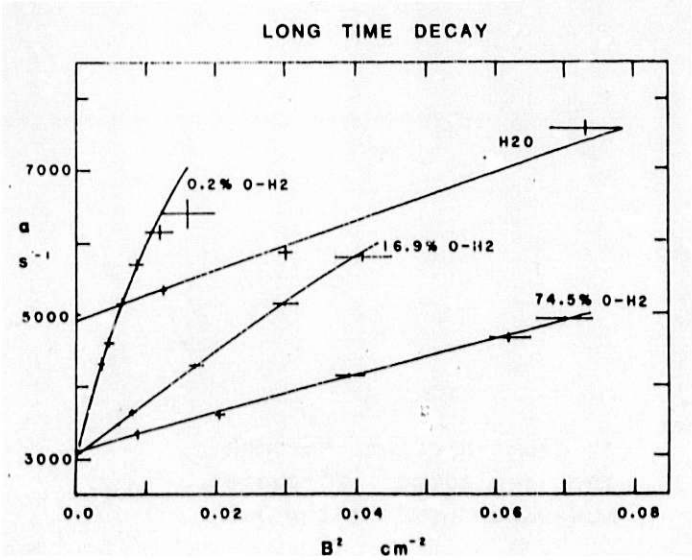

Fig. 6

The reciprocal of the long time decay mode plotted against B^2 for several values of the ortho fraction in liquid hydrogen [9].

Summary of Discussions on Reflector Studies, Neutron Flux and Energy Deposition Studies in the Session, Targets and Moderators: Designs and Tests

R. G. Fluharty

The discussion session on targer-reflector-moderator design included three sessions on moderator optimization and one each on target activation measurements and energy deposition. The Monte Carlo studies of G. Russell were on reflected systems and involved variations in the many parameters in an optimization approach. Generally this involves "tweaking" to make 5-20% gains in the neutron beam yields where the following points merit highlighting:

A. In his studies he found that the removal of the pre-moderator did not decrease the neutron yields. This rather clearly shows that the "reflector" enhancement is due to neutrons coming from the Be rather than being from reflections. This conclusion is based upon the available solid angles for reflection and return for the thin moderators without premoderator and the timing required for neutrons to pass from the moderator to Be and to return. The assumption here being that the incoming neutrons are epithermal >> 30 ev to be compatible with the narrow moderator pulse widths but are not fast neutrons. They are not fast neutrons because they would rapidly leak out of such small system before reaching thermal.

B. Studies of the size of Be reflector show that much smaller sizes are permissable allowing the addition of high Z shielding materials as composite reflectors. These are desirable to shield against fast neutrons from the source and moderator. In addition the reduced mass of the moderator without premoderator would reduce the number of fast particles scattered down the beam tube.

Andrew Taylor presented time dependent crystal diffraction data which show the rough equivalence of Be and Pb "reflectors". Because the time scale for lead moderated neutrons is much longer than Be the in-scattered neutrons from Pb must be above 18 Kev to be compatible with the Be argument above. Removal of the decoupler for a Be system shows a long time decay mode on the tail of the moderator pulses of very low amplitude. These are presumably due to neutrons representing the decay mode in the Be.

Data presented by M. Meier were based upon flux measurements on the moderator surface by means of gold foils. Elegant shape fitting routines provide surface flux shapes showing the areas of highest flux and allowing the choice to be made of where to locate the moderator and the areas of highest flux. Gains of ~ 20% should be available by these means.

The paper presented by D. Filges concerned proton activation measurements in the Pb and Uranium targets as functions of depth. Foils of the same materials were analysed by gamma spectrometry to show the major activities resulting from the proton activation. The information supplies data of immediate interest to machine operators and the designers of handling facilities. Such data will also serve as "bench mark" test material for code developers. Cu foil activations were obtained downstream from the target. These provided high energy neutron activations which show the presence of increasingly higher threshold reaction channels. Because these channels are ~ 8-15 Mev wide, a single foil has great potential for high neutron energy spectral analysis.

W. E. Fischer presented data on energy depositions in the D_2O moderating tank for the SIN Neutron Source. The energy deposition by the fast neutrons during thermalisation has been calculated, but at present only an upper bound estimate for the other contributions is available. The following contributions to the total energy have been calculated for a 1mA current:

1.	High energy neutrons	42.0 kW (UL)
2.	High energy protons	0.8 kW (UL)
3.	Charged pions	0.14 kW (UL)
4.	During thermalisation	18.2 kW (C)
5.	Gammas (from target)	2.6 kW (UL)
6.	Electrons (from target)	0.23 kW (UL)
7.	Gammas (from D(n,γ)T	2.7 kW (C)

where the qualifiers UL stand for Upper Limit and C for Calculated. This gives an upper limit of approximately 67 kW/mA.

The distribution of energy deposition by the neutrons during thermalisation indicates that 50% of their power contributions is deposited in approximately the first 6cm of the D_2O and 90% in the first 22cm. The peak energy density for this contribution is 1.0 W/cc at 1mA.

Summary of the Session
Target and Moderators: Design and Test

by
Walter E. Fischer
Schweizerisches Institut für Nuklearforschung
CH-5234 Villigen, Switzerland

In this session, the presentations were from three rather clearly distinguishable classes of neutron source:

i) The More or Less Established Sources IPNS, KENS and WNR:
They are running at an average beam power in the region of 10 kW. Their contributions to this session and also their status reports gave evidence of a trend to make contributions mainly on instrumentation.

ii) The Source(s) under Construction SNS:
It is designed for higher average beam power (above 100 kW). Very special technical problems have to be solved at this stage; they are down to the basic level of "nuts and bolts".

iii) The Sources in the Design Stage SIN, SNQ:
They have the ambition to deal with a high average beam power (beyond 1 MW). These projects are at the level of Mock-up experiments and technical design.

A particularly interesting result was reported by K. Inoue. Grooved cold moderators have given a 2.0 to 2.5 times higher neutron current in the 1 to 10 meV energy region than a corresponding flat moderator. Similar effects for thermal neutrons have been presented at previous meetings. Time-dependent measurements showed that the higher flux is mainly due to an increase of pulse width rather than to increased pulse height. These results have revived the discussions on Grooved moderators.

This example shows how the design of high power sources may still be influenced by basic data provided by the established sources. Decisions on large D_2-sources for the "modulated" SNQ and the "continuous" SIN-facilities should possibly be reconsidered in view of these results.

Evidence of the impressive progress of SNS has been presented by A. Carne and his colleagues. The engineering and build-up of the shielding, as well as the peripheral equipment such as control system, remote handling, drainage- and ventilating-systems, and described by B. Poulten, cover at this stage a considerable part of their activity. What could we learn from their presentations? My own (obviously biased) conclusions are the following:

1) At a rather late stage in the project, new technical insight may be obtained, demanding a high flexibility, even during the realisation phase. The SNS uranium target is an example: The cooling mechanism turned out to be more efficient than expected. Hence, thicker target plates may be used which leads to a higher target efficiency.

2) Components have to be built in spite of incertainties about some basic physical parameters. This became evident in the presentation on "Cold Moderator Design" by B. Diplock. Lack of precise knowledge of e.g. energy deposition by neutrons and gamma rays can become quite embarrassing: this even more so since the walls of cold moderators are "neither flat nor massless"!

There were several reports from the project groups of future high power sources. It seems that at the power level of several megawatts a stationary target is no longer practical. At SIN, a liquid metal target, using natural convection as cooling mechanism, has been chosen. In the paper by Y. Takeda (presented

by Ch. Tschalär), results of calculations in thermo-fluid dynamics gave evidence of the feasibility of the concept. Further investigations are still necessary to establish the reconciliation of neutronic and thermo-fluid dynamic requirements. With this target concept, investigations concerning the (stationary) beam window need special care. Therefore, irradiation tests of window material at a realistic beam power density are prepared at LAMPF. The target concept of SNQ for a beam power of 5 MW is a rotating wheel. Further details about the design was presented by J. Stelzer. Water cooled Pb-rods encased in $AlMg_3$ lead to a solution with mechanical stresses well below conventional limits. An advantage of this concept is the "moving window"; for a 5 MW beam power probably a necessity. On the neutronic side, flux distributions for thermal neutrons in a D_2O tank have been measured by the KFA/SIN-collaboration for a Pb-target, with and without a Be-sleeve. The results indicate that there is practically no gain in source strength from the (n,2n) reactions in the beryllium. This is in contradiction to theoretical calculations using the experimental neutron spectrum from a bare target.

From the contents of this session, we may draw the following conclusions:

i) The running sources do not suffer too much from the absence of basic physical data - they run! They could, however, still provide this kind of data for the projects in the design stage.

ii) SNS has to go ahead with construction, in spite of uncertainties - an embarrassing situation, which presumably cannot be escaped by any project in the realisation phase.

iii) The high power sources may still adjust their final design to new data.

From these conclusions we send a message to the running sources: Please continue to deliver basic technical and physical data in order to support the design of the future sources.

ICANS-VI

INTERNATIONAL COLLABORATION ON ADVANCED NEUTRON SOURCES

June 28 - July 2, 1982

SUMMARY OF DISCUSSION SESSION ON BEAMLINE SHIELDING CONSIDERATIONS FOR SPALLATION NEUTRON SOURCES

G. J. Russell and M. M. Meier
Los Alamos National Laboratory
Los Alamos, New Mexico 87545 USA

T. A. Broome
Rutherford and Appleton Laboratories
Chilton, Didcot, OXON OXII 0QX, UK

This was the first ICANS meeting where we specifically discussed problems associated with shielding beamlines at spallation neutron sources. These problems are difficult to tackle both computationally and experimentally. What makes the problem unique to spallation neutron sources is the possibility of high-energy (up to several hundred MeV) neutrons and charged particles contaminating the thermal neutron beams extracted from these sources. The high-energy neutrons and charged particles can themselves cause biological or instrument background problems or produce neutron and γ-ray progeny (by interacting with collimation systems, instrument components, and beam stops) which must be shielded against.

A typical beamline shield is illustrated in Fig. 1; questions relating to beamline shielding should be considered as a unit. Items needing attention are:

Interior to Bulk Shield

- energy of the proton beam
- target and moderator neutronic coupling
- angle (relative to the proton beam) at which neutron beams are extracted
- moderator field-of-view
- collimator design

Exterior to Bulk Shield

- collimator design
- lateral beamline shielding
- instrument shielding
- beam stop design .

Our discussions identified the following:

- There is a general concern about beamline shielding both from laboratories with operational spallation neutron sources as well as those laboratories planning and constructing spallation sources.
- Shields perform two distinct functions: a) biological shielding, and b) instrument background reduction.
- There is a clear need to establish reliable computational techniques and perform clean benchmark shielding measurements.

Neutron beams from a spallation source are characterized by a high-energy neutron contaminant. Gunter Bauer (KFA) recapped the results of measurements presented at ICANS V, and Tim Broome (RAL) gave the results of HETC calculations; both reports confirmed the likely presence of a high-energy (> 50 MeV) neutron contaminant.

Two other calculations were described:

1) Gary Russell (LANL) reported the results of 'idealized-geometry' Monte Carlo calculations. These computations (using HETC + MCNP) studied lateral shielding by simulating the high-energy beam contaminant with 100-MeV neutrons and allowing this beam to hit an iron cylinder giving the source term for the shield calculations. The beamline shield was comprised of layers of borated polyethylene, iron, regular polyethylene, and concrete. The neutron and γ doses outside the shield were calculated for various combinations of these materials. The calculations demonstrated that Monte Carlo techniques could be effectively used for simple flight path geometries to study fundamental systematics of beamline shielding problems.

2) Tim Broome (RAL) presented simple attenuation calculations; Tim used the Moyer method to determine the shield depth required to satisfy biological radiation protection requirements. These calculations gave the shield depth required assuming a point source description of the moderator flux and a parallel beam tube.

Other calculational techniques were discussed and a concensus emerged that the combination most likely to succeed would be two dimensional discrete ordinates codes with source terms calculated by Monte Carlo. The hope was expressed that calculations of simple geometries might be possible in the near future which could lead to the development of techniques to perform full collimator design calculations. One major limitation with the present codes is the inadequency of existing high-energy (> 20 MeV) neutron cross section libraries. At KFA, some theoretical effort will be expended to create an improved high-energy library. At the WNR, new (p,n) cross-section experiments will be performed in the near future. The physics models in the high-energy codes need improving, but the effort available for this is limited. As a preliminary to establishing a closer contact between ICANS members on the subject of codes, a simple HETC benchmark calculation will be circulated for interlaboratory code comparison.

Operating experience (at WNR, IPNS and KENS) with beamline shielding has shown that systems have evolved which perform satisfactorily at relatively low proton currents of 2-8 μA and at proton energies of 500-800 MeV. However, the shielding arrangements at these facilities are essentially ad hoc or empirical in nature. More work on beamline shielding needs to be done before beamlines can be adequately shielded at higher proton currents. Jack Carpenter (ANL) reported on background problems encountered at KENS during experimental studies of resonance detector systems. These problems stemmed mainly from a halo around the beam which was only eliminated with a substantial amount of lead shielding; the results suggested that the backgrounds were probably due to high- (rather than low-) energy neutrons.

A limited (but important) experimental program at the WNR was described which, together with the knowledge gained from existing flight path shielding, should help better understand beamline shielding problems. At the WNR, lateral beamline shielding questions will be investigated both experimentally and calculationally. A clear need for good benchmark experiments for code validation was identified, but the definition and execution of such experiments will require a great deal more thought. In particular, the measurement of the neutron beam spectrum requires a calibrated high-energy neutron detection system.

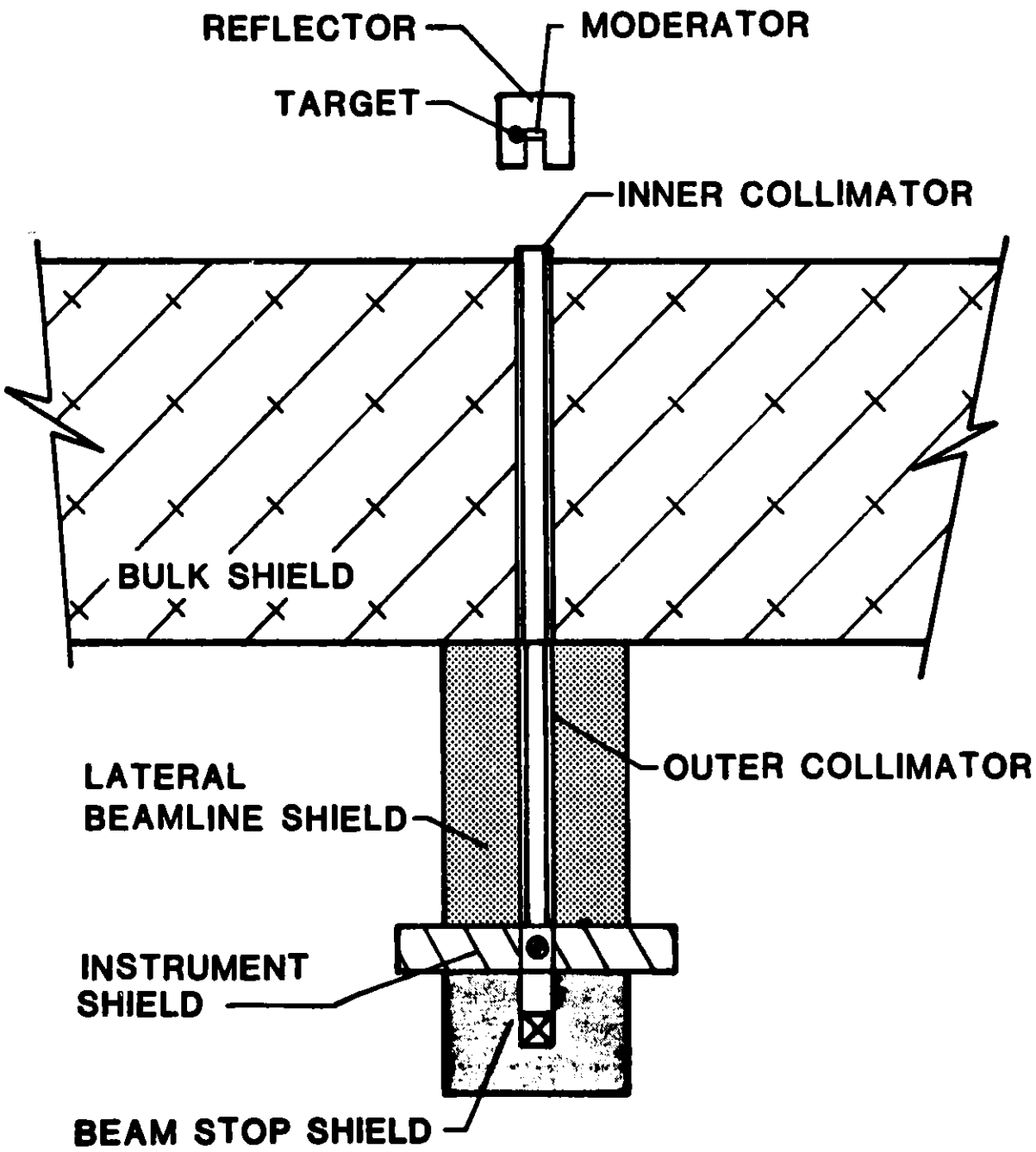

Fig. 1. Illustration of a typical beamline shield.

Summary of a Discussion on the Gain in Thermal Neutron Flux by using Grooved Hydrogenous Moderators

G. S. Bauer

Grooved moderators as investigated experimentally in various laboratories have a potential to yield a higher thermal neutron leakage from their surface than moderators with a flat surface. Gains reported are between a factor of about 1.3 and little more than two. During the discussion which was organized to try to get a better insight into how and under what conditions these gains come about, several sets of data were presented, most of which had already been given earlier. New results were shown at this meeting by the Japanese group (K. Inoue, et al, these proceedings) and by the Los Alamos group, presented by G. Russell.

In the Japanese experiments which referred to a cold moderator, the fin material forming the grooves was simply added to the surface of the flat moderator used for comparison. A gain by a factor 2 or more was found in the integrated yield but not in the peak flux which was reported to stay virtually unchanged. The thickness of the fins and their mutual separation was 1.6 cm which may be somewhat high relative to the mean transport length of about 0.5 cm or even less in a cold CH_4-moderator. The experimenters showed that most of the flux came from the bottom of the grooves between the fins.

Measurements by the Los Alamos group showed that the actual shape of the fins (rectangular, triangular or trapese-shaped cross section) is not of major importance. This is in accordance with the findings during the experiments done for the SNQ-project. It was of interest to see that there was no significant difference in gain whether the fins were arranged parallel or perpendicular to the target surface in a tangential geometry (wing-type geometry). This offset some of the earlier speculations that the improved coupling to the target brought about by the more extended moderator was the prime reason for the gain.

During the discussion it was felt that the magnitude of the gain does depend quite significantly on whether or not a reflected arrangement is used. This view was supported by the data presented by the SNQ-group at the ICANS-IV meeting (G. S. Bauer, proceedings of ICANS-IV). It does seem, however, that

it is also of importance whether or not a moderating reflector is used (e.g. Be as compared to Pb). In the data obtained during the SNQ-mockup experiments for the special arrangement chosen for the DIANE moderator-reflector system with a large target and a Pb reflector, a significant gain was found for the integrated flux as well as for the peak flux (fig. 1, after data presented at ICANS-V, Bauer et al). A summary of the integrated flux (the quantity of prime interest in an intensity modulated source) obtained at the CERN-Booster for various arrangements (Bauer et al, ICANS-V) is shown in Fig. 2. Here 1.0 is the reference value of the DIANE moderator-reflector design for all energies.

It was concluded, that the answer to the question, whether or not grooved moderators are of advantage in any given design, depends very much on the way in which the source will be used and what its time average power is. The slight pulse-broadening that may be introduced may offset the intensity gain in certain cases on a well reflected and decoupled moderator. If, however, the pulse is long anyway, e.g. because of a long source pulse or because excessive heating precludes the use of a decoupler, the gain from using a grooved moderator is certainly worth the effort.

Grooved moderators of hydrogenous materials essentially work like reentrant beam holes in a moderator of large transport length. In this sense it should be anticipated that there is also a gain in peak flux, which so far does not seem to have been confirmed unanimously.

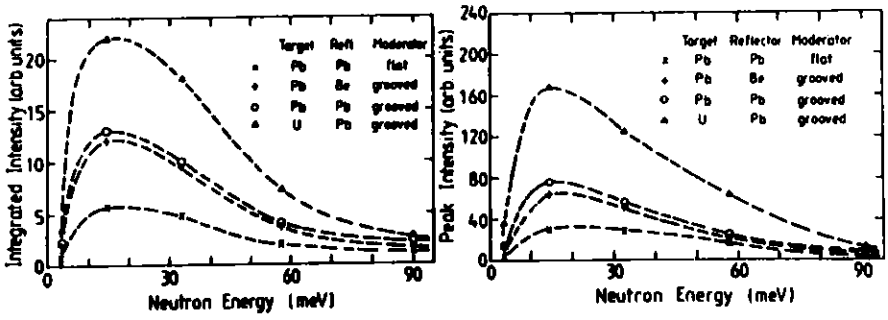

Fig. 1 Relative intensities measured for grooved and flat (polyethylene) moderators with Pb and Be-reflector using targets of Pb and depleted U. Data have not been corrected for crystal reflectivity as a function of energy (higher order reflections used).

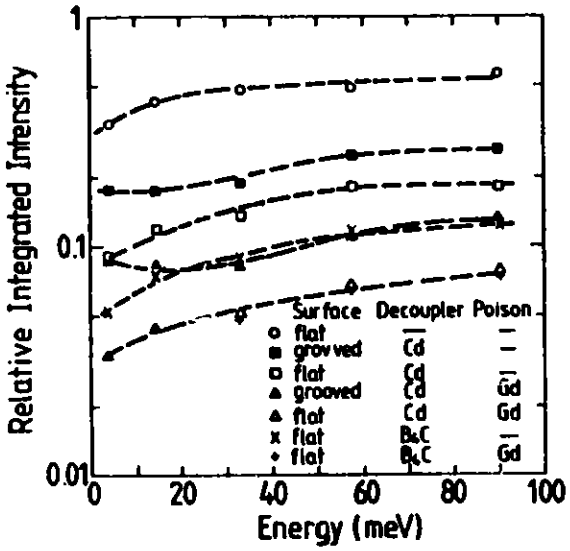

Fig. 2 Energy dependency of the integrated intensity of the reflections of a graphite analyser for various moderator configurations with and without decopling and poisonning relative to the intensity obtained from a moderator as proposed for DIANE.

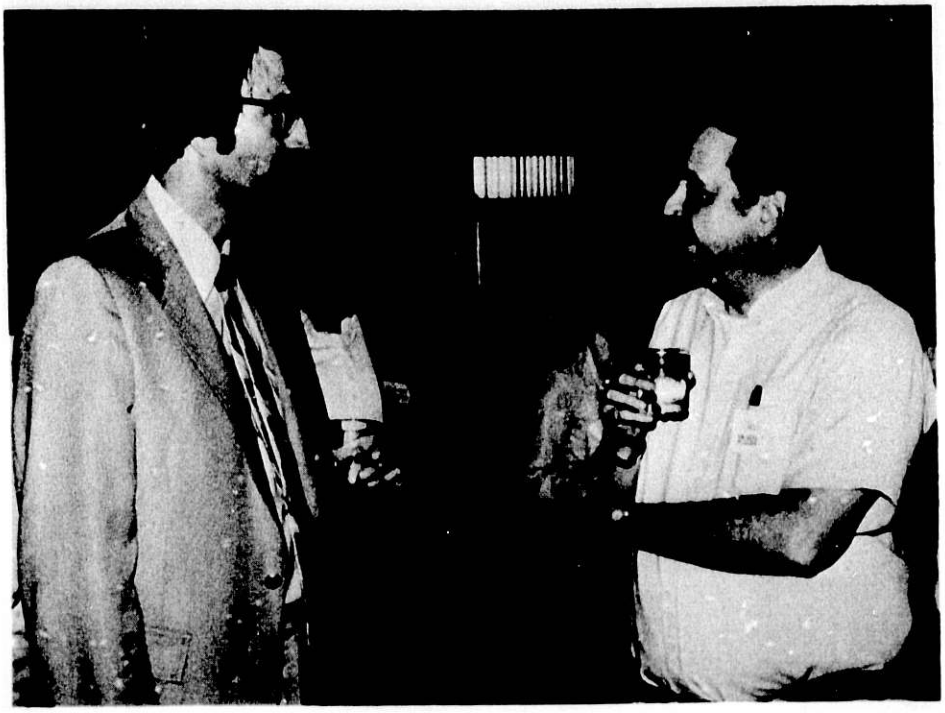

R. C. Birtcher, J. M. Meese

R. Jacobson, A. J. Schultz

T. G. Worlton, R. E. Prael

M. Loewenhaupt, J. E. Epperson

ICANS-VI
INTERNATIONAL COLLABORATION ON ADVANCED NEUTRON SOURCES
June 27 - July 2, 1982

COMPUTATIONAL METHODS FOR HIGH-ENERGY SOURCE SHIELDING

T.W. Armstrong*, P. Cloth, D. Filges

Institut für Reaktorentwicklung
Kernforschungsanlage Jülich GmbH
Postfach 1913
D-5170 Jülich 1, Germany

*KFA Consultant, P.O. Box 2807
La Jolla, California 92038, USA

ABSTRACT

The computational methods for high-energy radiation transport related to shielding of the SNQ-spallation source are outlined. The basic approach is to couple radiation-transport computer codes which use Monte Carlo methods and discrete ordinates methods. A code system is suggested that incorporates state-of-the-art radiation-transport techniques. The stepwise verification of that system is briefly summarized. The complexity of the resulting code system suggests a more straight forward code specially tailored for thick shield calculations. A short guide line to future development of such a Monte Carlo code is given.

COMPUTATIONAL METHODS FOR HIGH-ENERGY SOURCE SHIELDING

T.W. Armstrong*, P. Cloth, D. Filges

Institut für Reaktorentwicklung
Kernforschungsanlage Jülich GmbH
Postfach 1913
D-5170 Jülich 1, Germany

*KFA Consultant, P.O. Box 2807
La Jolla, California 92038, USA

INTRODUCTION

The SNQ shielding problem has special features and importance compared to usual accelerator shielding considerations. It presents difficult computational requirements because of the combination of a relatively high-energy source, large shielding dimensions, and geometric complexities. There does not presently exist a computer code system with an appropriate data base which is directly applicable to the SNQ shielding problems of concern.

In the following discussion, the step-wise development of such a shielding code system is suggested. The basic approach is to couple radiation computer codes which use both Monte Carlo methods (suitable for complex geometries) and discrete ordinates methods (suitable for deep-penetration) with a cross section data base extended to accomodate the SNQ beam energy of 1100 MeV. Further plannings to improve the system aiming at an all-Monte-Carlo procedure capable of deep penetration problems are outlined.

The main factors governing the bulk shield thickness required are the attenuation of high-energy particles (mainly neutrons) and the material density. This is because the flux (or dose) attenuation depends approximately exponentially on these factors, and only linearly with source strength (and dose rate criterion). That is, the flux spectrum at large distances (several mean free paths) from the source is roughly represented by

$$\Phi(E,x) \propto S \cdot f(E) \cdot \exp(-x\rho/\lambda_{att})/x^2. \qquad (1)$$

This can be seen e.g. in Fig. 1 from measurements and calculations. For the depht-dependence of high-energy particles see also Refs. 1 and 2.

In detailed code calculations the quasi material constant λ_{att} is not valid. In lieu of it the corresponding differencial cross section data are used. Providing of cross-sections will be discussed.

One might expect that since λ_{att} is so fundamental to shield design for high-energy radiations, accurate values for common shielding materials would be available from previous experiments and accelerator facility designs. This is not the case. For example, previous measurements of attenuation lengths for iron range from about 120 to 180 g/cm^2. (An HETC code calculation for a 500 MeV proton source and iron shield is reported by Brooms to give λ_{att} = 179 g/cm^2 /3/.) There is also a wide range of measured λ_{att} values reported for concrete ($\approx$110 to $\approx$ 172 g/cm^2). (A summary of all but the most recent measured values for λ_{att}, and descriptions of most of the experiments, is given in /4/.)

There are several reasons for these large variations in the measured values for λ_{att}. Some unaccounted for invalid assumptions have to be made in the measurements. Also λ_{att} has some spectral dependence, e.g., λ_{att} measured along the beam axis can be different from off-axis measurements because of differences in particle spectra.

SUGGESTED METHOD FOR SHIELDING CALCULATIONS

There are, of course, some alternatives as to the most appropriate calculational approach to take. However, only one procedure is outlined here, which is believed to be feasible and reasonably accurate, but which can probably be improved with further thought.

The basic approach here for the near future is to use a combination of Monte Carlo and discrete ordinates methods. While in principle it is feasible, even for the very thick shields envisioned, to use Monte Carlo methods alone, this would require some substantial modifications of existing codes, or eventually writing of new codes. This will be discussed later as an further improvement. The method outlined here can be applied nearer term.

The main advantage of the code system is that it incorporates state-of-the-art radiation transport developments and is, we believe, representative of the most accurate methods allowed by present day cross section data and computer capabilities.

The radiation transport codes suggested for use in the shielding code system are: 1. HETC /5/, for the Monte Carlo calculation of high-energy nucleons and pions, 2. MORSE /6/, for the

Monte Carlo transport of low-energy and γ-rays, 3. the discrete ordinates code ANISN /7/, for one-dimensional neutron and γ-ray transport, and 4. the discrete ordinates code DOT /8/, for two-dimensional neutron and γ-ray transport. It should be noted that, except for HETC, other comparable transport codes exist. In particular, there is the Los Alamos group of transport codes: the MCNP (continuous energy) and MCMG (multigroup) Monte Carlo codes /9/, which have capabilities similar to MORSE; and the discrete ordinates codes for 2-D and 1-D transport, TWOTRAN and ONETRAN /10/. The reasons for selecting MORSE, ANISN and DOT for the shielding code system are, in addition to representing state-of-the-art capabilities, they are compatible with the present IBM computer facilities at KFA and with the needed high-energy cross section data base.

COMPUTER CODES

Monte Carlo Codes

The high-energy transport code HETC and the low energy neutron/γ-ray transport code MORSE, which have been applied extensively during the SNQ reference design study /11/, would be used in the shielding calculations in their present form. It would however, probably be better to couple these two codes at a higher neutron energy (say 60 MeV) than that usually used (15 MeV). This could be done by extending the MORSE cross section to higher energies using the HILO library discussed below. This change is expected to have a negligible effect on bulk shielding estimates. However, it may be important in obtaining the high-energy portion of the neutron spectrum from the SNQ-neutron moderator. High-energy neutrons in the moderator which elastically scatter with oxygen would be more accurately treated by making this change.

Discrete Ordinates Codes

The discrete ordinates, or S_n, method is a means of numerically solving the Boltzmann transport equation in which the phase space is divided into a number of discrete points. A set of finite differences equations can then be formulated which can be solved by an iterative technique. (The detailed equations are given, for example, in Ref. /12/).

The radiation transport codes ANISN and DOT employ the discrete ordinates methods coupled with a multigroup deterministic solutions of the Boltzmann transport equation for neutrons and gamma rays. ANISN solves the one-dimensional form of the Boltzmann transport equation in slab, cylindrical or spherical geometries, whereas DOT solves the two-dimensional form in slab and R-Z or R-θ cylindrical geometries.

While ANISN is only 1-D, the computation and set-up times are much less than for DOT. Thus, ANISN will be very helpful in evaluating cross section sets, doing sensitivity studies, investigating parameter variations, etc. which would be too time consuming if only DOT were used.

Code Coupling Considerations

The ANISN and DOT codes transport only neutrons and (for appropriate cross section input) the secondary gamma-ray produced by neutrons. Therefore, a basic premise of the Monte Carlo/discrete ordinates coupling procedure suggested here is that the discrete ordinates codes are used only for transport in those spatial regions of the shield where neutrons are the dominate particles. One method of coupling is to consider an internal boundary in the shield at some depth sufficiently large that neu-

trons dominate. The Monte Carlo calculated neutron current across this boundary then constitutes the discrete ordinates code input. Both ANISN and DOT allow a boundary angular neutron source as an input option, so no code modifications are required.

"Coupling codes" will have to be written to put the Monte Carlo results in the quadrature set format needed to provide the neutron source for ANISN and DOT. HETC has previously been coupled with ANISN /13/, but for a volumetric ANISN neutron source and not for deep-penetration applications. A code called DOMINO /14/ for the opposite type of coupling, i.e., DOT output to Monte Carlo, is available. However, we are not aware of any previously documented experience in coupling Monte Carlo transport followed by discrete ordinates transport for the very deep penetration shielding applications of interest here.

All neutrons from the Monte Carlo calculations crossing the coupling plane in the "positive" (larger depth) directions for the first time then constitute a surface source for the ANISN or DOT calculations. This is illustrated in Fig. 2.

The coupling plane for defining the source for the discrete ordinates calculations should be located sufficiently deep into the shield that the neutrons are the dominate high-energy particles rather than protons, but yet no deeper than necessary to satisfy this criterion so that the statistics from the Monte Carlo calculations are as good as possible. Fig. 3 gives a good picture of the neutrons becoming the dominate high-energy cascade particle. It is also advantageous to have the coupling plane as shallow as possible so that there will be a "region of overlap" where results from the two calculations can be compared.

DATA BASES

The shielding code system suggested requires high-energy multigroup cross section data for the discrete ordinates transport calculations. Much of the needed cross section data are available, but the present data base is not completely compatible with SNQ application requirements because the maximum neutron energy considered is 400 MeV. Also, there are other approximations in the present data base whose accuracy is questionable for the very thick shields of interest for the SNQ.

The approach suggested here is to make ad hoc modifications to the present data to allow "Phase I" calculations to be made, which would include transport calculations to test the importance of present approximations.

Status of Present High-Energy Transport Cross Section Data Base

A multi-energy group cross section library (called HILO) for coupled neutron/γ-ray transport has recently been developed at ORNL in a format compatible with ANISN and DOT input requirements /15/. Features of this library are summarized in Table II. These data have been obtained by using experimental data at low energies (< 14.9 MeV) and theoretical models at high energies (14.9-400 MeV).

Some work has also been done at Los Alamos /16/ to obtain two high-energy cross section sets: 1. a 60 group library from thermal to 60 MeV, and 2. a 41 group library up to 800 MeV. The 41 group library contains the following elements: H, C, O, Al, Si, Fe, Mo, W, and Pb. A P_3 angular expansion is used for all elements except Fe, which is extended to P_8. These cross sections

were obtained in a manner similar to that of the HILO library, i.e., ENDF data at low energies (≤20 MeV) and optical model and intranuclear-cascade-evaporation model calculations for higher energies.

It should be noted that the Los Alamos cross section library does not include elastic scattering for nuclides other than H at high energies. Based on a test case for an iron shield (a rather "thin" one-dimensional spherical shield having diameter of 1.4 meters with a central isotropic neutron source from 50 MeV deuterons on Be), it was concluded that high-energy elastic scattering had a negligible effect on the dose equivalent at the edge of the shield /16/. However, calculations for a heavy concrete shield reported in Ref. /17/ (using the HILO library, for a spherical shell shield 3.7 m thick, point isotropic neutron source, ≤~60 MeV, from deuterons Li) show that the dose equivalent outside the shield is over estimated by more than three orders of magnitude if elastic scattering by heavy (other than H) elements at high energies (≥14.9 MeV) is neglected. (This may also have implications for the SNQ bulk shielding calculations in comparing iron vs. cast-iron since cast-iron contains nominally 20 atom per cent C and Si).

It is suggested here that the HILO high-energie cross section library be used (with modifications to allow higher-energies) for the initial discrete ordinates calculations related to SNQ shielding. The main consideration is that this data set includes elastic scattering (for all but the heaviest nuclei - W and Pb) whereas the Los Alamos library does not. Also, the HILO library includes γ-ray production and transport cross sections for γ-rays produced in low-energy (< 14.9 MeV) neutron collisions, which are neglected in the Los Alamos library. Furthermore, the HILO library has a higher order angular expansion at high

energies (p_5 vs P_3), except for Fe, and a finer energy group structure.

While the HILO library is recommended, it should be noted, however, that some of the considerations and assessments mentioned in Ref. /16/ in connection with the development of the Los Alamos library are very relevant to our interests. As an example, for the high-energy nonelastic cross sections of the HILO library, the results of intranuclear-cascade-evaporation model calculations are used directly above $\approx$ 60 MeV. In the Los Alamos library, such model cross sections are adjusted in some cases (e.g., upward by about 15 % for Fe) where some experimental data points are available.

SNQ-SHIELDING CALCULATIONS

Several "baseline" configurations are suggested here for setting up the initial shielding code system. There are a number of questions to be investigated using these simple shield arrangements, as outlined and discussed below.

Both 1-D and 2-D arrangements are suggested. The reasons for starting with a 1-D setup are: (a) To gain experience in Monte Carlo/discrete ordinates coupling with the simpler 1-D case. (There are no data presently available to check either the 1-D or 2-D cases, but the laterally integrated 2-D results can be compared with the 1-D calculations as a partial check.) (b) The 2-D calculations will require considerable computer time for deep penetrations, and many of the preliminary calculations (investigating quadrature sets, parameter variations, etc.) can be made with the 1-D set-ups. (c) For some of the eventual applications (e.g., accelerator shielding requirements due to proton beam losses) 1-D approximations are adequate.

Baseline Arrangements

A source/shield arrangement in cylindrical geometry for the 1-D case is shown in Figure 4. This set-up serves for baseline test calculations. Fig. 5 shows (upper case) a similar set-up for DOT calculations.

The lower arrangement in fig. 5 is to allow early estimates of bulk shielding dimensions using the initial code system and data base. The couplig surface is the target surface in this case.

Note also that the 1-D arrangement preserves the anisotropy of the neutron source at the coupling plane, so, for example, investigations of appropriate quadrature sets from the 1-D ANISN calculations should be relevant to the 2-D DOT calculations.

A target diameter of 10 cm is chosen to be consistent with the thickness of the reference design target wheel. We have indicated a target length L as approximately the range R of the primary proton range so that primary protons have a chance to produce neutrons within the target material. The angular and radial dependence of the neutrons at the coupling plane will depend upon L (the magnitude depending on L and the depth of the coupling plane). For example, for the reference design target wheel, where the wheel diameter was $\gtrsim 2$ range thicknesses, relatively few neutrons escape the target in the forward (0°) direction, and the neutron angular distribution is peaked at about 30°. Therefore, calculations for several target lengths (e.g., L=0, L R, and L 2R) would be of interest.

Arrangement with Beam Holes

Prediction of the doubly differential neutron and gamma-ray spectra emerging from a beam hole, taking into account interaction effects in the shield material around the hole, is a very demanding calculation. It will require the full extent of the transport codes as well as computer capabilities.

The first part would be to calculate the angular and spatially dependent neutron, proton, and charged pion energy spectrum leakage from the target surfaces adjacent to the moderators. The moderators should be included in these calculations to account for any second order effects; that is, particles which are "reflected" from the moderator back into the target region may produce additional particles which then can enter the moderator. A MORSE calculation will also be required to account for the neutrons which are produced in HETC below the cutoff energy. These spectra obtained become the source for part two of the HETC-MORSE calculation.

The second part of the calculation need only include the moderator since all back-scattered particles have been accounted for. The source calculation for the second HETC calculation will be the protons, charged pions and neutron leakage spectra obtained in the first part of the calculation. MORSE will be used twice during this step of the calculation: once to transport the low-energy neutrons leaking from the target, and once to transport the neutrons produced in the second HETC calculation. By using some of the biasing techniques already incorporated into the MORSE code, an improvement in the statistical accuracy of the low energy emerging neutrons can be obtained. It may also be necessary to incorporate some biasing techniques into HETC - for example, particle splitting in important regions and directions.

The DOT calculation will probably require a biased (asymmetric) angular quadrature, with most of the angles pointing down the collimator hole. In addiation, it will be necessary to define fine radial intervals (say $\sim$0.1 cm) for a short distance ($\sim$1 - 2 cm) into the shield material to properly account for "skin" effects. Since neutrons and gamma rays which are located more than several mean-free-paths into the shield material have little effect on the emerging particles at the end of the collimator, it is only necessary to make the thickness shield material surrounding the beam hole a few mean-free-paths thick. There is not, of course, experience to guide any of the above assumptions and test calculations will be necessary to refine the procedure. The arrangement is shown in Fig. 6.

It is not clear whether a single DOT calculation can simulate the entire length of the collimator. This is because the length-to-diameter ratio is very large (L/D$\sim$60) and a fine spatial grid is needed radially near the collimator surface. Therefore, array sizes may exceed computer storage capacities, and/or computation times may be prohibitive. If this should be the case, the problem can be divided into several parts, "overlapping" several DOT calculations for sequential segments of the collimator length (see Fig. 6). (This procedure is suggested by "overlap" discrete ordinates calculations which have been made for deep penetrations in air from neutron sources /18/.

FUTURE CODE SYSTEMS AND DATA BASE

The complexity of the presented code system ,the computer time and man power consuming running procedure for each problem case suggest a more straight forward computer code specially tailored for thick shielding calculation. If we realize the constraints of the above system, e.g., the strongly limited geometric capabilities, or the restriction to only neutral particle treatment (usually neutrons and gammas), we find, that Monte-Carlo techniques is the adequate means that should be tried for our purpose.

Thick Shield Monte Carlo Codes

The following is somewhat qualitative and serves only as a guide line in developing a special thick-shield Monte Carlo code. In thick shields as they occur in the SNQ case particles have to travel a large number of mean free paths to go through, whereas the average number of collisions that particles undergo during their lifetime (until energy has fallen below a certain level) is considerably smaller. Neutral particles, however, can travel any distance between collisions with, of course, low probability for larger path-lengths. Thus, a few particles can penetrate the thick shield, and the calculation of this small fraction is the deep penetration problem.

For simplicity reasons let us asume that the shield consists of only one single material and forget about the fact that the considered particle may change its identity from collision to collision and temporily may be a charged particle. This will only complicate the computational procedure but not affect the principle. The collision points of the particle tracks will be, according to what was discussed above, concentrated close to the

source, with more or less none of them in the far away shield regions near the surface. What is needed, however, is for bulk shielding calculations collision points near the surface, and for the case with beam tubes a more flat distribution.

The idea now is to calculate first a collision history of a particle without considering beforehand the free paths between collisions. This is justified as in our simpel model collision physics is space independent. After that, we sample a set of free tracks that has importance for our purpose. We do this in a way that the total migration length, that is the sum of all free paths of a track is in a certain range of high importance. Although there is some similarity to so called path-length stretching, which produces a wide variety of migration lengths, our procedure - and this is the advantage - gives control over the important parts of this variety.

Let us express the migration length in terms of the mean free path and denote it η, then the conditional probability of a collision history for agiven relative migration length η is a measure for the importance of this history to penetration of a shield of the thickness in the order of η. According to our discussion above η the number of mean free paths through the shield is (on average) larger than n the number of collisions.

While the bulk of histories has n values (collision numbers) near the average and well below η, there might be a small fraction of histories with n close to η having thus an extremely high importance yet being completely underrepresented in the n distribution provided e.g. by the intra-nuclear cascade calculation, as compared to their relevance for the shielding calculation (Fig. 7). It is not known how strong this effect could be, but it can be overcome by using biasing techniques already in the in-

tra-nuclear cascade model, which is a Monte-Carlo program itself. Obviously it is the extremely forward directed component of the cascade variety of extreme low energy loss, that can have exceptional high collision numbers. If this small history group plays a certain role, for which we have some indication, it has also to be considered in preparing cross-sections with HETC for use with the near term Monte-Carlo discrete ordinate system. So one of our next steps in code development is introduction of suitable biasing techniques in the intranuclear cascade part of HETC.

REFERENCES

1 S.P. Shen

Passage of High-Energy Particles in Matter: Nuclear Cascades Induced in Dense Media by 1-and 3-GeV Protons

BNL-8721,Brookhaven National Laboratory (1965).

2 T.W. Armstrong and R.G. Alsmiller

Monte Carlo Calculations of the Nucleon-Meson Cascade in Iron Initiated by 1- and 3-GeV Protons and Comparisons with Experiment

Nucl. Sci. Engr. 33, 291 (1972)

3 T.A. Broome

Shielding for the Spallation Neutron Source at the Rutherford Laboratory

Paper in "Meeting on Targets for Neutron Beam Spallation Sources"

G.S. Bauer (Ed.), Jül-conf-34, Januar 1980

4 W. Wade Patterson and Ralph H. Thomas
Accelerator Health Physics
Academic Press, New York, New York, 1973

5 T.W. Armstrong and K.C. Chandler
HETC - A High-Energy Transport Code
Nucl. Sci. Engr. 43 353 (1971)

6 E.A. Straker
The MORSE Code - A Multigroup Neutron and
Gamma-Ray Monte Carlo Transport Code
ORNL-4585, September 1970

7 W.W. Engle, Jr.,
ANISN, A One-Dimensional Discrete Ordinates
Transport Code with Anisotropic Scattering,
K-1693, March 1967
(also updated features described in ANISN
Code Package as distributed by the Radiation
Shielding Information Center, Oak Ridge, TN)

8 W.A. Rhoades, et.al.
The DOT-IV Two-Dimensional, Discrete-Ordinates
Transport Code with Space-Dependent Mesh and
Quadrature
ORNL-TM-6529, August 1978
(also, related documentation contained in DOT-IV
Code Package distributed by the Radiation Shielding
Information Center, Oak Ridge, TN)

9 W.L. Thompson and E.D. Cashwell
The Status of Monte Carlo at Los Alamos
LA-8353-MS, May 1980

10 T.R. Hill
ONETRAN, A Discrete Ordinates Finite Element Code for the Solution of the One-Dimensional Multigroup Transport Equation
LA-5990-MS, June 1975

11 T.W. Armstrong, P. Cloth, D. Filges, R.D. Neef
Theoretical Target Physics Studies for the SNQ Spallation Neutron Source
Jül-Spez-120, July 1981

12 F.R. Mynatt, F.J. Muckenthaler, and P.N. Stevens
Development of Two-Dimensional Discrete Ordinates Transport Theory for Radiation Shielding
CTC-INF-952, August 1969

13 T.W. Armstrong
Calculation of the Lunar Photon Albedo from Galatic and Solar Proton Bombardment
J. Geophys. Res. 77, 524 (1972)

14 M.B. Emmett, C.E. Burgart, and T.J. Hoffman
DOMINO, A General Purpose Code for Coupling Discrete Ordinates and Monte Carlo Radiation Transport Calculations
ORNL-4853, July 1973

15 HILO, 66 Neutron, 21-Gamma-Ray Group Cross Sections for Radiation Transport for Neutron Energies up to 400 MeV
ORNL Radiation Shielding Information Center Data Package
DLC-87 (1981)

16 W.B. Wilson
Nuclear Data Development and Shield Design for Neutrons Below 60 MeV
LA-7159-T, February 1978

17 R.G. Alsmiller, Jr., and J. Barish
Neutron -Photon Multigroup Cross Sections for Neutron Energies < 60 MeV
Nucl. Sci Engr. 69, 378 (1979)

18 J.V. Pace, III, F.R. Mynatt,and L.S. Abbott,
"A Study of the Overlap Conditions Required in Sequential Discrete Ordinates Transport Calculations for a 14-MeV Neutron Source in a 5000-m Radius Cylinder of Air",
ORNL-TM-3269, June 1971

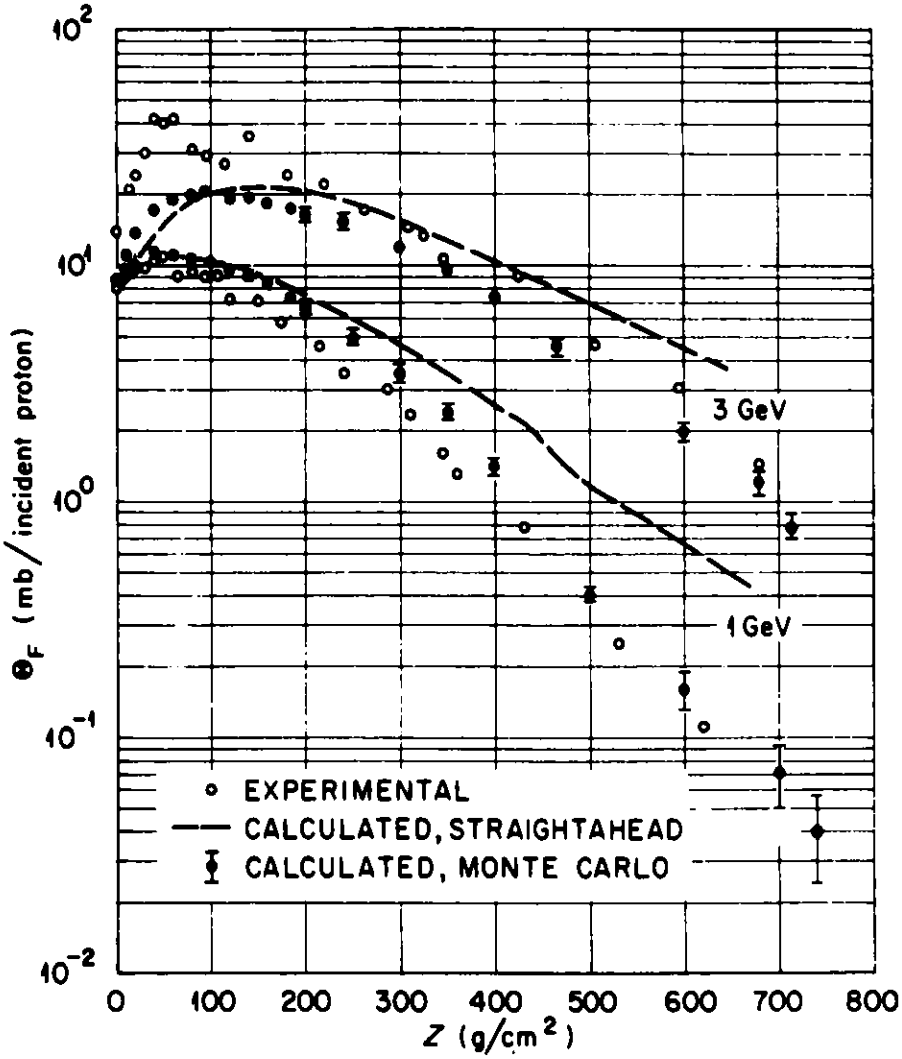

Fig. 1
Depth-dependence of high-energy particles in an iron shield bombarded by 1 and 3 GeV proton beams.(F-18 production in Al foils)
The experimental values are taken from Ref.1, the calculated values from Ref. 2.

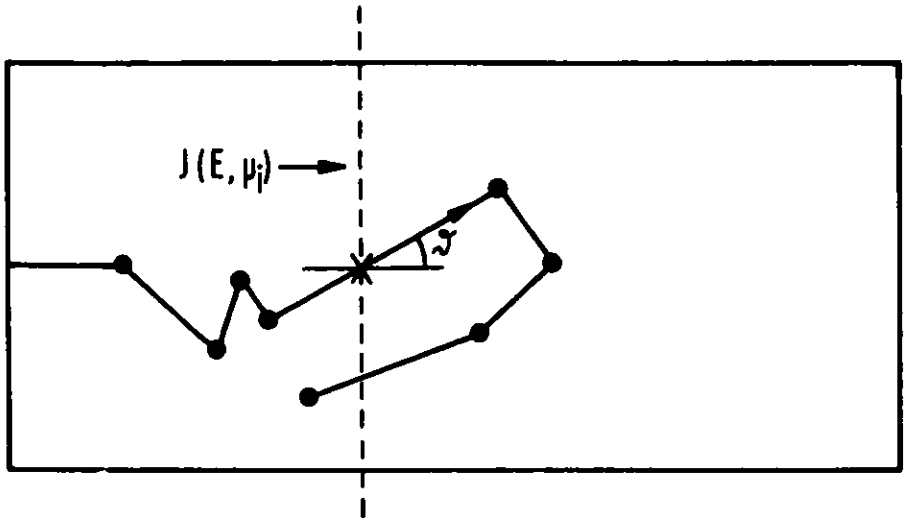

Fig. 2
Schematic of the contribution of a particle to the surface source at its first cross-over point on the surface.

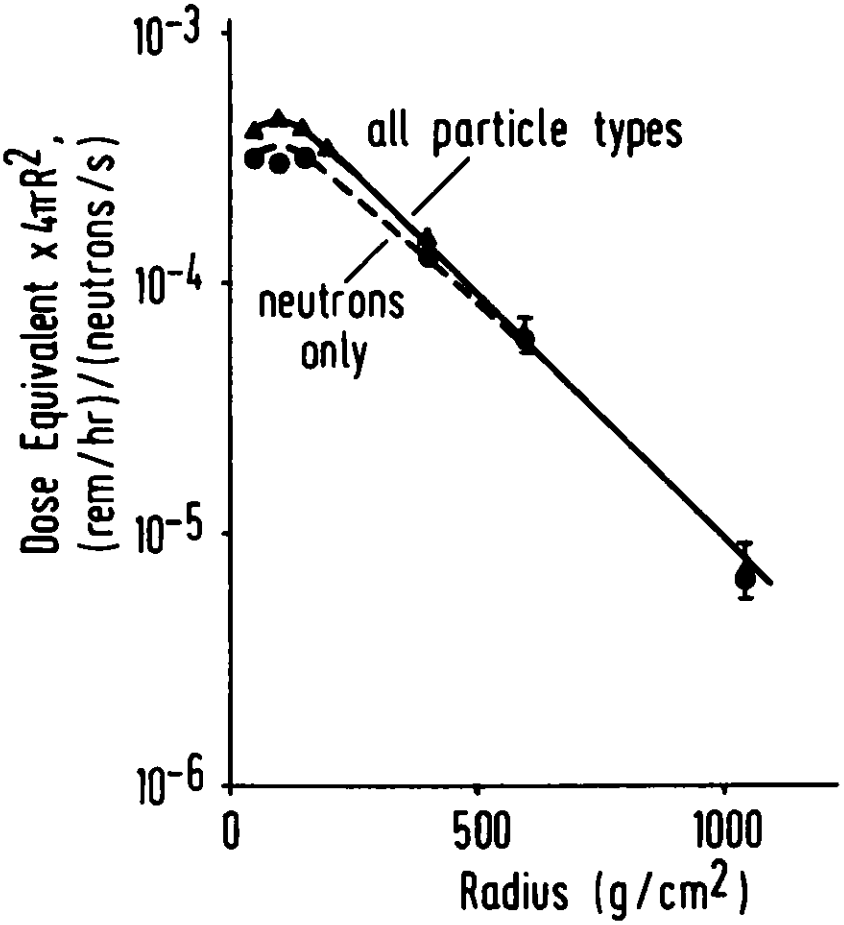

Fig. 3
Example showing that after a few high-energy mean-free-paths in the shield, the dominate particles are neutrons. This example is for the biological dose at the outside of a spherical iron shield due to an isotropic point source of 500 MeV neutrons, as calculated using the HET code.

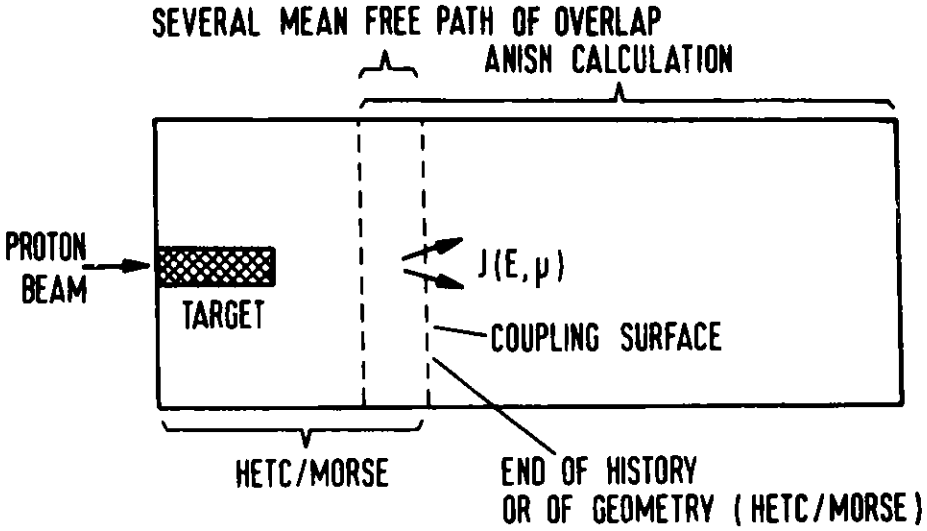

Fig. 4
1-D arrangement for source/shield test calculations in cylindrical geometry.

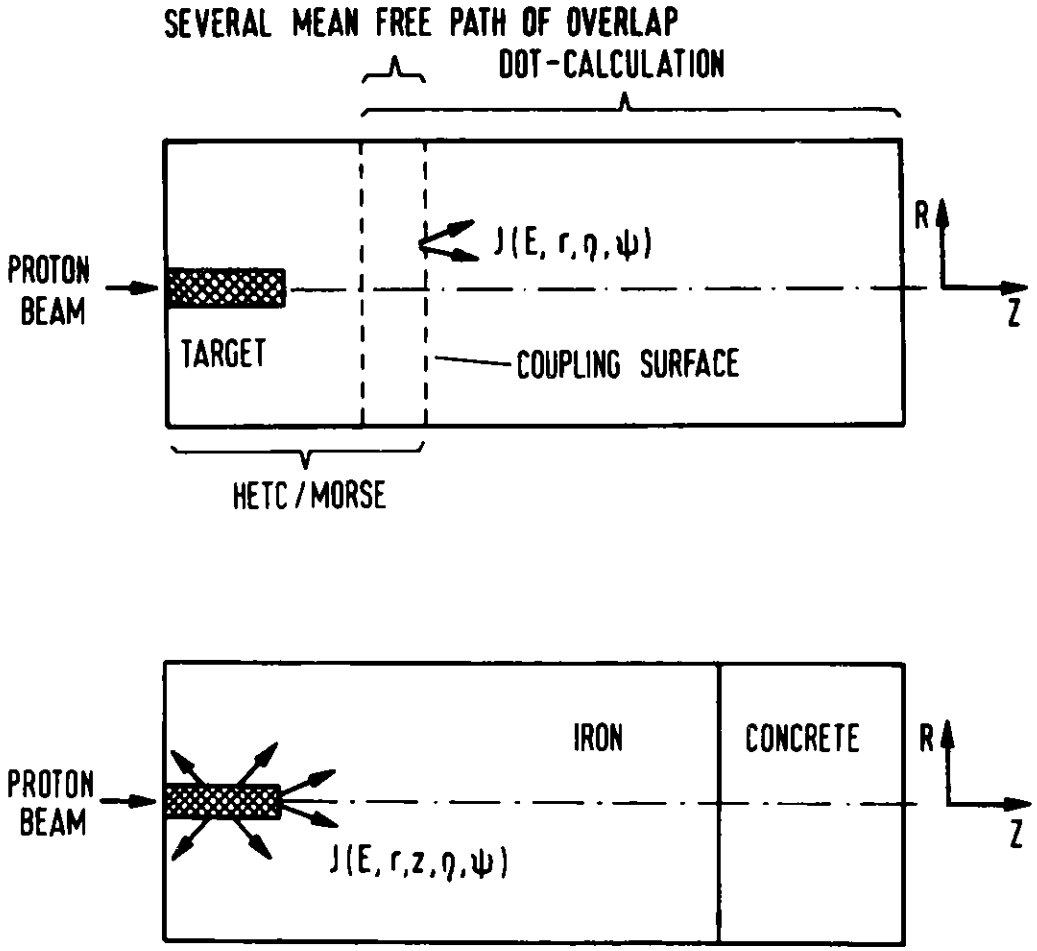

Fig. 5
2-D arrangement for test and early bulk shielding calculations using DOT in cylindrical geometry.

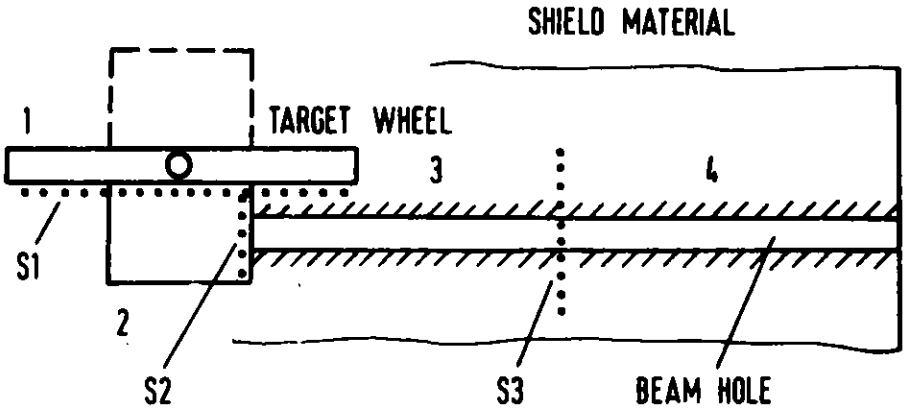

Fig. 6
Arrangement for 2-D SNQ-beam hole calculations with code coupling surfaces S1, S2 and S3.

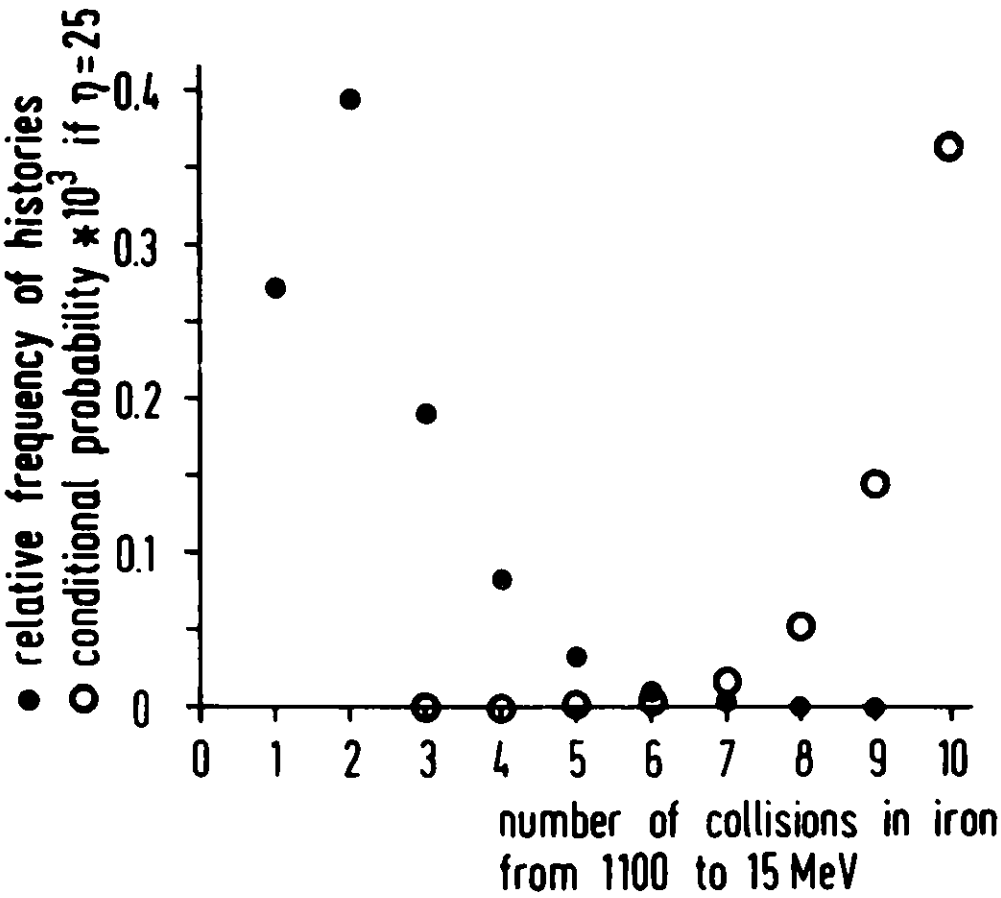

Fig. 7
Relative frequency of a particle collision history compared to its probability in penetrating a thick shield.

ICANS-VI
INTERNATIONAL COLLABORATION ON ADVANCED NEUTRON SOURCES
June 27 - July 2, 1982

HIGH-ENERGY FISSION MODELS VALIDATION AND COMPARISON WITH EXPERIMENTS

T.W. Armstrong*, P. Cloth, D. Filges, R.D. Neef

Institut für Reaktorentwicklung
Kernforschungsanlage Jülich GmbH
Postfach 1913
D-5170 Jülich 1, Germany

*KFA Consultant, P.O. Box 2807
La Jolla, California 92038, USA

ABSTRACT

Calculations including the high energy fission models were performed. Comparisons on BNL-Cosmotron arrangements of thermal neutron peak fluxes in the H_2O-moderator for lead and depleted uranium targets are given for different proton beam energies (540, 960, 1470 MeV) and two B_0-parameters (8 and 14 MeV) of the level density formula. Preliminary results of neutron spectra measurements for thin uranium targets are compared with HETC calculations at 590 MeV incident proton beam energy. The residual mass distributions are determined in thin uranium targets for proton beam energies of 0.3, 1.0, and 2.9 GeV. The calculations are done using the Rutherford and Appleton Laboratory high energy fission model (RAL) and are compared with respective calculations of the ORNL-model by Alsmiller et.al..

HIGH-ENERGY FISSION MODELS VALIDATION AND COMPARISON WITH EXPERIMENTS

T.W. Armstrong*, P. Cloth, D. Filges, R.D. Neef

Institut für Reaktorentwicklung
Kernforschungsanlage Jülich GmbH
Postfach 1913
D-5170 Jülich 1, Germany

*KFA Consultant, P.O. Box 2807
La Jolla, California 92038, USA

1. INTRODUCTION

From previous papers Ref. /1/ and /2/ at ICANS-V of the comparison of high energy fission (HEF) models for the High-Energy-Transport-Code (HETC) it was stated: Spectrum hardening with high energy fission models incorporated in the HET code is evident. The neutron captures in water surrounding finite depleted uranium targets are found to be 5-10 % higher with HEF. Significant differences of Rutherford and Appleton Laboratory (RAL) /3/ and the Oak Ridge National Laboratory (ORNL) /4/ high energy fission (HEF) models are found at incident proton beam energies above 1 GeV. The RAL model gives lower values than the ORNL model. The B_0 value seems to be model and energy dependend.

These investigations were continued studying the spatial dependence and thermal neutron peak fluxes in BNL-Cosmotron experiments (Refs. 5, 6). Preliminary comparisons for thin target measurements on uranium /Ref. 7/ with HETC calculations and predictions for residual mass distributions were also performed.

2. SPATIAL DEPENDENCE AND THERMAL NEUTRON PEAK FLUXES IN BNL-COSMOTRON EXPERIMENTS

The calculations were done for BNL-Cosmotron setups /5, 6/ at three proton beam energies (540, 960, and 1470 MeV) using HETC-, MORSE-CG-, and SIMPEL-spallation computer code system at KFA-IRE as described in Ref. 8. In Table 1 comparisons of the thermal peak fluxes in the H_2O-moderator for lead and uranium targets for different beam energies and several B_0-parameters of the level density formula are shown. In Table 2 the ratios of thermal peak fluxes for uranium and lead with different B_0-parameters are calculated.

In Fig. 1 the thermal peak fluxes for neutrons (n cm^{-2} s^{-1}) per proton are plotted as a function of proton beam energy for lead and uranium target with B_0=14. The uranium target system gives twice the thermal neutron peak flux of the lead system. The peak fluxes depend linearly on the incident proton beam energy upto 1 GeV. For higher energies there is only a weak increase of the neutron flux because of the spatial spreading out of the cascades.

In Fig. 2 and 3 the three-dimensional thermal flux distributions for the lead and uranium system at incident proton beam energy of 960 MeV are plotted meshwise. It is obvious that in the uranium case the flux distribution is more concentrated.

Energy MeV	Target	Evaporation Model	Thermal Peak Flux n $cm^{-2}s^{-1}$ per proton	Thermal Peak Flux n $cm^{-2}s^{-1}$ per 1 mA
	Pb	B_0=8,no RAL*	2.4×10^{-2}	1.5×10^{14}
540	Pb	B_0=14, RAL	2.15×10^{-2}	1.34×10^{14}
	U_{dep}	B_0=14, RAL	4.15×10^{-2}	2.59×10^{14}
	Pb	B_0=8,no RAL	4.7×10^{-2}	2.9×10^{14}
960	Pb	B_0=14, RAL	3.55×10^{-2}	2.2×10^{14}
	U_{dep}	B_0=8, RAL	8.9×10^{-2}	5.5×10^{14}
	U_{dep}	B_0=14, RAL	7.8×10^{-2}	4.8×10^{14}
	Pb	B_0=8,no RAL	6.25×10^{-2}	3.9×10^{14}
1470	Pb	B_0=14, RAL	5.1×10^{-2}	3.2×10^{14}
	U_{dep}	B_0=14, RAL	1.1×10^{-1}	6.9×10^{14}

* RAL = High Energy Fission Model /3/ of Rutherford and Appleton Laboratories

Table 1: Calculated thermal neutron peak fluxes for lead and uranium targets for two B_0 values at different incident proton beam energies

Energy	B_0	Peak flux ratio U_{dep}/Pb
540	14	1.93
960	8	1.9
960	14	2.2
1470	14	2.15

Table 2: Energy dependent ratios of thermal neutron peak fluxes for uranium and lead targets

3. NEUTRON SPECTRA COMPARISONS

The calculations are made using the intranuclear-cascade- evaporation model contained in the HETC code in combination with the standard Rutherford and Appleton Laboratory high energy fission model (RAL) with B_0 = 14 /3/. The cases considered are 590-MeV protons on U-238 target nuclei. The measured neutron spectra which are compared with here were kindly provided by S. Cierjacks of KfK, and are unpublished data from experiments performed at SIN. (The experimental method was summarized by Cierjacks, et.al. at ICANS-V /9/.) Cierjacks has indicated /7/ that the normalization of the measured data is to be checked in further experiments at SIN, so the comparisons here should be regarded as preliminary at present. Analyzed data for U targets at three angles (30, 90, and 150 degrees) are compared.

Figures 4-6 show comparisons of the present calculations and the KfK measurements for neutron spectra at 30^{o}, 90^{o}, and 150^{o} from thin uranium targets bombarded by 590-MeV protons.

To show better the low-energy neutron comparisons in the evaporation region, Fig. 7 gives the low-energy (< 10 MeV) neutron part of spectra with a linear scale. The calculated spectra here are averaged over all emission angles.

The basic conclusions from these comparisons are: (a) For uranium, there is rather good agreement in the evaporation region of the spectrum (few MeV and below). The magnitudes of the evaporation peaks agree within 25 %. The evaporation neutron maximum is lower in the calculations (1 MeV calculated vs. 2 MeV measured). In the "region of overlap" of the high-energy part of the evaporation spectrum and where the cascade production begins to dominate (i.e., in the energy range 10 - 25 MeV), the calculated

results are higher, by as much as a factor of 3 at 10 MeV. The high-energy part of the spectrum (> 50 MeV) is underestimated by the calculations, by a factor of 3 for small (e.g., 30^{o}) angles, with much worse agreement at the higher angles.

4. RESIDUAL MASS DISTRIBUTIONS IN THIN URANIUM TARGETS

The calculations made here are for proton beams having kinetic energies of 0.3, 1.0, and 2.9 GeV incident on thin U-238 targets. These were made using the Rutherford and Appleton Laboratory (RAL) high energy fission model and the results computed here are compared with available results for the same cases computed by the Oak Ridge National Laboratory (ORNL) model developed by Alsmiller, et.al. /4/.

A summary of the mass distribution results for the three beam energies as calculated using the RAL model is shown in Figure 8. The points shown are averages over $\Delta A = 5$ intervals, and are plotted at the midpoint of the intervals. Representative error bars (one standard deviation) are indicated. The normalization is per nonelastic proton-uranium collision, which can be converted from yields to production cross sections by multiplying by the computed total nonelastic cross section (Table 3). Note from Fig. 8 that the model predicts a "bump" in production in the mass region between that of the fission products ($A < 180$) and the mass region of the residual spallation product mass in which fission did not occur ($A > 220$); this is discussed in more detail later.

In Figures 9 and 10 results from the RAL model are compared with ORNL model predictions and measured data. The ORNL calculations are also averaged over $\Delta A = 5$ intervals. The normalization of the

measured data of Stevenson, et.al. /10/ at 300 MeV is taken from the ORNL paper /6/, in which the area under the experimental points in the mass region from 60 to 160 was normalized to be the same as the area under the ORNL calculated histogram in this mass region. (The 2.9 GeV experimental values are the absolute production cross sections given by Friedlander, et.al. /11/, converted to yields using the calculated nonelastic cross section.)

From Figures 9 and 10, the model predictions and measured data are all in good agreement in the vicinity of the peaks of the fission fragment mass distributions, although the RAL model seems to predict a somewhat wider fission fragment distribution.

As noted earlier, the RAL model predicts three peaks in the mass distribution: the fission fragment peak near A=110, the spallation peak near A=238, and an intermediate peak near A=200. This intermediate peak apparently results from spallation products which "survive" de-excitation through the mass region of high-fission probability into a lower mass region where further de-excitation by neutron emission is much more likely than fission. For illustration the mass distributions are calculated with and without fission competition for the 1-GeV beam case (Fig. 11). To get the fission probability versus mass number, subroutines of the RAL model are used to compute the fission probability for various arbitrarily selected isotopes covering the mass range from 175 to 250. Thus, while spallation products are produced down to A=160 (for 1-GeV, Fig. 11), and the model allows fission for these low masses, the fission probability determined for these masses is very small for A < 200, accounting for the peak in this region. This intermediate peak in the mass distribution is probably most evident at "medium" beam energies - i.e. at low beam energies (say, 100 MeV) there is not sufficient excitation energy to produce many nuclei in the lower mass region of low-

fission probability, whereas at high beam energies there is sufficient excitation energy that spallation products can be produced with very low masses which overlap with the higher mass fission fragments (as evidenced by the 2.9 GeV results).

Apparently, the ORNL model does not predict an intermediate peak in the mass distribution (Fig. 9), which seems somewhat surprising since the ORNL model neglects fission for nuclei having atomic numbers less than 91.

The results above were computed using a value of 14 for the parameter B_0 in the level density formula, which is the standard value incorporated in the RAL model program. As calculations with different B_0-parameters pointed out, the value of B_0 used has an important effect on neutron production, but has little influence on residual mass distributions.

	Proton Energy		
	0.30 GeV	1.0 GeV	2.9 GeV
σ_{nonel} (barns)	1.75	1.92	1.88
σ_f (barns)	1.38	0.93	0.92
$P_f = \sigma_f/\sigma_{nonel}$	0.79	0.48	0.49

Table 3: Calculated Nonelastic and Fission Cross Sections for Protons on U-238

5. CONCLUSIONS

For the thick target-moderator systems (large H_2O moderator) using lead and uranium as target material a factor of about 2 between uranium (0.2 % wt ^{235}U) and lead in thermal neutron peak fluxes is reachable. The B_0-dependence in lead target systems is larger than in uranium system, therefore in the new KFA version of HETC (HETC/KFA-1) mass dependent level density parameters in the evaporation model were introduced.

From the comparisons of neutron spectra calculations with measurements on this uranium targets the major deficiency of the present model is considered to be the underestimate of the high-energy neutrons. The comparisons here are with preliminary experimental data, and with only a small part of the KfK data which have been taken, so the magnitude of the experimental/theoretical differences may change if further comparisons are made. However, there is enough evidence from these, and other comparisons which have been made, to believe that the difference, at least at large angles, is real, even though the magnitude may be considered still questionable.

The RAL model predicts a somewhat wider fission fragment distribution than the experiment. Between the fission fragment peak and the spallation peak the RAL model predicts an intermediate peak near A=200. This peak results from spallation products which "survive" de-excitation through the mass region of high-fission probability into a lower mass region where further de-excitation by neutron emission is much more likely than fission. The ORNL model does not predict an intermediate peak in the mass distribution which seems somewhat surprising since the ORNL model neglects fission for nuclei having atomic numbers less than 91.

6. REFERENCES

/1/ T.W. Armstrong, P. Cloth, D. Filges, R.D. Neef, "A Comparison of High-Energy Fission Models for the HETC Transport Code, Part II: Thick Targets", Proceedings of the 5th Meeting of the International Collaboration on Advanced Neutron Sources", G.S. Bauer and D. Filges (Eds.), 22-26 June 1981, Jülich, Jül-Conf-45 (October 1981)

/2/ T.W. Armstrong, D. Filges, "A Comparison of High-Energy Fission Models for the HETC Transport Code, Part I: Thin Targets", Proceedings of the 5th Meeting of the International Collaboration on Advanced Neutron Sources", G.S. Bauer and D. Filges (Eds.), 22-26 June 1981, Jülich, Jül-Conf-45 (October 1981)

/3/ F. Atchison, "The Inclusion of Fission in the High-Energy Particle Transport Code, HETC", Bulletin of the American Physical Society 24, 874 (1979)

/4/ F.S. Alsmiller, R.G. Alsmiller Jr., T.A. Gabriel, R.A. Lillie, J. Barish, "A Phenomenological Model for Particle Production from the Collisions of Nucleons and Pions with Fissile Elements at Medium Energies", ORNL/TM-7528 (1981)

/5/ J.S. Fraser, et.al., "Neutron Production in Thick Targets Bombarded by High-Energy Protons", Phys. in Canada 21, 17 (1965)

/6/ R.G. Alsmiller Jr., T.A. Gabriel, J. Barish, F.S. Alsmiller
"Neutron Production by Medium Energy (1.5 GeV) Protons
in Thick Uranium Targets"
ORNL/TM-7527 (1981)

/7/ S. Cierjacks,
KfK unpublished, private communication 1981

/8/ T.W. Armstrong, P. Cloth, D. Filges, R.D. Neef,
"Theoretical Target Physics Studies for the SNQ
Spallation Neutron Source", Jül-Spez-120 (July 1981)

/9/ S. Cierjacks, et.al., "High-Energy Particle Spectra
Spallation Targets", Proceedings of the 5th Meeting
of the International Collaboration on Advanced
Neutron Sources, G.S. Bauer and D. Filges (Eds.)
22-26 June 1981 Jülich, Jül-Conf-45 (October 1981)

/10/ P.C. Stevenson, et.al., "Further Radiochemical
Studies of the High-Energy Fission Products",
Phys. Rev. 111, 886 (1958)

/11/ G. Friedlander, "Fission of Heavy Elements by High-
Energy Protons, in Physics and Chemistry of Fission",
1965, International Atomic Energy Agency, Vienna, 1965

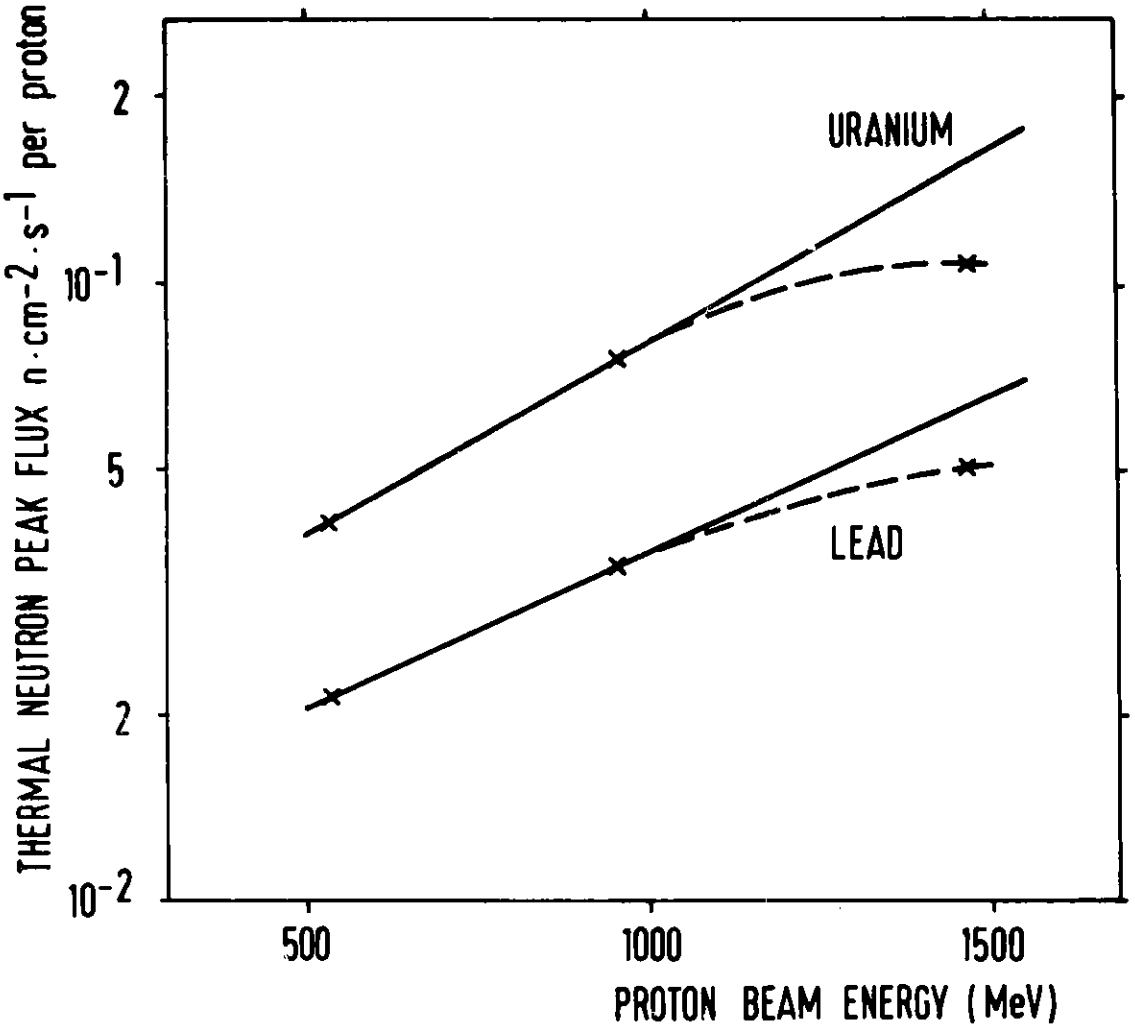

Fig. 1

Thermal neutron peak fluxes per proton as a function of proton beam energy (540, 960, 1470 MeV) for lead and uranium target with B_0 = 14 MeV

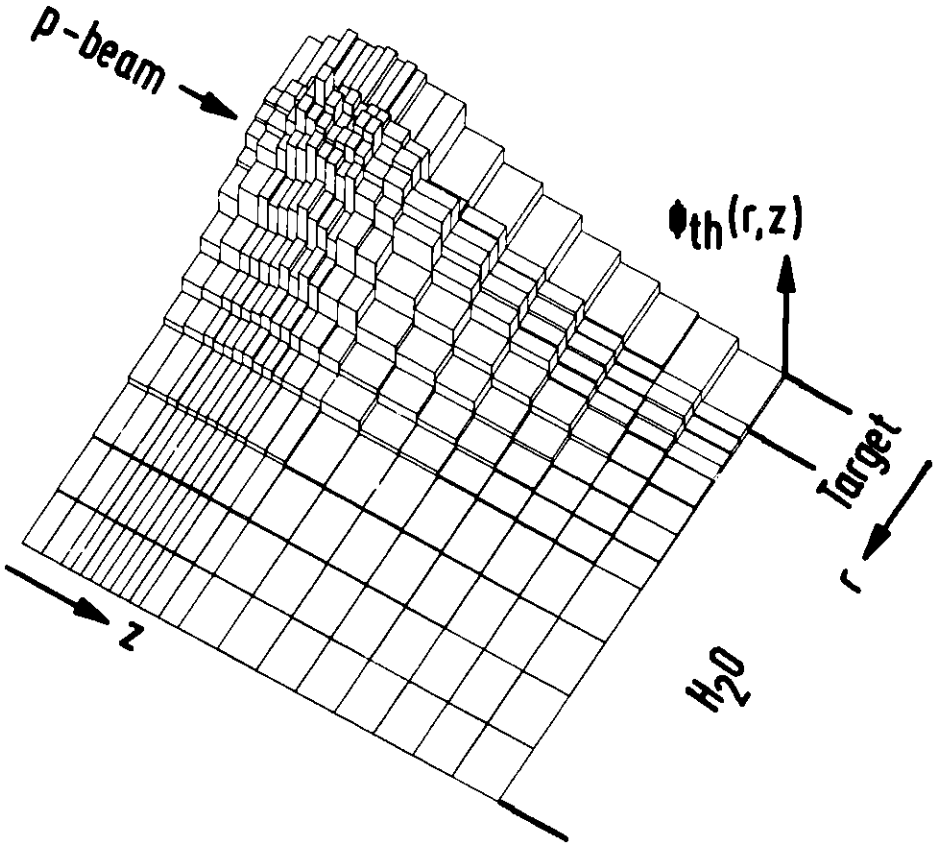

Fig. 2

Thermal neutron flux distribution for the lead system in R-Z plane (incident proton beam energy 960 MeV)

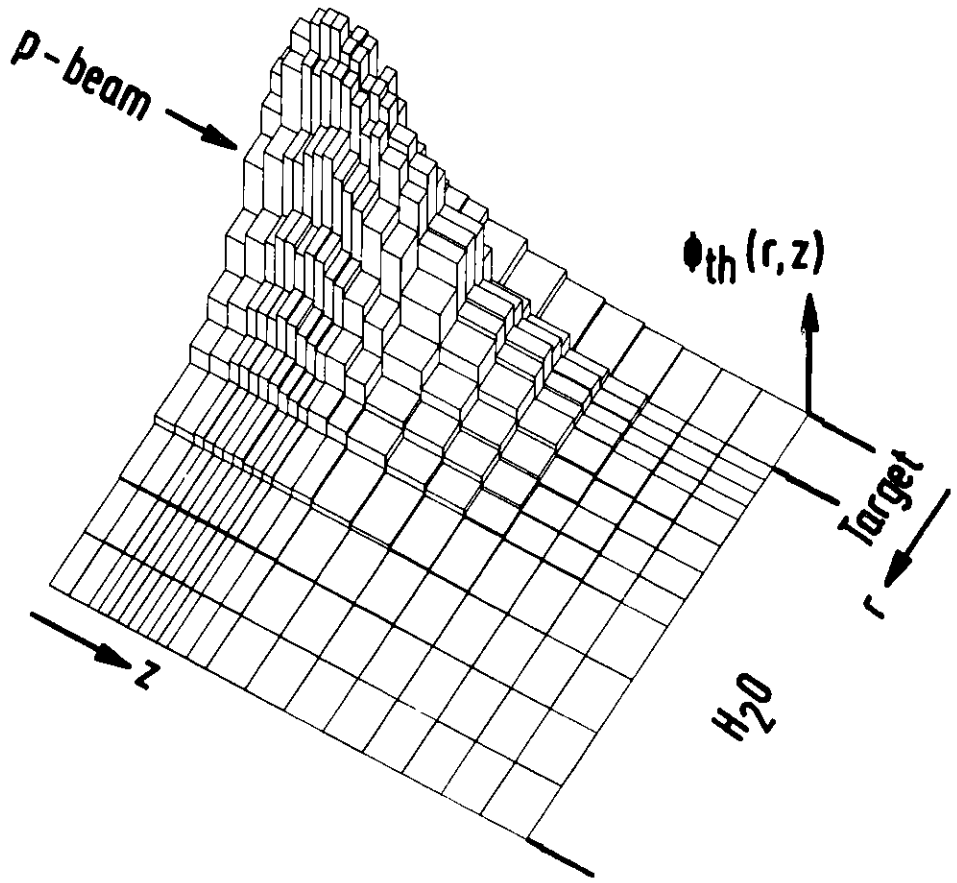

Fig. 3

Thermal neutron flux distriution for the uranium system in R-Z plane (incident proton beam energy 960 MeV)

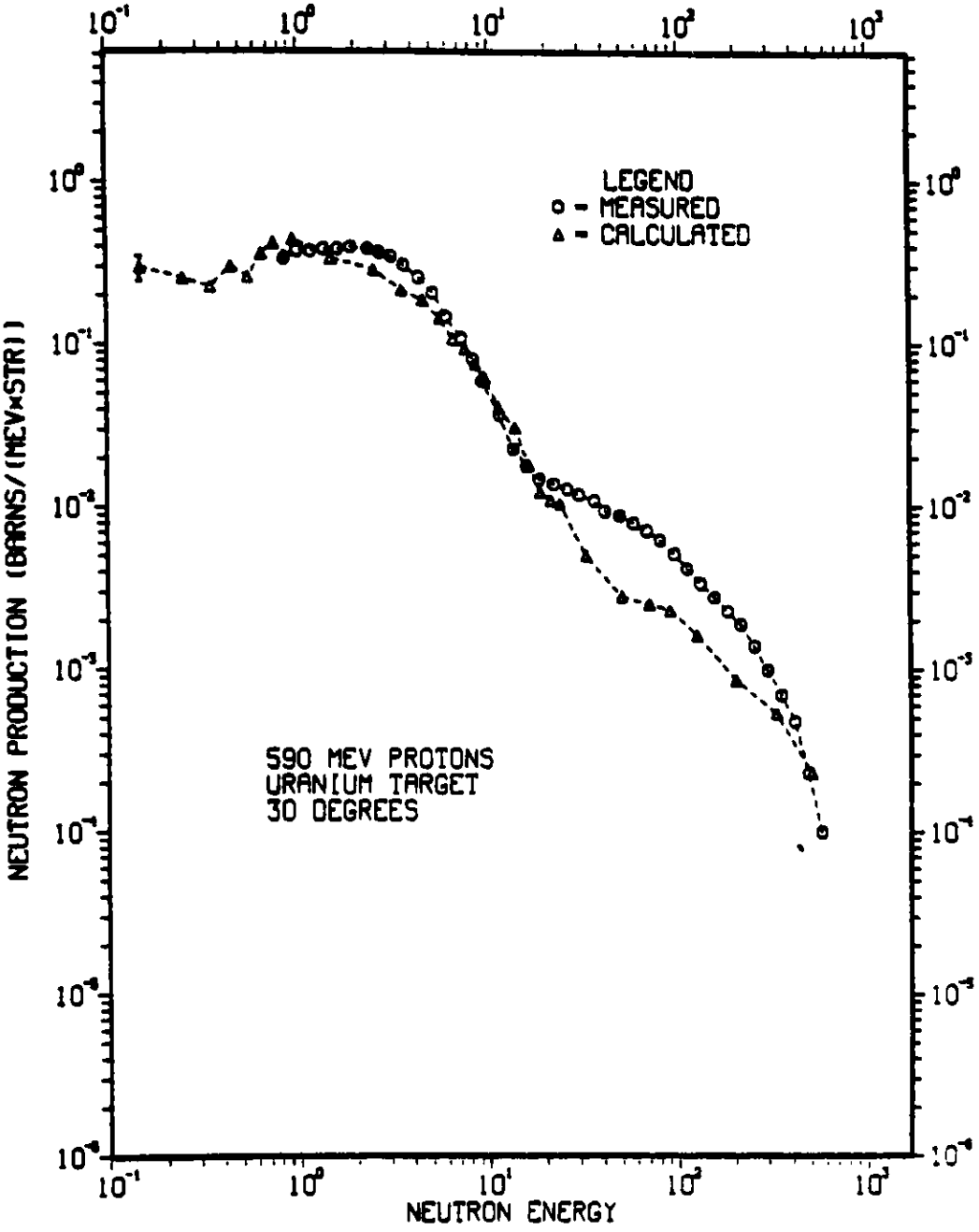

Fig. 4

Comparison of calculated and KfK measured neutron spectra at 30° from uranium target bombarded by 590-MeV protons

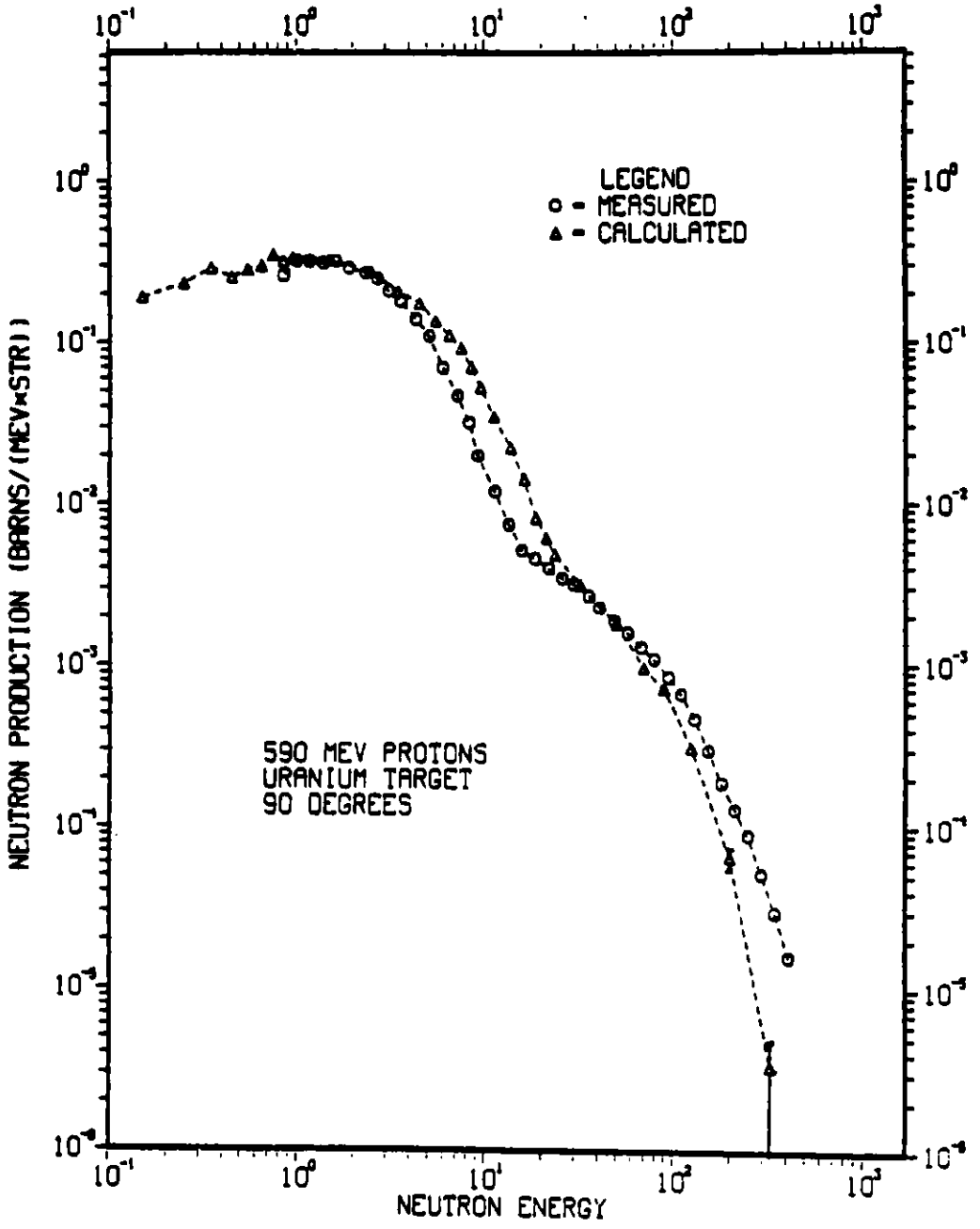

Fig. 5

Comparison of calculated and KfK measured neutron spectra at 90° from uranium target bombarded by 590-MeV protons

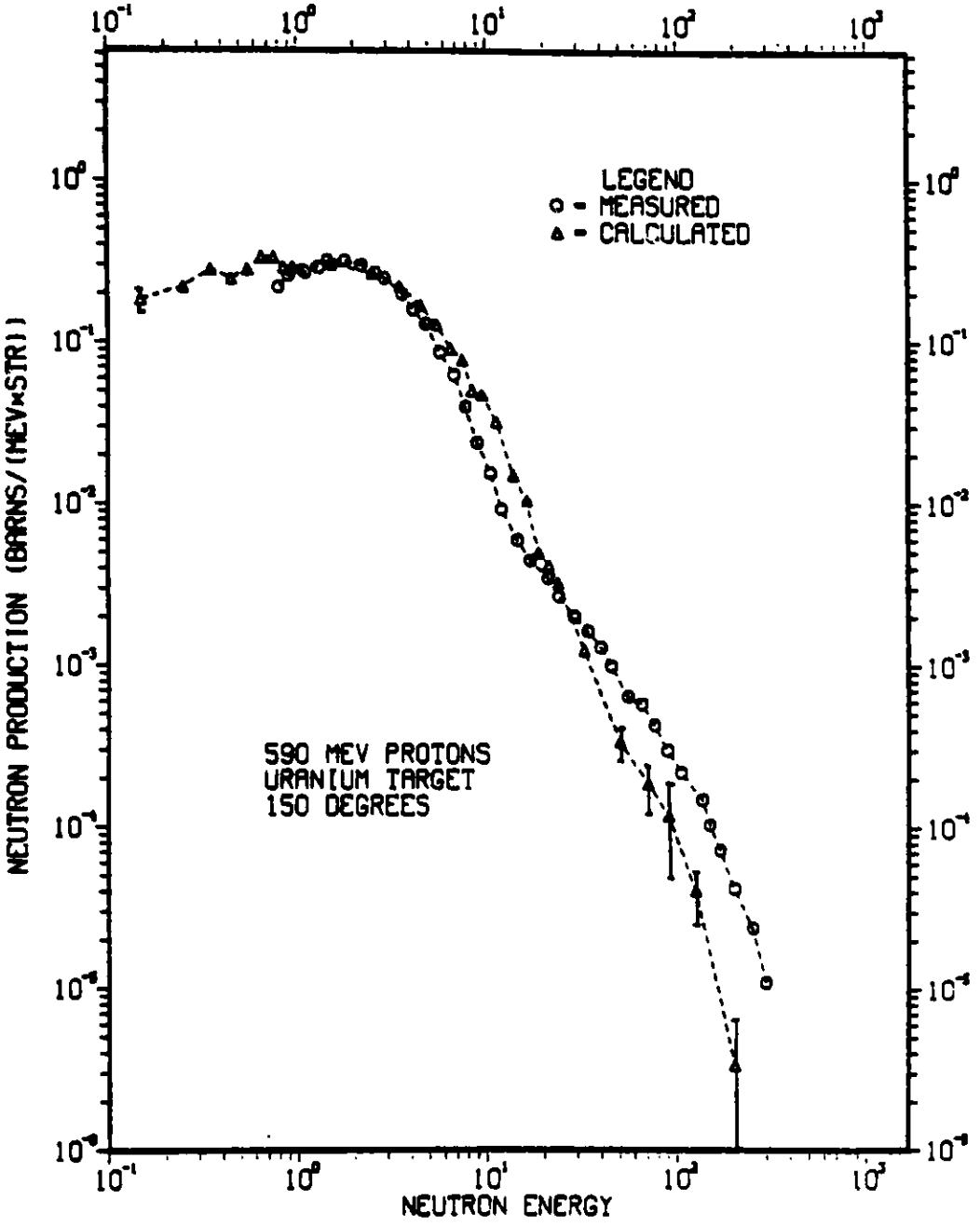

Fig. 6

Comparison of calculated and KfK measured neutron spectra at 150° from uranium target bombarded by 590-MeV protons

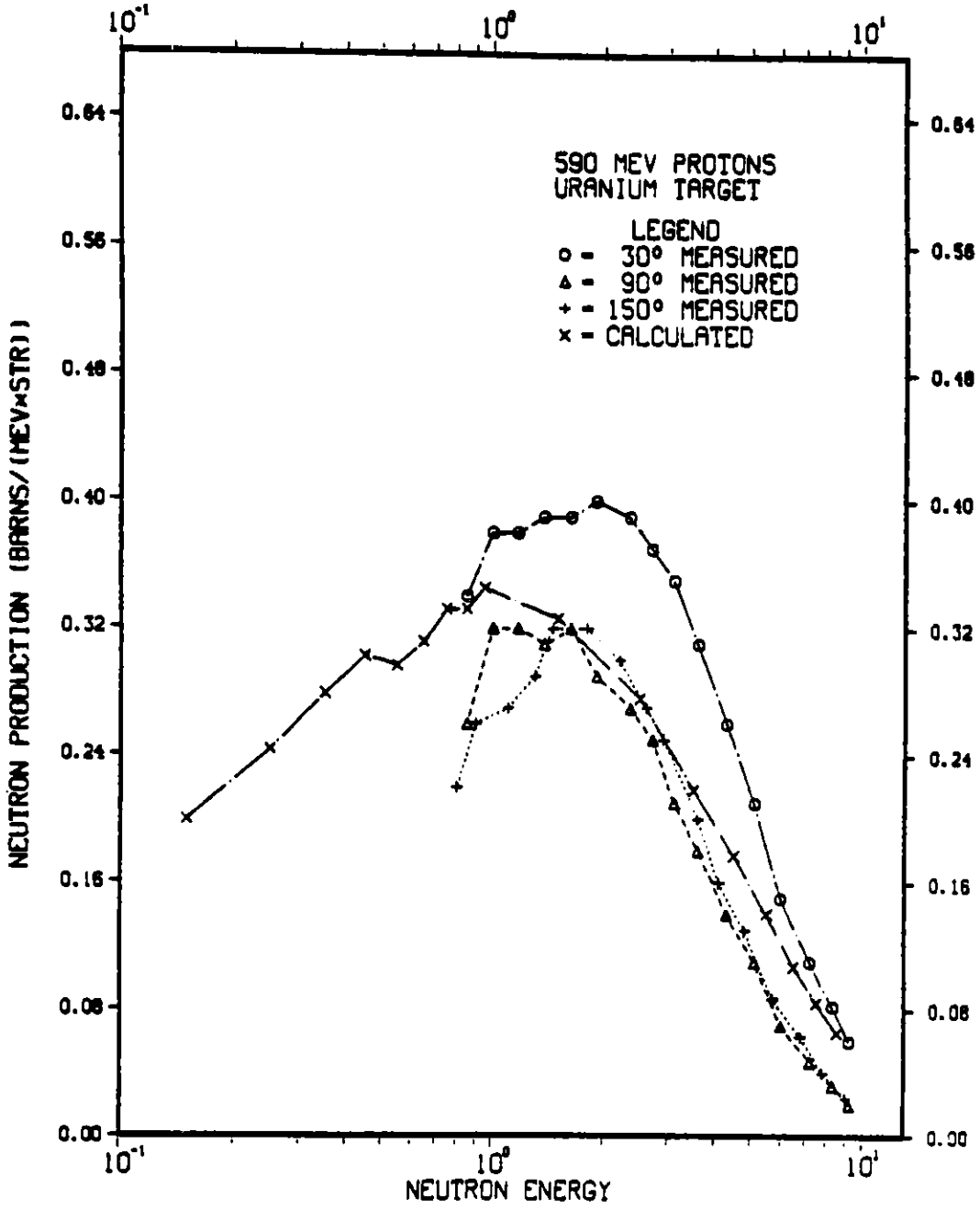

Fig. 7

Comparison of calculated and KfK measured neutron spectra at low energies from a thin uranium target bombarded by 590-MeV protons. The calculated spectrum ir averaged over all emission angles

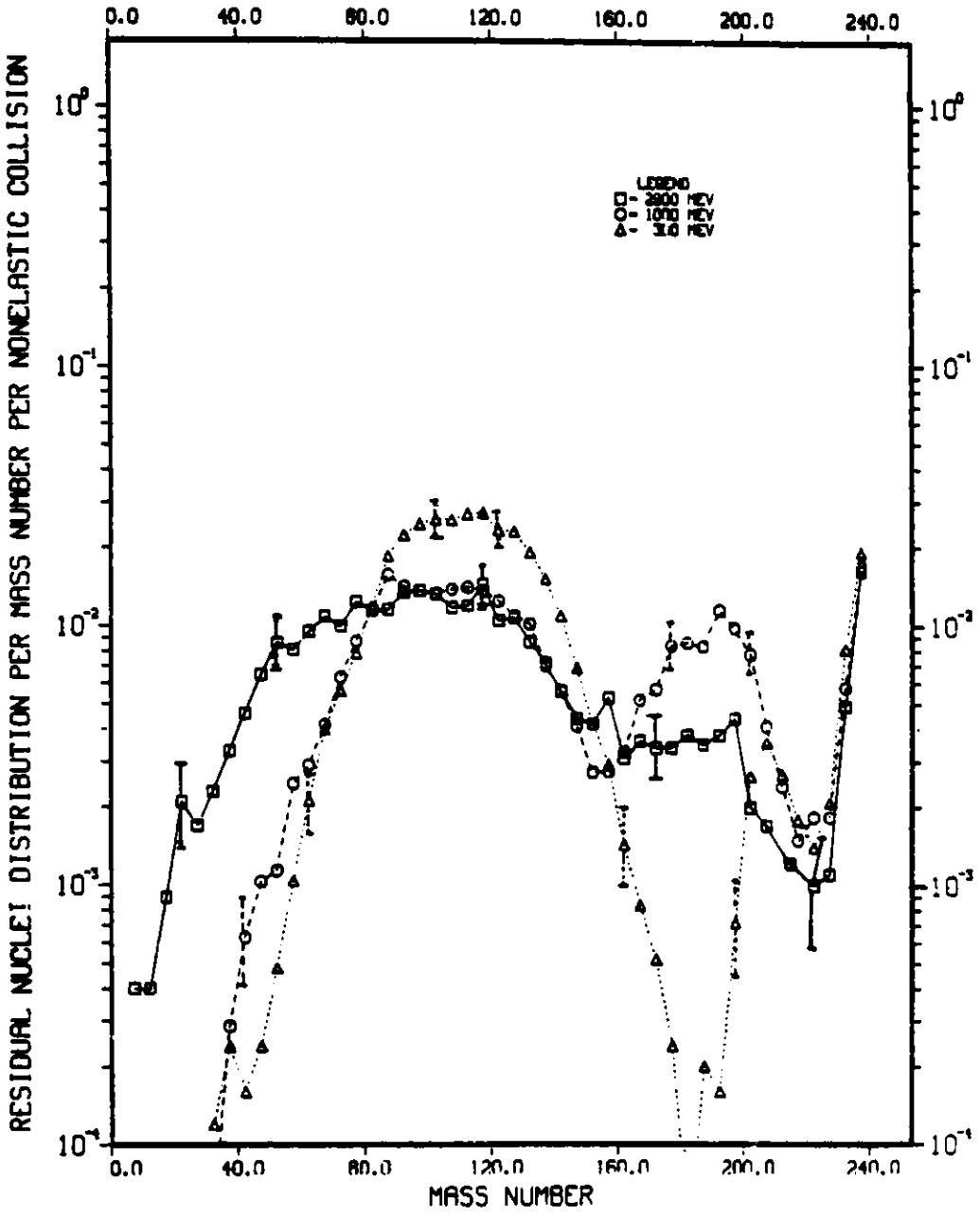

Fig. 8

Mass distributions predicted by RAL high-energy fission model for 300, 1000, and 2900 MeV protons on thin U-238 target

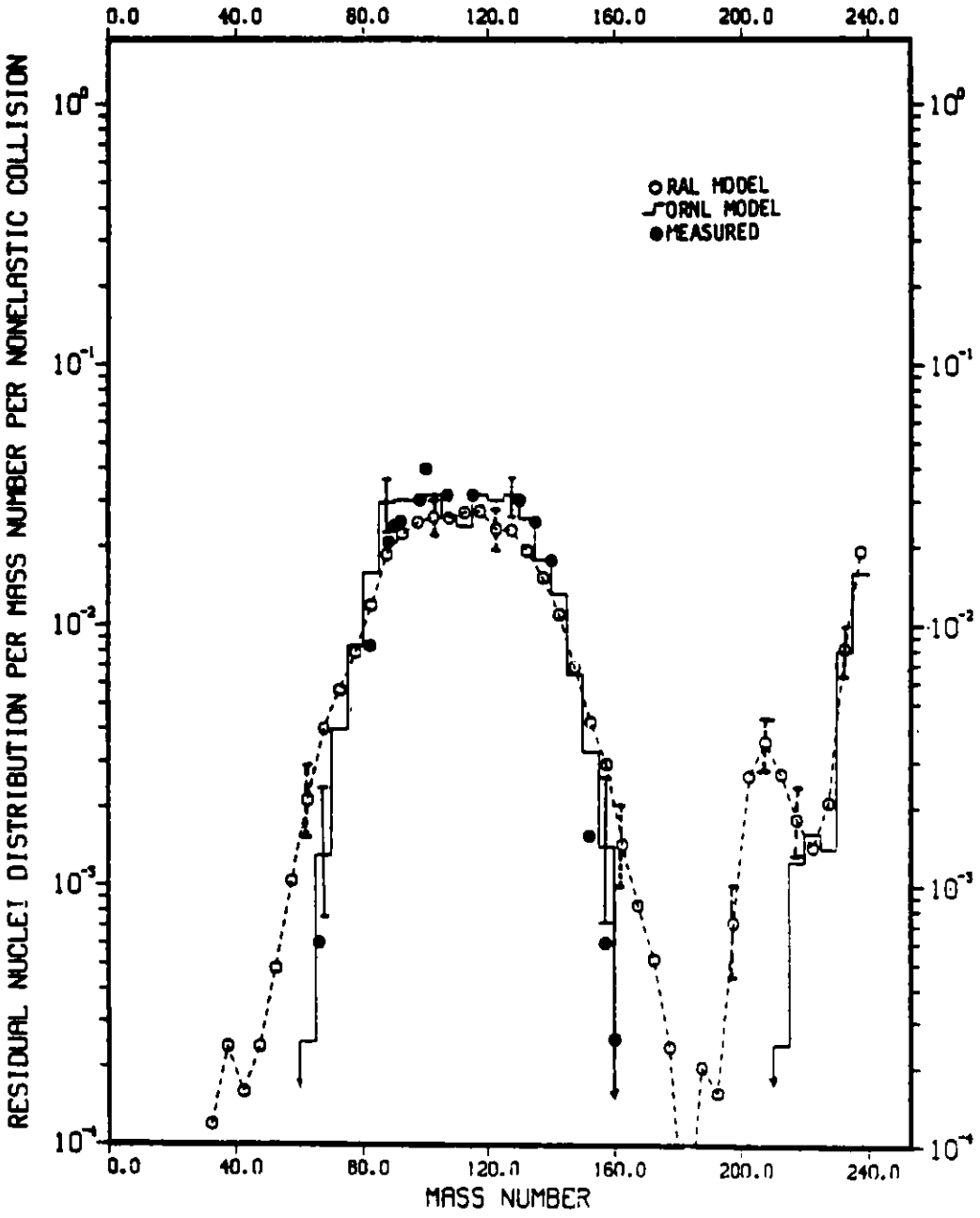

Fig. 9

Comparison of mass distributions computed using RAL model, from ORNL model calculations /6/, and from measurements of Stevenson, et.al. /10/ for 300 MeV protons on thin U-23[illegible] target

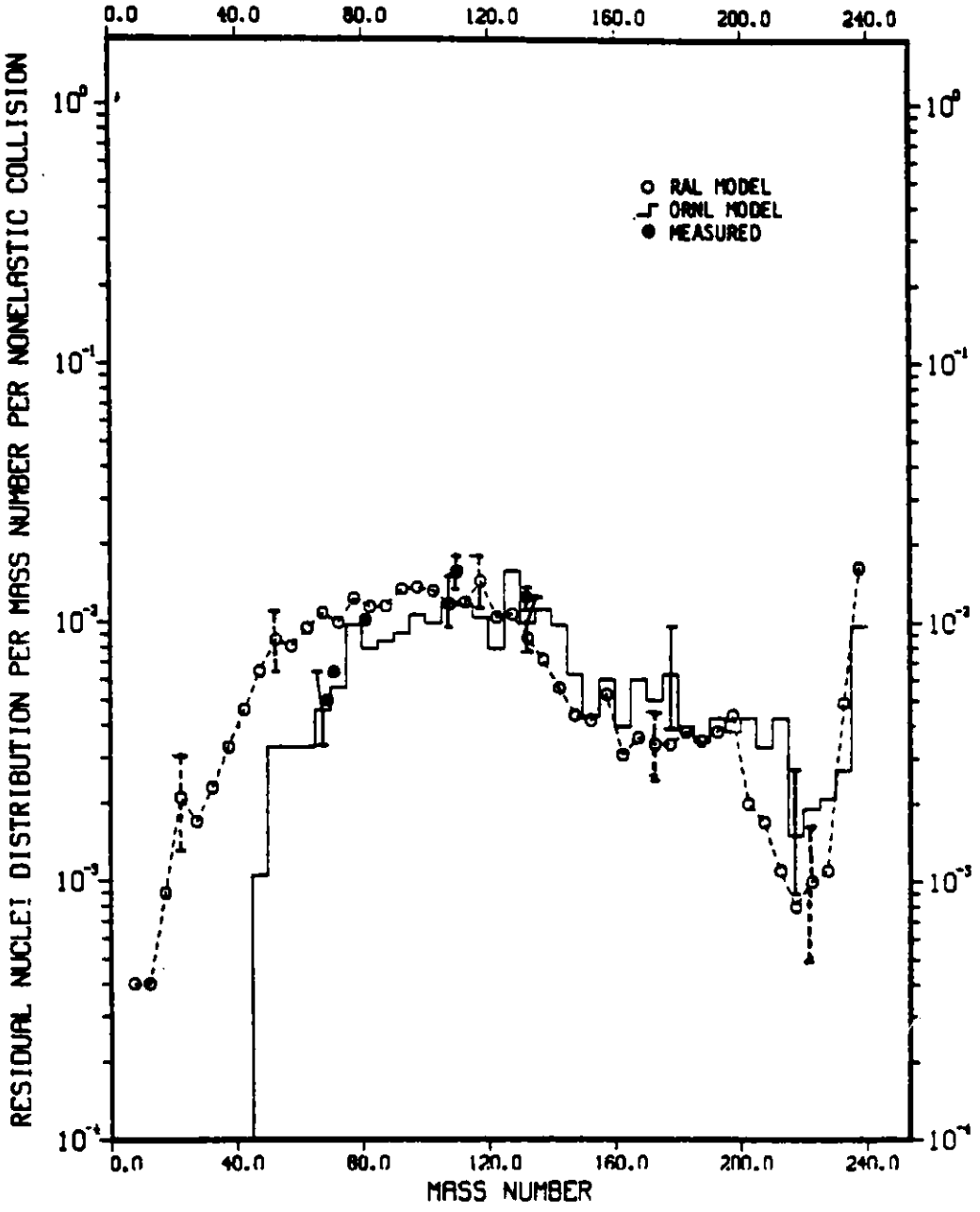

Fig. 10

Comparison of mass distributions computed using RAL model, from ORNL model calculations /6/, and from measurements of Friedlander, et.al. /11/ for 2900 MeV protons on thin U-238 target

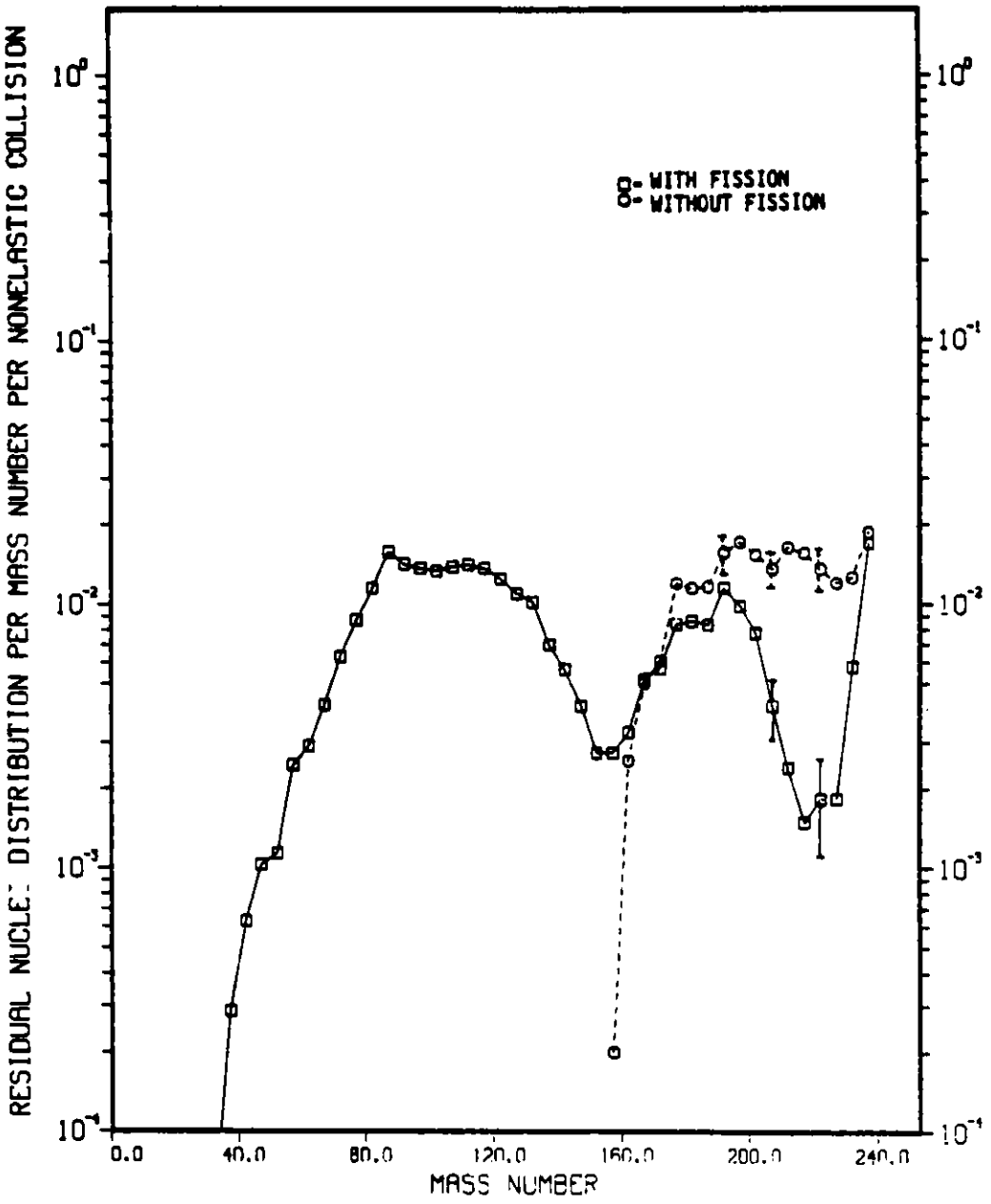

Fig. 11

Comparison of mass distributions with and without high-energy fission taken into account for 1-GeV protons on U-238

ICANS-VI
INTERNATIONAL COLLABORATION ON ADVANCED NEUTRON SOURCES
June 27 - July 2, 1982

MEASUREMENTS OF THE SPALLATION AND FISSION PRODUCT PRODUCTION FOR DEPLETED URANIUM AND NATURAL LEAD TARGETS BOMBARDED BY 1100 MEV PROTONS

W. Amian, N.F. Peek*, D.J. Shadoan*

Institut für Reaktorentwicklung
Kernforschungsanlage Jülich GmbH
Postfach 1913
D-5170 Jülich 1, Germany

*Physics Department, University of California,
Davis, California 95616

ABSTRACT

In order to simulate the spallation source target, 3 cm diameter by 1 mm thick disks of natural lead and depleted uranium were irradiated at 1100 MeV proton energy. The targets were inbedded between 5 cm thick bricks of the respective material. Gamma-ray spectrometric methods of gamma-peak and halflife analysis were developed to deduce mass yield distributions of the radionuclides produced. Both for lead and uranium fission products have been observed. The mass yield distributions and axial distributions of some isotopes are given. For lead the total production rates of some isotopes within an 100 x 50 x 450 mm target block are given.

MEASUREMENTS OF THE SPALLATION AND FISSION PRODUCT PRODUCTION FOR DEPLETED URANIUM AND NATURAL LEAD TARGETS BOMBARDED BY 1100 MEV PROTONS

W. Amian, N.F. Peek*, D.J. Shadoan*

Institut für Reaktorentwicklung
Kernforschungsanlage Jülich GmbH
Postfach 1913
D-5170 Jülich 1, Germany

*Physics Department, University of California,
Davis, California 95616

INTRODUCTION

Development of a high flux neutron source utilizing the spallation reaction necessarily involves extensive study of residual activity produced in the target material. To accomodate this task, gamma-ray spectrometric methods have been developed to deduce mass yield distributions for proton-induced spallation and fission reactions.

Measurements have been performed for thick targets of depleted uranium and natural lead bombarded by 1100 MeV protons. The axial distributions of the spallation and fission products observed within an 1.5 cm radial interval around the beam axis have been measured. Some of these results are given in this paper. For the uranium target especially the depth dependent production of Pu 239 by its precurson Np 239, the production of U 237 and of the fission product Ru 103 are given.

Preliminary mass yield distributions have been evaluated for 1 mm thick target foils exposed to the proton beam at the surface of the thick targets. Both for lead and uranium targets, fission products have been observed.

EXPERIMENTAL PROCEDURE

The experimental procedures involved irradiation of relatively thin, 1.0 mm thick, target foils embedded at equally spaced intervals in a larger target whose physical dimensions were similar to those of the proposed "infinitely thick" spallation target wheel. Two target materials were chosen for investigation, natural Pb and depleted U. An 1100 MeV proton beam at Saturne National Laboratory within the Centre d'Etudes Nucleaires de Saclay with an average intensity of up to 80 nA was used for irradiations. Once irradiated the target foils were removed and counted using high resolution gamma-ray spectroscopy. The resulting data were recorded on magnetic tape for subsequent computer analysis and isotope identification /1/. Figure 1 shows the configuration of the Pb target in detail. The first target foil shown was an aluminium foil (3.0 cm diameter by 1.0 mm thick) positioned 5.0 cm in front of the main target assembly. In this position it was utilized to monitor the incoming proton intensity. The next target foil (the first Pb foil) was positioned directly in front of the main assembly to receive full beam energy. Immediately behind the first Pb foil followed a 1.0 mm thick aluminium plate used to monitor the beam distribution.

The three target elements described above, Al foil, Pb foil, and Al plate, constituted a repetitive unit and appeared a total of 10 times; each unit separated by a 5.0 cm thick Pb brick. Individual target foils consisted of 3.0 cm diameter by 1.0 mm thick natural Pb disks. These dimensions were chosen as a compromise between adequate counting intensity and corrections due to self-absorption and non point-source geometry. Due to space limitations in the target area the total length,

45 cm, of the complete Pb target assembly was short of the "infinite thickness", 65 cm, required to completely absorb 1100 MeV protons. Stopping-power calculations indicated an energy loss of 700 MeV in 45 cm of Pb.

The uranium target foil assembly was identical except for two instances. First, the entire target assembly was infinitely thick at an overall length of only 35 cm and therefore the number of uranium target foils irradiated was eight in one run and nine in the next. Secondly, the uranium foils were vacuum encapsulated in aluminum cases to prevent the escaping of radioactive gases.

The data collection system included high resolution gamma-ray analysis electronics in conjunction with a 80 cm^3 Ge(Li) detector and an automatic sample changer mounted on rails to vary the distance to the detector easily. The detector was inclosed in lead shielding, 10 cm thick. The background due to photons with energies less than 100 keV, such as lead x-rays were excluded from the spectra by a lower level discriminator. The detector was calibrated against IAEA and PTB standard reference sources with + 2 % accuracy. The cross sections used to determine the number of protons striking the target for the respective proton reactions on aluminium are given in table 1. These have been taken from a review paper of Cummings /2/.

DATA REDUCTION

The gamma-ray spectra are analyzed by the computer code AGAMEMNON /3/. All spectra are corrected especially for energy calibration drift. The halflife analysis and nuclide identification code YELLOW /4/ is then applied to the peakfit results.

YELLOW sorts the outputs of AGAMEMNON by energy and time, plots the calculated activity for each peak-energy group as a function of time and identifies the reaction products based on their halflifes and known gamma-ray transitions. Besides the activity-time plot the system prints a list of all candidates which fit the experimental points best. The resulting decay curves of the best candidates are drawn in the graph (Fig. 2). If the decay is of parent-daughter nature, this is taken into consiuation. Any number of overlapping nuclides may be taken into account, experience, however, revealed that a maximum of three is sufficient (for parent daughter decay, six).

Finally the program outputs the complete list of candidate nuclides ordered by atomic number and mass number (Fig. 3). The number of nuclei produced as calculated by the halflife analysis is given for each of the isotope's gamma-ray transition lines. To accept a condidate nuclide the dominant gamma-ray transition lines have to fit the decay curves at the respectienergy most probably and these results have to agree within the experimental errors stated for the number of nuclei. These errors include besides the statistical errors of counting the fitting errors of the peakfit and the error of the halflife analysis. For dominant lines this is typically no more than 5 %. The list of candidate isotopes is derived from the compilation of Erdtmann and Soyka /5/, however the list of perent nuclei had to be enlarged for our purposes. For letargets the library is scanned from atomic number Z = 4(Be) up to Z = 84(Po), for uranium up to Z = 94(Pu).

All results given have been corrected for decay during irradiation and for gamma-ray attenuation in the sample.

EXPERIMENTAL RESULTS

Figures 4 and 5 show the axial distributions of Pt-191, Os-185, Y-88, Pb-203 and Hg-203 within 1,5 cm radial interval around beam axis.

The total number of reactions per proton within the target can be estimated by these data and by the measurements of the beam profile performed by looking at the Na-24 distribution on the aluminium plates inserted into the target. Table 2 gives the mean and FWHM of the vertical Gaussian beam profile, the Na-24 intensity and the fraction of the beam hitting the 3 cm-diameter target. The value of 15 % at a depth of 45 cm is near to a homogeneous activation of 14.1 % (target area/total area). The results of these calculations are given in table 3.

Figure 6 shows the number of reactions per proton and per (g/cm^2) for a lead foil at the front target face for various mass numbers. A distinction has been made between de-excitations from proton rich (β^+, ϵ) and neutron rich (β^-) states, respectively. Starting from the mass of the heaviest lead isotope (208) the production of radioactive proton rich isobars increases sharply to a mass number at 200 (stable isotopes may be produced in addition) and drops off about two orders of magnitude to a mass number of 140. At masses < 110 neutron rich fission products seem to be produced in competition with proton rich isobars.

The axial distribution of the fission product Rh-103, the Pu-239 precursor Np-239 and of the spallation product U-237 for the lead target bombarded at 1100 MeV proton energy are shown in figure 7. The distribution of Rh-103 is representa-

tive of the number of fissions and therefore for the energy deposition.

Figure 8 shows the number of reactions per proton and per (g/cm^2) for a uranium foil at the front target face for various mass numbers. Again a distinction has been made between neutron rich and proton rich isobars. The neutron rich isobars at masses between 85 and 155 are the normal fission products. Their distribution has the expected shape. Proton rich isobars are produced in that region, too, but at a one order of magnitude lower rate. In the gap between mass numbers 160 and 190 no nuclides could be identified with certainty. The gap between mass number 210 and 230 is not accessible to γ-spectrometry, because the nuclides are short lived α-emitters.*

It can be assumed, that the fissions observed are mainly due to neutrons. This is shown in figure 9 where the axial distributions of the fission products Ba-140 and Nd-147 and of the proton rich product Xe-127 are compared to the results for a foil exposed to the proton beam 20 cm upstream from the target. While the production rates for the fission products drop off sharply, the one of Xe-127 remains nearly unchanged. This result however, should be taken qualitatively only, because the neutron flux in the upstream position is not known from experiment.

---

*By integration of the distribution for neutron rich fission products using Simpson's Formula and relating it to 200 % yield an absolute yield of (5 + 2) % for mass 103 was estimated. Multiplying the numbers for Ru 103 in figure 9 by 20 gives the axial distribution of fission in the uranium target block in an 1.5 cm radial interval around beam axis.

CONCLUSION

The experiments described in this study allow to measure the axial distributions within natural lead and depleted uranium targets for those spallation and fission products, which show dominant γ-ray lines. Because no chemical separations are done the gamma-ray spectra contain numerous overlapping peaks. The presence of a nuclide like Lu 170, having 596 known gamma-ray lines, in the spectra of the lead targets illustrates this fact. This is why the analysis of the spectra necessarily calls for extensive studies of the halflifes identifiable.

For both target materials preliminary mass yield distributions have been evaluated for 1 mm thick target foils exposed to the proton beam at the surface of the thick target blocks. Fission products have been observed in each case.

For uranium the shape of the fission product disterbution for neutron rich isobars seems to imply the fission by low energy neutrons in competition to high energy particle processes. This is more substantiated by the fact, that a target foil irradiated 20 cm apart from the thick target shows a relatively higher decreas in the formation of neutron rich fission products as compared to proton rich fission products.

It is planned to compare our experimental data with calculated predictions using the Monte Carlo code HETC.

REFERENCES

/1/ N.F. Peek, D.J. Shadoan, W. Amian
Gamma-ray measurements of isotopes produced by 1.1 GeV protons on lead and uranium targets
ICANS-V, Jülich 1981

/2/ J.B. Cumming
Annual Review of Nuclear Science 13 (1963) 261

/3/ W. Amian
AGAMEMNON - a computer code to analyze complex gamma-ray spectra
(in preparation)

/4/ W. Amian, N.F. Peek, D.J. Shadoan
Gamma-ray spectrometric product identification and halflife analysis from proton induced spallation and fission reactions of lead and uranium
ICANS-V, Jülich 1981

/5/ G. Erdtmann, W. Soyka
The gamma-rays of the radionuclides
Verlag Chemie, Weinheim and New York 1979

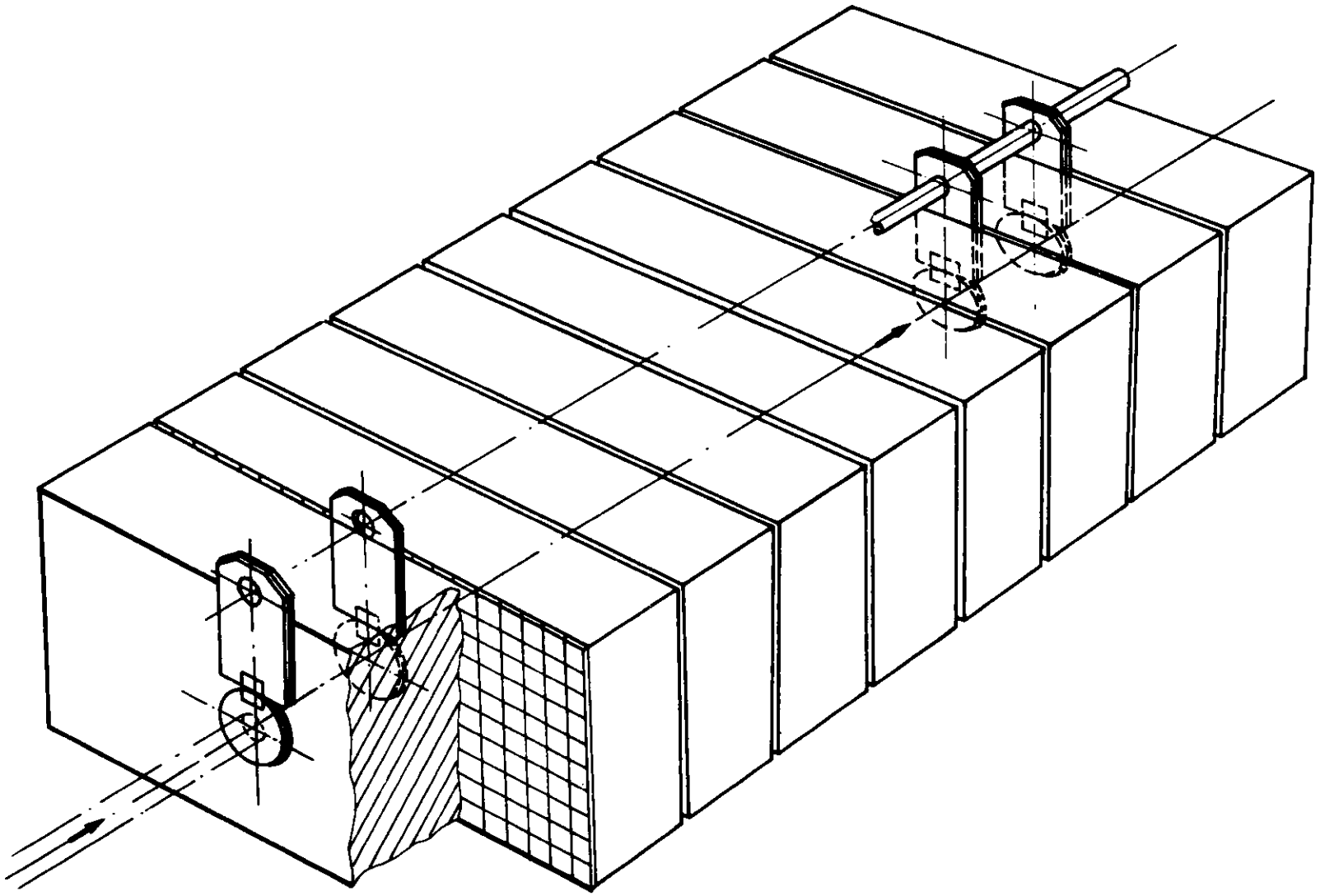

Fig. 1: Target configuration showing the small target disk followed by an aluminum disk and an aluminum plate along with the 5 cm thick Pb brick.

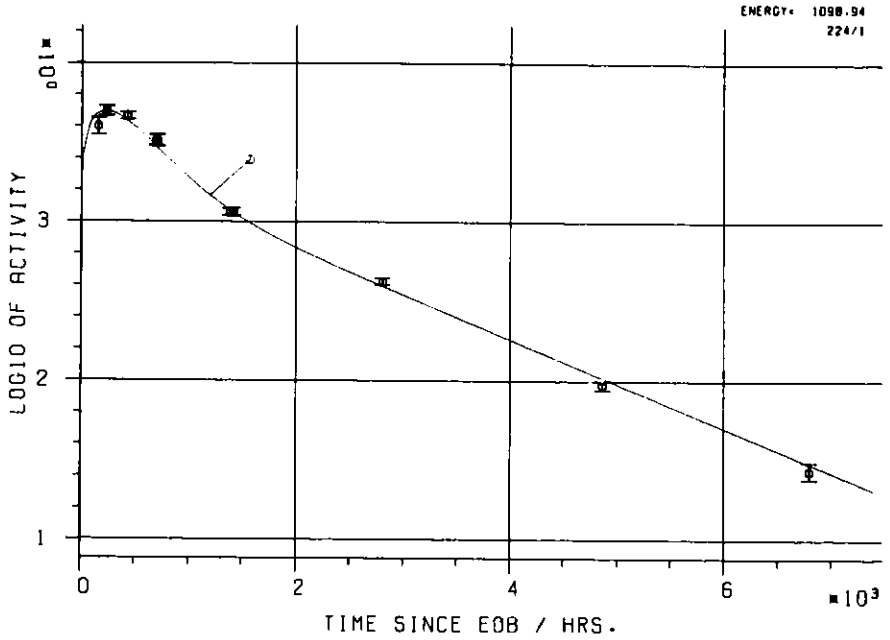


```
PT 188  -->      10.30 D AO= 9.49E+03+- 3.37E+00
  -->  77 IR 188  -->       1.73 D AO= 1.52E+01+- 1.61E+04 CHI= 1.50E+02

PO 206  -->       8.83 D AO= 1.47E+04+- 8.53E+01
  -->  83 BI 206  -->       6.24 D AO= 1.95E-02+- 7.10E+04 CHI= 1.15E+02
```

ENERGY	ERROR	CORR									
1098.94	0.62	1.051E+00									
ID	S-EOB	LIVETIME	% RESIDUE	CPS ERROR	CTS/S	ENERGY	FWHM	EFFICIENCY	DTCORR		
72U1 7530	1.593E+02	5.820E+02	4.834E+00	5.020E+02	3.991E+03	1098.37	2.723E+00	5.865E-04	1.080E+00		
72U1 7558	2.334E+02	1.508E+03	2.588E+00	3.510E+02	4.981E+03	1098.58	2.598E+00	5.865E-04	1.050E+00		
72U1 7589	4.209E+02	4.822E+03	2.469E+00	2.482E+02	4.637E+03	1098.76	2.668E+00	5.865E-04	1.022E+00		
72U1 7636	6.954E+02	8.364E+03	1.797E+00	2.445E+02	3.260E+03	1098.62	3.130E+00	5.865E-04	1.011E+00		
72U1 7640	7.083E+02	8.551E+03	1.831E+00	2.715E+02	3.244E+03	1098.66	3.111E+00	5.865E-04	1.011E+00		
72U1 7698	1.383E+03	1.928E+04	2.595E+00	6.219E+01	1.149E+03	1099.30	2.604E+00	5.865E-04	1.004E+00		
72U1 7702	1.415E+03	1.984E+04	2.571E+00	8.150E+01	1.158E+03	1099.24	2.621E+00	5.865E-04	1.004E+00		
72U1 7767	2.806E+03	3.351E+04	1.788E+00	2.203E+01	4.200E+02	1099.19	2.682E+00	5.865E-04	1.002E+00		
72U1 7819	4.868E+03	6.398E+04	1.046E+01	6.765E+00	9.430E+01	1099.36	2.709E+00	5.865E-04	1.000E+00		
72U1 7856	6.798E+03	8.640E+04	4.165E+00	3.385E+00	2.726E+01	1099.34	2.378E+00	5.865E-04	1.000E+00		

```
HLF=  8.30E+02 HRS    AO =  4.95E+03 1/SEC   LOG10(AO*SEC) =  3.69E+00   CHI2 =  2.00E+00
AO-LONG-    = 3.12E+03 1/SEC AO-SHORT-   = 2.72E+03 1/SEC HLF-LONG-   = 9.75E+02 HRS HLF-SHORT- = 8.37E+02 HRS
CHISQR-L-   = 5.15E-01  CHISQR-S-   = 1.81E+01
AO-LONG-    =( 2.21E+03 +- 2.36E+03) 1/SEC     HLF-LONG-   =( 1.08E+03 +- 3.69E+02) H
AO-SHORT-   =( 5.63E+03 +- 2.92E+03) 1/SEC     HLF-SHORT-  =( 3.54E+02 +- 2.80E+02) H    CHISQR = 5.50E+00
```

1098.94 224	HALFLIFE	HLF/H	AO	(E-EO)/N	DECAY	I/IO	PEAK	NR	LINE	INTENS
E121 26 FE 59	4.51E+01 D	1.09E+03	3.56E+03	1.11E+00	1.29E-02	1.00E+00	1098.94	224	1099.22	5.65E+01A
CHISQR= 3.79E+01		+- 2.28E+02					1291.47	249	1291.56	4.32E+01A
							190.59	23	192.34	3.11E+00A
							140.66	11	142.65	1.03E+00A
							336.24	63	334.80	2.60E-01A
E423 38 SR 83	1.35E+00 D	3.24E+01	6.36E+18	9.08E-01	6.91E-64	6.58E-01	511.61	99	511.00	5.40E+01A
CHISQR= 2.63E+05		+- 4.08E+17					0.00	0	762.50	3.00E+01A
							381.51	71	381.50	2.20E+01A
							778.14	154	778.40	1.80E+00A
							423.99	82	423.50	1.60E+00A
							388.57	73	389.20	1.60E+00A
DAUGHTERS: RB 83 KR 83M							1098.94	224	1098.00	2.00E-01A
E322 77 IR 188	1.73E+00 D	2.47E+02	9.49E+03	7.56E-01	5.27E-09	6.88E-01	154.44	14	155.03	3.34E+01A
CHISQR= 1.50E+02		+- 3.37E+00					633.67	123	633.10	2.16E+01A
							477.82	94	478.10	1.60E+01A
							0.00	0	2214.60	1.30E+01A
							1209.73	241	1210.00	6.75E+00A
							633.67	123	635.00	5.80E+00A
							1098.94	224	1097.00	1.35E+00A
E221 83 BI 206	6.24E+00 D	2.12E+02	1.47E+04	9.39E-01	2.21E-10	9.94E-01	803.39	162	803.05	1.00E+02A
CHISQR= 1.15E+02		+- 8.53E+01					881.33	181	881.00	6.78E+01A
							515.62	100	516.10	4.00E+01A
							1719.21	290	1718.65	3.40E+01A
							537.56	105	537.43	2.90E+01A
							341.97	84	343.50	2.40E+01A
							182.81	20	184.00	1.92E+01A
							497.25	98	497.20	1.55E+01A
							894.99	184	895.00	1.53E+01A
							1098.94	224	1098.20	1.33E+01A

```
G PO 206  -->       8.83 D AO= 6.88E+03+- 1.14E+02
   -->  83 BI 206  -->       6.24 D AO= 3.91E-03+- 5.51E+02
    AND   26 FE  59   1.08E+03 H  AO= 2.38E+03+- 6.64E+01 CHI= 1.71E+00

  PT 188  -->      10.30 D AO= 5.65E+03+- 2.54E+02
   -->  77 IR 188  -->       1.73 D AO= 1.17E-02+- 4.31E+02
    AND   26 FE  59   1.08E+03 H  AO= 2.48E+03+- 8.91E+01 CHI= 7.38E+00

   38 SR  83   3.24E+01 H  AO= 6.88E+04+- 1.18E+04
    AND   26 FE  59   1.08E+03 H  AO= 2.89E+03+- 1.78E+02 CHI= 2.92E+01
```

Fig. 2: Decay plot and typical output information of YELLOW

```
 40 ZR  95    6.440E+01 D  5.564E+06 SEC  1.546E+03 H
DAUGHTERS: NB 95MNB 95
GENESE:    NFI 6.500 NTH ZR 94 NFA MO 98
PARENT1:            0.000E+00
PARENT2:            0.000E+00
  4 LINES
                                        ENERGY    NUCLEI     SIGMA    PARENT     SIGMA   CHISQR PAGE PARENT
 724.18  44.2000A    E1;Z0;D0;->E1<-  724.31  7.61E+11  3.85E+10  0.00E+00  0.00E+00  6.07E-01 143   0
 756.72  54.8000A    E1;Z0;D0;->E1<-  756.85  7.56E+11  3.67E+10  0.00E+00  0.00E+00  1.44E+00 150   0
  1 LINES MISSING WITH TOTAL INTENSITY OF     0.0200
-------------------------------------------------------------------------------------------------------
*
*
-------------------------------------------------------------------------------------------------------
 44 RU 103    3.935E+01 D  3.400E+06 SEC  9.444E+02 H
DAUGHTERS: RH103M
GENESE:    NTH RU102 NFI 3.090 NFA RH103
PARENT1:            0.000E+00
PARENT2:            0.000E+00
 23 LINES
                                        ENERGY    NUCLEI     SIGMA    PARENT     SIGMA   CHISQR PAGE PARENT
 294.98   0.2420A    E8;Z1;D0;->Z1<-  294.36  1.01E+12  2.23E+11  0.00E+00  0.00E+00  1.57E+00  51   0
 317.72  -1.0000A
 443.80   0.3110A    E5;Z*;D0;->Z*<-  444.70  1.88E+12  1.74E+11  0.00E+00  0.00E+00  8.63E+00  87   0
 497.08  86.4000A    E1;Z0;D0;->E1<-  497.25  1.03E+12  5.37E+10  0.00E+00  0.00E+00  8.35E-01  98   0
 557.04   0.7800A    E1;Z4;D0;->Z4<-  557.65  1.11E+12  7.84E+10  0.00E+00  0.00E+00  1.72E+00 110   0
 610.33   5.3000A    E1;Z0;D0;->E1<-  610.55  9.98E+11  5.66E+10  0.00E+00  0.00E+00  1.36E+00 119   0
 13 LINES MISSING WITH TOTAL INTENSITY OF     0.1790
-------------------------------------------------------------------------------------------------------
*
*
-------------------------------------------------------------------------------------------------------
57 LA 140    4.027E+01 H  1.105E+06 SEC  3.070E+02 H
DAUGHTERS:
GENESE:    NFI 6.300 NTH LA139 NFA CE140
PARENT1:   BA 140   1.279E+01 D
PARENT2:            0.000E+00
 41 LINES
                                        ENERGY    NUCLEI     SIGMA    PARENT     SIGMA   CHISQR PAGE PARENT
 131.12   0.5300A    E*;Z0;D0;->E*<-  129.67  1.83E+15  3.19E+14  0.00E+00  0.00E+00  8.41E+02   7   0
 241.96   0.4200A    E2;Z0;D0;->E2<-  242.22  4.99E+11  1.54E+11  0.00E+00  0.00E+00  2.05E-01  38   0
 266.55   0.5200A    E4;Z*;D0;->Z*<-  267.64  2.28E+06  7.38E+08  1.68E+07  2.74E+09  5.62E+00  45   1
 328.75  18.5000A    E1;Z0;D0;->E1<-  329.02  6.68E+07  1.26E+11  5.28E+11  9.28E+09  5.13E+00  61   1
 432.55   2.9800A    E1;Z1;D0;->Z1<-  432.80  5.48E+04  2.23E+07  5.09E+11  1.04E+08  1.01E+00  84   1
 487.03  43.0000A    E1;Z1;D0;->Z1<-  487.45  2.35E+08  3.47E+09  5.12E+11  7.17E+09  1.13E+00  96   1
 510.95   0.3500A    E6;Z*;D0;->Z*<-  511.61  4.95E+13  2.35E+12  2.99E+13  1.52E+12  3.86E+00  99   1
 574.20  -1.0000
 751.79   4.1900A    E1;Z0;D0;->E1<-  751.81  1.54E+07  1.27E+11  5.25E+11  9.51E+09  6.36E+00 149   1
 815.80  22.3200A    E1;Z1;D0;->Z1<-  816.21  2.96E+06  3.08E+08  5.23E+11  8.22E+08  8.29E+00 167   1
 867.86   5.3600A    E1;Z1;D0;->Z1<-  868.02  7.62E+04  1.34E+08  4.99E+11  6.02E+08  1.65E-01 178   1
 919.60   2.6100A    E1;Z1;D0;->Z1<-  919.57  2.82E+05  3.57E+06  4.97E+11  1.67E+07  2.52E+00 192   1
 925.25   6.9200A    E1;Z3;D0;->Z3<-  925.52  3.16E+08  1.40E+09  4.96E+11  2.98E+09  2.66E+00 194   1
 951.02   0.4900A    E3;Z5;D0;->Z5<-  951.95  1.65E+06  3.20E+09  4.10E+09  1.50E+10  6.25E+00 199   1
1085.20  -1.0000
1596.20  95.4700A    E1;Z1;D0;->Z1<- 1596.61  1.37E+04  1.58E+09  5.15E+11  7.42E+09  2.64E-01 282   1
 16 LINES MISSING WITH TOTAL INTENSITY OF     0.4300
-------------------------------------------------------------------------------------------------------
*
*
*
```

Fig. 3: List of candidate nuclides

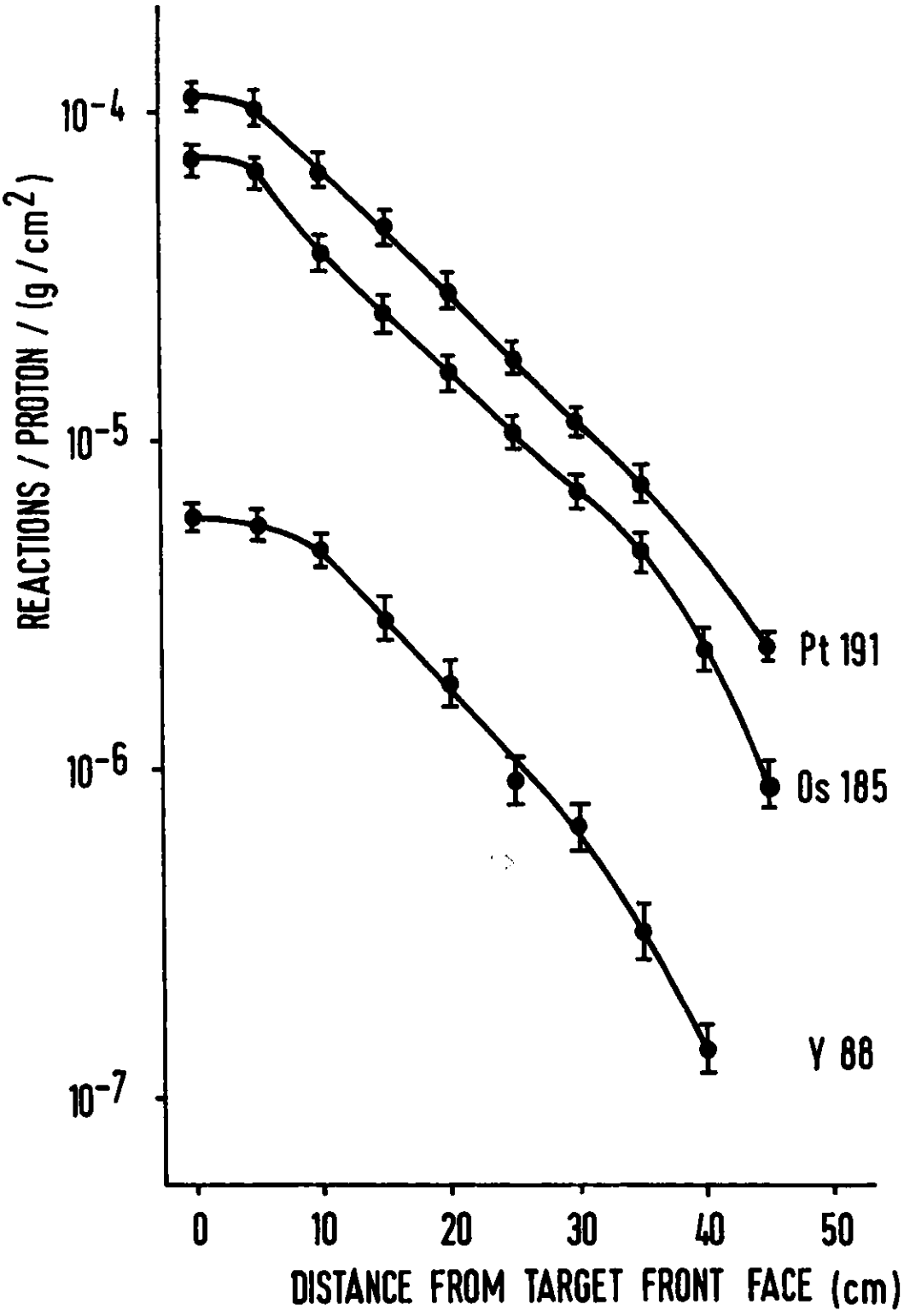

Fig. 4: Axial distributions of Pt191, Os185 and Y88 within an 1.5 cm radial interval around beam axis

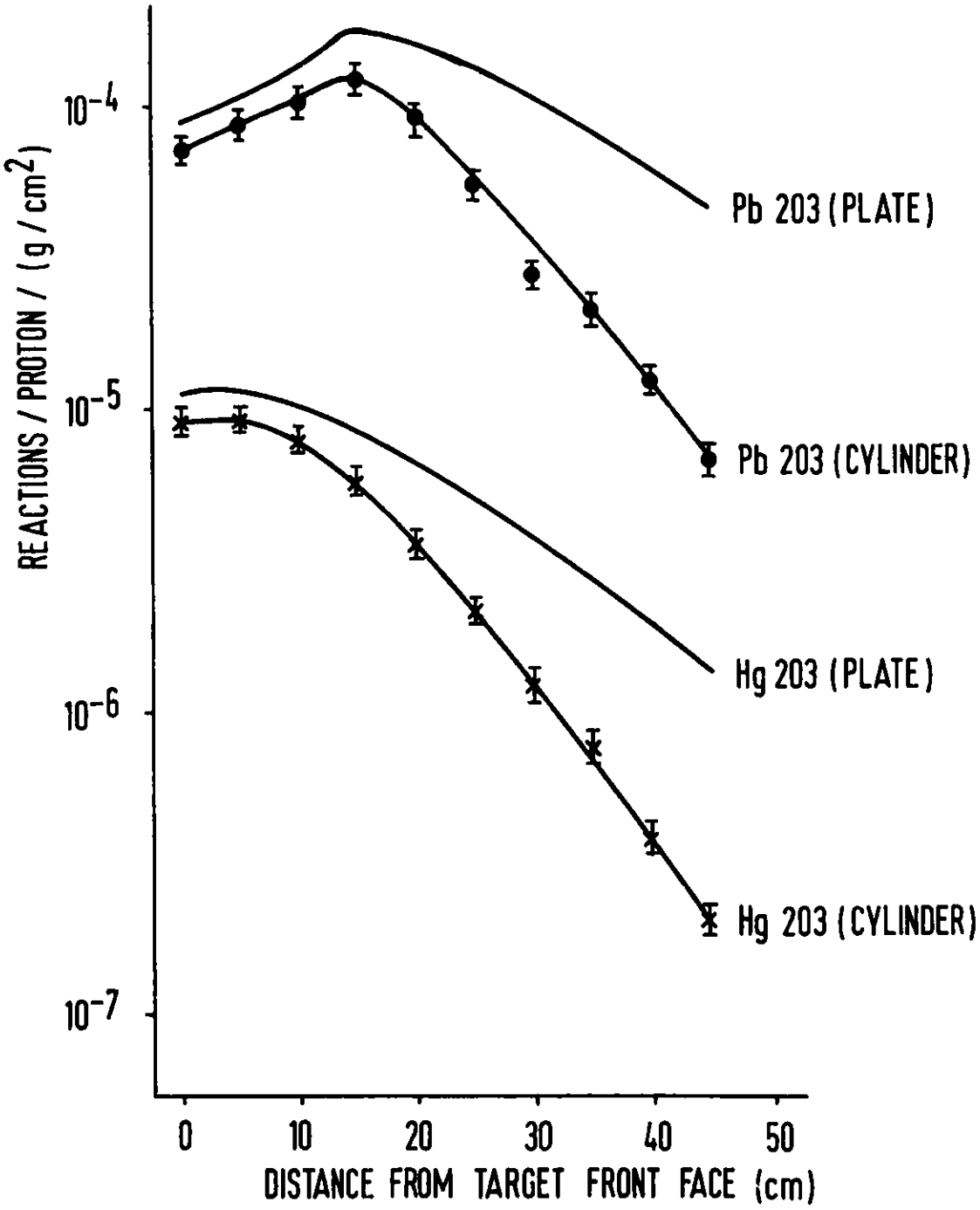

Fig. 5: Axial distributions of Pb203 and Hg203 within an 15 mm diameter cylinder around beam axis and within an 100 x 50 x 1 mm plate

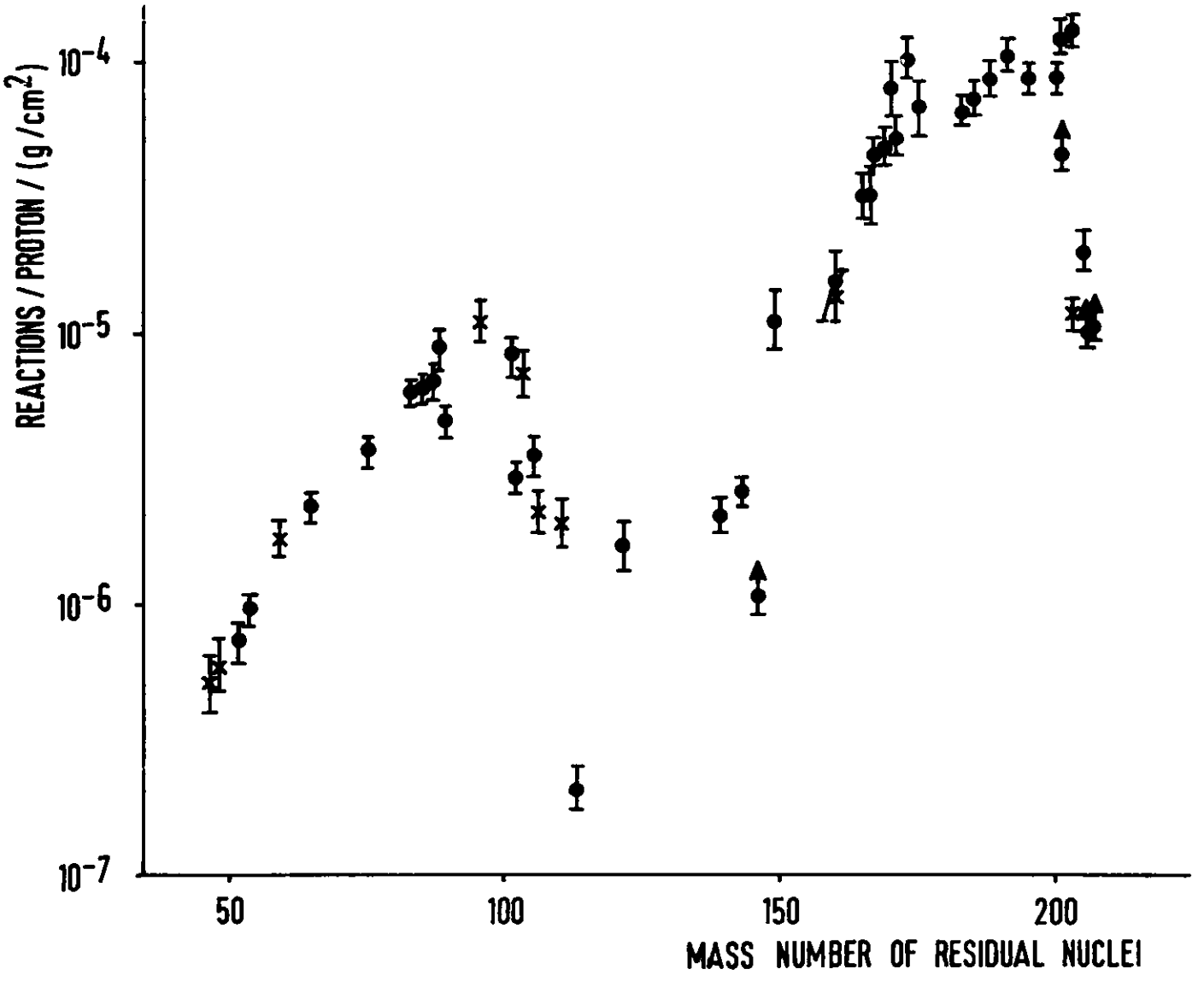

Fig. 6: Mass yield distribution for natural lead at target front face at 1100 MeV (● β^+, ε; X β^-)

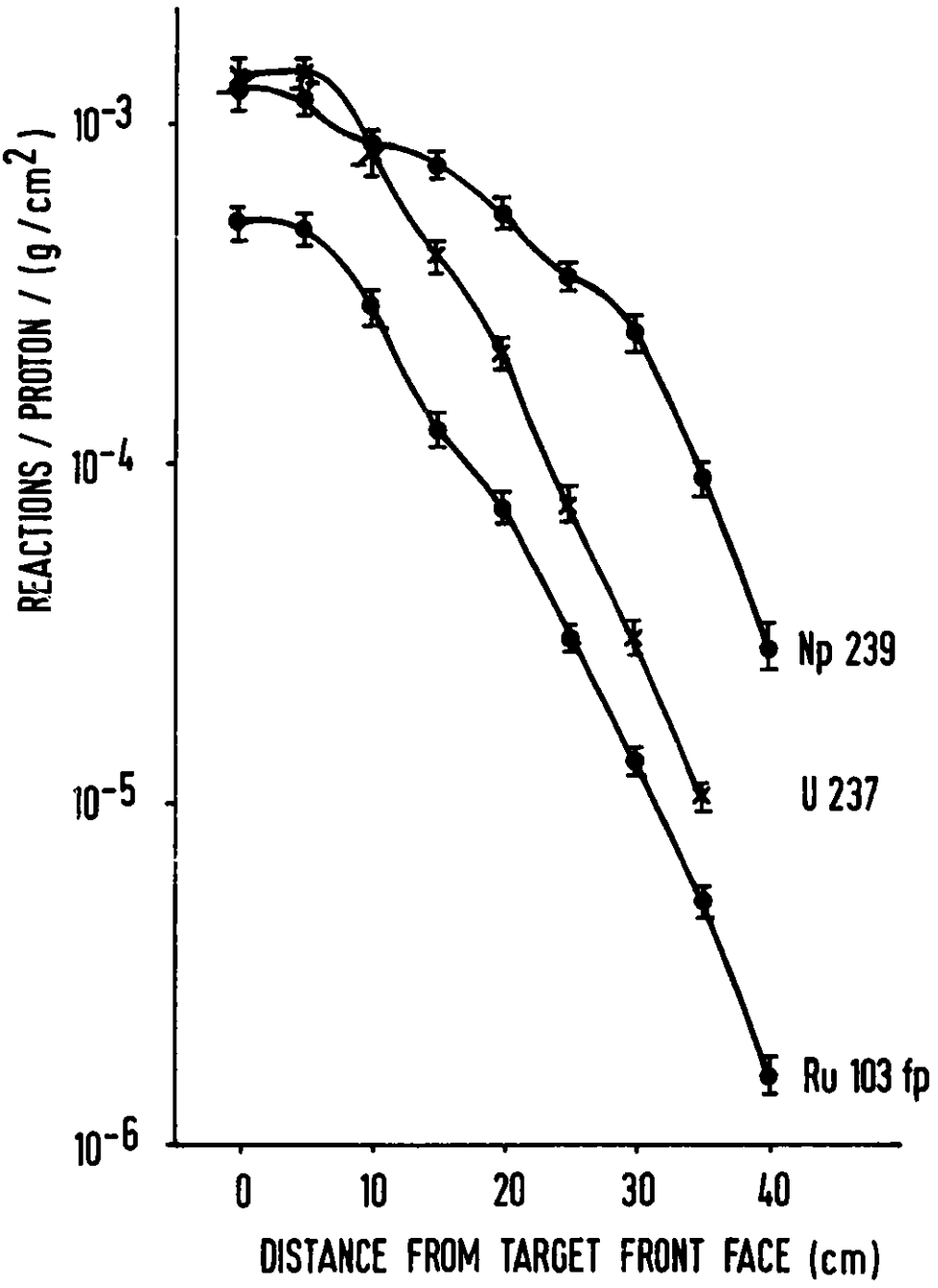

Fig. 7: Axial distributions of Np239, U237 and Ru103 within an 1.5 cm radial interval around beam axis. The distribution of fissions is ∿ 20 times that of Ru103 (uranium, 1100 MeV)

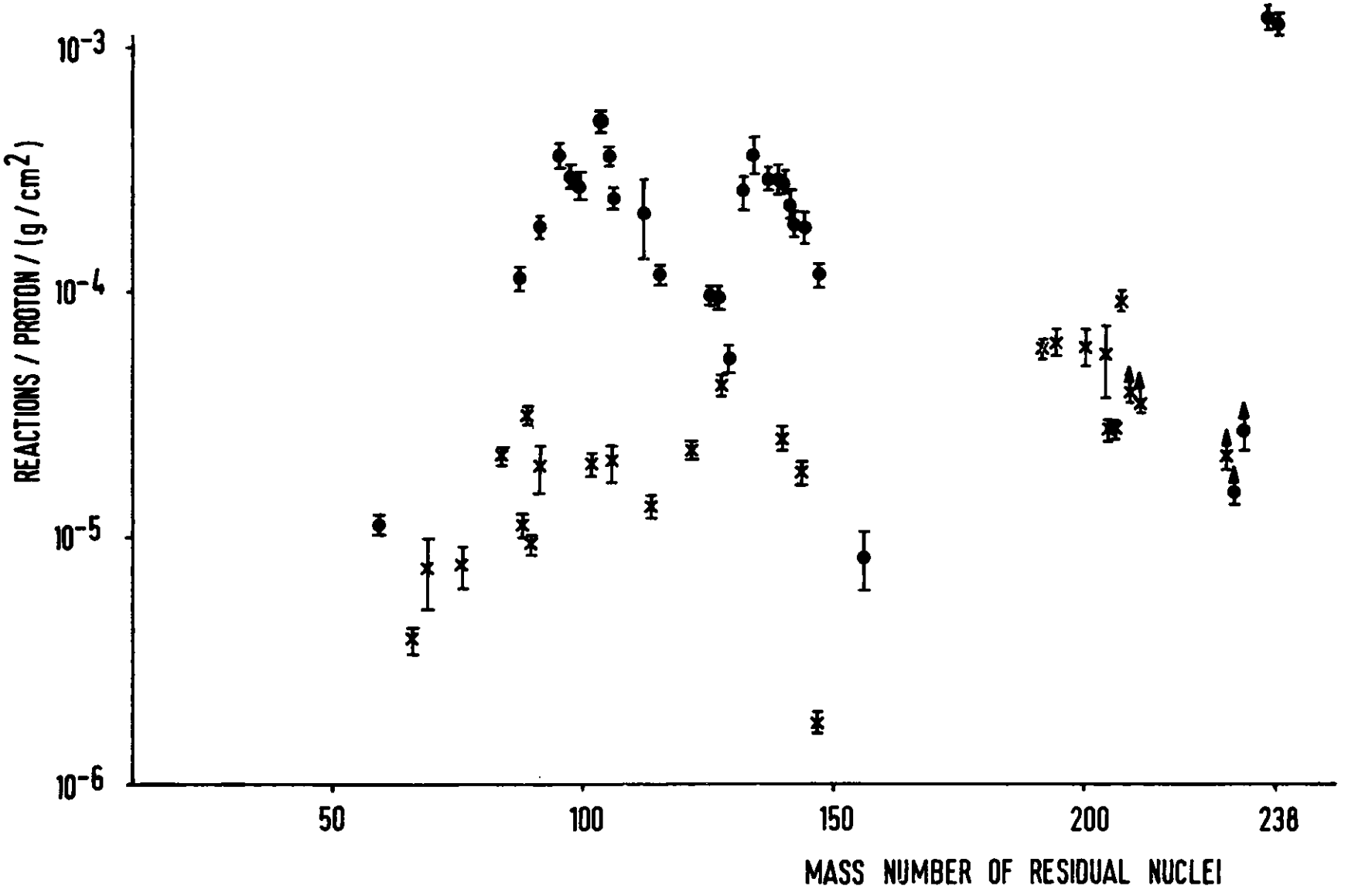

Fig. 8: Mass yield distribution for depleted uranium at target front face at 1100 MeV (● β^-; X β^+, ε)

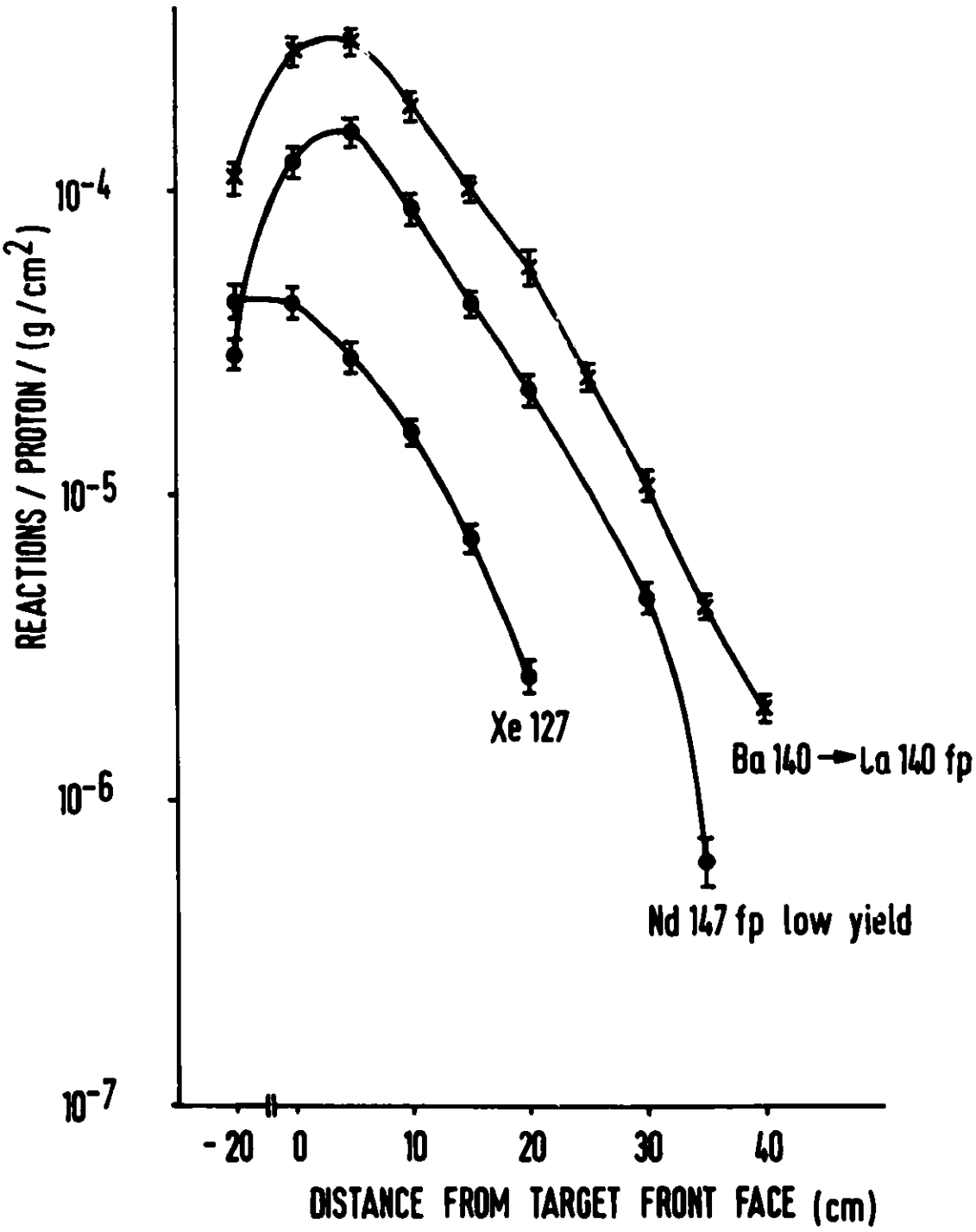

Fig. 9: Axial distributions of Ba140, Nd147, Xe127 compared to thin foil results 20 cm in front of the target (uranium, 1100 MeV)

Reaction	Cross Section (mb)
$^{27}Al(p,x)^{24}Na$	11
$^{27}Al(p,x)^{22}Na$	12
$^{27}Al(p,x)\ ^{7}Be$	8

Table 1: Al monitor foil data for 1100 MeV protons

Target	Depth (cm)	μ_{vert} (cm)	FWHM (Γ cm)	Intensity (c/sec)	% on Target
1	0	-1.24	1.3	255	81
2	5	-1.13	1.8	230	80
3	10	-1.06	2.4	172	76
4	15	- .97	3.2	100	67
5	20	- .89	4.3	58	56
6	25	- .80	5.8	33	45
7	30	- .73	7.9	19	34
8	35	- .62	10.6	11	28
9	40	- .54	14.4	6.2	19
10	45	- .46	19.4	4.6	15

(μ_{horiz} = + .095 cm)

Table 2: Beam Parameters from ^{24}Na Measurements for the

Nuclide	Halflife	Activity at Saturation* (MBq/nA)
Hg 203	46.6 d	20
Pb 203	52.1 h	380
Tl 201	73.5 h	220
Pt 191	2.8 d	190
Os 185	94.0 d	110
Re 183	71.0 d	120
Zr 95	64.0 d	20
Y 88	108.0 d	11

*numbers estimated to be correct within a factor of two

Estimated activities at saturation for some dominant α-emitters

Nuclide	Halflife	Activity at Saturation (MBq/nA)
Pt 190	$6.1\ 10^{11}$a	180
Os 186	$2.0\ 10^{15}$a	140
Hf 174	$2.0\ 10^{15}$a	130

Table 3: Activity at saturation per nA proton current of 1100 MeV within a 45 cm long, 10 cm * 5 cm area lead target

ICANS - VI

INTERNATIONAL COLLABORATION ON ADVANCED NEUTRON SOURCES

June 27 - July 2, 1982

CASCADE NEUTRON YIELDS FROM ENERGETIC HEAVY ION INTERACTIONS

Marcel M. Barbier
Marcel M. Barbier, Inc.

ABSTRACT

Experimental data on heavy ion production of cascade neutrons (neutron energy above 20 MeV) is collected and reviewed. Cascade neutron production figures per unit solid angle are given as a function of emission angle for projectiles up to Ar 40 and incident energies up to 2100 MeV/AMU. Total cascade neutron yields per event are derived and found not to increase when going to heavier projectiles.

CASCADE NEUTRON YIELDS FROM ENERGETIC HEAVY ION INTERACTIONS.

Marcel M. Barbier
Marcel M. Barbier, Inc.

1. NEUTRON DIFFERENTIAL PRODUCTION CROSS-SECTIONS.

There has been numerous measurements of neutron production by protons, light, and heavy ions, which are in part reported in the bibliography. In order to compare them, we have plotted the cascade neutron single differential cross-sections

$$\frac{d\sigma}{d\Omega} = \int_{20\,MeV}^{\infty} \frac{d\sigma}{dE\,d\Omega}\,dE \quad \text{barn/sterad}$$

as a function of neutron emission angle θ in fig. 1. In the forward direction ($\theta = 0$) there is generally a peak, whereas between 15° and 150° the data can in most cases be approximated by an exponential with angle of the form $\exp(-k\theta)$, where k (rad^{-1}) can be found from the figure.

Fig. 2 groups recent data collected by measurement at the Berkeley Bevalac. Some of these curves are proton production measurements, upgraded by the neutron proton ratio in the target nucleus. One sees that as the energy and the masses of the projectile and target increase, there tends to be more cascade neutrons produced, and more neutrons are produced at larger emission angles.

2. NUCLEAR REACTION CROSS-SECTIONS.

Is is useful to have a value for the nuclear interaction cross-section, which is approximately the inelastic one σ_{inel}, as this serves to calculate the yield at each angle, which is the neutron differential cross-section $d\sigma/d\Omega$ divided by σ_{inel}. We have used the values published by Barshay, Dover and Vary and drawn by extrapolation the graph given in fig. 3 which gives approximative values of σ_{inel} as a function of projectile and target masses A_P and A_T.

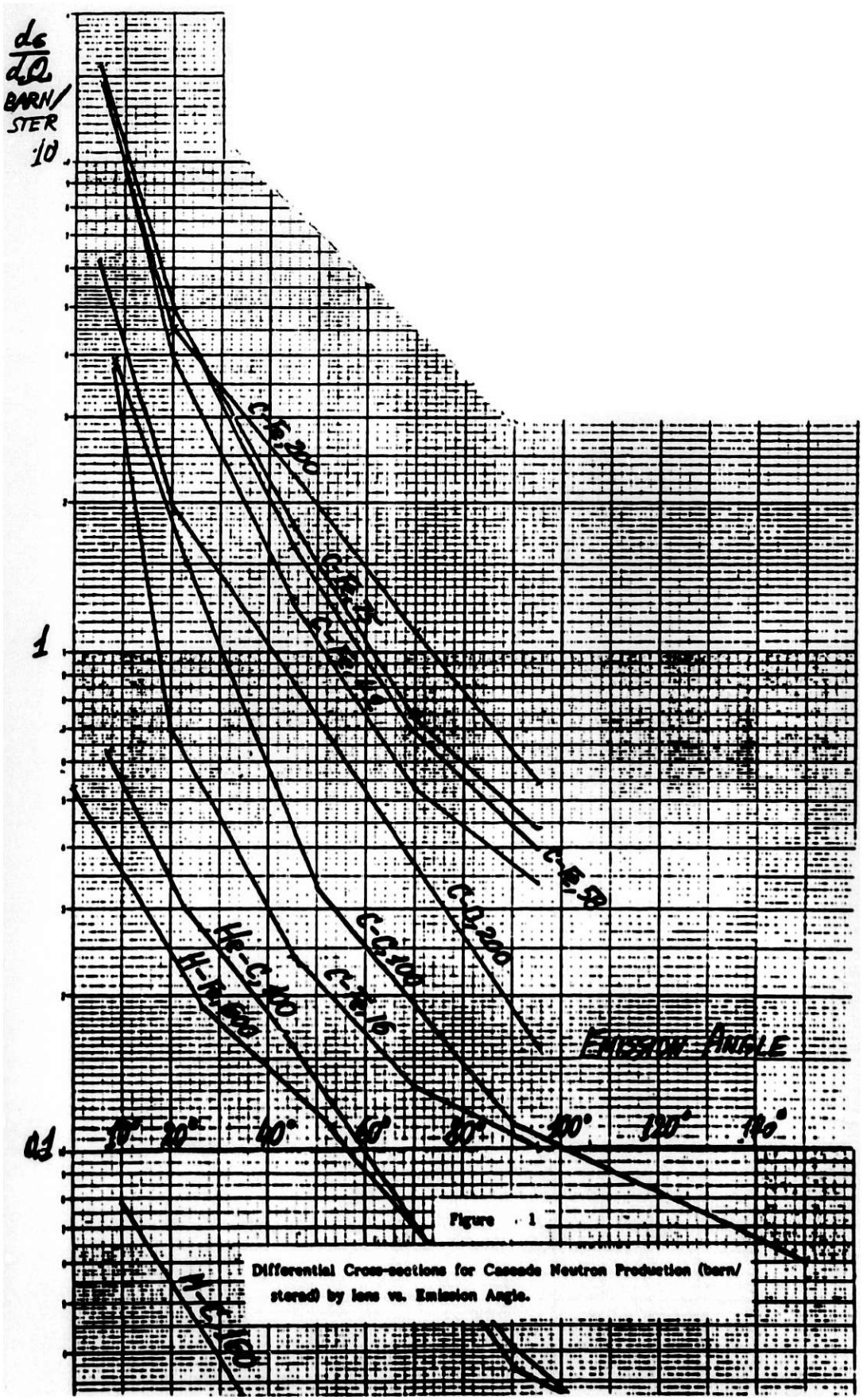

Figure 1

Differential Cross-sections for Cascade Neutron Production (born/ steradian) by Ions vs. Emission Angle.

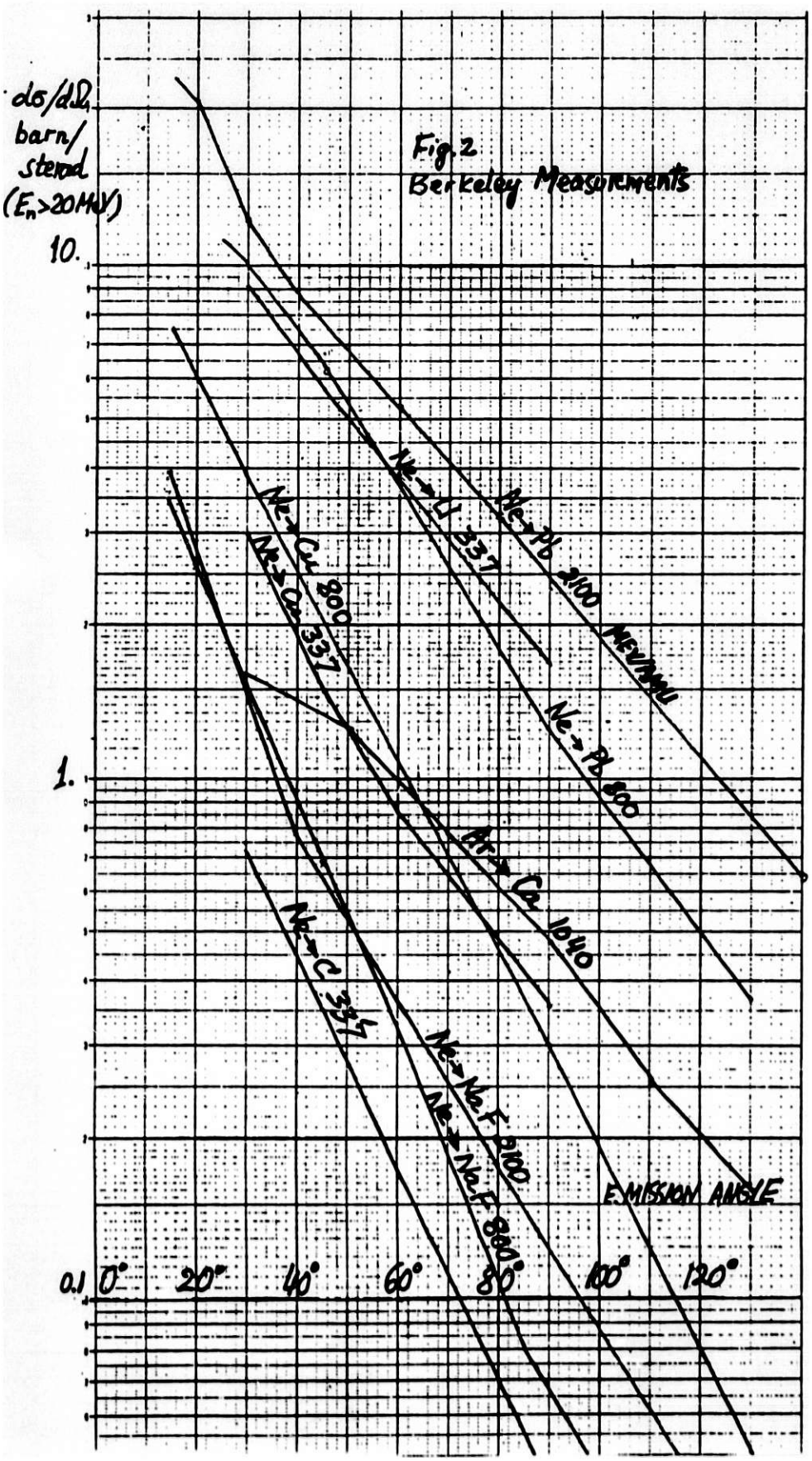
dσ/dΩ, barn/steradian (E_n>20MEV)
10.
1.
0.1
Fig. 2
Berkeley Measurements
Ne→U 337
Ne→Pb 2100 MEV/AMU
Ne→Cu 800
Ne→Cu 337
Ne→Pb 800
Ar→Ca 1040
Ne→C 337
Ne→NaF 2100
Ne→NaF 800
EMISSION ANGLE
0°
20°
40°
60°
80°
100°
120°

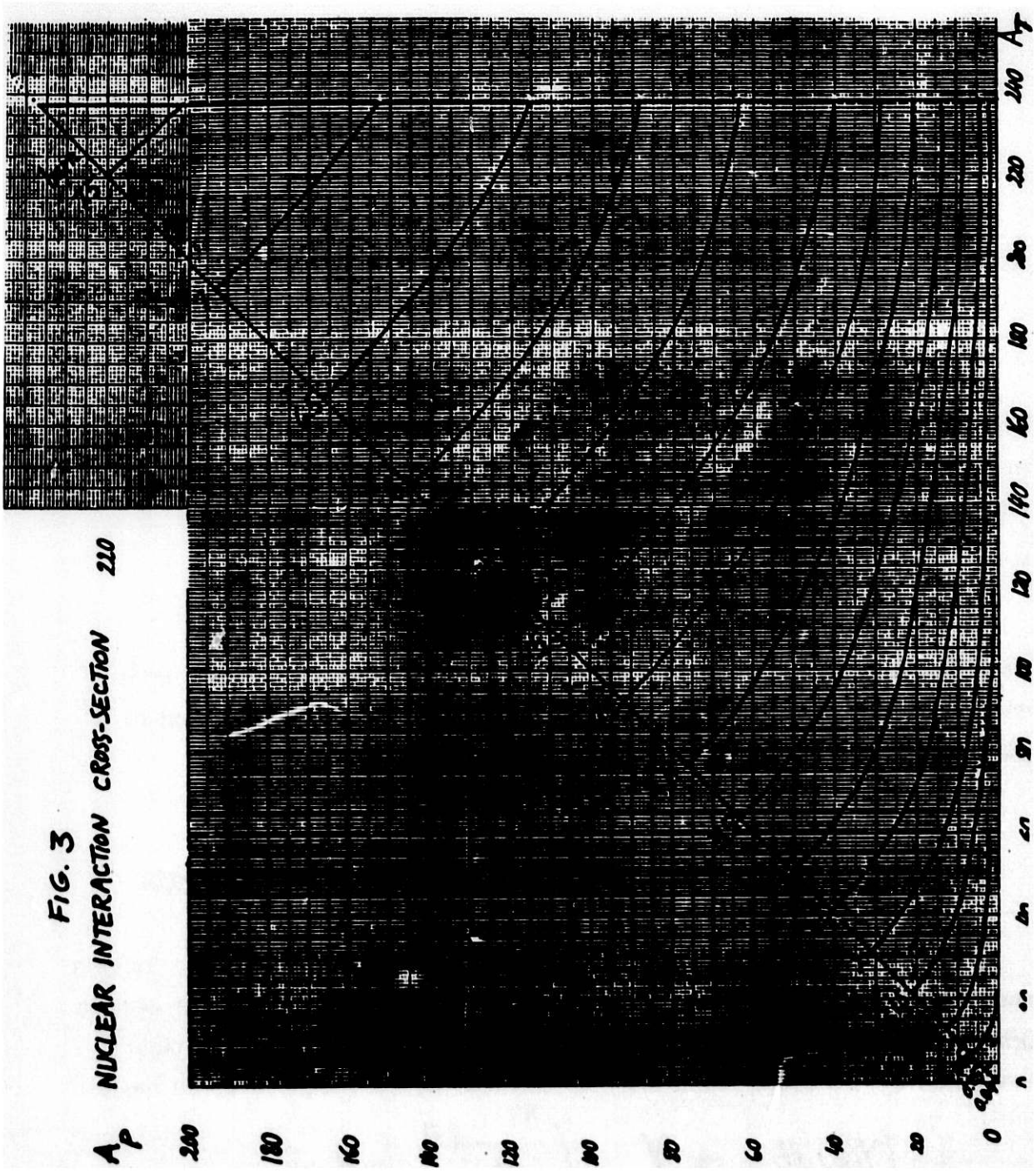
A_P
240
180
160
140
120
100
80
60
40
20
0
A_T
240
220
200
180
160
140
120
100
80
60
40
20
0
NUCLEAR INTERACTION CROSS-SECTION
FIG. 3

The σ_{inel} values given are smaller than the geometric cross-sections. It is a recognized fact that grazing incidence (tangential nuclei) is not enough for inelastic interactions to take place: there must be a volume common to both nuclei.

3. CASCADE NEUTRON YIELD.

The cascade neutron yield at a given angle, as mentioned previously, is given by:

$$Y(\theta) = \frac{1}{\sigma_{inel}} \frac{d\sigma}{d\Omega} \qquad \text{neutron/sterad}$$

The division of the $d\sigma/d\Omega$ values by σ_{inel} has the advantage of grouping the numerical values together. Excepting the forward direction, where neutron emission is always enhanced, the yield then takes the form:

$$Y(\theta) = Y_o\, e^{-k\theta} \qquad \text{neutron/sterad}$$

where Y_o is a mathematical quantity describing the practically exponential decay with θ between 15° and 150°. Practically, it is the intersection of the straight line on linear-log paper with the ordinate axis at $\theta = 0$.

4. TOTAL NUMBER OF CASCADE NEUTRONS PER INTERACTION.

To compare cascade neutron production from various projectiles, targets and energies, it is convenient to take in a simplistic fashion the total neutron production as a figure of merit. This is obtained by integrating the yield multiplied by the proper solid angle differential at each angle over all angles:

$$N = \int Y(\theta)\, d\theta = 2\pi Y_o \int_0^{\pi} e^{-k\theta} \sin\theta\, d\theta$$

$$= 2\pi Y_o (1 - e^{-k\pi}) / (1 + k^2) \simeq 2\pi Y_o / (1 + k^2)$$

The values obtained are plotted in fig. 4 as a function of projectile incident energy for various projectiles and targets.

5. ENERGY DEPENDENCE.

A pattern seems to emerge from fig. 4. which suggests an energy dependence following the expression $E^{0.3}$ in most cases.

6. PROJECTILE, TARGET DEPENDENCE.

The total neutron production N extrapolated or intrapolated from fig. 4 at a common energy of 1,000 MEV/AMU is shown for all targets as a function of projectile mass up to Ar 40 in fig. 5. Neutron production, which begins to increase with projectile mass up to carbon 12, shows a systematic decrease for all targets when going to projectile mass 20 (Neon). This could be explained by the fact that channels involving creation of charged fragments carrying neutrons with them (such as deuterons, alphas and other light atoms) tend to be favored when the projectile mass increases.

As of now there are no known production measurements with projectiles above Ar 40. It would be useful to do such measurements, with heavier atoms in the future.

Pending such measurements, theoretical calculations such as the fire streak and fireball calculations can be applied. Dr. Walt Schimmerling at Berkeley has told me that he is working with Professor Meadey of Kent University on deriving theoretically a formula which will give the inclusive neutron production as a function of projectile and target masses. Inclusive refers in this case to the total number of reaction channels which produce at least one neutron (and in some cases more).

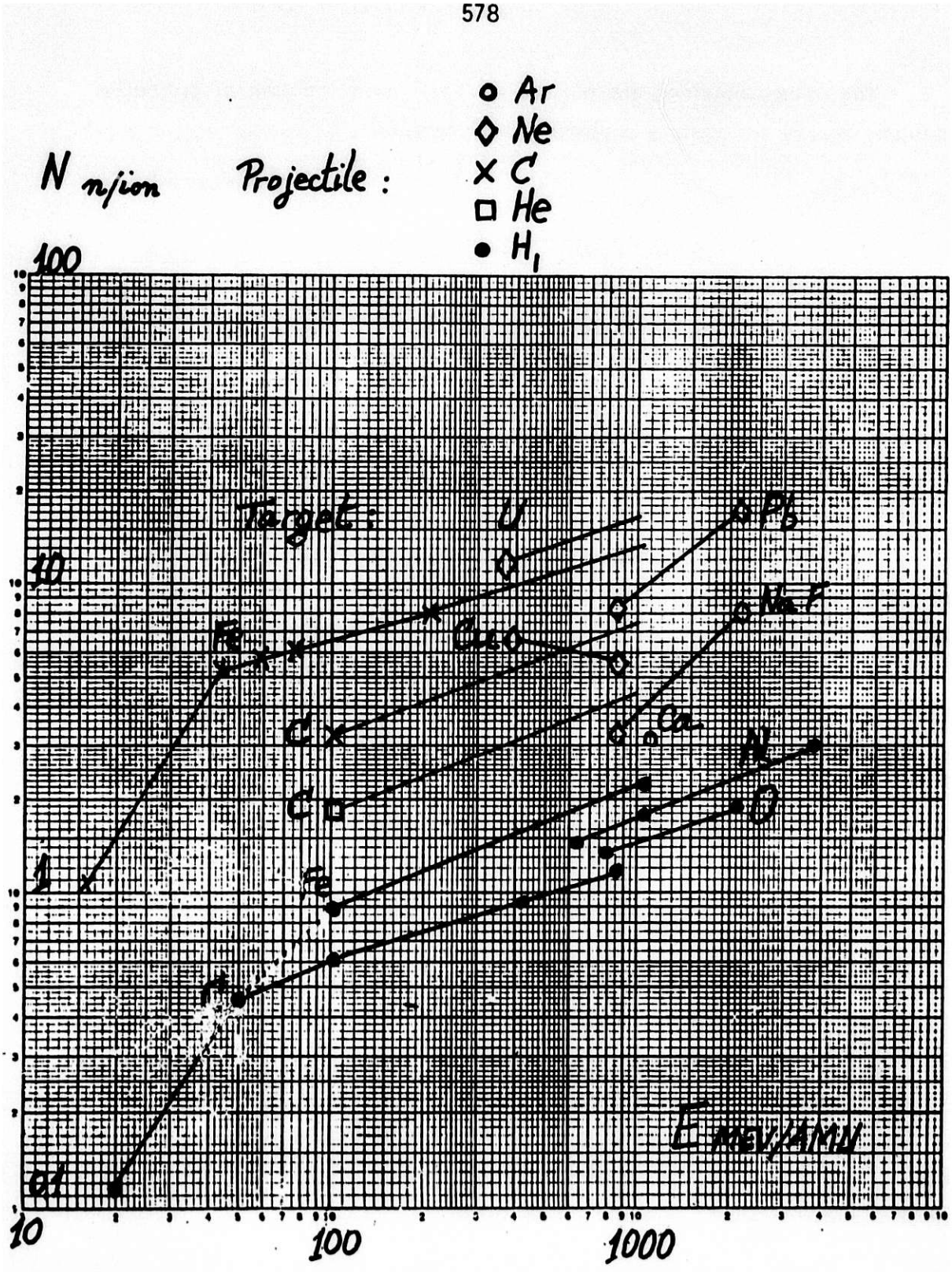

Fig. 4. Cascade neutron production vs projectile energy for various projectiles and targets.

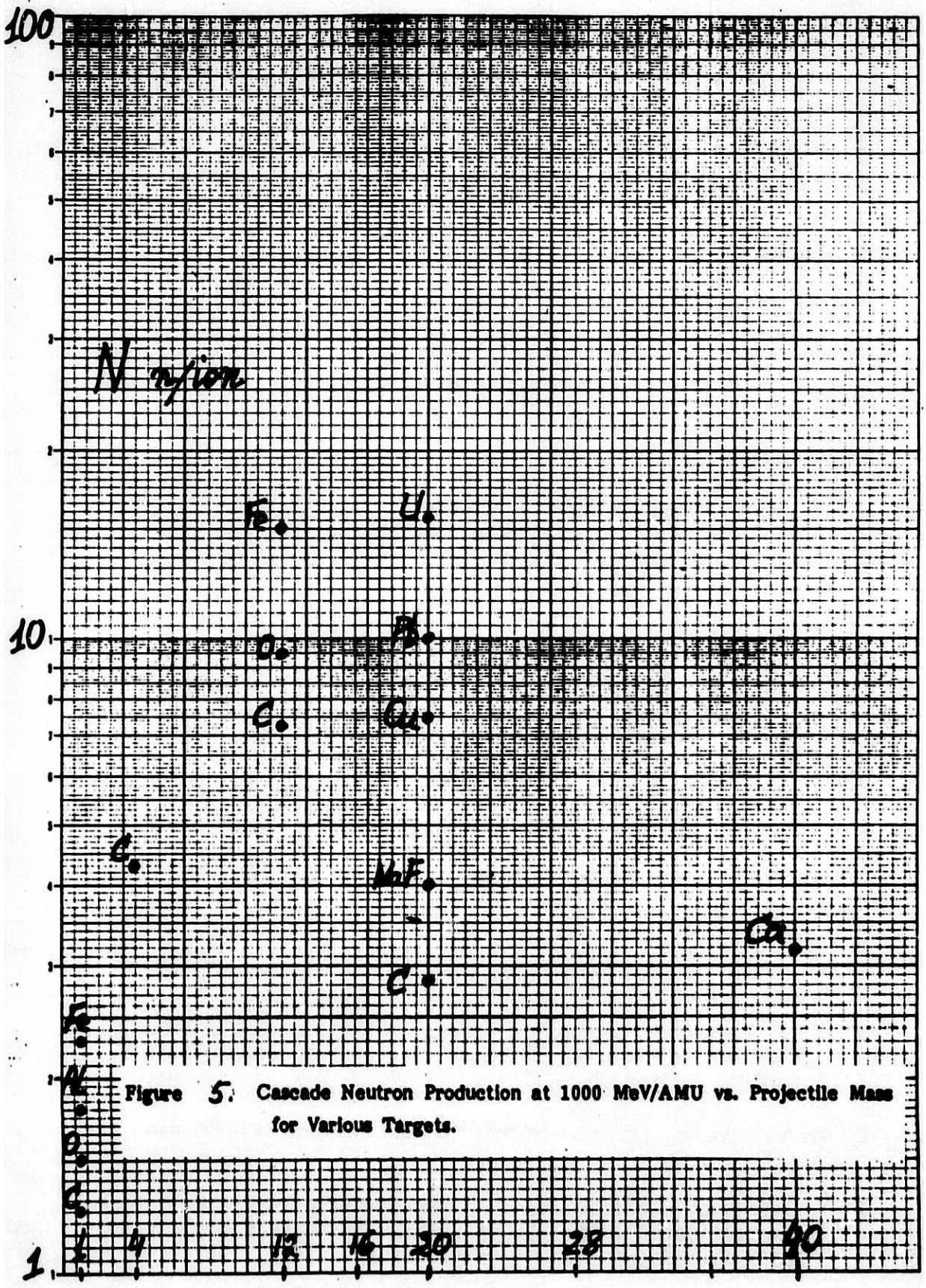

Figure 5. Cascade Neutron Production at 1000 MeV/AMU vs. Projectile Mass for Various Targets.

BIBLIOGRAPHY.

R. G. Alsmiller Jr., R. T. Santoro, J. Barish, Shielding Calculations for a 200 MeV Proton Accelerator and Comparison with Experimental Data, Particle Accelerators 1975, Vol. 7, pp. 1-7.

T. M. Amos, Jr., Neutron Yields from Proton Bombardment of Thick Targets, Thesis, Department of Physics, Michigan State University, EastLansing, 1972.

S. Barshay, C. B. Dover, J. P. Vary, Nucleus-Nucleus Cross-Sections and the Validity of the Factorization Hypothesis at Intermediate and High Energies, Phys. Rev. C, Vol 11, No 2, Feb. 1975, pp. 360-369.

H. W. Bertini, Secondary Particle Spectra from the Interaction of 30-340 MeV Protons on Complex Nuclei ORNL-TM-1652, Feb. 27, 1967, Oak Ridge, TN.

H. W. Bertini, Preliminary Data from Intranuclear-Cascade Calculations of 0.75-, 1-, and 2-GeV Protons on Oxygen, Aluminium and Lead, and 1-GeV Neutrons on the same Elements, ORNL-TM-1996, Oak Ridge National Laboratory, December 1967.

H. W. Bertini et al., HIC-1: a First Approach to the Calculation of Heavy Ion Reactions at Energies above 50 MeV/Nucleon, ORNL-TM-4134, Jan. 1974.

H. W. Bertini, T. A. Gabriel, R. T. Santoro, Predicted Proton Spectrum at Forward Angles for 29.4 GeV Nitrogen on Carbon, Phys. Rev. C, Vol. 9, No. 2, Feb. 1974.

H. W. Bertini, R. T. Santoro, O. W. Hermann, Calculated Nucleon Spectra at Several Angles from 192-, 500-, 700-, and 900- MeV ^{12}C on ^{56}Fe, Phys. Rev. C, Vol. 14, No. 2, Aug. 1976.

H. Blosser, private communication 1980, Michigan State University, East Lansing.

R. Deltenre, European Organization for Nuclear Research, Geneva, Switzerland, private communication, 1971.

W. Everette, Differential Neutron Production Cross-sections vs. Angle for Neon, C, NaF, Cu, Pb, U, unpublished, private communication, Lawrence Berkeley Laboratory, 1982.

D. Graham Foster, Los Alamos Scientific Laboratory, private communication, 1979.

T. A. Gabriel et al, Calculated Secondary Particle Spectra from Alpha-Particle- and Carbon-Induced Nuclear Reactions, ORNL-TM 4334, Oct. 1973, Oak Ridge, TN.

J. Gosset, J. I. Kapusta, G. D. Westfall, Phys. Rev. C 18, 844, 1978.

M. C. Lemaire, S. Nagamiya, O. Chamberlain, G. Shapiro, S. Schnetzer, H. Steiner, I. Tanihata, Table of Light Fragments Inclusive Cross-sections in Relativistic Heavy Ion Collisions, Part I, LBL-8463 UC-34c, Berkeley, Nov. 1978.

Ph. Tardy-Joubert, Etude du Rayonnement Autour d'un Accélérateur de Haute Energie, CEA-R2975, CEN Saclay, France.

A. Sandoval et al., Spectra of p, d, and t from Relativistic Nuclear Collisions, LBL-8771, Berkeley.

R. T. Santoro, private communication, Engineering Physics, Oak Ridge National Laboratory, May 1981.

W. Schimmerling et al., Measurement of the Inclusive Neutron Production by Relativistic Neon Ions on Uranium, Phys. Rev. Letters, Vol 43, No. 27, Dec 31, 1979.

J. W. Wachter, W. R. Burrus, W. A. Gibson, Neutron and Proton, Spectra from Targets Bombarded by 160 MeV Protons, Phys. Rev, Vol. 161, No. 4, Sept. 20, 1967.

ICANS-VI

INTERNATIONAL COLLABORATION ON ADVANCED NEUTRON SOURCES

June 27 - July 2, 1982

MEASURED AND CALCULATED NEUTRON YIELDS FOR 100 MeV PROTONS ON THICK TARGETS OF Pb AND Li

by

R.T. Jones, M.A. Lone, A. Okazaki, B.M. Townes,
D.C. Santry and E.D. Earle
Atomic Energy of Canada Limited
Chalk River Nuclear Laboratories
Chalk River, Ontario K0J 1J0

J.K.P. Lee, J.M. Robson, R.B. Moore and V. Raut
McGill University
Montréal, Québec

ABSTRACT

The neutron yield per proton from thick targets of lead and lithium irradiated with 100 MeV protons has been measured and calculated. The water bath method was used to measure the neutron production, and a Faraday cup for the the beam current determination. Measured yields are 0.343 $\pm$ 0.021 for lead and 0.123 $\pm$ 0.007 for lithium. Corresponding yields calculated with the nucleon-meson transport code NMTC are 0.363 $\pm$ 0.002 and 0.160 $\pm$ 0.001. Measured and calculated thermal neutron distributions in the water bath are also compared.

June 1982

MEASURED AND CALCULATED NEUTRON YIELDS FOR 100 MeV PROTONS ON THICK TARGETS OF Pb and Li

R.T. Jones, M.A. Lone, A. Okazaki, B.M. Townes
D.C. Santry and E.D. Earle
Atomic Energy of Canada Limited
Chalk River Nuclear Laboratories
Chalk River, Ontario K0J 1J0

J.K.P. Lee, J.M. Robson, R.B. Moore and V. Raut
McGill University
Montréal, Québec

1. INTRODUCTION

AECL has a research and development program aimed at constructing an accelerator and neutron producing target for economic breeding of fissile material, the so-called Breeder Accelerator (BA)[1,2]. The planned stages of the program are:

(1) ZEBRA (Zero Energy BReeder Accelerator)

Beam: 300 mA protons at 10 MeV

Purpose: To gain understanding of accelerator operation at high current and low energy.

(2) EMTF (Electronuclear Materials Test Facility)

Beam: 70 mA protons at 200 MeV

Purpose: Further accelerator development and materials testing using neutrons from a Pb-Bi target.
Thermal neutron source for fundamental research. (Flux available $\sim 10^{15}$ n.cm^{-2}.s^{-1})

(3) PILOT BA

Beam: 70 mA protons at 1000 MeV

Purpose: Accelerator development and target blanket development at moderate power levels.

(4) DEMO BA

Beam: 300 mA protons at 1000 MeV

Purpose: Full scale demonstration of electro-nuclear breeding.

The work described here is to help with the design and performance assessment of the target for the EMTF. There are very few measurements of neutron yields from thick targets for protons with energies in the range 50 to 400 MeV. We have measured such yields from targets of lead and lithium for 100 MeV protons. These measurements will provide a benchmark for the computer codes used to design the EMTF target-moderator assembly. We also present results calculated using the codes NMTC and MORSE for the experimental geometry.

2. EXPERIMENTS

2.1 General Description

The 100 MeV proton beam of the McGill Cyclotron was used to irradiate thick targets of Pb (1.6 cm thick by 6.2 cm diameter) and Li enriched to 99.995 wt.% Li-7 (17.4 cm long by 5.7 cm diameter). A large tank of light water surrounding the targets thermalized and captured the neutrons produced and also served as part of the Faraday cup for proton current measurement. The neutron source strength was derived from measurements of the thermal neutron flux distribution in the water.

2.2 Beam Current Measurement

The beam line and target arrangement are shown in Figure 1. The remotely controlled quartz scintillator was used to initially align the

beam and to periodically monitor its alignment and profile during an irradiation. Continuous monitoring of the current on the 2.5 cm ID brass collimator also safeguarded against abrupt changes in beam profile or position and ensured that only the target was irradiated. Post-irradiation autoradiography of a lead target confirmed that the beam spot although not quite circular was only $\sim$1 cm in diameter.

To measure the integrated charge on the target, the target tube and the water tank were electrically connected and insulated from ground to form a large Faraday cup. This was connected to a low impedance, low noise current integrator. Extensive tests were performed to check the accuracy of the current integration.

The current integrator was calibrated with a precision current source which verified its accuracy to $\pm$0.1% on the 10^{-8} and 10^{-9} A ranges. A portable current source was used to measure the effect of the shunt impedance of the Faraday cup with no beam. This made less than 0.4% difference to measurements of currents of about 50 nA.

With the beam on, other systematic errors in the current measurement are possible. Ionization current in the residual gas in the target tube was calculated to be negligible due to the low pressure of the gas and the large length (75 cm) and small diameter (6.3 cm) of the tube. The geometry of the tube also helped to suppress the loss of secondary electrons from the Faraday cup as did permanent magnets placed near its outer end. Leakage of charge from the Faraday cup due to ionization in the target room was measured by stopping the beam upstream in a thick copper block. The beam was adjusted such that the measured radiation level in the target room was similar to that experienced in an actual irradiation. This test indicated a systematic error of less than 0.8%.

Radio frequency pick-up on the Faraday cup was negligible from the cyclotron but considerable from a nearby television transmitter. A π filter in the lead to the integrator reduced this effect by several orders

of magnitude. Residual current due to RF pick-up was of the order of 0.1 nA and was monitored during the irradiation by occasionally switching off the beam. The integrated charge was corrected for this effect which introduced an uncertainty of less than 0.2%. The filter circuit also provided protection against pulse saturation of the integrator due to the pulsed nature of the synchrocyclotron beam.

Typical average beam currents were about 50 nA with an estimated overall uncertainty of less than 1.5%.

2.3 Neutron Yield Measurement

The basis of the method is that the fate of the great majority of neutrons produced in the target is moderation followed by capture in the water bath. A measurement of the volume integrated thermal flux combined with the absorption cross section of water can therefore be equated with the neutron yield, provided the small corrections for leakage, fast neutron absorption, and thermal neutron absorption in other than water can be made.

To minimize leakage a large tank in the form of a vertical cylinder (1.7 m high by 1.5 m diameter) was used (Fig. 2). The back face of the targets was located about 60 cm from the front surface of the tank at its mid-height.

The method chosen to measure the neutron flux was activation of gold foils attached to a lucite frame in the vertical plane above the target tube. About 70 foils of thickness either 0.254 mm or 0.051 mm and diameter 11.3 mm were used, distributed as indicated in Fig. 2. This gives the spatial flux distribution which must be integrated. To minimize the number of foils used most measurements were made in the plane above the target tube. The frame was, however, equipped with arms below and to either side at the position immediately downstream from the target. These enabled azimuthal asymmetries in the flux distribution, due to non uniformities in the beam profile or radial displacement of the beam from the target centre,

to be measured. A correction for azimuthal variation was made to the measured fluxes before integration.

The gamma activity of the foils was counted on an automatic system with two NaI(Tl) detectors connected to counting channels biased at 50 keV. Preliminary data analysis corrected for counter dead time, room background and radioactive decay during and since the irradiation. The efficiency of the counter system for Au-198 activity had been previously established using standardized gold foils of the same diameter as those used here but of different thickness (0.025 mm). A correction for the different gamma-ray absorption in the present foils allowed their Au-198 activity content to be calculated.

To obtain the neutron flux from the activity the effective macroscopic absorption cross section for gold, $\hat{\Sigma}$, is required. We use the Westcott convention[3] to define this

$$\hat{\Sigma} = \hat{\Sigma}_o(GBg + G_r rs)$$

where Σ_o is the macroscopic cross section for 2200 $m \cdot s^{-1}$ neutrons (5.835 cm^{-1}), g and s are the Westcott cross section parameters [defined in (3)], and r is the Westcott epithermal flux index. G and B are factors accounting for thermal neutron flux depression in the foil and in the moderator around the foil, respectively. G_r is a similar quantity to G but for neutrons at the Au-197 resonance energy (4.9 eV).

The epithermal flux index, as a function of distance from the target, was obtained from an irradiation in which some of the foils were covered with cadmium. G_r was calculated from (4) and s taken from (5), the resulting correction for epi-cadmium activation was ~3.6% for 0.254 mm foils and ~6.4% for 0.051 mm foils. Values for the product GB were obtained from subsidiary experiments: GB = 0.715 for 0.254 mm foils and 0.923 for 0.051 mm foils.

3. RESULTS

The measured thermal flux distributions, normalized to a 1 mA proton current, are shown in Figs. 3 and 4. That for the lithium target is much less steeply sloped. This may be ascribed to a higher average neutron energy in the source spectrum and a spatially more distributed source. These fluxes have been corrected for azimuthal variation of the flux measured in the previously described manner. The largest of these corrections was about 10%. This occurred before alignment of the beam was finalized. With better beam alignment the corrections fell in the range 1% to 4%.

To integrate the flux over the measurement volume cubic splines were fitted to the logarithm of the flux. This was done first for the axial (z) distributions at each radius (r) where measurements had been made, then radially. The lines in Figs. 3 and 4 are the fitted splines. Because of the discontinuity in the measurement array caused by the target tube the integration was done for positive and negative z separately. The zero of the z co-ordinate is shown in Figs. 2 and 3.

Various checks were made on the accuracy of the integration method. These included reversing the order of integration (r then z), including measurements at extra radial positions for one irradiation and integrating over all z at once. The results showed systematic differences in the range $\pm$1%.

For the lithium target results it was necessary to extrapolate the fluxes beyond the measurement volume. An exponential extrapolation was used and increased the integral by $\sim$ 5%.

To obtain the neutron absorption rate in the water, the integrated flux is multiplied by the appropriate macroscopic absorption cross section (0.0220 cm^{-1} was used). This can be equated to the neutron source strength

if allowance is made for the small numbers of neutrons lost in other ways. These include thermal neutron absorptions in the target and target tube ($\ll$1% for both targets), absorption of non-thermal neutrons ($\sim$1.4% for Pb target, $\sim$1.9% for Li), and leakage of neutrons of all energies (0.3% for Pb target, 0.5% for Li). The first of these corrections was based on the measured thermal fluxes and known cross sections, the other two were derived from the calculations described in the next section.

The measured neutron yields for three irradiations with Pb targets and one with a Li-7 target are shown in Table 1. The uncertainty in the measurement, derived from the three results for lead, is $\pm$3%. A separate error analysis in which errors were assigned to each of the separate factors needed to derive the measured yield indicated an overall error of $\pm$6%. These estimates are in reasonable agreement since the first cannot detect some systematic effects which were included in the second.

4. CALCULATION OF NEUTRON YIELDS AND FLUXES AND COMPARISON WITH MEASURED VALUES

4.1 Method of Calculation

The calculations for these experiments were performed using a combination of computer codes and nuclear data which were originally set up for accelerator breeder target studies at CRNL.

The (p,n) production and neutron transport down to neutron energies below a 14.9 MeV cut-off energy were computed using NMTC[6], a nucleon-meson transport code. This code employs Monte Carlo techniques to provide a detailed description of the transport process using the intranuclear-cascade-evaporation model of nuclear interactions. The intranuclear-cascade calculation is based on Bertini's medium-energy

intranuclear-cascade code[7], and the evaporation calculation is carried out using a version of Guthrie's evaporation code[8]. Slowing down of charged particles due to excitation and ionization of atomic electrons is treated using the continuous slowing down approximation, and elastic collisions with all nuclei other than hydrogen are neglected. When the neutron energy falls below the 14.9 MeV cut-off its location, energy and direction are stored, and a random sample of these neutrons is used as an input source distribution for the MORSE[9,10] code, which tracks each neutron until it is absorbed or escapes.

A 23-group neutron cross section library for use with the MORSE code was produced using SUPERTOG[11] to derive a 100 group (GAM-II 99 groups + 1 thermal group) cross-section set from ENDF/B-IV data files for each material of interest. Data for each material were combined into an ANISN format P-3 library using DLC-2, and this set was further condensed to 23 groups. The group condensations were done assuming a fission spectrum joined by a 1/E distribution to a 300°K Maxwellian.

4.2 The Experimental Simulation

The CRNL version of the NMTC code can only accommodate cylindrical geometry, and, although the detailed geometry of the beam tube, target tube, target can, and target was represented exactly, the water bath had to be approximated in the NMTC calculation by a concentric cylinder of length 152.4 cm and radius 85.73 cm.

In MORSE calculations the same horizontal beam tube, target tube, target can, and target were represented but the experimental vertical water bath orientation was treated explicitly as a cylinder of 152.4 cm diameter and 171.45 cm height. In both calculations the aluminum tank was ignored.

In order to determine a calculated flux distribution the water bath was split into zones for the MORSE calculations, the mesh chosen being a compromise between providing large enough regions for acceptable statistical accuracy and yet small enough to enable the flux variation to be reasonably defined.

4.3 Results and Comparisons

The calculated neutron yields are shown in Table 1. Agreement with the measured value is good for the lead target but not for the lithium. This is perhaps not surprising since NMTC was designed for targets of heavy nuclei and for proton beams of energy >100 MeV.

To compare the measured fluxes with those from MORSE it was necessary to integrate the measured distribution over the large zones used in the calculation. The same integration method as for the yield calculation was used. For the lead target axial distributions are compared in Fig. 5 and radial in Fig. 6. Normalization is to the same proton current and agreement is generally good. The error bars represent the statistical errors of the Monte Carlo calculation. Similar results for the lithium target are shown in Figs. 7 and 8. Here the agreement is not good; even if the difference in neutron yield is removed by renormalization, the calculated fluxes clearly fall off more rapidly than the measured.

5. CONCLUSIONS AND FUTURE PLANS

We have measured the neutron yield from thick targets of Pb and Li-7 irradiated with 100 MeV protons with a precision of about $\pm$6%. The computer code NMTC calculates a neutron yield from the high mass number target which is in satisfactory agreement with the measured value. This is not true of the Li-7 target where the calculated value is some 33% higher than that measured. The combination of codes NMTC and MORSE provide a satisfactory description of the thermal neutron distribution in light water moderator surrounding the Pb target. For the Li-7 target they predict a

more rapid fall off of the flux than is observed. This is consistent with the calculated neutron source spectrum being too soft.

We plan future measurements on both light (Be,D_2O) and heavy (U,Th) target materials. It is also expected that we will measure yields from accelerator structural materials such as the medium-weight elements Cu and Fe.

6. REFERENCES

1. G.A. Bartholomew, Research Opportunities with Prototype Accelerators for an Accelerator Breeder, Proc. ICANS-V, Julich, June 1981.

2. J.S. Fraser et al., A Review of Prospects for an Accelerator Breeder, Atomic Energy of Canada Limited, Report AECL-7260, 1981.

3. C.H. Westcott et al., Effective Cross Sections and Cadmium Ratios for the Neutron Spectra of Thermal Reactors, Atomic Energy of Canada Limited, Report AECL-612, 1958.

4. G.M. Roe, The Absorption of Neutrons in Doppler Resonances, KAPL-1241, (1954).

5. C.B. Bigham et al., Experimental Effective Fission Cross Sections and Neutron Spectra on a Uranium Fuel Rod, Part II, Atomic Energy of Canada Limited, Report AECL-1350, 1961.

6. W.A. Coleman and T.W. Armstrong, The Nucleon-Meson Transport Code NMTC, ORNL-4606, 1970.

7. H.W. Bertini, Intranuclear-Cascade Calculation of the Secondary Nuclear Spectra from Nuclear-Nucleus Interactions in the Energy Range 340 to 2900 MeV and Comparison with Experiment, Phys. Rev. 188, 1711, 1969.

8. M.P. Guthrie, EVAP-4: Another Modification of a Code to Calculate Particle Evaporation from Excited Compound Nuclei, ORNL-TM-3119, 1970.

9. E.A. Straker, P.N. Stevens, D.C. Irving and V.R. Cain, The MORSE Code - A Multigroup Neutron and Gamma-Ray Monte Carlo Transport Code, ORNL-4585, 1970.

10. E.A. Straker, W.H. Scott Jr. and N.R. Byrn, The MORSE Code with Combinatorial Geometry, DNA-2860 T, 1972.

11. R.Q. Wright, N.M. Greene, J.L. Lucius and C.W. Craven Jr. SUPERTOG: A program to Generate Fine Group Constants and Pn Scattering Matrices from ENDF/B, ORNL-TM-2679, Rev. 1973.

TABLE 1

Measured and Calculated Neutron Yields

Target Material	Au Foil Thickness Used (mm)	Measured Yield (n/p)	Calculated Yield (n/p)
Pb	0.254	0.330	0.363 ± 0.002
"	0.254	0.346	
"	0.051	0.353	
Li-7	0.254	0.123	0.160 ± 0.001

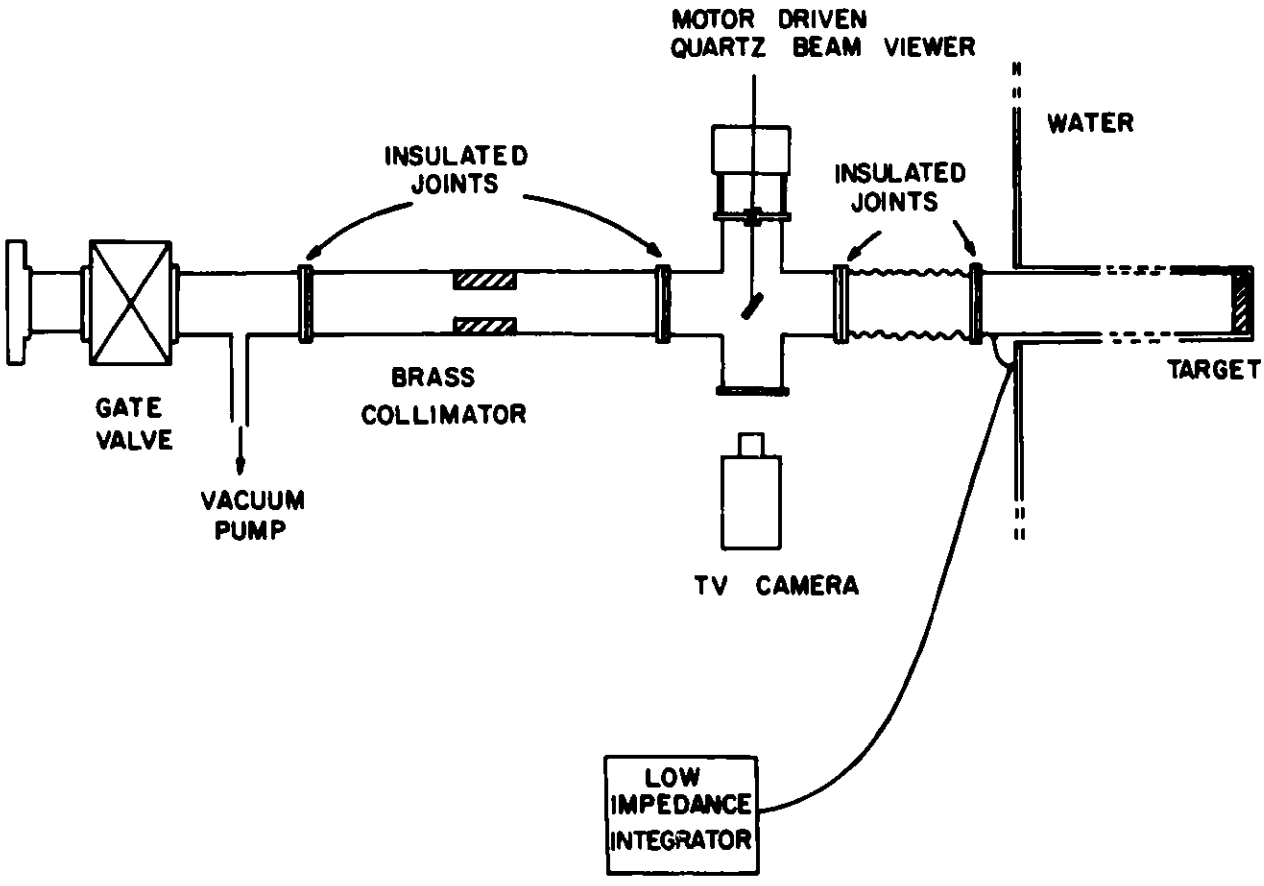

Fig. 1: Beam Line and Target Arrangement

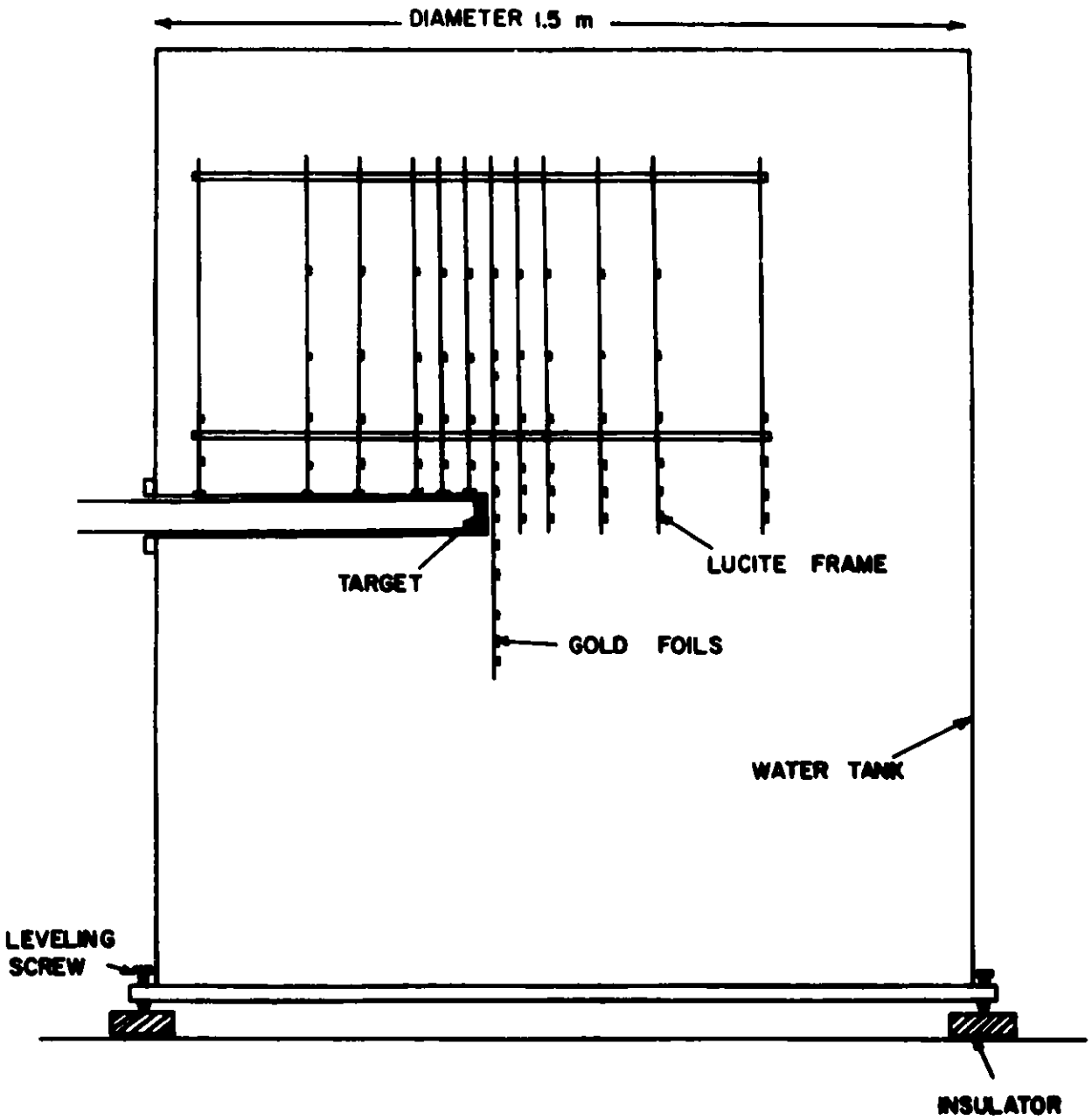

Fig. 2: Water Tank and Foil Array

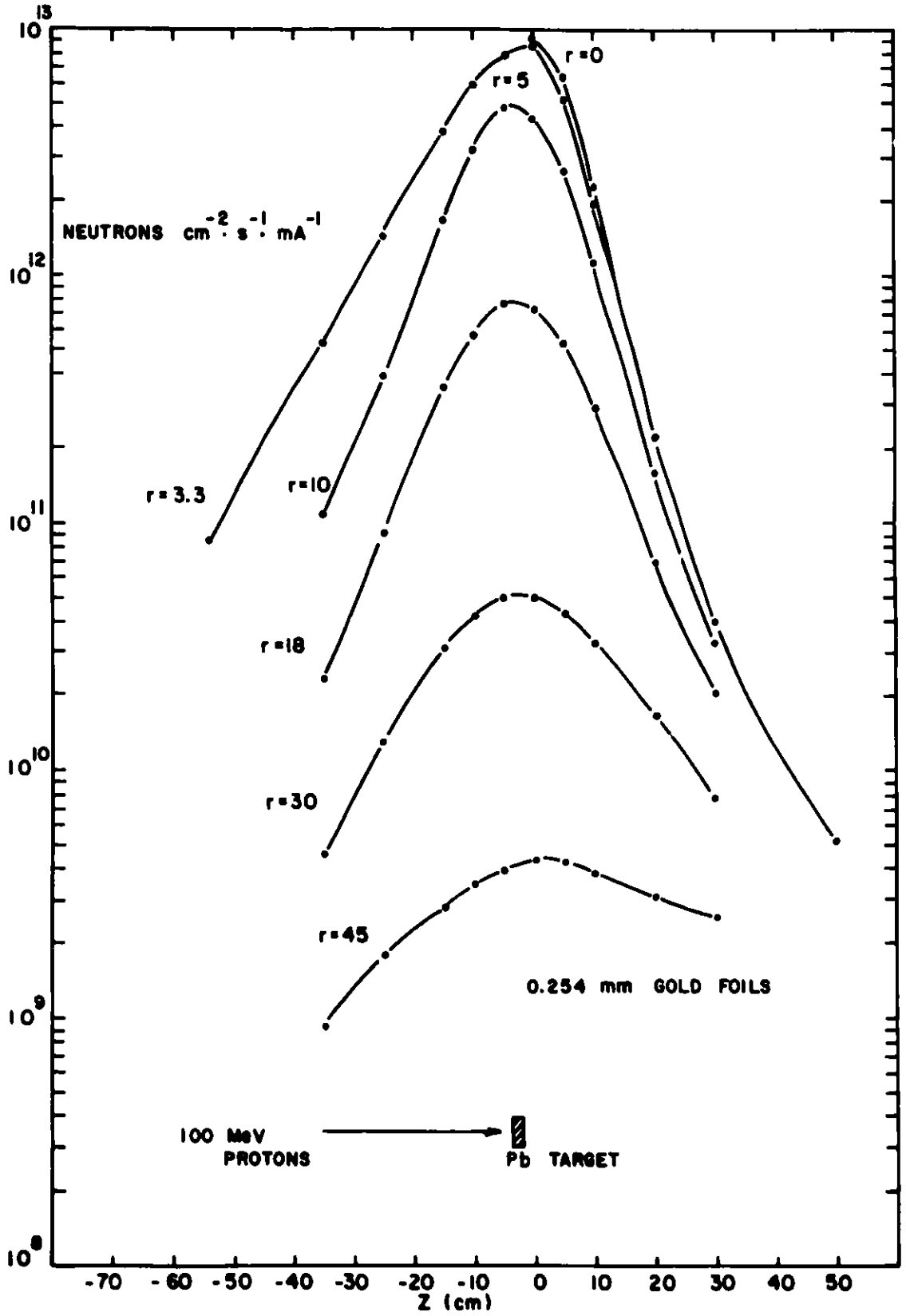

Fig. 3: Thermal Neutron Flux Distribution (Pb Target)

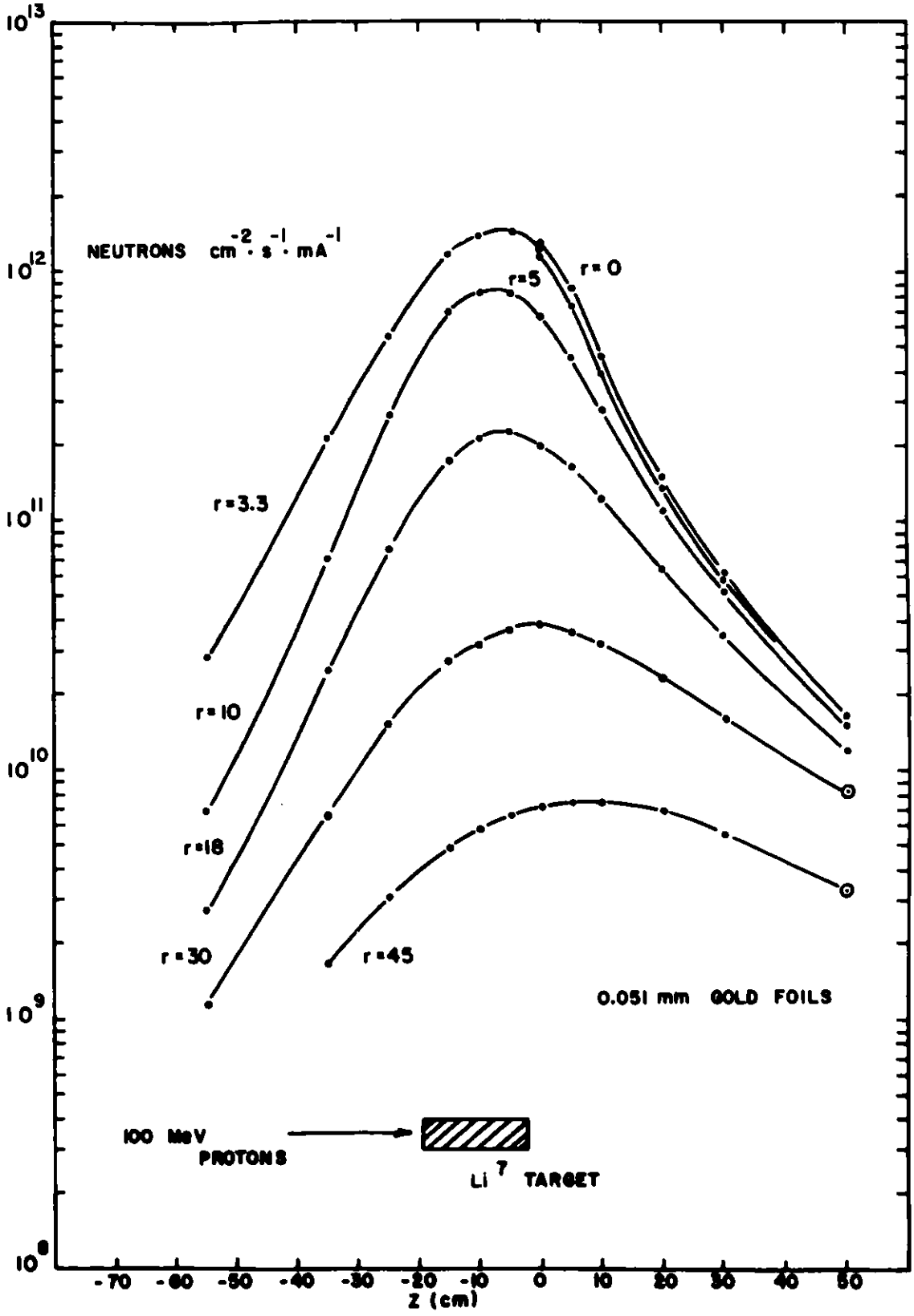

Fig. 4: Thermal Neutron Flux Distribution (Li-7 Target)

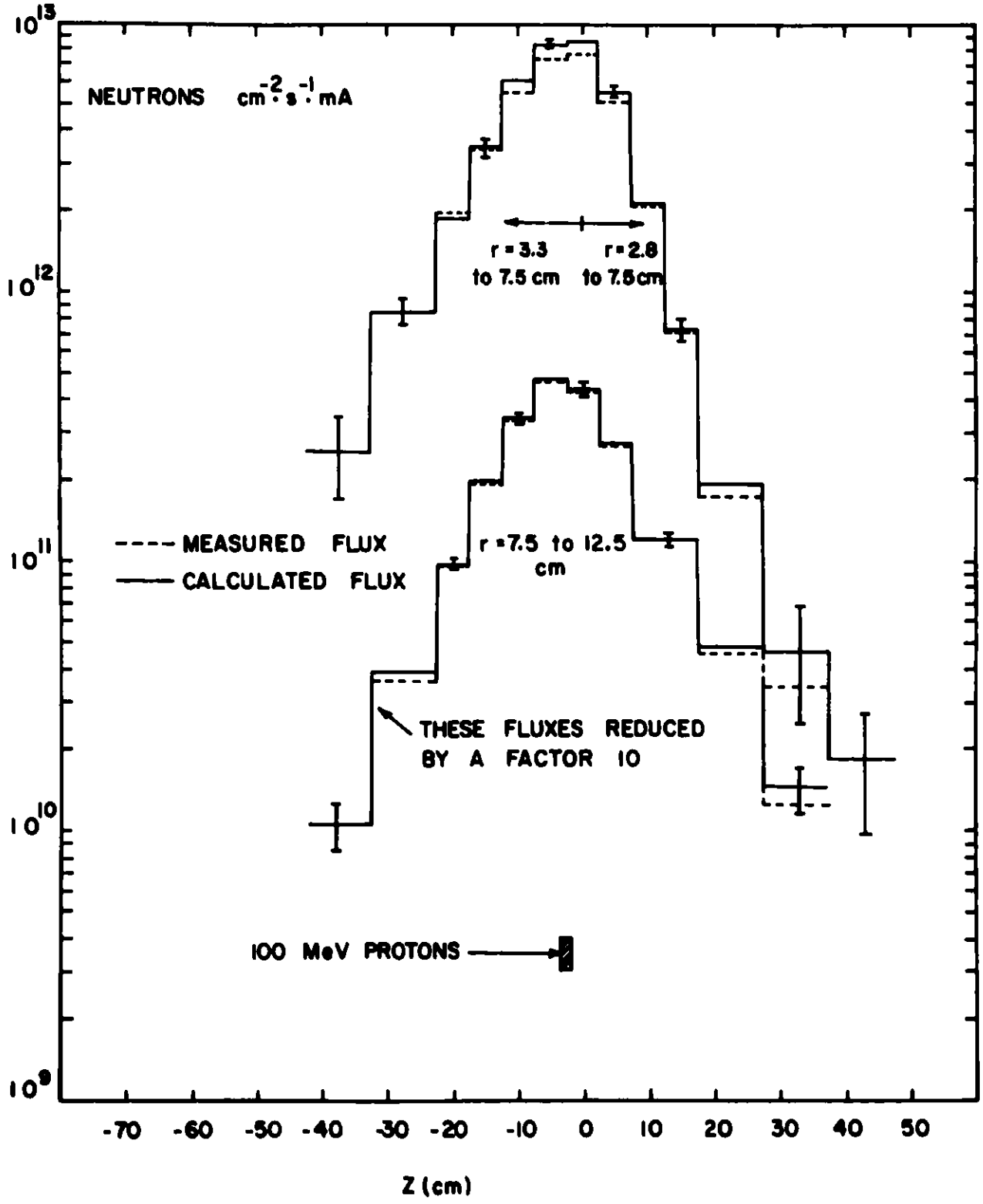

Fig. 5: Comparison of Axial Flux Distributions (Pb Target)

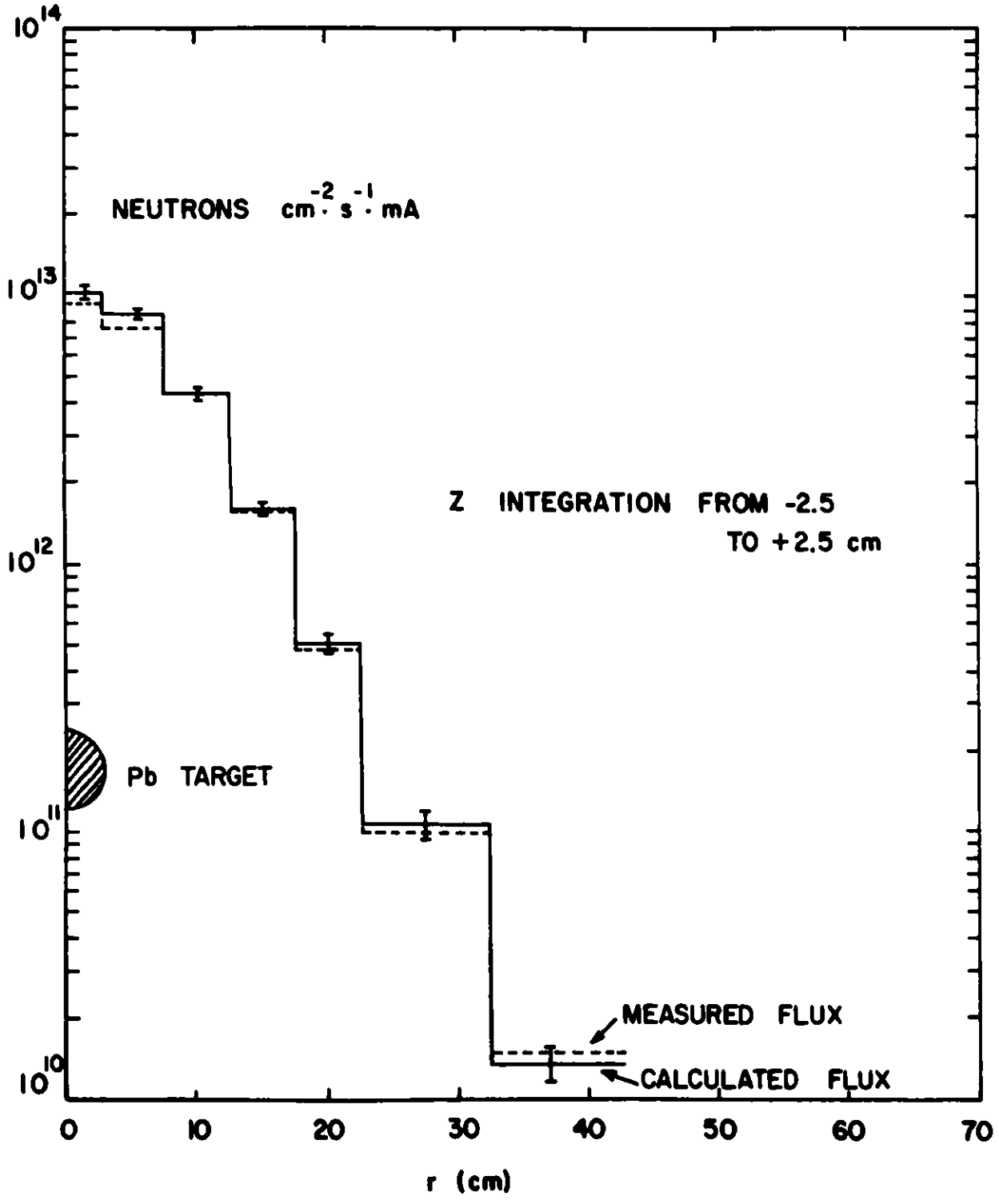

Fig. 6: Comparison of Radial Flux Distributions (Pb Target)

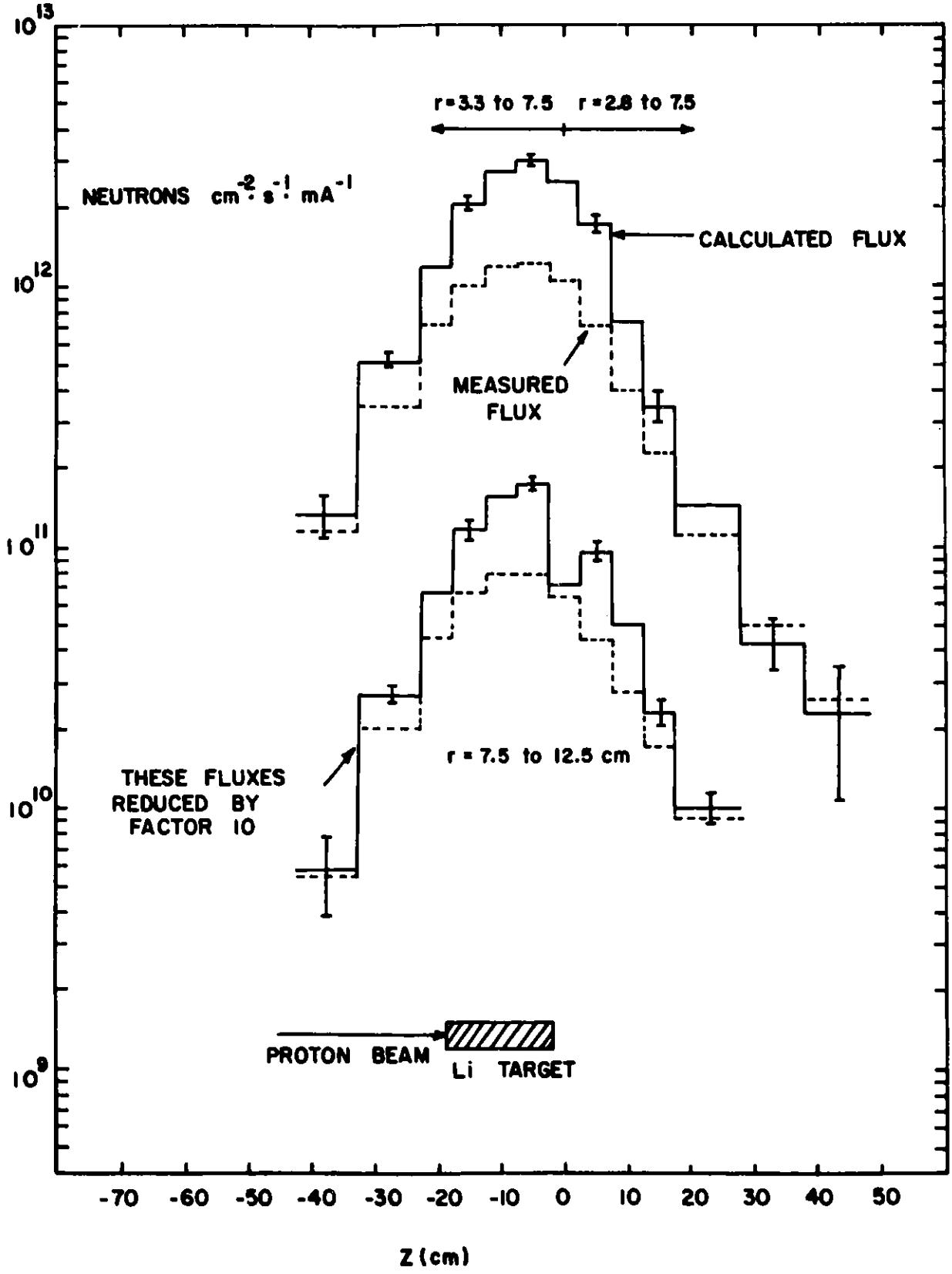

Fig. 7: Comparison of Axial Flux Distributions (Li-7 Target)

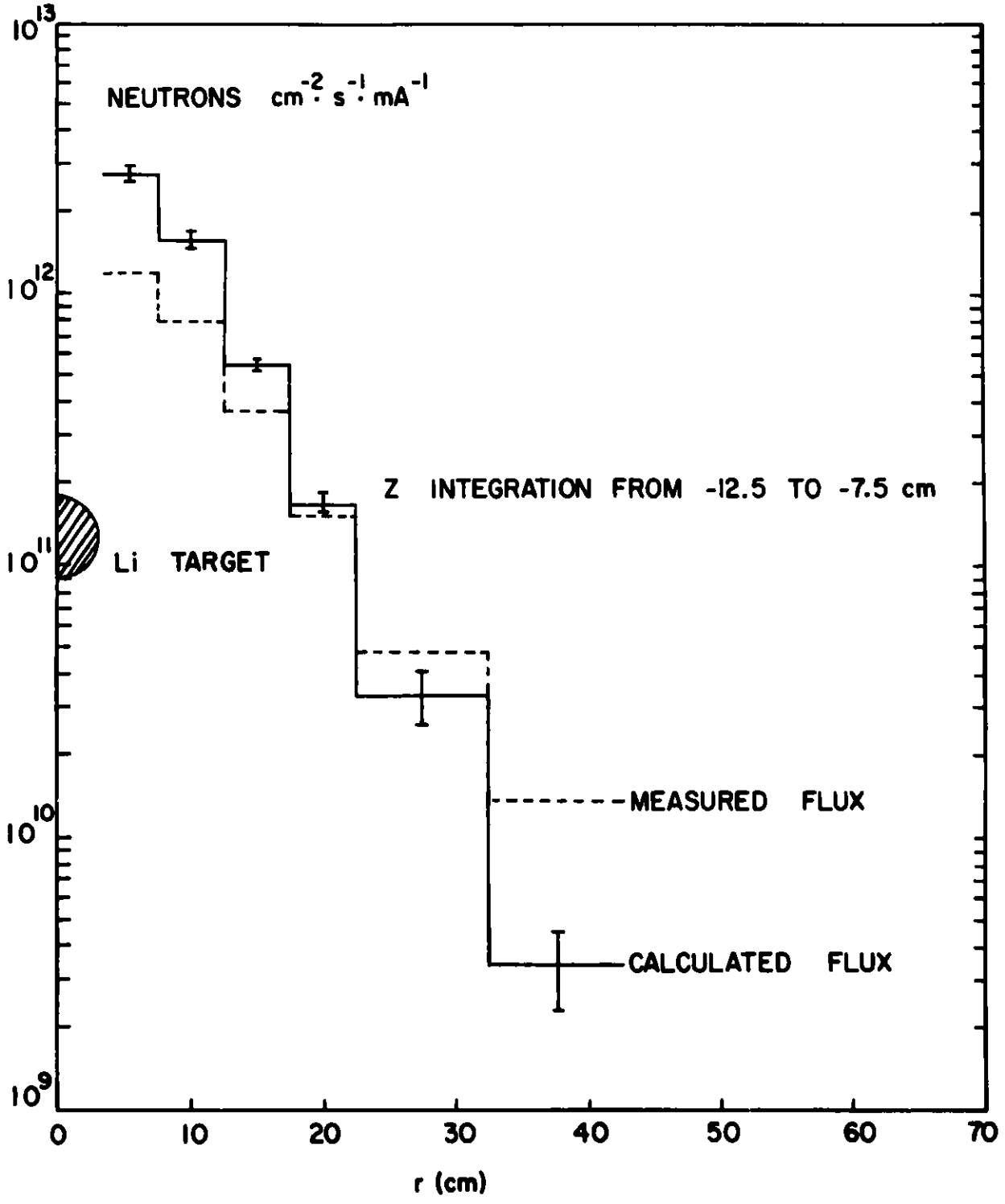

Fig. 8: Comparison of Radial Flux Distributions (Li-7 Target)

ICANS-VI

INTERNATIONAL COLLABORATION ON ADVANCED NEUTRON SOURCES

June 27 - July 2, 1982

METHODS OF NEUTRON AND PROTON DOSIMETRY AT SPALLATION SOURCES

L. R. Greenwood and R. J. Popek

Argonne National Laboratory

ABSTRACT

A variety of techniques are being developed to measure the neutron and proton fluxes and energy spectra at spallation neutron sources. Multiple-activation dosimetry is being used to adjust the neutron energy spectrum by a least-squares procedure. Primary beam protons are measured by the $^{27}Al(p,*)^{22}Na$ reaction and secondary protons by (p,n) reactions on ^{7}Li, ^{51}V, and ^{65}Cu. Lithium fluoride thermoluminescent dosimeters are used to measure the neutron dose rate, although we have been unable to determine the much weaker gamma dose rate. Neutron fluxes, displacement damage, gas production and transmutation, and dose rates are now routinely determined for materials irradiations with uncertainties of 10-15%.

METHODS OF NEUTRON AND PROTON DOSIMETRY AT SPALLATION SOURCES

L. R. Greenwood and R. J. Popek
Argonne National Laboratory

1. INTRODUCTION

In order to understand radiation damage measurements at spallation neutron sources, we need to fully characterize these facilities in terms of neutron flux and energy spectra and the resultant displacement damage, transmutation, and dose rate. A companion paper at this conference[1] describes the results of such measurements[2] at the Radiation Effects Facility (REF) of the Intense Pulsed Neutron Source (IPNS) at Argonne National Laboratory. The present paper discusses the techniques used in these measurements.

Neutron flux and spectral measurements were made using the multiple-activation technique.[3] This method has been developed for fusion material irradiations and has been successfully applied in a wide variety of neutron sources including fission reactors, 14 MeV T(d,n) sources, and Be(d,n) sources.[4] This method measures activation products induced simultaneously in a number of materials. These integral activities are chosen to span all neutron energy regions of interest. Each integral is equal to the neutron flux-spectrum times the activation cross section. The flux-spectrum is then adjusted to obtain the best fit to the integral measurements. The final neutron spectrum is then used to calculate damage parameters. This can be done routinely with integral uncertainties of ±10 - 15%.

2. NEUTRON FLUX AND SPECTRAL MEASUREMENTS

In order to obtain the best analysis of the IPNS neutron spectrum, more than 30 different activation products were measured using Ge(Li) gamma spectrometry. Twenty-eight reactions were used to adjust the neutron flux

spectrum.[1] The starting spectrum was calculated with the HETC[5] and VIM[6] computer codes. The spectral adjustment was performed with the STAYSL computer code.[7] In this technique uncertainties and covariances are assigned to the integral activities, activation cross sections, and starting spectrum. A simultaneous least-squares adjustment is then made to all of the data. Cross sections were taken from ENDF/B-V[8] and extended to 44 MeV[9] using available data and calculations.

The resultant flux spectra are shown in Figures 1 and 2. Figure 1 shows the spectrum for the REF (VT2) and Figure 2 compares spectra for the REF and NSF targets. This latter difference is due to the moderators, Pb for the REF and C-Be for the NSF. These data are summarized in Table I. Flux gradients were also measured, as discussed in reference 1. Typical gradients are shown in Figures 3 and 4. Clearly, dosimetry is probably required in most materials experiments to precisely locate samples in the rather steep flux and spectral gradients.

Table I. Neutron Fluxes at IPNS
Neutrons/m^2-proton (400 MeV)

Energy, MeV	REF (VT2)	NSF (H2)
Total	218	194
>0.1 MeV	151	55
Thermal	1.2	44
<1	157	180
1-5	51	10.8
5-10	4.4	1.04
10-20	1.54	0.45
>20	4.0	1.3

Several problems were considered which might interfere with this technique. First of all, if protons are present as well as neutrons, then confusion is possible as to the source of reaction products. For example, a (p,d) reaction is indistinguishable from a (n,2n) reaction. Fortunately, the proton flux is quite low, as discussed in section 4. Hence, proton interference is generally less than 1%. Secondly, our present activation cross sections do not extend above 44 MeV. This high energy flux can be neglected for all of the reactions we have used since both the cross sections and fluxes are very weak above 44 MeV. The only exception to this rule is that we apparently see interference with (n, α) reactions from high-energy spallation products. Activation rates from ^{54}Fe, ^{63}Cu, and ^{60}Co were all much higher than expected (40-80%). The most likely explanation is that the activation products can also be produced by spallation from the neglected high-energy neutrons. As proof of this we note that the worst cases appear to be those elements which have the least abundant isotopes (i.e., ^{54}Fe (n,α) may be overshadowed by ^{56}Fe spallation).

On the other hand, spallation cross sections could be extremely valuable in defining the neutron spectrum above 30 MeV. J. Routti and J. Sandberg have recently demonstrated this technique using spallation products from copper.[10] We have observed these spallation products in many of our materials and plan to develop this technique, although the cross sections are not very well known. In general, neutron cross sections are very poorly known above 20 MeV, a fact which hampers neutronic and shielding calculations as well as dosimetry.

3. PROTON BEAM DOSIMETRY

The $^{27}Al(p,*)^{22}Na$ reaction has been used to monitor the direct proton beam. Originally this was done to measure beam profiles and currents. However, with improvements in the beam monitoring system we are now able to study the cross section. The measurements were performed by placing a stack of three Al foils (5 mils thick, 4" by 4" square) directly in the proton beam. The center foil was then gamma counted, the others being used to correct for recoil losses. We have focused on ^{22}Na since we want a long-lived monitor for irradiations lasting a week or more. Thus, ^{24}Na is too short-lived. We also measure ^{7}Be; however, the data has not been repeatable, possibly due to the longer recoil ranges of ^{7}Be ions compared to those for ^{22}Na.

The results of several measurements are listed in Table II. As can be seen the ^{22}Na results are quite consistently lower than measurements with the toroids and faraday cup. The ^{22}Na yield was taken from a French evaluation.[11] Our results indicate that the most likely cross section at 400 MeV is 13.4 mb (±10%), considerably lower than the recommended value of 17.8 mb.

Table II. $^{27}Al(p,*)^{22}Na$ Cross Section Measurements

Proton Energy = 400 MeV
Previous Cross Section = 17.8 mb

Date	Protons, x 10^{17}		Ratio
	^{22}Na	Toroid	(^{22}Na/Toroid)
11-16-81	1.20	1.63	0.74
11-20-81	1.32	1.72	0.77
02-08-82	16.4	21.9	0.75
		Average =	0.75

Adjusted cross section = 13.4 mb (±10%)

4. SECONDARY PROTON DOSIMETRY

As mentioned previously, some concern was raised over the possibility of protons interferring with neutron dosimetry measurements. Another more serious concern is that low energy protons may deposit very high energy losses in insulators under study for radiation damage. The following measurements show that neither of these effects are significant.

In order to measure secondary proton fluxes, several materials were irradiated to look for (p,n) reactions. The $^{65}Cu(p,n)^{65}Zn$ and $^{51}V(p,n)^{51}Cr$ reactions gave the best results, mainly since neither target has any strong neutron-activation products, except from spallation. The $^{56}Fe(n,p)^{56}Co$ reaction is overwhelmed by neutron activities. Lithium fluoride was also tried; however, ^{7}Be from the $^{7}Li(p,n)$ reaction appears to be weaker than the ^{7}Be produced by spallation in fluorine. The Cu and V results are listed in Table III.

Table III. Secondary Proton Dosimetry
REF-VT2-400 MeV
Pb Absorption Result < E > ≈100 MeV

Reaction	Rate/μC (x 10^{-18})	σ, mb	Flux/cm^2-μC (x 10^8)
$^{51}V(p,n)^{51}Cr$	2.41	10-20	∿1.6
$^{65}Cu(p,n)^{65}Zn$	2.50	10-20	∿1.7
$^{58}Ni(n,p)^{58}Co$	5493.	40.8	1346.

Secondary protons/neutrons ∿1/800

Flux at 10 μA: neutrons: 1.3 x 10^{12} n/cm^2-s
protons: ∿1.6 x 10^9 p/cm^2-s

Since these two reactions have very similar thresholds and cross section values, little can be deduced about proton fluxes or energies. Another experiment was thus performed where the Cu and V samples were embedded at 16 locations in a lead cylinder measuring 1-7/8" in diameter by 3" long. Although these samples are still being analyzed, preliminary results indicate a rather even distribution of ^{65}Zn. This implies that the protons must have rather high energies, certainly above 100 MeV and more likely 150-200 MeV. The even distribution is then explained since the decrease in proton flux across the cylinder is balanced by the increase in cross section as the protons lose energy. Each of these effects is roughly a factor of two for our experimental geometry.

Since we know that the protons must have an average energy above 100 MeV, then the (p,n) activation cross sections must be in the 10-20 mb range (although neither reaction is well-known at 100-200 MeV). The proton flux must thus be about 1.6×10^8 protons/cm^2-μC or about 1.6×10^9 protons/cm^2-s at 10 μA beam current. This secondary proton flux is only about 1/800 of the neutron flux, as shown in Table III. These measurements are still in progress and we hope to refine our knowledge of the secondary proton flux. In any case, the present results indicate that these protons are of little concern to radiation damage and dosimetry measurements. The most likely explanation for these particles is that we are seeing protons elastically or inelastically scattered from the target and that these nearly 400 MeV protons lose about 200 MeV in the uranium target and lead moderator before we detect them.

5. DOSE MEASUREMENTS

Insulator irradiations now being done for the fusion materials program require knowledge of the total dose deposited in the samples. This dose is primarily due to neutrons, but may be weakly influenced by gammas, protons, or other charged particles. Thermoluminiscent dosimeters (LiF-TLD700) were irradiated in an attempt to more accurately determine dose rates. These dosimeters were calibrated at known ^{226}Ra and ^{60}Co sources prior to their use at IPNS. The samples were irradiated in polyethelene tubing.

Nickel wires were also irradiated to determine the neutron flux using the $^{58}Ni(n,p)^{58}Co$ reaction. In order not to saturate the dosimeters it was necessary to reduce the IPNS beam-cycling rate to 1 hertz (normally 30 hz) and to expose the samples for only 1-15 minutes.

The TLD results are listed in Table IV along with background gamma

Table IV. Dose Measurements at IPNS
LiF - TLD 700
E_p = 400 MeV; 1 Hz; ~7 x 10^{13} P

Location (REF)	Dose (Rads/μC) Exp. (±10%)	Calc. (neutron) (±15%)
VT2	18.7	19.1
VT1	17.0	18.1

Background Gamma Dose

Run Time (m)	Gamma Dose, R/hr (±10%) Pre-Run	Post-Run
1	77	92
15	82	150

doses before and after short irradiations at reduced (1/30) beam power. The calculated doses (neutron only) were determined by averaging ^{7}Li and F Kerma factors[12] over our measured neutron spectra, normalized to the $^{58}Ni(n,p)$ activation rate. As can be seen, the calculations overpredict the measured rates, although values agree within the estimated errors. One possible source of this overprediction is that the kerma factors include the full beta-particle energies even though our samples (1 mm OD by 6 mm long) will not stop all of the betas. We estimate that this effect might reduce our calculated values by as much as 10%, although more exact calculations have not been performed. In any case, it would appear that most of the dose seen in the TLD's is due to neutrons. Estimates of the gamma flux[13] suggest that the gamma dose should be no more than 10-20% of the neutron dose and we have already shown that secondary protons are negligable. Nevertheless, it would appear that TLD measurements and calculations are not sufficiently accurate at present to really measure the weaker gamma dose and other techniques may be needed.

6. CONCLUSIONS

Techniques have been developed to characterize neutron and proton fluxes and energy spectra at spallation neutron sources. Routine neutron measurements are now being performed to provide materials experimenters with exposure data including calculated displacement, transmutation, and dose rates. These integral parameters can generally be determined to ±10-15% accuracy, although some problems remain. In particular, nuclear cross sections need further development above 20 MeV. Spallation cross sections (e.g., for Cu) would be especially useful and might allow us to extend the spectral adjustment technique up to the proton beam energy. Further work is also needed to measure the gamma flux at spallation sources. The use of TLD's

is questionable for this purpose due to uncertainties in the measurements and calculations. Proton dosimetry also could be improved with more nuclear reactions and better dosimetry. Work is continuing in all of these areas, although we feel that the IPNS is now sufficiently well-characterized for routine materials experiments.

REFERENCES

1. R. C. Birtcher, M. A. Kirk, T. H. Blewitt, and L. R. Greenwood, Measurement of Neutron Spectra and Fluxes at the IPNS Radiation Effects Facility, proceedings of this conference.
2. M. A. Kirk, R. C. Birtcher, T. H. Blewitt, L. R. Greenwood, R. J. Popek, and R. R. Heinrich, J. Nucl. Mater. 96, (1981) 37.
3. L. R. Greenwood, Review of Source Characterization for Fusion Materials Irradiations, BNL-NCS-51245, (1980) 75.
4. L. R. Greenwood, R. R. Heinrich, M. J. Saltmarch, and C. B. Fulmer, Nucl. Sci. Eng. 72, (1979) 175.
5. K. C. Chandler and T. W. Armstrong, Oak Ridge National Laboratory Report, ORNL-4744 (1972).
6. F. M. Gelbard and R. E. Prael, Argonne National Laboratory Report, ANL-75-2 (1974).
7. F. G. Perey, Least-Squares Dosimetry Unfolding: The Program STAYSL, ORNL-TM-6062 (1977); modified by L. R. Greenwood (1979).
8. Evaluated Nuclear Data File, Part B, Version V, National Neutron Cross-Section Center, Brookhaven National Laboratory (1979).
9. L. R. Greenwood, "Extrapolated Neutron Activation Cross-Sections for Dosimetry to 44 MeV", ANL-FPP-TM-115 (1979).

10. J. T. Routti and J. V. Sandberg, Computer Physics Communications 21, (1980) 119.

11. J. Tobailem, C. H. Lassus-St. Genies, and L. Leveque, CEA Report-N-1446 (1971).

12. M. A. Abdou, Y. Gohar, and R. Q. Wright, MACK-IV; A Program to Calculate Nuclear Response Functions from Data in ENDF/B Format, Argonne National Laboratory Report, ANL-FPP-77-5 (1978).

13. M. Kimura, J. M. Carpenter, and D. F. R. Mildner, Calculations of the Heat Deposition and the Expected Rate of Temperature Rise in Moderator, Reflector, and Decoupler Materials at IPNS-I, Argonne National Laboratory Report, ANL-81-22 (1981).

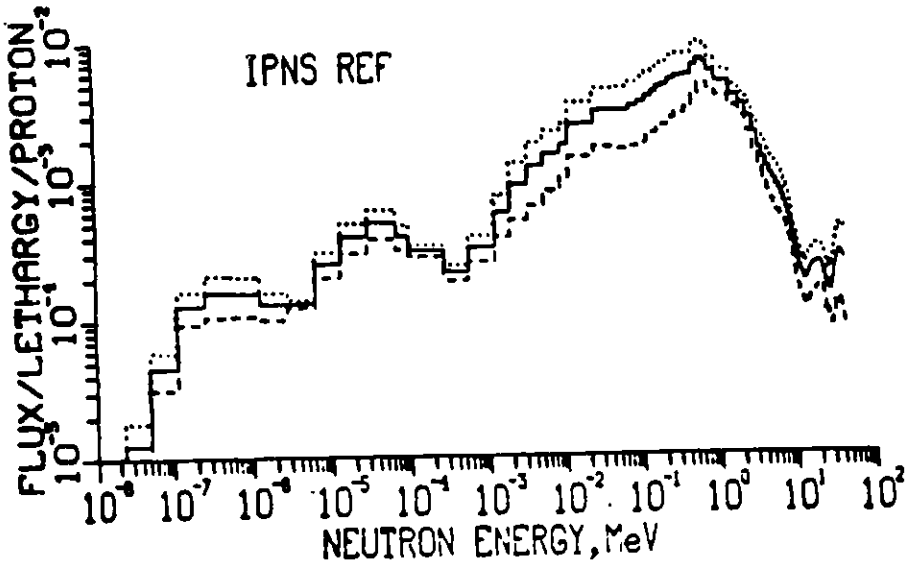

Figure 1. Neutron spectrum unfolded at the Intense Pulsed Neutron Source. The dotted and dashed lines represent one standard deviation. At least 28 activation reactions were measured. The spectrum extends to 500 MeV (not shown).

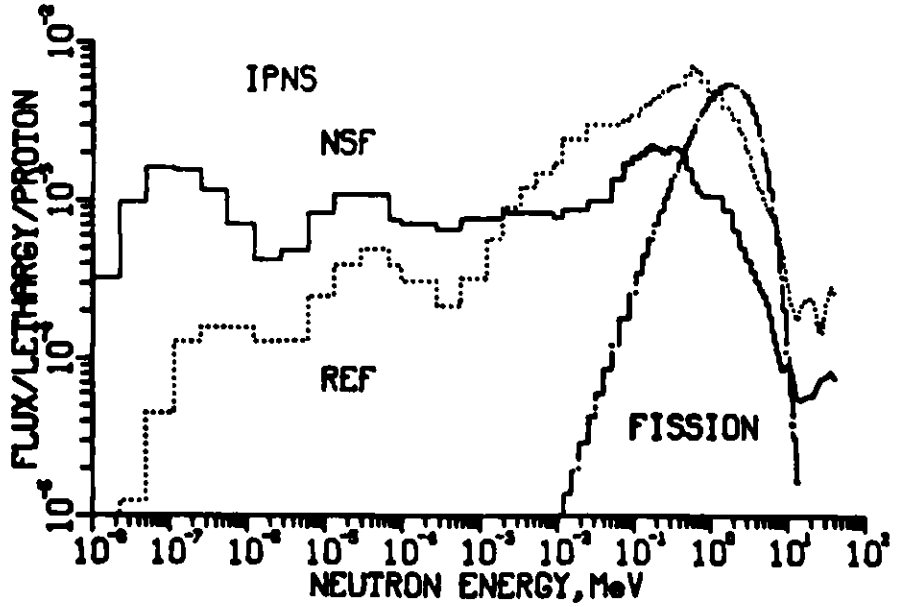

Figure 2. Comparison of neutron spectra at the Radiation Effects Facility (Pb moderator), the Neutron Scattering Facility (C-Be moderator), and a pure fission spectrum.

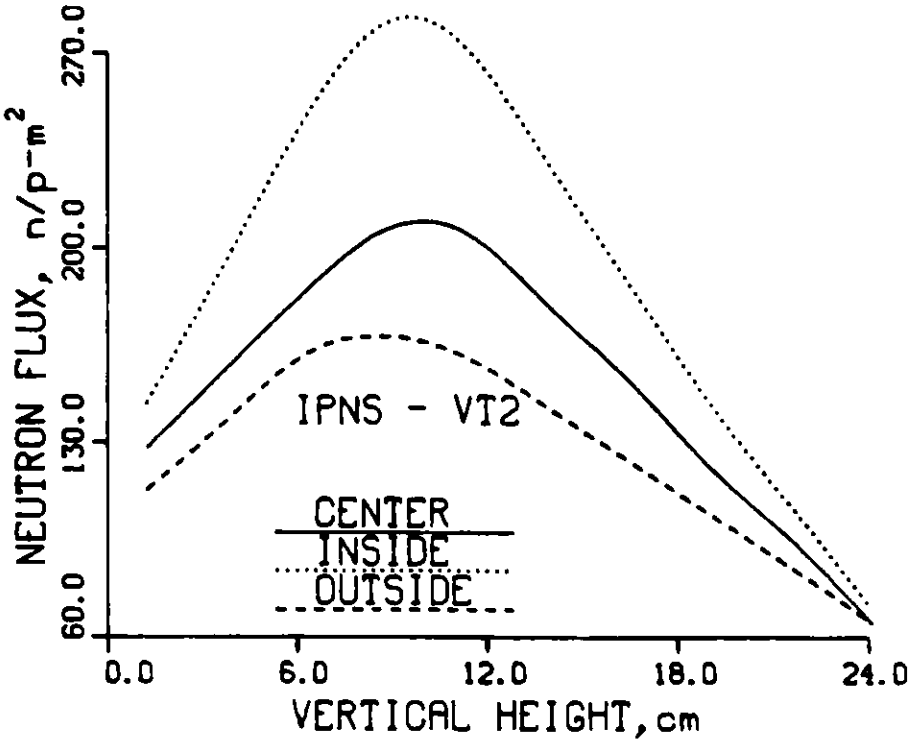

Figure 3. Vertical flux gradients in the vertical thimble 2 of IPNS-REF. The solid line was at the center of the tube; the dotted line was on the inside radius, 2 cm closer to the target; the dashed line was on the outside radius, 2 cm farther from the target.

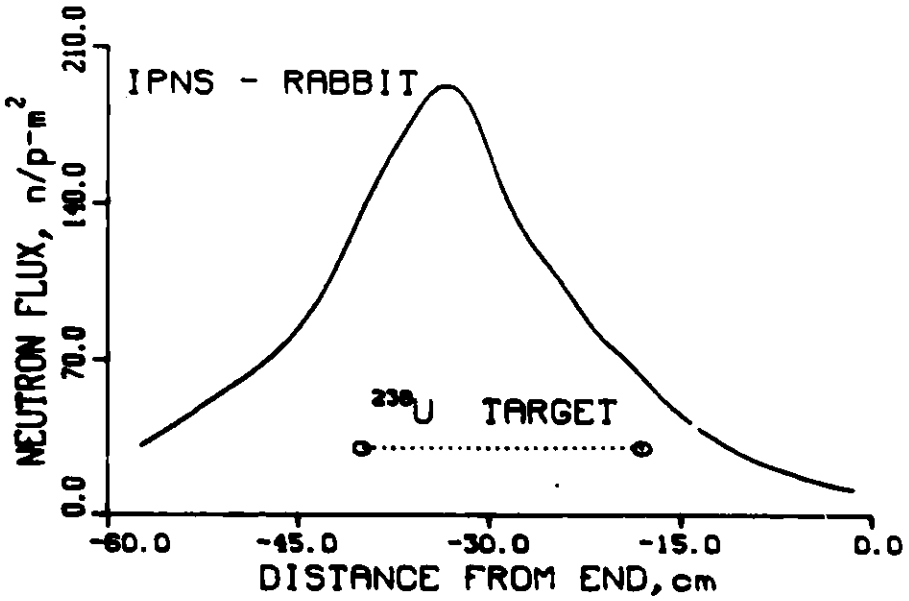

Figure 4. Horizontal flux gradients measured in the center of the IPNS-REF rabbit tube, parallel to the ^{238}U target. Distances are relative to the end of the rabbit hole. The target location is shown. The beam is incident from the left.

ICANS-VI

INTERNATIONAL COLLABORATION ON ADVANCED NEUTRON SOURCES

June 27 - July 2, 1982

HOW MUCH THERMAL NEUTRON FLUX IS GAINED USING DEUTERONS INSTEAD OF PROTONS?

G.S. Bauer, H.M. Conrad, K. Grünhagen and H. Spitzer
Institut für Festkörperforschung der KFA Jülich GmbH
W.Germany

G. Milleret
Labortoire National SATURNE, Saclay, France

ABSTRACT

The neutron leakage fluxes from hydrogeneous moderators have been measured as a function of the energy of protons and deuterons impinging on lead and depleted uranium targets. A gain in thermal neutron yields has been observed in any case using deuterons. The gains depend on both primary particle energies and target materials. The economic advantage employing deuterons instead of protons can be stated in two ways: firstly, using 850 MeV deuterons and a lead target the same thermal leakage flux is obtained as with 1100 MeV protons, or secondly, using 1100 MeV deuterons a flux increase of about 30% is gained. The figures for a uranium target are 900 MeV deuterons or 23% flux gain respectively.

HOW MUCH THERMAL NEUTRON FLUX IS GAINED USING DEUTERONS INSTEAD OF PROTONS?

G.S. Bauer, H.M. Conrad, K. Grünhagen and H. Spitzer
Institut für Festkörperforschung der KFA Jülich GmbH
W.Germany

G. Milleret
Labortoire National SATURNE, Saclay, France

1. INTRODUCTION

Loss of kinetic energy of charged particles due to ionization of matter penetrated by high energy ions are the reason for the very low neutron yields at particle energies below 100 MeV /Bartholomew, 1966/. Clearly, neutral particles cannot be produced with, or accelerated to, the high kinetic energies necessary for efficient spallation reactions. On the other hand, heavier nuclii containing neutrons can be used as vehicles for neutral projectiles. Although ionization losses may become very severe for multiply charged ions, numerical calculations by Barashenkov (1974) indicated that an appreciable gain in neutron yield may be obtained by using deuterons instead of protons (deuterons are stripped on impinging on matter giving two particles with half the kinetic energy each; binding energy of -2.2 MeV neglected).

As neutron production by spallation is a power consumptive, i.e. a costly procedure, each possibility for increasing its efficiency should be checked. For the German spallation project (SNQ project) this might mean a reduction in investment expenses and particularly in running costs if a lower-energy linac for deuterons could be envisaged. In order to improve the basis for this dis-

cussion we performed measurements of the thermal neutron leakage fluxes from hydrogeneous moderators in a target-moderator-reflector geometry as proposed for the SNQ project. We decided to measure the gains in thermal fluxes in realistic arrangements instead of determining the fast neutron yields from targets in order to be independent of any subsequent corrections and conversions.

2. EXPERIMENTAL

The experiments have been performed at the synchrotron of the Laboratoire National SATURNE. The set-up is the same as used in our former investigations and details are described elsewhere /Bauer et al., 1981c/. With the present measurements we used for the first time the actual H_2O-moderator planned for use in the SNQ, its size and shape (grooved surfaces!) being the result of our former studies /Bauer; 1981a, 1981b/. This moderator is shown in figure 1.

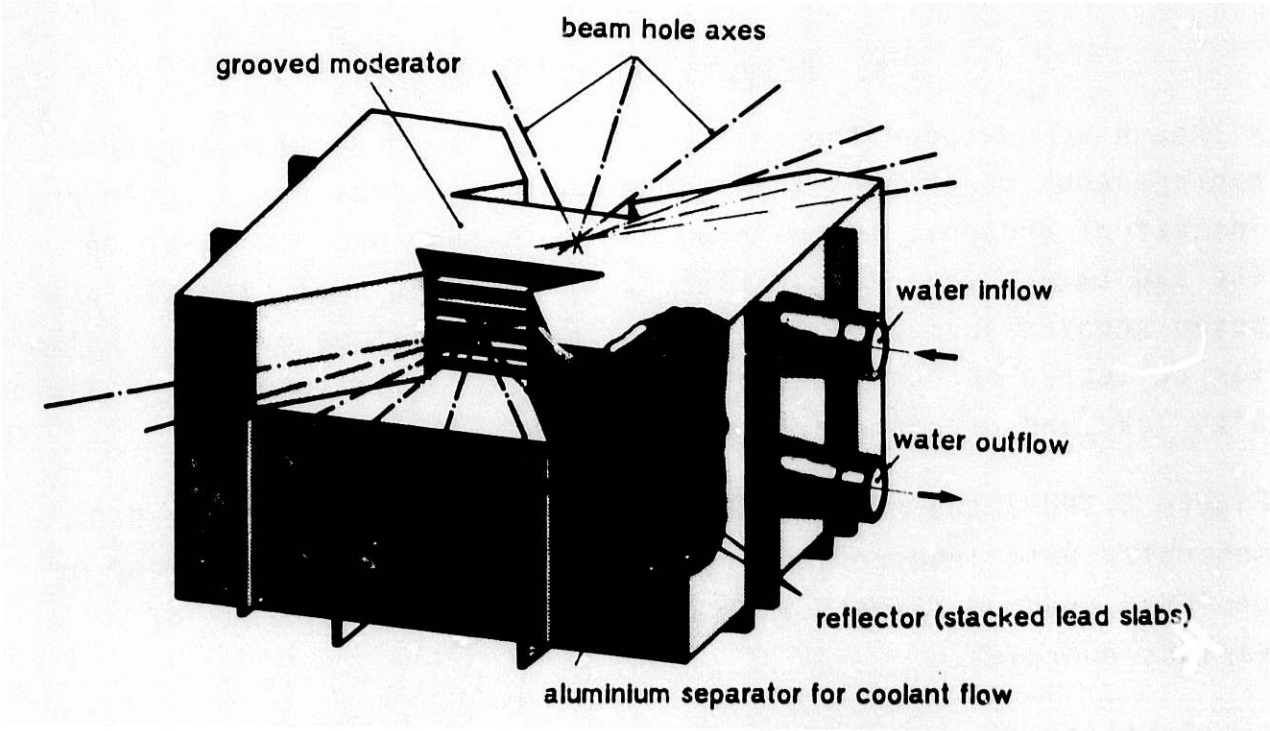

Fig. 1
Grooved-surface H_2O-moderator with lead reflector

The SNQ mock-up used for our measurements can be briefly characterized as follows: lead target with dimensions 10x50x75 cm^3 (height x width x depth), the H_2O-moderator with lead reflector, a graphite block of 40x60x60 cm^3 (simulating the D_2O-moderator) below the target and an overall lead shielding of about 50 cm thickness. The uranium target had the dimensions 10x45x50 cm^3.

The proton energies used were 400 MeV, 600 MeV, 750 MeV and 1100 MeV. With deuterons we utilized only the lower three values, 750 MeV being the highest energy which could be diverted into our experimental area. The absolute numbers of protons and deuterons impinging on our targets were determined by carbon activation in separate short calibration irradiations in which the counts simultaneously recorded with secondary emission chambers (SEC) and ionizations chambers (IC) were related to the activation results. In the actual experiments the SEC and IC counts were used as a measure of the number of the primary particles.

3. RESULTS AND DISCUSSION

Although we measured the gain of thermal neutrons emerging from hydrogeneous moderators in various configurations using deuterons instead of protons, the main emphasis in this paper will be on the SNQ target-moderator-reflector arrangement employing the proposed grooved-surface H_2O-moderator mentionned above. The results for reflected and unreflected polyethylene moderators both measured with lead and uranium targets are quoted only briefly.

Figure 2 shows the thermal neutron leakage fluxes from the H_2O-moderator with lead reflector, resulting from bombarding lead or depleted uranium targets with both protons and deuterons of various energies.

As mentionned in the caption of figure 2, the lines drawn through the experimental data points are guides to the eye only. The reader should keep in mind that the data of figure 2 do not exhi-

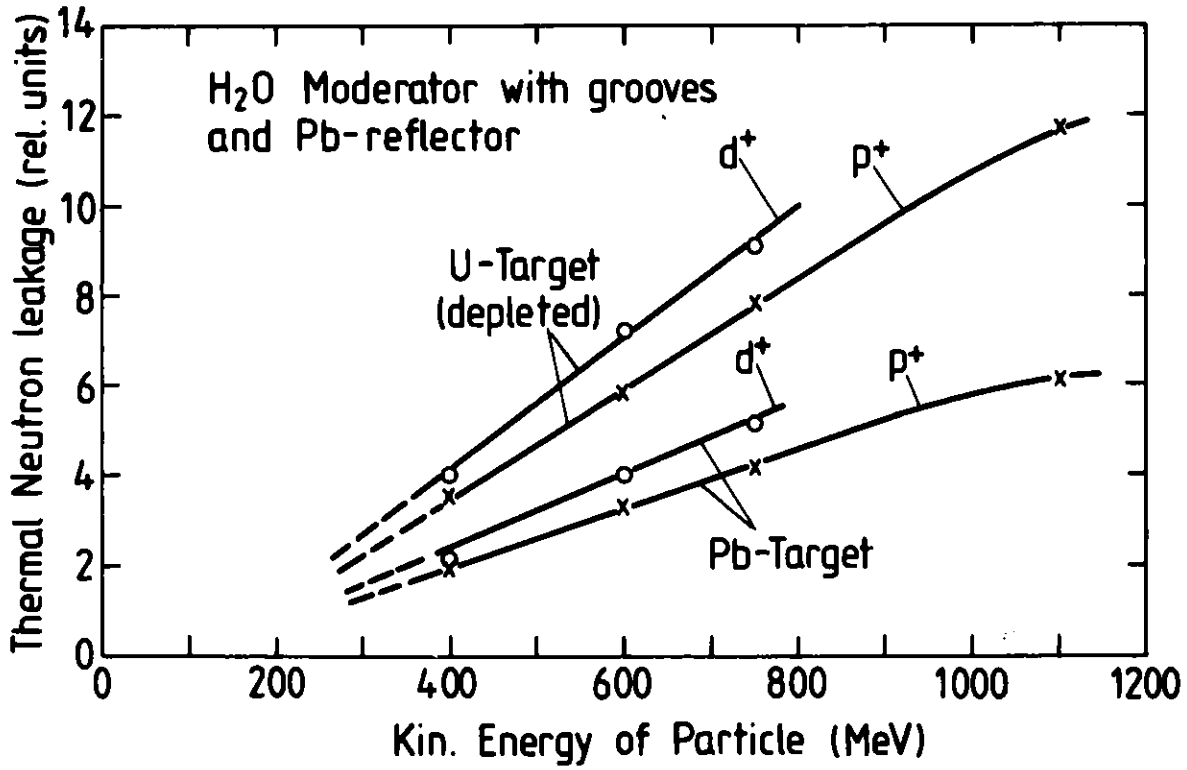

Fig. 2

Relative thermal neutron leakage measured from an H_2O-moderator for slab targets (10 cm high) of Pb and depleted U as a function of kinetic energy for protons and deuterons. The geometry was the same for all energies and for protons and deuterons. Curves are a guide to the eye only.

bit the total fast neutron yield as a function of energy as, for instance, given in the paper of Barashenkov /1974/. The plotted thermal neutron leakages represent the expected fluxes of a realistic target-moderator-reflector configuration. The data therefore contain physical parameters like target-moderator geometry, penetration depth of the primary protons or deuterons and coupling efficiency for fast neutrons from target into moderator. The increasing penetration depth of the primary particles with increasing kinetic energy in conjunction with the finite size of the moderator may explain the downward bending of the leakage curves for protons at higher energies. In fact the bending is less pronounced for the uranium target. This is consistent with the smaller penetration depth of protons in that material.

Despite the difficulties in expressing our experimental data in mathematical relations, as discussed so far, we may answer the following question without stressing our results too much. What is the kinetic energy of deuterons yielding the same thermal neutron flux per primary particle as do protons of 1100 MeV?

Inspection of figure 2 shows that only a slight (linear) extrapolation of the deuteron lines is necessary to see that 850 MeV deuterons on a lead target will yield the same thermal flux like 1100 MeV protons. For the uranium target we find that 900 MeV deuteron are sufficient to yield the same flux as 1100 MeV protons.

If we linearly extrapolate the deuteron lines to 1100 MeV, we can estimate the flux gain we would obtain in employing deuterons instead of protons. (This extended extrapolation appears to be justified because the deuterons are likely to have a shorter effective range in the target relative to protons.) Under this assumption the flux gain with 1100 MeV deuterons is found to be about 30% for a lead target and about 23% for a depleted uranium target.

Table 1 shows a comparison of the gains according to our experimental data for the lead target and the results of Barashenkov's /1974/ numerical calculations. Although Barashenkov calculated total fast neutron yields the comparison with our data is certainly justified for the lower energies, where minor coupling and penetration effects influence the proportionality of fast neutron yields and thermal leakages. A comparison with Barashenkov's uranium data is omitted because these results refer to natural uranium whereas we employed depleted uranium.

For the sake of completeness we have added table 2, in which the results for the other target-moderator-reflector configurations are listed. Most of these data may be of academic interest only.

E [MeV]	Theory [Barashenkov] (lead target)	This experiment (lead target)	This experiment (depleted uranium)
	N_{d^+} / N_{p^+}	Φ_{d^+} / Φ_{p^+}	Φ_{d^+} / Φ_{p^+}
400	1.11	1.10	1.13
600	1.18	1.22	1.24
750	1.16	1.23	1.16
1100	(1.13)	(1.30)	(1.23)
	extrapolated values		

Table 1: Comparison of numerical calculations /Barashenkov, 1974/ of fast neutron gain N_{d^+}/N_{p^+} with experimental data for the thermal neutron leakage gain Φ_{d^+}/Φ_{p^+} on changing from protons (p^+) to deuterons (d^+). The comparison is for a lead target. The column on the right are experimental values for a depleted uranium target.

E [MeV]	Φ_{d^+} / Φ_{p^+}			
	grooved polyethylene moderator			
	lead target		depleted uranium target	
	lead shielding no reflector	no reflector + shielding	lead shielding no reflector	no reflector + shielding
400	1.11	1.07	-	-
600	1.18	1.26	-	-
750	1.20	1.24	-	1.19

Table 2: Thermal neutron leakage gain factors for a grooved polyethylene moderator in several configurations. Dimensions of the moderator are 13.5x10x20 cm^3 with 1 cm wide and 6 cm deep grooves pointing toward the neutron beam tube.

4. CONCLUSION

It is obvious that a thorough discussion of the advantages and disadvantages of employing deuterons, even on the basis of our experimental results, is beyond the scope of this report since this would involve accelerator technology quite heavily. Moreover, not every aspect can be formulated as a quantitative argument, so the final decision will have to balance quantitative economic aspects and qualitative reasons. We shall only give a brief summary of the pros and cons. There are mainly two pros: Firstly, an 850 MeV deuteron linac has less than 70 % of the length of an 1100 MeV proton linac if we utilize the same rf-frequency. This reduces investment costs at about the same ratio. Secondly lowering the primary particle energy reduces the power consumption of the linac and thereby the running costs of the spallation source, which are the dominating part (> 50%) thereof.

The two essential cons are: Firstly, under the assumption of a fixed pre-accelarator (dc-accelerator) energy, deuterons would leave that injector part with lower velocity, whence shorter drift- tubes or lower rf-frequency for the Alvarez-linac were necessary. Both is unfavourable because of weaker beam focussing and worse economics respectively. This drawback may be circumvented utilizing an RFQ-structure instead of the electrostatic pre-accelerator, because these structures are expected to reach about 2 MeV. Secondly, deuterons produce activation due to d-d reactions already in the low-energy injector structures, a fact which might impede the operation. This latter disadvantage is certainly not easily transferrable into quantitative economic terms.

REFERENCES

V.S. Barashenkov, V.D. Toneev, and S.E. Chigrinov;
Atomnaya Énergiya, 37, 480 (1974) (engl. translation: Sov. J. Atomic Energy 37, 1256 (1975))

G.S. Bauer, J.P. Delahaye, H. Spitzer, A.D. Taylor, and K. Werner (1981 a)
"Relative Intensities and Time Structure of Thermal Neutron Leakage from Various Moderator-Decoupler Systems for a Spallation Neutron Source"
paper D2-3 in "ICANS V" pp. 417-444, G.S. Bauer and F. Filges, eds., report Jül-Conf-45, Kernforschungsanlage Jülich

G.S. Bauer, W.E. Fischer, F. Gompf, M. Küchle, W. Reichardt, and H. Spitzer (1981 b)
"Thermal Neutron Leakage and Time Structure Measured for Various Target-Moderator-Reflector Configurations for a Spallation Neutron Source"
paper D2-4 in "ICANS V" pp. 445-474, G.S. Bauer and D. Filges, eds., report Jül-Conf-45, Kernforschungsanlage Jülich

G.S. Bauer, H.M. Conrad, H. Spitzer, K. Friedrich, and G. Milleret (1981 c)
"Measurement of Time Structure and Thermal Neutron Spectra for Various Target-Moderator-Reflector Configurations of an Intensity-Modulated Spallation Neutron Source"
paper D2-5 in "ICANS V" pp. 475-488, G.S. Bauer and D. Filges, eds., report Jül-Conf-45, Kernforschungsanlage Jülich

ICANS-VI

INTERNATIONAL COLLABORATION ON ADVANCED NEUTRON SOURCES

June 27 - July 2, 1982

MONTE CARLO STUDY OF THE ENERGY DEPOSITION OF A FLUX OF SPALLATION NEUTRONS IN VARIOUS SAMPLES

M. Pepin
Schweizerisches Institut für Nuklearforschung
CH-5234 Villigen, Switzerland

ABSTRACT

The flux of spallation neutrons produced on a sample by a 10 μA beam of 520 MeV protons incident on a 25 cm long cylindrical lead target of 7.7 cm radius was estimated with the Monte Carlo codes HET and O5R. In order to save computing time, the simulation was done in two steps, and the number of high-energy neutrons in the region of interest could be enhanced at the end of the first step. The calculated flux was compared with the values measured by S. Cierjacks, M.T. Rainbow, M.T. Swinhoe, and L. Buth at 590 MeV. The energy deposed in the sample by nuclear reactions above 15 MeV and by elastic recoils was estimated for the materials Be, C, Al, Fe, Cu, W, Pb, Bi and D_2O. For a 10 μA incoming beam, the total energy deposition varies between 1.02×10^{-4} cal/cm^{3}sec for Bi and 3.30×10^{-4} cal/cm^{3}sec for D_2O. The fraction of this energy which is deposed through elastic recoils varies from 6 % for Bi to 88 % for D_2O.

MONTE CARLO STUDY OF THE ENERGY DEPOSITION OF A FLUX OF SPALLATION NEUTRONS IN VARIOUS SAMPLES

M. Pepin
Schweizerisches Institut für Nuklearforschung
CH-5234 Villigen, Switzerland

1. INTRODUCTION

The design of high-intensity spallation neutron sources requires a better knowledge of the heating effects of the neutron flux on the components of the source than is now available. In order to learn more about these effects, an experiment to measure the heat-up of samples of the nine materials Be, C, Al, Fe, Cu, W, Pb, Bi and D_2O in the flux of the TRIUMF neutron source is being planned as a collaboration between KFA Jülich and SIN, and will be carried out at the end of this year.

In preparation for this experiment we have used the Monte Carlo codes HET [1] and O5R [2] to estimate

(i) the neutron flux expected at the sample position in conditions approximating the planned experiment, and
(ii) the expected values of heat deposition through high-energy nuclear interactions and through elastic recoils for all nine sample materials.

2. GEOMETRY OF THE SOURCE

The geometry assumed for the computation is a simplified version of the TRIUMF neutron source (see Fig. 1). In particular, the walls containing the moderator baths are omitted and only a central volume of 75 x 100 x 100 cm^3 is considered.

The production target is a lead cylinder, 25 cm in length and of 7.7 cm radius. It is surrounded by a H_2O/D_2O moderator assembly which includes an iron shielding block above the target and two vertical irradiation shafts. In the planned experiment, the samples will be placed in the rectangular shaft to the side of the target. To obtain sufficient statistics, a 5 x 5 x 2 cm^3 sample was chosen for the Monte Carlo run, although the experiment will use samples approximately one order of magnitude smaller in volume. The relative positions of target and sample are shown in Fig. 2.

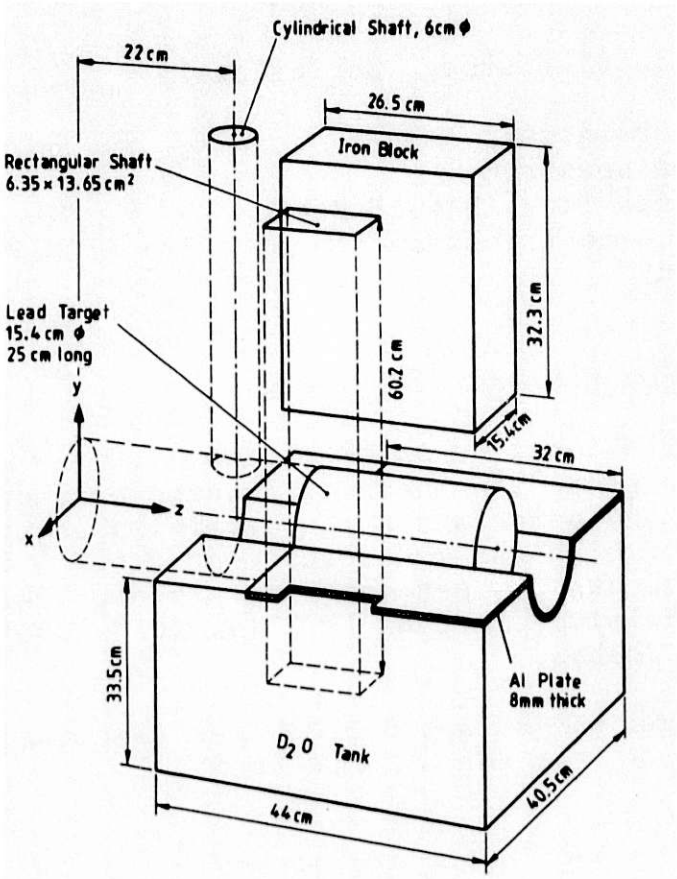

Fig. 1
Simplified geometry of the central region of the TRIUMF neutron source, as used in the Monte Carlo study.

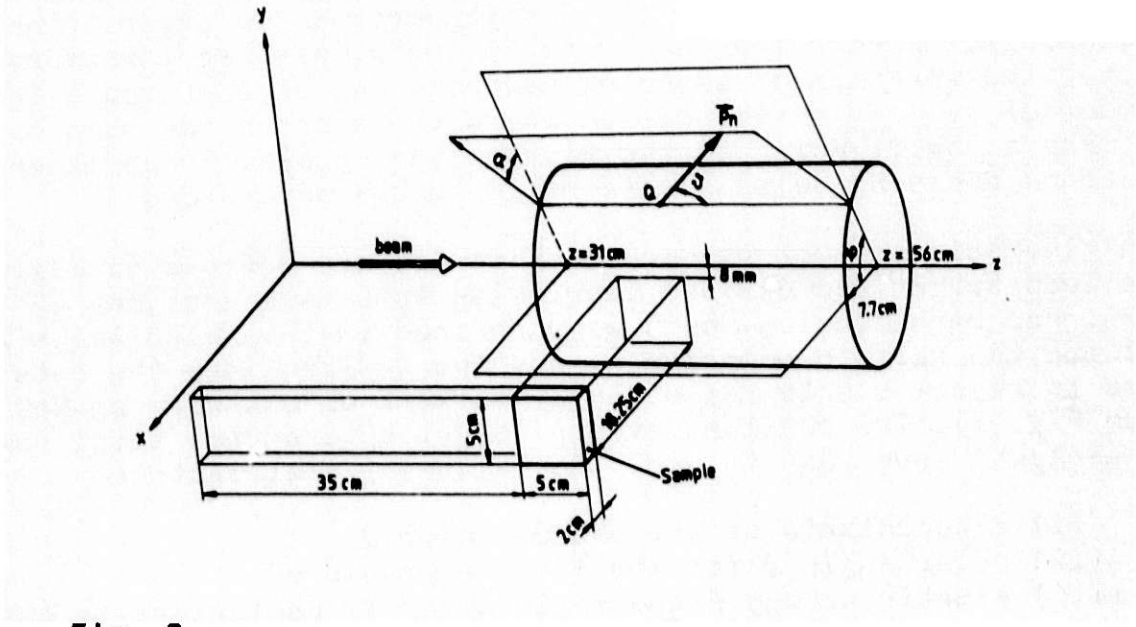

Fig. 2
Sketch showing the position of the sample with respect to the lead target, and the definition of the kinematic parameters used to describe the escaping neutrons.

3. ORGANISATION OF THE RUN

The calculation was done in five steps, as follows:

(i) HET run for the Pb target,
(ii) fit to the escape spectrum,
(iii) high-energy neutron flux (E > 15 MeV),
(iv) low-energy neutron contribution (10 eV < E < 15 MeV),
(v) energy deposition.

4. HET RUN FOR THE LEAD TARGET

The beam used in the calculation is a 15 mm radius, 300 π x 250 π mm mrad beam of 520 MeV protons. One hundred thousand cascades were generated and followed to the point where the particles escape from the lead. The yield of high-energy escapes was 0.627 ± 0.003 neutrons and 0.006 ± 0.0002 protons per incoming proton. There were also (9 ± 1)x 10^{-4} positive pion and (5 ± 1)x 10^{-4} negative pion escapes per incoming proton.

The energy deposition in the target was 360 MeV per incoming proton, corresponding to 860 cal/sec for a 10 μA beam.

5. FIT TO THE ESCAPE SPECTRUM

It is clear that a straightforward one-pass Monte Carlo simulation of the whole target-moderator-sample system requires a prohibitively large number of incoming protons in order to obtain a meaningful spectrum of neutrons at the sample. We therefore fitted the spectrum of escaping neutrons and regenerated a large number of escapes in the region where the neutron has some chance to make a contribution to the flux on the sample. Propagation of neutrons escaping outside this region could be dropped.

The kinematic parameters used in this fit are defined in Fig. 2. The lead target was divided lengthwise into five sections of 5 cm each. For each section, cuts were defined in the polar angle ϑ between the neutron momentum $\vec{p}_n$ and the z-direction; the cuts were used to reject events too strongly forward or backward peaked (see Fig. 3). The retained events (about 30 % of the total number of escapes) were used to plot the following distributions:

(i) z-coordinate of the escape point Q
(ii) polar angle ϑ for the five intervals of z
(iii) kinetic energy E and angle α for 12 subregions in the z-ϑ space.

These distributions were used to generate escaping neutrons. For the azimuthal angle φ of the escape point, an isotropic distribution

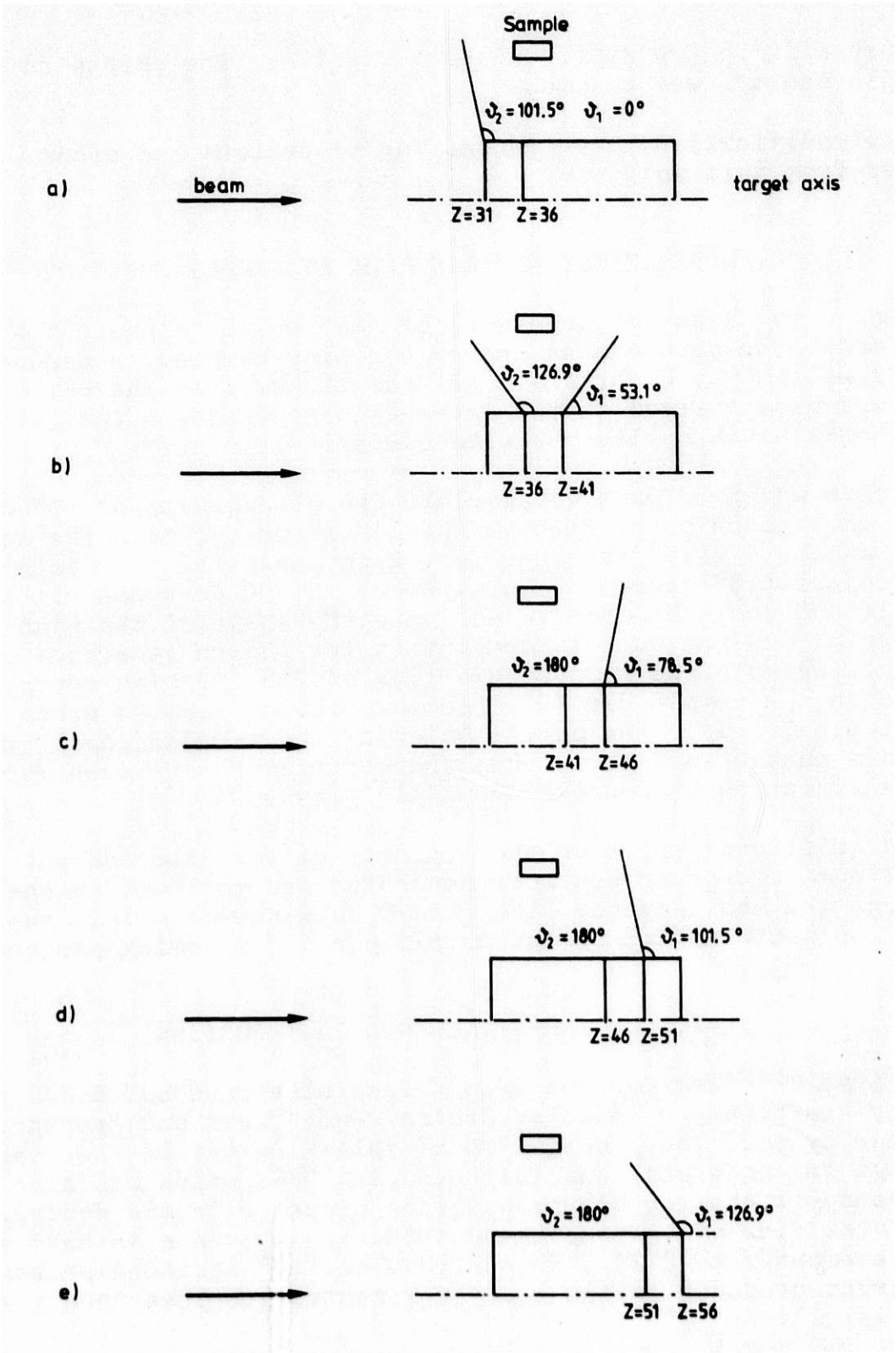

Fig. 3
Limiting values ϑ_1 and ϑ_2 of the polar angle ϑ for the five sections of the lead target. These cuts define the neutron escapes selected for fitting.

within a 36-degree sector whose bissecting line points to the sample center, was assumed.

For simplification, the propagation of protons and pions was abandoned from this point on.

6. HIGH-ENERGY NEUTRON FLUX AT SAMPLE POSITION

In order to allow the treatment of D_2O, which is present both in the moderator bath and as one of the nine samples, a Glauber type model written by F. Atchison [3] was linked into the HET code, and was used instead of the intranuclear cascade evaporation model for non-elastic collisions with deuterium.

The code was then used to simulate the propagation of 10^5 neutrons from the escape point through the moderator and onto the sample. As a check, 5×10^4 neutrons were also generated from each of the two adjacent 36-degree sectors. About 12'800 neutrons hit the sample and could be used to estimate the shape of the high-energy spectrum. Scaling back to compensate for the re-generated particles, we obtained an absolute flux of 256 ± 5 high-energy neutrons on the sample per 10^5 incoming protons (quoted error is statistical only). The contribution of the two "adjacent" sectors to this number is 7 %, so that the contribution of even more distant sectors can certainly be neglected.

As an additional check on the validity of our fits and cuts, a small number of cascades were generated and followed in one pass through the whole system. The result obtained from this run was 300 ± 55 neutron hits on the sample per 10^5 incoming protons.

7. LOW-ENERGY NEUTRON CONTRIBUTION

The first HET pass for the lead target also produced 9.37 low-energy neutrons per incoming proton, which were not transported further by HET. The propagation of this flux out of the lead and through the moderator was followed with O5R, which was also used to transport the low-energy neutrons produced in the moderator. The total flux of low-energy neutrons ($10\ eV < E < 15\ MeV$) on the sample amounts to 6121 ± 80 neutrons per 10^5 incoming protons (neutrons produced in the moderator contribute less than 1 % to this value).

The neutron spectrum obtained at sample position (low- and high-energy ranges combined) is given in Table I; the Table also shows the flux of neutrons at target surface and at approximately 90^o ($-0.2 < \cos \vartheta < 0.2$).

Table I

Monte Carlo computed spectra of neutrons at sample position, and at target surface

Energy Interval (MeV)	Flux on Sample (n/p MeV cm^2)	90° Flux at Target Surface (n/p MeV sr)
10^{-5} - 10^{-4}	3.53	
10^{-4} - 10^{-3}	3.94×10^{-1}	
10^{-3} - 10^{-2}	4.11×10^{-2}	17.8×10^{-2}
10^{-2} - 10^{-1}	5.05×10^{-3}	41.7×10^{-2}
0.1 - 1.0	6.13×10^{-4}	41.0×10^{-2}
1.0 - 1.5	1.87×10^{-4}	21.7×10^{-2}
1.5 - 2	1.27×10^{-4}	15.1×10^{-2}
2 - 3	9.45×10^{-5}	89.9×10^{-3}
3 - 5	3.38×10^{-5}	31.7×10^{-3}
5 - 7	1.55×10^{-5}	13.1×10^{-3}
7 - 10	9.81×10^{-6}	65.1×10^{-4}
10 - 15	4.18×10^{-6}	25.5×10^{-4}
15 - 25	3.33×10^{-6}	12.87×10^{-4}
25 - 35	1.77×10^{-6}	6.80×10^{-4}
35 - 45	1.18×10^{-6}	4.65×10^{-4}
45 - 55	8.94×10^{-7}	3.55×10^{-4}
55 - 65	6.28×10^{-7}	2.65×10^{-4}
65 - 75	5.12×10^{-7}	2.03×10^{-4}
75 - 85	3.74×10^{-7}	1.55×10^{-4}
85 - 95	3.17×10^{-7}	1.23×10^{-4}
95 - 105	2.62×10^{-7}	9.55×10^{-5}
105 - 115	1.86×10^{-7}	7.36×10^{-5}
115 - 135	1.30×10^{-7}	5.73×10^{-5}
135 - 155	1.00×10^{-7}	2.75×10^{-5}
155 - 175	5.75×10^{-8}	1.59×10^{-5}
175 - 195	3.28×10^{-8}	9.15×10^{-6}
195 - 215	2.59×10^{-8}	4.58×10^{-6}
215 - 235	1.51×10^{-8}	2.38×10^{-6}
235 - 255	1.31×10^{-8}	1.59×10^{-6}
255 - 175	5.04×10^{-9}	0.32×10^{-6}
275 - 295	3.84×10^{-9}	
295 - 315	2.32×10^{-9}	
315 - 335	1.52×10^{-9}	

In Fig. 4 the flux obtained at sample (plotted with circles) is compared to the flux emitted above 15 MeV at target surface (black dots). One sees how the material between target and sample selectively depresses the less energetic part of the flux. The results are also compared to the values measured at 90° by S. Cierjacks,

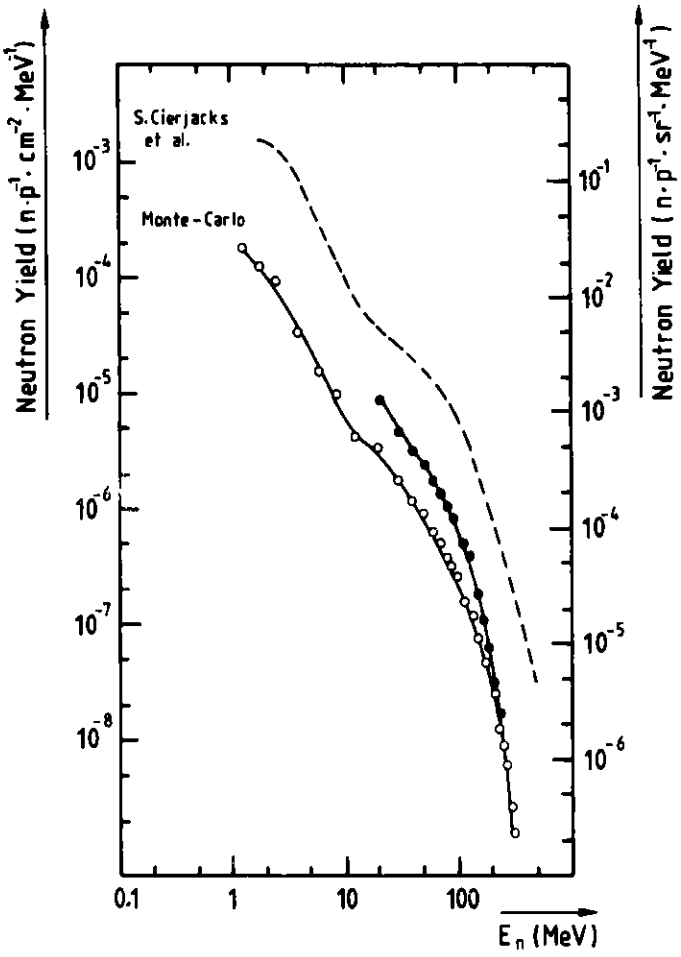

Fig. 4
Monte Carlo computed energy spectra of the neutrons emitted at 90° ($-0.2 < \cos\vartheta < 0.2$) from the target surface (black dots, right vertical scale), and of the neutrons incident on the sample (circles, left vertical scale), for an incoming proton energy of 520 MeV. For comparison, one of the spectra measured by S. Cierjacks et al. [4] is also shown (dashed line, right vertical scale; 90° neutrons, integrated over the first 35 cm of a thick lead target, incoming proton energy 590 MeV).

M.T. Rainbow, M.T. Swinhoe and L. Buth [4] for 590 MeV incoming protons and a thick lead target (dashed line). Our calculated flux at target surface is weaker than the measured one by a factor varying between about 5 (at 15 MeV) and 20 (at 300 MeV). Another short HET run indicates that the calculated yield of neutrons increases by 24 % when the incoming proton energy is taken to be 590 MeV.

8. ENERGY DEPOSITION

Two main processes were considered up to now for estimating the energy deposition in the sample:

(i) non-elastic interactions of the neutrons with the sample nuclei at higher energies, and
(ii) recoils of the sample nuclei following elastic collisions.

The energy deposition of non-elastic interactions was estimated by making, for each sample material, a HET run with incident neutrons generated according to the high-energy part (E > 15 MeV) of our spectrum. The history tapes were then examined with the heat depositon analysis programme ENDEN5 [5].

The number of recoils from elastic collisions was obtained from our neutron spectrum and from the compilation of neutron cross-sections by D.I. Garber and R.R. Kinsey [6]. The total energy deposition through this mechanism depends on the angular distribution of the recoils. In this estimation we assumed, as a simple model, a linear distribution of the cosine μ of the center-of-mass scattering angle,

$$P(\mu) = \frac{1}{2} (1 + 3.f_1.\mu)$$

with f_1 values taken from the ENDF/B data. For lack of better data, it was also assumed that the f_1 values at 20 MeV were valid at all higher energies. The results are shown in Table II.

Table II

Heat deposition from nuclear reactions above 15 MeV E_r and from elastic recoils E_{el} for a 10 μA incoming proton beam, and corresponding initial rate of sample heat-up for nine materials.

	Energy deposition (cal/10 μA · sec · cm^3)			$\frac{dT}{dt}$
	E_r	E_{el}	$E_r + E_{el}$	(^oC/sec)
Be	1.08×10^{-4}	1.78×10^{-4}	2.86×10^{-4}	3.5×10^{-4}
C	0.99×10^{-4}	1.03×10^{-4}	2.02×10^{-4}	7.6×10^{-4}
Al	0.99×10^{-4}	0.42×10^{-4}	1.41×10^{-4}	2.4×10^{-4}
Fe	2.32×10^{-4}	0.28×10^{-4}	2.60×10^{-4}	3.1×10^{-4}
Cu	2.27×10^{-4}	0.32×10^{-4}	2.59×10^{-4}	3.1×10^{-4}
W	2.20×10^{-4}	0.12×10^{-4}	2.32×10^{-4}	3.8×10^{-4}
Pb	1.06×10^{-4}	0.08×10^{-4}	1.14×10^{-4}	3.3×10^{-4}
Bi	0.96×10^{-4}	0.06×10^{-4}	1.02×10^{-4}	3.5×10^{-4}
D_2O	0.41×10^{-4}	2.89×10^{-4}	3.30×10^{-4}	3.0×10^{-4}

A noteworthy feature of these results is that the energy deposition through elastic recoils is the major contribution for light nuclei, and remains a sizeable effect for medium-heavy ones (e.g. 12 % for copper).

ACKNOWLEDGEMENTS

I owe a great deal to F. Atchison, who suggested the "guided" Monte Carlo method in order to make this study feasible on a VAX-11/780 computer, and who supplied the Glauber model and heat analysis programmes [3,5]. His advice and help during the run were most valuable, and he suggested many improvements to the writing of this paper.

REFERENCES

[1] HETC, ORNL 4744.
[2] O5R, ORNL Report CCC-161/NMTC and CCC-17.
[3] F. Atchison, private communication.
[4] S. Cierjacks, M.T. Rainbow, M.T. Swinhoe, and L. Buth, Primärbericht KfK 3097 B, Fig. 6.
[5] F. Atchison, ENDEN5, private communication.
[6] D.I. Garber and R.R. Kinsey, Neutron Cross Sections, BNL 325.

ICANS-VI
INTERNATIONAL COLLABORATION ON ADVANCED NEUTRON SOURCES
June 27 - July 2, 1982

POSSIBLE USE OF COPPER SPALLATION REACTIONS TO MEASURE HIGH ENERGY PARTICLE SPECTRA IN SHIELDING EXPERIMENTS

W. Amian, V. Drüke, M. Kloda, W. Litzow

Institut für Reaktorentwicklung
Kernforschungsanlage Jülich GmbH
Postfach 1913
D-5170 Jülich 1, Germany

ABSTRACT

The formation of spallation products in copper foils has been used to derive the high energy part of the neutron energy spectra from spallation reactions. Spectra for lead and uranium spallation targets have been measured. The method allows to derive the neutron energy spectra by unfolding of the measured residual nuclei in the energy region of 100 MeV up 650 MeV with reasonable precision, which is illustrated by the confidence limits of the neutron spectra derived.

POSSIBLE USE OF COPPER SPALLATION REACTIONS TO MEASURE HIGH ENERGY PARTICLE SPECTRA IN SHIELDING EXPERIMENTS

W. Amian, V. Drüke, M. Kloda, W. Litzow

Institut für Reaktorentwicklung
Kernforschungsanlage Jülich GmbH
Postfach 1913
D-5170 Jülich 1, Germany

INTRODUCTION

Experiments have been performed to measure the formation of spallation products in copper foils by high energy neutrons emerging from thick cylindrical spallation targets of lead and uranium, respectively, bombarded by 1100 MeV protons. In addition "normal" threshold reaction foils have been used. While these reactions cover the energy region between about 1 MeV and 20 MeV, the copper spallation reactions have thresholds upto about 100 MeV. The cross sections for the "normal" threshold reactions have been taken from /1/, those for the copper spallation reactions are known only from calculations /2/. The unfolding of the measured activities has been performed with the code LOUHI78 /3/ to derive the neutron energy spectrum.

EXPERIMENTAL

The copper foils and "normal" threshold reaction foils were about 10 cm downstream from the beam entrance to the target (rectangular parallelepiped of 15 x 15 x 90 cm^3) immediately on the target surface. The protonbeam of 1100 MeV energy had 11.2 nA intensity for the uranium target, 22.5 nA for the lead tar-

get, respectively. The formation of Fe59, Co58, Co57, Co56, Mn52, V48, Sc46 and Sc44 in the copper foils and of the respective isotopes in the "normal" threshold foils has been measured by gamma-ray spectrometry using Ge(Li)-detectors. Table I gives the saturation activities in units of decays per second per detector nucleus per proton.

The copper foils have been measured about three hours after the end of bombardment and afterwards about three months later. This explains why Cr48 and Na24 which have relatively long halflifes and low production cross sections have not been observed. Later experiments should reveal their existence by counting at intermediate cooling times. Strong overlapping activities at short times (hours) stem from Cu61, Mn56, Ni65, Cu64.

RESULTS AND DISCUSSION

The spallation yield cross sections of different products for copper as calculated according to the Rudstam formulas /2/ are presented in figure 1. In the case of the "normal" threshold reactions, the cross sections have been set to zero above the highest energy known from the literature /1/.

The unfolding of the neutron energy spectra measured with the copper spallation reactions and the "normal" threshold reactions has been performed with the code LOUHI78. The comparison of the measured activities and the ones calculated for the spectrum derived are given in tables II and III, respectively.

The agreement of measured and calculated saturation activities is fairly well. However, since the product yield cross sections for the copper spallation reactions are not very well known this reasonable agreement has to be expected. Figure 2 gives the unfolded spectrum in units of neutrons per cm^2 per second per MeV and per proton for the uranium target, figure 3 for the lead target.

The confidence bands reveal that only the regions between 3 MeV and 15 MeV and between 100 MeV and 650 MeV can be unfolded with sufficient precision. This uniquely corresponds to the regions, where the cross sections dominantly contribute to the reactions observed. Further reactions with lower and higher thresholds are needed to get detailed information outside these regions.

REFERENCES

/1/ D.I. Garber, R.R. Kinsey
Neutron Cross Sections, Volume II, Curves
BNL 325, Brookhaven National Laboratory (1976)

/2/ G. Rudstam
Z. Naturforschung 21 a (1966) 1027

/3/ J.T. Routti, J.V. Sandberg
Computer Physics Communications 21(198) 119

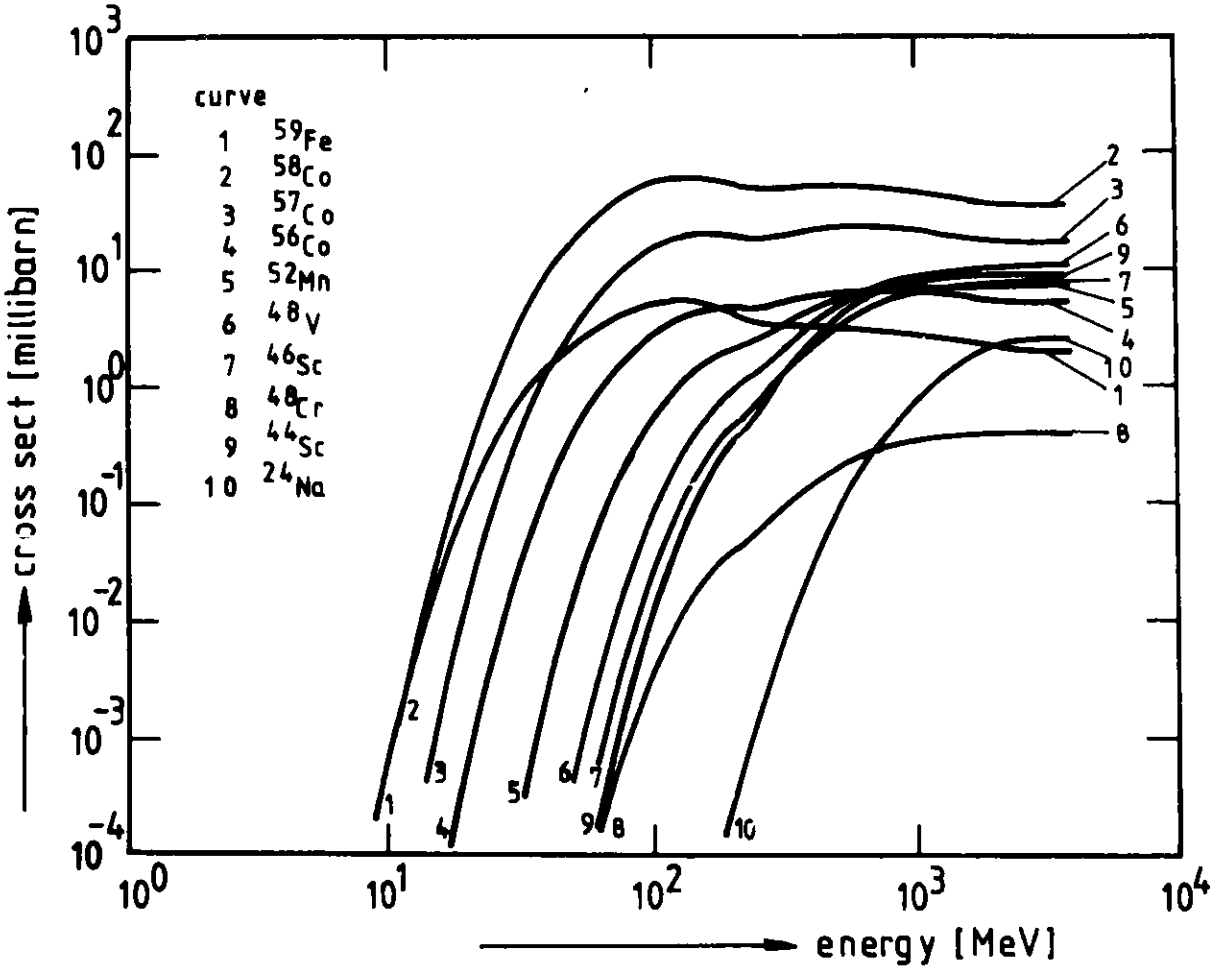

Fig. 1: Calculated spallation cross sections for copper

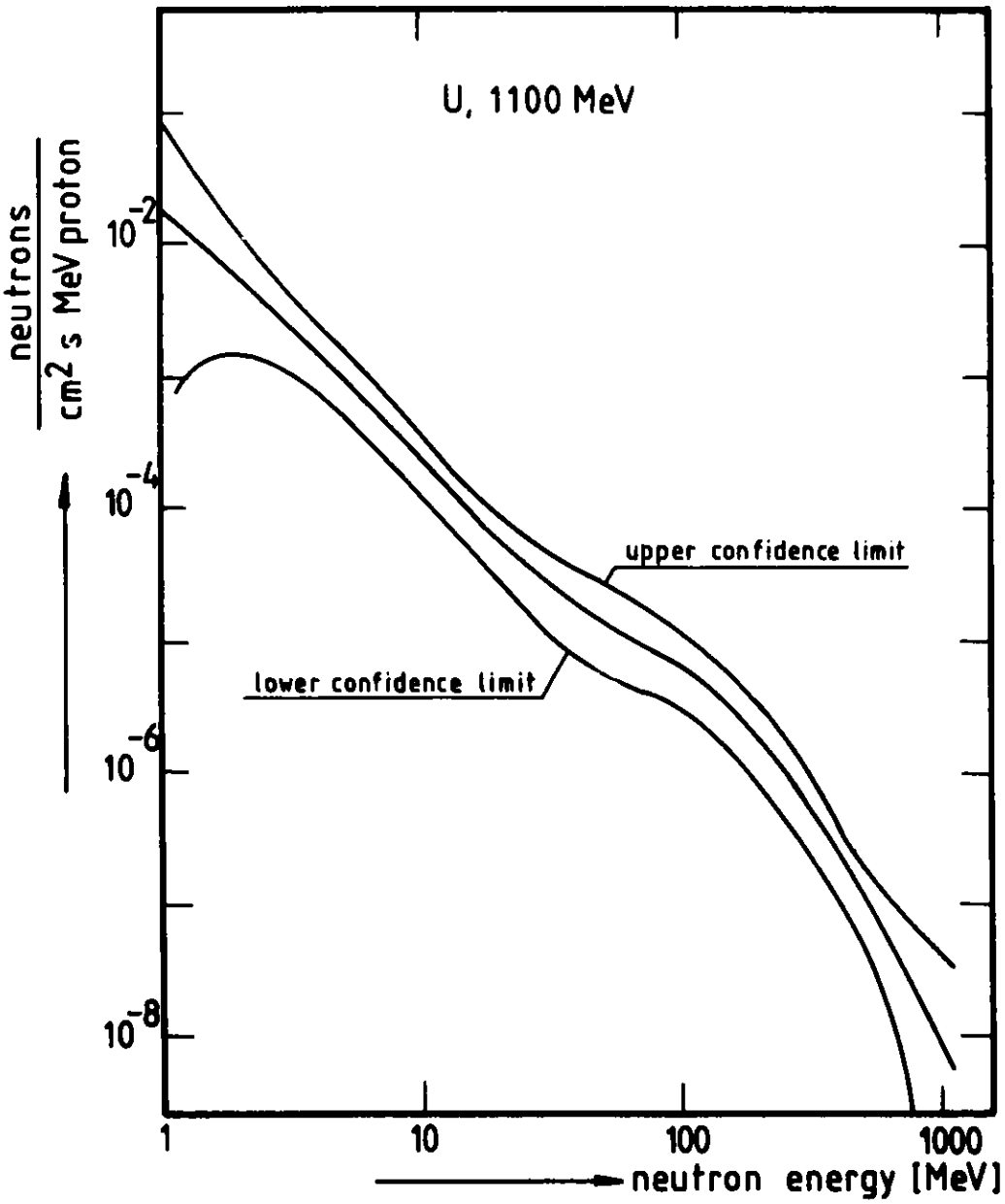

Fig. 2: Unfolded neutron energy spectrum at the surface, 10 cm from beam entry, for a rectangular uranium target (15 x 15 x 90 cm^3) at 1100 MeV

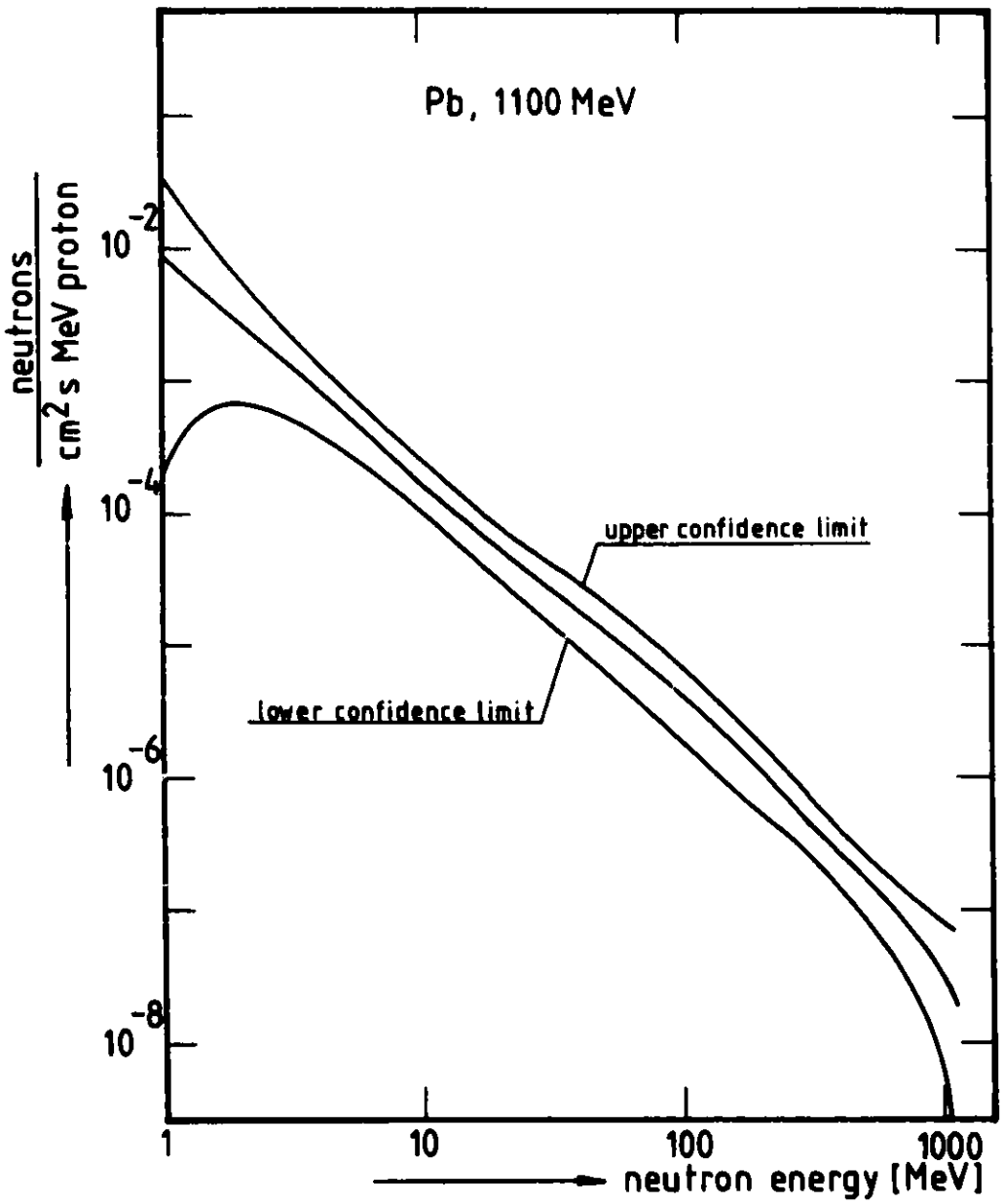

Fig. 3: Unfolded neutron energy spectrum at the surface, 10 cm from beam entry, for a rectangular lead target (15 x 15 x 90 cm^3) at 1100 MeV

Nuclide	Halflife	Gamma-Energy (keV	Saturation Activity (sec^{-1}/proton/nucleus) Uranium	Lead
Fe59	45.1 d	1099.22;1291.56	$3.9\ 10^{-30}$	$3.3\ 10^{-30}$
Co58	70.78 d	811.75	$5.1\ 10^{-29}$	$4.9\ 10^{-29}$
Co57	270.00 d	122.07; 136.43	$2.7\ 10^{-29}$	$2.9\ 10^{-29}$
Co56	77.30 d	846.75;1238.28	$3.6\ 10^{-30}$	$4.2\ 10^{-30}$
Mn52	5.70 d	1434.30; 935.60	$2.0\ 10^{-30}$	-
V48	16.10 d	983.50;1311.60	$7.7\ 10^{-31}$	$9.4\ 10^{-31}$
Sc46	83.85 d	1120.52; 889.26	$4.4\ 10^{-31}$	$6.6\ 10^{-31}$
Sc44	3.93 h	1156.95;	$2.2\ 10^{-31}$	$2.8\ 10^{-31}$
Cr48	23.00 h	306.00; 116.00	-	-
Na24	15.03 h	1368.55;2754.10	-	-

Table I: Saturation activities for the copper spallation products produced from neutrons emerging from lead and uranium spallation targets, respectively

Reaction	Saturation Activity (sec^{-1}/proton/nucleus) Measured	Calculated	% Difference
Cu(n,sp)Fe59	$3.9\ 10^{-30}$	$5.1\ 10^{-30}$	32.2
Cu(n,sp)Co58	$5.1\ 10^{-29}$	$5.1\ 10^{-29}$	1.2
Cu(n,sp)Co57	$2.7\ 10^{-29}$	$1.5\ 10^{-29}$	44.2
Cu(n,sp)Co56	$3.6\ 10^{-30}$	$3.1\ 10^{-30}$	14.6
Cu(n,sp)Mn52	$2.0\ 10^{-30}$	$1.1\ 10^{-30}$	43.8
Cu(n,sp)V48	$7.7\ 10^{-31}$	$5.5\ 10^{-31}$	28.7
Cu(n,sp)Sc46	$4.4\ 10^{-30}$	$3.2\ 10^{-30}$	26.4
Cu(n,sp)Sc44	$2.2\ 10^{-30}$	$3.0\ 10^{-30}$	40.8
Fe54(n,p)Mn54	$5.8\ 10^{-27}$	$2.7\ 10^{-27}$	53.7
In115(n,n')In115m	$4.7\ 10^{-27}$	$4.8\ 10^{-27}$	1.5
Ni58(n,p)Co58	$2.9\ 10^{-27}$	$3.5\ 10^{-27}$	18.8
Co59(n,α)Mn56	$5.4\ 10^{-29}$	$4.1\ 10^{-29}$	25.4
Nb93(n,2n)Nb29m	$3.5\ 10^{-28}$	$3.9\ 10^{-28}$	14.6
Zr90(n,2n)Zr89	$1.1\ 10^{-27}$	$1.1\ 10^{-27}$	3.3

Table II: Saturation activities of the reactions observed in comparison to the calculated saturation activities for the uranium target at 1100 MeV proton energy

Reaction	Saturation Activity (sec^{-1}/proton/nucleus) Measured	Calculated	% Difference
Cu(n,sp)Fe59	$3.3\ 10^{-30}$	$3.9\ 10^{-30}$	17.3
Cu(n,sp)Co58	$4.9\ 10^{-29}$	$3.9\ 10^{-29}$	20.9
Cu(n,sp)Co57	$2.9\ 10^{-29}$	$1.1\ 10^{-29}$	60.5
Cu(n,sp)Co56	$4.2\ 10^{-30}$	$2.4\ 10^{-30}$	43.2
Cu(n,sp)V48	$9.4\ 10^{-31}$	$6.2\ 10^{-31}$	34.3
Cu(n,sp)Sc46	$6.6\ 10^{-31}$	$4.0\ 10^{-31}$	39.5
Cu(n,sp)Sc44	$2.8\ 10^{-31}$	$4.2\ 10^{-31}$	48.9
Fe54(n,p)Mn54	$4.5\ 10^{-27}$	$1.7\ 10^{-27}$	62.3
In115(n,n')In115m	$2.9\ 10^{-27}$	$2.7\ 10^{-27}$	7.3
Ni58(n,p)Co58	$1.8\ 10^{-27}$	$2.2\ 10^{-27}$	21.7
Co59(n,α)Mn56	$4.2\ 10^{-29}$	$3.4\ 10^{-29}$	18.8
Nb93(n,2n)Nb29m	$2.8\ 10^{-28}$	$3.4\ 10^{-28}$	21.8
Zr90(n,2n)Zr89	$1.0\ 10^{-27}$	$1.1\ 10^{-27}$	10.0

Table III: Saturation activities of the reactions observed in comparison to the calculated saturation activities for the lead target at 1100 MeV proton energy

Summary of Afternoon Session, Tuesday, June 29, 1982

A. Carne & T. Broome

Though the session was nominally on Nuclear Data and Codes it did also contain some papers from the morning session. I believe our early change to have the Tuesday sessions in series rather than in parallel turned out to be the right one because of the overall interest that the Target Station designers have in the whole range of topics.

The Session was a broad ranging one so that it is difficult to make a general summary, and it may be easier to quickly run through the papers and try to pick out salient features.

The first report we heard was on the IPNS Radiation Effects Facility given by Bob Birtcher. The requirement of a good REF was of course high flux (> 10^{12} n/cm^2/sec E_n > 0.1 MeV), pure n beams with no charged particles or γ's (particularly because of their effect on the cryogenics), easy access, large volumes and control of flux achieved by control of the accelerator. Some of the features were described with the conclusion that a uranium target was better than tantalum giving about 50% more neutrons in total and 73% more with energies above 0.1 MeV. Flux distributions were as expected and the neutron spectrum was rather similar to that of the irradiation facility at CP-5 except for the much higher component of neutrons above 1 MeV. Overall the performance met reasonably well with the predictions of HETC/VIM. We of the RAL were encouraged by this report where we hope to achieve similar performance, but where we will be parasiting on the main target assembly.

The paper by Harold Conrad discussed the time structure of pulses from H_2O and D_2O moderators. Experiments were carried out at SIN at 590 MeV using the proton chopper. Several combinations of moderator, target and reflector were examined including slab targets of Pb, ^{238}U and W. Also examined was a heavily grooved "starlight" moderator to simulate 6 beam tube faces, which however appeared to act as a flux trap. The data displayed could be characterized by two neutron dwell times. The conclusion from the talk was to propose halving the SNQ pulse length to 250μs and doubling the peak intensity to maintain the same average proton current. The resulting shortened dwell time would increase $\hat{\phi}_{th}$ by 100%.

The third paper was a first ever report on γ calculations for spallation targets. The target was Pb, rather than Pb-Bi, 5 cm dia., 530 MeV at 1.5 μA

(σ = 2 cm, truncated at 10 cm). The various sources of γ production and transport were examined with some surprising results of spectrum softening and strong absorption in the target. The overall photon emission in the target was about 17.5 kW of which about 20%, i.e. 3.9 kW, escaped from the target to which must be added a further 0.34 kW from e^+, e^- pair production etc. In broad terms the γ escape was about 1/10 of the neutron escape.

The next two papers were presented by Detlef Filges. The first was a very comprehensive review on "Computational Methods in Beam Tube Shielding". It is clear that standard attenuation methods are inadequate to deal with complex geometries. Further the material attenuation length is a vital parameter but is poorly known. As an example the SNQ requires 17 decades of shielding, ie a material attenuation of e^{30} or 6 m of iron; however a 10% error in $\lambda_{att.}$ is equivalent to about 1 m of iron or 1 - 2 orders of magnitude in radiation dose. For SNQ the code system of HETC plus MORSE + ANISN or DOT is being used and the calculations to be done on beam holes were described. Note that ANISN and DOT deal only with neutrons and gammas so there is a need for validations to ensure that they are dominating. There is a need for high energy multigroup cross-section data particularly for the high energies of SNQ. Finally the use of importance sampling in HETC and for charged particles was proposed.

The second paper discussed high energy fission models. The Cosmotron experiments were mocked up for 540, 960, 1470 MeV, Pb and ^{238}U . At 960 MeV (the energy closest to SNQ) the thermal neutron flux ratio for U to Pb was 2. The recoil products add greatly to energy deposition when high energy fission is included. Thin target experiments of Cierjacks with 590 MeV protons on ^{238}U for several angles were compared with the RAL model (with B_o = 14). In angular distribution agreement appeared to be within about 25% and good agreement in spectra apart from $\leq$ few MeV in the evaporation part. Compared with the limited experimental data the model appeared to underestimate high energy neutron and proton production. On residual mass the RAL and Alsmiller codes were compared at 1 GeV. In the vicinity of the fission peak there was good agreement, but the RAL code predicted a wider fission product mass range. There was a second (spallation) peak and a third, intermediate peak predicted by the RAL code but not produced at all by the Alsmiller code.

Marcel Barbier discussed in a short paper neutron production in heavy ion interactions. The interest is strong for heavy ion fusion and could be also for some future neutron source. From some, as yet, rather limited data some

estimates of neutron production were presented.

The next paper by Rick Jones of CRNL was on Neutron Yields for 100 MeV protons on Pb and Li. The basis was from the original specification at the EMTF* proposal (70 mA at 200 MeV on Pb-Bi) which was one of four projects among the Canadian plans towards electronuclear breeding, the last of which was the 300 mA 1 GeV accelerator. The experiment itself used the now familiar water bath technique, but where very careful examination of experimental errors in systematics was done. From a Pb target 1½ cm long a yield of neutrons of 0.34 n/p was obtained in good agreement with the codes, but less good for Li. There was good agreement with the calculations using NMTC/MORSE.

Larry Greenwood discussed the methods of neutron and proton dosimetry at spallation sources, particularly using activation methods to characterize particle spectra both in IPNS NST & REF. He used $^{27}A\ell$ foils in the beam using the $^{27}A\ell(p,x)^{22}Na$ reaction to get long lifetime because of foil access problems. There appeared to be a discrepancy between beam toroid and the foils which gave a lower apparent beam. The LANL people reported that they had used $^{27}A\ell$ foils to give ^{7}Be, ^{22}Na and ^{24}Na and obtained agreement with toroid readings of better than 10%.

The last paper of the day was that of Harold Conrad, comparing deuterium with protons for the primary beam for a neutron source. He examined d, p on Pb and U over several energies and concludes that d would give a gain in neutron production over p at 1.1 GeV of about 30%, and 10-15% at 400 MeV. The 30% gain was equivalent to saying that an 850 MeV d linac was equivalent to a 1.1 GeV proton one, ie an accelerator of about 2/3 the length. This remark was questioned by some members of the audience but it was felt that it would be a good challenge to offer to the other 1/3 of the ICANS collaboration - the accelerator experts. Such papers (with that of M. Barbier) are good ones to end a session for they remind us that not only must we help each other on todays sources but we must also look forwared to the bigger and better ones of the future.

*ElectroMagnetic Test Facility

6th Meeting of the International
Collaboration on Advanced Neutron Sources
June 28 — July 2, 1982
Argonne National Laboratory
Argonne, Illinois U.S.A.

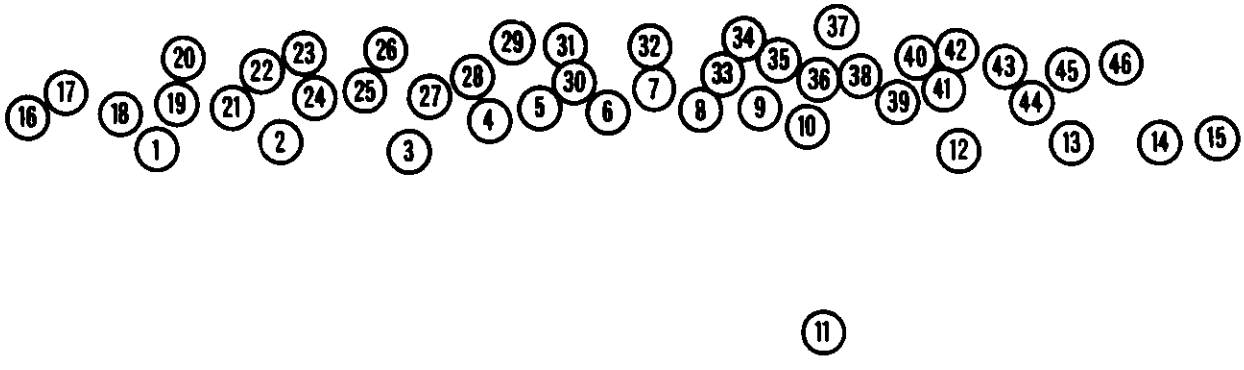

Pictured

1. Bohringer, D.
2. Filges, D.
3. Goldstone, J.
4. Taylor, A.
5. Woods, R.
6. Carpenter, J.
7. Carne, A.
8. Silver, R.
9. Crawford, R. K.
10. Bauer, G. S.
11. Watanabe, N.
12. Loewenhaupt, M.
13. Armstrong, A. W.
14. Fluharty, R. G.
15. Inoue, K.
16. Diplock, B. R.
17. Dorem, J. H.
18. Howells, W. S.
19. Stelzer, J. F.
20. Schulke, A. W.
21. Holden, T.
22. Prael, R. E.
23. Brun, T. O.
24. Hecker, R.
25. Felcher, G. P.
26. Brugger, R. M.
27. Russell, G. J.
28. Mildner, D. F. R.
29. Lander, G. H.
30. Williams, W. G.
31. Roach, P.
32. Barbier, M. M.
33. Robinson, H.
34. Broome, T. A.
35. Worlton, T. G.
36. Jones, R. T.
37. Tschalär, C.
38. Poulten, B.
39. Conrad, H. M.
40. Epperson, J. E.
41. Mizuki, J.
42. Wroe, H.
43. Mueller, M. H.
44. Kohgi, M.
45. Fischer, W. E.
46. Jorgensen, J. D.

Missing from Picture

Amian, W.
Birtcher, R. C.
Borso, C.
Brown, B. S.
Carlile, C. J.
Chidley, B. G.
Cloth, P.
Copley, J. R. D.
Eckert, J.
Faber, J., Jr.
Gray, D. A.
Greenwood, L.
Kazadi, S. M.
Kliewer, K. L.
Meese, J.
Meier, M. M.
Mezei, F.
Moon, R. M.
Ottinetti, L.
Popek, R.
Price, D. L.
Rotella, F. J.
Satija, S. K.
Schultz, A. J.
Sinha, S. K.
Smither, R.

List of Attendees
6th Meeting of the International
Collaboration on Advanced Neutron Sources
June 27 - July 2, 1982
Argonne National Laboratory
Building 362 Auditorium

	Name	Affiliation
1.	Amian, W.	KFA Jülich GmbH
2.	Armstrong, Tony	KFA Consultant
3.	Barbier, Marcel	Marcel M. Barbier, Inc.
4.	Bauer, Günter S.	Kernforschungsanlage Jülich
5.	Birtcher, R. C.	Argonne National Laboratory
6.	Bohringer, D. E.	Argonne National Laboratory
7.	Borso, C.	Argonne National Laboratory
8.	Broome, Timothy	Rutherford Appleton Laboratory
9.	Brown, Bruce S.	Argonne National Laboratory
10.	Brugger, Robert M.	Los Alamos National Laboratory
11.	Brun, T. O.	Argonne National Laboratory
12.	Carlile, C. J.	Rutherford Appleton Laboratory
13.	Carne, Alan	Rutherford Appleton Laboratory
14.	Carpenter, J. M.	Argonne National Laboratory
15.	Chidley, Bruce G.	Atomic Energy of Canada Ltd.
16.	Cloth, P.	KFA Jülich GmbH
17.	Conrad, Harald Manfred	KFA Jülich GmbH
18.	Copley, John R. D.	McMaster University
19.	Crawford, R. Kent	Argonne National Laboratory
20.	Diplock, Brian	Rutherford Appleton Laboratory
21.	Eckert, J.	Los Alamos National Laboratory
22.	Epperson, J. E.	Argonne National Laboratory
23.	Faber, J., Jr.	Argonne National Laboratory
24.	Felcher, G.	Argonne National Laboratory
25.	Filges, Detlef	KFA Jülich GmbH
26.	Fischer, Walter	Swiss Institute for Nuclear Research
27.	Fluharty, Rex G.	Universe Radiations Inc.
28.	Goldstone, Joyce A.	Los Alamos National Laboratory
29.	Gray, David A.	Rutherford Appleton Laboratory
30.	Greenwood, Lawrence R.	Argonne National Laboratory

	Name	Affiliation
31.	Hecker, Rudolf	KFA Jülich GmbH
32.	Holden, Thomas M.	Atomic Energy of Canada Ltd.
33.	Howells, William Spencer	Rutherford Appleton Laboratory
34.	Inoue, Kazuhiko	Hokkaido University
35.	Jones, Richard Thomas	Chalk River Nuclear Laboratories
36.	Jorgensen, James D.	Argonne National Laboratory
37.	Kazadi, S. M.	Argonne National Laboratory
38.	Kliewer, K. L.	Argonne National Laboratory
39.	Kohgi, Masahumi	Tohoku University
40.	Lander, Gerard H.	Argonne National Laboratory
41.	Loewenhaupt, M.	Institut fur Festkorperforschung
42.	Meese, J.	University of Missouri
43.	Meier, Michael M.	Los Alamos National Laboratory
44.	Mezei, Ferenc	Institut Laue-Langevin
45.	Mildner, D. F. R.	University of Missouri-Columbia
46.	Mizuki, Junichiro	McMaster University
47.	Moon, Ralph M.	Oak Ridge National Laboratory
48.	Mueller, M. H.	Argonne National Laboratory
49.	Norem, J. H.	Argonne National Laboratory
50.	Ottinetti, Luca	Argonne National Laboratory
51.	Popek, R.	Argonne National Laboratory
52.	Poulten, Bernard H.	Rutherford Appleton Laboratory
53.	Prael, Richard E.	Los Alamos National Laboratory
54.	Price, David L.	Argonne National Laboratory
55.	Roach, Pat	Argonne National Laboratory
56.	Robinson, Harold	Los Alamos National Laboratory
57.	Rotella, Frank J.	Argonne National Laboratory
58.	Russell, G. J.	Los Alamos National Laboratory
59.	Satija, S. K.	Brookhaven National Laboratory
60.	Schulke, A. W.	Argonne National Laboratory
61.	Schultz, A. J.	Argonne National Laboratory
62.	Silver, Richard	Los Alamos National Laboratory
63.	Sinha, S. K.	Argonne National Laboratory

	Name	Affiliation
64.	Smither, R.	Argonne National Laboratory
65.	Stelzer, Johann F.	KFA Jülich GmbH
66.	Taylor, Andrew D.	Los Alamos National Laboratory
67.	Tschalär, Christoph	Swiss Institute for Nuclear Research
68.	Watanabe, Noboru	KEK-Nat. Lab. for High Energy Physics
69.	Williams, W. Gavin	Rutherford Appleton Laboratory
70.	Woods, R.	Los Alamos National Laboratory
71.	Worlton, T. G.	Argonne National Laboratory
72.	Wroe, Harold	Rutherford Appleton Laboratory

List of Authors

List of Authors (continued)

Distribution for ANL-82-80

Internal:

E. S. Beckjord
R. C. Birtcher
D. E. Bohringer
C. Borso
B. S. Brown
T. O. Brun
J. M. Carpenter (42)
R. K. Crawford
E. Crosbie
J. E. Epperson
J. Faber
G. Felcher
B. R. T. Frost
L. R. Greenwood
J. D. Jorgensen
S. M. Kazadi
T. Khoe
M. Kirk
K. L. Kliewer (2)
R. L. Kustom
G. H. Lander
W. E. Massey
M. H. Mueller
J. H. Norem
L. Ottinetti
R. Popek
D. L. Price
P. Roach
F. J. Rotella
A. W. Schulke
A. J. Schultz
D. Shaftman
S. K. Sinha
R. Smither
T. G. Worlton
ANL Contract File
ANL Patent Dept.
ANL Libraries (3)
TIS Files (6)

External:

DOE-TIC (27)
Manager, Chicago Operations Office, DOE
W. Amian, KFA Jülich Gmbh, Jülich, Germany
T. Armstrong, LaJolla, Calif.
J. D. Axe, Brookhaven National Lab.
M. Barbier, Marcel M. Barbier, Inc., Herndon, Va.
G. S. Bauer, Kernforschungsanlage, JÜlich, Germany (3)
M. Blume, Brookhaven National Lab.
T. Broome, Rutherford Appleton Lab., Abingdon, England
W. L. Brown, Bell Labs., Murray Hill, N. J.
J. Browne, Los Alamos National Lab.
R. M. Brugger, Los Alamos National Lab.
C. J. Carlile, Rutherford Appleton Lab., Abingdon, England
A. Carne, Rutherford Appleton Lab., Abingdon, England
B. G. Chidley, Atomic Energy of Canada Ltd., Chalk River (3)
P. Cloth, KFA Jülich Gmbh, Jülich, Germany
J. B. Cohen, Northwestern U.
H. M. Conrad, KFA Jülich GmbH, Jülich, Germany
J. R. D. Copley, McMaster Univ., Hamilton, Ont., Canada
B. Diplock, Rutherford Appleton Lab., Abingdon, England
J. Eckert, Los Alamos National Lab.
P. A. Egelstaff, Univ. of Guelph, Guelph, Canada
D. M. Engelman, Yale Univ.
B. E. Fender, Institut Laue-Langevin, Grenoble, France
D. Filges, KFA JÜlich GmbH, Jülich, Germany
W. E. Fischer, Swiss Institute for Nuclear Research, Villigen, Switzerland (3)
R. G. Fluharty, Universe Radiations Inc., Los Alamos
J. A. Goldstone, Los Alamos National Lab.
D. A. Gray, Rutherford Appleton Lab., Abingdon, England
R. L. Harlow, E. I. duPont de Nemours & Co., Inc., Wilmington, Del.
R. Hecker, KFA JÜlich GmbH, Jülich, Germany
T. M. Holden, Atomic Energy of Canada Ltd., Chalk River
W. S. Howells, Rutherford Appleton Lab., Abingdon, England
K. Inoue, Hokkaido Univ., Sapporo, Japan
Y. Ishikawa, Tohoku Univ., Sendai, Japan (3)

G. A. Jeffrey, Univ. of Pittsburgh
R. T. Jones, Chalk River Nuclear Laboratories, Canada
M. Kohgi, Tohoku Univ., Sendai, Japan
B. Larson, Oak Ridge National Lab.
M. Loewenhaupt, Institut für Festkorperforschung, Jülich, Germany
J. P. McTague, Brookhaven National Lab.
J. Meese, Univ. of Missouri
M. M. Meier, Los Alamos National Lab.
F. Mezei, Institut Laue-Langevin, Grenoble, France
D. F. R. Mildner, Univ. of Missouri-Columbia
J. Mizuki, McMaster Univ., Hamilton, Canada
R. M. Moon, Oak Ridge National Lab.
R. Peele, Oak Ridge National Lab.
B. H. Poulten, Rutherford Appleton Lab., Abingdon, England
R. E. Prael, Los Alamos National Lab.
H. Robinson, Los Alamos National Lab.
J. M. Rowe, National Bureau of Standards
G. J. Russell, Los Alamos National Lab. (3)
H. Sasaki, KEK-National Lab. for High Energy Physics, Ibaraki-ken, Japan (3)
S. K. Satija, Brookhaven National Lab.
R. Silver, Los Alamos National Lab.
J. F. Stelzer, KFA Jülich GmbH, Jülich, Germany
G. C. Stirling, Rutherford Appleton Lab., Abingdon, England (3)
A. D. Taylor, Los Alamos National Lab.
I. M. Thorson, Simon Fraser Univ., Burnaby, Canada (3)
C. Tschalär, Swiss Inst. for Nuclear Research, Villigen, Switzerland
P. J. Vergamini, Los Alamos National Lab.
J. E. Vetter, KFK-Karlsruhe GmbH, Germany (3)
N. Watanabe, KEK-National Lab. for High Energy Physics, Ibaraki-ken, Japan
M. Wilkinson, Oak Ridge National Lab.
W. G. Williams, Rutherford Appleton Lab., Abingdon, England
R. Woods, Los Alamos National Lab.
H. Wroe, Rutherford Appleton Lab., Abingdon, England